The volcanic and magmatic evolution of Tongariro volcano, New Zealand

Leo Robert Pure

A thesis submitted to the Victoria University of Wellington in partial fulfilment of the requirements for the degree of Doctor of Philosophy in Geology

Victoria University of Wellington
School of Geography, Environment and Earth Sciences

Wellington, New Zealand
December 2019

Abstract

Detailed mapping studies of Quaternary stratovolcanoes provide critical frameworks for examining the long-term evolution of magmatic systems and volcanic behaviour. For stratovolcanoes that have experienced glaciation, edifice-forming products also act as climate-proxies from which ice thicknesses can be inferred at specific points in time. One such volcano is Tongariro, which is located in the southern Taupō Volcanic Zone of New Zealand's North Island. This study presents the results of new detailed mapping, geochronological and geochemical investigations on edifice-forming materials to reconstruct Tongariro's volcanic and magmatic history which address the following questions:

(1) Does ice coverage on stratovolcanoes influence eruptive rates and behaviour (or record completeness)?
(2) What is the relationship between magmatism, its expression (i.e. volcanism) and external but related processes such as tectonics?
(3) How are intermediate composition magmas assembled and what controls their diversity?
(4) What are the relative proportions of mantle-derived and crust-derived materials in intermediate composition arc magmas?
(5) Do genetic relationships exist between andesite and rhyolite magmas in arc settings?

Samples from 250 new field localities in under-examined areas of Tongariro were analysed for major oxide, trace element and Sr-Nd-Pb isotope compositions. Analyses were performed on whole-rock, groundmass and xenolith samples. The stratigraphic framework for these geochemical data was established from field observations and 29 new $^{40}Ar/^{39}Ar$ age determinations, which were synthesised with volume estimates and petrographic observations for all Tongariro map units. Mapping results divide Tongariro into 36 distinct map units (at their greatest level of subdivision) which were organised into formations and constituent members.

New $^{40}Ar/^{39}Ar$ age determinations reveal continuous eruptive activity at Tongariro from at least 230 ka to present, including during glacial periods. This adds to the discovery of an inlier of old basaltic-andesite (512 ± 59 ka) on Tongariro's NW sector that has an unclear source vent. Hornblende-phyric andesite boulders, mapped into the Tupuna Formation (new), yield the oldest $^{40}Ar/^{39}Ar$ age determination (304 ± 11 ka) for materials confidently attributed to Tongariro. Tupuna Formation andesites are correlated with Turakina Formation debris flows that were deposited between 349 to 309 ka in the Wanganui Basin, ~100 km south of Tongariro, which indicates that Ruapehu did not exist at this time, at least not in its current form.

Tongariro has a total edifice volume of ~90 km^3, 19 km^3 of which is represented by exposed mapped units. The total ringplain volume immediately adjacent to Tongariro contains

~60 km^3 of material. The volume of exposed glacial deposits are no more than 1 km^3. During periods of major ice coverage, edifice-building rates on Tongariro were only 17-21 % of edifice-building rates during warmer climatic periods. Because shifts in edifice-building rates do not coincide with changes in erupted compositions, differences in edifice-building rates reflect a preservation bias. Materials erupted during glacial periods were emplaced onto ice masses and conveyed to the ringplain as debris, which explains reduced preservation rates at these times.

MgO concentrations in Tongariro stratigraphic units with ages between 230 and 0 ka display successive and irregular cyclicity that occurs over ~10-70 kyr intervals, which reflect episodes of enhanced mafic magma replenishment. During these cycles, more rapid (≤10 kyr) increases in MgO concentrations to ≥5-9 wt% are followed by gradual declines to ~2-5 wt%, with maxima at ~230, ~160, ~117, ~88, ~56, ~35, ~17.5 ka and during the Holocene.

Contemporaneous variations in Tongariro and Ruapehu magma compositions (e.g. MgO, Rb/Sr, Sr-Nd-Pb isotope ratios) for the 200-0 ka period coincide with reported zircon growth model-ages in Taupō magmas. This contemporaneity reflects regional tectonic processes that have externally regulated and synchronised the timings of elevated mafic replenishment episodes versus periods of prolonged crustal residence at each of these volcanoes.

Isotopic Sr-Nd-Pb data from metasedimentary xenoliths, groundmass separates and whole-rock samples indicate that two or three separate metasedimentary terranes (in the upper 15 km of the crust) were assimilated into Tongariro magmas. These are the Kaweka terrane and the Waipapa or Pahau terranes (or both). Subhorizontal juxtapositioning of these terranes is indicated by the coexistence of multiple terranes in the same eruptive units.

Paired whole-rock and groundmass (interstitial melt) samples have effectively equal Sr-Nd-Pb isotope ratios for the complete range of Tongariro compositions. Despite intra-crystal isotopic heterogeneities that are likely widespread, the new data show that crystal fractionation and assimilation occur in approximately equal balance for essentially all Tongariro eruptives.

Assimilated country rock accounts for 22-31 wt% of the average Tongariro magma. Initial evolution from a Kakuki basalt-type to a Tongariro Te Rongo Member basaltic-andesite reflects the addition of 17 % assimilated metasedimentary basement with a mass assimilation rate/mass crystal fractionation rate ratio—a.k.a. 'r-value' of 1.8-3.5. Subsequent evolution from a Te Rongo Member basaltic-andesite to other Tongariro eruptive compositions represents 5-14 % more assimilated crust (r-values of ~0.1-1.0). Magma evolution from high (>1) to lower (0.1-1.0) r-values can explain the dearth of andesitic melt inclusions in (bulk) andesite magmas observed globally. High relative assimilation rates characterise rapid evolution from basalt to basaltic-andesite bulk compositions which contain andesitic interstitial melts. Thus, andesitic melt

inclusions have a reduced chance of being preserved in crystals which can explain their low representation in global datasets.

Acknowledgements

The mapping component of this thesis was encompassed within a larger mapping project of the entire Tongariro National Park led by GNS Science. The Ngati Tūwharetoa people are thanked for the privilege to collect materials from Tongariro for scientific examination. Funding awarded by the Earthquake Commission (grant 16/U735) supported extensive geochemical analytical work which complemented the mapping work. My study was supported by a Victoria Doctoral Scholarship and subsequent support was provided by the Ministry of Business, Innovation and Employment via Colin Wilson and the ECLIPSE program. Opportunities to travel for conferences, field trips and a collaborative research exchange were supported by Victoria University of Wellington (VUW) Faculty of Graduate Research and the S. T. Lee Student Fellowship to the University of Alaska, Fairbanks, awarded by the Antarctic Research Council at VUW. In no particular order, the following people are recognised and thanked for their role in the success of this thesis.

To Colin Wilson, your enthusiasm from the word "go" was obvious from your initial three-page email reply and our two-hour phone call where you spoke for two hours. Your no-nonsense approach to supporting students and your professionalism is a model for everyone. I've learned loads from your critical thinking and your 'no half measures' approach to science has shown me the value of integrity and working for the longer-term payoff. You deserve all the good things that come your way.

To Bruce Charlier, thank you for your warmth and friendship, and for showing me what it takes to be a real geochemist. I was happy to be a guinea pig getting the lab back on its feet, and I look back fondly on the many laughs we've had along the way. Sick!

To Dougal Townsend, your attentiveness and endless patience cannot be overstated. I consider myself incredibly fortunate to have worked with you. You have made me a better geologist and are a reminder to everyone that cultivating young scientists can always be done constructively and with warmth – thank you.

To John Gamble, thank you for the encouragement, insights and generosity at every step of the way. Your 70th was the best house party I've been to in New Zealand and all the little things you did helped me to feel at home despite being overseas. Here's to the Sunday afternoon car repairs, smoked fish and surprise drams – sláinte!

To Graham Leonard, you are a logistical lifeline. Thanks for making everything happen, for taking care of me in the field and in San Francisco, and for replacing my sledgehammer after I decapitated the first one – long live Raskolnikov! The beers, positivity and encouragement have helped me stay above the water.

To Luisa Ashworth, Julie Vry and Ian Schipper, thank you for your technical guidance in the geochemical, microscopy and electron microprobe laboratories.

To my field companions, Rosie Cole, Stan Mordensky and Andrew Galloway, thank you for keeping my spirits up and keeping me out of my own head. To Andrew, we covered a lot of hard country (1500 km by my estimates) and went to some places I would never have gone to by myself. The creeks, spiders and vegetables were as infinite as they were beautiful.

To all people, past and present, who have overlapped with me at VUW, thank you for the community and laughs we've shared in our rickety wail-sail that is the Cotton Building. By name: my big-bird bro/sensei Chris 'Condor' Conway, Elliot Swallow, Jürgen Österle, Marcel Mizera, Céline Mandon, Jamey Stutz, Katelyn Johnson, Kostas Michailos, Valerie van der Bos, Will Gonzalez, Ben Hines, Tom Womack, Nick Hitt, Kate Mauriohooho, Hannah Elms, Andrea Davies, Finn Illsley-Kemp and Simon Barker.

To Will Critchlow, Jake Church and Jonno Mandeno at 26 Raroa, thanks for the good times and grounding me to the real world with laughter and sometimes too many homebrews. Our culinary adventures have shown me that there is no thing as too much spice or too much butter. I feel incredibly lucky to have shared such a formative part of my life with such colourful young men. The endless Borat jokes will be sorely missed.

To mum and dad, thank you for the letting me find myself in my own time. Your love and support have had a tremendous influence on my wellbeing and the quality of my work – thank you.

To my brother, Ross, thank you for checking up on me in Wellington. You have a heart of gold. Despite the appalling weather, you've kept coming back. It'll be great to have you here when this thing is printed and done.

To my best friend, Tharika Liyanage, thank you for sharing this ride with me. You are my star. It's not possible to articulate in words how much I think of you. Your love and support are bottomless, and it is only in this respect that I can match you. I'm so excited for what the future holds for us.

Table of contents

CHAPTER 1 – Introduction 1
1.1. Significance of stratovolcanoes 3
1.1.1. Scientific importance 3
1.1.2. Historical background 3
1.2. Outstanding questions in the study of stratovolcanoes and intermediate composition arc magmas 4
1.2.1. Stratovolcano geomorphology 4
1.2.2. Magmatism, volcanism and tectonics 6
1.2.3. Compositional diversity of intermediate composition arc magmas 6
1.2.4. Crustal versus mantle inputs into magmas 7
1.2.5. Relationships between arc andesite and rhyolite magmas 8
1.3. Structure of thesis 8
1.4. Background 10
1.4.1. Geological setting of the southern Taupō Volcanic Zone (TVZ) 10
1.4.2. Tongariro within the southern TVZ 13
1.4.3. Previous edifice studies of Tongariro 14
1.4.4. Broader context of this project 17

CHAPTER 2 – Methodologies 19
2.1. Field geology 21
2.1.1. Sample collection 21
2.1.2. Mapping process and coordinates 21
2.2. Rock crushing and powdering 24
2.3. $^{40}Ar/^{39}Ar$ geochronology 24
2.4. X-ray fluorescence (XRF) 26
2.5. Electron probe microanalysis (EPMA) 27
2.6. Beaker and plasticware cleaning 28
2.7. Reagents for wet chemistry 28
2.8. Sample digestions for isotopic and trace element analysis 29
2.9. Solution inductively coupled plasma mass spectrometry (ICP-MS) 29
2.9.1. Solution ICP-MS analytical protocols 29
2.9.2. Dilution factors and batches 31
2.9.3. Solution ICP-MS uncertainties 31
2.10. Thermal ionisation mass spectrometry (TIMS) 34
2.10.1. Purification and column separation procedures for isotopic analysis 34
2.10.1.1. Strontium (Sr) 34
2.10.1.2. Neodymium (Nd) 36
2.10.1.3. Lead (Pb) 39
2.10.1.4. Matrix-rich samples 41
2.10.2. Filament loading procedures 42
2.10.3. TIMS instrumental operating conditions 43
2.10.4. Blanks for Sr-Nd-Pb isotope analyses 44
2.10.5. TIMS uncertainties 46
2.10.6. Normalisation to reference standards 46
2.10.6.1. Sr-Nd-Pb data from this study 46
2.10.6.2. Sr isotope data from other studies 47
2.10.6.3. Nd isotope data from other studies 48
2.10.6.4. Pb isotope data from other studies 48

CHAPTER 3 – A high resolution $^{40}Ar/^{39}Ar$ edifice construction history of lavas and pyroclastic deposits on Tongariro volcano, New Zealand 51
3.1. Introduction 53
3.1.1. Previous work 55
3.1.2. Geological setting 55
3.2. Methods 59
3.2.1. Field studies and sampling 59
3.2.2. Whole-rock geochemistry 59
3.2.3. $^{40}Ar/^{40}Ar$ geochronology 59
3.2.4. Volume estimates of exposed stratigraphic units 60
3.3. Eruptive stratigraphy 61
3.3.1. Introduction 61
3.3.2. Systematic descriptions of stratigraphic units 71
3.3.2.1. Otamatereinga Formation (between 571 and 453 ka) – OT 71
3.3.2.2. Tupuna Formation (between 349 and 293 ka) – TU 72
3.3.2.3. Haumata Formation (between 290 and 189 ka) – HA 73
3.3.2.3.1. Lower Tama Member (between 290 and 242 ka) – alt 73
3.3.2.3.2. Tutangatahiro Member (between 229 and 220 ka) – mtu 74
3.3.2.3.3. Tawhairauiki Member (between 220 and 214 ka) – atw 74
3.3.2.3.4. Upper Tama Member (between 214 and 207 ka) – aut 74
3.3.2.3.5. Toatoa Member (between 207 and 200 ka) – ato 78
3.3.2.3.6. Pukekaikiore Member (between 200 and 190 ka) – apk 78
3.3.2.3.7. Waipoa Member (between 195 and 189 ka) – awp 79
3.3.2.3.8. Undifferentiated Haumata Formation products – uha 80
3.3.2.4. Mangahouhounui Formation (189 and 130 ka) – MH 80
3.3.2.4.1. Te Pakiraki Member (between 189 and 130 ka) – dpk 80
3.3.2.4.2. Waiaruhairiki Member (between 152 and 150 ka) – awh 81
3.3.2.4.3. Tātaramoa Member (between 189 and 130 ka) – mtm 83
3.3.2.4.4. Undifferentiated Mangahouhounui Formation products – umh 83
3.3.2.5. Taiko Formation (between 133 and 52 ka) – TA 83
3.3.2.5.1. Rahuituki Member (between 129 and 119 ka) – arh 84
3.3.2.5.2. Pungarara Member (between 130 and 102 ka) – apg 85
3.3.2.5.3. Mangahouhouiti Member (between 130 and 96 ka) – mhi 85
3.3.2.5.4. Mangatepopo Member (between 133 and 102 ka) – amp 86
3.3.2.5.5. Te Porere Member (between 102 and 96 ka) – dtp 86
3.3.2.5.6. Otamangakau Member (between 96 and 92 ka) – aok 87
3.3.2.5.7. Waitakatorua Member (between 96 and 79 ka) – awu 87
3.3.2.5.8. Te Rurunga Member (between 92 and 84 ka) – atr 87
3.3.2.5.9. Te Wakarikiariki Member (between 86 and 79 ka) – ati 87
3.3.2.5.10. Rotopaunga Member (between 79 and 61 ka) – arp 88
3.3.2.5.11. Te Tatau Member (between 61 and 52 ka) – att 88
3.3.2.6. Undifferentiated Otukou lava (between 91 and 79 ka) – uol 89
3.3.2.7. Te Whaiau Formation (between 50 and 45 ka) – TW 89
3.3.2.8. Pukeonake Formation (between 40 and 30 ka) – PN 91
3.3.2.9. Mokomoko Formation (between 45 and 23 ka) MK 92
3.3.2.9.1. Rangitaupahi Member (between 45 and 36 ka) – ari 92
3.3.2.9.2. Mangatapate Member (between 36 and 24 ka) – amt 93
3.3.2.9.3. Te Wai Whakaata Member (between 33 and 23 ka) – aww 93
3.3.2.10. Te Maari Formation (before 25.4 ka to present) – TM 94
3.3.2.11. Makahikatoa Formation (~17.5 ka) – MK 94
3.3.2.12. Red Crater Formation (between 11.0 and 0.1 ka) – RC 96

3.3.2.13. Te Pupu Formation (between 7? ka and 1975 CE) – TP..... 96
3.4. Volumes..... 97
3.4.1. Volumes of formations and members..... 97
3.4.2. Total edifice volume of Tongariro..... 99
3.4.3. Ring plain volume..... 99
3.5. Discussion..... 100
3.5.1. Review of geochronological data..... 100
3.5.2. Evolution of the Tongariro edifice..... 102
3.5.3. Glacial history of Tongariro volcano..... 109
3.5.4. Volume-time reconstructions..... 114
3.5.5. Explosive versus effusive volcanism comparison on Tongariro..... 119
3.5.6. Ruapehu versus Tongariro growth history comparison..... 119
3.5.7. New geochronological results for Pihanga and Ruapehu eruptives..... 122
3.6. Conclusions..... 123

CHAPTER 4 – The geochemistry and petrogenesis of basaltic-andesite to dacite magmas at Tongariro volcano, New Zealand 127
4.1. Introduction..... 129
4.1.1. Previous work..... 129
4.1.2. Basement geology of the southern TVZ..... 131
4.2. Analytical methods..... 131
4.3. Results..... 132
4.3.1. Whole-rock samples..... 133
4.3.1.1. Petrography..... 133
4.3.1.2. Major oxides..... 133
4.3.1.3. Trace elements..... 135
4.3.1.4. Sr-Nd-Pb isotopes..... 141
4.3.2. Xenolithic materials..... 143
4.3.2.1. Petrography..... 143
4.3.2.2. Major oxides..... 149
4.3.2.3. Trace elements..... 152
4.3.2.4. Sr-Nd-Pb isotopes..... 160
4.3.2.5. Unusual xenolith samples..... 163
4.3.3. Groundmass separates from Tongariro lavas..... 164
4.3.3.1. Petrography..... 164
4.3.3.2. Major oxides..... 164
4.3.3.3. Trace elements..... 166
4.3.3.4. Sr-Nd-Pb isotopes..... 167
4.4. Discussion..... 171
4.4.1. Crystallisation, differentiation and fractionation..... 171
4.4.2. Crustal lithologies..... 173
4.4.2.1. Metasedimentary basement..... 173
4.4.2.1.1. Relationships between isotope ratios in xenoliths versus protoliths..... 174
4.4.2.1.1.1. Strontium..... 174
4.4.2.1.1.2. Neodymium..... 175
4.4.2.1.1.3. Lead..... 176
4.4.2.1.2. Interpretation of metasedimentary basement terranes(s) 178
4.4.2.2. Crustal structure beneath Tongariro..... 179
4.4.2.3. A metasedimentary basement composition for modelling..... 184
4.4.3. Fractional crystallisation and assimilation..... 184
4.4.3.1. Assimilation: bulk or partial protolith incorporation? 185

4.4.3.2. A two-stage scenario for estimating crustal inputs into Tongariro magmas 186
4.4.3.3. AFC and mixing model parameters 190
4.4.3.4. AFC and mixing model results 192
4.4.4. Magma assembly processes at Tongariro 193
4.5. Conclusions 196

CHAPTER 5 – An integrated time-space-composition evolution of edifice-forming eruptives at Tongariro volcano, New Zealand 199
5.1. Introduction 201
5.2. Methods and datasets 201
5.3. Results 202
5.3.1. Petrography versus time 203
5.3.2. Major oxides versus time 203
5.3.3. Trace elements versus time 206
5.3.4. Sr-Nd-Pb isotopes versus time 210
5.4. Discussion 210
5.4.1. Summary of time-composition relationships 210
5.4.2. Composition-volume relationships 216
5.4.3. Tongariro versus Ruapehu time-composition relationships 218
5.4.4. The petrogenesis of early Tongariro and Ruapehu magmas 221
5.4.4.1. Tongariro: Tupuna Formation (between 349 and 293 ka) 221
5.4.4.2. Ruapehu: Te Herenga Formation (between 200 and 150 ka) 223
5.4.4.3. Classification scheme for basement rocks 227
5.4.5. Links between regional andesitic and rhyolitic activity in the TVZ 228
5.4.6. Implications for popular petrogenetic models 234
5.5. Conclusions 237

CHAPTER 6 – Synthesis and conclusions 241
6.1. Introduction 243
6.2. Outstanding questions 243
6.2.1. Stratovolcano geomorphology 243
6.2.2. Magmatism, volcanism and tectonics 246
6.2.3. Compositional diversity of intermediate composition arc magmas 249
6.2.4. Crustal versus mantle inputs into magmas 252
6.2.5. Relationships between arc andesite and rhyolite magmas 253
6.3. Other results and conclusions 257
6.3.1. Results and conclusions for the southern TVZ area 257
6.3.2. Analytical and methodological findings 258
6.4. Suggestions for future studies 259

REFERENCES 263

APPENDICES
A1. $^{40}Ar/^{39}Ar$ step heating age analysis data 283
A2. Features used to define and discriminate formations and members on Tongariro 305
A3. Revised and new formations and members for the Te Hoata Group (Tongariro volcano) 329
A4. Sample list and analytical batch numbers 347
A5. Whole-rock major oxide, trace element and Sr-Nd-Pb isotopic compositions 357
A6. Groundmass major element, trace element and Sr-Nd-Pb isotopic compositions 389

A7. Xenolith major oxide, trace element and Sr-Nd-Pb isotopic compositions..... 399
A8. Electron probe microanalysis (EPMA) data..... 405

LIST OF FIGURES

Fig. 1.1. Map of intermediate composition volcanoes in the southern TVZ..... 12
Fig. 1.2. Tongariro volcano and its landforms and vent foci..... 15
Fig. 1.3. Previous and new sample localities of edifice-forming eruptives on Tongariro..... 16
Fig. 2.1. Example of the 'sombrero' method for spatially plotting compositional data..... 23
Fig. 2.2. Summary cartoon of column separation procedures for Sr, Nd and Pb..... 35
Fig. 2.3. LN-spec column calibration profile for ^{139}La, ^{140}Ce, ^{141}Pr, ^{146}Nd and ^{147}Sm..... 38
Fig. 3.1. Map of intermediate composition volcanoes in the southern TVZ (duplicate of Fig. 1.1) 57
Fig. 3.2. Tongariro volcano and its landforms and vent foci (duplicate of Fig. 1.2)..... 58
Fig. 3.3. Space-time relationships of map units (pseudo-stratigraphic column)..... 63
Fig. 3.4. Distribution of Tongariro eruptives from ~0.5 Ma to 189 ka..... 72
Fig. 3.5. View of northwestern Tongariro from an aerial photograph, overlain with map unit annotations, looking SE 79
Fig. 3.6. Lava-ice interaction features on Tongariro..... 82
Fig. 3.7. Distribution of Taiko Formation and other eruptives between 133 to 52 ka..... 84
Fig. 3.8. Distribution of the Pukeonake, Mokomoko and Te Whaiau formations..... 90
Fig. 3.9. Distribution of the Makahikatoa, Te Maari, Red Crater and Te Pupu formations..... 95
Fig. 3.10. Comparisons between K/Ar and ^{40}Ar/^{39}Ar age determinations for the same map units..... 101
Fig. 3.11. REE concentration diagram for the Tupuna, Turakina and Te Herenga formations..... 103
Fig. 3.12. Vent age comparison against vent lifespan at Tongariro..... 106
Fig. 3.13. Moraines and sedimentary deposits on Tongariro and its ring plain..... 110
Fig. 3.14. Time-series of cumulative preserved volumes of map units, a global δ^{18}O climate proxy record and erupted compositions at Tongariro..... 117
Fig. 4.1. Major oxides versus SiO_2 for Tongariro whole-rock samples..... 134
Fig. 4.2. Trace elements in Tongariro whole-rock samples..... 137
Fig. 4.3. REE concentration diagram for Tongariro whole-rock samples..... 140
Fig. 4.4. Sr-Nd-Pb isotope ratios diagrams for Tongariro whole-rock samples..... 142
Fig. 4.5. Flatbed scanner images of thin sections containing metasedimentary xenoliths..... 144
Fig. 4.6. Petrographic features of metasedimentary xenoliths..... 145
Fig. 4.7. Major oxide variation diagrams for metasedimentary xenoliths from Tongariro... 151
Fig. 4.8. Trace element variations for Rb, Sr, Ba, Cs, Ca, Na in metasedimentary xenoliths from Tongariro..... 153
Fig. 4.9. REE concentration diagram for metasedimentary xenoliths and LP168X from Tongariro..... 154
Fig. 4.10. Trace element variations for Sm, Nd, Eu/Eu* and P in metasedimentary xenoliths from Tongariro..... 155
Fig. 4.11. Trace element variations for U, Pb, Th, Zr and Hf in metasedimentary xenoliths from Tongariro..... 157
Fig. 4.12. Sr-Nd-Pb isotope ratios in Tongariro metasedimentary xenoliths and LP168X.. 162
Fig. 4.13. Major oxide variation diagrams for Tongariro lava groundmass separates..... 165
Fig. 4.14. REE concentration diagram for Tongariro lava groundmass separates..... 167
Fig. 4.15. Sr-Nd-Pb isotope ratios in paired Tongariro whole-rock and groundmass samples..... 169

Fig. 4.16. Sr-Nd-Pb isotope ratio comparison between Tongariro lava groundmass..... 170
separates, whole-rock samples, metasedimentary xenoliths, LP168X, regional basalts and greywacke reference samples
Fig. 4.17. Pb isotope ratios versus Th/U ratios in Tongariro metasedimentary xenoliths... 178
Fig. 4.18. Suggested crustal structure beneath Tongariro..... 180
Fig. 4.19. AFC and mixing modelling results for Tongariro samples (stage 2)..... 191
Fig. 5.1. Total crystal concentrations versus time for Tongariro eruptives..... 203
Fig. 5.2. Major oxide concentrations versus time for Tongariro eruptives..... 205
Fig. 5.3. Trace element concentrations versus time for Tongariro eruptives..... 207
Fig. 5.4. Sr-Nd-Pb isotope ratios versus time for Tongariro eruptives..... 209
Fig. 5.5. Interpreted composition versus time relationships for Tongariro eruptives..... 211
Fig. 5.6. Time-composition comparison for Tongariro and Ruapehu, and zircon model... 220
ages from Taupō
Fig. 5.7. Sr-Nd isotope plot for Ruapehu Te Herenga Formation versus other southern... 224
TVZ eruptives, regional basalts and xenolith samples
Fig. 5.8. REE concentration diagram for unusual xenoliths, Ruapehu Te Herenga..... 226
Formation eruptives and regional basalts
Fig. 5.9. Schematic NNE cross-section along the TVZ arc from Ruapehu to Taupō..... 230
Fig. 6.1. Time-series of cumulative preserved volumes of map units, a global $\delta^{18}O$..... 245
climate proxy record and erupted compositions at Tongariro (duplicate of Fig. 3.14)
Fig. 6.2. Time-composition comparison for Tongariro and Ruapehu, and zircon model.... 248
ages from Taupō (reproduced from Fig. 5.6)
Fig. 6.3. Sr-Nd-Pb isotope ratios in paired Tongariro whole-rock and groundmass..... 251
samples (reproduced from Fig. 4.15)
Fig. 6.4. Comparison of SiO_2 in paired whole-rock, interstitial melts and melt inclusion.... 255
samples for Tongariro and global data
Fig. A1. $^{40}Ar/^{39}Ar$ step heating age analysis data for Tongariro and southern TVZ..... 287
eruptives
Fig. A8.1. LP007 opx3 analysis locations..... 410
Fig. A8.2. LP011 opx1 analysis locations..... 410
Fig. A8.3. LP011 opx2 analysis locations..... 411
Fig. A8.4. LP032 glass analyses within MS1 for locations 1-3..... 411
Fig. A8.5. LP032 glass analyses within MS1 for locations 4-13..... 412
Fig. A8.6. LP058 CC1 analysis locations..... 412
Fig. A8.7. LP064 MS1 analysis locations..... 413
Fig. A8.8. LP064 MS1 analysis locations..... 413
Fig. A8.9. LP064 MS1 analysis locations..... 414
Fig. A8.10. LP096 ol1 analysis locations..... 414
Fig. A8.11. LP096 ol1 analysis locations..... 415
Fig. A8.12. LP096 ol1 analysis locations..... 415
Fig. A8.13. LP140 opx1 analysis locations..... 416
Fig. A8.14. LP140 opx2 analysis locations..... 416

LIST OF TABLES

Table 2.1. EPMA instrumental operating conditions for silicate glass analyses..... 27
Table 2.2. Chronological summary of beaker cleaning process..... 28
Table 2.3. Instrumental operating conditions for solution ICP-MS analyses..... 30
Table 2.4. External reproducibility of trace element analyses by ICP-MS on standards..... 33
Table 2.5. Results from Pb leaching experiments on sample powder to quantify loss..... 40
Table 2.6. Sr-Nd-Pb isotope ratio blank amounts for all TIMS analyses..... 45

Table 2.7. External reproducibility of isotope analyses on NBS987 (Sr), JNdi-1 (Nd)..... 47
and NBS981 (Pb)
Table 3.1. Summary of new $^{40}Ar/^{39}Ar$ age determinations on Tongariro lavas..... 64
Table 3.2. Summary of age determinations and mapping discriminants for Tongariro..... 65
stratigraphic units
Table 3.3. Summary of petrological and lithological features for Tongariro stratigraphic... 69
units
Table 3.4. Representative major oxide, Sr and Ba concentrations for Tongariro..... 75
stratigraphic units
Table 3.5. Areas, thicknesses and volumes of exposed edifice-forming materials on..... 98
Tongariro
Table 3.6. Comparison of features and histories of Tongariro and Ruapehu volcanoes..... 121
Table 4.1. Interpreted crystal fractionation order relative to major oxide concentrations... 136
in Tongariro eruptives
Table 4.2. Petrographic summary for xenoliths analysed geochemical and LP234X..... 148
Table 4.3. Major oxide concentrations in metasedimentary xenoliths and LP168X..... 150
Table 4.4. Trace element data for metasedimentary xenoliths and LP168X..... 158
Table 4.5. Radiogenic Sr-Nd-Pb isotope ratios for metasedimentary xenoliths and..... 161
LP168X
Table 4.6. Geochemical data for AFC and mixing model calculations..... 188
Table 5.1. Regression equations for linear segments in MgO, Rb/Sr. $^{143}Nd/^{144}Nd$ and..... 213
$^{206}Pb/^{204}Pb$ time-composition arrays from Figs. 5.6 and 5.6
Table A1. Summary of new $^{40}Ar/^{39}Ar$ age determinations on Tongariro lavas (duplicate... 286
of Table 3.1)
Table A4. List of samples, coordinates, stratigraphic units and analytical batch numbers... 349
Table A5. Whole-rock major oxide, trace element and Sr-Nd-Pb isotope compositions.... 359
Table A6. Groundmass major oxide, trace element and Sr-Nd-Pb isotope compositions.. 391
Table A7. Xenolith major oxide, trace element and Sr-Nd-Pb isotope compositions..... 401
Table A8.1. EPMA analysis and external reproducibility summary for VG-A99..... 406
Table A8.2. EPMA analysis and external reproducibility summary for VG-568..... 407
Table A8.3. EPMA analyses of non-homogenised silicate melt inclusions..... 408

Chapter 1

Introduction

"Models tell you what you know, I'm interested in what we don't know"

C. J. N. Wilson (c. 2017)

1.1. The significance of stratovolcanoes

1.1.1. Scientific significance

The most archetypical surficial expressions of arc magmatism are large (tens to hundreds of km^3) edifices of composite stratovolcanoes that are generally andesitic in composition (Gill, 1981; Sigurdsson et al., 2015). Reviews of andesite magmas and their petrogenesis have demonstrated an intimate relationship with proximity to convergent plate boundaries (Gill, 1981) and it is perhaps unsurprising that the average composition of the continental crust is approximated by andesites and dacites (Rudnick and Gao, 2003). Stratovolcanoes pose considerable societal risk because their violent, often unpredictable eruptions can cause loss of life, damage infrastructure, disrupt land and air traffic, damage electrical connectivity, contaminate water supplies and destabilise economies. In contrast, stratovolcanoes are also associated with hydrothermal systems that can be harnessed as geothermal energy sources and are intimately related with globally significant mineral deposits. Managing the risks posed by stratovolcanoes, and understanding geothermal and mineralisation processes, therefore requires an accurate understanding of how arc magmas are assembled and erupted. One avenue for studying these processes is to examine the long-term records of lavas and pyroclastic rocks that comprise edifice-forming materials and which essentially preserve a sequential record of how magma compositions (and erupted volumes) have varied over stratovolcano lifecycles. Where these studies have been undertaken around the world, they provide case examples that improve local hazard preparedness and contribute to comparisons and contrasts of how volcanism and magmatism are expressed globally. Relatively few high-resolution chronostratigraphic records of stratovolcanoes exist globally (e.g. Dungan et al., 2001; Gamble et al., 2003; Fierstein et al. 2011; Conway et al., 2016; Calvert et al., 2018), and to address this, this study contributes a new case example from Tongariro volcano in New Zealand.

1.1.2. Historical background

Tongariro National Park (TNP) was the first national park established in New Zealand, and one of the oldest in the world. In 1887, the Ngati Tūwharetoa people entered a partnership with the Crown to ensure that the area that would later become TNP would remain protected (DOC, 2019). The TNP was later inscribed as an UNESCO World Heritage Site in 1990 for its outstanding natural values and then in 1993 recognising its cultural significance to tangata whenua. At present, TNP is administered and managed by the Department of Conservation (DOC) and receives hundreds of thousands of visitors annually.

This study was carried out in collaboration with the Ngati Tūwharetoa people who have a strong partnership with DOC regarding the management of the TNP and also with the other iwi (tribes) at the southern end of the park. The other organisations involved with this study were DOC, Victoria University of Wellington and GNS Science, with funding provided by Victoria University, the Earthquake Commission and the Ministry of Business, Innovation and Employment. The privilege to access Tongariro volcano and collect materials for study follows strong rapport that has been built and maintained with the Ngati Tūwharetoa people over previous decades.

Consultations with T. 'Bubs' Smith from Ngati Tūwharetoa (pers. comm., 2019) greatly improved the cultural significance of the geological mapping undertaken as part of this study. Stratigraphic units defined from geological mapping were accurately and respectfully named after words and names in the Māori language and Ngati Tūwharetoa dialect, which are specific to the area and historical events. Because of the scale and detail of mapping work undertaken here, it is hoped that these names will become entrenched in published scientific literature and survive as a record of both New Zealand's natural and human histories.

The oldest stratigraphic unit confidently associated with Tongariro volcano is the Tupuna Formation, which takes its name from the Ngati Tūwharetoa word of 'ancestor'. In balance with this, the youngest stratigraphic unit on Tongariro is the Matariki Member that is defined as all lavas and pyroclastic deposits erupted between 1870 and 1975 CE from the Ngauruhoe vent and which represent the youngest magmatic eruptives on Tongariro. Whilst the name 'Matariki' is taken from a nearby waterfall west of Tongariro, it has a greater cultural significance. In the Māori language 'Matariki' is the name of the stars forming the Pleiades cluster in the constellation of Taurus, and the first appearance of these stars in late May, which defines the Māori new year.

1.2. Outstanding questions in the study of stratovolcanoes and intermediate composition arc magmas

1.2.1. Stratovolcano geomorphology

The question arises: why do some stratovolcanoes possess simple cone geometries, such as the Ngauruhoe cone on Tongariro volcano, whereas others possess irregular or "ice-ravaged" geometries (Hildreth and Lanphere, 1994; Lescinsky and Sisson, 1998; Schmidt and Grunder, 2009; Conway et al., 2015, 2016)? Glacial processes have long been recognised to affect stratovolcano eruptive processes and morphologies (Mathews, 1952; Lescinsky and Sisson, 1998; Schmidt and Grunder, 2009; Conway et al., 2015), however the processes by which these occur have yet to be globally recognised (cf. Singer et al., 1997; Dungan et al., 2001; Singer et al., 2008;

Jicha et al., 2012). Explicit evidence for lava-ice interaction at previously-glaciated stratovolcanoes indicates that the presence and absence of ice strongly controls where erupted material can and cannot be preserved (Lescinsky and Sisson, 1998; Conway et al., 2015; Vallance and Sisson, 2017). On Earth, glaciovolcanic deposits have been identified on all continents except Australia (Edwards et al., 2015) but are potentially under-recognised at many stratovolcanoes around the world, as demonstrated by the recent recognition of previously unrecognised glaciovolcanic deposits on Tongariro volcano (Townsend et al., 2017; Cole et al., 2018, 2019).

Other processes that influence stratovolcano geomorphologies and produce irregular landforms are mass wasting and sector collapse events (e.g. the Te Whaiau Formation debris flows on Tongariro: Lecointre et al., 2002). In many examples, mass wasting is associated with glaciation, such as the Osceola Mudflow from Mount Rainier (Vallance and Scott; 1997) and the Murimotu Formation sector collapse deposits from Ruapehu volcano (Palmer and Neall, 1989; Conway et al., 2016; Townsend et al., 2017). Both of these units are Holocene in age and are inferred to have occurred soon after deglaciation, probably due to the reduced support of unstable edifice-material that had been confined by ice. At Mount Rainier, Pleistocene diking and subsequent hydrothermal alteration is inferred to have weakened the edifice to failure point, but collapse did not occur until deglaciation was relatively advanced (Vallance and Scott, 1997; Reid et al., 2001; Sisson et al., 2001; Vallance and Sisson, 2017).

Understanding of the processes that shape stratovolcano morphologies provides the fundamental basis for reconstructing edifice growth histories and eruptive volumes, including volumes that are not preserved as part of the edifice. Traditional models have explained stratovolcano morphologies as the result of intervals of (perfect) cone growth that alternate with periods of inactivity and erosion (often accompanied by glacial activity), which imply large volumes of eroded edifice material (e.g. Singer et al., 1997; Dungan et al., 2001; Singer et al., 2008; Jicha et al., 2012). These models contrast with the syn-glacial growth models summarised previously, wherein irregular stratovolcanic landforms are the products of edifice growth in the presence of ice, where erosion is thought to be a secondary factor. In pursuit of testing these contrasting growth models, this study contributes a new chronostratigraphic reconstruction of edifice growth for Tongariro, as presented in Chapter 3. The results favour a syn-glacial growth model wherein the present-day ~350-0 ka edifice is approximately representative of its original volume, with the distinction that a significant proportion of originally erupted material has never preserved as part of the edifice.

1.2.2. Magmatism, volcanism and tectonics

At all volcanoes, there is a complex relationship between magmatism, its expression (i.e. volcanism) and external but related processes such as regional tectonics. Since the advent of accurate geochronological techniques for Quaternary volcanic rocks, models proposed for the interplay between magmatism, volcanism and tectonics and have become testable by examining contemporaneity (or lack thereof) between neighbouring regional volcanic systems (e.g. within ~100 km: Bacon and Duffield, 1981; Bacon, 1985). The spatial alignment of vent foci in volcanic arcs demonstrates that upper crustal stress regimes and tectonic processes must regulate the volcanic expression of magmatism (Bacon, 1985) in ways beyond magma production via mantle flux melting (Gill, 1981; Morris et al., 1990; Sisson and Layne, 1993). Some studies have suggested that synchronised volcanism has occurred at isolated volcanoes within the same arc, such as within the Taupō Volcanic Zone (TVZ) of New Zealand for 12-10 ka explosive eruptions at Taupō, Tongariro and Ruapehu volcanoes (Kohn and Topping, 1978; Nairn et al., 1998). Other studies from the TVZ have inferred above-average slip-rates (extensional) that occurred contemporaneously with the 25.4 ka ~530 km^3 Orunaui eruption from Taupō volcano (Wilson, 2001; Gómez-Vasconcelos et al., 2016), which indicates that tectonically-regulated arc magmatism and volcanism may be an under-recognised global phenomenon. To test whether external (i.e. tectonic) processes are likely to have affected the expression of volcanism and magmatism at Tongariro volcano, time-composition records from Tongariro (Chapter 5 in this study) and Ruapehu volcano (Gamble et al., 2003; Price et al., 2012; Conway et al., 2016, 2018) are compared with zircon (residence) model-ages in eruptives from Taupō volcano (Charlier et al., 2005; Wilson and Charlier, 2009; Barker et al., 2014). These data span from ~230 ka to the Holocene and are examined for the presence and/or absence of synchronised patterns.

1.2.3. Compositional diversity of intermediate composition magmas

How are arc magmas assembled and what controls their compositions? Compositional diversity in arc magmas is the norm and is strongly influenced by open system processes (Eichelberger, 1975; Gamble et al., 1999; Izbekov et al., 2004; Humphreys et al., 2006a). Salient examples have demonstrated that compositional variations in arc magmas are not unidirectional through time (Eichelberger et al., 2006), as was previously thought (e.g. Bowen, 1928). Further complexity is observed in the diverse crystal cargoes, interstitial melts and xenolithic materials incorporated into arc magmas. The recycling of older populations of crystals into younger magmas within the same magmatic system, termed "antecrysts" following Hildreth (presentation at Penrose Conference on 'Longevity of Rhyolitic Magma Systems', 2001) and Charlier et al. (2005), have

been identified as ubiquitous features in many arc magmas (e.g. Charlier et al., 2007). Andesite and dacite arc magmas typically possess rhyolitic melt inclusions and interstitial melts, as do rhyolites themselves, despite their contrasting whole-rock compositions (Reubi and Blundy, 2009; Price et al., 2012; Kent, 2013; Lee and Bachman, 2014; Conway et al., 2018). The presence of xenolithic inclusions derived from the mantle (e.g. Gruender et al., 2010; Tollan et al., 2017), deep-crustal cumulates (e.g. Arculus and Wills, 1980; Gruender et al., 2010; Sisson et al., 2014) and mid- to shallow-crustal rocks (e.g. Barley, 1987; Graham, 1987; Charlier et al., 2008, 2010; Price et al., 2012) attest to the diverse range of contaminants in arc magmas.

The relationship between interstitial melts and whole-rock compositions in intermediate composition arc magmas is examined in this study with geochemical comparisons between paired whole-rock and groundmass samples from Tongariro volcano. Groundmass separates were collected opportunistically in tandem with aliquots for $^{40}Ar/^{39}Ar$ geochronology, and therefore mostly also have precise age determinations. Paired groundmass and whole-rock sample were analysed for major oxides, trace elements and Sr-Nd-Pb isotopes to interrogate the relationship between intermediate arc magmas and their interstitial melts across a representative spectrum of bulk-rock concentrations. These data are reported and discussed in full in Chapter 4.

1.2.4. Crust versus mantle inputs into magmas

What are the relative proportions of mantle-derived and crust-derived materials in intermediate composition arc magmas? Arc magmas often show direct petrographic evidence in their xenolith cargoes for mantle and crustal inputs during magma assembly (e.g. Rudnick et al., 1986; Barley, 1987; Graham, 1987, Graham et al., 1988; Gruender et al., 2010; Tollan et al., 2017). Where the isotopic characteristics of mantle and crustal end-members are known, mixing and assimilation-fractional crystallisation models can be used to estimate their relative proportions (DePaolo, 1981; Bohrson and Spera, 2001). These have fundamental implications for the thermodynamic processes involved with magma assembly, such as energy-balanced crustal fusion and magma crystallisation. Despite this, previous estimates of the percentage of assimilated crust in intermediate composition arc magmas are relatively few (e.g. Sisson et al., 2014).

In this study, a representative suite of 16 crustal xenoliths derived from basement rocks beneath Tongariro were sampled. These xenoliths were analysed for major oxides, trace elements and Sr-Nd-Pb isotopes to characterise metasedimentary basement rocks and provide a basis for estimating the percentage of assimilated crust in Tongariro magmas. These new data are reported and discussed in Chapter 4 and build on previous studies of crustal xenoliths in arc volcanics from the southern TVZ (Graham, 1985, 1987; Graham et al., 1988, 1990).

1.2.5. Relationship between arc andesite and rhyolite magmas

Do genetic relationships exist between andesite and rhyolite magmas in arc settings? The common observation that arc andesites contain dacitic to rhyolitic melt inclusions and interstitial melts has inspired numerous models of andesite petrogenesis and remains a source of scientific debate (Gill, 1981; Price et al., 2005; Reubi and Blundy, 2009; Lee and Bachmann, 2014). Intimately associated with such models is the genetic relationship, or lack thereof, between arc andesite and rhyolite magmas. Some studies have suggested that andesites are primarily the product of basalt mixing with dacite-rhyolite magmas (Reubi and Blundy, 2009) whereas others have argued the opposite (Lee and Bachmann, 2014). Elsewhere, other models have proposed that crystal-poor rhyolites are the product of crystal-melt segregation from crystal-rich andesite-dacite magmas (e.g. Bachmann and Bergantz, 2004). In New Zealand however, some Quaternary rhyolitic ignimbrites have overlapping crystal concentrations with typical andesites (20-40 vol%: Gill, 1981), which include the ~1.21 Ma Ongatiti ignimbrite (20-50 vol% crystals: Cooper and Wilson, 2014) and the ~349 ka Whakamaru Group ignimbrites (~35 vol% crystals: Ewart, 1965; Brown et al., 1998; Downs et al., 2014), whereas the 25.4 ka Oruanui ignimbrite and subsequent rhyolite eruptives are relatively crystal-poor (≤2-15 vol% crystals: Sutton et al., 1995, 2000; Vandergoes et al., 2013).

In New Zealand, a relationship between andesite and rhyolite magmas has also been suggested to be of age-progression, wherein the andesite volcanoes in the southern TVZ (Tongariro and Ruapehu) will evolve to become rhyolite volcanoes as the TVZ rift propagates southwards (Price et al., 2005). This suggestion is seemingly contradicted by the occurrence of White Island/Whakaari volcano—which is andesitic—in the Bay of Plenty (continental crust basement) where the rifting rate (~15 mm/yr) exceeds that of the rhyolite-dominated central TVZ (Gamble et al., 1993; Wallace et al., 2004; Villamor and Berryman, 2006). Clearly, available observations show that whilst a genetic relationship between andesite and rhyolite magmas is plausible, it must also be complex. New geochemical data from Tongariro, presented from chapters 3-5, will be integrated in Chapter 6 to address the potential genetic relationship between andesite and rhyolite magmas.

1.3. Structure of this thesis

This thesis is built around detailed geological mapping of Tongariro volcano, coupled with radiometric dating of samples to provide a chronological framework, within which a detailed study of the geochemical and isotopic characteristics of whole-rock and groundmass samples could be placed. Following this introduction and description of the analytical methods

(Chapter 2), chapters 3-5 are presented as journal style manuscripts. Because of the need to set the context for chapters 3-5, there is some repetition of introductory material within those chapters.

Chapter 1: Introduction

This chapter introduces the scope of the thesis. The significance of stratovolcanoes in cultural and scientific terms is summarised. A number of outstanding research questions relating to the study of stratovolcanoes and intermediate composition arc magmas, relevant to and address in this study, are also briefly introduced. This chapter also provides a summary of the content in the chapters of this thesis (this section). A brief overview of Tongariro's geological setting and previous work follows. This overview includes a comparison of new sampling campaigns relative to previous coverage (Cole, 1978, 1979; Wahyudin, 1993; Hobden, 1997) and how this study fits into the ongoing larger mapping project of the TNP (Townsend et al., 2017).

Chapter 2: Analytical methodologies

Analytical techniques and methodologies are reported in this chapter. These include analytical operating conditions and protocols, internal and external analytical reproducibility, procedural blanks and technique calibrations. The descriptions in this chapter take the place of fully-detailed methods sections in chapters 3 and 4, and will be integrated in when respective chapters are submitted for publication.

Chapter 3: A high-resolution $^{40}Ar/^{39}Ar$ lava chronology and edifice construction history for Tongariro volcano, New Zealand

Mapping results from 250 new localities, 219 new samples with major oxide concentrations and 29 new $^{40}Ar/^{39}Ar$ age determinations are reported here. The data are combined with pre-existing datasets from Cole (1978, 1979), Wahyudin (1993) and Hobden (1997) for Tongariro eruptives to define a new chronostratigraphy for edifice-forming materials on Tongariro. Formal definitions of stratigraphic formations and members are provided in Appendix 3 to supplement this chapter. Methods relating to this chapter are fully described in Chapter 2.

Chapter 4: The geochemistry and petrogenesis of basaltic-andesite to dacite magmas at Tongariro volcano, New Zealand

This chapter presents all the geochemical data collected during the course of this study. Major oxide and trace element concentrations and Sr-Nd-Pb isotope ratios are reported for whole-rock

samples, groundmass separates and metasedimentary crustal xenoliths. The geochemical characterisation of crustal xenoliths and assessment of compositional arrays in whole-rock samples provide a basis for estimating the proportions of (a) assimilated crust, (b) fractionated crystalline material and (c) primitive mantle-derived magma in Tongariro magmas, which was pursued with modelling in this chapter. Comparisons of paired whole-rock and groundmass compositions from the same samples are also reported here for major oxide, trace element and Sr-Nd-Pb isotopes. Methods relating to this chapter are fully described in Chapter 2.

Chapter 5: The time-space-composition evolution of edifice-forming eruptives at Tongariro volcano, New Zealand
The chronostratigraphic framework of Chapter 3 and the geochemical data of Chapter 4 are integrated in this chapter to examine time-composition relationships over Tongariro's lifespan. Tongariro data are compared with time-composition data from Ruapehu volcano (Gamble et al., 2003; Price et al., 2012; Conway et al., 2016, 2018) and with zircon (residence) model-ages from Taupō volcano for the ~230 ka to Holocene period (Charlier et al., 2005; Wilson and Charlier, 2009; Barker et al., 2014). Arising from these comparisons is an examination of whether or not these records display synchronised variations, which if present might suggest simultaneous regulation of two or three of these volcanoes by an external factor.

Chapter 6: Synthesis and conclusions
This chapter synthesises and summarises the results and conclusions of chapters 3-5. These are presented within the context of the 'outstanding questions in the study of stratovolcanoes and intermediate composition arc magmas' posed in section 1.2. Recommendations for future studies are provided in relation to both local geology in New Zealand and globally.

1.4. Background

1.4.1. Geological setting of the southern Taupō Volcanic Zone (TVZ)

Tongariro is an active, composite stratovolcano situated in the central North Island of New Zealand (Fig. 1.1). Tongariro has erupted lavas and pyroclastic rocks of basaltic-andesite to dacite compositions since at least ~300 ka (Stipp 1969; Hobden et al., 1996; this study). Together with Ruapehu, located ~20 km to the south, Tongariro defines the southern portion of the Taupō Volcanic Zone (TVZ), which is one of the most spectacular and productive sites of continental arc volcanism recently active on Earth (Wilson et al., 1995). A salient observation is that the central TVZ, that, for the purposes of this study occurs northwards of the Pihanga and Kakaramea edifices (Fig. 1.1), is dominated by rhyolitic volcanism (Wilson et al., 1995). In

contrast, volcanism in the southern TVZ—from Pihanga and Kakaramea to the south—does not display any rhyolitic volcanism. All known eruptive products in the southern TVZ are basaltic-andesites to dacites in composition (Cole, 1978, 1979; Cole et al., 1983; Hobden, 1997; Gamble et al., 2003; Cameron et al., 2010; Price et al., 2012; Conway et al., 2016, 2018; Townsend et al., 2017).

The TVZ is a continental volcanic arc that is fuelled by the westward subduction of the Pacific Plate beneath the overriding Indo-Australian Plate, which converge at this latitude at a rate of ~43 mm/yr (Nicol et al., 2007; DeMets et al., 2010). Active since ~2 Ma (Leonard et al., 2010; Mortimer et al., 2010), the TVZ is the ~300 km, southernmost continental segment of the larger-scale ~2800 km Tonga-Kermadec oceanic island arc that continues northwards offshore of New Zealand (Cole and Lewis, 1981; Gamble et al., 1993; Luyendyk, 1995; Mortimer, 2004; Smith and Price, 2006: Fig. 1.1). The TVZ is established within continental crust whereas the Tonga-Kermadec arc is established within oceanic crust (Fig. 1.1) (Gamble et al., 1993; Wilson et al., 1995). Whilst situated above a convergent plate boundary, the TVZ also undergoes active extension due to either slab rollback (Seebeck et al., 2014) or frictional contrasts at the subduction interface that arise due to buoyancy differences between the Hikurangi Plateau and other subducting materials (Wallace et al., 2004). Current measurements of extension show rifting of ~2-7 mm/yr at the latitude of the southern TVZ which increases northwards to ~15 mm/yr at the Bay of Plenty coastline (Fig. 1.1) (Wallace et al., 2004; Villamor and Berryman, 2006). In the Wanganui Basin ~100 km further SW, the tectonic regime becomes actively compressional.

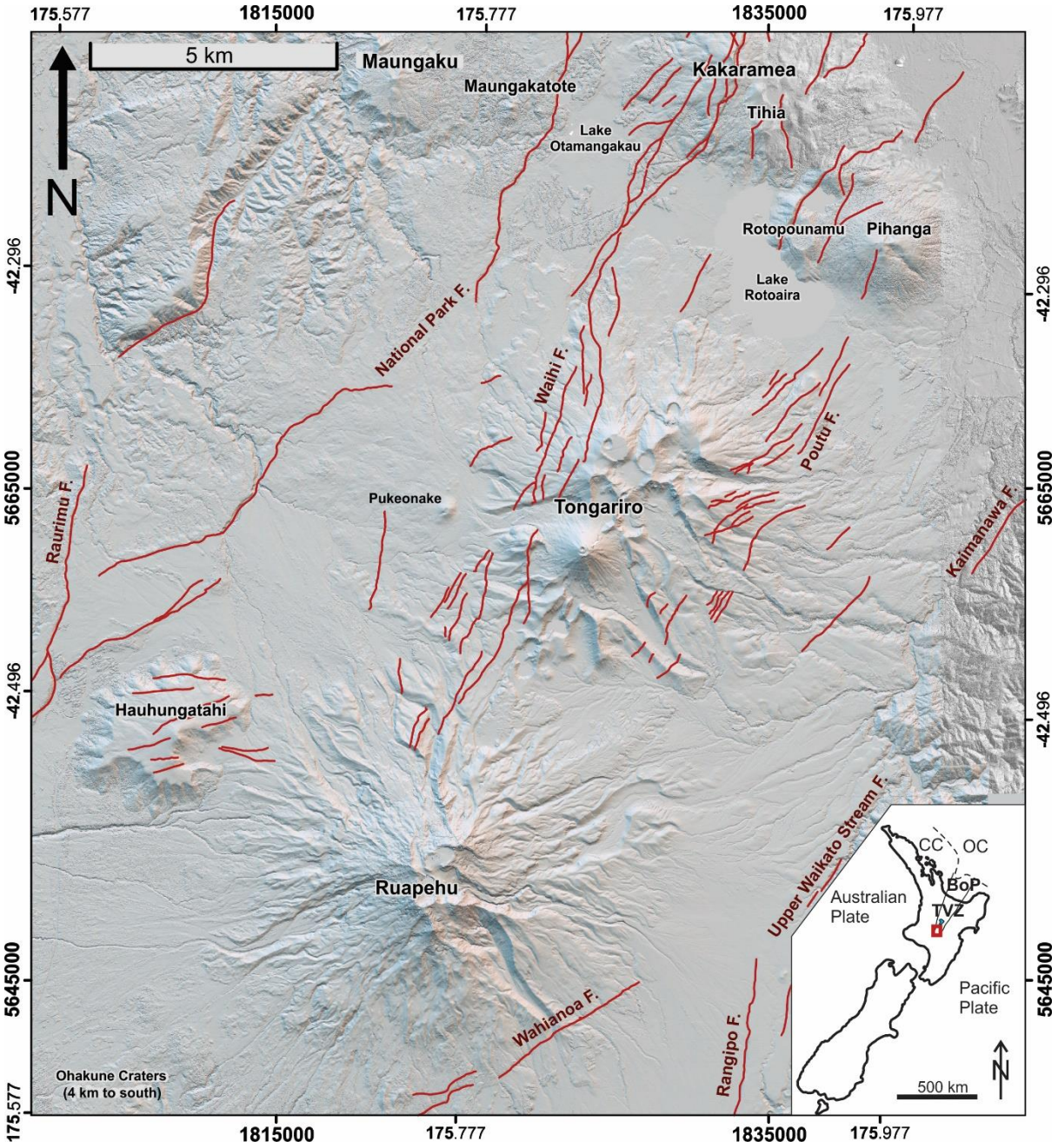

Figure 1.1. Map of intermediate composition volcanoes that dominate the southern TVZ, with inset showing the position (red box) in New Zealand's North Island. Red lines indicate faults active during the Quaternary, following Townsend et al. (2017). The boundary between the continental crust (CC) and oceanic crust (OC) after Gamble et al. (1993), offshore from the Bay of Plenty (BoP). Subduction of the Pacific Plate is westward beneath the Australian Plate at ~2-5 cm/yr from south to north along the North Island. Map projection is the New Zealand Transverse Mercator 2000 (NZTM2000). The 2 m-resolution digital surface model (DSM), which is the basis for this map and all others in the thesis, was developed by GNS from photogrammetry of aerial photos obtained in 2010 and 2012 and is reported with methodologies by Gómez-Vasconcelos et al. (2016).

Surrounding the Tongariro and Ruapehu massifs are other dormant stratovolcanoes, listed clockwise from north: Kakaramea (N), Tihia (NNE), Pihanga (NE), Hauhungatahi (SW)

and Maungakatote and Maungaku (NW) (Fig. 1.1). Satellite vents are found to the southwest of Ruapehu (Ohakune Craters) and directly west of Tongariro (Pukeonake) (Cole, 1978). Of these vents, direct age determinations exist for the lavas of Hauhungatahi (933 ± 46 ka; Cameron et al., 2010); Kakaramea (229 ± 1 ka: Stipp, 1969 via decay constants of Steiger and Jaeger, 1977); Tihia, which is a vent on the SE of Kakaramea (198 ± 23 ka: Stipp, 1969 via decay constants of Steiger and Jaeger, 1977) and Pihanga (>180 ka in this study [Chapter 3] which conflicts with a previous K./Ar age determination of 123 ± 10 ka: Stipp, 1969 via decay constants of Steiger and Jaeger, 1977), and for a radiocarbon age determination on twigs from tephra of the Ohakune Craters (31.5 ± 0.3 ka: Froggatt and Lowe, 1990). Elsewhere, the only available age constraints are stratigraphic relations with respect to the regional Whakamaru Group ignimbrites (349 ± 4 ka: Downs et al., 2014) and the Oruanui eruption deposits (25,360 ± 320 a: Vandergoes et al., 2013). Maungakatote and Maungaku were constructed mostly after emplacement of the Whakamaru Group ignimbrites but possibly beforehand too (Topping, 1974; Cashman, 1979) and Pihanga and Pukeonake were most recently active prior to the Oruanui eruption (Topping, 1974). Activity at Tongariro began by 304 ± 11 ka (2 s.d.) as indicated by a new $^{40}Ar/^{39}Ar$ age determination on a lava collected from nearby Lower Tama Lake area of southern Tongariro (Fig. 1.2, below; age in Chapter 3), which is consistent with previous K/Ar age determinations of ~270 ka (Stipp, 1969; Hobden et al., 1996).

1.4.2. Tongariro volcano within the southern TVZ

Tongariro's composite edifice is constructed from the lavas of demonstrably multiple vents but many of the locations of these vents remain unclear (Gregg, 1960; Cole, 1978; Hobden et al., 1996). Existing estimates propose a total of 17 vents (Hobden, 1997) but the exact number is uncertain because the locations of many pre-50 ka vents are no longer visible. Younger vents—such as Ngauruhoe, Red Crater and Te Maari Craters—are obvious from their prominence and immediately adjacent lava flows. This, however, does not hold for older vents (>50 ka), the locations of which are obscured by younger eruptives or have been destroyed by erosion (Fig. 1.2). North Crater is potentially the oldest vent (or vents) the location of which is well-constrained. Further clarifying the positions of older vents is an objective of this study. Glacial valleys and streams (Oturere, Mangatepopo, Mangahouhounui, Makahikatoa, Waihohonu), cirques and explosion craters (Blue Lake, possibly Tama Lakes and North Crater, Te Maari Craters) demonstrate the variety of geological processes that modify landforms at Tongariro. New interpretations of Tongariro's geomorphology consider two endmember growth models, as summarised in section 1.2.1 (above), which are (a) stop-start growth that is punctuated by periods

of glacial erosion and (b) relatively continuous growth that occurs syn-glacially during cool climatic periods.

1.4.3. Previous edifice studies of Tongariro

European accounts of Tongariro volcano span over 150 years. Initially the focus of naturalists (e.g., Hochstetter, 1864) and mapping surveys (Cussen, 1891; Gregg, 1960), Tongariro has since received strengthening scientific attention. Pioneering work by Cole (1978, 1979) was the first overarching geochemical investigation of volcanoes in the southern TVZ. Later Tongariro-specific geochemical studies were undertaken by Wahyudin (1993) and Hobden (1997). However, during recent decades research on Tongariro has failed to keep pace with advancing analytical tools and contemporary models of stratovolcano construction. These shortcomings are exacerbated further by the paucity of sampling in northwestern and northeastern quadrants of Tongariro (Fig. 1.3) that has served to limit confidence in the surviving interpretations of Tongariro's volcanic and magmatic evolution.

Pre-Holocene lavas represent >95% of Tongariro's lifespan (Stipp, 1969; Hobden et al., 1996) but have received limited attention (Cole, 1978, 1979; Patterson and Graham, 1988; Wahyudin, 1993; Hobden et al., 1996). Many studies of Tongariro's lavas focus on those erupted from the youngest vents, particularly Red Crater (Stevens, 2002; Wadsworth et al., 2015; Shane et al., 2017) and Ngauruhoe (Graham et al., 1988; Rogan and Blake, 1994; Hobden et al., 2002; Price et al., 2010; Coote and Shane, 2016; Shane et al., 2019). Furthermore, many graduate theses continue to re-examine Ngauruhoe's lavas but rarely proceed to scientific journal publication (e.g., Hora, 2003; Krippner, 2009; Bova, 2010; Sanders, 2010; Barton, 2011). The most representative sampling campaign of Tongariro's lavas obtained 459 specimens, 370 of which have determined compositions; of these, 178 (48%) were taken from lavas younger than 25 ka, which represent only ≤10% of Tongariro's lifespan (Hobden, 1997).

The other shortcoming in geochemical studies of Tongariro's lavas is the underutilisation of modern geochronological techniques. The only age determinations of Tongariro's lavas are from Stipp (1969) and Hobden et al. (1996), both of which use the (now largely superseded) K/Ar dating method. The results of bulk-rock K/Ar age determinations are questionable when the contribution of excess argon to measured concentrations is unknown. Excess argon is known to exist in some phenocrystic melt inclusions and groundmass glass, which are abundant in Tongariro's lavas, and has the potential to shift determined ages to different and geologically-insignificant values (e.g. Esser et al., 1997). It is possible that excess argon affected previous K/Ar age determinations that were performed on whole-rock Tongariro samples that commonly

contained glassy groundmass material (cf. Hobden et al., 1996). To address this, $^{40}Ar/^{39}Ar$ analyses in this study were performed on thoroughly devitrified groundmass separates that were free of phenocryst fragments. This follows specifically designed sampling techniques and the $^{40}Ar/^{39}Ar$ dating technique, which have been developed over recent decades and offer substantial reductions in analytical uncertainties by up to an order of magnitude, following Gamble et al. (2003) and Conway et al. (2016) for the context of Ruapehu, when compared with K/Ar methods. An existing partnership with the Menlo Park office of the United States Geological Survey (USGS) has afforded access to world-class radioisotopic dating facilities, which is where $^{40}Ar/^{39}Ar$ age determinations on Tongariro lavas were performed.

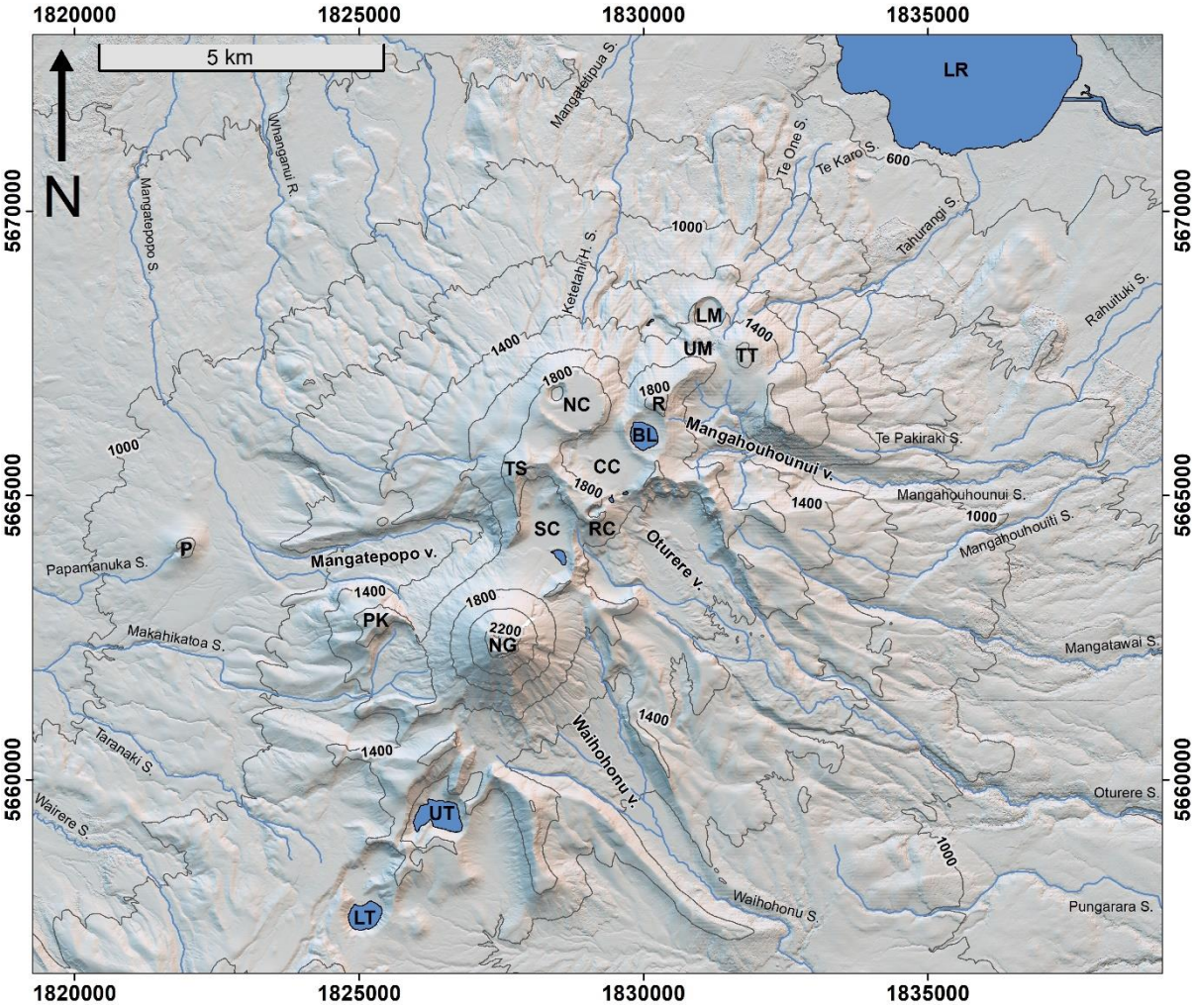

Figure 1.2. Tongariro volcano and its landforms and vent foci with contours (labelled every 200 m) relative to sea level. Contours were taken from 1:50,000 Topo50 series digital topographic maps (published by Land Information New Zealand). Abbreviations are as follows. Valley (V), stream (S), BL = Blue Lake, CC = Central Crater, LR = Lake Rotoaira, LM = Lower Te Maari Crater, LT = Lower Tama Lake, NC = North Crater, NG = Ngauruhoe, P = Pukeonake, PK = Pukekaikiore, R = Rotopaunga summit, RC = Red Crater, TS = Tongariro summit, TT = Te Tatau summit, SC = South 'Crater' Cirque (e.g. Cole et al., 2018), UM = Upper Te Maari Crater, UT = Upper Tama Lake.

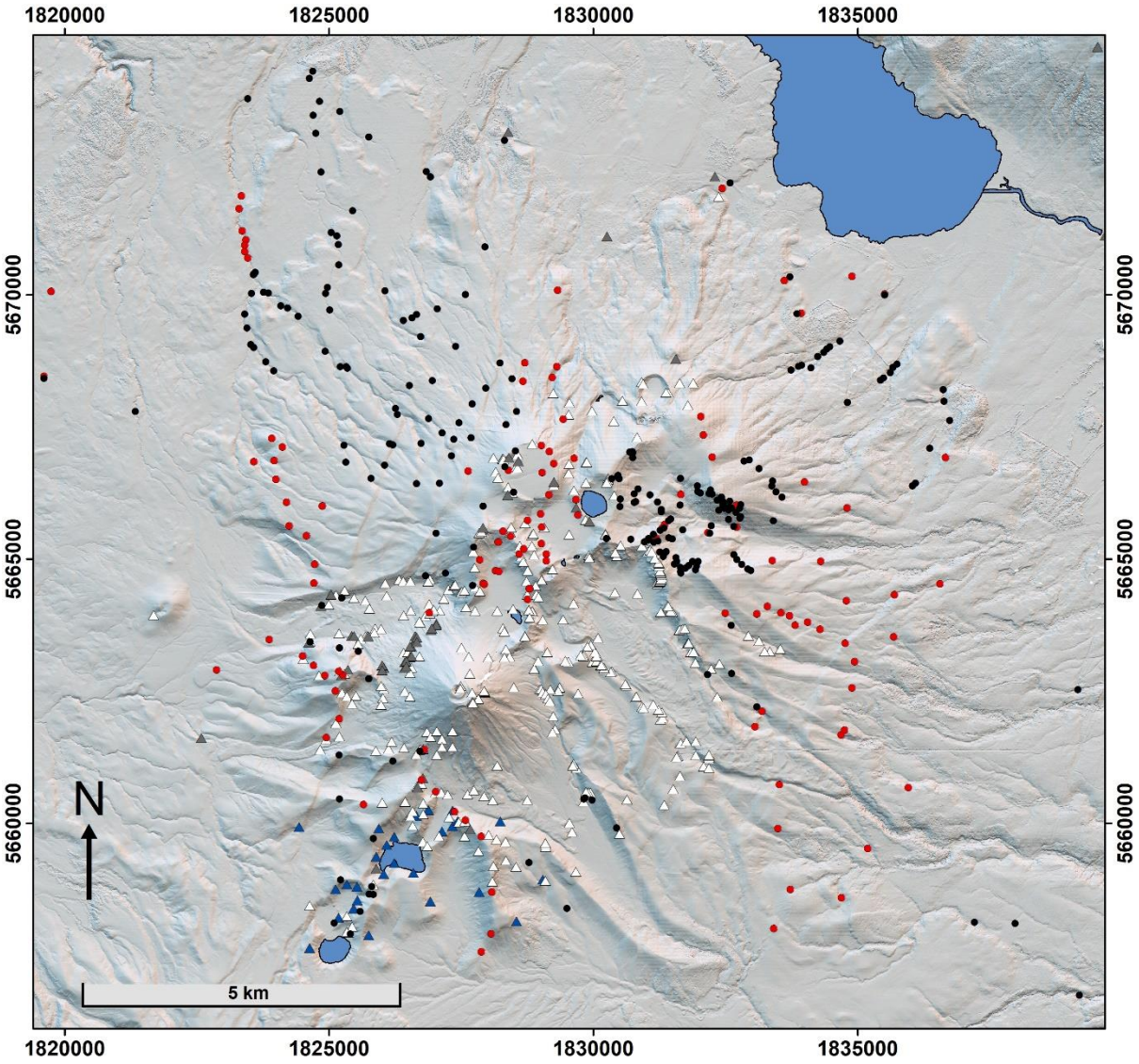

Figure 1.3. Previous samples (triangles) and new samples (circles) of edifice-forming eruptives from Tongariro. New samples are from this study (black) and collaborators involved with the broader TNP mapping project of TNP (G. S. Leonard, D. B. Townsend, C. E. Conway, M. Rattenbury, R. P. Cole, pers. comm., 2016-2018) (red). Previous samples represented by triangles are from Cole (1978, 1979) (grey), Wahyudin (1993) (blue) and Hobden (1997) (white).

A fundamental consideration for improving Tongariro's eruptive stratigraphy is the edifice construction model within which observations are interpreted. The existing edifice growth model for Tongariro proposed by Hobden et al. (1996) is open to reinterpretation because it overlooks the role of contemporaneous glaciation and volcanism in shaping edifice growth. Hobden et al.'s (1996) model invoked 17 separate volcanic vents that developed individual cone structures; these cones experienced episodic activity that was punctuated by periods of glacial erosion, which occurred in temporal isolation. However, age determinations (Hobden et al., 1996; this study) demonstrate that lavas were commonly erupted during glacial periods. Crucially, the presence and absence of ice masses have been demonstrated elsewhere to control the locations at

which lavas are preserved (Lescinsky and Sisson, 1998; Lescinsky and Fink, 2000; Conway et al., 2015). At Tongariro, the applicability of lava-ice models is corroborated by explicit textural evidence for lava-ice interaction, in the form of cooling structures preserved on the peripheries of lavas (Cole et al., 2018, 2019; this thesis). The absence of contemporaneous glacial and volcanic interplay as part of Tongariro's existing edifice construction model suggests that interpreted vent locations, lava sequencing (and consequential geochemical sequencing), geomorphological evolution, estimated lava volumes and eruption rates are all open to re-examination.

1.4.4. Broader context of this project

The mapping component of this study, which is chiefly represented by the results in Chapter 3, was encompassed under a larger mapping project of the entire Tongariro National Park. Output from this project is primarily represented by the 1:60,000 map of Townsend et al. (2017) which will be re-published as a second edition in 2020 and incorporate the new mapping results of Tongariro from this thesis. Other recent PhD theses that have made significant contributions to this work are Eaves (2015) (glaciation and moraines), Conway (2016) (edifice mapping of Ruapehu), Gómez-Vasconcelos (2017) (structural evolution of the southern TVZ) and Cole (2019) (glaciovolcanic deposits on Tongariro).

Chapter 2

Methodologies

"Quantitare aut mori"

C. J. N. Wilson (c. 2016)

2.1. Field geology

2.1.1. Sample collection

Samples were collected during field mapping campaigns in the summers of 2016-2018 at Tongariro volcano. Permission to undertake scientific sampling was granted by the Ngati Tūwharetoa iwi through the Department of Conservation to GNS Science, to personnel G. S. Leonard, D. B. Townsend and their graduate students for the period 1 December 2015 to 31 December 2020 (PAM 05 07 19). About 30 additional samples were contributed by G. S. Leonard, D. B. Townsend, M. Rattenbury, C. E. Conway and R. P. Cole between 2016-2019, which were collected during field and helicopter-assisted campaigns. Sample coordinates were obtained with a Garmin GPS unit at the time of collection, and were cross-examined with field notes, field photographs and by plotting spatially in ArcGIS software. These locations are accurate to about ± 10 m, following Townsend et al. (2017).

2.1.2. Mapping process and coordinates

The geological mapping undertaken here defines the exposed eruptive materials exposed on Tongariro's edifice. Surficial alluvium, fan deposits, till, glacial outwash and other sedimentary deposits were not differentiated. Where these covering materials occur in relatively thin veneers (i.e. <2 m), the mapping unit chosen is the underlying eruptive material. Because of this approach, it is likely that the mapped unit boundaries in this study will differ from the forthcoming update of the TNP map (due 2020, following Townsend et al., 2017).

Mapping was undertaken using field-based examination and ArcGIS software, which aided the identification, interpretation and cross-comparison with geomorphological features on aerial photographs, topographic maps and a digital surface elevation model (DSM). All resources and sample location information were handled in the New Zealand Transverse Mercator 2000 (NZTM2000) map projection. Aerial photographs taken by Land Information New Zealand (LINZ) were provided by GNS Science (D. B. Townsend, pers. comm., 2016). Contours were obtained from 1:50,000 Topo50 series digital topographic maps (published by Land Information New Zealand). The 2 m-resolution DSM used is this study was developed by GNS from photogrammetry of aerial photos obtained in 2010 and 2012 and is reported using the methodologies of Gómez-Vasconcelos et al. (2016). Formwork lines drafted by D. B. Townsend (pers. comm., 2016) for geomorphological features in the park were used as a basis for defining map unit boundaries in ArcGIS software. Some of these formwork lines were later published (relatively unchanged) as unit boundaries in the map of Townsend et al. (2017).

This study adopted a novel approach to spatially representing geochemical data which greatly aided the mapping process. The technique has become known as the 'sombrero' method (G. S. Leonard, pers. comm., 2016) and involves linking a Microsoft Excel spreadsheet that contains geochemical data to spatially-plotted samples in ArcGIS software, based on corresponding sample IDs. A simple case is shown in Fig. 2.1 which demonstrates how geochemical data, colour-coded as different concentric rings, can provide a powerful spatial representation of quantitative compositional data. In the example shown, the SiO_2-MgO-K_2O data clearly distinguish between the Rangitaupahi Member (**ari**) from adjacent units. Other geochemical parameters such as TiO_2-Ba-Sr were plotted to distinguish between other units that have relatively similar SiO_2-MgO-K_2O concentrations. The scatterplot matrix function in ArcMap further aided this process. To differentiate the edifice-forming volcanic materials on Tongariro, new geochemical data were plotted using the 'sombrero' method to iteratively refine unit boundaries that were previously drawn from geomorphological features that were visible in the DSM and in aerial photographs (Townsend, pers. comm., 2016). Note that because mineral mode data were obtained from hand specimen estimates with the charts of Terry and Chilingar (1955), and not via point counting, they are less precise than whole-rock XRF data and were not plotted as sombreros. Mapped units were stratigraphically ordered with observations of field relationships and radioisotopic age determinations obtained for this study and from elsewhere (see Chapter 3).

Figure 2.1. (Next page.) Example of the 'sombrero' method for displaying geochemical data spatially, based on corresponding sample IDs that link a spreadsheet containing geochemical data with ArcGIS sample localities (G. S. Leonard, pers. comm., 2016). Note the strong spatial association with symbols and mapped lavas. Data are from NW Tongariro. Map unit abbreviations and corresponding unit names are: Rahuituki Member (**arh**), Te Porere Member (**dtp**), Otamangakau Member (**aok**), Te Rurunga Member (**atr**), Rotopaunga Member (**arp**), Te Whaiau Formation (**TW**), Rangitaupahi Member (**ari**), Pukeonake Formation (**PN**), Mangatapate Member (**amt**). Symbology shows SiO_2 (outer ring), MgO (middle ring) and K_2O (centre dot) from evolved (blue) to mafic (red) concentrations, in wt% normalised to 100% anhydrous totals. Coordinates are in NZTM2000. DSM after Gómez-Vasconcelos et al. (2016): see text for details in section 2.1.2, above.

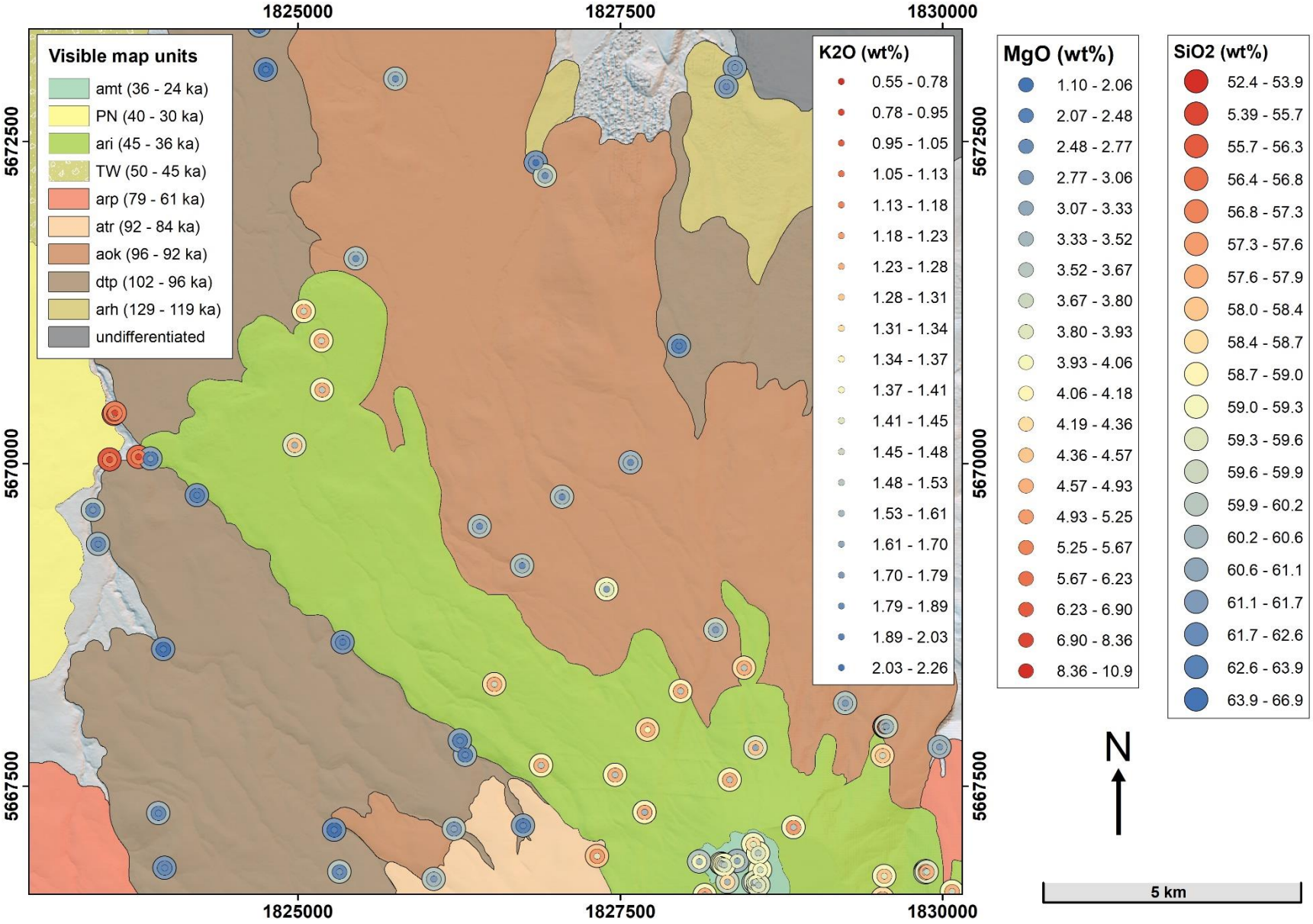
1825000
1827500
1830000
5672500
5670000
5667500
Visible map units
amt (36 - 24 ka)
PN (40 - 30 ka)
ari (45 - 36 ka)
TW (50 - 45 ka)
arp (79 - 61 ka)
atr (92 - 84 ka)
aok (96 - 92 ka)
dtp (102 - 96 ka)
arh (129 - 119 ka)
undifferentiated
K2O (wt%)
0.55 - 0.78
0.78 - 0.95
0.95 - 1.05
1.05 - 1.13
1.13 - 1.18
1.18 - 1.23
1.23 - 1.28
1.28 - 1.31
1.31 - 1.34
1.34 - 1.37
1.37 - 1.41
1.41 - 1.45
1.45 - 1.48
1.48 - 1.53
1.53 - 1.61
1.61 - 1.70
1.70 - 1.79
1.79 - 1.89
1.89 - 2.03
2.03 - 2.26
MgO (wt%)
1.10 - 2.06
2.07 - 2.48
2.48 - 2.77
2.77 - 3.06
3.07 - 3.33
3.33 - 3.52
3.52 - 3.67
3.67 - 3.80
3.80 - 3.93
3.93 - 4.06
4.06 - 4.18
4.19 - 4.36
4.36 - 4.57
4.57 - 4.93
4.93 - 5.25
5.25 - 5.67
5.67 - 6.23
6.23 - 6.90
6.90 - 8.36
8.36 - 10.9
SiO2 (wt%)
52.4 - 53.9
5.39 - 55.7
55.7 - 56.3
56.4 - 56.8
56.8 - 57.3
57.3 - 57.6
57.6 - 57.9
58.0 - 58.4
58.4 - 58.7
58.7 - 59.0
59.0 - 59.3
59.3 - 59.6
59.6 - 59.9
59.9 - 60.2
60.2 - 60.6
60.6 - 61.1
61.1 - 61.7
61.7 - 62.6
62.6 - 63.9
63.9 - 66.9
N
5 km

2.2. Rock crushing and powdering

All ~220 samples collected in this study were prepared for compositional analyses at Victoria University of Wellington (VUW: Kelburn, Wellington) and GNS Science (Gracefield, Lower Hutt). Samples were trimmed of weathered, lichen-covered and altered material until only uniformly-coloured grey-black interior material remained. Hand-sized pieces of samples were crushed in a Rocklabs® Boyd Crusher (high-Cr steel) at VUW or a roller mill at GNS Science, Gracefield (hardened steel, manufactured in-house before 1970). For whole-rock samples, at least 100 g of material was crushed, but usually 200-500 g which ensured sample representativity. Whole-rock samples were powdered in a Rocklabs® agate ring mill (Scott® Automation, NZ). Crushing equipment was cleaned between samples with compressed air guns, vacuum cleaners, tap-water and then ethanol using paper towels until surfaces were dry and completely-dust free. The agate ring mill was cleaned the same way, in addition to running the milling process using pure quartz sand to recondition the inner surface of the milling pot.

2.3. $^{40}Ar/^{39}Ar$ geochronology

Radioisotopic age determinations were performed on strategically chosen lava samples collected in this study and one obtained from the collection of Hobden (1997). Sample collection and most preparation procedures up to the irradiation stage were undertaken at VUW. Prepared samples were later irradiated in the United States then analysed at the United States Geological Survey (USGS) geochronological laboratories in Menlo Park, California.

Analyses were performed on holocrystalline groundmass separates rather than whole-rock or phenocryst materials. This follows Hildreth and Lanphere (1994) and Gamble et al. (2003). Hildreth and Lanphere (1994) demonstrated that holocrystalline samples yield more precise age results, which are consistent with field relationships. Gamble et al. (2003) showed that $^{40}Ar/^{39}Ar$ precision was further improved by analysing groundmass separates (also holocrystalline), relative to less precise measurements on phenocrysts or whole-rock materials of similar samples. For typical andesites, potassium is generally incompatible and accumulates in the groundmass (melt) which is also favourable for precise analyses because of greater radiogenic argon yields.

Comparisons between previous K/Ar age determinations (Hobden et al., 1996) and new $^{40}Ar/^{39}Ar$ age determinations (this study) for the same stratigraphic units at Tongariro indicate that, in general, holocrystalline samples yield results that are consistently more accurate than glassy samples (section 3.5.1). K/Ar age determinations also become systematically more accurate with increasing K_2O concentrations, and within error of $^{40}Ar/^{39}Ar$ determinations above 1.8 wt%

K_2O, irrespectively of whether the samples are glassy or holocrystalline. The percentage of phenocrysts (which can host melt inclusions with excess argon) does not correlate with the accuracy of whole-rock K/Ar age determinations, despite the phenocrysts not having been removed from the K/Ar samples (Hobden et al., 1996).

Samples selected for analysis typically had <5 vol% groundmass glass, although there are some exceptions (Appendix 1). For all samples, fresh lava fragments were cut with a diamond saw then crushed (see section 2.2) and sieved to obtain the 250-355 μm size fraction. Dust adhering to the grains was washed away by repeatedly filling and decanting a glass beaker containing sieved samples with water, until clear. The grains were dried overnight in a warm oven at <100 °C. Grains of groundmass material were separated with a hand magnet by exploiting the abundance of highly-magnetic titanomagnetite in holocrystalline groundmass material relative to phenocrystic components. For up to 10 cycles each of 20-40 mins, the grains were washed in glass beakers filled with tap-water in an ultrasonic bath, with the water decanted between cycles, then the grains dried overnight at <100 °C. Dried grains were handpicked to obtain pure groundmass separates, free of phenocryst shards. These grains were washed in glass beakers in four 20 min cycles in an ultrasonic bath. The first wash was with acetone that was later decanted, which was followed by three washes of 15 MΩ H_2O with the water decanted between cycles. The grains were then dried overnight at <100 °C. Total yields of groundmass separates in the 250-355 μm size fraction were ~200-300 mg, with 88-210 mg used for irradiation and analysis. Two samples (LP001 and LP007) were prepared and analysed for 60-90 μm size fractions. Estimates of groundmass glass abundance in all samples are provided in Appendix 1.

Written details of irradiation and analytical procedures specific to this study were provided by USGS personnel at Menlo Park (A. T. Calvert, written communication, 2019) and are quoted directly as follows.

> "$^{40}Ar/^{39}Ar$ geochronology was performed using groundmass segregated by crushing, sieving, and magnetic techniques. Samples were carefully handpicked under a binocular microscope. For irradiation, 88-210 mg separates were packaged in metal foil and placed in a cylindrical quartz vial, together with fluence monitors of known age and K-glass and fluorite to measure interfering isotopes from K and Ca. The quartz vials were wrapped in 0.5 mm-thick Cd foil to shield samples from thermal neutrons during irradiation. The majority (37 of 39) of samples were irradiated in four separate irradiations, each for one hour in the central thimble of the U.S. Geological Survey TRIGA reactor in Denver, Colorado (Dalrymple et al., 1981). The reactor vessel was rotated continuously during irradiation to avoid lateral neutron flux gradients and oscillated vertically to minimize

vertical gradients. Due to a temporary reactor shutdown, samples LP097 and LP239 were irradiated in the CLICIT facility at the TRIGA reactor at Oregon State University (OSU). Reactor constants determined for the Denver irradiations were indistinguishable from recent irradiations, and a weighted mean of constants obtained over the past five years yields $^{40}Ar/^{39}Ar_K = 0.0010 \pm 0.0004$, $^{39}Ar/^{37}Ar_{Ca} = 0.00071 \pm 0.00005$, and $^{36}Ar/^{37}Ar_{Ca} = 0.000281 \pm 0.000006$. We utilized reactor constants from Niespolo et al. (2017) for the OSU irradiation, once corrected for an obvious typographical error in the $^{36}Ar/^{37}Ar_{Ca}$ correction: $^{40}Ar/^{39}Ar_K = 0.000730 \pm 0.000092$, $^{39}Ar/^{37}Ar_{Ca} = 0.000702 \pm 0.000012$, and $^{36}Ar/^{37}Ar_{Ca} = 0.0002702 \pm 0.0000040$. Bodie Hills sanidine (BHs, Fleck et al., 2019) was used as a fluence monitor with an age of 9.797 Ma. BHs is a secondary standard calibrated against the primary intralaboratory standard, GA1550 biotite, that has an age of 98.79 ± 0.96 Ma (McDougall and Wellman, 2011). Fluence monitors were analyzed using a continuous CO_2 laser system and MAP 216 mass spectrometer described by Dalrymple (1989). Unknowns were heated either with a Stuadacher-type resistance furnace or a continuous diode laser system, then analyzed on the MAP spectrometer. Gas was purified continuously during extraction using two SAES ST-175 getters operated at 4A and 0A."

"Mass spectrometer discrimination and system blanks are important factors in the precision and accuracy of $^{40}Ar/^{39}Ar$ age determinations of Pleistocene samples because of low radiogenic yields. Discrimination is routinely monitored by analyzing splits of atmospheric Ar from a reservoir attached to the extraction line. Typical system blanks including mass spectrometer backgrounds were $1.5x10^{-18}$ mol of m/z = 36, $9x10^{-17}$ mol of m/z = 37, $3x10^{-18}$ mol of m/z = 39 and $1.5x10^{-16}$ mol of m/z = 40, where m/z is mass/charge ratio."

2.4. X-ray fluorescence (XRF)

Major oxide, Sr and Ba concentrations were analysed by X-ray fluorescence (XRF) spectrometry at the University of Waikato (UW) after sample preparation at VUW. Loss-on-ignition (LOI) measurements were determined from ~2 g (whole-rock) or 0.2-1.0 g (xenoliths, because of limited material) of powdered sample in alumina crucibles at VUW. Pre-ignited crucibles (1 hr at 1050 °C) and rock powders were ignited for 1 hr at 1050 °C in a muffle furnace. Whole-rock and xenolith sample powders (0.8 g) were fused with 12:22 $BLiO_2$ flux (8.0 g) at 1050 °C in an automated Claisse Neo Furnace over a 25-min heating and cooling cycle at the UW. All sample weighings were performed on an Ohaus (USA) balance with an external reproducibility (2 s.d.) of

± 0.00005 g determined using a 10 g reference weight, therefore errors can be considered insignificant compared with XRF precision and accuracy and for LOI determinations. XRF analyses were performed on a Bruker AXS (WDS detector) S8 Tiger at UW. Analytical precision and accuracy were monitored with standards AGV-1, BCR-2, BHVO-2, OREAS, WS-E and an internal standard (LP009B). Analytical accuracy is within 5 % (1 r.s.d.) for each oxide concentration but generally ≤2.5 % (1 r.s.d.), as determined with rock standards compared with the recommended values of Jochum et al. (2016). Duplicate analyses of LP009B indicate an external precision (2 s.d.) better than 5 % for all major oxides and Sr, however Ba reproducibility is ~13 %.

2.5. Electron probe microanalysis (EPMA)

Major oxide concentrations in silicate melt inclusions and interstitial glasses were measured with a JEOL JXA-8230 Superprobe at VUW equipped with five WDS detectors. Calibrations and measurements were made at 8 nA (Ti, Mn and Mg) and 2 nA (Si, Al, Fe, Ca, Na, K, P) with a 15 kV accelerating voltage and 10 μm beam, following recommendations by Humphreys et al. (2006b), with identical operating procedures for calibration and sample measurements. Currents, peak and background counting times and detector channels are summarised in Table 2.1. Sample data were quantified with a ZAF correction using JEOL software (where Z = atomic number, A = absorption, F = fluorescence). Instrument calibration sequences were performed immediately prior to and following sample analyses with the silicate glass standards VG-A99 and VG-568. All sample data were processed offline (Off-Quant in JEOL software) to minimise the effects of instrument drift that commonly occurred over >5 hr analytical sessions. Trial and error combinations of standardisation data for VG-A99 and VG-568 were used to determine a calibration that most closely reproduced these standard compositions when analysed as unknowns, in each analytical session. Replicate analyses of VG-A99 and VG-568 are presented in Appendix 8 along with sample data.

Table 2.1. EPMA instrumental operating conditions for major elements analyses in silicate glasses.

Element	Channel	Current (nA)	Peak counting time (s)	Background counting time (s)
Si	3	2	30	15
Ti	1	8	40	20
Al	3	2	30	15
Fe	4	2	60	20
Mn	5	8	60	20
Mg	2	8	40	20
Ca	1	2	40	20
Na	2	2	15	8
K	4	2	40	20
P	2	2	60	20

2.6. Beaker and plasticware cleaning

All rock acid digestions were performed in 15 mL or 22 mL Savillex™ PFA (USA) beakers. Beakers were thoroughly pre-cleaned between digestion batches. Table 2.2 summarises the beaker cleaning process and the grades of acid used for cleaning. Between each cleaning stage, beakers were washed with 18 MΩ H_2O, henceforth referred to as MQ H_2O. The same collection of beakers were used for isotope dilution (ID) Sr blanks and double-spike (DS) Pb analyses which were always used and cleaned separately from beakers used for natural (un-spiked) materials. This includes cleaning ID and DS beakers in separate Teflon vats, different glass beakers and their storage in separate plastic boxes.

Table 2.2. The beaker cleaning process in chronological order, starting with from step 1. See text for additional details.

Stage	Location[1]	Containing vessel	Cleaning reagent[2]	Temperature (°C)	Purpose
1	WC	uncontained	8-9 M analar grade HCl, fresh	120	internal cleaning
2	WC	~4L Teflon vat	8-9 M analar grade HCl, reused up to 3 times	120	internal and external cleaning
3	WC		8-9 M analar grade HNO_3, reused up to 3 times	120	
4-6 (x3)	WC	Borosilicate glass beaker w/ watchglass	18 MΩ H_2O dispensed from Nalgene carboy, then decanted	to boiling	
7-8 (x2)	UC	uncontained	6M TD HCl, 2-3 mL to cover bottom surfaces of beakers	120	internal cleaning
9	UC	uncontained	(empty, trace 18 MΩ H_2O)	60-70	drying

[1] WC = wet chemistry laboratory, UC = ultra-clean laboratory with positive pressure.

[2] TD = Teflon distilled acid produced in-house at VUW from Primar Plus grade stock, checked for blank contribution and found to be sub-ppt (parts per trillion) for most elements. Fresh = new acid from the stock bottle that had not previously been used for cleaning.

2.7. Reagents for wet chemistry

This subsection summarises the liquids and their sources used for wet chemistry in this study. Water used for all wet chemistry was purified to a resistivity of 18.2 MΩ with an Elga™ water filtration system installed in the ultra-clean geochemistry lab at VUW. All acids ultimately came from ThermoFisher™ (USA), in either Primar Plus™ or Optima™ grades (the former certified at 10-100 ppt, the latter at sub-ppt for most elements). Concentrated Primar Plus™ HNO_3 and HCl acids were sub-boiling distilled in Savillex™ (USA) Teflon distillers to produce highly pure acid with trace element concentrations similar to, or better than the commercial Optima™ grade acids. Teflon distilled (TD) HNO_3 and TD HCl were diluted and analysed with solution inductively coupled plasma mass spectrometry for blank testing before use of every batch. HBr, HF, H_2SO_4 and H_3PO_4 were all Optima™ grade from ThermoFisher (USA) and used as-is. Unless otherwise stated, all acids used in the following descriptions are TD or Optima™ grade in purity.

2.8. Sample digestions for isotopic and trace element analysis

Rock powders were digested following conventional HF and HNO_3 procedures for all samples (whole-rock, xenoliths, groundmass separates). Concentrated Optima grade HF was added at a 20:1 volumetric ratio with concentrated TD HNO_3 to sample powders using 2 mL HF per 100 mg of powder (and 100 μL of HNO_3). Digested powder masses were always ≤200 mg and usually 50-100 mg. Rock digestions were completed by overnight fluxing at 120 °C with the HF-HNO_3 mixture. After complete digestion, the volatile SiF_4 was evaporated from the solutions at 120-140 °C. Gels and biscuits of digested samples remaining after the first step were re-dissolved in 6M HCl, fluxed at 120 °C overnight and then dried down to a gel. This step was repeated twice in total to ensure the complete removal of fluoride complexes. After the second HCl dry-down, samples were re-dissolved in either 9 mL of 1M HNO_3 (for trace element analyses) or 2 mL of 9M HNO_3 (for Sr and Nd purification). Solutions with any remaining undissolved material were re-processed through the necessary previous steps until a limpid solution was obtained.

2.9. Solution inductively coupled plasma mass spectrometry (ICP-MS)

2.9.1. Solution ICP-MS analytical protocols

Trace element concentrations were measured by solution inductively coupled plasma mass spectrometry (ICP-MS) in samples digested with conventional HF-HNO_3 procedures (see section 2.8, above). All ICP-MS analyses were performed on a Thermo Scientific Element II sector-field ICP-MS at VUW. At the start of analytical sessions, counting rates were calibrated against at least five gravimetric multi-element solution standards with concentrations between 0.2-20.0 ppb per element (usually 0.2-10.0 ppb were used) that were prepared from high-purity (usually 1000 ppm) single-element solutions (Inorganic Ventures, USA). All elements were calibrated from a single multi-element standard for batches T1-8. However, high-field-strength elements (HFSEs: Ti, Ta, Sn, Zr, Hf, Th, Nb) were calibrated with their own multi-element standard for batches T9-10 to minimise complexing and loss of HFSEs from solution during long-term storage at low concentrations (e.g. Makishima et al., 2009). Samples were analysed alongside both total procedural blanks (TPB) and rock standards (AGV-2, BHVO-2, WS-E) to examine background contamination levels and to check for accuracy against published values internationally recognised rock standards. Measured trace element concentrations were generally accurate to 5-11 % (2 s.d.), which is described in section 2.9.3, below. Typical instrument operating conditions are summarised in Table 2.3.

Table 2.3. Operating conditions for sector-field Element II solution ICP-MS analyses.

Variable	Typical value
forward (RF) power	1200 W
reflected power	7-12 W
sample gas flow	1.1 L/min
auxiliary gas flow	0.8 L/min
oxide production	≤5 % on UO/U, always lower for Ba
high vacuum before plasma starts	7×10^{-8} mbar
high vacuum after plasma starts	2×10^{-7} mbar
fore vacuum before plasma starts	2×10^{-7} mbar
fore vacuum after plasma starts	2×10^{-3} mbar
medium resolution intensity	7-10 % of low resolution intensity
high resolution intensity	1-3 % of low resolution intensity
relative stability on ^{7}Li, ^{115}In, ^{238}U at tune-up	≤1 % (but often ≤0.5 %)
acid used for sample solutions and washes	1 % HNO_3 (batches T1-8) and 3 % HNO_3 (batches T9-10)
peristaltic pump speed	12 rpm
wash time between samples	3 minutes
take-up time for samples	90 seconds
drift monitor replicate analyses	bracketing every 4-6 sample analyses, followed by an additional wash 'sample' before sample (unknown) analyses resume

During each analytical session, mass offsets were determined and manually adjusted where necessary to ensure that counting occurred on the central portions of each mass peak. The isotopes used for quantification for each element were chosen taking into account their relative abundances versus any isobaric interferences from other elements or polyatomic species. During instrument tune-up, oxides were minimised to generally <5 % to reduce isobaric interferences (Table 2.3).

ICP-MS data reduction was carried out by first subtracting the contribution to the total signal from the TPB (measured in counts) from sample intensities. This included TPB contributions for calibration standards themselves. Calibration lines were determined for each analytical session with linear regression slopes of measured counts against gravimetrically determined concentrations (see above). Typical r^2 values were 0.9994-1.0000 for 4-point to 6-point regressions for all elements except Ta, which in some batches had r^2 values of 0.9870 (Batch T4), 0.9695 (Batch T5), 0.9469 (Batch T6). This occurred due to complexation and loss of Ta from calibration solutions in 1 % HNO_3 after prolonged storage for several weeks (Makishima et al., 2009). The Ta calibration line for Batch T9 had an r^2 value of 0.9990. Ta calibration lines from batches T7-8 and T10 had r^2 values of ~0.5-0.8. In this situation, Ta concentrations were calculated instead using single-point regressions with AGV-2, BHVO-2 or WS-E anchored through zero for these analytical sessions only.

Drift corrections were applied by normalising sample intensities with linearly interpolated adjustment factors that were determined by repeatedly measuring a 1.0 ppb multi-element standard every 4-6 samples. Post-analytical comparisons between measured and recommended concentrations for AGV-2, BHVO-2 and WS-E trace element concentrations (Jochum et al.,

2016) were used to verify the success of digestions, by comparing concentrations determined independently using the multi-element solution standard approach (above). A secondary normalisation was applied to the unknowns based on the recommended concentrations of AGV-2, BHVO-2 and WS-E reported by Jochum et al. (2016). This was necessary for quantifying Lu concentrations in batches T1-3 because Lu was missing from older multi-element standards but was measured on the instrument.

2.9.2. Dilution factors and batches

Dilution factors were 10^{-5} (sample powder/solution mass) for batches T5-10. Experimentation with both higher (10^{-3}) and lower (10^{-6}) dilution factors in earlier batches (T1-4) was undertaken in efforts to maximise signal-to-noise ratios for all elements whilst also preventing the counting of more abundant elements (Sr, Ba, V, Zr) from being switched from the electron multiplier to the Faraday cup 'analog-mode' and attendant nonlinearity issues at high counting rates. To monitor this issue, Ba, Sr and Zr were analysed on low and medium resolution simultaneously (where medium resolution offers a ~90% attenuation of the beam - see Table 2.3). Batch T4 samples were analysed twice, first at a dilution factor of 10^{-3}, for which Cs, all rare earth elements (REEs), Hf, Ta and Tl concentrations were determined. The concentrations of other elements in Batch T4 samples were determined at a dilution factor of 10^{-6} using new solution mixtures from the same digest stock which enabled most elements to be measured within the middle of the instrument's dynamic range at concentrations comparable to multi-element solution calibration standards.

2.9.3. Solution ICP-MS uncertainties

The uncertainties associated with calculated trace element concentrations produced via solution ICP-MS analysis can be caused by several factors. Blanks were measurable and were typically <0.01 ppb or <1 % of sample concentrations, and blank corrections were applied to all data (see section 2.9.1). Counting stability was generally excellent, with internal, within-run r.s.d. values of ~0.5-2.0 % for all elements, although up to ~5.0 % for some elements in Batch T4 (Nb, Ta, Th, REEs). The external reproducibility of internationally recognised rock standards (AGV-2, BHVO-2 and WS-E) was generally between 5-10 % (2 s.d.), which is summarised for all elements in Table 2.4. After data normalisation with the recommended rock standard values of Jochum et al. (2016) (e.g. using AGV-2), the trace element concentrations of other rock standards not used to calculate normalisation factors (e.g. BHVO-2 and WS-E) were generally within <1-2 % (1 r.s.d.) of values recommended by Jochum et al. (2016). Uncertainties introduced from

weighing inaccuracies were effectively insignificant, because the external precision of repeated reference mass measurements (20 mg to 10 g) was 0.00002-0.00004 g (2 s.d.) introduced at most 0.04-0.20 % uncertainty into measured sample powder masses of 20-100 mg. Quadratic addition of the uncertainties associated with the two subsequent gravimetric dilution steps were ≤0.04 %. When all sources of uncertainty are quadratically added, typical total analytical errors for solution ICP-MS analyses are 5.5-11.3 % (2 s.d.).

Table 2.4. External reproducibility of rock standards AGV-2, BHVO-2 and WS-E for all batches.

	AGV-2 (n = 11)			BHVO-2 (n = 5)			WS-E (n = 12)		
Isotope	**Average**	**2 s.d.**	**2 s.d. (%)**	**Average**	**2 s.d.**	**2 s.d. (%)**	**Average**	**2 s.d.**	**2 s.d. (%)**
Low resolution									
^{7}Li	11.49	2.02	17.6	4.84	0.85	17.6	13.50	0.26	1.9
^{85}Rb	66.6	7.8	11.7	9.3	0.2	2.3	25.5	1.4	5.5
^{88}Sr	654	36	5.5	391	17	4.3	406	13	3.3
^{89}Y	19.63	0.93	4.7	26.19	0.40	1.5	31.42	1.70	5.4
^{90}Zr	234	14	5.8	174	3	1.9	203	8	4.2
^{93}Nb	14.03	0.59	4.2	18.12	0.37	2.0	17.84	0.63	3.5
^{95}Mo	2.18	0.30	13.7	4.86	0.55	11.3	3.32	0.77	23.1
^{111}Cd	0.15	0.15	98.5	0.13	0.04	33.2	0.13	0.04	30.3
^{115}In	0.04	0.03	87.6	0.08	0.07	77.3	0.08	0.11	138.7
^{118}Sn	2.03	0.91	44.7	2.03	0.40	19.7	15.63	3.41	21.8
^{133}Cs	1.20	0.14	11.4	0.10	0.04	35.1	0.48	0.04	7.9
^{137}Ba	1116	56	5.0	129	5	3.7	336	13	3.8
^{139}La	36.53	4.86	13.3	15.04	0.34	2.3	26.61	0.98	3.7
^{140}Ce	67.4	6.2	9.2	37.3	1.4	3.8	59.7	1.9	3.2
^{141}Pr	7.94	0.75	9.4	5.32	0.14	2.7	7.74	0.26	3.4
^{146}Nd	29.60	2.37	8.0	24.32	0.15	0.6	32.71	1.16	3.6
^{147}Sm	5.42	0.40	7.5	6.03	0.13	2.2	8.61	0.43	5.0
^{151}Eu	1.60	0.19	11.7	2.04	0.04	2.0	2.17	0.14	6.4
^{157}Gd	5.06	0.45	8.8	6.12	0.24	3.9	7.07	0.54	7.6
^{159}Tb	0.657	0.043	6.5	0.935	0.025	2.7	1.079	0.053	4.9
^{163}Dy	3.46	0.17	5.0	5.27	0.09	1.7	6.16	0.35	5.7
^{165}Ho	0.670	0.035	5.3	0.983	0.018	1.8	1.176	0.072	6.2
^{166}Er	1.84	0.10	5.5	2.53	0.05	2.0	3.02	0.27	8.8
^{169}Tm	0.259	0.013	5.1	0.336	0.003	0.8	0.430	0.046	10.6
^{172}Yb	1.62	0.09	5.3	1.98	0.06	3.2	2.50	0.12	4.6
^{175}Lu	0.245	0.020	8.4	0.273	0.018	6.6	0.359	0.015	4.2
^{178}Hf	5.41	0.73	13.5	4.68	0.37	7.9	5.04	0.72	14.2
^{181}Ta	0.89	0.26	28.9	1.23	0.11	9.2	1.08	0.21	19.1
^{205}Tl	0.26	0.19	70.3	0.08	0.13	162	0.20	0.04	18.9
^{208}Pb	14.20	3.59	25.3	1.87	0.44	23.3	12.63	1.09	8.6
^{232}Th	6.17	0.54	8.7	1.23	0.07	5.7	2.94	0.17	5.9
^{238}U	1.85	0.08	4.1	0.41	0.01	3.3	0.62	0.02	3.6
Medium resolution									
^{45}Sc	12.41	0.90	7.2	31.35	1.27	4.1	27.90	1.71	6.1
^{51}V	117.1	5.4	4.6	318	5.1	1.6	335.5	10.8	3.2
^{52}Cr	15.61	1.62	10.4	297	14.65	4.9	96.8	3.83	4.0
^{59}Co	15.58	0.68	4.4	44.83	1.34	3.0	44.73	2.07	4.6
^{60}Ni	18.45	1.36	7.3	120.1	3.95	3.3	53.9	3.52	6.5
^{63}Cu	52.9	3.2	6.0	133.7	4.7	3.5	65.2	4.5	6.9
^{66}Zn	88.5	5.2	5.9	103.3	6.4	6.2	112.2	6.2	5.5
^{69}Ga	19.96	1.14	5.7	20.92	0.78	3.7	21.56	0.98	4.6
^{88}Sr	662	28	4.2	389	6	1.5	406	22	5.4
^{90}Zr	232	12	5.0	172	2	1.4	201	13	6.4
^{137}Ba	1121	67	6.0	131	3	2.5	334	18	5.3

2.10. Thermal ionisation mass spectrometry (TIMS)

Sr, Nd and Pb isotopes were measured on a ThermoFisher™ Triton thermal ionisation mass spectrometer (TIMS) at VUW. Pure separates of Sr, Nd and Pb were produced following conventional techniques (e.g. Pin et al., 2014) that are described in section 2.10.1, below. This includes the calibration profile for new LN-spec resin columns constructed in this study for separating Nd from other REEs (section 2.10.1.2) and tests that quantified the amount of Pb lost during pre-digestion leaching with HCl. Operating conditions for TIMS analyses are given in section 2.10.3. Blanks for all Sr-Nd-Pb batches (prefixed 'I' for isotope ratio batches and 'T' for trace elements: cf. section 2.9, above) are summarised in section 2.10.4 and Table 2.6. The treatment of internal and external precision is explained in section 2.10.5. Isotope ratio normalisation to internationally certified Sr-Nd-Pb isotope reference standards is summarised for data from this study and other studies that are used for comparison in section 2.10.6.

2.10.1. Purification and column separation procedures for isotopic analysis

Cation and anion exchange columns were used to separate Sr, Nd and Pb from dissolved samples, following digestions that are outlined in section 2.8, above. Column chemistry methodologies broadly follow those of Pin et al. (2014), with minor modifications that are summarised below. An illustrated summary of column Sr-Nd-Pb separation is shown in Fig. 2.2.

2.10.1.1. Strontium (Sr)

Columns were fashioned from 1 mL Eppendorf™ plastic pipette tips that were loaded with a porous polyethylene frit cut with a stainless-steel cork borer. Trial and error experimentation showed that cutting the pipette tips diagonally at their ends below the frit maximised drip rates (done with a stainless steel razor blade cleaned with ethanol and MQ H_2O), as shown for Sr-spec™ and TRU-spec™ (Triskem International), and AG1-X8™ (Biorad) columns in Fig. 2.2. These columns were cleaned then stored in a Teflon vat filled with 3 % HNO_3, and were removed at the time with of use Teflon tweezers, dried with clean-room wipes (3M™, USA) and placed into a custom-made perspex stand. Flow-rates were checked initially using MQ H_2O to ensure that subsequently loaded resin would be free-draining. This setup procedure also applies to TRU-spec™ and AG1-X8™ columns.

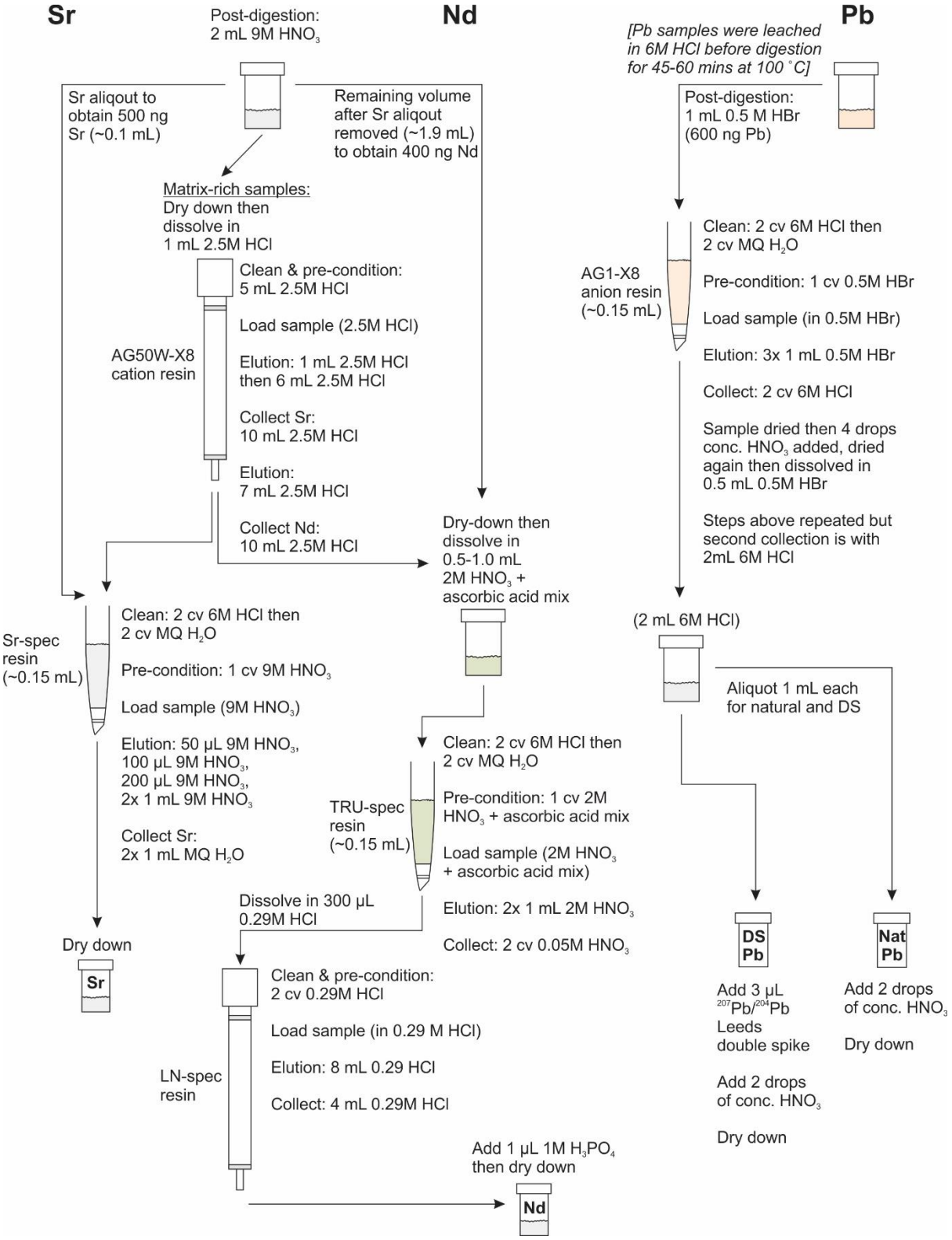

Figure 2.2. Summary cartoon showing chemical column separation procedures for Sr, Nd and Pb, following the methods of Pin et al. (2014).

About 7 drops of Sr-spec™ resin (~0.15 mL) were loaded into these columns and cleaned with two full column volumes (CV) of 6M HCl and MQ H_2O each, in that order. Waste was collected in plastic shot-glasses beneath the dripping columns. This step onwards is summarised in Fig. 2.2. HCl and MQ H_2O were dispensed from PFA squeezy bottles. The resin was then pre-conditioned with 1 CV 9M HNO_3. The required volume of sample needed for 500 ng Sr, already dissolved in 9M HNO_3 (usually ~0.1 mL for andesite samples in this study, from the same digestion used for Nd separation: section 2.10.1.2, below), was pipetted onto the resin gently, dripped from a 1 mL Eppendorf™ pipette down the sides of the column. Successive elution volumes were added, then allowed to drain, before the next elution followed. Elution steps were in volumes 50 μL, 100 μL, 200 μL, 1 mL then another 1 mL. Waste was discarded and the sample was collected into a pre-cleaned 3 mL Savillex™ PFA (USA) beaker (section 2.6) with 2 mL MQ H_2O. This was dried down at 100-120 °C, sometimes overnight, within sealed laminar flow cabinets.

Sr-spec™ resin used for chemical separation was pre-cleaned according to the following procedure (Charlier et al., 2006; see Table 2.6 for Sr blanks). Using a plastic retort stand, a 2 ml Biorad™ plastic column with reservoir extension filled with dry Sr-spec™ resin was suspended above a waste acid receptacle. The column was repeatedly filled with ~250 mL of acid that dripped through the resin according to the following cycle, after initially wetting the resin with MQ H_2O. (1) MQ H_2O, (2) 6M HCl, (3) 0.05M HNO_3, (4) 0.2M H_2SO_4. This was repeated a total of five times. During cleaning, the funnel was left covered with a sheet of Parafilm™ (Bemis Company, USA).

2.10.1.2. Neodymium (Nd)

Chemical separation of Nd required two sets of columns: the first with TRU-spec resin (to remove most matrix elements and provide a REE-enriched solution) and the second with LN-spec resin (to provide a purified Nd sample). TRU-spec resin was loaded into columns fashioned from 1 mL Eppendorf tips as described for Sr separation in section 2.10.1.1, above. LN-spec columns were constructed with larger 2 ml columns (Eichrom™) and calibrated chromatographically, which process is described below. The sequence for Nd separation is as follows.

Sample aliquots for Nd separation were already dissolved in 9M HNO_3 (from the same digestion used for Sr separation) were dried down after the Sr aliquot had been processed. These were then re-dissolved in a mixture of 2M HNO_3 + ascorbic acid that was made by dissolving 2.5 g of crystalline ascorbic acid (Sigma Aldrich™) in 50 mL of 2M HNO_3 within a pre-cleaned

PFA centrifuge tube (this volume being sufficient for processing 12 samples through TRU-spec resin). Ascorbic acid is used to reduce the iron to Fe^{2+} from Fe^{3+} as a better separation is achieved with the Fe in a reduced state (Pin et al., 2014). Once a clear solution was obtained, 0.5 mL of the 2M HNO_3 + ascorbic acid mix was added to the dried samples and beaker lids were closed tightly. Most andesitic samples examined in this study turned a murky olive-green/black colour on account of the Fe reduction; some Fe-poor samples (e.g. AGV-2) immediately achieved a transparent olive-green colour. The addition of 2M HNO_3 + ascorbic acid solution to dried samples was done ≤1 hr prior to commencing column separation. Any re-dissolved samples that were originally murky, that became transparent (as AGV-2), were diluted with a further 0.5 mL of 2M HNO_3 + ascorbic acid solution to ensure the Fe remained in its reduced state.

TRU-spec resin was loaded into columns fashioned from 1 mL Eppendorf pipette tips (see above), and cleaned with two full CV of 6M HCl and MQ H_2O each, in that order. Waste was collected in plastic shot-glasses beneath the dripping columns. This step onwards is summarised in Fig. 2.2. The resin was then pre-conditioned with 1 CV 2M HNO_3 + ascorbic acid mixture and the sample was loaded gently from a 1 mL Eppendorf™ pipette into the column. Elution volumes were added, then allowed to drain, before the next elution followed. The elution steps were 2x 1 CV 2M HNO_3 (not mixed with ascorbic acid) which was collected as waste then discarded. Samples were collected into pre-cleaned 7 mL Savillex™ PFA (USA) beakers (section 2.6) with 2x 1 CV 0.05M HNO_3. This was dried down at 100-120 °C, never overnight, in laminar flow cabinets, then re-dissolved in 300 μL 0.29M HCl in preparation for LN-spec columns (below).

A note on preparing 0.29M HCl: the 0.29M HCl used for dissolving samples and eluting with in LN-spec columns must closely match the concentration of the 0.29M HCl used to calibrate the LN-spec columns originally. This is because the separation of Nd from other REEs follows a chromatographic scheme, and depends on reproducible conditions to maximise the collection of the most Nd-enriched aliquot of eluted HCl, relative to other REEs. Over the course of this study, two batches of 0.29M HCl were made in 2 L PFA bottles. Using density-concentration relationships, the required masses of 6M HCl and MQ H_2O needed to produce 0.292M[1] HCl were calculated. First the densities of 6M HCl and MQ H_2O were measured with a density meter accurate to 0.0001 g/cm^3. For the second 0.29M HCl batch, these had densities of ϱ = 1.1011 g/cm^3 at 19.3 °C (6.230M HCl) and ϱ = 0.9993 g/cm^3 at 20.4 °C (MQ H_2O). For

[1] 0.292M is specified, despite rounding to 0.29M elsewhere in the text, to be consistent with subsequent densities, stock acid molarities and temperatures.

each batch, the predicted 0.29M HCl density was cross-checked with a density meter and found to be exactly as predicted (ϱ = 1.0034 at 20.3 °C) in the first batch (20 Sep 2018) and very similar (ϱ = 1.0036 at 20.4 °C) in the second batch (27 Feb 2019), with the small difference considered insignificant in changing the position of the Nd cut in the column elution profile.

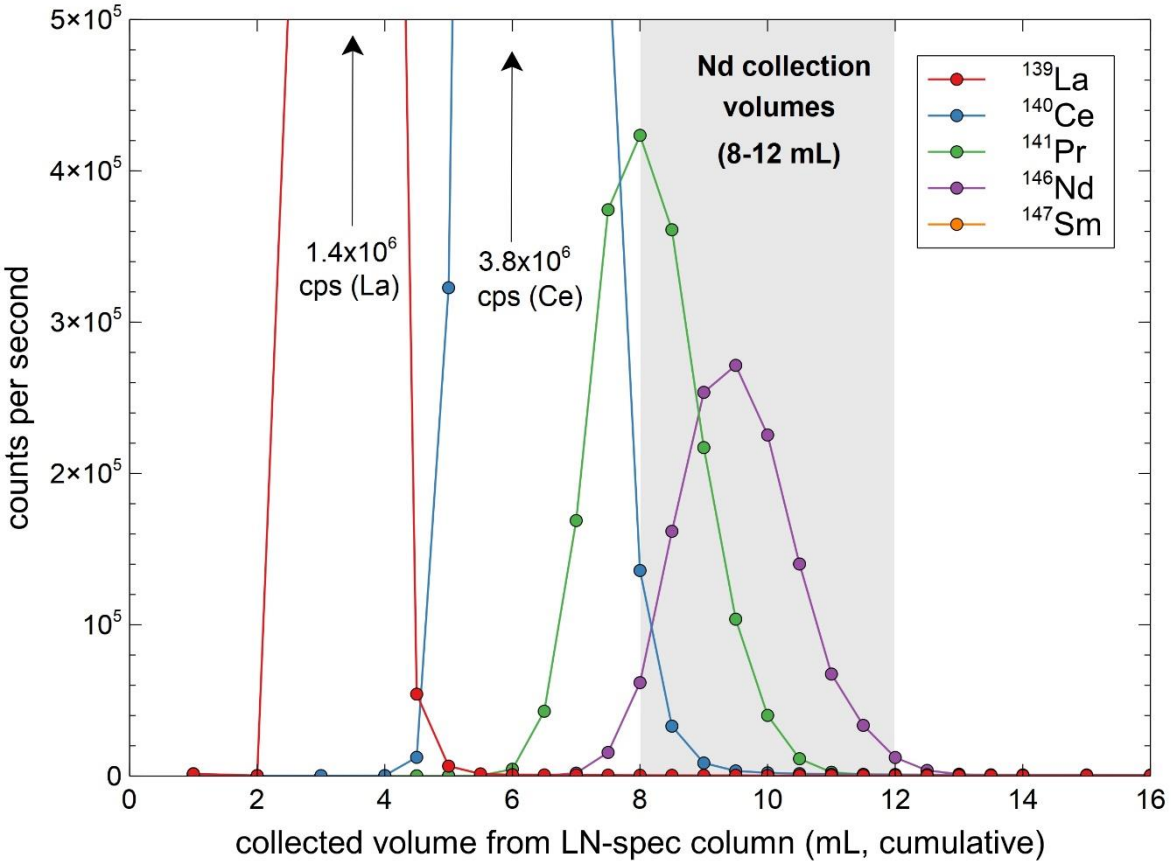

Figure 2.3. LN-spec column calibration profile for La, Ce, Pr, Nd and Sm as used for batches I2-6 in this study. Calibration was performed on Tongariro andesite sample LP009B which was previously passed through a TRU-spec column then re-taken up in 2 M HNO_3 + ascorbic acid ≤1 hr prior to column pass. Elutions were performed with 0.29M HCl. ^{147}Sm occurs in low concentrations that obscure its visibility.

The column separation of Nd from other REEs in this study used two sets of LN-spec columns. An older set of columns calibrated by Swallow (2018) were used for Batch I1, which were shorter and contained less resin. This resulted in poorer separation of neighbouring REEs from the Nd and thus greater isobaric interferences with other REEs (principally Ce) during TIMS analysis. To address this, a second set of LN-spec columns were constructed from new resin that was used for batches I2-6. The new LN-spec columns were cleaned with MQ H_2O and repeated washes with 6M HCl before first ever use. The calibration for this second set of columns was made with an internal standard (andesite sample LP009B) with 0.292M HCl prepared as described above. Column elutions were collected in 1.0 mL increments (0-4 mL;

14-20 mL) and 0.5 mL increments (4-14 mL) and analysed by solution ICP-MS, following procedures described above (section 2.9). Count rates were measured for ^{139}La, ^{140}Ce, ^{141}Pr, ^{146}Nd and ^{147}Sm, as shown in Fig. 2.3. The results of this calibration indicate that the optimal elution volumes to collect for Nd are the 8th, 9th, 10th and 11th millilitres (from zero) (Fig. 2.3).

LN-spec columns were cleaned immediately after preceding Nd separation with 2 CV 6M HCl, then further cleaned and conditioned with 2 CV 0.29M HCl. Before use, these columns were taken from storage (with 0.29M HCl) and re-conditioned with 2 CV 0.29M HCl before samples were loaded and eluted. Samples were previously dissolved in 300 μL 0.29M HCl, which was loaded gently into the columns with a 1 mL Eppendorf™ pipette. The columns were then eluted with 8 mL 0.29M HCl in 1 mL increments, which were allowed to drain before the subsequent elution was added, with these first 8 mL discarded as waste. The subsequent 8th, 9th, 10th and 11th mL 0.29M HCl elutions (from zero) were collected in pre-cleaned 7 mL Savillex™ PFA (USA) beakers, after first adding 1 μL 1M H_3PO_4 to each beaker with a 10 μL Eppendorf™ pipette (although it is recommended to use 0.01M H_3PO_4 for any future users of this method) (Figs. 2.2-2.3). These collections were dried down at 100-120 °C, never overnight, in sealed cabinets. Subsequent cleaning and storage procedures of the LN-spec columns are described above.

2.10.1.3. Lead (Pb)

Pb separation was performed using the traditional 'bromide method' (Strelow and Toerien, 1966) on AG1-X8 resin anion columns (Fig. 2.2), following techniques that are similar to those described by Kempton (1995). Two elution cycles, with an intermediate collection and dry-down stage, were used to obtain a highly pure Pb separate from digested samples. Sample masses weighed for digestions contained 600 ng Pb, which may be relatively high but was intended to compensate for Pb lost during leaching. Sample powders were leached before beginning digestions, following Baker et al. (2004) and Todd et al. (2015), which was important for removing anthropogenic contamination (from past usage of leaded petrol). Leaching also removes sub-millimetre isotopic heterogeneities that can develop in ~zero-age volcanic rocks between alteration minerals and their coexisting protoliths (e.g. Todd et al., 2015).

Initial attempts to separate Pb failed because of undissolved gel-like material in HBr solutions that were introduced to the columns. Investigations here deduced that the gel-like material inhibits flow through the column and binds to the resin, reducing its capacity to sorb the Pb from the mobile phase during the elution process with HBr. Consequently, Pb is generally lost as elution waste and elements other than Pb are over-represented in final collections, which

characteristically poisons the Pb ionisation during TIMS analysis. In the process of identifying this issue, tests were undertaken to ascertain whether poor Pb yields were due to excessive Pb loss during leaching. These experiments analysed the supernatant fluid (6M HCl) that was removed after leaching three samples with between 4.6-14.3 ppm Pb, following leaching in 6M HCl at 100 °C for 45-60 mins. Analyses were made via solution ICP-MS, per procedures outlined in section 2.9, above. Results of these experiments are reported in Table 2.5 and show that leaching removed 16-35 % of Pb in the samples (a basaltic-andesite [LP097], an andesite [LP039] and a dacite [LP234]).

Table 2.5. Results from Pb leaching tests wherein the Pb lost into the leachate was analysed.

Sample	Pb in powder (ppm)	Powder leached (mg)	Total Pb in powder (ng)	Total Pb in leachate (ng)	% Pb lost as leachate
LP039	9.8	109.98	172	1078	15.9
LP097	4.6	94.77	154	436	35.3
LP234	14.3	99.36	417	1421	29.3

The Pb separation process is summarised as follows. Prior to digesting samples for Pb separation, all samples were leached in 6M HCl for 45-60 mins at 100 °C, with the supernatant discarded. Immediately after leaching, HF + HNO_3 was administered to begin digestions in addition to <300 μL remaining after the leach. These were separate from Sr-Nd digestions. When Pb digestions were completed, following procedures outlined in section 2.8, samples were dried down to a gel then re-dissolved in 0.5M HBr. These solutions typically contained undissolved gel-like material, and to ensure only pure solutions were used for Pb separation, the HBr solutions were centrifuged for 5 mins in 2.5 mL centrifuge tubes that were pre-rinsed with 1 mL 0.5M HBr. Note that because Pb is highly soluble in 0.5M HBr, it is unnecessary (and undesirable—see below) to include the separated gel-like material during column separation.

Columns fashioned from 1 mL Eppendorf™ pipette tips, as for Sr separation (described in section 2.10.1.1, above), were loaded with 7 drops of AG1-X8™ resin (~0.15 mL) and cleaned with 2x CV of 6M HCl and MQ H_2O each, in that order. Waste was collected in plastic shot-glasses beneath the dripping columns. This step onwards is summarised in Fig. 2.2. The resin was then pre-conditioned with 1 CV 0.5M HBr. In their respective columns, samples were gently dripped from a 1 mL Eppendorf™ pipette down the sides of each column onto the resin bed. Elution volumes were added, then allowed to drain, before the next elution followed. The elution steps were 3x 1 CV 0.5M HBr, then the sample was collected in the original digestion beaker that had been cleaned during the elution process. To clean the 15-22 mL beaker for reuse, all gel-like material was washed out with MQ H_2O and discarded, then the beaker was filled with 3 mL 6M HCl and fluxed at 120 °C for 20 mins. The HCl was then discarded and the beaker was re-

rinsed with MQ H_2O, then used to re-collect the sample. Samples were collected with 2x 1 CV 6M HCl, which was dried down at 120-140 °C, then briefly re-dissolved with ~4 drops of conc. HNO_3 to remove HBr and destroy organic compounds derived from the resin. This was dried to a gel then re-dissolved in 0.5-1.0 mL 0.5M HBr. The process from pre-conditioning the columns to collecting samples was repeated in the same columns, with two differences: (1) only 2x (not 3x) 1 CV 0.5M HBr were eluted and (2) collection was with 2x 1 mL (not CV) 6M HCl into a pre-cleaned 2 mL Savillex™ PFA (USA) beaker. From this collection, 1 mL was aliquoted into a separate beaker, after first adding 3 μL of $^{207}Pb/^{204}Pb$ Leeds double-spike (DS). The amount of added DS was chosen based on tests with NBS982-DS mixtures that minimised the error magnification during data deconvolution (B. L. A. Charlier, pers. comm., 2017; following Thirlwall, 2000). The spike was added before the dry-down stage to ensure full sample-spike equilibration in the DS aliquot. About 2 drops of conc. HNO_3 were added to both natural and DS aliquots and then dried down at 120-140 °C on separate hotplates in separate cabinets. Note again, beakers used for DS collections were never mixed with beakers used for natural samples.

2.10.1.4. Matrix-rich samples

A number of samples prepared for Sr and Nd isotope ratio analysis repeatedly failed because column purification did not satisfactorily remove matrix material. Consequently, TIMS analyses failed because of poor ionisation and loss of sample (loads were characterised by ~1 mm tall mounds on loaded filaments). These samples (LP113, LP113GM, LP149, LP149GM, LP187X) possessed either flat CI-normalised REE profiles or positive Eu anomalies (LP113GM and LP187X). To achieve successful analyses on these samples, new digested material was prepared and separated in AG50W-X8™ cation columns in order to remove matrix elements. The appropriate collections from these initial pre-concentration columns were then processed as per standard procedures for Sr and Nd separation (sections 2.10.1.1-2.10.1.2, above). A description of the separation process follows.

The (reused) AG50W-X8™ cation columns were cleaned and pre-conditioned with 5 mL 2.5M HCl. Samples were previously dissolved in ~2 mL 2.5M HCl after digestions, and were loaded gently in to the column and allowed drain before beginning elutions. The separation on AG50W-X8™ cation columns is a chromatographic process and requires two successive cuts to be collected to give Sr-bearing and Nd-bearing solutions. The AG50W-X8™ columns used in this study were calibrated by Swallow (2018) and the elution process is described as follows. First, the columns were eluted with 1 mL 2.5M HCl, then another 6 mL 2.5M HCl once the first elution had dripped through. During this elution step, the original digestion beaker was rinsed

with MQ H_2O then with 6M HCl then MQ H_2O again. Another 10 mL 2.5M HCl was added to the column and collected into the rinsed digestion beaker. This collection was the Sr-bearing aliquot and was subsequently processed according to procedures outlined in section 2.10.1.1 to obtain Sr for TIMS analysis. After the Sr-bearing collection, further 7 mL 2.5M HCl was eluted through the columns, which was discarded as waste. A further 10 mL 2.5M HCl was added and collected into a separate, previously-cleaned 15-22 mL Savillex PFA (USA) beaker. This cut contained the Nd fraction and was processed according to the Nd separation procedure described in section 2.10.1.2.

2.10.2. Filament loading procedures

Filament componentry was cleaned after being stripped of previously-analysed Re filaments, with components used for spiked versus natural sample analysis dealt with separately here and in all subsequent steps. Filament shields were scrubbed with a fibreglass brush and boiled alongside filament mounts, blank-plates and slit-plates in a Pyrex® (Corning Inc.) beaker filled with MQ H_2O (~1 L) and a cap-full of 30-volumes concentrated H_2O_2. After boiling, the samples were dried in an oven in boats shaped from aluminium foil overnight at 80 °C. New Re filaments were cut to size with ceramic scissors, formed using a filament bending gauge then welded onto the filament mounts using a spot welder. Using a ThermoScientific™ outgasser unit, all filaments were heated to 4 A twice over a 66 minute cycle that was initiated under a 5-6 $x10^{-7}$ mbar vacuum. Filaments were stored in plastic boxes inside a desiccator until required.

Inside a laminar flow cabinet, each filament was loaded by first fusing small ~0.3 mm mounds of Parafilm™ (Bemis Company, USA) onto the Re filament wire that was heated with a 0.85 A current passing through it. The specific reagents used for Sr, Nd and Pb samples were administered with 10 μL Eppendorf™ pipettes. These reagents were evaporated to dryness at ~0.8 A and then quickly heated with a ~1.5-2.0 A current for 2 seconds to burn off the Parafilm™. Loading procedures for Sr, Nd and Pb are described as follows.

Sr single filaments (samples and NBS987 standards) were first loaded with 0.7 μL Ta_2F_5, (following Charlier et al., 2006), which is an activator that improves the ionisation efficiency of Sr. The samples obtained after drying Sr column collections (section 2.10.1.1) were re-dissolved in 1 μL of conc. HNO_3 and loaded onto Ta_2F_5 as it evaporated, and then the activator-sample mix was fully dried together. The NBS987 solution used in this study had a concentration of 901 ng/μL Sr and was loaded in amounts of 1 μL per each standard.

After column separation and drying, Nd samples were dissolved in 1-3 μL of 1M H_3PO_4 for batches I1-3 and with 0.01M H_3PO_4 for batch I6 and loaded onto double filaments. Note that

0.01M H_3PO_4 produced loads that were 80-90 % smaller than loads with 1M H_3PO_4; smaller loads from 0.01M H_3PO_4 were preferred for analysis. JNdi-1 (551 ng/μL) solution was loaded on filaments in amounts of 1 μL per standard.

Dried samples obtained from chemical separation of Pb (section 2.10.1.3) were dissolved in 1 μL silica gel (Gerstenberger and Haase, 1997). The gel was loaded onto each single filament then fused and quenched to produce a Pb-Si glass by ramping the filament current from 0.85 A to ~2.0 A over 1-2 seconds. The accuracy of Pb isotope ratio measurements was determined by analysing filaments loaded with NBS981 (for natural Pb) and an optimal mixture of NBS981-Leeds $^{207}Pb/^{204}Pb$ DS (for DS Pb). Both natural and DS Pb solutions (50 ng/μL) were loaded at a rate of 3 μL per filament, after first loading 1 μL of silica gel and partially drying the gel before adding the NBS981 solution.

2.10.3. TIMS instrumental operating conditions

All samples were analysed on Re filaments from the TIMS source chamber with a vacuum better than 2 x 10^{-7} mbar. All analyses were performed with various permutations of the standard nine Faraday cup configuration. For analyses in batches I1-3, the Faraday collectors were connected to 10^{11} Ω feedback amplifiers whereas samples in batches I4-6 were analysed after five 10^{13} Ω feedback amplifiers were installed in exchange for five of the stock 10^{11} Ω amplifiers during early 2019. After the 10^{13} Ω amplifiers were installed and the instrument was baked out, multiple daily gain calibrations for all amplifiers over subsequent weeks showed an initially rapid re-stabilisation of gain results. Variable gain sensitivities after the upgrade did not affect data comparability because gains were measured daily and all analyses were run with multiple internationally certified reference standards that were later used to externally normalise the analytical results (section 2.10.6, below).

Sr isotope measurements were performed on single outgassed Re filaments over 24 cycles of 10 block ratio measurements after a 20 second pre-baseline wait and 120 second baseline. Typical beams on ^{88}Sr were 4-6 V, which effectively ensured ^{84}Sr beams were at ~40 mV. For Batch I6, cups L1 (mass 84) and C (mass 85: Rb) were assigned to a 10^{13} Ω amplifiers to improve the stability of relatively low beam voltages on ^{84}Sr and ^{85}Rb which improved analytical precision. Inference corrections for ^{87}Rb on ^{87}Sr used the measured abundance of ^{85}Rb and $^{87}Rb/^{85}Rb$ = 0.385707 (Rosman and Taylor, 1997). During analysis, Sr isotope data was corrected for instrumental mass fractionation using $^{88}Sr/^{86}Sr$ = 8.37512, which is equivalent to $^{86}Sr/^{88}Sr$ = 0.1194 using the exponential mass fractionation law (Thirlwall, 1991). All sample wheels contained at least three NBS987 standards which were later used to determine external

precision and normalise data to allow robust comparisons between analytical batches and published data. Sr blanks were calculated via isotope dilution (ID) using an ^{84}Sr-enriched tracer, measured at the end of analytical sessions after all samples were completed.

Nd isotope measurements were performed over 24 cycles of 10 block ratio measurements for batches I1-3 and 18 cycles for batches I4-6. For all Nd analyses this was after a 20 second pre-baseline wait and 120 second baseline. Nd isotope analyses use closely-spaced opposing double outgassed Re filaments (separated by as little as 100 μm). One filament (evaporation side) was loaded with the sample and the opposing filament (ionisation side) was not loaded. Typical ionisation (unloaded) filament temperatures during analysis were ~1840 °C. Typical beams on ^{144}Nd were 0.5-3.0 V, which were strongly dependent on the closeness of the filament spacing (stronger beam = closer spacing). Nd isotope data were corrected for instrumental fractionation using ^{146}Nd/^{144}Nd = 0.7219 (O'Nions et al., 1977) and the exponential law, following Thirlwall (1991). All sample wheels contained at least three JNdi-1 samples to monitor accuracy and to determine the external precision. Standard-normalised data could then be used for robust comparisons between analytical batches and with published data.

Pb isotope measurements were performed on samples loaded onto single outgassed Re filaments with the double-spike (DS) method, following Thirlwall (2000). Pb natural and double-spike (DS) aliquots were analysed separately on different sample wheels. Except for a single sample (LP103) analysed in Batch I1, all other analyses of natural Pb aliquots were performed with a 10^{13} Ω amplifier assigned to the cup measuring ^{204}Pb (least abundant Pb isotope), which improved analytical precision (batches I4-5). Natural Pb aliquots were analysed for 24 cycles (Batch I1) or 18 cycles (batches I4-5) of 10 block ratio measurements. DS Pb aliquots were analysed for 18 cycles (Batch I1) or 12 cycles (batches I4-5) of 10 block ratio measurements. All measurements were performed after a 20 second pre-baseline wait and 120 second baseline. Measured natural and DS Pb isotope data were deconvolved using a modified Newtown-Raphson inversion (B. L. A. Charlier, pers. comm., 2017) with within-run uncertainties calculated using a 2000-iteration Mote-Carlo regression. All sample wheels contained at least three NBS981 standards to determine external reproducibility and to normalise data to allow robust comparisons between analytical batches and with published data.

2.10.4. Blanks for Sr-Nd-Pb isotope analyses

Blanks were determined for Sr-Nd-Pb isotope ratio analyses with solution ICP-MS and isotope dilution (ID) methods. Blanks analysed by solution ICP-MS did not include loading blanks whereas spiking methods did. ID spikes were sometimes used to determine Sr TPBs and a

$^{202}Pb/^{205}Pb$ DS was sometimes used to determine Pb TPB amounts and isotope ratios. Blank amounts are summarised in Table 2.6.

Table 2.6. Sr-Nd-Pb isotope ratio blank amounts for all TIMS samples.

Batch	Element[1]	Blank type[2]	Sr (pg)	Nd (pg)	Pb (pg)	Blank method	Date	Comment
I1	Sr	EF	83.3			ICP-MS	1/08/2018	
	Nd	EF		28.0		ICP-MS	1/08/2018	
	Pb	ND						Only LP103 run in this batch: SRM981 data are accurate and LP009B and LP024 Pb analyses are in excellent agreement with LP103 result from the same stratigraphic unit
I2	Sr	TPB	83.9			ID TIMS	17/08/2019	
	Nd	EF		13.4		ICP-MS		B. L. A. Charlier (pers. comm., 2019)
I3	Sr	TPB	37.8			ID TIMS	8/02/2019	
I4	Pb							Assume as for Batch I5 because of done in same period from same resin and materials
I5	Pb	TPB			126.4	^{202}Pb-^{205}Pb DS	10/07/2019	From wheel 0540 in $^{202}Pb/^{205}Pb$ spreadsheet provided by B. L. A. Charlier (pers. comm., 2019); the isotopic composition is available for this blank
I6	Sr (normal)	TPB	15.0			ID TIMS	17/07/2019	All samples except LP113GM and LP149GM
	Sr (MQ wash)	EF	3140			ICP-MS	2/07/2019	For samples LP113GM and LP149GM
	Nd	EF		400		ICP-MS	2/07/2019	

[1] 'normal' and 'MQ wash' refer to different sample treatment between most samples versus LP113GM and LP149GM, respectively. See text in section 2.10.4 for details.
[2] TPB = total procedure blank which includes loading, EF = full procedure except for filament loading, ND = not determined.

All blanks for Sr-Nd-Pb chemistry were generally excellent, being between 13.4-83.9 pg (Table 2.6), and can be considered negligible against the amount of sample analysed. However, two samples analysed for Sr were only available as ~1 mg amounts of powder smeared over the inner surfaces of 2 cm x 7 mm glass vials, and were collected with water from an old MQ H_2O squirt bottle, which was evidently less clean than all other reagents used for Sr-Nd-Pb wet chemistry (Table 2.6). The blank amount for these samples (LP113GM and LP149GM) is ~3140 pg, which for ~1 mg of sample with 230-258 ppm Sr, equates to 1.2-1.4 % of the Sr in the sample. These samples are groundmass separates that have paired whole-rock Sr isotope ratio

measurements, which follow the trend observed in other data where blanks were negligible (section 4.3.3.4). This provides confidence that the analyses for LP113GM and LP149GM are accurate.

2.10.5. TIMS uncertainties

The sources of uncertainty contributing to TIMS analyses of Sr-Nd-Pb isotope ratios were primarily the counting statistics for each individual measurement, and external reproducibility on independent repeated measurements of the standards. Blanks were negligible and were discussed in section 2.10.4, above. Internal precision was generally 5-10 ppm for $^{87}Sr/^{86}Sr$ analyses, 5-30 ppm for $^{143}Nd/^{144}Nd$ analyses, 30-50 ppm for $^{206}Pb/^{204}Pb$ and $^{207}Pb/^{204}Pb$ analyses, 40-60 ppm for $^{208}Pb/^{204}Pb$ analyses, 10 ppm for $^{207}Pb/^{206}Pb$ analyses and 15-20 ppm for $^{208}Pb/^{206}Pb$ analyses. External reproducibility was generally 2- to 3-times poorer than internal precision and is summarised in Table 2.7. Both internal precision (2 s.e.) and external reproducibility (2 s.d.) were quadratically added to give a robust representation of the overall uncertainty associated with an analysis. Uncertainties calculated in this fashion are used in geochemical plots presented in this thesis.

2.10.6. Normalisation to reference standards

2.10.6.1. Sr-Nd-Pb data from this study

All Sr-Nd-Pb isotope data produced in this study, and data from other studies used in comparisons, were normalised to recommended values of internationally certified reference standards. This was done to ensure comparability of data between separate analytical batches. Standards used to monitor external accuracy and precision during analytical sessions in this study were NBS987[2] (Sr), JNdi-1 (Nd) and NBS981 (Pb). Sample data was normalised to NBS987 $^{87}Sr/^{86}Sr = 0.710248$ (Thirlwall, 1991) and JNdi-1 $^{143}Nd/^{144}Nd = 0.512115$ (Tanaka et al., 2000) which is equivalent to LaJolla $^{143}Nd/^{144}Nd = 0.511858$ (Carlson and Langmuir, 1978). Pb isotope ratios were normalised to NBS981 with the values of $^{206}Pb/^{204}Pb = 16.9409$, $^{207}Pb/^{204}Pb = 15.4956$, $^{208}Pb/^{204}Pb = 36.7228$, $^{207}Pb/^{206}Pb = 0.91469$, $^{208}Pb/^{206}Pb = 2.16770$ from first row of Table 9 "this study, preferred values" in Thirlwall (2000).

[2] NBS987, as named here, is synonymous and isotopically identical with the more commonly known SRM987. NBS987 used in this study was purchased before 1990 (B. L. A. Charlier, pers. comm., 2019). Subsequent corporate changes from the manufacturer have resulted in originally-named National Bureau of Standards (NBS) materials as being renamed Standard Reference Materials (SRM).

Table 2.7. External reproducibility of $^{87}Sr/^{86}Sr$ (NBS987), $^{143}Nd/^{144}Nd$ (JNdi-1) and Pb isotope ratios (NBS981).

		NBS987	JNdi-1	NBS981				
B	**Stat.**	**$^{87}Sr/^{86}Sr$**	**$^{143}Nd/^{144}Nd$**	**$^{206}Pb/^{204}Pb$**	**$^{207}Pb/^{204}Pb$**	**$^{208}Pb/^{204}Pb$**	**$^{207}Pb/^{206}Pb$**	**$^{208}Pb/^{206}Pb$**
I1	n	5	3	9	9	9	9	9
	Ave.	0.710269	0.512080	16.9423	15.5000	36.7265	0.91487	2.16774
	2 s.d.	0.000002	0.000044	0.0004	0.0006	0.0016	0.00002	0.00005
	2 s.d. ppm	2	87	26	38	44	21	22
I2	n	3	8					
	Ave.	0.710267	0.512105					
	2 s.d.	0.000023	0.000008					
	2 s.d. ppm	32	15					
I3	n	9	10					
	Ave.	0.710270	0.512104					
	2 s.d.	0.000010	0.000017					
	2 s.d. ppm	15	32					
I4	n			9	9	9	9	9
	Ave.			16.9433	15.5018	36.7328	0.91492	2.16798
	2 s.d.			0.0014	0.0021	0.0064	0.00006	0.00024
	2 s.d. ppm			80	136	175	70	110
I5	n			28	28	28	28	28
	Ave.			16.9418	15.4998	36.7265	0.91488	2.16780
	2 s.d.			0.0029	0.0043	0.0090	0.00012	0.00020
	2 s.d. ppm			171	275	246	130	94
I6	n	7	4					
	Ave.	0.710267	0.512099					
	2 s.d.	0.000009	0.000004					
	2 s.d. ppm	12	8					

B = batch number, Stat. = statistic, Ave. = average, n = number of standard analyses in this batch.
NBS987 (901 ng/μL) was loaded with 0.7 μL Ta_2F_5 activator 1 μL of standard.
JNdi-1 (551 ng/μL) was loaded with 1.0 μL 1M H_3PO_4 and 1 μL of standard.
NBS981 (50 ng/μL) was loaded with 1.0 μL silica gel 3 μL of standard.

2.10.6.2. Sr isotope data from other studies

Data from other studies were normalised to NBS987 $^{87}Sr/^{86}Sr = 0.710248$ (Thirlwall, 1991) as follows. Hobden (1997) and Hobden et al. (1999) reported data relative to NBS987 $^{87}Sr/^{86}Sr = 0.710248$ (samples TG001, TG020, TG051, TG074, TG080, TG098, TG112, TG115, TG135, TG152, TG156, TG161, TG163, TG182, TG242, TG262, TG280, TG288, TG289, TG376, TG381) and NBS987 $^{87}Sr/^{86}Sr = 0.710249$ (samples TG276B, TG269) and SRM987 $^{87}Sr/^{86}Sr = 0.710234$ (samples TG035, TG086, TG272, TG273). Price et al. (2015) reported data relative to NBS987 $^{87}Sr/^{86}Sr = 0.710230$ for all samples. Sutton (1995) reported data relative to NBS987 $^{87}Sr/^{86}Sr = 0.710250$ for sample R623. Gamble et al. (1993) reported data relative to NBS987 $^{87}Sr/^{86}Sr = 0.710195$ for all samples. Lee (2008) reported data relative to NBS987 $^{87}Sr/^{86}Sr = 0.71024$ for all samples.

2.10.6.3. Nd isotope data from other studies

Data from other studies were normalised to LaJolla $^{143}Nd/^{144}Nd = 0.511858$ (Carlson and Langmuir, 1978) which is equivalent to JNdi-1 $^{143}Nd/^{144}Nd = 0.512115$ (Tanaka et al., 2000), sometimes via equivalent values from other reference standards, as follows. Hobden (1997) reported $^{143}Nd/^{144}Nd$ ratios normalised to the Aldrich standard value of 0.511427 for all samples, which shifts to 0.511419 when normalised to LaJolla $^{143}Nd/^{144}Nd = 0.511858$ (Langmuir and Carlson, 1978). Price et al. (2015) reported $^{143}Nd/^{144}Nd$ ratios normalised to LaJolla = 0.511860 for all samples. Sutton (1995) reported replicate analyses of $^{143}Nd/^{144}Nd$ for the Open University (UK) J&M standard = 0.511780, which shifts to 0.511833 when normalised to LaJolla $^{143}Nd/^{144}Nd = 0.511858$ (B. L. A. Charlier pers. comm., 2019). Gamble et al. (1993) reported BCR-1 = 0.512653, which shifts to 0.512629 when normalised to LaJolla $^{143}Nd/^{144}Nd = 0.511858$ (Thirlwall, 1991; Raczek et al., 2003). Lee (2008) reported Nd isotope analyses on xenolith samples collected by Graham (1985), some of which were analysed for Nd isotopes by Graham et al. (1990), but not the samples used for comparison in this study (17423 and 17457). Graham et al. (1990) reported $^{143}Nd/^{144}Nd$ ratios relative to BCR-1 = 0.512654±5, and for samples that were re-analysed for Nd isotopes by Lee (2008), the Graham et al. (1990)/Lee (2008) average normalisation factor (± 2 s.d.) was 1.000031201±34133. Thus, Lee (2008) $^{143}Nd/^{144}Nd$ ratios for samples 17423 and 17457, which were collected by Graham (1985) but not analysed for Nd isotopes by Graham et al. (1990), relative to the La Jolla values in this study have an overall normalisation factor of 0.999951 to make them equivalent to La Jolla $^{143}Nd/^{144}Nd = 0.511858$ (Lugmair and Carlson, 1978). The quadratically combined uncertainties from normalisation factors, the BCR-1 reproducibility of Graham et al. (1990) and Lee (2008) internal and external uncertainties, are ±0.000028 (sample 17423) and ±0.000025 (sample 17457).

2.10.6.4. Pb isotope data from other studies

Pb isotope data from other studies, except Price et al. (2015), were normalised to the values for NBS981 recommended by Thirlwall (2000) of $^{206}Pb/^{204}Pb = 16.9409$, $^{207}Pb/^{204}Pb = 15.4956$, $^{208}Pb/^{204}Pb = 38.7228$, $^{207}Pb/^{206}Pb = 0.91469$, $^{208}Pb/^{206}Pb = 2.16770$. The Pb isotope data of Hobden (1997) were not used because they were calculated using external normalisation (i.e., not via DS methodologies) and are subject to large uncertainties that are equivalent to inter-sample variation. Gamble et al. (1996) reported replicate analyses of NBS981 with mean values of $^{206}Pb/^{204}Pb = 16.937$, $^{207}Pb/^{204}Pb = 15.492$ and $^{208}Pb/^{204}Pb = 38.708$. Price et al. (2015) reported Pb isotope data collected via multi-collector (MC) ICP-MS with the Tl-doping technique, after samples were leached for an uncertain time in room-temperature 6M HCl, with analyses

performed at the University of Melbourne (UM). Multi-year averages reported for BCR-2 by Price et al. (2015) at the UM MC-ICP-MC laboratory are $^{206}Pb/^{204}Pb$ = 18.759±9, $^{207}Pb/^{204}Pb$ = 15.619±10 and $^{208}Pb/^{204}Pb$ = 38.726±35. These BCR-2 values are in agreement with reference values for non-leached BCR-2 analyses but are outside of analytical error for leached BCR-2 analyses reported by Todd et al. (2015) for the Tl-doping technique, which indicates that if similar leaching procedures were employed for most MC-ICP-MS BCR-2 analyses at the University of Melbourne, then leaching was less thorough than the Todd et al. (2015) procedures (60 mins in cold 6M HCl in an ultrasonic bath, then washed twice with water, then 30 mins in fresh 6M HCl at 100 °C), which seems likely. All BCR-2 Pb isotope ratios reported by Todd et al. (2015) are effectively normalised to the NBS981 Pb isotope ratios reported by Galer and Abouchami (1998) which are in close agreement with those of Thirlwall (2000, cited above) that were determined via $^{207}Pb/^{204}Pb$ DS TIMS analyses. On this basis, no external normalisation was made to the Price et al. (2015) Pb data because they should correspond, within analytical error, to equivalent NBS981 Pb isotope ratios of Thirlwall (2000) that were used for normalisation in this study. Pb isotope data reported by Shane et al. (2017) were also performed at the UM MC-ICP-MS laboratory, following pre-digestion leaching procedures (6M HCl for 1 hr at 100 °C) that are also less thorough than those of Todd et al. (2015). The multi-year BCR-2 Pb isotope values reported by Shane et al. (2017: $^{206}Pb/^{204}Pb$ = 18.758±9, $^{207}Pb/^{204}Pb$ = 15.619±10 and $^{208}Pb/^{204}Pb$ = 38.726±35) are effectively identical to those of Price et al. (2015). On this basis, the Pb isotope data reported by Shane were not normalised because they should be equivalent to NBS981 Pb isotope ratios of Thirlwall (2000) that were used for normalisation in this study.

Chapter 3

A high-resolution $^{40}Ar/^{39}Ar$ edifice construction history of lavas and pyroclastic deposits on Tongariro volcano, New Zealand

"Once a valley, always a valley"

T. W. Sisson (c. 2016)

3.1. INTRODUCTION

The most typical surficial expressions of arc magmatism are large (tens to hundreds of cubic kilometres) composite stratovolcanoes (Gill, 1981; Sigurdsson et al., 2015). The temporal and spatial records of how stratovolcanoes grow and their associated eruptive compositions provide a window into arc magmatic processes on scales of the order of 10^4-10^5 years or more. The keys to tracing and interrogating such processes lie with detailed mapping and the recognition of compositionally-related eruptive units, coupled with accurate age determinations to quantify stratigraphic ordering. $^{40}Ar/^{39}Ar$ geochronology has been key to establishing the stratigraphic chronology of stratovolcanoes because it is applicable to some lavas (e.g. Dungan et al., 2001; Gamble et al., 2003; Fierstein et al., 2011; Conway et al., 2016), which are generally the best-preserved volcanic products on stratovolcano edifices (e.g. Singer et al., 1997; Hildreth and Fierstein, 2012; Sisson et al., 2014). Pyroclastic deposits are both highly vulnerable to erosion on the edifice itself and tend to weather rapidly during soil formation at lower elevations. Because of these factors, records of pre-Holocene explosive eruption deposits are incomplete and are biased towards preserving only the larger events (≥1 km^3) (Watt et al., 2013; Weller et al., 2015).

This study presents the results of a mapping campaign that focussed on the lavas of Tongariro volcano, New Zealand. New field observations, along with new and existing geochemistry and $^{40}Ar/^{39}Ar$ geochronology results, are used to establish a high-resolution eruptive chronology for edifice-forming products on Tongariro volcano, as well as eruptions from peripheral vents. The resulting map provides a platform for exploring fundamental questions regarding volcanic behaviour and the completeness of records on mid-latitude stratovolcanoes, as follows.

- Are there biases in exposure and/or preservation in volcanic materials on stratovolcano edifices that relate to various degrees of ice coverage during glacial/interglacial cycles?
- Are valleys cutting into previously-glaciated Quaternary stratovolcanoes primarily erosional features, or are could they in contrast represent constructional landforms produced by the preferential emplacement of lava flows along the ridges between valleys (Conway et al., 2015)?
- Does deglaciation cause an increase in eruption rates at stratovolcanoes due to edifice de-loading and depressurisation?

The chronostratigraphy established in this chapter also provides a basis for examining how compositional and isotopic compositions of erupted magmas vary over Tongariro's lifespan, which is explored in Chapter 5.

It has been shown that the presence and absence of glacial ice determines emplacement behaviour and the preservation potential of erupted materials at stratovolcanoes (e.g. Mathews, 1952; Lescinsky and Sisson, 1998; Conway et al., 2015). Lescinsky and Sisson (1998) report abundant Pleistocene ice-impounded lavas on Mount Rainier that did not flow onto valley floors because the valleys were occupied by glaciers. Hildreth and Fierstein (2012) report rare ponds of welded ignimbrite erupted from Katmai volcano that were emplaced over glaciers at ~23 ka, during the coldest part of the Last Glaciation, and are not preserved where ice existed at this time. These ponded ignimbrite deposits are found 21 km east of Katmai, which indicates that a large volume of erupted material is absent from proximal, *in situ* records. In an older example, tephra deposits up to 30 cm thick are preserved at Lake Tapps, 200 km from their vent source at Kulshan caldera in Washington State. The only proximal deposit from this eruption is the caldera fill, and there are no preserved extra-caldera ashfall or pyroclastic deposits (Hildreth, 1996). The area between the preserved tephra deposits and the caldera source was a previously glaciated part of Puget Sound (Pringle, 2008), and it is inferred that ice coverage precluded the *in situ* preservation of eruption products. Lava emplacement over snow has also been observed historically at Tolbachik volcano where the likelihood of preservation is related to whether lavas burrow down to bedrock or remain above ice masses (Edwards et al., 2015). At times of significant ice coverage on stratovolcanoes, the latter is evidently more likely (e.g. Lescinsky and Sisson, 1998).

Glaciovolcanism has been previously recognised at Tongariro and Ruapehu volcanoes in New Zealand (Conway et al., 2015, 2016; Townsend et al., 2017; Cole et al., 2018). Tongariro displays evidence for extensive Quaternary glaciation in the form of moraines (Eaves et al., 2016a) and lava-ice interaction textures (Cole et al., 2018). However, the degree to which glaciation has affected preserved volumes and edifice growth styles has not previously been quantified on Tongariro. As a counterpoint to the potential for interaction with glacial ice, a traditional view has been that stratovolcanoes grow as symmetrical cones during bursts of eruptive activity (like Tongariro's Ngauruhoe cone in the present context) and are subsequently scoured out by glaciers to produce valleys (Hobden et al., 1996; Singer et al., 1997; Dungan et al., 2001). In such models, alternating phases of growth (e.g. during interglacials or when edifice-building outpaces glacial erosion) and erosion (e.g. during glacial periods and eruptive quiescence) are favoured to explain stratovolcano geomorphology. However, accumulating evidence for lava-ice interactions at many stratovolcanoes favours syn-glacial edifice growth models. In opposition to traditional models, syn-glacial growth models interpret valleys as being constructional landforms where the valley walls and ridgetops are built up around ice masses. Syn-glacial edifice

growth readily explains how some unusual and asymmetric landforms can form in upper edifice regions, without needing to assume caldera collapse or sector collapse. Debate also surrounds whether eruptive rates at stratovolcanoes increase after deglaciation. Some studies suggest that depressurisation of a magma system due to ice loss and edifice unloading triggers increased eruptive rates (Jicha et al., 2012; Rawson et al., 2016). However, the spectrum of documented case examples shows contradictions: in some, peak eruptive rates are occur within glacial periods (e.g. Calvert et al., 2018), whereas in others, increased eruptive rates occur within interglacial periods.

3.1.1. Previous work

Before the recent mapping project of Tongariro National Park (Conway et al., 2016; Townsend et al., 2017), mapping at Tongariro volcano had been limited to the compilation by Gregg (1960), work on the northern flanks undertaken by Nairn (1996) and regional scale (1:250,000) compilations with some new interpretations (Lee et al., 2011). The most substantial previous geochemical and geochronological studies were by Hobden (1997) and Hobden et al. (1996), respectively, building on earlier work on edifice-forming materials by Topping (1974), Cole (1978) and Wahyudin (1993). Other areally-limited but peer-reviewed mapping studies are from Hobden et al. (2002) on Ngauruhoe and Cole et al. (2018) on parts of Tongariro's upper edifice. Building on these pre-existing datasets, the current study presents a suite of new geochronological and geochemical data that are used to revise the stratigraphic framework set out in Townsend et al. (2017). New observations are integrated with earlier work to produce a detailed map of edifice-forming volcanic products on Tongariro and to reinterpret the edifice construction history of the volcano.

3.1.2. Geological setting

Tongariro volcano is located in the southern Taupō Volcanic Zone (TVZ) where volcanism has produced primarily intermediate-composition products, in contrast to the rhyolite-dominated central TVZ ≥30 km to the north (Wilson et al., 1995). The TVZ is an actively rifting continental volcanic arc (also referred to as the Taupō Rift: Villamor et al., 2017) fuelled by the westward subduction of the Pacific Plate beneath the Indo-Australian Plate. Whilst the TVZ is a rift, the convergence rate projected from rigid motion of the Pacific and Australian plates is ~43 mm/yr in the central and southern TVZ (Nicol et al., 2007; DeMets et al., 2010). Active extension is greatest (~15 mm/yr) in the northern TVZ arc at the Bay of Plenty coast and decreases to ~7 mm/yr at the latitude of Tongariro, as demonstrated by GPS measurements (Wallace et al., 2004;

Beavan et al., 2016; Gomez-Vasconcelos et al., 2017). Rifting terminates ~20 km south of Ruapehu volcano, which is ~20 km south of Tongariro itself (Fig. 3.1; Wallace et al., 2004; Villamor and Berryman, 2006).

Both Tongariro and Ruapehu occupy active grabens between uplifted eastern (Kaimanawa Range) and western shoulders that are underlain by Mesozoic greywackes, argillites and sandstones. This graben is superimposed on pre-existing structures associated with the NNW-trending Hauraki Rift (Hochstein and Ballance, 1993) and is parallel to the vent alignment of both Tongariro and Ruapehu (Townsend et al., 2017). Despite evidence for previous and ongoing active extension (Villarmor and Berryman, 2006; Wallace et al., 2004; Jiao et al., 2014; Beavan et al., 2016), it is unclear whether rifting-related subsidence in the southern TVZ has shifted the summit elevations of Tongariro or Ruapehu relative to sea level. If, however, summit elevations have been shifted >100 m higher or lower, relative to sea level, over the lifespans of Tongariro and Ruapehu, this will have possibly affected the extent of ice cover during glacial periods on these volcanoes. Tongariro has also experienced more advanced intra-edifice down-faulting for similar-age materials than at Ruapehu (Fig. 3.1). In the case of Tongariro, this has lowered central edifice areas relative to flank regions (Gomez-Vasconcelos et al., 2017).

Tongariro and Ruapehu are the only Quaternary stratovolcanoes in New Zealand that have supported substantial glaciers repeatedly over their lifespans (McArthur and Shepherd, 1990; Spörli and Rowland, 2006; Conway et al., 2015; Eaves et al., 2016a; Townsend et al., 2017; Cole et al., 2018). Moraine deposits are recorded at both volcanoes for at least three periods of major glacial advance in their 200-300 kyr histories (Conway et al., 2015; Eaves et al., 2016a; Townsend et al., 2017) but are absent from other volcanic edifices in the southern TVZ. Tongariro's composite edifice is constructed from volcanic products erupted from multiple vent foci (Gregg, 1960; Cole, 1978; Hobden et al., 1996; Townsend et al., 2017; Cole et al., 2018). Previous studies propose as many as 17 vents (e.g. Hobden et al., 1996) but the exact number is uncertain. Younger vents, such as Ngauruhoe and Red Crater, are obvious from their prominence in the landscape and the presence of lava flows that can be traced back to their source vents (Fig. 3.2). However, the locations of older vents (>50 ka to much older) is less clear because they are buried by younger eruptive materials, sediments, or are represented by missing edifice material. From the work presented here, the oldest erupted products that can be directly (physically) linked with their source vent are those forming North Crater (Fig. 3.2), with a new adopted age of 45-36 ka (see section 3.3.2.9 and Appendix 2).

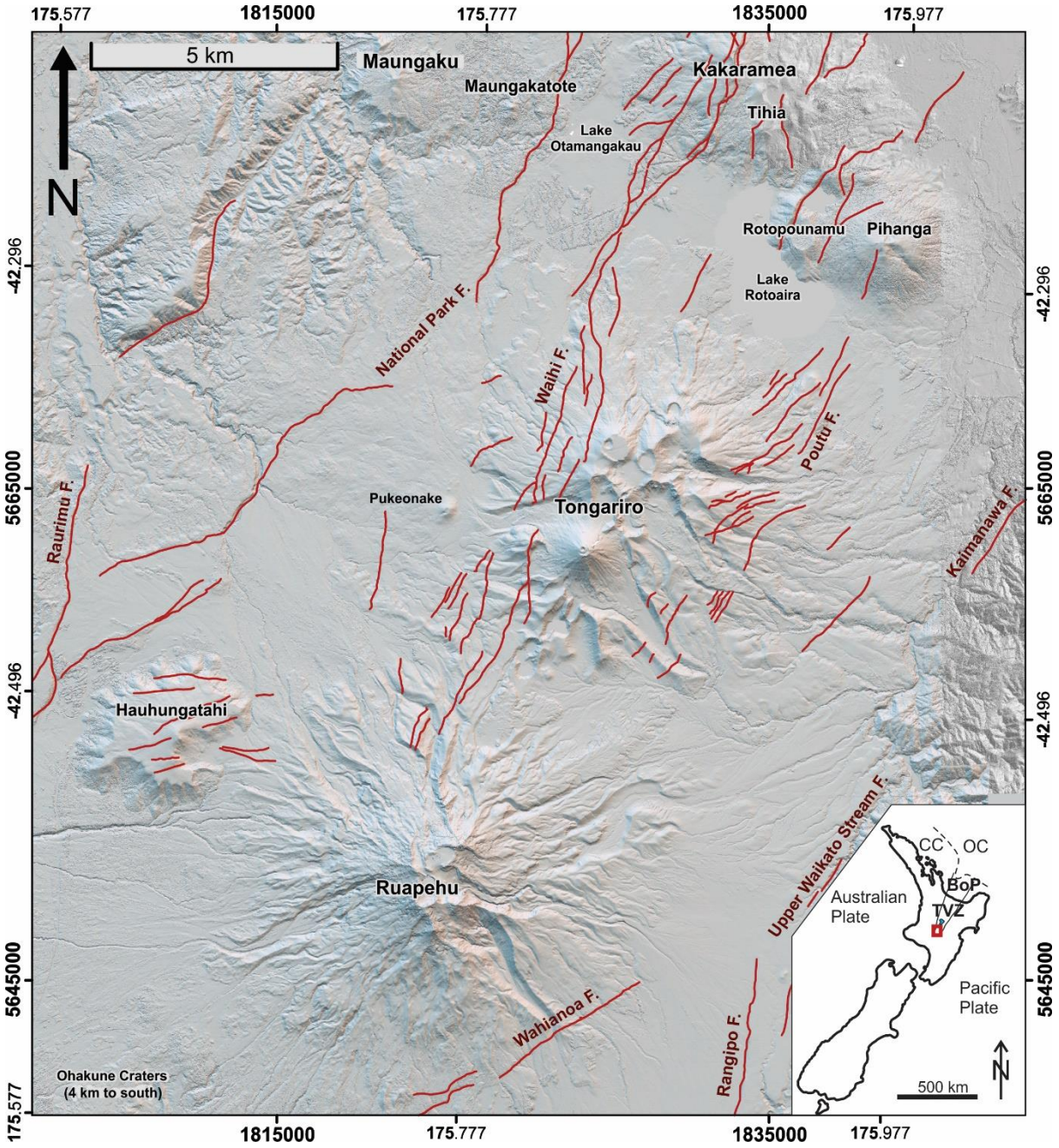

Figure 3.1. (Duplicate of Fig. 1.1.) Map of intermediate composition volcanoes that dominate the southern TVZ, with inset showing the position (red box) in New Zealand's North Island. Red lines indicate traces of faults that were active during the Quaternary, following Townsend et al. (2017), which trend strongly to the NNE-SSW, parallel to Tongariro and Ruapehu vents. The boundary between the continental crust (CC) and oceanic crust (OC) is after Gamble et al. (1993), and occurs near the Bay of Plenty (BoP). Subduction of the Pacific Plate is westward beneath the Australian Plate at ~2-5 cm/yr from south to north along the North Island. Map projection is the New Zealand Transverse Mercator 2000 (NZTM2000). The 2 m-resolution digital surface model (DSM), which is the basis for this map and all others in the thesis, was developed by GNS Science from photogrammetry of aerial photos obtained in 2010 and 2012 and is reported with methodologies by Gómez-Vasconcelos et al. (2016).

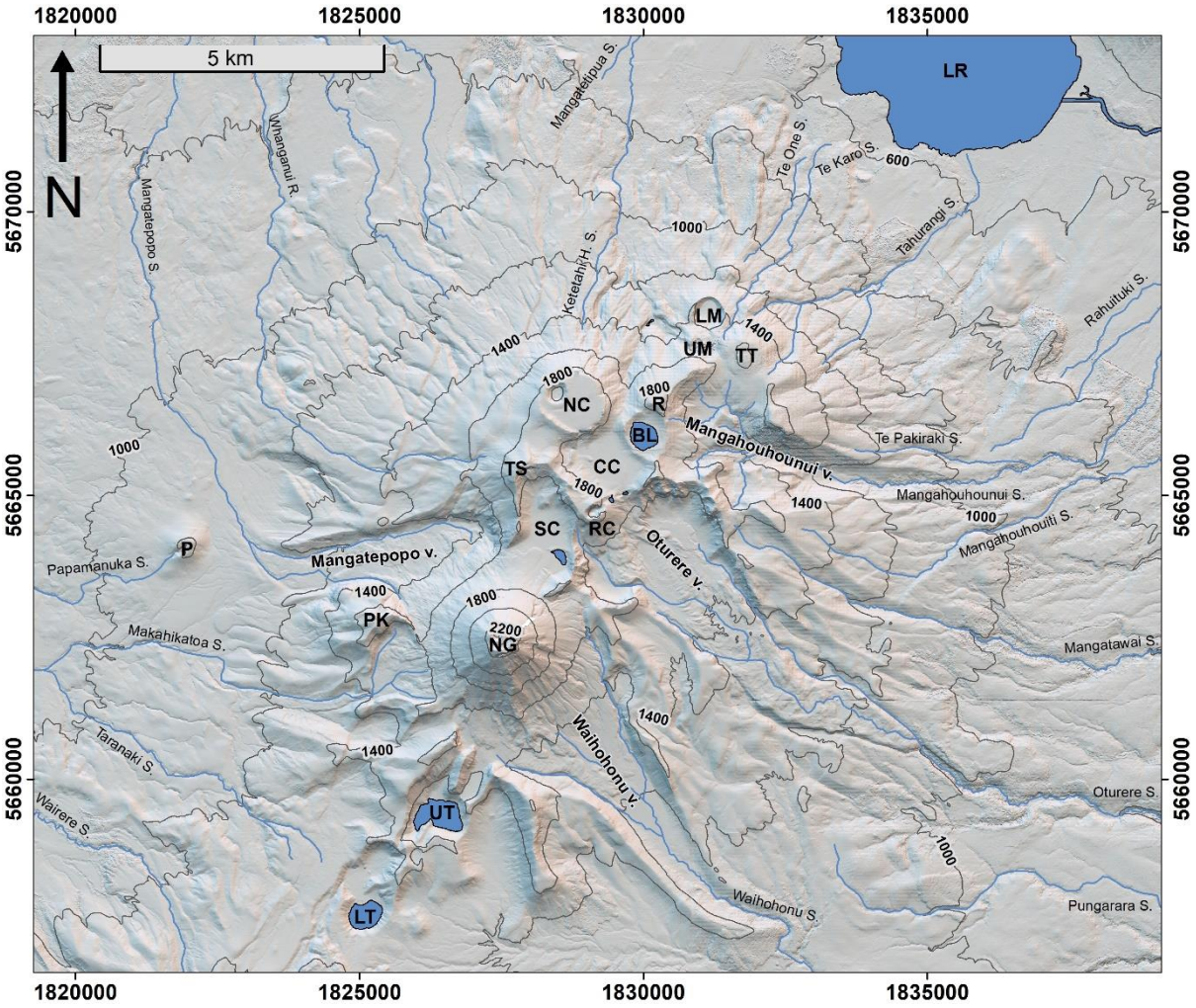

Figure 3.2. (Duplicate of Fig. 1.2.) Major landmarks on and around Tongariro volcano. Water bodies are shaded blue. BL = Blue Lake, CC = Central Crater, LR = Lake Rotoaira, LM = Lower Te Maari Crater, LT = Lower Tama lake, NC = North Crater, NG = Ngauruhoe, P = Pukeonake, PK = Pukekaikiore, R = Rotopaunga summit, RC = Red Crater, TS = Tongariro summit, TT = Te Tatau summit, SC = South 'Crater' Cirque (e.g. Cole et al., 2018), UM = Upper Te Maari Crater, UT = Upper Tama lake.

3.2. METHODS

3.2.1. Field studies and sampling

Sampling predominantly targeted the forested NW, NE and E sectors that constitute ~40% of the edifice's area, and which were previously under-sampled. Most samples (n = 219) were analysed for major oxide concentrations and were petrographically characterised using hand specimens and thin sections. Another ~30 samples were contributed by colleagues, as described fully in Chapter 2. Samples were grouped into eruptive formations and members based on field observations, geochronological results, petrographic features examined in thin sections and hand specimens and major oxide, Sr and Ba concentrations. A detailed explanation of how unit boundaries were mapped is given in section 2.1.2.

3.2.2. Whole-rock geochemistry

Major oxide, Sr and Ba concentrations were determined by XRF, with full details provided in Chapter 2. Analytical precision and accuracy were monitored with standards AGV-1, BCR-2, BHVO-2, OREAS, WS-E and an internal standard (LP009B). Analytical accuracy is within 5 % (1 r.s.d.) for each oxide concentration but generally ≤2.5 % (1 r.s.d.). Duplicate analyses of LP009B indicate an external precision (2 s.d.) better than 5 % for all oxides and Sr; however, Ba reproducibility is ~13 %. XRF analyses by Hobden (1997) of the same map units sampled in this study show good agreement, generally within 5 % (1 r.s.d.) of XRF data presented here. XRF data from Cole (1978, 1979) and Wahyudin (1993) are less accurate and generally within 5-10 % (1 r.s.d.) of data from this study, and were only used to inform mapping when more accurate data from this study or Hobden (1997) were unavailable.

3.2.3. $^{40}Ar/^{39}Ar$ geochronology

New $^{40}Ar/^{39}Ar$ ages were determined for 29 lava samples from Tongariro volcano. Sampling targeted the holocrystalline materials which are sometimes found in the interiors of lava flows, which cool more slowly and are thoroughly devitrified, as distinct from chilled glassy margins that are unsuitable for current dating methods (e.g. Gamble et al., 2003). Ages were determined on crystalline groundmass separates with <5 vol% glass (to minimise excess argon hosted in glass) that contained feldspars >10 μm (to minimise reactor recoil), following Hildreth and Lanphere (1994), Gamble et al. (2003), Fierstein et al. (2011) and Conway et al. (2016). Analytical uncertainties (2 s.d.) are generally ~5 kyr irrespective of age (Table 3.1), but exceptions exist for low-K_2O samples or analyses where isochron results are preferred over weighted plateau mean ages (WPMA). Samples were irradiated in TRIGA reactors in the United States (USGS Denver,

Colorado and CLICIT, Oregon State University) and were analysed at the USGS geochronological facility in Menlo Park. Full sample preparation, irradiation and analytical details are provided in Chapter 2.

3.2.4. Volume estimates of exposed stratigraphic units

The volume of each edifice-forming map unit on Tongariro was estimated, based on their known or inferred areas multiplied by their thicknesses. Exceptions are eruptives from the Otamatereinga Formation (poorly exposed inlier of unclear origin) and the Tupuna Formation (not exposed *in situ*), which were not estimated. In most cases, map units are partially obscured by younger overlying eruptives. To address this, estimated volumes were multiplied by 'f'-values that account for buried area, which connect known exposures to their source vent location, as inferred from field relations. Inferred vent locations are noted in respective unit descriptions of section 3.3.2, below. Tongariro's total edifice volume was also calculated. The estimated value strongly depends on the elevation on which Tongariro was constructed. A discussion of this paleo-topography elevation accompanies total edifice volume estimates in section 3.4.2, below. The total edifice volume was estimated with the "Zonal Statistics as Table" tool in ArcMap on a DSM, which returns the total area and average thickness above sea level. (For this calculation, Pukeonake Formation eruptives were calculated separately because they were erupted from a satellite vent system.) The elevation of the volcanic base that separates Tongariro's eruptives from underlying sediments was then subtracted from the average elevation above sea level (a.s.l.), computed in the previous step. The total edifice volume was computed by multiplying the average volcano thickness by its total area. This calculation is mathematically equivalent to subtracting a DSM of a pre-Tongariro landscape from a present-day landscape DSM but is less computationally-intensive.

3.3. ERUPTIVE STRATIGRAPHY

3.3.1. Introduction

This section presents a mostly new stratigraphic framework for Tongariro volcano. The mapping results reported here subdivide Tongariro's edifice-forming materials into 12 new formations (including 5 new definitions), some of which are subdivided into members. All new units are formally defined in Appendix 2. Collectively, these formations and members form 35 distinct stratigraphic units at their greatest level of subdivision, which does not include the Te Whaiau Formation debris flows or any undifferentiated edifice-forming units. This breakdown is comparable with the four formations and constituent members that collectively form 22 distinct edifice-forming units on neighbouring Ruapehu volcano (Conway, 2016; Conway et al., 2016; Townsend et al., 2017).

Like at Ruapehu, map units on Tongariro are jointly defined by a combination of field relations, geochronological data, sample petrography, geochemistry, spatial distributions and lithological characteristics. Regarding spatial distinctions, the following system applies: vent areas are defined as having a ≤1 km diameter, whereas where vent areas are separated by ≥2 km, they are considered as being distinct. The naming conventions used here are consistent with recent geological mapping at Ruapehu. Formations and members are named after nearby landmarks, flora or fauna in the Māori language. The naming process strongly benefited from the contributions of T. 'Bubs' Smith from Ngati Tūwharetoa (pers. comm., 2019). In this study, formations are abbreviated with uppercase two-letter codes. Members are abbreviated with lowercase three-letter codes, where the first letter denotes the most distinctive composition observed (e.g. Fierstein et al., 2011. In the case of this study: m = basaltic-andesite, a = andesite, d = dacite. No true basalts or rhyolites have been found at Tongariro.

The map unit boundaries presented here reflect the uppermost edifice-forming volcanic materials, as defined by landscape geomorphology (after Townsend et al., 2017) and sample data. This is for practical reasons because most of the area mapped is densely forested or covered in colluvium and fan deposits, and outcrops on the volcano's flanks are sparse. Geochronological, petrographic and geochemical data used for mapping are presented alongside previous Tongariro data. All radiometric age results are cited with 2 s.d. analytical uncertainties. This study contributes a total of 29 new $^{40}Ar/^{39}Ar$ age determinations (Table 3.1) that are integrated with previous K/Ar age determinations by Stipp (1969) and Hobden et al. (1996) for each map unit (Table 3.2). The age ranges specified in the titles and descriptions of map units below reflect adopted ages that are suggested from joint consideration of both field relationships and

geochronological data. Explanations of how each age range was established are provided in Appendix 2.

The confidence in mapping results are rated with a factor for each unit from 0 to 10 (low to high), weighted linearly (Table 3.2). Petrographic observations, SiO_2 and MgO concentrations, and unit lithologies are summarised for each map unit in Table 3.3. Major oxide (and Sr and Ba) concentrations are reported for representative samples in Table 3.4 and the full dataset is presented in Appendix 5. The petrographic observations and major oxide concentrations contributed by this study are supplemented with data from Cole (1978, 1979), Wahyudin (1993), Hobden (1997), D. B. Townsend and G. S. Leonard (pers. comm., 2019) and a small number of XRF analyses in GNS PETLAB from pre-1980 investigations.

Figure 3.3. (Next page.) Space-time relationships of map units (not a stratigraphic log). 'Age' boundaries represent the adopted range of ages for each map unit but do not indicate continuous activity during these intervals. Bold lines indicate observed field contacts; dashed bold lines indicate adjacent and inferred contacts. The horizontal position and width of each map unit box represents the approximate distribution across N-E-S-W sectors, but does not indicate runout distance. Grey dashed lines show key time horizons of regional rhyolitic tephra deposits from central TVZ volcanoes (≥50 km to north): see text and Appendix 2 for details regarding which Tongariro units they provide age control for. Question marks indicate poorly constrained age boundaries. Note the time break (~450-350 ka) and change in scale (~235 ka). $^{40}Ar/^{39}Ar$ age determinations and 2 s.d. uncertainties are symbolised with white circles and error bars; one K/Ar age determination from Hobden et al. (1996) is shown for unit **alt** with a yellow square with error bars. Mean values for $^{40}Ar/^{39}Ar$ age determinations on **awh** (LP245) and **dpk** (LP118) indicate stratigraphic ordering that is opposite to field relations: arrows emanate from the field positions of these samples and point to their respective age symbols. See headings in section 3.3.2 or tables 3.2-3.3 for map unit abbreviations. Members are grouped by their parent formations as indicated by grey boxes in the background. The inset hillshade model of Tongariro is annotated with N-E-S-W directions and the approximate positions of each formation (abbreviated) except the Taiko Formation (**TA**).

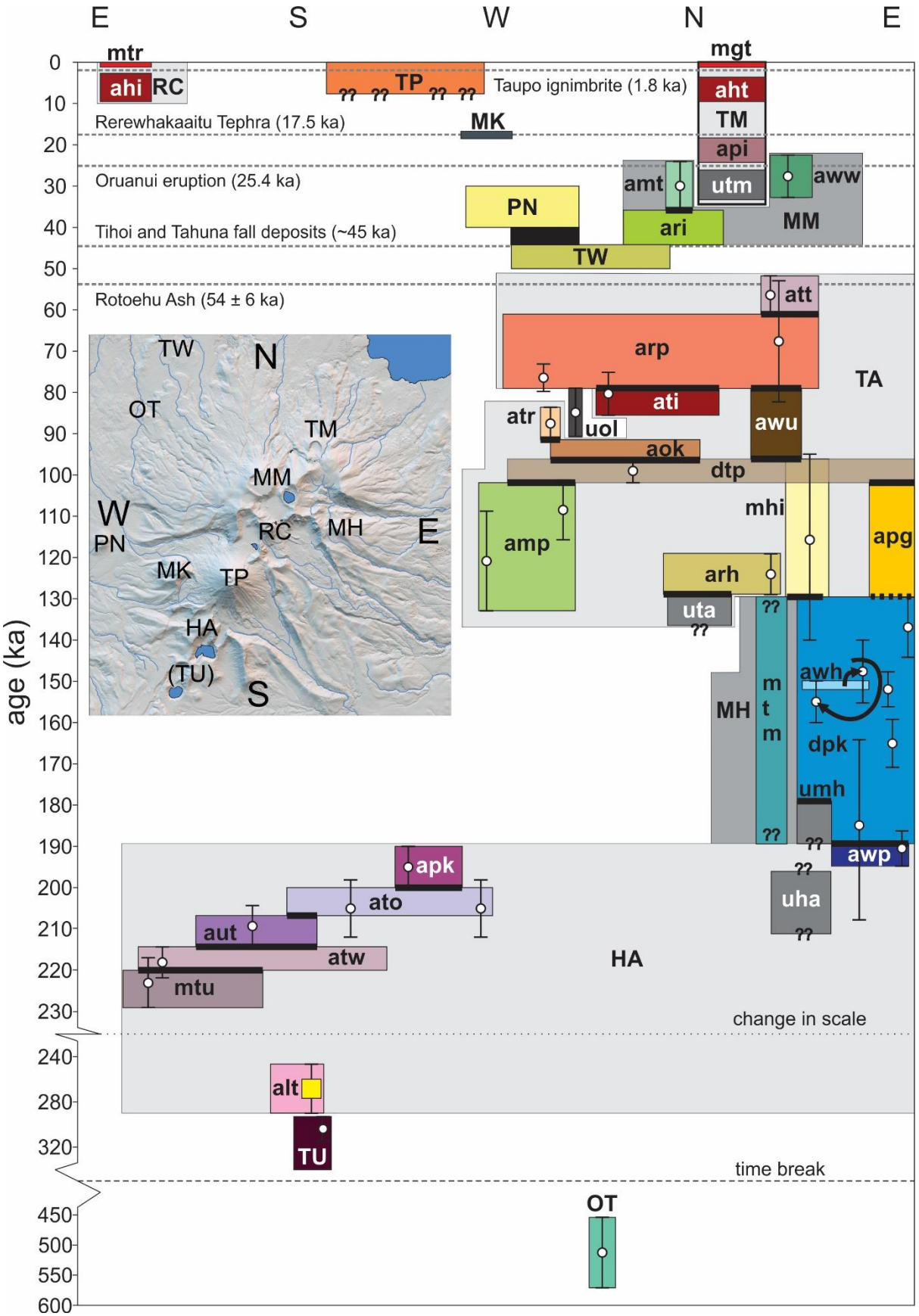
E
S
W
N
E
age (ka)
0
10
20
30
40
50
60
70
80
90
100
110
120
130
140
150
160
170
180
190
200
210
220
230
240
280
320
450
500
550
600
mtr
ahi
RC
TP
?? ?? ?? ??
Taupo ignimbrite (1.8 ka)
Rerewhakaaitu Tephra (17.5 ka)
MK
Oruanui eruption (25.4 ka)
Tihoi and Tahuna fall deposits (~45 ka)
Rotoehu Ash (54 ± 6 ka)
mgt
aht
TM
api
utm
amt
aww
MM
PN
ari
TW
att
arp
TA
ati
atr
uol
awu
aok
dtp
mhi
apg
amp
arh
uta
??
??
MH
m
t
m
??
awh
dpk
umh
??
??
awp
??
uha
??
apk
ato
aut
atw
mtu
HA
change in scale
alt
TU
time break
OT
TW
N
OT
TM
MM
W
PN
RC
MH
E
MK
TP
HA
(TU)
S

Table 3.1. Summary of new $^{40}Ar/^{39}Ar$ age determinations for Tongariro lavas.

Sample	Formation – Member (member abbreviation)[1]	Plateau age[2]				Isochron age[2]				Total gas age
		n/N	$\%^{39}Ar$	MSWD	(ka ± 2 s.d.)	$\%^{39}Ar$	MSWD	(ka ± 2 s.d.)	$^{40}Ar/^{36}Ar_i$ (± 2 s.d.)	(ka ± 2 s.d.)
TG088	RC – Te Ahititi (**ahi**)	6/10	77.8	2.07	**12.9 ± 11.8**	77.8	2.40	8.3 ± 25.4	301.4 ± 22.4	21.8 ± 10.2
LP147	MM – Te Wai Whakaata (**aww**)	11/11	100.0	0.46	**28.3 ± 5.2**	100.0	0.50	29.3 ± 7.6	298.0 ± 3.5	27.2 ± 6.0
LP151	MM – Mangatapate (**amt**)	5/10	69.3	0.41	**30.1 ± 6.0**	69.3	0.49	26.8 ± 14.8	305.0 ± 33.7	51.6 ± 6.2
GL2223	TA – Te Tatau (**att**)	11/11	100.0	1.31	**56.2 ± 4.6**	100.0	1.05	59.5 ± 5.4	296.3 ± 2.8	54.8 ± 4.8
LP211	TA – Rotopaunga (**arp**)	9/10	98.9	3.47	86.4 ± 12.4	**98.9**	**1.60**	**68.3 ± 15.4**	319.3 ± 18.4	96.0 ± 7.6
GL2007	TA – Rotopaunga (**arp**)	9/10	97.4	0.44	**76.1 ± 3.5**	97.4	0.38	78.4 ± 5.9	291.2 ± 10.1	73.3 ± 4.1
RPC110	TA – Te Wakarikiariki (**ati**)	4/11	63.6	0.98	**80.6 ± 4.8**	63.6	1.13	74.8 ± 15.2	304.0 ± 15.7	82.9 ± 6.0
LP062	undifferentiated Otukou lava (**uol**)	10/10	100.0	0.87	**85.0 ± 6.0**	100.0	0.86	89.7 ± 11.6	296.7 ± 4.4	83.8 ± 6.6
LP023	TA – Te Rurunga (**atr**)	6/11	58.7	1.07	**87.5 ± 4.2**	58.7	0.79	84.2 ± 6.2	304.0 ± 9.0	96.0 ± 4.0
LP103	TA – Te Porere (**dtp**)	4/10	71.2	0.69	**98.9 ± 2.6**	71.2	0.96	101.1 ± 14.2	290.7 ± 55.7	98.5 ± 3.0
LP010	TA – Mangatepopo (**amp**)	8/10	96.4	1.80	**108.5 ± 8.4**	96.4	1.73	102.9 ± 15.6	305.1 ± 21.2	119.1 ± 7.2
MSR15019	TA – Mangahouhouiti (**mhi**)	10/11	99.2	0.89	**116.8 ± 23.4**	99.2	0.88	141.4 ± 56.2	297.3 ± 3.1	108.0 ± 25.4
LP250	TA – Mangatepopo (**amp**)	7/10	70.5	2.12	**121.1 ± 12.2**	70.5	1.83	114.3 ± 14.6	307.0 ± 21.4	169.2 ± 9.0
LP214	TA – Rahuituki (**arh**)	7/10	75.9	0.77	**124.4 ± 4.8**	75.9	0.78	124.2 ± 5.4	297.4 ± 6.2	135.0 ± 5.6
TG084	MH – Te Pakiraki (**dpk**)	8/10	90.5	0.84	**136.5 ± 7.0**	90.5	0.79	130.8 ± 11.8	304.2 ± 12.6	153.3 ± 7.6
LP245	MH – Waiaruhairiki (**awh**)	7/10	81.8	0.30	**147.3 ± 7.4**	81.8	0.35	148.9 ± 17.4	296.9 ± 17.2	174.9 ± 7.6
LP234	MH – Te Pakiraki (**dpk**)	8/10	96.0	0.92	**151.8 ± 4.0**	96.0	0.62	146.7 ± 7.4	310.5 ± 18.0	158.9 ± 4.6
LP118	MH – Te Pakiraki (**dpk**)	8/10	88.2	1.35	**155.4 ± 5.2**	88.2	1.48	157.1 ± 13.4	297.0 ± 11.3	152.6 ± 5.0
LP129	MH – Te Pakiraki (**dpk**)	10/10	100.0	1.13	**164.9 ± 5.8**	100.0	1.23	166.2 ± 12.2	296.8 ± 11.5	164.9 ± 5.8
LP239	MH – Te Pakiraki (**dpk**)	3/10	58.2	2.43	203.8 ± 9.6	**58.2**	**1.12**	**185.5 ± 22.4**	319.1 ± 28.2	296.9 ± 8.6
MSR15018	HA – Waipoa (**awp**)	6/11	74.0	1.19	**191.1 ± 4.4**	74.0	0.72	195.8 ± 7.0	292.2 ± 8.5	196.4 ± 4.2
LP039	HA – Pukekaikiore (**apk**)	7/10	95.1	0.38	**194.7 ± 5.0**	95.1	0.40	197.7 ± 12.6	296.1 ± 11.0	192.6 ± 5.8
LP036	HA – Toatoa (**ato**)	8/10	**96.3**	**Recoil**	**205.1 ± 6.0**	100.0	7.97	208.9 ± 7.4	293.0 ± 17.7	208.8 ± 4.2
LP149	HA – Toatoa (**ato**)	4/10	67.2	1.72	**205.1 ± 6.0**	67.2	1.48	191.3 ± 23.4	311.0 ± 24.4	225.6 ± 5.0
GL2132	HA – Upper Tama (**aut**)	6/11	85.2	0.74	**209.1 ± 4.9**	85.2	0.84	211.8 ± 17.9	290.9 ± 31.0	201.9 ± 5.7
LP072	HA – Tawhairauiki (**atw**)	10/10	100.0	0.72	**217.7 ± 4.4**	100.0	0.76	219.0 ± 6.6	296.6 ± 7.2	215.6 ± 5.6
LP074	HA – Tutangatahiro (**mtu**)	6/10	89.0	0.66	**223.3 ± 5.6**	89.0	0.45	214.1 ± 16.2	305.5 ± 13.9	221.2 ± 6.6
LP113	TU	5/10	67.0	1.85	**304.4 ± 11.4**	67.0	1.06	285.5 ± 58.8	342.9 ± 109.5	376.4 ± 10.6
LP097	OT	3/11	62.2	0.51	**512.0 ± 59.4**	62.2	0.52	631.1 ± 338.4	294.6 ± 12.6	931.1 ± 57.4

[1] Formation abbreviations: OT = Otamatereinga, TU = Tupuna, MH = Mangahouhounui, HA = Haumata, TA = Taiko, MM = Mokomoko, RC = Red Crater.
[2] n/N = number (n) of heating steps used for plateau age calculation out of total (N) steps in age analysis. $\%^{39}Ar$ is the percentage of radiogenic argon released over the selected plateau steps of the total radiogenic argon. Recoil ages are noted where used instead of plateau ages—see Appendix 1 for heating step data. $^{40}Ar/^{36}Ar_i$ = denotes the isochron intercept value. Preferred ages appear in bold typeface. Details of heating step experiments, $^{40}Ar/^{36}Ar$ intercepts, isochrons and plateau spectra are provided in Appendix 1.

Table 3.2. Summary of age determinations and mapping discriminants for new Tongariro formations and members of this study.

Formation	Member	K/Ar ages [1, 2] (ka ± 2 s.d.)	$^{40}Ar/^{39}Ar$ ages relevant to unit (ka ± 2 s.d.)	Previous mapping reference [3, 4, 5, 6, 7]	Mapping discriminants (C, F, G, S, L)[9]	Confidence factor (0 to 10)[10]
Te Pupu (**TP**)	Matariki (**mmt**)			Te Pupu Formation[3]	Witnessed	10
	undifferentiated (*utp*)				F	2
	Toakakura (**mtk**)				F	8
	Papamānuka (**mpa**)				F	8
Red Crater (**RC**)	Te Rongo (**mtr**)			Red Crater Formation[3]	C, F	9
	Te Ahititi (**ahi**)		13 ± 12 (TG088)		C, F	9
Te Maari (**TM**)	Mangatetipua (**mgt**)			Te Maari Formation[3]	C, F	9
	Heretoa (**aht**)				F	7
	Paungaiti (**api**)				F	7
	undifferentiated (*utm*)				F	7
Makahikatoa (**MK**)	(no members)			Makahikatoa Formation[3]	C, F, S, L	9
Pukeonake (**PN**)	(no members)			Pukeonake Formation[3]	C, F, S	9
Mokomoko (**MM**)	Te Wai Whakaata (**aww**)		28 ± 5 (LP147)	Blue Lake Formation[3]	F, G, S	9
	Mangatapate (**amt**)		30 ± 6 (LP151)	North Crater Formation[3]	C, F, G, S	9
	Rangitaupahi (**ari**)				C, F, L	9
Te Whaiau (**TW**)	(no members)			[3, 7]	L	6
(Formation unclear)	undifferentiated Otukou lava (**uol**)	85 ± 6 (3258)[2]	85 ± 6 (LP062)	Otukou Quarry Andesite[6]	C, G, S	8

[1] K/Ar ages from Hobden et al. (1996). Sample numbers in parentheses.
[2] K/Ar ages from Stipp (1969) via Hobden et al. (1996), who recalculated ages with the decay constants of Steiger and Jaeger (1977). Sample numbers in parentheses.
[3] (Where defined names are identical to previous usage, only reference numbers are given.) Townsend et al. (2017); [4] Gregg (1960); [5] Cole et al. (2018); [6] Stipp (1969); [7] Lecointre et al. (2002).
[9] C = compositional from any combination of major oxides, trace elements and petrography; F = field relations; G = geochronology, S = spatial separation, L = lithological differences (see supplementary material for details). [10] 0 = zero confidence, 1-5 = will probably require revision when more data becomes available, 6-9 = unlikely to change with future work, 10 = total confidence; linear scale.

Table 3.2. Continued (Taiko Formation).

Formation	Member	K/Ar ages [1, 2] (ka ± 2 s.d.)	$^{40}Ar/^{39}Ar$ ages relevant to unit (ka ± 2 s.d.)	Previous mapping reference [3, 4, 5, 6, 7]	Mapping discriminants (C, F, G, S, L)[9]	Confidence factor (0 to 10)[10]
Taiko (**TA**)	Te Tatau (**att**)		56 ± 5 (GL2223)	Te Tatau Formation[3]	C, F, G, L	4
	Rotopaunga (**arp**)	64 ± 22 (TG330)[1] 79 ± 18 (TG147)[1] 87 ± 10 (TG051)[1]	68 ± 15 (LP211) 76 ± 4 (GL2007)	Rotopaunga Formation[3]	C, F, G, L	8
	Te Wakarikiariki (**ati**)		81 ± 5 (RPC110)	overlap w/ units in [5]	C, F, G	7
	Te Rurunga (**atr**)		88 ± 4 (LP023)	[new]	C, F, G, S	9
	Waitakatorua (**awu**)	104 ± 26 (TG227)[1] 105 ± 24 (TG258)[1] 122 ± 20 (TG247)[1] 128 ± 24 (TG123)[1] 164 ± 24 (TG249)[1]		[new]	C, F, L	6
	Otamangakau (**aok**)			Undiff. central Tongariro deposits[3]	C, F	6
	Te Porere (**dtp**)	68 ± 22 (TG235)[1] 81 ± 34 (TG228)[1] 91 ± 18 (TG182)[1] 91 ± 14 (TG144)[1] 95 ± 20 (TG178)[1] 110 ± 12 (TG138)[1] 107 ± 20 (3257)[2]	99 ± 3 (LP103)		C, F, G, L	9
	Mangatepopo (**amp**)		109 ± 8 (LP010) 121 ± 12 (LP250)		C, F, G	7
	Mangahouhouiti (**mhi**)	123 ± 32 (TG109)[1] 202 ± 46 (TG400)[1]	117 ± 23 (MSR15019)	[new]	C, F	9
	Pungarara (**apg**)	77 ± 28 (TG077)[1] 103 ± 24 (TG171)[1]		Undiff. central Tongariro deposits[3]	C, F, S	5
	Rahuituki (**arh**)		124 ± 5 (LP214)	[new]	C, F, G	5
	undifferentiated (*uta*)				F	1

Table 3.2. Continued (Mangahouhounui Formation).

Formation	**Member**	**K/Ar ages [1, 2] (ka ± 2 s.d.)**	**$^{40}Ar/^{39}Ar$ ages relevant to unit (ka ± 2 s.d.)**	**Previous. mapping reference [3, 4, 5, 6, 7]**	**Mapping discriminants (C, F, G, S, L)[9]**	**Confidence factor (0 to 10)[10]**
Mangahouhounui (**MH**)	Tātaramoa (**mtm**)			[new]	C, S	8
	Waiaruhairiki (**awh**)		147 ± 7 (LP245)	[3]	C, F	6
	Te Pakiraki (**dpk**)	97 ± 20 (TG084)[1] 123 ± 20 (TG114)[1]	137 ± 7 (TG084) 152 ± 4 (LP234) 155 ± 5 (LP118) 165 ± 6 (LP129) 186 ± 22 (LP239)		C, F, G, S	7
	undifferentiated (*umh*)				F	2

(continued below)

Table 3.2. Continued (Haumata, Tupuna and Otamatereinga formations).

Formation	Member	K/Ar ages [1, 2] (ka ± 2 s.d.)	$^{40}Ar/^{39}Ar$ ages relevant to unit (ka ± 2 s.d.)	Prev. mapping reference [3, 4, 5, 6, 7]	Mapping discriminants (C, F, G, S, L)[9]	Confidence factor (0 to 10)[10]
Haumata (**HA**)	Waipoa (**awp**)	173 ± 20 (TG098)[1] 229 ± 22 (TG111)[1] 247 ± 20 (TG048)[1]	191 ± 4 (MSR15018)	[new]	S, (G)	5
	undifferentiated (*uha*)				F	2
	Pukekaikiore (**apk**)	121 ± 46 (TG151)[1]	195 ± 5 (LP039)	Pukekaikiore Formation[3] Pukekaikiore Andesite[4]	C, F, G	6
	Toatoa (**ato**)	158 ± 28 (TG265)[1] 190 ± 18 (TG155)[1] 204 ± 30 (TG373)[1] 204 ± 26 (TG383)[1]	205 ± 6 (LP036) 205 ± 6 (LP149)	Tama Trig Formation[3]	C, F	7
	Upper Tama (**aut**)		209 ± 5 (GL2132)		C, F	7
	Tawhairauiki (**atw**)	91 ± 62 (TG298)[1] 203 ± 22 (TG292)[1] 206 ± 28 (TG382)[1] 208 ± 28 (TG389)[1] 209 ± 32 (TG294)[1] 216 ± 28 (TG028)[1]	218 ± 4 (LP072)		C, F, G	9
	Tutangatahiro (**mtu**)	207 ± 36 (TG300)[1]	223 ± 6 (LP074)		C, F, G	9
	Lower Tama (**alt**)	266 ± 24 (N89)[1]		Tama Formation[3]	C, F	9
Tupuna (**TU**)	(no members)	273 ± 44 (TG136)[1] 266 ± 6 (3254)[2]	304 ± 14 (LP113)		C, F, G	7
Otamatereinga (**OT**)	(no members)		512 ± 59 (LP097)	[new]	C, F, G, S	9

Table 3.3. Petrographic features of Tongariro eruptive formations and members in approximate stratigraphic order.

Formation	Member	Lithology	SiO_2 (wt%)[1]	MgO (wt%)[1]	Total xtals (vol%)[2]	Vesicles (vol%)	Relative phase proportions[3]	Other petrographic features[3]
Te Pupu (**TP**)	Matariki (**mmt**)	lava, pyroclastics	55.5-57.6	4.2-5.4	20-35	0-20	pl > opx > cpx > ox ~ ol	sometimes no ol and/or ox
	Toakakura (**mtk**)	lava, pyroclastics	56.9-57.6	4.0-4.9	30-35	0-10	pl > opx ~ cpx > ox > ol	sometimes no ol and/or ox
	Papamānuka (**mpa**)	lava	54.5-58.3	2.2-4.9	35-45	0-15	pl > opx > cpx > ox > ol	sometimes no ol and/or ox
Red Crater (**RC**)	Te Rongo (**mtr**)	lava, scoria, spatter	53.6-55.7	6.3-7.7	25-35	2-10	pl > cpx > ol > opx	trace ox
	Te Ahititi (**ahi**)	lava, agglutinates	59.1-60.9	3.8-4.5	25-35	0-2	pl > cpx ~ opx > ol ~ ox	-
Te Maari (**TM**)	Mangatetipua (**mgt**)	lava	~56.3	~6.9	25-30	n.d.	pl > ol ~ cpx > opx > ox	-
	Heretoa (**aht**)	agglutinates, lava	57.3-59.8	3.6-4.5	35	0-(?)5	pl > cpx > opx > ox	no ol or ap
	Paungaiti (**api**)	agglutinates, lava	58.5-60.3	3.2-4.1	25-35	0	pl > opx ~ cpx > ox	trace ap adjoined to opx-cpx-pl clots
	undifferentiated (*utm*)	lava	58.9	3.6	-	-	-	-
Makahikatoa (**MK**)	(no members)	scoria, lava	57.1-57.4	6.9-7.1	15-20	0-40	cpx ~ opx > pl ~ ol ~ ox	-
Pukeonake (**PN**)	(no members)	scoria, lava	56.0-56.9	7.9-8.9	20-35	30-35	cpx ~ pl > opx > ol > ox	-
Mokomoko (**MM**)	Te Wai Whakaata (**aww**)	lava, agglutinates	56.9-58.5	3.9-4.3	25-35	0-15	pl > cpx ~ opx > ox	trace ap adjoined to cpx-pl clots
	Mangatapate (**amt**)	lava, agglutinates	59.1-59.9	3.8-4.2	25-35	0-2	pl > opx > cpx > ox	no ol or ap
	Rangitaupahi (**ari**)	lava, spatter, agglutinates	58.6-59.9	4.4-5.1	25-40	0-40	pl > cpx > opx > ox	trace ol, trace ap adjoined to cpx-pl clots
Te Whaiau (**TW**)	-	debris flows	-	-	-	-	-	contains clasts of OT lava
(formation unclear)	undiff. Otukou lava (**uol**)	lava	~58.6	~5.9	~7	0	pl > cpx ~ opx > ol	trace hb-ox

Note: major oxide abundances are normalised to 100 % anhydrous totals. Representative major oxide XRF data are presented in Table 3.4; full data in Appendix 5.

[1] XRF whole-rock major oxide data primarily from this study and Hobden (1997), but also Wahyudin (1993), Cole (1978, 1979); pre-1980 samples from Stevens and Stirling via GNS PETLAB, D. B. Townsend and G. S. Leonard pers. comm. (2016). Values are normalised to 100 % anhydrous totals.

[2] Normalised to vesicle-free basis.

[3] Abbreviations: pl = plagioclase, opx = orthopyroxene, cpx = clinopyroxene, ol = olivine, ox = Fe-Ti oxide, hb = hornblende, hb-ox = Fe-Ti oxide pseudomorphs after amphibole, ap = apatite.

Table 3.3. Continued (Taiko and Mangahouhounui formations).

Formation	Member	Lithology	SiO_2 (wt%)[1]	MgO (wt%)[1]	Total xtals (vol%)[2]	Vesicles (vol%)	Relative phase proportions[3]	Other petrographic features[3]
Taiko (**TA**)	Te Tatau (**att**)	lava, scoria, agglutinates	57.4-59.5	4.2-6.5	20-30	0-45	pl > cpx ~ opx > ox	trace ol, no ap
	Rotopaunga (**arp**)	agglutinates, lava, lapilli tuff breccias	57.6-61.3	3.0-4.2	25-35	0-15	pl > opx > cpx > ox	trace ap adjoined to cpx-pl clots
	Te Wakarikiariki (**ati**)	lava	58.9-59.1	4.0-4.6	30-35	0	pl > cpx > opx > ox	≤7 mm pl
	Te Rurunga (**atr**)	lava, scoria, agglutinates	58.1-58.3	4.9-5.0	40-45	0-20	pl > cpx > opx > ox ~ ol	-
	Waitakatorua (**awu**)	lava, bedded lapilli tuffs	56.7-59.2	4.8-5.8	30-40	0-5	pl > cpx > opx > ox	trace ol, no ap
	Otamangakau (**aok**)	lava, agglutinates	59.4-61.7	3.4-3.9	35-40	0-5	pl > opx > cpx > ox	trace ol, trace ap adjoined to opx clots
	Te Porere (**dtp**)	lava, lapilli tuffs (also as breccias), agglutinates, hyaloclastites	59.4-63.9	1.7-3.1	35-50	0-7	pl > opx > cpx > ox	trace ap in some samples
	Mangatepopo (**app**)	lava	58.6-59.5	4.2-4.9	30	0	pl > cpx > opx > ox	trace ol
	Mangahouhouiti (**mhi**)	lava, agglutinate	55.6-58.6	5.5-7.1	10-20	0-5	cpx ~ ol > pl ~ opx > ox	-
	Pungarara (**apg**)	lava	57.8-62.7	2.5-3.9	20-30	0	pl > opx > cpx > ox	trace hb-ox
	Rahuituki (**arh**)	lava	60.4-61.3	2.9-3.4	30-40	0-2	pl > cpx ~ opx > ox	no ap or ol
Manga-houhounui (**MH**)	Tātaramoa (**mtm**)	lava	~53.9	~5.3	20	25	pl > cpx > opx	trace opx and ox, no ol, ≤9 mm pl and ≤8 mm cpx
	Waiaruhairiki (**awh**)	lava, agglutinates	57.0-58.6	5.4-6.2	35-40	0	pl > cpx ~ opx > ox	≤9 mm pl and ≤8 mm cpx
	Te Pakiraki (**dpk**)	lava, agglutinates, glacial-lateral breccias	56.7-64.6	2.5-4.8	30-40	0	pl > opx > cpx > ox	trace ap in dacites and hi-SiO_2 andesites; ≤9 mm pl and ≤8 mm cpx

Table 3.3. Continued (Haumata, Tupuna and Otamatereinga formations).

Formation	Member	Lithology	SiO_2 (wt%)[1]	MgO (wt%)[1]	Total xtals (vol%)[2]	Vesicles (vol%)	Relative phase proportions[3]	Other petrographic features[3]
Haumata (**HA**)	Waipoa (**awp**)	lava	59.6-62.4	3.1-4.5	30-40	0	pl > cpx > opx > ox ~ hb-ox	trace serpentinised ol xenocrysts, trace ap
	Pukekaikiore (**apk**)	lava	60.0-61.5	3.6-4.2	35	0	pl > cpx > opx > hb-ox > ox	trace ol, no ap
	Toatoa (**ato**)	lava	60.1-61.6	3.4-4.6	30-35	0	pl > cpx ~ opx ~ hb-ox > ox	trace ap
	Upper Tama (**aut**)	lava, pumice, pyroclastics	59.1-63.0	2.4-2.9	30-40	0-? (PDCs)	pl > cpx > opx > hb-ox > ox	trace ap
	Tawhairauiki (**atw**)	lava	59.0-60.6	3.8-4.7	35-40	0	pl > opx ~ cpx > ox > hb-ox	trace ap
	Tutangatahiro (**mtu**)	lava	56.1-57.6	3.7-5.5	40-45	0	pl > cpx > opx > hb-ox> ox	≤6 mm cpx clots, no ap
	Lower Tama (**alt**)	lava	61.2-62.7	3.0-3.1	35	0	pl > cpx ~ opx > hb-ox > ox	-
Tupuna (**TU**)	(no members)	lava (not in-situ)	59.2-60.5	3.8-4.1	35	0	hb ~ pl > ox > cpx ~ opx	-
Otama-tereinga (**OT**)	(no members)	lava	56.0-57.0	5.3-5.4	40-45	1-7	pl > cpx > opx > ol ~ ox	ol has scythe-shaped ox + opx reaction rims

3.3.2. Systematic descriptions of stratigraphic units

3.3.2.1. Otamatereinga Formation (between 571 and 453 ka) – OT

An exposure of basaltic-andesite lava on Tongariro's western flank (Fig. 3.4) yielded an $^{40}Ar/^{39}Ar$ age of 512 ± 59 ka (Table 3.1). This is the oldest dated material on Tongariro, but probably represents an older edifice that is almost entirely buried. The Otamatereinga Formation is observed at two localities surrounded by outcrops of younger Tongariro eruptives: the 102-96 ka Te Porere Member (section 3.3.2.5.5) and the 40-30 ka Pukeonake Formation (section 3.3.2.9).

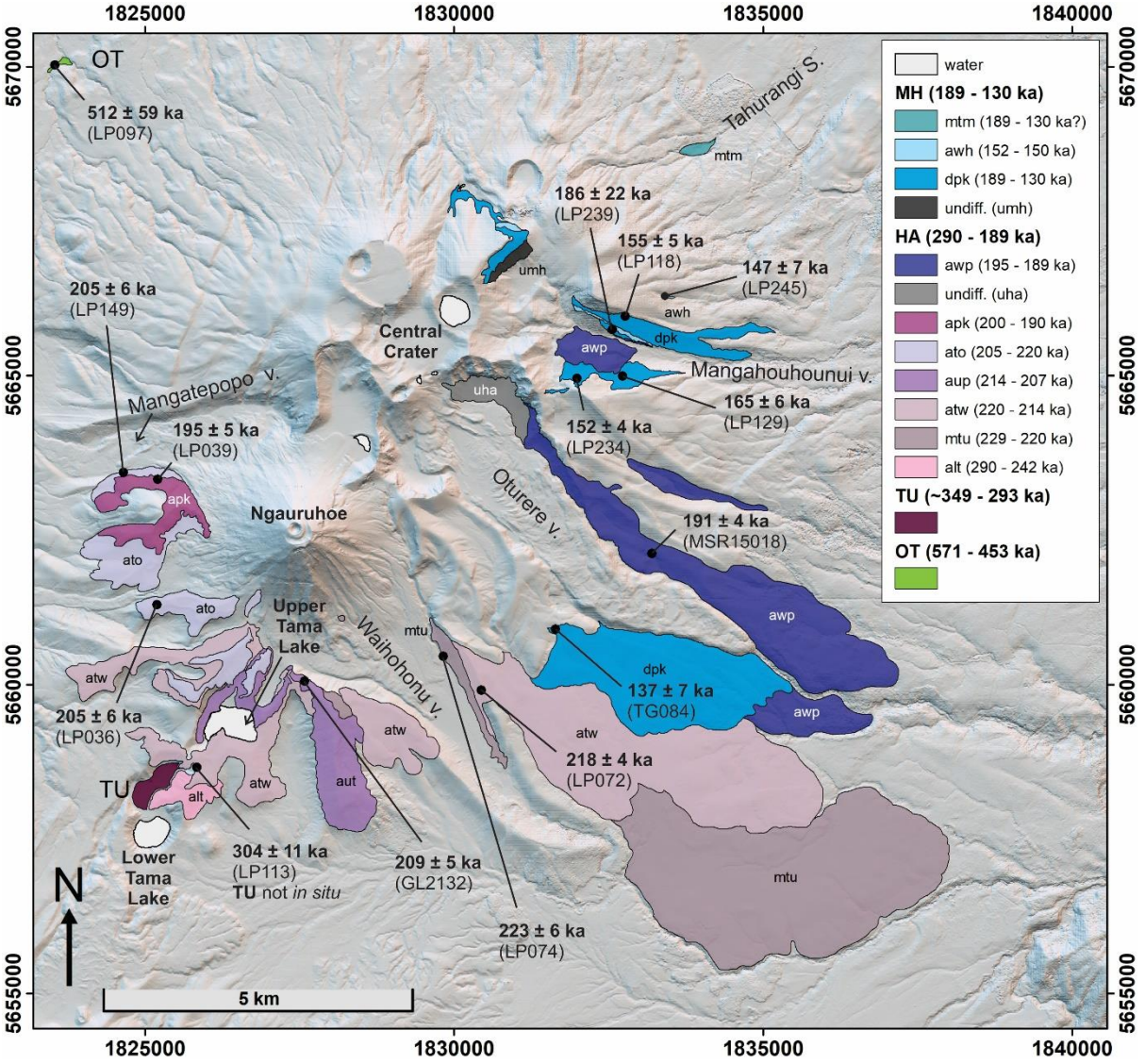

Figure 3.4. Distribution of oldest eruptive units on Tongariro from ~0.5 Ma to 189 ka. Formations are: Otamatereinga (**OT**), Tupuna (**TU**), Haumata (**HA**). Member abbreviations are: Lower Tama (**alt**), Tutangatahiro (**mtu**), Tawhairauiki (**atw**), Upper Tama (**aut**), Toatoa (**ato**), Pukekaikiore (**apk**), Waipoa (**awp**), Te Pakiraki (**dpk**), Waiaruhairiki (**awh**), Tātaramoa (**mtm**). Key landmarks mentioned in the text are labelled. See Table 3.1 for $^{40}Ar/^{39}Ar$ age results and Table 3.2 for summary of K/Ar (Hobden et al., 1996) and $^{40}Ar/^{39}Ar$ age results for each unit.

3.3.2.2. Tupuna Formation (between 349 and 293 ka) – TU

The Tupuna Formation is not found *in situ*. It is represented by boulders of hornblende-phyric andesite lava up to 0.4 m across, found predominantly eastwards of and up to ~3 km from Lower Tama lake (Fig. 3.4) (Hobden, 1997; Nairn et al., 1998). The distribution of these boulders matches the dispersal direction of juvenile material in the ~10 ka Wharepu eruption (cf. PM5: Nairn et al., 1998). Hornblende-bearing lithics are also abundant in the tephra deposits of the Wharepu eruption. This association suggests that Tupuna Formation boulders represent an old Tongariro lava flow or flows that were excavated during the Wharepu eruption episode as

accidental lithics from beneath what is now Lower Tama lake (Fig. 3.4). A single $^{40}Ar/^{39}Ar$ age determination on a Tupuna Formation boulder of 304 ± 11 ka (Table 3.1: LP113) has mixed agreement with previous K/Ar age determinations. K/Ar dating by Stipp (1969) of 259 ± 6 ka was revised by Hobden et al. (1996) with the decay constants of Steiger and Jaeger (1977) to give 266 ± 6 ka (Table 3.2: sample 3254). Hobden et al. (1996) re-dated the same unit by K/Ar methods and obtained a result of 273 ± 44 ka (Table 3.2: TG136). The compositions of boulders in the 349-309 ka (Pillans, 1983; Downs et al., 2014) Turakina Formation debris flows (Tost and Cronin, 2015) are similar to Tupuna Formation andesites. These debris flows are reported from a location ~100 km SW of Tongariro along the Turakina River in the Wanganui Basin (Tost and Cronin, 2015). This association would imply that at least some of the Tupuna Formation eruptives must pre-date 309 ka, consistent with the 304 ± 11 ka age result reported here (see section 3.5.2 for discussion of this correlation).

3.3.2.3. Haumata Formation (between 290 and 189 ka) – HA

The Haumata Formation consists of lavas and minor volumes of ignimbrite erupted between 290 and 198 ka. It is divided into seven members, and an eighth undifferentiated unit is added because its inferred age falls within this time period. Spatial overlap with map units defined in previous studies is summarised in Table 3.2. Haumata Formation eruptives are characterised by the presence of Fe-Ti oxide pseudomorphs after amphibole (1-5 vol%) that are more abundant than in other Tongariro eruptives (always ≤1 vol%). Haumata Formation eruptives are primarily exposed in the southern portion of Tongariro's edifice. All but one member of the Haumata Formation are distributed from an area around present-day Ngauruhoe, which overlies their inferred vent area (Fig. 3.4), although Ngauruhoe itself is a Holocene feature (Moebis et al., 2011; Townsend et al., 2017). The exception is the 195-189 ka Waipoa Member, which was probably erupted from a vent near present-day Central Crater.

3.3.2.3.1. Lower Tama Member (between 290 and 242 ka) – alt

This member consists of low-K_2O andesites exposed exclusively in ~100 m thick sections on the ridge to the east of Lower Tama lake, within ~1 km of the lake itself (Fig. 3.4). Samples contain abundant Fe-Ti oxide pseudomorphs after amphibole (denoted hb-ox in Table 3.3), which suggest similar magmatic histories and possibly a shared magma system with the hornblende-phyric, 349-293 ka Tupuna Formation. Amphibole pseudomorphs occur in other >190 ka Tongariro lavas (≤2 vol%) but are most abundant in the Lower Tama Member lavas (~5 vol%).

The only age estimate for this member is a K/Ar age determination by Hobden et al. (1996) of 266 ± 22 ka (Table 3.2: N89).

3.3.2.3.2. Tutangatahiro Member (between 229 and 220 ka) – mtu

Basaltic-andesite lavas of the Tutangatahiro Member are exposed in the SW and NE walls of Waihohonu valley and as an inlier on the Ngauruhoe cone at the head of Waihohonu valley (Fig. 3.4). No lower contact is observed (Fig. 3.3). The lavas occur as a conformable succession of at least seven flows, best exposed in the NE wall of the Waihohonu valley, where they are collectively up to 150 m thick. The farthest-travelled lava of this member is exposed on State Highway 1, ~10 km from the inferred vent location now buried beneath Ngauruhoe. A single $^{40}Ar/^{39}Ar$ age for this unit of 223 ± 6 ka (Table 3.1: LP074) is within error of Hobden et al.'s (1996) K/Ar determination of 207 ± 36 ka (Table 3.2: TG300).

3.3.2.3.3. Tawhairauiki Member (between 220 and 214 ka) – atw

The Tawhairauiki Member comprises at least four conformably overlying, ridge-forming andesite lavas, collectively ~60 m thick. Runout distances are up to 9 km from the inferred vent, now buried beneath Ngauruhoe (Fig. 3.4). In the NE Waihohonu valley, Tawhairauiki Member lavas overlie Tutangatahiro Member basaltic-andesites (Figs. 3.3-3.4). Tawhairauiki Member lavas contain Fe-Ti oxides pseudomorphing after amphibole, but they are less abundant (≤2 vol%) than other ≥190 ka lavas. However, their presence indicates a similar magmatic history and possibly a shared magma system with other eruptives of the Haumata and Tupuna formations. One $^{40}Ar/^{39}Ar$ age determination on a Tawhairauiki Member lava of 218 ± 4 ka (Table 3.1: LP072) is within error of five K/Ar determinations by Hobden et al. (1996) of 216 ± 28, 209 ± 32, 208 ± 28, 206 ± 28 and 206 ± 28 ka (Table 3.2). A fifth K/Ar age determination on a Tawhairauiki Member lava of 91 ± 62 ka (Hobden et al., 1996) is considered here to be an analytical outlier.

3.3.2.3.4. Upper Tama Member (between 214 and 207 ka) – aut

The Upper Tama Member is composed of andesitic lavas and minor volumes of ignimbrite near Upper Tama lake (Fig. 3.4). Upper Tama Member eruptives form the basal halves (~60 m) of bluffs surrounding the lake. At the Tama-trig ridgeline, located ~1.5 km east of Upper Tama lake, a sequence of ~20 m-thick lavas capping ~50 m of pyroclastic deposits is included in this member. Southwards, these capping lavas thicken to ~200 m (Nairn, 1996; Hobden, 1997; Townsend et al., 2017). The aforementioned pyroclastic deposits are pumice-rich ignimbrite

deposits and are preserved only where capped by coherent lava flows. Lava thickening away from the vent area suggests impoundment by ice, as does the confinement of the Upper Tama Member products to ridgelines (e.g., Conway et al., 2015). A single $^{40}Ar/^{39}Ar$ age determination of 209 ± 5 ka (Table 3.1: GL2132; G. S. Leonard, pers. comm., 2019) is consistent with the age of the underlying Tawhairauiki Member (Fig. 3.3).

Table 3.4. Representative major oxide (wt%) and Sr and Ba (ppm) concentrations for all map units (except undifferentiated).

Sample	LP097	LP113	LP109	LP074	LP072	GL 2132	LP036	LP149	LP039	MSR 15018
Fm.[1]	OT	TU	HA	HA	HA	HA	HA	HA	HA	HA
Mbr.[2]	-	-	alt	mtu	atw	aut	ato	ato	apk	awp
SiO_2	55.54	59.41	62.46	56.14	59.05	61.32	60.46	59.98	60.07	59.99
TiO_2	0.68	0.54	0.43	0.66	0.57	0.56	0.59	0.62	0.61	0.65
Al_2O_3	16.66	16.91	16.97	17.82	16.23	17.30	15.60	16.47	16.39	17.10
Fe_2O_3*	8.79	6.93	5.85	8.24	7.50	6.24	6.89	6.94	6.98	6.99
MnO	0.15	0.13	0.11	0.14	0.13	0.12	0.12	0.11	0.12	0.12
MgO	5.34	3.92	3.05	4.23	4.70	2.72	4.53	3.97	4.02	3.74
CaO	7.88	6.46	5.26	7.53	6.71	6.35	6.80	6.47	6.55	6.75
Na_2O	2.74	3.40	3.58	3.32	3.15	3.66	3.07	3.30	3.29	3.42
K_2O	0.80	1.04	1.13	0.89	1.17	1.45	1.40	1.30	1.30	1.28
P_2O_5	0.14	0.13	0.14	0.16	0.13	0.18	0.13	0.13	0.13	0.14
SO_3	0.04	0.01	0.04	0.04	0.04	-	0.04	0.04	0.04	0.04
LOI	0.40	0.16	0.57	-0.22	0.11	0.10	0.61	0.03	-0.04	0.19
Total	99.22	99.10	99.64	99.21	99.56	99.23	100.31	99.43	99.56	100.46
Sr	293	247	242	260	272	-	239	261	275	233
Ba	239	324	279	280	257	-	344	277	270	307

All data by XRF. Full whole-rock major oxide dataset is reported in Appendix 5. MSR and GL samples from G. S. Leonard (pers. comm., 2016). TG samples from Hobden (1997). Samples 24269 and 24266 from Cole (1979).

*Data from solution ICP-MS.

[1] Fm. = formation. Otamatereinga (**OT**), Tupuna (**TU**), Haumata (**HA**), Mangahouhounui (**MH**), Taiko (**TA**), Mokomoko (**MM**), Pukeonake (**PN**), Makahikatoa (**MK**), Te Maari (**TM**), Red Crater (**RC**), Te Pupu (**TP**).

[2] Mbr. = member. Lower Tama (**alt**), Tutangatahiro (**mtu**), Tawhairauiki (**atw**), Upper Tama (**aut**), Toatoa (**ato**), Pukekaikiore (**apk**), Waipoa (**awp**), Te Pakiraki (**dpk**), Waiaruhairiki (**awh**), Tātaramoa (**mtm**), Rahuituki (**arh**), Pungarara (**apg**), Mangahouhouiti (**mhi**), Mangatepopo (**amp**), Te Porere (**dtp**), Otamangakau (**aok**), Waitakatorua (**awu**), Te Rurunga (**atr**), Te Wakarikiariki (**ati**), Rotopaunga (**arp**), Te Tatau (**att**), undifferentiated Otukou lava (**uol**), Rangitaupahi (**ari**), Mangatapate (**amt**), Te Wai Whakaata (**aww**), Paungaiti (**api**), Heretoa (**ahi**), Mangatetipua (**mgt**), Te Ahititi (**ahi**), Te Rongo (**mtr**), Papamānuka (**mpa**), Toakakura (**mtk**), Matariki (**mmt**).

Table 3.4. Continued.

Sample	LP239	LP129	LP234	LP118	LP229	TG084	LP245	LP209	LP051	LP214
Fm.[1]	MH	MH	MH	MH	MH	MH	MH	MH	TA	TA
Mbr.[2]	dpk	dpk	dpk	dpk	dpk	dpk	awh	mtm	arh	arh
SiO_2	61.89	58.34	64.84	57.46	58.55	58.69	58.39	53.77	61.14	60.99
TiO_2	0.73	0.73	0.65	0.82	0.71	0.73	0.66	0.83	0.73	0.65
Al_2O_3	16.71	16.62	16.13	16.74	16.94	16.96	15.28	17.92	16.51	17.05
Fe_2O_3*	6.67	8.20	5.30	8.32	7.70	7.51	7.83	9.50	7.10	6.91
MnO	0.10	0.13	0.09	0.13	0.12	0.12	0.13	0.16	0.10	0.12
MgO	3.03	3.95	2.52	4.23	4.20	3.86	5.56	5.32	2.91	3.18
CaO	5.56	6.67	4.67	6.91	6.90	7.21	7.57	7.91	5.40	5.99
Na_2O	3.27	3.02	3.30	3.04	3.15	3.23	2.87	2.72	3.27	3.28
K_2O	1.74	1.50	2.27	1.47	1.15	1.30	1.28	0.74	2.05	1.75
P_2O_5	0.17	0.16	0.17	0.17	0.15	0.14	0.14	0.15	0.18	0.14
SO_3	0.03	0.04	0.01	0.04	0.00	-	0.00	0.00	0.04	0.02
LOI	0.33	-0.06	0.37	-0.17	0.39	-0.18	-0.08	0.74	0.28	0.25
Total	100.30	99.43	100.39	99.40	100.01	99.57	99.79	99.81	99.78	100.38
Sr	189	229	200	260	222	267	357	258	222	225
Ba	366	298	435	340	255	304	251	297	343	330

Sample	TG077	MSR 15019	LP010	LP250	LP024	LP103	LP071	LP140	LP023	LP161
Fm.[1]	TA	TA	TA	TA	TA	TA	TA	TA	TA	TA
Mbr.[2]	apg	mhi	amp	amp	dtp	dtp	aok	awu	atr	ati
SiO_2	57.15	56.77	58.80	59.41	61.96	60.89	60.10	58.38	58.39	57.78
TiO_2	0.88	0.68	0.76	0.76	0.92	0.94	0.77	0.68	0.75	0.68
Al_2O_3	17.72	15.54	16.49	15.49	16.75	16.93	16.55	15.98	16.18	16.94
Fe_2O_3*	7.90	7.82	7.78	8.19	7.43	7.73	7.21	7.30	7.99	7.72
MnO	0.13	0.14	0.13	0.13	0.12	0.12	0.12	0.12	0.13	0.13
MgO	3.29	6.31	4.23	4.88	2.01	1.97	3.44	5.12	4.89	4.44
CaO	6.93	8.14	6.95	6.40	5.32	4.91	5.92	6.90	7.13	7.56
Na_2O	3.53	2.76	3.22	3.09	3.74	3.54	3.27	3.10	3.10	3.13
K_2O	1.28	0.99	1.51	1.56	1.94	1.94	1.84	1.41	1.43	1.16
P_2O_5	0.17	0.13	0.15	0.15	0.18	0.19	0.17	0.15	0.14	0.14
SO_3	-	-	0.04	0.00	0.04	0.04	0.05	0.04	0.04	0.00
LOI	-0.12	0.86	0.30	-0.04	0.14	0.24	0.00	0.10	0.14	0.12
Total	98.86	100.18	100.42	100.13	100.61	99.51	99.53	99.38	100.37	99.84
Sr	313	363*	259	226	236	260	262	348	246	223
Ba	310	226*	337	303	418	434	395	310	272	225

Table 3.4. Continued.

Sample	LP211	GL 2223	LP247	LP249	LP062	LP063	LP151	LP147	LP001	TG152
Fm.[1]	**TA**	**TA**	**TA**	**TA**	**-**	**MM**	**MM**	**MM**	**PN**	**MK**
Mbr.[2]	**arp**	**att**	**att**	**att**	**uol**	**ari**	**amt**	**aww**	**-**	**-**
SiO_2	61.03	57.90	58.37	56.25	58.33	58.58	59.88	57.57	55.35	56.89
TiO_2	0.76	0.79	0.67	0.66	0.66	0.72	0.74	0.82	0.68	0.57
Al_2O_3	16.44	16.71	15.24	15.68	14.99	15.88	16.20	17.15	14.23	14.59
Fe_2O_3*	7.50	7.65	7.88	8.26	7.48	7.62	7.53	8.17	7.60	7.93
MnO	0.13	0.12	0.13	0.14	0.12	0.13	0.13	0.14	0.12	0.13
MgO	3.34	4.60	5.58	6.56	5.91	4.71	4.21	4.04	9.47	7.02
CaO	5.94	7.40	7.55	7.23	7.53	6.83	6.47	7.13	7.22	9.18
Na_2O	3.27	3.23	2.88	2.44	2.99	3.08	3.16	3.04	2.64	2.37
K_2O	1.76	1.33	1.29	1.12	1.24	1.49	1.55	1.38	1.30	0.89
P_2O_5	0.16	0.17	0.14	0.14	0.15	0.16	0.16	0.17	0.14	0.08
SO_3	0.01	-	0.00	0.11	0.04	0.05	0.01	0.04	0.04	-
LOI	-0.15	0.96	-0.12	1.55	-0.25	0.01	-0.07	-0.14	1.27	-0.47
Total	100.40	100.97	99.80	100.20	99.51	99.32	100.10	99.69	100.15	99.18
Sr	233	319	358	314	386	260	252	257	264	634
Ba	423	266	244	222	250	337	351	329	297	198

Sample	LP003	24269	24266	TG088	TG112	TG266	TG017	TG039
Fm.[1]	**TM**	**TM**	**TM**	**RC**	**RC**	**TP**	**TP**	**TP**
Mbr.[2]	**api**	**aht**	**mgt**	**ahi**	**mtr**	**mpa**	**mtk**	**mmt**
SiO_2	59.52	56.57	56.19	59.39	53.38	54.87	55.30	54.80
TiO_2	0.74	0.75	0.71	0.73	0.72	1.05	0.87	0.75
Al_2O_3	16.21	17.37	15.86	16.54	15.45	17.60	18.13	16.61
Fe_2O_3*	7.53	7.31	7.65	7.31	9.70	9.18	9.50	8.82
MnO	0.12	0.14	0.15	0.12	0.16	0.16	0.16	0.15
MgO	3.97	4.47	6.86	4.37	7.71	4.52	3.89	5.32
CaO	6.33	7.55	8.05	7.29	10.49	8.03	8.51	8.26
Na_2O	3.20	3.12	2.85	3.16	2.43	3.40	3.11	2.79
K_2O	1.64	1.16	1.29	1.48	0.63	1.08	0.94	1.09
P_2O_5	0.17	0.08	0.13	0.14	0.13	0.20	0.14	0.14
SO_3	0.04	-	-	-	-	-	-	-
LOI	-0.01	0.12	0.04	-0.54	-0.71	0.25	-1.52	-0.52
Total	99.54	98.68	99.81	99.99	100.09	100.34	99.03	98.21
Sr	301	162	155	295	278	316	214	245
Ba	322	233	233	317	134	204	166	204

3.3.2.3.5. Toatoa Member (between 207 and 200 ka) – ato

Toatoa Member andesite lavas overlie andesites of the Tawhairauiki and Upper Tama members on Tongariro's southern flank (Figs. 3.3-3.4). Toatoa Member lavas also form the basal bluffs of the Pukekaikiore landform, where they form a single ≥100 m thick unit with a rubbly upper surface and no apparent interior layering. In both areas, these features are taken to indicate lava impoundment by ice. Two $^{40}Ar/^{39}Ar$ age determinations for the Toatoa Member, both yielding 205 ± 6 ka (Table 3.1: LP036 and LP149), have mixed agreement with Hobden et al.'s (1996) K/Ar age determinations of 204 ± 30, 204 ± 26, 190 ± 18 and 158 ± 28 ka (Table 3.2). In particular, the 205 ± 6 ka ($^{40}Ar/^{39}Ar$: LP149) and 158 ± 28 ka (K/Ar) age determinations are from samples of the same outcrop, but do not overlap within analytical uncertainties. Toatoa Member andesites contain Fe-Ti oxides pseudomorphing after amphibole that suggest a similar magma assembly history, and potentially a shared magmatic system, with other Haumata Formation eruptives.

3.3.2.3.6. Pukekaikiore Member (between 200 and 190 ka) – apk

The Pukekaikiore Member corresponds to the upper of two ~100 m-thick andesite lava flows that form bluffs on the northern side of the Pukekaikiore landform (Figs. 3.4-3.5). As for the Toatoa Member (above), the presence of a single, thick lava flow exposed as a bluff implies that the Pukekaikiore Member was impounded by ice when emplaced. The inferred vent location is now buried beneath Ngauruhoe. A new $^{40}Ar/^{39}Ar$ age determination for the Pukekaikiore Member of 195 ± 5 ka (Table 3.1: LP039) does not overlap within analytical uncertainty with the K/Ar age determination by Hobden et al. (1996) of 121 ± 46 ka (Table 3.2: TG151). The 'old' and 'young' Pukekaikiore of Patterson and Graham (1988) and Hobden (1997) differ from the Pukekaikiore Member defined here because this member comprises the upper half of the aforementioned 'old' Pukekaikiore, with the lower half represented by the Toatoa Member (Fig. 3.3). The 'young' Pukekaikiore refers to the Makahikatoa Formation (Fig. 3.5) which is described in section 3.3.2.11, below.

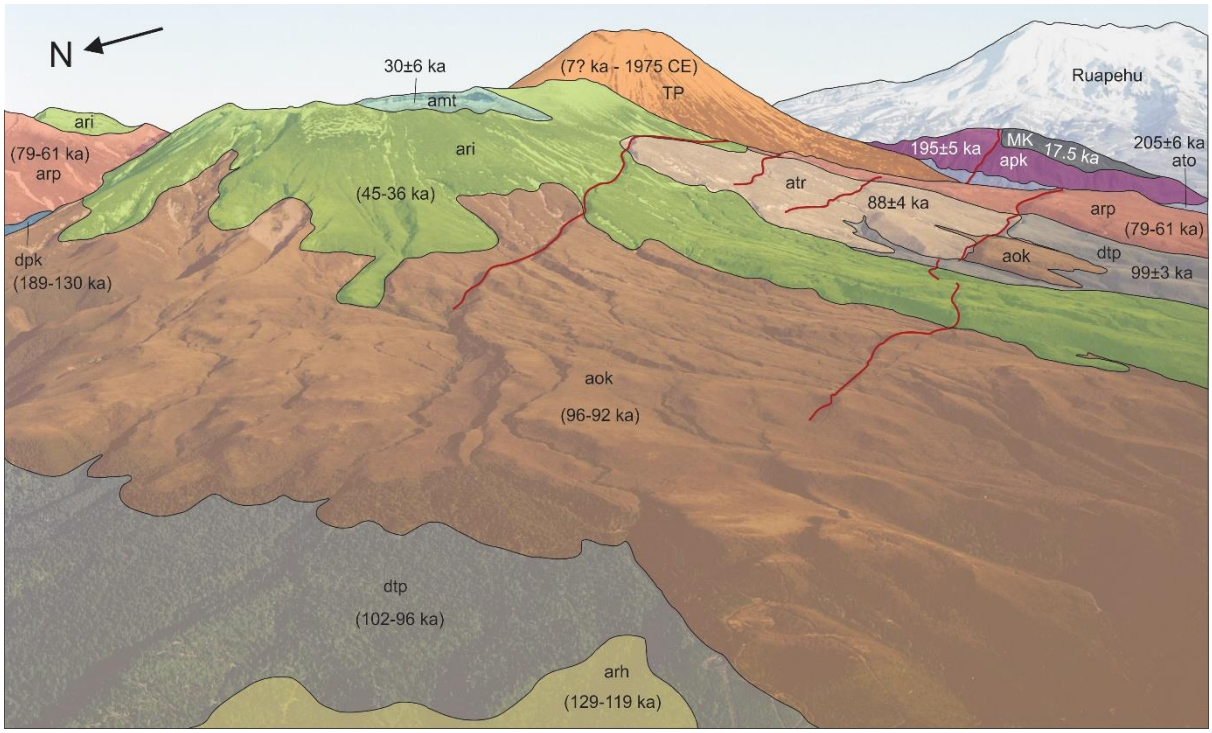

Figure 3.5. View of northwestern Tongariro, looking SE. Ngauruhoe (Te Pupu Formation: **TP**) and Ruapehu in background. NNE-trending Waihi Fault traces are shown in red (extensional). Note the ~17.5 ka Makahikatoa flank vent (**MK**) occurs immediately east of one of these Waihi Fault traces. Member abbreviations: Toatoa (**ato**), Pukekaikiore (**apk**), Te Pakiraki (**dpk**), Rahuituki (**arh**), Te Porere (**dtp**), Otamangakau (**aok**), Te Rurunga (**atr**), Rotopaunga (**arp**), Rangitaupahi (**ari**), Mangatapate (**amt**).

3.3.2.3.7. Waipoa Member (between 195 and 189 ka) – awp

Waipoa Member andesite lavas are the oldest eruptives on Tongariro that were demonstrably erupted from an area near present-day Central Crater (Fig. 3.4). Up to five conformable Waipoa Member lavas, totalling up to 100 m in thickness, are exposed on the NE Oturere valley wall, with other, lesser exposures in the Mangahouhounui valley and Mangatawai Stream. A single $^{40}Ar/^{39}Ar$ age determination for the Waipoa Member of 191 ± 4 ka (Table 3.1) contrasts with K/Ar determinations by Hobden et al. (1996) of 247 ± 20, 229 ± 22 and 173 ± 20 ka (Table 3.2). These K/Ar determinations are all from exposures at similar stratigraphic levels in the NE Oturere valley that, based on other well-dated exposures elsewhere on the mountain, are unlikely to span >70 kyr of eruptive activity, suggesting that some of these K/Ar age determinations are inaccurate. The new $^{40}Ar/^{39}Ar$ age determinations suggests that the Waipoa Member may have been erupted contemporaneously with the Pukekaikiore Member (section 3.3.2.3.6, above) but, because they are preserved on different parts of the mountain (Fig. 3.4), there are no field contacts with which to constrain their stratigraphic order (Fig. 3.3). The distributions of these two members indicate a shift in vent focus from the southern edifice (Pukekaikiore Member) to

the northern edifice (Waipoa Member) (Figs. 3.3-3.4), with the eruption of similar-composition magma (Tables 3.3-3.4).

The alternative hypothesis, that Waipoa Member lavas were erupted from a southern vent and travelled northwards over ice, is considered unlikely. Outcrops at equal elevation on both walls of the SE-trending Oturere valley only contain Waipoa Member lavas on the NE wall (Fig. 3.4). Given that that the dominant extensional faulting orientation is perpendicular to the Oturere valley (Fig. 3.1), Waipoa Member lavas should occur on the SW Oturere valley wall at similar elevations as the NE wall (up to 1560 m a.s.l.) if the vent location was near Ngauruhoe's present location, but this is not observed (Fig. 3.4). Outcrops of Waipoa Member lavas in the NE wall of the Oturere valley point back towards Central Crater and therefore this area is considered the most likely to be source vent location. The basal contact of the Waipoa Member has not been observed.

3.3.2.3.8. Undifferentiated Haumata Formation products – uha

The landscape-forming unit in the upper NE Oturere valley is composed of volcanic products with poor exposure due to a thick mantling of fan and tephra deposits (Fig. 3.4). The base of the unit is not exposed, but field relations imply that it underlies the Waipoa Member and therefore most likely belongs to the Haumata Formation or, less likely, the Tupuna Formation or Otamatereinga Formation (Fig. 3.3).

3.3.2.4. Mangahouhounui Formation (between 189 and 130 ka) – MH

Products of the Mangahouhounui Formation were erupted from a vent area in the present-day position of Central Crater, except for the Tātaramoa Member, which was possibly erupted from a flank vent (Fig. 3.4). Most Mangahouhounui Formation products occur in the Mangahouhounui valley, but minor exposures also occur in the distal SW Oturere valley and on the NE flank of Tongariro (Fig. 3.4). Mangahouhounui Formation eruptives are characterised by common 8-9 mm-long plagioclase and clinopyroxene phenocrysts (Table 3.3). Other Tongariro eruptives have smaller plagioclase and pyroxene phenocrysts, generally both <5 mm.

3.3.2.4.1. Te Pakiraki Member (between 189 and 130 ka) – dpk

As many as 20 lava flows and agglutinates exposed in the Mangahouhounui valley and distal SW Oturere valley constitute the Te Pakiraki Member (Fig. 3.4). Compositions range from basaltic-andesite to dacite but, overall, high-silica andesite predominates (Tables 3.3-3.4). Large

plagioclase (up to 9 mm) and clinopyroxene (up to 8 mm) phenocrysts are characteristic, and apatite (≤300 μm) is common in more silicic flows (Table 3.3).

Five new $^{40}Ar/^{39}Ar$ age determinations for Te Pakiraki Member lavas build on two previous K/Ar age determinations (Table 3.2). The $^{40}Ar/^{39}Ar$ age determinations are 186 ± 22, 165 ± 6, 155 ± 5, 152 ± 4 and 137 ± 7 ka (Table 3.1). The oldest of these age results is from a lava that overlies the 195-189 ka Waipoa Member (Fig. 3.3). The youngest $^{40}Ar/^{39}Ar$ age (137 ± 7 ka) is a re-dated aliquot of TG084 (Hobden et al., 1996) and was prepared from the original sample. The reported K/Ar age for this sample is 97 ± 20 ka, which does not overlap within 2 s.d. error of 137 ± 7 ka (Table 3.2). The other K/Ar age result of 123 ± 20 ka (TG114: Hobden et al., 1996) from the NE Oturere valley is within error of only the 137 ± 7 ka $^{40}Ar/^{39}Ar$ age determination (Table 3.2) and might reflect the younger end of the age range of this member.

Te Pakiraki Member eruptives possess some of the most conspicuous textures indicative of lava-ice interaction on Tongariro. In the Mangahouhounui valley, eruptive products are confined to the valley walls and display overthickened margins that occasionally bulge out towards the valley's centre. In the SW Mangahouhounui valley, ridge-confined lavas contain joints with ≤15-20 cm spacing that define horizontal columns (Fig. 3.6b), which are indicative of ice-contact cooling (e.g. Lescinsky and Sisson, 1998; Conway et al., 2015). On both sides of the Mangahouhounui valley the Te Pakiraki Member is associated with monomict breccias that are composed of volcaniclastic materials intercalated with coherent lavas (Fig. 3.6a). The petrographic features and major oxide concentrations of breccia clasts are most similar to the nearest lavas exposed uphill. These intercalated lava-breccia deposits have metre-scale layering and plaster the slopes, parallel to the valley walls, and are interpreted as deposits associated with the emplacement of lavas alongside glaciers.

3.3.2.4.2. Waiaruhairiki Member (between 152 and 150 ka) – awh

The Waiaruhairiki Member is intercalated between upper and lower sequences of Te Pakiraki eruptives in the NE wall and headwall of the Mangahouhounui valley (Fig. 3.4). Field relations show that Te Pakiraki Member products were erupted penecontemporaneously with the 152-150 ka Waiaruhairiki Member. On the NE wall of the Mangahouhounui valley, a single 20-40 m thick exposure of Waiaruhairiki Member lavas occurs between lower (~100 m) and upper (~150 m) successions of Te Pakiraki Member (Fig. 3.3). This relationship is repeated in the headwall of the Mangahouhounui valley. Waiaruhairiki lava also occurs as an inlier on the

planèze[1] north of the Mangahouhounui valley. Examinations of time-composition relationships in (section 3.5.4) indicate cyclic mafic replenishment episodes that appear to be represented by the Waiaruhairiki and Tātaramoa (section 3.3.2.4.3) members.

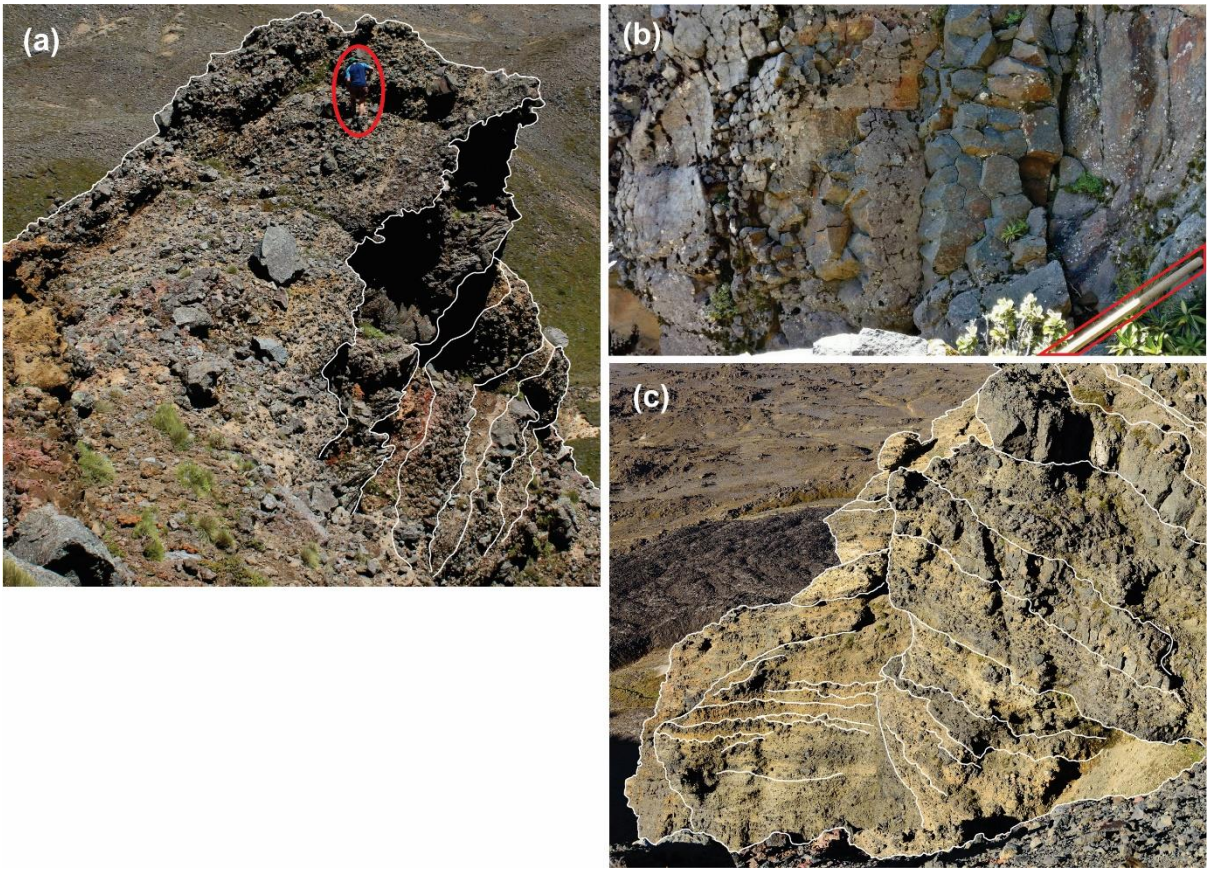

Figure 3.6. Lava-ice interaction features on Tongariro. **(a)** Alternating layers of intercalated coherent lava and monomict breccia deposits composed of subangular lava fragments in Te Pakiraki Member lava with an inferred age between 150-130 ka at this locality, northern Mangahouhounui valley [E1832474, N5665970, 1580 m a.s.l.]. Geologist circled in red is ~1.8 m tall. **(b)** Horizontal column joints in Te Pakiraki Member lava with an inferred age between 150-130 ka at this locality, southern Mangahouhounui valley [E1831657, N5664737, 1610 m a.s.l.]. Column diameters are between 10-25 cm. Sledgehammer handle (red) is 1 m. **(c)** Layers of lapilli tuff breccia (5-70 cm thick) intercalated with layers of fine sediment (grain sizes <<1 cm, layers 1-10 cm thick) and coherent lavas (≥60 cm thick) in Waitakatorua Member ridge-top deposits between the Oturere and Mangahouhounui valleys [E1831362, N5664691, 1680 m a.s.l.]. Photo courtesy of D. B. Townsend (recorded 2015).

Like Te Pakiraki eruptives, Waiaruhairiki lavas contain large plagioclase (up to 9 mm) and clinopyroxene (up to 8 mm) phenocrysts, which suggests similar magma assembly conditions, possibly in the same magma system, despite their distinct MgO concentrations (Tables 3.3-3.4). A single $^{40}Ar/^{39}Ar$ age determination for the Waiaruhairiki Member of 147 ± 7 ka (Table 3.1:

[1] An elevated, sloping, triangular landform that forms a flank on a composite volcano.

LP245) has a younger mean value than a Te Pakiraki $^{40}Ar/^{39}Ar$ age determination of 155 ± 5 (Table 3.1: LP118) from a lava that is inferred to overlie the Waiaruhairiki Member. This relationship implies that the age of the Waiaruhairiki Member is between 152-150 ka (further explanation provided in Appendix 2).

3.3.2.4.3. Tātaramoa Member (between 189 and 130 ka) – mtm

A small outcrop (<300 m of streambed exposure) of basaltic-andesite in the Tahurangi Stream on NE Tongariro is only known outcrop of the Tātaramoa Member (Fig. 3.4). Association with Mangahouhounui Formation eruptives is based on the petrography of the lava, which contains plagioclase and clinopyroxene crystals up to 8 or 9 mm in length. No radiometric age analyses have been attempted for the Tātaramoa Member because known outcrops are comprised of glassy and vesicular lava (Table 3.3). Its age is inferred based on its distinct petrography that is unique to the 198-130 ka Mangahouhounui Formation. This age is consistent with the Rotopaunga Member that overlies the Tātaramoa Member at this site (68 ± 15 ka: LP211 in Table 3.1). The spatial separation and mafic composition of the Tātaramoa Member relative to other Mangahouhounui Formation eruptives (Tables 3.3-3.4) suggest that it may have been erupted from a flank vent. A possible vent location is the dome-like Te Tatau summit, located ~2 km uphill of the Tātaramoa Member outcrop location in Tahurangi Stream (Fig. 3.2).

3.3.2.4.4. Undifferentiated Mangahouhounui Formation products – umh

Landscape-forming materials in the lower part of the Mangahouhounui valley headwall are poorly exposed and have not been sampled because they are covered in fan deposits and tephra. The stratigraphic levels of Te Pakiraki and Waiaruhairiki members in the headwall of the Mangahouhounui valley (Fig. 3.4) suggest that these undifferentiated materials are likely to be part of the Mangahouhounui Formation. However, given the available stratigraphic constraints, they could be part of the older (290-189 ka) Haumata Formation (Fig. 3.3).

3.3.2.5. Taiko Formation (between 133 and 52 ka) – TA

Products forming the Taiko Formation are lithologically diverse and spatially extensive, covering about 40% of Tongariro's surficial edifice area (Fig. 3.7). They were erupted from vent foci in the area of present-day Central Crater. However, the dips of Taiko Formation eruptives on Tongariro's upper edifice project back towards possible vent sources above 2000 m a.s.l., higher than any surviving landform in the Central Crater area. The Taiko Formation therefore, represents the last phase of edifice growth from which the source vent(s) are not preserved, and

all subsequent activity has been from vents that are presently visible in the landscape. The 'missing' edifice material is interpreted to have collapsed, forming the voluminous Te Whaiau Formation debris flow deposits (section 3.3.2.7, below).

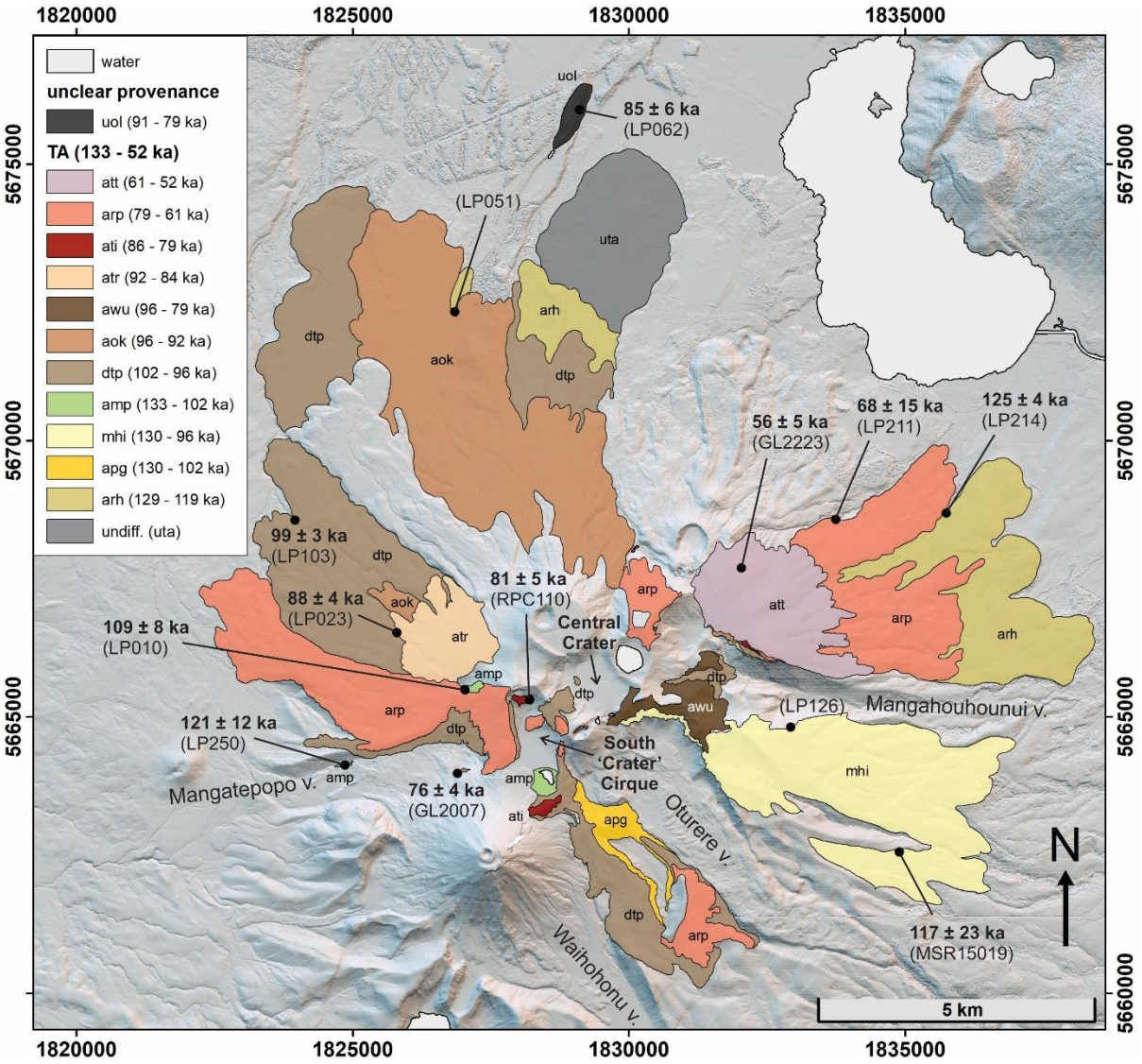

Figure 3.7. Distribution of the Taiko Formation (**TA**) eruptives for the interval between 133 to 52 ka. The source edifice of the undifferentiated Otukou lava (**uol**) is unclear. Member abbreviations are: Rahuituki (**arh**), Pungarara (**apg**), Mangahouhouiti (**mhi**), Mangatepopo (**amp**), Te Porere (**dtp**), Otamangakau (**aok**), Waitakatorua (**awu**), Te Rurunga (**atr**), Te Wakarikiariki (**ati**), Rotopaunga (**arp**), Te Tatau (**att**). Key landmarks are labelled. $^{40}Ar/^{39}Ar$ age determinations on LP051 and LP126 were adversely affected by groundmass glass but are indicated here because heating step results are provided in Appendix 1 for these samples. $^{40}Ar/^{39}Ar$ age results are presented in Table 3.1 and summarised with K/Ar age results (Hobden et al., 1996) in Table 3.2 for each stratigraphic unit.

3.3.2.5.1. Rahuituki Member (between 129 and 119 ka) – arh

The Rahuituki Member comprises andesite lavas on Tongariro's distal NE and NW flanks. These lavas have runout lengths of up to 9 km from an inferred source area at present-day Central

Crater (Fig. 3.7). This distribution contrasts with older eruptives of the Mangahouhounui Formation that are generally confined to valley walls and have smaller runout distances (up to 6 km). A single $^{40}Ar/^{39}Ar$ age determination of 124 ± 5 ka from the NE flank is the only reliable radiometric age constraint for the Rahuituki Member, which is consistent with field relations (Table 3.1: LP214).

3.3.2.5.2. Pungarara Member (between 130 and 102 ka) – apg

The Pungarara Member is composed of andesite lavas exposed on the upper SW Oturere valley wall (Fig. 3.7). Two K/Ar age determinations by Hobden et al. (1996) yielded ages of 103 ± 24 ka (TG171) and 77 ± 28 ka (TG077) (Table 3.2). At this locality, 102-96 ka Te Porere Member lavas overlie Pungarara Member andesites, which is compatible within the analytical uncertainty of the dates (Fig. 3.3). Pungarara Member andesites contain trace amounts of Fe-Ti oxide pseudomorphs after amphibole, which distinguishes them from the 129-119 ka Rahuituki Member. This petrographic difference may imply similar magmatic storage conditions and histories between the Pungarara Member and the Haumata and Tupuna formations, which also possess this petrographic feature.

3.3.2.5.3. Mangahouhouiti Member (between 130 and 96 ka) – mhi

The Mangahouhouiti Member is Tongariro's largest unit that contains olivine as the dominant phenocrystic mineral, which was sourced from an upper-edifice vent location. This unit is also distinguished by its high MgO concentration of ~6.3 wt% (Table 3.4). It comprises basaltic-andesite lava flows and minor agglutinates that occur only on the planèze between the Mangahouhounui and Oturere valleys, a distribution that implies a source vent near the present-day area of Central Crater (Fig. 3.7). However, the confinement of Mangahouhouiti Member to this planèze and its mafic composition suggest it was probably erupted from a flank vent at the head of the planèze. The overall thickness of the Mangahouhouiti Member is 20-40 m and consists of two to three conformable lavas. Two $^{40}Ar/^{39}Ar$ age determinations have been attempted on lavas from the Mangahouhouiti Member: of these, one was adversely affected by glass in the groundmass material and is reported only in Appendix 1 (LP126) but its location is shown in Fig. 3.7. The other age determination of 117 ± 23 ka is the preferred radiometric constraint for this member (MSR15019: Table 3.1, Fig. 3.7), which has mixed agreement with previous K/Ar determinations of 202 ± 46 and 123 ± 32 ka by Hobden et al. (1996). The Mangahouhouiti Member overlies the 195-189 ka Waipoa Member, consistent with age results (Fig. 3.3).

3.3.2.5.4. Mangatepopo Member (between 133 and 102 ka) – amp

The Mangatepopo Member is composed of poorly exposed andesite lavas, both on ridgetop and valley-floor locations in the Mangatepopo valley and Tongariro's upper edifice (Fig. 3.7). Of two $^{40}Ar/^{39}Ar$ ages determinations for this member, the oldest is 121 ± 12 ka from a lava in the floor of the Mangatepopo valley (Table 3.1: LP250). The valley-floor position indicates that Tongariro was relatively ice-free at the time of this lava's emplacement. Another $^{40}Ar/^{39}Ar$ age of 109 ± 8 ka was determined on an inlier north of Mangatepopo valley (Table 3.1: LP010).

3.3.2.5.5. Te Porere Member (between 102 and 96 ka) – dtp

The Te Porere Member consists of high-silica andesites and low-silica dacites. Outcrops on Tongariro's NW, NE and SW flanks triangulate towards a vent area in the present-day location of Central Crater (Figs. 3.5, 3.7). This map unit covers a large part of central Tongariro that was mapped by Nairn (1996) but left as undifferentiated by Townsend et al. (2017). A recent study by Cole et al. (2018) remapped and sampled some of these deposits on the upper central-edifice but not on flank areas. Te Porere Member eruptives are lithologically diverse: they include minor volumes of hyaloclastites, lapilli tuffs and lapilli tuff breccias (labelled ERh, ERltb and PLT in Cole et al., 2018), but are mostly composed of lavas and agglutinates. The hyaloclastites and lapilli tuff deposits on Tongariro's upper edifice indicate transient subaerial to subglacial eruptive activity (Cole et al., 2018, 2019). The thickest sequence of Te Porere Member lavas is on the northern wall of the Mangatepopo valley, where up to eight conformable lavas of 100-120 m total thickness occur. Here, lavas commonly display knuckles[2], locally increasing in thickness by up to ~40% (~8 m for flows ~20 m thick), which is taken to indicate that these lavas were impounded by ice (e.g. Conway et al., 2015). In the SW Oturere valley, a succession of up to six conformable lavas is 80-90 m thick. These lavas are exposed on ridges and on planèzes adjacent to the valley, but are not observed on the valley floor, which is further evidence for the syn-glacial emplacement of Te Porere Member eruptives. A single $^{40}Ar/^{39}Ar$ age determination for this member of 99 ± 3 ka (Table 3.1: LP103) is within error of most of the previous K/Ar determinations: 110 ± 12, 97 ± 20, 95 ± 20, 95 ± 20, 91 ± 18, 81 ± 34, 68 ± 22 ka (Hobden et al., 1996) and 107 ± 20 ka (Stipp, 1969). The Te Porere Member is inferred to overly the Mangatepopo Member in the floor of the Mangatepopo valley (dated at 121 ± 12 ka at this locality: Table 3.1), which is consistent with Te Porere Member radiometric age results (Table 3.2; Fig. 3.3).

[2] Protrusions of lava that ponded in void space at the lava-ice interface (e.g. Conway et al., 2015).

3.3.2.5.6. Otamangakau Member (between 96 and 92 ka) – aok

The Otamangakau Member consists of andesite lavas and agglutinates found primarily on Tongariro's NW flank and in the Mangahouhounui valley (Figs. 3.5, 3.7). Otamangakau Member andesites are compositionally similar to Te Porere Member eruptives, but are distinguished by higher MgO concentrations above 3.1 wt% (Table 3.3). No radiometric age analyses exist for the Otamangakau Member, but field relationships show that it overlies 102-96 ka Te Porere Member (Figs. 3.3, 3.5, 3.7).

3.3.2.5.7. Waitakatorua Member (between 96 and 79 ka) – awu

The Waitakatorua Member forms a prominent ridge that separates the Oturere and Mangahouhounui valleys and it also occurs in the Mangahouhounui valley (Fig. 3.7). It comprises coherent lava flows intercalated with bedded lapilli tuffs (Fig. 3.6c) which were erupted from a vent focus near present-day Central Crater. The presence of lapilli tuff breccias, which are sometimes reworked (Fig. 3.6c), and the ridge-confined locations of Waitakatorua Member materials are suggestive of syn-glacial emplacement. The alternating emplacement of coherent lavas and water-reworked lapilli tuff breccias suggests a vent focus that transitioned between subaerial and subaqueous (or subglacial) eruptive activity (e.g. Cole et al., 2018). Five previous K/Ar determinations of 164 ± 24, 128 ± 24, 122 ± 20, 105 ± 24 and 104 ± 26 ka by Hobden et al. (1996) exist for Waitakatorua Member (Table 3.2). The 164 ± 24 ka K/Ar result conflicts with field relations showing Waitakatorua Member eruptives directly overlying the 130-96 ka Mangahouhouiti Member (Fig. 3.3) in the Mangahouhounui valley (Fig. 3.7).

3.3.2.5.8. Te Rurunga Member (between 92 and 84 ka) – atr

The Te Rurunga Member is composed of andesitic welded agglutinates, scoria and lava in a ~1 km^2 exposure on Tongariro's upper western slopes (Figs. 3.5, 3.7). A single $^{40}Ar/^{39}Ar$ age of 88 ± 4 ka (Table 3.1: LP023) was determined on a boulder that is correlated with Te Rurunga Member on compositional grounds; all *in situ* material was texturally unsuitable for dating due to high proportions of glassy matrix (e.g. Gamble et al., 2003). The age result is consistent with field relations that show the Te Rurunga Member overlying the 102-96 ka Te Porere and 96-92 ka Otamangakau members (Fig. 3.3).

3.3.2.5.9. Te Wakarikiariki Member (between 86 and 79 ka) – ati

This member consists of several isolated lavas on Tongariro's upper edifice and in the Mangahouhounui valley and is partly equivalent to Cole et al.'s (2018) unit labelled dL (Fig. 3.7).

Some Te Wakarikiariki Member lavas are characterised by up to 7 mm plagioclase crystals, the sizes of which may suggest similar magma storage conditions and crustal residence times to the older Mangahouhounui Formation (Table 3.3). A single $^{40}Ar/^{39}Ar$ age determination of 81 ± 5 ka (Table 3.1) for Te Wakarikiariki Member lava was previously reported by Cole et al. (2018), which is compatible with field relationships observed in this study (Fig. 3.3).

3.3.2.5.10. Rotopaunga Member (between 79 and 61 ka) – arp

The Rotopaunga Member is synonymous with the Rotopaunga Formation of Townsend et al. (2017). Here, the Rotopaunga Member includes lavas and agglutinates on Tongariro's NE, SE and W flanks (Fig. 3.7). It also includes hyaloclastites and lapilli tuff breccias on Tongariro's upper edifice mapped by Cole et al. (2018; their units ERh and ERltb). These lithologies indicate a vent location that alternated between subaerial and subglacial eruptive activity. Other outcrops of the Rotopaunga Member on Tongariro's NE, SE and W flanks triangulate to a source region in the present-day Central Crater area (Fig. 3.7). Two $^{40}Ar/^{39}Ar$ ages determined for Rotopaunga Member lavas add to three previous K/Ar determinations (Table 3.2). A lava in the head of the Mangatepopo valley yielded an age of 76 ± 3 ka $^{40}Ar/^{39}Ar$ (Table 3.1: GL2132; G.S. Leonard, pers. comm., 2019), which compares well with a previous K/Ar age of 79 ± 18 ka from the same location (Hobden et al., 1996). The second $^{40}Ar/^{39}Ar$ age determination from NE Tongariro has a result of 68 ± 15 ka (Table 3.1: LP211). Both $^{40}Ar/^{39}Ar$ age results are indistinguishable within uncertainty of two other K/Ar determinations of 87 ± 20 ka (TG051) and 64 ± 22 ka (TG330) reported by Hobden et al. (1996) (Table 3.2). All radiometric age results are consistent with observed field relations showing Rotopaunga Member eruptives overlying 102-96 ka Te Porere and 86-79 ka Te Wakarikiariki members (Fig. 3.3).

3.3.2.5.11. Te Tatau Member (between 61 and 52 ka) – att

The Te Tatau Member is synonymous with the Te Tatau Formation of Townsend et al. (2017). It comprises andesitic scoria, agglutinates and lavas exposed on Tongariro's upper NE flank (Fig. 3.7). They present no lithological or textural indication of syn-glacial eruptive activity which distinguishes them from the earlier 96-79 ka Waitakatorua (cf. Fig. 3.6c), 86-79 ka Te Wakarikiariki and 79-61 ka Rotopaunga members. A single $^{40}Ar/^{39}Ar$ age determination of 56 ± 5 ka is consistent with field relations showing Te Tatau Member eruptives overlying the Rotopaunga Member, which is dated at 68 ± 15 ka (Table 3.1: LP211) 1-2 km NE of Te Tatau Member exposures (Fig. 3.7).

3.3.2.6. Undifferentiated Otukou lava (between 91 and 79 ka) – uol

This unit comprises a crystal-poor andesite lava dated at 85 ± 6 ka by both K/Ar (Stipp, 1969) and $^{40}Ar/^{39}Ar$ methods (Table 3.1). It is exposed in a ~30 m section on the Waihi Fault scarp near the Otukou settlement, ~9 km north of Tongariro (Fig. 3.7), also previously reported by Cole (1979). Its composition is similar to Tongariro's 86-79 ka Te Wakarikiariki and 61-52 ka Te Tatau members. However, field relations do not support associations between these members and the Otukou lava. Tongariro's older 96-92 ka Otamangakau, 102-96 ka Te Porere and 129-119 ka Rahuituki members occur between the Otukou outcrop and appearances of the Te Wakarikiariki and Te Tatau members on northern Tongariro, which should be buried by more recently erupted Otukou lava if Tongariro was the source. Other studies (e.g. Lecointre et al., 2002) have attributed the lava's source to the small edifice of Maungakatote, ~15 NNW of Tongariro. Other possibilities include the Rotopounamu vent area on Pihanga's SW flank and the Kakaramea edifice (Fig. 3.1). However, available compositional data (Cole, 1978; Cashman, 1979; Cole et al., 1983; this study) are unable to confidently associate the Otukou lava with any of these vent foci in a manner compatible with field relations. The Otukou lava is overlain by 50-45 ka Te Whaiau Formation debris flows (Lecointre et al., 2002) but field relations with other southern TVZ eruptives are unclear.

3.3.2.7. Te Whaiau Formation (between 50 and 45 ka) – TW

The Te Whaiau Formation usage here follows Prebble (1995), Lecointre et al. (2002) and Townsend et al. (2017). The formation represents a significant volume of material that was removed from Tongariro's upper edifice and conveyed as numerous debris flows to the NW ring plain (Fig. 3.7; Table 3.5). A significant proportion of this material probably represents missing edifice material, probably from the Taiko Formation's vent area near Central Crater (Figs. 3.7-3.8). Thus, Taiko Formation materials are expected to be the dominant constituents of Te Whaiau Formation debris. However, one clast sampled from the Te Whaiau Formation is compositionally similar to the Otamatereinga Formation (Table 3.3) and indicates that representative clast sampling is needed to properly assess which source materials comprise Te Whaiau Formation deposits.

The depositional mechanism of the Te Whaiau Formation may not have been as a cohesive debris flow as suggested by Lecointre et al. (2002). Evidence for successive debris flows with varied clast sizes is indicated by m-scale bedding in type locality outcrops on State Highway 47 ~8-9 km NW of Tongariro, previously reported by Lecointre et al. (2002). The distribution of Te Whaiau Formation deposits, as mapped here (Fig. 3.8) and elsewhere

(Lecointre et al., 2002; Townsend et al., 2017), may incorporate unrelated ring plain deposits because poor exposure and forestation on NW Tongariro have discouraged representative investigations of Te Whaiau Formation deposits.

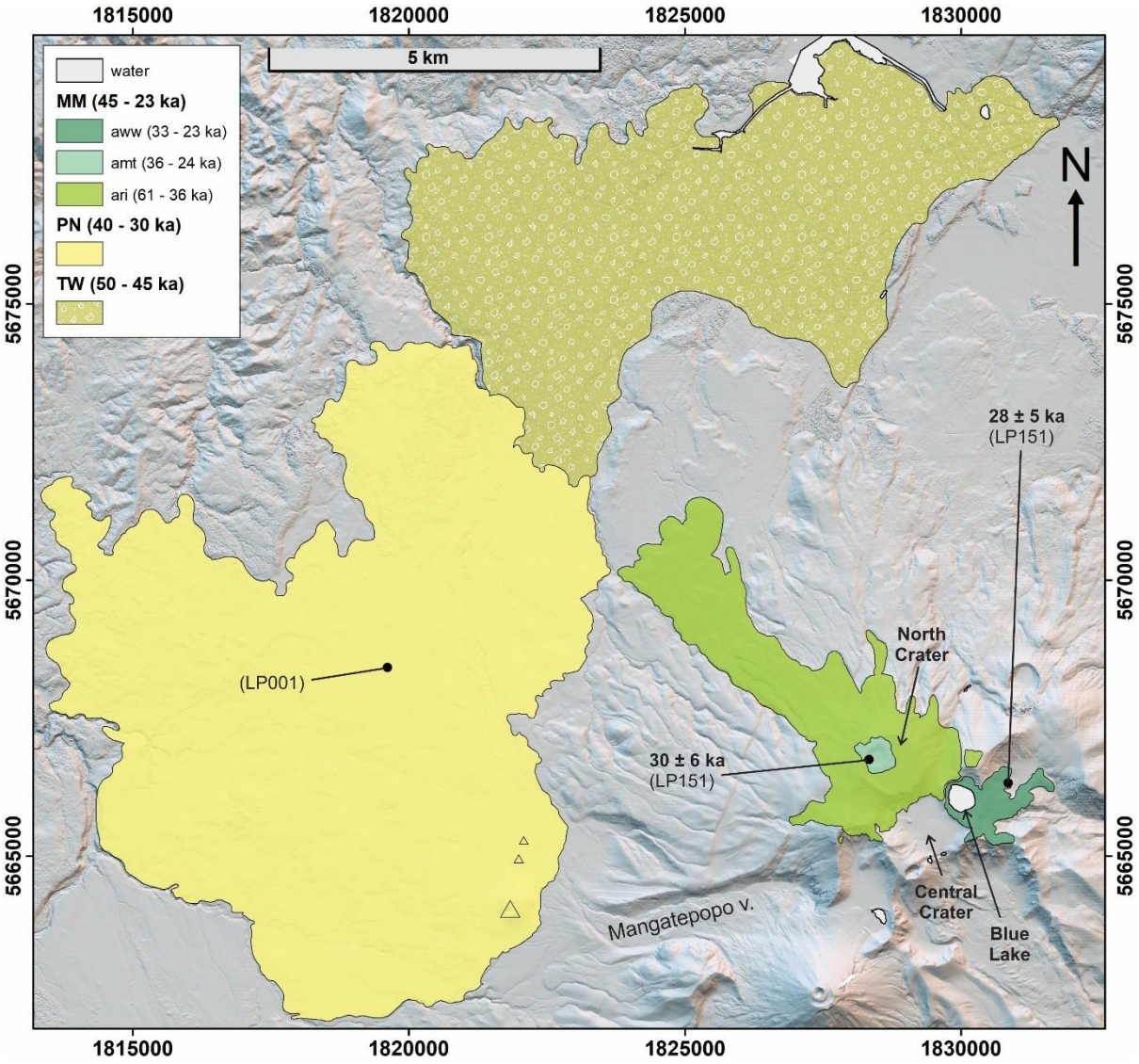

Figure 3.8. The distribution of Pukeonake Formation (**PN**) and Mokomoko Formation (**MM**) eruptives and the Te Whaiau Formation debris flow deposits (**TW**). The Pukeonake Formation was vented from one or more satellite cones, shown by triangles, with the main cone as the largest triangle. Pukeonake Formation lavas overlie the Te Whaiau Formation. Rangitaupahi (**ari**) and Mangatapate (**amt**) members were erupted from North Crater vents. The Te Wai Whakaata Member (**aww**) was erupted from a vent at the present-day location of Blue Lake. Field relationships indicate that at the time the North Crater and Blue Lake vents were growing, Central Crater was filling with reworked erupted material. Key landmarks are labelled. See Table 3.1 for $^{40}Ar/^{39}Ar$ age results. LP001 is indicated without an age value because $^{40}Ar/^{39}Ar$ age analysis was adversely affected by groundmass glass, but heating step results are presented in Appendix 1.

Te Whaiau Formation deposits must pre-date Mokomoko Formation eruptives on NW Tongariro (section 3.3.2.9), although age relationships with 133-52 ka Taiko Formation eruptives are challenging to assess and remain inconclusive. The age of Te Whaiau Formation is not directly known but constraints are provided by relationships with the regionally-dispersed Rotoehu Ash, which the Te Whaiau Formation overlies (Fig. 3.3) (Lecointre et al., 2002). Te Whaiau Formation deposits are also reported to overlie undifferentiated Otukou lava (section 3.3.2.6) which have a well-constrained age of 85 ± 6 ka (Tables 3.1-3.2). Lecointre et al. (2002) suggest the age of the Te Whaiau Formation is between 60 and 55 ka based on radiocarbon dating of material within the debris flows. However, these radiocarbon results are within error of background and could also post-date 55 ka. Recent age investigations on the underlying Rotoehu Ash (e.g. Flude and Storey, 2016 and references therein) indicate an age of 54 ± 6 ka, which serves as a maximum age for the Te Whaiau Formation as presently mapped. Tihoi (and Tahuna) rhyolitic fall deposits from the central TVZ with ages around 45 ka (Wilson and Charlier, 2009) overlie the Te Whaiau Formation (Lecointre et al., 2002) which provide a minimum age. From consideration of these field relationships and the debated age of the Rotoehu Ash (e.g. Berryman, 1992; Danišík et al., 2012; Flude and Storey, 2016), an age of between 50 to 45 ka is adopted for the Te Whaiau Formation. Further justification for this age is given in Appendix 2.

3.3.2.8. Pukeonake Formation (between 40 and 30 ka) – PN

This formation is the same as the Pukeonake Formation defined by Townsend et al. (2017) and the Pukeonake lavas of Grindley (1960). The Pukeonake Formation includes all eruptives vented from the Pukeonake system, which is currently represented by a surviving scoria cone beyond the western end of the Mangatepopo valley (Fig. 3.8). However other vent sites may exist, such as two ~20 m-high mounds found 800 m and 1100 m northwards of the main Pukeonake cone that possibly represent sites of lava venting and are now covered by spatter (Topping, 1974). Pukeonake eruptives are MgO-rich (7.9-8.9 wt%) basaltic-andesites with pyroxene-dominated phenocryst assemblages (Tables 3.3-3.4) that include prominent forsteritic olivines (Hobden, 1997; Beier et al., 2017). Only one direct radiometric age determination ($^{40}Ar/^{39}Ar$) exists for the Pukeonake Formation (LP001: Fig. 3.8), which was only partially successful. The age analysis data for LP001 are reported in Appendix 2 for which the preferred WMPA age has a mean value of ~37 ka, which is consistent with field relations (Fig. 3.3). However, because of low confidence in the $^{40}Ar/^{39}Ar$ age determination, the age of the Pukeonake Formation is constrained primarily by field relations. It overlies the Te Whaiau Formation (Townsend et al., 2017) and is overlain by

25.4 ka Oruanui fall deposits (Topping, 1974), from which an age between 40 and 30 ka is adopted (further explained in Appendix 2).

3.3.2.9. Mokomoko Formation (between 45 and 23 ka) – MM

The Mokomoko Formation defined here includes all products erupted from North Crater and Blue Lake. In earlier publications, Blue Lake and North Crater eruptives were mapped as separate formations (e.g. Gregg, 1960; Nairn, 1996; Townsend et al., 2017). However, close similarities in eruptive ages (shown by new data here: Table 3.1) and compositions (Tables 3.3-3.4) favour the grouping of these eruptives into a single map unit at the formation level. Within the Mokomoko Formation, subdivisions are made at the member level, jointly relating to compositions and vent locations: North Crater for the Rangitaupahi and Mangatapate members and Blue Lake for the Te Wai Whakaata Member.

3.3.2.9.1. Rangitaupahi Member (between 45 and 36 ka) – ari

This Member consists of andesitic lavas, agglutinates and minor lapilli tuffs that form the North Crater landform, and a 5 km-long lava flow to the NW of the cone (Fig. 3.7). Bedded lapilli tuffs and associated lavas exposed in the headwall of South Cirque, about 1 km to the southwest of North Crater, are probably the oldest Rangitaupahi Member eruptives. Together with the volumetrically-dominant Rangitaupahi Member agglutinates and lavas elsewhere, the bedded lapilli tuffs are taken as evidence of initial subglacial eruptive activity from a proto-North Crater vent (Cole et al., 2018: their corresponding bedded lapilli tuff and lava units are labelled LTa, LTac, LTb, LTc, LTd, LTo). This interpretation is supported by paleomagnetic studies on the aforementioned bedded lapilli tuffs that show random orientations of magnetism in juvenile clasts which indicate rapid cooling and waterlain deposition contemporaneously with eruption (Cole et al., 2019). During the later stages of activity from North Crater, the vent became subaerially emergent and dispersed agglutinates up to 1 km away during fire-fountaining eruptions. This activity generated the 5 km-long flow-banded lava to the NW of North Crater. Other studies have inferred the presence of a lava lake that filled the crater floor (Townsend et al., 2017 and references therein), which is consistent with the prominence of younger Mangatapate Member eruptives (section 3.3.2.9.2, below) that are evidently perched above the main crater floor on a shallow substratum. A 300 m diameter cap of Rangitaupahi Member spatter is preserved on the ridge to the north of Blue Lake, about 1 km east of North Crater. This spatter rests on Rotopaunga Member agglutinates, implying a post-61 ka age (Fig. 3.3).

3.3.2.9.2. Mangatapate Member (between 36 and 24 ka) – amt

The Mangatapate Member is represented by lava, agglutinates and proximal ashy and blocky ejecta in and around the 400 m-wide crater on the NW summit floor of North Crater (Fig. 3.8). Holocrystalline lava in the pit's inner walls was likely exposed during an explosive phase that deposited the rim-draping agglutinates and surrounding blocks and tephra. The pit lava is compositionally distinct from Rangitaupahi Member eruptives. A sample of this pit lava yields a $^{40}Ar/^{39}Ar$ age of 30 ± 6 ka and is the first radiometric age determination for any North Crater lava (Table 3.1). Because this explosion pit is the youngest volcanic feature on the North Crater, the age results provides a minimum age for the cone and indicates that most of the cone must have developed by 30 ± 6 ka. This result is inconsistent with suggestions that North Crater is entirely post-25.4 ka in age that were based on relationships between tephras inferred to have been erupted from North Crater that overlie 25.4 ka Oruanui fall deposits (Shane et al., 2008). This discrepancy is discussed further in section 3.5.2, below.

3.3.2.9.3. Te Wai Whakaata Member (between 33 and 23 ka) – aww

Andesitic lavas and agglutinates erupted from a vent now occupied by Blue Lake form the Te Wai Whakaata Member (Fig. 3.8), which is equivalent to the Blue Lake Formation of Townsend et al. (2017). Te Wai Whakaata Member eruptives are distinguished from other Mokomoko Formation products by their separate vent location which is ~1 km east of North Crater (Fig. 3.8). Like Rangitaupahi Member products, Te Wai Whakaata Member eruptives contain trace amounts of xenocrystic olivine and are compositionally identical to Mangatapate Member eruptives in major oxides, within analytical uncertainty, which suggests a magmatic consanguinity (Tables 3.3-3.4). Te Wai Whakaata Member eruptives include a succession of conformable lavas that flowed eastwards from the Blue Lake vent into the Mangahouhounui valley. To the southeast, Te Wai Whakaata Member agglutinates overlie Waitakatorua Member lavas at an elevation 50-100 m above Blue Lake itself (~1740 m a.s.l.), which is taken to indicate deposition by fire-fountaining from an ice-free vent area (Fig. 3.8). Te Wai Whakaata Member lavas on the floor of the Mangahouhounui valley appear to be subtly overthickened by ≤20 m and are overlain by a thin (<20 m) veneer of moraine at ~1500 m a.s.l. A lava at the head of the Mangahouhounui valley was $^{40}Ar/^{39}Ar$ dated to yield an age of 28 ± 5 ka, which overlaps in time with the Mangatapate Member's age of 30 ± 6 ka (Table 3.1). This indicates that Tongariro was relatively ice-free when Te Wai Whakaata Member lavas were erupted, but subsequently experienced increased ice coverage.

3.3.2.10. Te Maari Formation (before 25.4 ka to present) – TM

This formation is synonymous with the Te Maari Formation of Townsend et al. (2017) and is composed of three new members and an undifferentiated mapping unit. The members are defined by their stratigraphic relationships with respect to regional and local tephras with established ages: 25.4 ka Oruanui Formation (Vandergoes et al., 2013), 17.5 ka Rerewhakaaitu Tephra (Lowe et al., 2013), Pahoka-Mangamate sequence and the 3.5 ka Papakai Tephra (Topping, 1974; Donoghue et al., 1995a; Nairn et al., 1998). The age of the youngest member (Mangatetipua Member) is constrained by dendrochronology and witnessed events (Topping, 1974; Scott and Potter, 2014). More details are provided in Appendix 2.

In general, the Te Maari Formation eruptives are less well studied than other Tongariro eruptives for which exisiting geochemical and petrographic data are summarised in Tables 3.3-3.4. Eruptives of the oldest three subunits (undifferentiated lava [**utm**], Paungaiti Member [**api**] and Heretoa Member [**aht**]) are all andesites whereas the youngest Mangatetipua Member (**mgt**) is basaltic-andesite. Undifferentiated pre-Oruanui lava (before 25.4 ka) was possibly erupted from a now-buried vent located ~500 m east of Lower Te Maari Crater (Cronin, 1996; Townsend et al., 2017). This lava is overlain by the Paungaiti Member, which was erupted between 25.4 and 17.5 ka from the Lower Te Maari Crater (Cronin, 1996; Lecointre et al., 2004; Townsend et al., 2017). Paungaiti Member eruptives flowed ~6.5 km northwards to what is now Lake Rotoaira's eastern shoreline (Townsend et al., 2017). Younger Heretoa Member andesites were erupted between 11.0 and 3.5 ka from a vent focus ~500 m north of Lower Te Maari Crater, and flowed northwards, some as far as what is now Lake Rotoaira's southern shoreline. Subsequently basaltic-andesite lava was erupted from Upper Te Maari Crater at 1528 CE (Topping, 1974; Cole, 1978), forming a 3.5 km-long, leveed flow. The Mangatetipua[3] Member, defined here, includes this basaltic-andesite lava and all subsequent Te Maari eruptives, including products of the 2012 eruptions from Upper Te Maari Crater.

3.3.2.11. Makahikatoa Formation (~17.5 ka) – MK

Basaltic-andesite scoria, lava and spatter erupted from a post-glacial vent on top of the Pukekaikiore landform constitute the Makahikatoa Formation, following the usage of Townsend

[3] The name 'Mangatipua' that is used for a local stream on local topographic maps (e.g. Topo50 series [Land Information New Zealand]) but was apparently mis-named. It has been used for the 'Mangatipua mudflow', a debris flow originating from the Ketetahi Springs area on the slopes of nearby Mount Tongariro, that occurred in c. 1896 (Topping 1974). The correct name for the stream, 'Mangatetipua', is used here for the youngest member of the Te Maari Formation.

et al. (2017). The vent location appears to be related to where the southern extension of the Waihi Fault cuts the Pukekaikiore landform (Figs. 3.5, 3.9). Field relations provide a well-constrained age estimate for Makahikatoa Formation eruptives of about 17.5 ka. This is constrained by the age of the Rerewhakaaitu Tephra (Lowe et al., 2013) that is interbedded between horizons of Makahikatoa Formation scoria (Topping, 1974). This age result is also consistent with field relations that show Makahikatoa Formation lava having been diverted around Marine Isotope Stage (MIS) 2 moraines that were deposited prior to glacial retreat at ~18 ka (Eaves et al., 2016a).

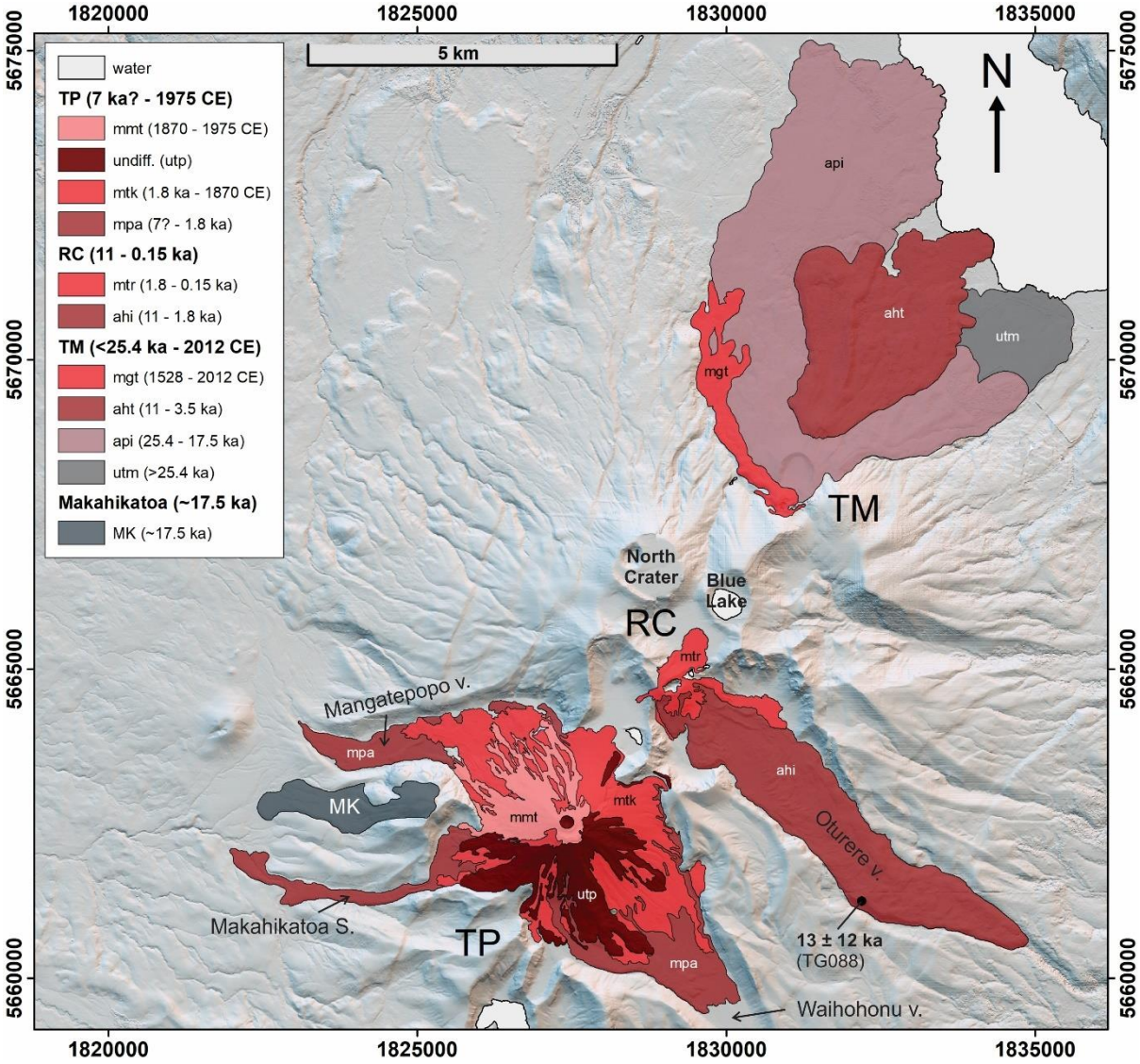

Figure 3.9. Eruptives from the Te Pupu Formation (Ngauruhoe – **TP**), Red Crater Formation (**RC**), Te Maari Formation (**TM**) and the Makahikatoa Formation (**MK**). Identical colours reflect similar ages between these contemporaneously active separate vent systems. Age relationships are largely determined from tephrostratigraphy, as explained in sections 3.3.2.10-3.3.2.13 and in Appendix 2. $^{40}Ar/^{39}Ar$ age determination data for TG088 are provided in Table 3.1. Key landmarks are labelled.

3.3.2.12. Red Crater Formation (between 11.0 and 0.1 ka) – RC

The Red Crater Formation is synonymous with the usage of Townsend et al. (2017) and two new members are defined. It comprises lava, spatter and scoria erupted from Red Crater at the head of the Oturere valley (Fig. 3.9). Volcanic products on Tongariro's edifice record as many as 12 distinct eruptions from Red Crater (Topping, 1974; Shane et al., 2017) and tephra records suggest up to 16 eruptions since ~1660 CE (Moebis et al., 2011). The first edifice-forming products of Red Crater comprise the Te Ahititi Member (**ahi**), represented by valley-filling andesitic lava flows in the Oturere valley (Fig. 3.9). The largest of these lavas was erupted during the early Holocene, which is consistent with Holocene tephra stratigraphy, including the overlying 232 CE Taupō ignimbrite (Topping, 1974; Hogg et al., 2012). This flow yielded an $^{40}Ar/^{39}Ar$ age of 13 ± 12 ka (Table 3.1: TG088, age from this study). This lava is 6.5 km long and has a volume of ~0.5 km^3 (Stevens, 2002). In contrast, post-232 CE eruptions produced mainly basaltic-andesite scoria, spatter and lavas (Topping, 1974), which make up the Te Rongo Member (**mtr**). Te Rongo Member eruptives are less voluminous and less widespread than Te Ahititi Member eruptives as shown by blocky Te Rongo lavas that flowed a maximum distance of only 1800 m from Red Crater's vent in N, E and W directions (Fig. 3.9). The Te Rongo Member includes a prominent dike on the inner walls of the Red Crater cone (Hobden, 1997; Wadsworth et al., 2015).

3.3.2.13. Te Pupu Formation (between 7? ka and 1975 CE) – TP

Previously defined by Townsend et al. (2017), the Te Pupu Formation comprises all edifice-forming products erupted from the Ngauruhoe cone (Fig. 3.9). The formation is subdivided into three members and an undifferentiated unit, defined by two time-stratigraphic markers: the 232 CE Taupō ignimbrite (Hogg et al., 2012) and European arrival in New Zealand. In a practical sense, the latter corresponds to the earliest witnessed "historical" lava eruption of Ngauruhoe in 1870 CE that produced edifice-building materials (Hobden et al., 2002). In eruptive order, the Te Pupu Formation comprises the Papamānuka (**mpa**: between 7? ka and 232 CE), Toakakura (**mtk**: between 232 CE and 1870 CE) and Matariki (**mmt**: from 1870 CE to 1975 CE) members. An undifferentiated unit (**utp**) encompasses all eruptives for which age relations are either undocumented or observations are unclear. Papamānuka Member eruptives have the furthest runout lengths from the Ngauruhoe cone, up to 5.5 km from the present-day vent position (Fig. 3.9). These flows are demonstrably Holocene because they are present on the floors of all key drainages around Ngauruhoe that were previously glaciated in MIS 2: Mangatepopo valley, Makahikatoa Stream and Waihohonu valley (Eaves et al., 2016a). Overlying and younger Te Pupu

Members have shorter runout distances of <3 km (Toakakura) and <2 km (Matariki). All Te Pupu subunits include basaltic-andesites that have a large degree of compositional overlap with each other (Tables 3.3-3.4). Detailed field mapping and compositional data was used by Hobden et al. (2002) to define five distinct groups. However, their study notes that older compositional "types" reappear after evidenced time-breaks, which precludes the assignment of ages from compositional data alone. The equivalence between map units of this study and those of Hobden et al. (2002) and Townsend et al. (2017) is given in Appendix 2. The age of onset of activity at Ngauruhoe (Te Pupu Formation) is discussed in section 3.5.2, below.

3.4. VOLUMES

The volumes of edifice-forming materials on Tongariro have been estimated for all mapped formations and members. The total volume for exposed Tongariro eruptives is 19 km^3. In comparison, the adopted value for Tongariro's total edifice volume is ~90 km^3, for which only 21% is presently visible. The estimation of these values is explained as follows.

3.4.1. Volumes of formations and members

The areas, average thicknesses and volumes of edifice-forming units are presented in Table 3.5. A total volume of 19 km^3 is computed for all mappable primary volcanic products exposed on Tongariro's edifice, which does not include materials that are buried or missing (section 3.4.2, below). The volumes of three generations of moraines were also estimated assuming triangular cross-sectional profiles, which collectively sum to ~0.8 km^3, or 4% of all mapped volcanic units. The Te Whaiau Formation, which is the most voluminous debris unit associated with Tongariro (Prebble, 1995; Lecointre et al., 2002; Townsend et al., 2017) has an estimated volume of ~0.6 km^3 (Table 3.5). Time-volume relationships, and whether they represent eruptive rates, are discussed in section 3.5.5.

Table 3.5. Areas, thicknesses and volumes of edifice-forming materials on Tongariro.

Volcanic deposits						
Formation	**Package**	**Visible area (km^2)**	**'f'-factor ***	**Inferred total area (km^2) ***	**Average thickness (m)**	**Volume (km^3)**
Te Pupu (**TP**)	Matariki (**mmt**)	2.1	1	2.1	15	0.03
	undifferentiated (*utp*)	2.9	1.1	3.2	20	0.06
	Toakakura (**mtk**)	4.3	2	8.5	20	0.17
	Papamānuka (**mpa**)	4.4	3	13.1	20	0.73
Red Crater (**RC**)	Te Rongo (**mtr**)	1.1	1	1.1	50	0.05
	Te Ahititi (**ahi**)	6.6	1	6.6	80	0.53
Te Maari (**TM**)	Mangatetipua (**mgt**)	1.7	1	1.7	30	0.05
	Heretoa (**aht**)	7.2	1	7.2	50	0.36
	Paungaiti (**api**)	15.7	1.3	20.4	30	0.61
	undifferentiated (*utm*)	2.2	2	4.4	30	0.13
Makahikatoa (**MK**)	(no members)	1.4	1	1.4	40	0.06
Mokomoko (**MM**)	Te Wai Whakaata (**aww**)	1.4	1	1.4	40	0.06
	Mangatapate (**amt**)	0.3	1	0.3	30	0.01
	Rangitaupahi (**ari**)	11.5	1.1	12.6	40	0.50
Pukeonake (**PN**)	(no members)	77.5	1	77.5	10	0.77
Taiko (**TA**)	undifferentiated (*uta*)	5.5	3	16.5	15	0.25
	Te Tatau (**att**)	4.8	2	9.6	30	0.29
	Rotopaunga (**arg**)	13.8	1.5	20.7	90	1.86
	Te Wakarikiariki (**ati**)	0.3	15	4.4	50	0.22
	Te Rurunga (**atr**)	2.3	2.2	5.2	40	0.21
	Waitakatorua (**awu**)	1.2	2	2.3	130	0.30
	Otamangakau (**aok**)	16.1	1.5	24.2	60	1.45
	Te Porere (**dtp**)	16.0	2.5	40.1	50	2.00
	Mangatepopo (**amp**)	0.3	8	2.1	20	0.04
	Mangahouhouiti (**mhi**)	10.8	1.1	11.9	50	0.59
	Pungarara (**apg**)	1.0	1.3	1.3	100	0.13
	Rahuituki (**arh**)	9.1	3	27.2	40	1.09
Mangahouhounui (**MH**)	undifferentiated (*umh*)	0.1	1	0.1	60	0.01
	Tātaramoa (**mtm**)	0.1	5	0.4	20	0.01
	Waiaruhairiki (**awh**)	0.1	8	0.9	30	0.03
	Te Pakiraki (**dpk**)	1.2	7	8.5	130	1.34
Haumata (**HA**)	undifferentiated (*uha*)	0.6	1	0.6	90	0.05
	Waipoa (**awp**)	7.1	1.8	12.8	100	1.28
	Pukekaikiore (**apk**)	1.0	1.3	1.3	100	0.13
	Toatoa (**ato**)	2.4	1.5	3.6	90	0.33
	Upper Tama (**aut**)	2.1	1.5	3.2	130	0.41
	Tawhairauiki (**atw**)	12.2	1.7	20.7	60	1.24
	Tutangatahiro (**mtu**)	10.8	2	21.6	60	1.30
	Lower Tama (**alt**)	0.9	4	3.5	100	0.35
Tupuna (**TU**)	(no members)	0	-	-	-	?
Otamatereinga (**OT**)	(no members)	0.1	-	-	-	?
Total for exposed map units		**220**	**-**	**220**	**410**	**19.03**

Non-volcanic deposits					
Deposit type	**Glacial period**	**Visible area (km^2)**	**Thickness (m)**	**Volume for rectangular profile (km^3)**	**Volume with triangular profile (km^3)**
Moraines	MIS 7-5	4.9	60	0.30	0.15
	MIS 4	9.1	60	0.54	0.27
	MIS 3-2	11.5	60	0.68	0.34
Te Whaiau Fm	-	52.8	2-26 (~12)	0.63	-

* Inferred total area is the visible area multiplied by the 'f'-factor. 'f'-factor represents the proportion of buried area that connects units to their inferred source vent location, as determined by field relations. Erosion is not accounted for. Limited outcrop of TU and OT are not adequate for estimating volumes.

3.4.2. Total edifice volume of Tongariro

The total volume of Tongariro's edifice is ~90 km^3. This value was computed as the difference between Tongariro's present-day surface and a base elevation surface. The base datum represents the average elevation of a horizon that separates Tongariro's volcanic edifice from older deposits. The preferred base datum elevation that was used for computing Tongariro's total edifice volume is 750 m a.s.l. This value is the midpoint between 900 and 600 m a.s.l. contours that define the base datum's northward-sloping surface from southern to northern Tongariro, respectively, which can be inferred from the elevations of flow fronts on distal lavas (Robertson and Davey, 2018). An average datum value of 750 m a.s.l. is supported by gravity survey data that shows the volcanic base boundary at 750-850 m a.s.l. under Ngauruhoe (Robertson and Davey, 2018). This value is in general agreement with other geophysical studies. Jointly-considered gravity, aeromagnetic and magnetotelluric survey data presented by Cassidy et al. (2009) indicate a datum elevation between 750-800 m a.s.l. that separates Tertiary (probably Miocene) sediments and overlying mixed volcanic deposits, in the saddle between Tongariro and Ruapehu. Other gravity survey data presented by Miller and Williams-Jones (2016) show an average density of 2300 kg/m^3, which corresponds to Miocene sediments (Robertson and Davey, 2018), occurs at ~750 m a.s.l. If alternative datum elevations are used for computing the total edifice volume, the results are 101 km^3 (for 700 m a.s.l.) and 79 km^3 (for 800 m a.s.l.).

3.4.3. Ring plain volume

The volume of ring plain deposits surrounding Tongariro is ~60 km^3, depending on the choice of areal extent. This value corresponds to a ~550 km^2 ring-shaped area with Tongariro's edifice-forming materials omitted from the centre. The volume calculation here follows the same procedure as for the total edifice with the same base datum value of 750 m a.s.l. (sections 3.2.4 and 3.4.2, above). Use of the same base datum value is justified because ring plain deposits are sourced from the volcano and because Tongariro sits in the centre of the rift zone (Fig. 3.1).

3.5. DISCUSSION

3.5.1. Review of geochronological data

A total of 29 new $^{40}Ar/^{39}Ar$ age determinations presented in this study (Table 3.1) build on 38 K/Ar age determinations by Hobden et al. (1996) and three by Stipp (1969) (Table 3.2). These data reveal an age range of ~300 ka to present for known Tongariro eruptives, which partly bury an older edifice that is at least ~500 ka in age. This section also evaluates previous K/Ar datasets against new $^{40}Ar/^{39}Ar$ age results and field observations.

The $^{40}Ar/^{39}Ar$ age determinations presented here refine the timings of edifice-building activity at Tongariro and establish the ages of previously under-sampled edifice regions, primarily on the NW and NE flanks. Field relations and superposition provide an independent check on the accuracy of all radioisotopic age data from Tongariro. $^{40}Ar/^{39}Ar$ ages are fully consistent with field relations within analytical uncertainties. At every locality where $^{40}Ar/^{39}Ar$ ages were determined on successively overlying units, ages are either within analytical error or the overlying units are younger. Less precise and less accurate K/Ar ages have hampered detailed stratigraphic studies previously (Hobden, 1997; Townsend et al., 2017).

Comparisons between K/Ar and $^{40}Ar/^{39}Ar$ ages reveal the factors leading to inaccuracies in K/Ar age determinations, as shown for samples collected from the same stratigraphic units and analysed with K/Ar and $^{40}Ar/^{39}Ar$ dating methods (Fig. 3.10). For these comparisons, $^{40}Ar/^{39}Ar$ ages (WMPA or isochron) are considered accurate because they are fully consistent with field relations. Total gas $^{40}Ar/^{39}Ar$ ages are usually close to preferred WMPA or isochron values, but not always (Table 3.1; Fig. 3.10b). Comparisons show that K/Ar ages are inaccurate at low K_2O concentrations, particularly for samples with glass-bearing groundmass material (Fig. 10b-c). K/Ar and $^{40}Ar/^{39}Ar$ age values appear to systematically converge with increasing whole-rock K_2O concentrations, becoming consistently within error above 1.8 wt% (Fig. 3.10b-c). Likewise, differences between $^{40}Ar/^{39}Ar$ and K/Ar ages are greater for low K_2O samples, particularly below 1.2 wt%. Differences between $^{40}Ar/^{39}Ar$ and K/Ar ages do not systematically vary with the percentages of crystals in the K/Ar samples (Fig. 3.10d); inaccuracies appear due to low K_2O concentration. Across all comparisons, whole-rock K/Ar age determinations on samples with holocrystalline groundmasses are consistently more accurate than glassy samples, for both low-K_2O and phenocryst-rich samples. This supports observations elsewhere that K/Ar and $^{40}Ar/^{39}Ar$ age determinations are most accurate for holocrystalline samples (e.g. Hildreth and Lanphere, 1994; Gamble et al., 2003).

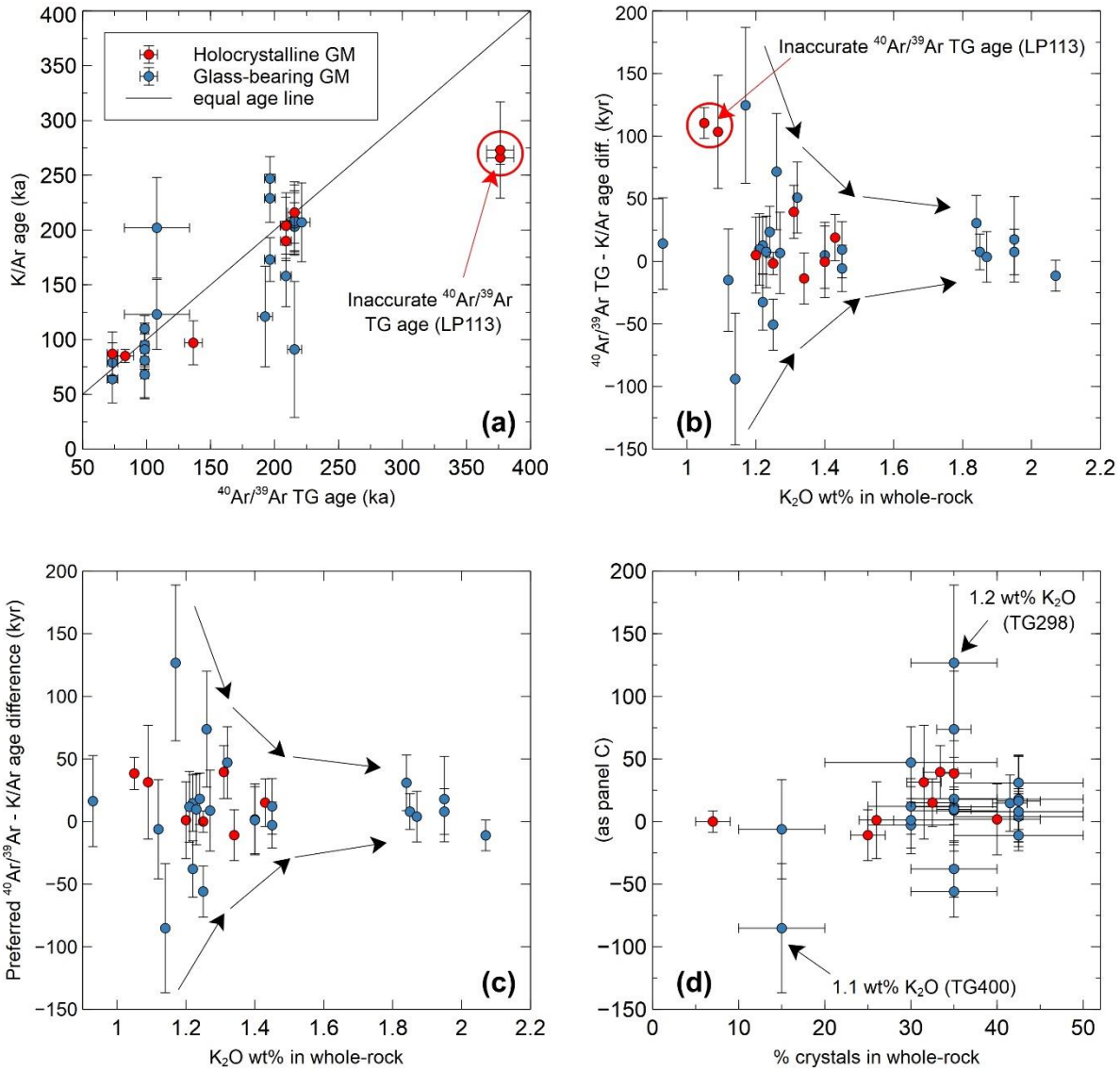

Figure 3.10. Comparisons between K/Ar and $^{40}Ar/^{39}Ar$ age determinations for the same map units (e.g. Table 3.2), coloured by K/Ar sample groundmass (GM) texture: red (holocrystalline) and blue (glass-bearing). $^{40}Ar/^{39}Ar$ ages are total gas (TG) and weighted mean plateau ages (WPMA) as indicated. Source data in Table 3.1. LP039 and GL2007 $^{40}Ar/^{39}Ar$ ages are used for comparisons against K/Ar ages for the Toatoa and Rotopaunga members because other $^{40}Ar/^{39}Ar$ ages in these members are recoil and isochron values, respectively (Table 3.1). Whole-rock K_2O concentrations are from Hobden et al. (1996). Crystal percentages and groundmass textures from Hobden (1997) and this study (Table 3.3). **(a)** TG $^{40}Ar/^{39}Ar$ age determinations vs. K/Ar age determinations by Stipp (1969) and Hobden et al. (1996): errors are 2 s.d. **(b)** Whole-rock K_2O concentrations in K/Ar samples vs. the difference between TG $^{40}Ar/^{39}Ar$ ages and K/Ar ages (positive value = older $^{40}Ar/^{39}Ar$ age). Reference sample (LP113) with an inaccurate TG $^{40}Ar/^{39}Ar$ age is annotated for two K/Ar comparisons (TG136 – Hobden et al., 1996; 3254 – Stipp, 1969). **(c)** Whole-rock K_2O concentrations in K/Ar samples vs. the difference between preferred $^{40}Ar/^{39}Ar$ ages (either WMPA or isochron ages) and K/Ar ages (positive value = older $^{40}Ar/^{39}Ar$ age). Exceptions for (**b-c**): K_2O concentrations used for comparisons with Stipp (1969) K/Ar results are from this study: 3254 (LP113) and 3258 (LP062). **(d)** The difference between preferred $^{40}Ar/^{39}Ar$ ages and K/Ar ages (either WMPA or isochron ages), as in (**c**) vs. the concentrations of crystals in whole-rock K/Ar samples.

3.5.2. Evolution of the Tongariro edifice

Tongariro's edifice has been constructed by lava flows and pyroclastic deposits since at least ~350 ka (Fig. 3.4). The 571-453 ka Otamatereinga Formation marks the earliest known eruptive activity expressed by materials exposed on the edifice (Figs. 3.3-3.4). However, the source vent location of Otamatereinga Formation lavas is unclear and may not be on Tongariro. Alternatives include the poorly studied Maungaku and Maungakatote cones, which are located 12 and 10 km NW of Tongariro, respectively (Fig. 3.1). Geochemical data presented by Cole et al. (1983) for Pihanga, Kakaramea and Maungakatote edifices cannot be uniquely associated with Otamatereinga Formation compositions reported in this study.

Any eruptive activity that occurred before ~350 ka on Tongariro is not represented by any well-examined materials exposed on the edifice. Undifferentiated materials in the Oturere (**uha**) and Mangahouhounui (**umh**) valleys, and on northern Tongariro (**uta**), might represent some of the oldest Tongariro eruptives but have not been sampled and are poorly exposed (Fig. 3.4). Drill cores from the Poutu-Tokaanu hydro canal contain andesite boulders overlying ~349 ka Whakamaru ignimbrite (Bayly and Quinlan, 1965; M. Rosenberg, pers. comm, 2018), which is consistent with a post-349 ka age (Downs et al., 2014) for Tongariro, although available drill cores are not deep enough to examine pre-Whakamaru age volcanism in the southern TVZ.

The oldest materials that are confidently attributed to Tongariro are represented by the 349-293 ka Tupuna Formation. Although it is not found *in situ*, petrographic features suggest that the hornblende-phyric Tupuna Formation is magmatically related to the 290-189 ka Haumata Formation, both of which contain abundant pseudomorphs after amphibole (Table 3.3). These petrographic similarities suggest similar magma storage conditions that may represent the same magma system. This is consistent with the overlapping distributions of Haumata Formation eruptives and inferred (buried) Tupuna Formation lavas on southern Tongariro (Fig. 3.4).

Haumata Formation eruptives are represented *in situ* on southern Tongariro, which implies that Tupuna Formation eruptives also originated from Tongariro. Tupuna Formation eruptives are also compositionally similar to amphibole-phyric andesite boulders in the 349-309 ka Turakina Formation debris flow deposits exposed 100 km SW of Tongariro, along the Whanganui coastline (Gamble et al., 2003; Tost and Cronin, 2015). This contrasts with the interpretation of Tost et al. (2016) who suggest that andesite boulders in the Turakina Formation represent eruptives from Ruapehu because they have overlapping rare earth element (REE) concentrations with Ruapehu's Te Herenga Formation (cf. Price et al., 2012), which Tost et al. (2016) show to be distinct from REE concentrations in Tongariro eruptives. However, a unique compositional association between Ruapehu eruptives and Turakina Formation boulders could

not be established here (Fig. 3.11). Data from this study and Hobden (1997) show that Tupuna Formation (and Lower Tama Member) andesites have clear compositional overlap with both the Te Herenga (Price et al., 2012; Conway et al., 2018) and Turakina (Tost et al., 2016) formations. On the basis of REE compositions, neither a Tongariro nor Ruapehu source can be confidently established (cf. Tost and Cronin, 2015; Tost et al., 2016).

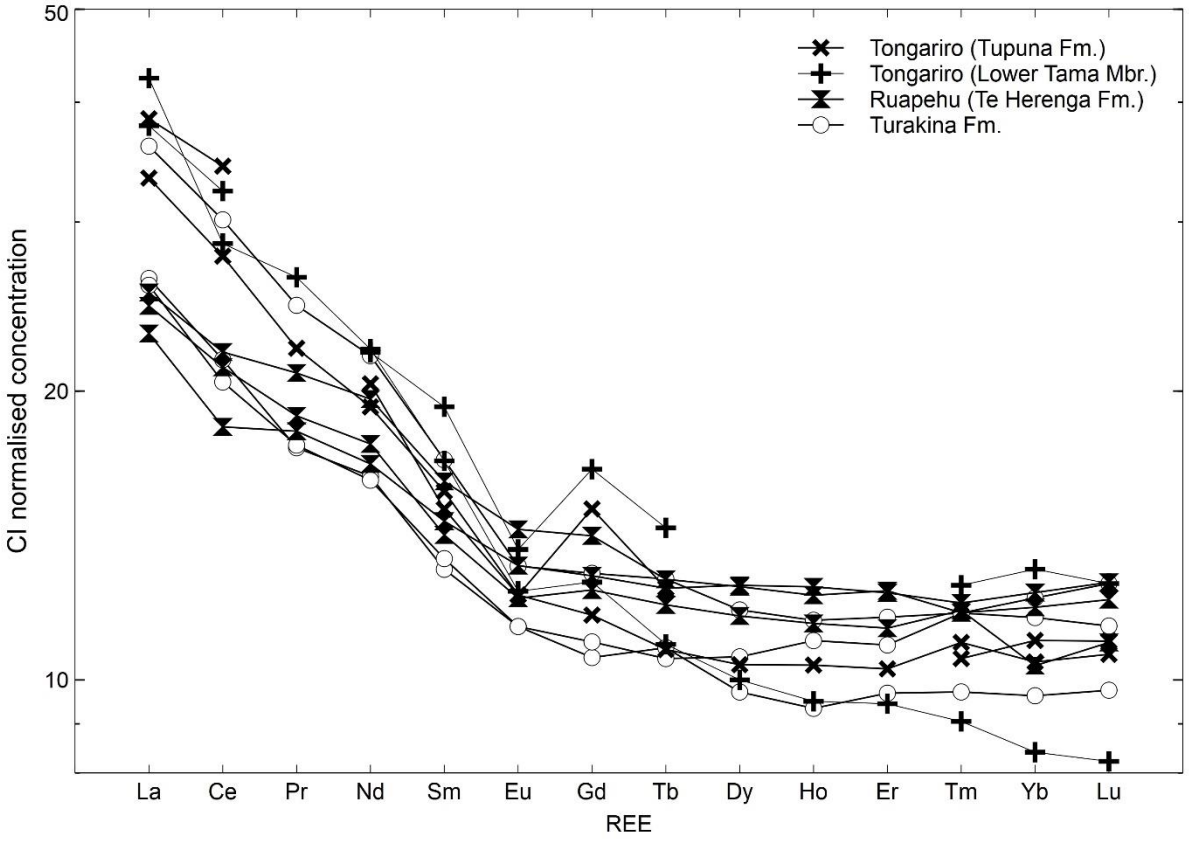

Figure 3.11. CI-normalised rare earth element (REE) concentrations for hornblende-phyric andesite boulders in the Turakina Formation debris flows (Tost et al., 2016) compared with Tongariro's Tupuna Formation and Lower Tama Member (Haumata Formation), which are hornblende-phyric and contain pseudomorphs after amphibole, respectively. REE concentrations in Ruapehu's clinopyroxene-dominant Te Herenga Formation (Conway et al., 2018) are shown for comparison. Tongariro trace element data are from this study (reported in Appendix 5) and Hobden (1997: samples with incomplete REEs [TG136, TG292]). All compositional fields for Tongariro, Ruapehu and Turakina materials are indistinguishable within analytical uncertainty. CI chondrite normalisation uses the values of McDonough and Sun (1995).

Despite inconclusive REE comparisons, a Tongariro source for Turakina Formation boulders is supported by two additional observations. First, Ruapehu's Te Herenga Formation does not contain hornblende or pseudomorphs after amphibole whereas (respectively) these features are observed in Tongariro's Tupuna and Haumata formations (Table 3.3). In contrast, Te Herenga Formation eruptives are characterised by clinopyroxene-dominated phenocryst assemblages (over plagioclase) with clinopyroxene crystals and glomerocrysts up to 12 mm

(Hackett, 1985; Price et al., 2012; Conway et al., 2016). Second, the oldest $^{40}Ar/^{39}Ar$ age yet determined for Te Herenga Formation is 205 ± 27 ka (Gamble et al., 2003) whereas hornblende-phyric lava from Tupuna Formation yields an $^{40}Ar/^{39}Ar$ age of 304 ± 11 ka (Table 3.1). The age of the Tupuna Formation is closer in time to the depositional age of the Turakina Formation debris flows, between 349-309 ka, which is based on correlations with marine terraces and regional tephras with known ages (Pillans, 1983; Tost and Cronin, 2015; Downs et al., 2014). Therefore, if the andesite boulders in the Turakina Formation represent Tongariro (Tupuna Formation) eruptives, then volcanism at Tongariro must have initiated between 349-309 ka or earlier. A caveat of associating Turakina Formation volcaniclastics to Tongariro is that Ruapehu probably did not exist when the Turakina Formation was deposited. Currently, Ruapehu physically separates Tongariro from the Turakina River headwaters, along which Turakina Formation debris flows were transported, which implies that Ruapehu is younger than ~309 ka. Another possibility is that Tupuna Formation lavas were erupted from a proto-Ruapehu, although comparisons discussed above indicate that a Tongariro source is more likely based on comparisons of age and petrography.

From 290-190 ka, Haumata Formation lavas and pyroclastic materials were erupted from a southern vent focus beneath the present-day position of Ngauruhoe (Figs. 3.3-3.4). In contrast, the youngest member of the Haumata Formation, the Waipoa Member, was erupted from a vent further north in the area of present-day Central Crater (Figs. 3.3-3.4). Emplacement of the Waipoa Member between 195-189 ka was possibly contemporaneous with the emplacement of the Pukekaikiore Member between 200-190 ka, which was erupted from the southern vent focus. Both members probably tapped the same magma body because their compositions are indistinguishable within analytical uncertainty (Tables 3.3-3.4).

Eruptions continued from a vent focus in the area of present-day Central Crater between 189 and 130 ka with the emplacement of the Mangahouhounui Formation. Diverse magma compositions ranging from basaltic-andesite to dacite characterise the Te Pakiraki Member within the Mangahouhounui Formation. Field relations and $^{40}Ar/^{39}Ar$ age determinations indicate that the 189-130 ka Te Pakiraki Member was erupted and emplaced in the Mangahouhounui valley contemporaneously with the 152-150 ka Waiaruhairiki Member. The occurrence of 8-9 mm plagioclase and clinopyroxene phenocrysts in both the Te Pakiraki and Waiaruhairiki members suggest a shared magmatic system and a discrete phase of generating high-MgO andesite magma (5.4-6.2 wt%: Tables 3.3-3.4). This episode was probably broadly contemporaneous with the emplacement of the Tātaramoa Member (basaltic-andesite) on NE Tongariro that may have been erupted from a flank vent, possibly represent by a buried vent at the Te Tatau trig point on NE

Tongariro (Fig. 3.2). Despite this, Tātaramoa Member MgO concentrations of ~5.3 wt% tend towards the lower range observed for Waiaruhairiki Member andesites (Tables 3.3-3.4), despite being a basaltic-andesite.

Between 133-52 ka eruptions continued from a northern vent area within roughly the location of present-day Central Crater (Fig. 3.7). These are represented by lavas, hyaloclastites, lapilli tuff breccias, agglutinates and spatter of the Taiko Formation. Dip directions of Taiko Formation materials on Tongariro's upper edifice triangulate towards an elevation that exceeds 2000 m a.s.l., which is higher than any surviving landforms in this area. Missing edifice material relating to this eruptive period is probably represented by clastic material in Te Whaiau Formation debris flows (Fig. 3.8). Te Whaiau Formation debris flows extend 10-15 km NW of the inferred northern vent area for the Taiko Formation and have independent age constraints that imply deposition between 50-45 ka, which is consistent with the adopted minimum age of the Taiko Formation of 52 ka (Fig. 3.3). The volume of the Te Whaiau Formation estimated in this study (~0.6 km^3: Table 3.5) is similar to 0.5 km^3 estimated by Lecointre et al. (2002) who invoked a cone-shaped landform on upper Tongariro that collapsed to explain the volume of volcaniclastic material in the debris flow deposits. An alternative is that erupted materials were emplaced onto a glacier in the Central Crater area and were later conveyed away as debris. However, this interpretation probably requires a vent or vent(s) surrounding Central Crater to explain the distribution of Taiko Formation eruptives on all flanks (especially the voluminous 102-96 ka Te Porere Member), and the lack of such vent-proximal landforms of Taiko Formation age in the surviving edifice indicate that some mass wasting events have occurred.

Subsequent edifice construction on Tongariro involved eruptions from vents that are still presently visible but have had shorter lifespans than the vent foci of older formations. The 45-23 ka Mokomoko Formation (North Crater and Blue Lake vents), >25.4 ka to 2012 CE Te Maari Formation, ~17.5 ka Makahikatoa Formation (young vent on top of the Pukekaikiore landform), 11-0.15 ka Red Crater Formation and the 7(?) ka to 1975 CE Te Pupu Formation (Ngauruhoe vent) were erupted from vents with inferred lifespans of <25 ka (Fig. 3.12). In contrast, field observations indicate that vent areas for the Haumata, Mangahouhounui and Taiko formations were persistent for intervals of 50-150 kyr within areas of ≤1 km^2 each, except for the Tātaramoa and Mangahouhouiti members that were possibly erupted from flank vents. This observation reveals a trend wherein vents have become shorter-lived, more geographically dispersed and more numerous over Tongariro's lifespan.

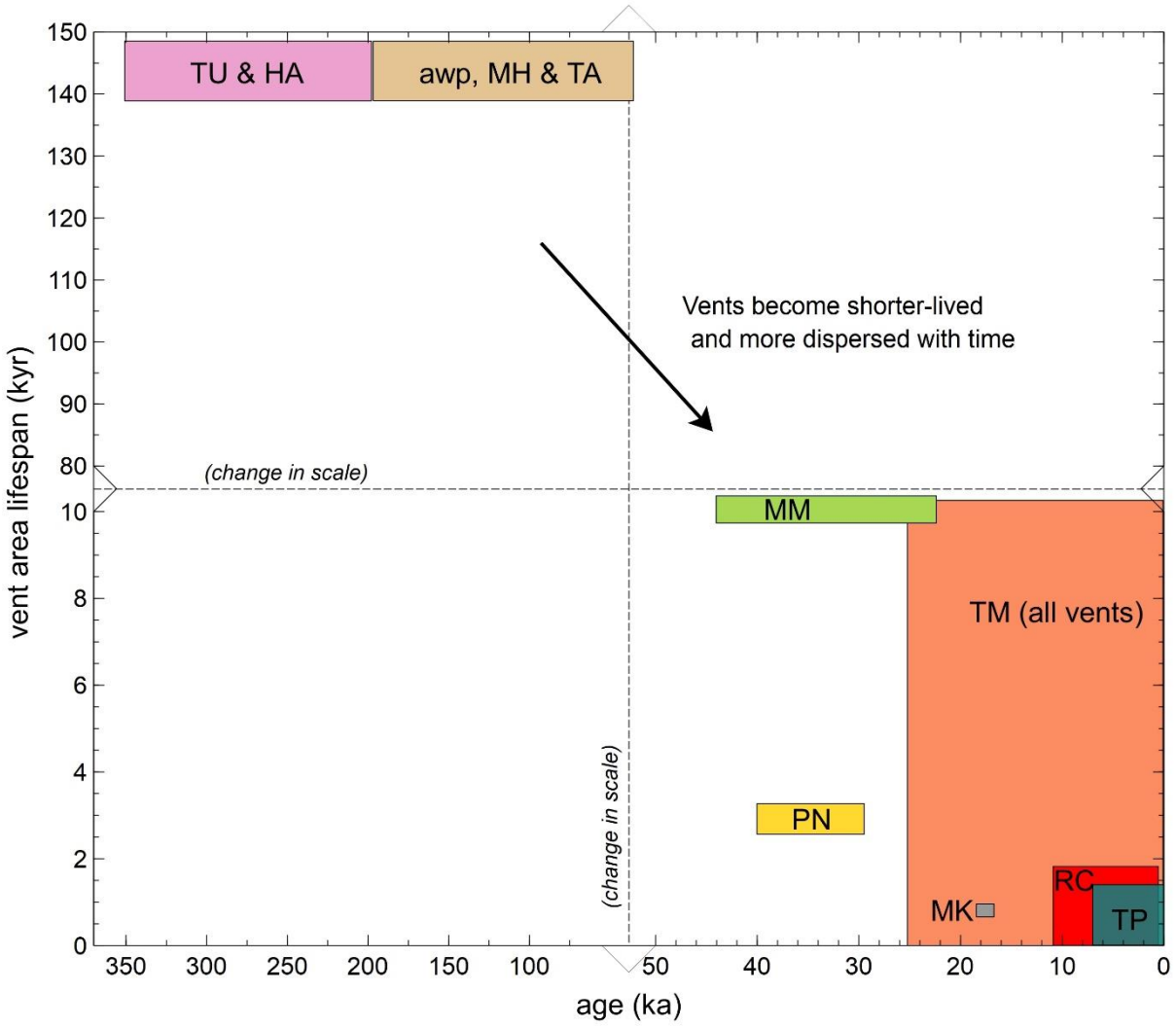

Figure 3.12. Vent age comparison against vent lifespan at Tongariro. Formations and members are organised into groups with continuously sustained vent position with new boxes reflecting vent position shifts. Vents are grouped into distinct clusters within 1 km² and labelled here by formation: Tupuna (**TU**), Haumata (**HA**) which includes the Waipoa Member (**awp**), Mangahouhounui (**MH**), Taiko (**TA**), Mokomoko (**MM**: North Crater and Blue Lake vents), Pukeonake (**PN**), Te Maari (**TM**), Makahikatoa (**MK**), Red Crater (**RC**) and Te Pupu (**TP**: Ngauruhoe is the vent).

The previously reported age range of North Crater between 25.4 and 14.0 ka is not entirely consistent with the findings of this study. Andesitic tephras deposited after the 25.4 ka Oruanui eruption and before the 14.0 ka Waiohau eruption were correlated with proximal scoria deposits on North Crater by Shane et al. (2008), using ages from Vandergoes et al. (2013) and Lowe et al. (2013), which provide the most recent age estimates for North Crater before this study, as adopted by Townsend et al. (2017). These tephra associations indicate that North Crater was active after 25.4 ka, however, the age determination for the Mangatapate Member indicates that most of the North Crater cone was constructed prior to 30 ± 6 ka (Table 3.1; section 3.3.2.9.2). These andesitic tephras, named Rt1, Rt2 and Rt3 by Shane et al. (2008), have

ages of between 25.4 and 17.5 ka (Rt1-2) and ~16.6 ka (Rt3). If tephras Rt1-2 were erupted from North Crater, available observations indicate their ages must be between 25.4 ka (post-Oruanui) and 24 ka (minimum Mangatapate Member age at 2 s.d.: Table 3.1). Given that North Crater was constructed by 30 ± 6 ka, it is considered unlikely that the Rt1-3 tephras were erupted from North Crater. Similar arguments are valid for Blue Lake a potential source vent, because of the Te Wai Whakaata age determination of 28 ± 5 ka (Table 3.1). Therefore, the vent source(s) of Rt1-3 deposits cannot be identified based on available published information.

During the Holocene there have been at least three co-existing and contemporaneously active magma systems that are expressed as the Te Maari, Red Crater and Te Pupu (Ngauruhoe) formations (Figs. 3.3, 3.9). Other craters (predominantly phreatic or phreatomagmatic) also formed amongst these locations at Emerald Lakes (between Red Crater and Blue Lake: Fig. 3.2) and in South Cirque (e.g. Topping, 1974; Hobden, 1997; Nairn et al., 1998). The products of the Te Maari, Red Crater and Te Pupu formations were vented from three distinct vent areas separated by distances greater than 2 km. Distinct compositional features both within and between these formations have been revealed by unit-specific studies (e.g. Hobden et al., 1999; Coote and Shane, 2016; Shane et al., 2017). This observation echoes similar findings at Ruapehu that show coexisting magmas of distinct compositions persisted throughout the volcano's lifespan (Gamble et al., 1999; Price et al., 2012; Conway et al., 2016). At Tongariro, however, there are general compositional similarities between the Te Maari, Red Crater and Te Pupu formations that have not been acknowledged. Early Holocene eruptives from Te Maari Craters (11-3.5 ka Heretoa Member) and Red Crater (11-1.8 ka Te Ahititi Member) are andesitic with a dominance of plagioclase phenocrysts over pyroxene over olivine (Table 3.3). Later Holocene eruptives in all three formations are basaltic-andesites that show increases in olivine as a percentage of their total phenocryst cargoes (Table 3.3). This observation is consistent with a volcano-wide input of mafic magma into dispersed magma reservoirs that acquired their own distinct compositions during crustal processing according to the idiosyncrasies of their specific reservoirs and residence times. Note that the Te Pupu Formation's maximum age is not well constrained (cf. Moebis et al., 2011) and could be as young as 2.5 ka (Topping, 1974), which could explain the petrological distinctions between early and late Holocene eruptives mentioned above. If so, this would imply that the expression of volcanism at Tongariro has been significantly more dispersed spatially during the Holocene than earlier in the volcano's history, which is in good agreement with the waning longevities of vent systems over time (Fig. 3.12). Similar suggestions of contemporaneous magmatism and volcanism were inferred for the early Holocene Pahoka-Mangamate tephra sequence (Nairn et al., 1998). This sequence represented

contemporaneous eruptions of diverse composition magmas from separate vent foci between northern Tongariro to northern Ruapehu (>10 km linear vent alignment), which include Te Maari Crater(s), upper/central Tongariro vents, Tama lakes vents and Saddle Cone (Ruapehu) (Nakagawa et al., 1998).

A further point of debate surrounding Tongariro's evolution is the age of the Ngauruhoe cone and its associated eruptives, for both effusive and explosive materials. It has been suggested that Ngauruhoe's construction was underway by ~7 ka (Moebis et al., 2011). This age is consistent with field evidence for construction in an ice-free environment (Ngauruhoe is a perfect cone) and lava flows that fill drainage systems that were glaciated before the Holocene: Mangatepopo valley, Makahikatoa Stream and Waihohonu valley (Eaves et al., 2016a; Townsend et al., 2017). The older age boundary of ~7 ka was established by associating Ngauruhoe with tephra in Papakai Formation that underlies the ~6.9 ka Motutere rhyolitic tephra (Moebis et al., 2011). This association was established from similarities in glass compositions between Ngauruhoe's 1954 CE and 1975 CE eruptions and >6.9 ka tephra from the Papakai Formation, which contrast with tephra glass compositions in the Tufa Trig Formation of Ruapehu (between 1.8 ka and 1314 CE: Donoghue et al., 1995a; Donoghue and Neall, 1996; ages from Hogg et al., 2012 and Lowe et al., 2013) and Te Rongo Member scoria from Red Crater (between 1.8 ka and 1800 CE: Topping, 1973; Greve et al., 2016). However, in opposition to arguments put forward by Moebis et al. (2011), the available data indicates that Red Crater is a more likely source vent for >6.9 ka tephra in the Papakai Formation. Whole-rock compositions from Red Crater's Te Ahititi Member (between 11-1.8 ka) are more evolved than the Ngauruhoe-sourced Papamānuka Member (older than 1.8 ka: **ahi** and **mpa** data in Table 3.4, above), which is the reverse relation to Red Crater versus Ngauruhoe tephra glass compositions reported by Moebis et al. (2011). In contrast, Moebis et al. (2011) excluded Red Crater as a possible source vent for >6.9 ka tephra in the Papakai Formation because its <1.8 ka compositions are more mafic than Ngauruhoe-sourced eruptives, although this argument is not applicable for materials older than 1.8 ka. Available isopach data for the Papakai Formation cannot distinguish between Ngauruhoe and Red Crater as source vents (Donoghue et al., 1995a), and also indicate a contribution of Ruapehu-sourced material to the Papakai Formation (Topping, 1973). Further detailed tephra provenance studies are required in order to constrain the timing of the onset of Ngauruhoe cone-building.

3.5.3. Glacial history of Tongariro volcano

Tongariro has supported large ice masses during its lifespan, within both glacial and interglacial periods. Previous summit ice caps had thicknesses exceeding 150 m (Cole et al., 2018) and some valley-occupying glaciers were as thick as 250 m. Till deposits are observed for at least three periods of major glacial advance (Fig. 3.13), which probably correlate with the timings of Marine Isotope Stage (MIS) 6 (191-130 ka), MIS 4 (71-57 ka) and MIS 3-2 (57-14 ka) (Lisiecki and Raymo, 2005; Eaves et al., 2016a). However, there is also field evidence for less substantial ice coverage in the later part of MIS 7 (Townsend et al., 2017; this study) and varied but significant ice coverage in MIS 5 (Townsend et al., 2017; Cole et al., 2018). Because ice coverage determines emplacement behaviour and the preservation potential of erupted materials, syn-glacial edifice growth models can be used (in 'reverse') to infer ice coverage (e.g. Lescinsky and Sisson, 1998; Conway et al., 2016). This framework is used to estimate paleoclimatic conditions on Tongariro, in combination with complementary studies of moraine ages (Eaves et al., 2016a) and energy-balance ice coverage modelling results (Eaves et al., 2016b).

Haumata Formation eruptives (290-189 ka) are the oldest *in situ* deposits confidently attributed to a vent source on Tongariro, and display evidence for varied ice coverage when they were emplaced. Inferences regarding the amount of ice coverage on Tongariro before 220 ka are not possible because volcanic materials older than this are poorly exposed. Haumata Formation eruptives indicate persistent valley-filling glaciers in the Waihohonu and Mangatepopo valleys for at least the 220-190 ka period, which corresponds to the later part of MIS 7 (243-191 ka: Lisiecki and Raymo, 2005). These glaciers appear to have thickened from ~80 to ~250 m over this 30 kyr period. From 220-214 ka, the Tawhairauiki Member was probably emplaced syn-glacially because it overlies 229-220 ka Tutangatahiro Member eruptives, but does not fill any adjacent drainage systems such as the Waihohonu valley. At this time, valley-filling glaciers were probably ~80-100 m thick. The 214-207 ka Upper Tama Member contains lavas 60 m thick that are locally overthickened up to 200 m, which imply ice thicknesses in the Tama lakes area of ~200 m for this period. Two ~100 m-thick lavas stacked between the Makahikatoa Stream and Mangatepopo valley, which correspond to the 207-200 ka Toatoa and 200-190 ka Pukekaikiore members, indicate an ice thickness of 200-250 m for the 207-190 ka period. These inferences suggest growing ice coverage in the lead-up to the MIS 6 glacial period.

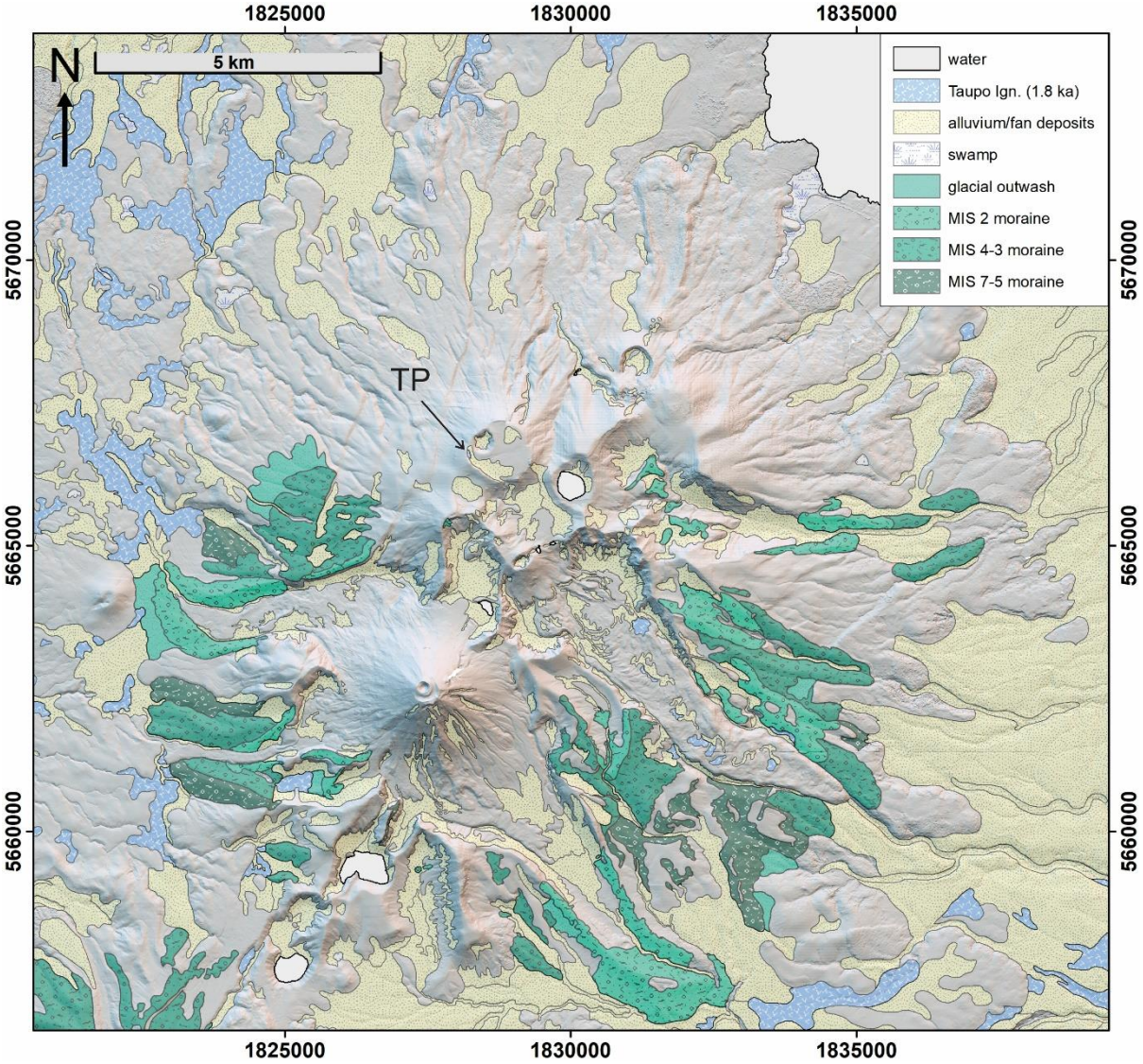

Figure 3.13. Moraines and sedimentary deposits on Tongariro and its ring plain, and the distribution of the 1.8 ka Taupō ignimbrite. Note the small remnant above 1800 m a.s.l. on North Crater's summit (labelled TP). Glacial outwash fan deposits and swamp areas are also indicated. Geology adapted from Eaves et al. (2016a) and Townsend et al. (2017).

The transition from MIS 7 to MIS 6 (191 ka: Lisiecki and Raymo, 2005) closely coincides with the age boundary between the Haumata and Mangahouhounui formations (189 ka). Eruptives of the 189-130 ka Mangahouhounui Formation are predominantly represented by ~250 m-thick successions of lavas, breccias and agglutinates on both sides of the Mangahouhounui valley (Fig. 3.4). The presence of breccia deposits of interpreted glacier-margin origin, the absence of Mangahouhounui Formation eruptives in valley-floor positions and horizontal columnar-jointed lava indicates ice thicknesses up to 250 m for the 189-130 ka period (Fig. 3.6a-b).

Taiko Formation eruptives were emplaced between 133 and 52 ka, and coincide with a complex part of New Zealand's Quaternary glacial history, which is defined partly by speleothem growth layers from Aurora Cave, Fiordland (Williams et al., 2015). The Taiko Formation is broadly contemporaneous with the 130-57 ka MIS 5 period of Lisiecki and Raymo (2005). This period is initially reflected by the 129-119 ka Rahuituki Member and an older part of the Mangatepopo Member dated at 121 ± 12 ka (Table 3.1) that were likely emplaced in relatively ice-free conditions. The Rahuituki Member has relatively long runout distances of ~9 km onto the NW and NE flanks, and an older Mangatepopo Member lava (121 ± 12 ka) occurs in the floor of the Mangatepopo valley (Fig. 3.7), which is normally filled with ice during glacial periods (e.g. Eaves et al., 2016a). These observations suggest relatively minimal ice coverage on Tongariro for the ~130-120 ka interval. In contrast, the Mangahouhouiti Member, dated at 117 ± 23 ka, and a younger lava from the Mangatepopo Member (109 ± 8 ka: Table 3.1) are confined to upper flank and planèze positions (Fig. 3.7), which indicates an increase in the presence of ice between ~118-102 ka. These interpretations are in good agreement with the 128-118 ka Kaihinu Interglacial (MIS 5e), 117-109 ka stadial (MIS 5d) and the initially cool 108-98 ka interstadial (MIS 5c) periods defined by Williams et al. (2015) from speleotherm records, after Barrell (2011).

The younger 102-96 ka Te Porere Member contains hyaloclastites and lapilli tuff breccias that are considered indicative of syn-glacial emplacement on upper edifice areas (e.g. Cole et al., 2018). Elsewhere, the Te Porere Member is comprised of lava flows confined to flanks and planèzes (Fig. 3.7). Tongariro's NW sector lacks surficially-exposed moraines (Fig. 3.13), probably due to a later collapse of this part of the mountain and loss of any glacial record (sections 3.3.2.7, 3.5.2). Successions of Te Porere Member lavas in the Oturere and Mangatepopo valleys suggest the presence of glaciers up to ~100 m thick. Younger 96-79 ka Waitakatorua and 86-79 ka Te Wakarikiariki members were emplaced both subaerially and subglacially in the presence of ice, as indicated by ice-impounded lavas and lapilli tuff breccias that are confined to ridgetop positions (Waitakatorua Member – Fig. 3.6c; Te Wakarikiariki Member – 'dL' in Cole et al., 2018). These possible age ranges correspond to the 97-88 ka stadial (MIS 5b) and 87-73 ka (MIS 5a) Otamangakau Interstadial periods defined by Williams et al. (2015), who note a possible glacial excursion between 84-80 ka, which is consistent with the ice-damned Te Wakarikiariki lava dated at 81 ± 5 ka (Table 3.1). This age result was previously presented by Cole et al. (2018) who also noted its occurrence within the Otamangakau Interstadial. The distribution and features of the 79-61 ka Rotopaunga Member indicate varied levels of ice-coverage on Tongariro for this period, similar to that at the time of the 102-96 ka Te Porere Member. On Tongariro's upper edifice, alternating deposits of hyaloclastites, lapilli tuffs and coherent lavas in the Rotopaunga

Member indicate transitions between subglacial and subaerial eruptive activity, previously noted by Cole et al. (2018) for their equivalent units. A Rotopaunga Member lava that erupted on the NE flank without evidence for impoundment by ice is dated at 68 ± 15 ka (Table 3.1). The mean value of this age result is close to the peak glacial advance (66-61 ka) within the New Zealand Last Glacial Cycle (72-62 ka) defined by Williams et al. (2015). This indicates either that the $^{40}Ar/^{39}Ar$ age determination is inaccurate with a true age closer to 80-70 ka, or that differences exist between North Island and South Island glacial advances for this period, or that glacial advance on the northern flank of Tongariro was minor during this period. The first and last options are considered more likely given the relatively large uncertainty (± 15 ka) on this age determination and the good agreement between inferred ice coverages in the North Island (this study) and South Island (Barrell, 2011; Williams et al., 2015) as discussed above. The youngest Taiko Formation eruptives are represented by the 61-52 ka Te Tatau Member, which displays no evidence for syn-glacial emplacement, and coincide with the early part of the relatively warm Aurora Interstadial of Williams et al. (2015).

Around 0.5 km^3 of edifice material was removed from Tongariro's northern-central edifice after ~52 ka based on estimates of a collapse cone-structure (e.g. Lecointre et al., 2002), and is likely represented by the volcaniclastic constituents of the 50-45 ka Te Whaiau Formation debris flows (Fig. 3.8) (Lecointre et al., 2002; Townsend et al., 2017). The source vent area of Taiko Formation eruptives exceeded 2000 m a.s.l., which is higher than surviving landforms in the northern-central part of Tongariro's edifice. Dip directions of eruptives within the Te Porere, Te Wakarikiariki, Waitakatorua and Rotopaunga members triangulate towards a summit vent position above 2000 m a.s.l. that was removed during or after these units were emplaced. Climate proxy records presented by Williams et al. (2015) suggest a warm period between 61-49 ka that was probably associated with deglaciation on Tongariro (late MIS 4/early MIS 3), as also inferred from the ice-free emplacement of Te Tatau Member eruptives. Earlier edifice growth prior to ~61 ka (see above) in the presence of ice probably created asymmetric and irregularly-shaped landforms that were unstable (e.g. Townsend et al., 2017). Subsequent deglaciation in the 61-49 ka period may have removed ice masses that held these unstable landforms in place. Local examples (e.g. the 5.2 ka Mangaio Formation and 10.5 ka Murimoto Formation sector collapse deposits on Ruapehu: Palmer and Neall, 1989; Eaves et al., 2016a; Conway et al., 2016; Townsend et al., 2017) and global examples (e.g. the Osceola Mudflow on Mount Rainier: Vallance and Scott; 1997) show that voluminous mass-wasting events commonly follow deglaciation events, because the loss of supporting ice masses encourages the collapse of unstable landforms (Capra, 2006). Deglaciation is considered to be the most likely explanation for the

consecutive timings of syn-glacial >61 ka edifice growth and the interglacial deposition of the 50-45 ka Te Whaiau Formation debris flows at Tongariro.

Edifice growth on upper Tongariro resumed with the 45-23 ka Mokomoko Formation. Lapilli tuff breccias and related blocks of coherent lava mapped as the 45-36 ka Rangitaupahi Member (Cole et al., 2018) demonstrate that North Crater's initial eruptive activity was subglacial but later became subaerially emergent. Despite this, MIS 4-2 moraines are not observed on NW Tongariro and may relate to a lack of suitable topography for accumulating glacial ice masses (i.e. pre-existing valleys). It is possible that North Crater was constructed soon after the mass-wasting events that produced the 50-45 ka Te Whaiau Formation debris flows when remaining ice masses on the edifice were waning. Such behaviour is observed at other historically active volcanoes where edifice mass-loss is quickly followed by dome-growth and edifice-rebuilding, such as Bezymianny after 1956 CE (Girina, 2013) and Mount St. Helens after 1980 CE. Subsequent eruptive activity at Tongariro resumed with the 36-24 ka Mangatapate (North Crater vent) and 33-23 ka Te Wai Whakaata (Blue Lake vent) members which display limited evidence for syn-glacial emplacement. Te Wai Whakaata Member lavas that entered the Mangahouhounui valley have steep sides that imply minor overthickening (Fig. 3.8), suggesting ice up to ~20 m thick was present in the valley floor. These lavas are capped by till in the upper Mangahouhounui valley which indicates glacial advance after 28 ± 5 ka (Table 3.1).

The 45-23 ka period described above coincides with the ages of moraines on Tongariro determined by cosmogenic ^{3}He dating (Eaves et al., 2016a). The middle-aged and the youngest moraines north of the Mangatepopo Valley (Fig. 3.13) have reported mean ages between 57-45 ka (~MIS 3) and 30-18 ka (~MIS 2), respectively (Eaves et al., 2016a). During these periods, glaciers were up to ~80-100 m thick in the Mangatepopo and Oturere valleys as indicated by moraine elevations relative to valley floors (Fig. 3.13; Eaves et al., 2016a; Townsend et al., 2017). These periods of moraine deposition probably correspond to varied amounts of ice coverage across New Zealand for this interval as inferred by Williams et al. (2015), with possible glacial advances at 49-47 ka and 32-28 ka. This suggestion is consistent with field observations for limited valley-confined ice masses when the 33-23 ka Te Wai Whakaata Member was erupted. This contrasts with inferred glacier thicknesses at Ruapehu for this period by Conway et al. (2016) which were ~80-120 m thick at equivalent elevations (between ~1400 and 1900 m a.s.l.), although Ruapehu's greater catchment may explain differences in ice accumulation during this interval. However, it is clear that Tongariro was re-glaciated between ~28-18 ka as indicated by the moraines capping Te Wai Whakaata lavas in the Mangahouhounui valley and many other Last Glacial moraines mapped around the lower parts of the edifice (Eaves et al., 2016a; Townsend et al., 2017). Glacier

modelling by Eaves et al. (2016b) indicates that the temperatures were, on average, -5 to -6 °C cooler than present during glacial advances for these ~57-45 ka and ~30-18 ka periods. It is possible that temperature differences needed to retain ~80-100 m valley-filling glaciers earlier in Tongariro's history were less extreme because the edifice occupies the centre of a rift, and summit elevations may have been higher in the 290-52 ka period. Alternatively, if Ruapehu is a younger volcano than Tongariro (section 3.5.2), it follows that rain shadow effects from Ruapehu would have been initially small for south-westerly weather fronts, therefore permitting more precipitation and ice development on Tongariro.

Subsequent edifice construction on Tongariro provides no evidence for syn-glacial eruptive activity. The >25.4 ka to 2012 CE Te Maari Formation is composed of materials erupted from north-facing vents at relatively low elevations (<1600 m a.s.l.) that do not display evidence for syn-glacial emplacement. Early Holocene eruptives from Red Crater and Te Pupu (Ngauruhoe vent) formations include lavas in valley-floor positions of the Makahikatoa Stream and Mangatepopo, Waihohonu and Oturere valleys, which could not have contained significant ice when the lavas were emplaced (Fig. 3.9).

3.5.4. Volume-time reconstructions

Volume-time patterns have been widely used to examine variations in volcanic eruptive rates with time (e.g. Miller and Smith, 1987; Singer et al., 1997; Sinton et al., 2005; Singer et al., 2008; Maclennan et al., 2002; Rawson et al., 2016, Yamamoto et al., 2018). However, in most studies of stratovolcano construction histories there is little discussion of whether estimated volumes are representative of volcanic productivity (Frey et al., 2004; Vallance and Sisson, 2017; Calvert et al., 2018). For stratovolcanoes that have supported glaciers over their lifespans, abundant evidence for lava-ice interactions indicates that both the presence and absence of ice dictates where and how much erupted material is preserved (Lescinsky and Sisson, 1998; Hildreth and Fierstein, 2012; Conway et al., 2015). Whether volume-time trends reflect true variations in eruptive rates depends on whether preservation rates are consistent between periods of syn-glacial and inter-glacial edifice growth. Arguments that deglaciation triggers increased eruptive rates at stratovolcanoes are not supported in cases were variations in preservation rates exceed variations in eruptive rates. To explore this issue, time-volume trends at Tongariro are quantified and interpreted in the context of New Zealand's climate variability since ~230 ka.

Cumulative volume versus time patterns reveal five periods in Tongariro's history with distinctly different edifice-building rates (Fig. 3.14a: source data in Table 3.5). The gradients for these periods reflect distinct edifice-building rates over time. Periods of increased and decreased

edifice-building alternate with one another, as shown by the red and blue lines in Fig. 3.14a, which correspond to periods with distinct gradients and are coloured to reflect relatively warm (red) versus relatively cool periods (blue). Climate proxy data from benthic $\delta^{18}O$ records are annotated with MIS periods for comparison, after Lisiecki and Raymo (2005), which are shaded grey for periods of major ice coverage on Tongariro (Fig. 3.14b). Shifts in edifice-building rates appear to closely coincide with the boundaries of marine isotope stages (Fig. 3.14a-b). Beginning at ~230 ka in late MIS 7 (interglacial), Tongariro's edifice-building rate was 0.08 km^3/kyr, which decreased to 0.02 km^3/kyr during MIS 6 (glacial). This is in general agreement with inferred glacier thickening from ~100 m to ~200 m between ~220-190 ka (late MIS 7), and the persistence of 200-250 m-thick glaciers between ~190-130 ka (~MIS 6: see section 3.5.4, above). A subsequent increase in edifice-building rate to 0.12 km^3/kyr is observed for the 130-70 ka period, during which glaciers expanded (up to ~100 m-thick) and contracted repeatedly, but overall Tongariro had significantly less ice coverage compared with the ~190-130 ka (MIS 6) period. Between ~70-11 ka, which approximates MIS 4-2, the edifice-building rate decreased to 0.04 km^3/kyr. This is the second period in Tongariro's history with an identifiable decline in edifice-building rate that coincided with increased ice coverage (see section 3.5.4, above). The most recent period, from ~11 ka to present is defined by greatest edifice-building rate (0.19 km^3/kyr) observed for Tongariro during a period of no ice influence. These data clearly show that increased edifice-building rates coincide with warm climatic periods, and vice versa. Two opposing interpretations are considered to explain this pattern.

(1) Increased edifice-building rates during warm periods reflect true increases in eruptive rate that are triggered by reduced ice coverage on the volcano, which depressurises the magmatic system.
(2) 'Preservation bias': when the volcano is covered in large volumes of ice, the percentage of preserved erupted materials declines. This is because materials emplaced on top of ice bodies will later be lost to the ring plain as debris (e.g. Hildreth and Fierstein, 2012; Conway et al., 2016).

If the first hypothesis is true, geochemical patterns should coincide with changes in edifice-building rate and ice coverage, as has been observed elsewhere. In Iceland, Maclennan et al. (2002) report contemporaneous increases in eruptive rates and increased variation in whole-rock MgO concentrations in early postglacial lavas (12-7 ka) compared with glacial lavas (>12 ka) for the Krafla and Theistareykir systems. Lavas erupted more recently (<7 ka) revert to glacial-like eruptive rates and geochemical features, indicating that magmatic and volcanic responses (pulses) to deglaciation are relatively rapid, occurring within ~5 kyr after significant reductions in ice

coverage (glacial ice thicknesses were up to 1 km in this example). These findings are supported by another study in the Western Volcanic Zone of Iceland. Sinton et al. (2005) report similar geochemical and eruptive rate shifts between glacial (>12 ka), early postglacial (12-9 ka) and recent (<9 ka) lavas. The volcanic and magmatic responses to deglaciation at mid-latitude stratovolcanoes are unlikely to be as extreme, however, but the Icelandic examples provide end-member scenarios for testing the first hypothesis. If variations in MgO concentrations are synchronised with shifts in ice coverage at stratovolcanoes, this would provide evidence to support deglaciation as a trigger of increased eruptive rates during periods of warm climate.

Figure 3.14. (Next page.) **(a)** Cumulative volumes of map units. Width of crosses reflects the adopted age range of each stratigraphic unit (section 3.3.2). One is exception are Te Pakiraki Member (**dpk**) eruptives which is subdivided into pre- and post-151 ka (Waiaruhairiki Member) ages. Red and blue lines are regressions calculated from midpoints of adopted age ranges (section 3.3.2) and average volumes (Table 3.5) for five intervals of distinct edifice-building rates, which correspond to warm and cool climatic periods, respectively. **(b)** Benthic $\delta^{18}O$ record and MIS intervals after Lisiecki and Raymo (2005). Blue-shaded periods reflect major periods of ice coverage on Tongariro. **(c)** Time-composition systematics for SiO_2 concentrations in each stratigraphic unit (whole-rock samples), shown as crosses. Te Pakiraki Member subdivided as in (a). Cross heights represent the range of mean values for all samples of that unit. Red symbols are flank vents: 189-130 ka Tātaramoa Member (mtm), 40-30 ka Pukeonake Formation (PN), ~17.5 ka Makahikatoa Formation (MK). See data in Tables 3.3 and 3.4. **(d)** Time-composition systematics for MgO concentrations in all stratigraphic units, symbolised as in (c). Regression lines calculated between interpreted vertices D_1-D_9 are reported in Table 5.1. Typical r^2 values are 0.50-0.98.

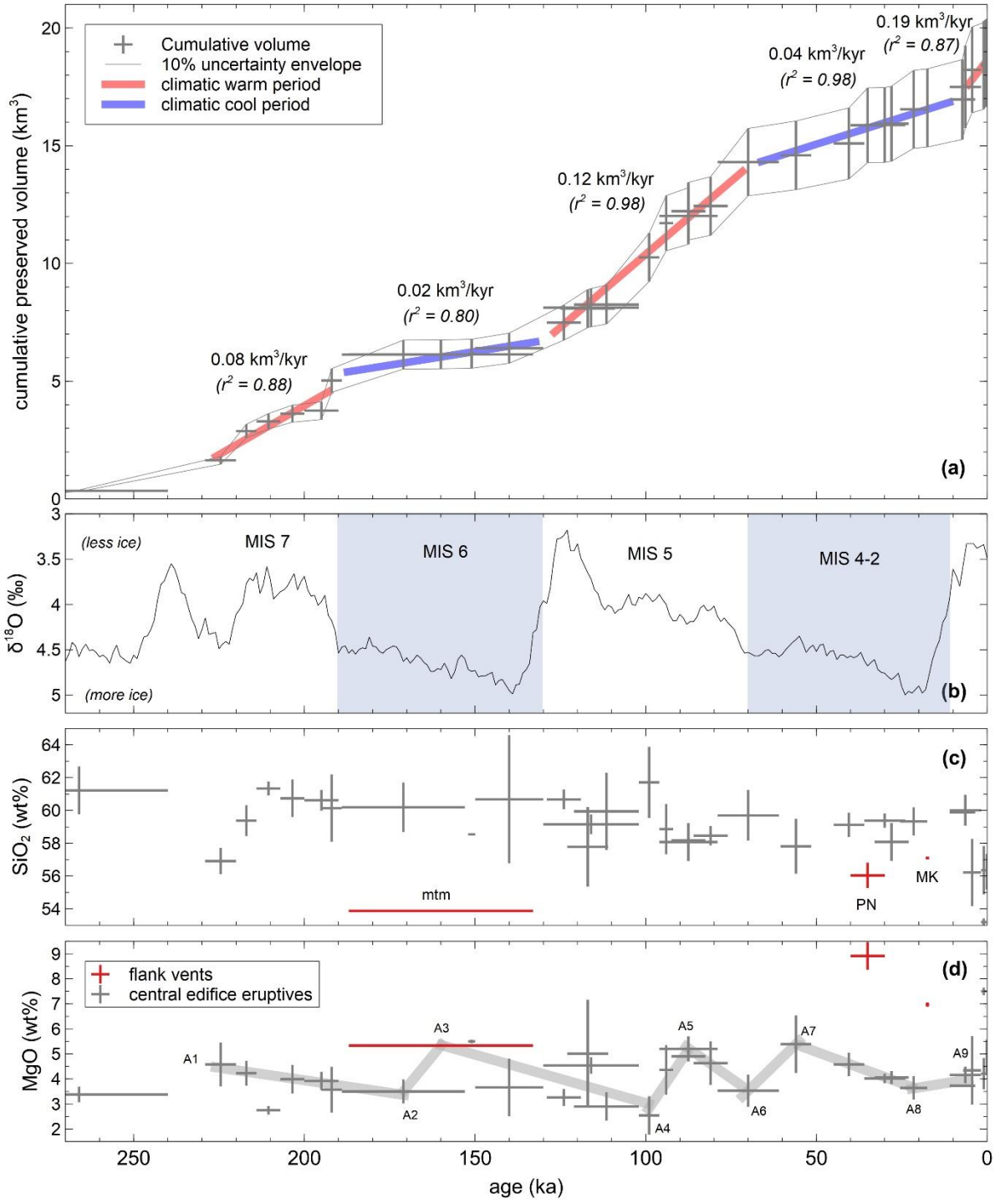

At Tongariro, variations in SiO_2 and MgO concentrations since ~230 ka do not correlate with periods of warmer or cooler climate (Fig. 3.14b-d). Variations in MgO concentrations show periods of rapid increase at ~230, ~160, ~88, ~56 ka and during the Holocene, followed by periods of gradual decline (Fig. 3.14d). This suggests that increased mafic recharge events occur at Tongariro, but not at times of contemporary ice loss. Increases in MgO at ~230, ~160, ~88, ~56 ka and the Holocene occur within mid-MIS 7 (interglacial), mid-MIS 6 (glacial), mid-MIS 5

(interglacial) and early-MIS 4 (New Zealand's greatest Last Glacial advance: Williams et al., 2015), respectively. Furthermore, high-MgO flank vents appear between ~160 ka (189-130 ka), at ~117 ka, ~35 ka and ~17.5 ka, which are all periods of significant ice coverage on Tongariro (section 3.5.3, above). In contrast, SiO_2-time systematics do not show patterns over Tongariro's lifespan (Fig. 3.14c). Collectively, SiO_2-time and MgO-time systematics do not support deglaciation as a trigger for increased eruptive rates on Tongariro. By elimination, these observations favour the second hypothesis whereby reduced edifice-building rates in ice-dominant periods represent periods of reduced volcanic record completeness. This contrasts with suggestions by other authors that deglaciation triggers increased eruptive rates at mid-latitude stratovolcanoes (Miller and Smith, 1987; Singer et al., 1997, 2008; Rawson et al., 2016). The findings of this study echo results from other rigorous time-volume reconstructions that do not find evidence to support deglaciation as a trigger of increased eruptive rates for effusive records (Conway et al., 2016; Calvert et al., 2018) or explosive eruption records (Watt et al., 2013; Weller et al., 2015).

Differences in periodic edifice-building rates can also be used to quantify the preservation bias that occurs during ice-dominant periods. The ratios of the edifice-building rates in ice-dominant periods versus subsequent warm climatic period are 21 % (MIS 4-2/MIS 1) and 17 % (MIS 6/MIS 5) (Fig. 3.14a). These values approximate the preservation rate of effusive eruptives at Tongariro during ice-dominant climate periods, relative to normal preservation rates, although preservation is unlikely be 100 % during warm periods. Similar preservation rates probably apply to other mid-latitude stratovolcanoes that have supported glaciers in their lifespans. This interpretation contrasts with the proposal of Singer et al. (1997) who suggested that erosion is the primary agent of volcanic record incompleteness at previously-glaciated stratovolcanoes.

It is suggested here that glacial erosion is a secondary geomorphological process at mid-latitude Quaternary stratovolcanoes. Moraine volumes on Tongariro (<1 km^3) equate to ≤5 % of the surficially-exposed edifice-forming materials (Table 3.5). A similar result is obtained for Ruapehu (~150 km^3 total edifice: Gamble et al., 2003; Conway et al., 2016) that has ~2 times more moraine (Townsend et al., 2017) than Tongariro (~90 km^3), which indicates that till accounts for <5 vol% of Ruapehu's total edifice. The stratovolcano growth model supported by the results of this study is one whereby valley walls and other irregular or asymmetric landforms are primary landforms that were constructed around existing ice masses: i.e., 'starfish'-shaped growth. This contrasts with traditional models that invoke periods of (perfect) cone-building that alternate with periods of inactivity and glacial erosion (e.g. Hobden et al., 1996; Singer et al.,

1997): i.e., episodic 'cone-building' growth. The choice of growth model has fundamental implications for reconstructing eruptive and original edifice volumes.

3.5.5. Explosive versus effusive volcanism comparison on Tongariro

Holocene volcanic records for Tongariro are mostly complete. Here, effusive and explosive eruption volumes are compared to assess how volcanic productivity is expressed for contrasting eruption styles. Eruptive activity since ~12 ka has produced ~6.2 km^3 of pyroclastic and tephra deposits (Topping, 1973; Donoghue et al., 1995a; Nairn et al., 1998) and ~1.5 km^3 of lava, which is explained as follows.

Large explosive eruptions occurred primarily in the early Holocene with the 12-11 ka Pahoka-Mangamate eruption sequence (Nairn et al., 1998). Pahoka-Mangamate tephra and pyroclastic deposits have a volume of ~5.9 km^3, about 4.5 km^3 of which can be attributed to vents on Tongariro (Nairn et al., 1998). Other Tongariro-sourced tephras from the Mangatawai, Ngauruhoe and Papakai tephra formations are ~1.3 km^3 (Topping, 1973; Donoghue et al., 1995a). Holocene pyroclastic volumes in the Te Pupu, Red Crater and Te Maari formations are ~0.4 km^3, based on proportions of effusive versus explosive eruptive distributions (areally) for each of these formations, as encountered during field investigations and inferred from aerial imagery. (Explosive deposits are primarily in the Te Rongo Member [Red Crater] and Matariki Member [Ngauruhoe].) Together, these sum to ~6.2 km^3 in total or ~1.7 km^3 if early Holocene Pakoha-Mangamate materials are excluded.

Holocene effusive volumes for the Te Pupu, Red Crater and Te Maari formations are collectively ~1.6 km^3 (e.g. Table 3.5). Thus, explosive products are ~3 times more voluminous than effusive products for Tongariro during the Holocene, or approximately equal if Pahoka-Mangamate explosive volumes are excluded. Tongariro's poorly-examined and fragmentary pre-Holocene tephra record precludes any meaningful comparisons of effusive versus explosive volumes for Tongariro's longer-term history.

3.5.6. Ruapehu versus Tongariro growth history comparison

Tongariro and Ruapehu are andesitic composite stratovolcanoes of similar-age, located ~20 km apart along the axis of the TVZ arc. Both volcanoes have comparable but also contrasting growth histories which are summarised in Table 3.6. In general, Tongariro is older, probably by ~100 kyr or more. Tongariro's edifice is more extensively faulted and consists of more dispersed vent locations than Ruapehu (Gómez-Vasconcelos et al., 2017; Townsend et al., 2017). Recent studies of *in situ* materials on Tongariro (this study) and Ruapehu (Conway et al., 2016) show that

eruptive activity at each volcano has been more or less continuous throughout their lifespans, which opposes previously interpreted models of growth punctuated by periods of erosion at Tongariro (Hobden et al., 1996; Hobden, 1997) and eruptive hiatuses on Ruapehu (Hackett, 1985; Gamble et al., 2003). The only major exception is the 80-50 ka period on Ruapehu which is not represented by any known edifice-forming materials. However, new examination and geochemical analysis of a lava flow exposed in the Tongariro River, located 1-2 km east of State Highway 1, indicate that it was erupted from Ruapehu within this time period. Evidence for this association is discussed further in section 3.5.7, below.

The glacial histories of each volcano also differ (Table 3.6). Tongariro does not have any known moraines on its northern flank, which Ruapehu does. Ruapehu also has a greater representation of younger moraines from MIS 2-1 whereas Tongariro has a greater representation of MIS 7-5 moraines than Ruapehu (Eaves et al., 2016a; Conway et al., 2016; Townsend et al., 2017; Cole et al., 2018). Two possible explanations for this observation are suggested as follows. First, more productive edifice-building and MIS 4-1 glacial deposits may be obscuring exposure of MIS 6-5 moraines on Ruapehu. Second, when Ruapehu was a smaller edifice around ~200-150 ka, as inferred above (section 3.5.2), its rain shadowing effect on Tongariro for south-westerly weather fronts would have been weaker. During this interval, Tongariro would have experienced comparatively greater ice development from precipitation, all else being equal. South-westerly weather fronts are common today and tephra dispersal patterns indicate that south-westerly winds were also common in the Holocene (Topping, 1973; Donoghue et al., 1995a; Nain et al., 1998).

Volume-time systematics cannot be compared in detail between the two volcanoes because of contrasting assumptions and methods used for estimating volumes. However, Ruapehu has a larger edifice of ~150 km^3 constructed within ~200 kyr (Gamble et al., 2003; Conway et al., 2016) that compares with ~90 km^3 for Tongariro that was constructed over ~300 kyr, which implies Ruapehu's edifice-building rate is about twice that of Tongariro's (Table 3.6). The proportions of explosive versus effusive eruptive outputs at each volcano are opposite for Holocene records (Table 3.6). Tongariro has erupted ~3 times more volume explosively (~6.2 km^3, following section 5.5, above: Topping, 1973; Donoghue et al., 1995a; Nairn et al., 1998; Hitchcock and Cole, 2007) than effusively (~2.0 km^3). In contrast, Ruapehu erupted ~6 times more volume effusively (~9.6 km^3: Conway et al., 2016) than explosively (~1.5 km^3: Topping, 1973; Donoghue et al., 1995a; Donoghue and Neall, 1996) in the Holocene.

Table 3.6. Comparison of features and histories of Tongariro and Ruapehu volcanoes.

Feature	Sub-aspect	Tongariro	Ruapehu
Relative age	Oldest edifice age determination	304 ± 11 ka [$^{40}Ar/^{39}Ar$] (this study: Table 3.1)	205 ± 27 ka [$^{40}Ar/^{39}Ar$] (Gamble et al., 2003)
	Oldest associated material	<349 ka andesite boulders overlying Whakamaru Ignimbrite [~9 km N of edifice] (M. Rosenberg, pers. comm., 2018; Bayly and Quinlan, 1965; Downs et al., 2014) 349-309 ka Turakina Formation debris flows [~100 km S] (Tost and Cronin, 2015; Whakamaru age from Downs et al., 2014; marine terrace stratigraphy from Pillans, 1983)	180-160 ka Oreore Formation [~30 km S of Ruapehu] (Tost and Cronin, 2015)
Volcano growth history	Vent spacing*	Within ~8 km on transect	Within ~4 km on transect
	Sector collapse events that can be linked to observable collapse scars/obvious deposits	50-45 ka Te Whaiau Formation [NW flank] (Lecointre et al., 2002; Townsend et al., 2017)	~5.2 ka Mangaio Formation [SE flank] (Donoghue and Neall, 2001; age via OxCal reprocessing by Townsend et al., 2017) ~10.5 ka Murimotu Formation [NW flank] (Palmer and Neall, 1989; Eaves et al., 2016a)
	Flank and peripheral vents	40-30 ka Pukeonake Formation [6 km W of edifice] (Townsend et al., 2017) 130-96 ka Mangahouhouiti Member [within 1 km W of upper edifice] 189-130 ka Tātaramoa Member [possibly vented from Te Tatau summit, which is 2 km NE of Central Crater: cf. Fig. 3.2]	11.4-8.6 ka Saddle Cone Member [4 km N of edifice] (Hitchcock and Cole, 2007; Conway et al., 2016; Greve et al., 2016; Townsend et al., 2017) undifferentiated spatter cone near State Highway 1 [14 km E of edifice: E1835957 N5648515 elev. 1082 m (NZTM2000)] (B. M. Kennedy, pers. comm., 2016; Townsend et al., 2017)
	Total number of vents	14 effusive vents (this study) + 3 Holocene explosive-only vents (Topping, 1973; Nairn et al., 1998) [compares with 16 effusive vents + 3 Holocene explosive-only vents in Hobden (1997)]	At least 5, with older vent areas reactivated after 5-100 kyr hiatuses (Conway et al., 2016)
Glacial history	Moraine distribution	Not known on N north flank	On all flanks
	Moraine ages	MIS 7-2 [~220-18 ka] (Eaves et al., 2016a; Townsend et al., 2017; Cole et al., 2018) MIS 7-5 moraines more common than on Ruapehu (labelled t6 in Townsend et al., 2017)	MIS 6-1 [~200-5 ka] (Conway et al., 2016; Townsend et al., 2017) MIS 6-5 moraines only on NW flank. MIS 2-1 much more abundant than on Tongariro (labelled t2 and t1 in Townsend et al., 2017)
Volumes	Total edifice	~90 km^3 (see section 3.4.2)	~150 km^3 (Gamble et al., 2003; Conway et al., 2016)
	Effusive (Holocene)	~2.0 km^3 (see section 3.5.5)	~9.6 km^3 (Conway et al., 2016)
	Explosive (Holocene)	~6.2 km^3 (see section 3.5.5)	~1.5 km^3 (see section 3.5.6)

* Refers to all inferred previous and all presently visible vent foci referenced to an upper-edifice transect in NNE direction, parallel to the TVZ arc axis.

3.5.7. New geochronological results for Pihanga and Ruapehu eruptives

New $^{40}Ar/^{39}Ar$ age determinations on lavas from Pihanga's summit and the Tongariro River provide improved age control on Pihanga and Ruapehu eruptives. A single $^{40}Ar/^{39}Ar$ age determination on a basaltic-andesite lava from Pihanga's summit indicates an age of >180 ka, which contradicts earlier K/Ar dating by Stipp (1969) (Fig. 3.1 for edifice location). The Pihanga sample contains large clinopyroxene phenocrysts and glomerocrysts (up to 11 mm across) with plagioclase only as a microphenocryst phase (<0.3 mm). This lava was probably one of the last materials erupted by Pihanga because of its position at the summit. In contrast, a K/Ar age determination of 123 ± 10 ka (revised with the decay constant of Steiger and Jaeger, 1977) was determined by Stipp (1969) on a boulder in the Poutu Canal that drains Lake Rotoaira, south of Pihanga. Stipp (1969) reports the dominance of plagioclase phenocrysts in this sample, which suggests it was sourced from a younger, probably separate edifice. The $^{40}Ar/^{39}Ar$ age determination does not display a consistent plateau age between progressive heating steps, despite the microcrystalline texture of analysed groundmass (CC351: Appendix 1). However, for the sample's low K_2O concentration (0.95 wt%), a stable radiogenic argon yield is observed for heating steps at 550-700 °C, which probably represents degassing groundmass and the sample's minimum age (~180 ka). Note that the total gas $^{40}Ar/^{39}Ar$ age (~360 ka) grossly exceeds Stipp's (1969) result of 123 ± 10 ka. From these observations, it is suggested that Pihanga was mostly constructed by ~180 ka. The geomorphology of Pihanga's edifice also indicates that it was not glaciated during growth or subsequently.

A voluminous lava flow, intermittently exposed in the Tongariro River, 1-2 km east of State Highway 1, was previously inferred to represent the oldest lava from Tongariro (cf. Grindley, 1960). New geochronological data summarised here indicate the lava was erupted between ~60-70 ka. Moreover, concentrations of K_2O and SiO_2 of ~1.9-2.1 wt% and ~59 wt%, respectively, resemble those of the Wahianoa Formation (166-80 ka) and early Mangawhero Formation (50-15 ka) lavas from Ruapehu (Price et al., 2012; Conway et al., 2016). A single $^{40}Ar/^{39}Ar$ age determination attempted for this lava was adversely affected by glassy groundmass material (LP007: Appendix 1). However, all reasonable interpretations of the heating step spectra indicate an age centred around 60-70 ka, which is within the 80-50 ka 'eruptive hiatus' suggested for Ruapehu by Conway et al. (2016). This time period coincides with New Zealand's peak glacial advance between 66-61 ka during the Last Glacial (Williams et al., 2015), which likely explains the absence of edifice-forming materials on Ruapehu in this period (Gamble et al., 2003; Conway et al., 2016). If the Tongariro River lava was erupted during the peak glacial advance, it was probably conveyed over ice until reaching exposed bedrock where it is preserved.

Petrographically, the lava is dominated by complexly-zoned plagioclase crystals relative to other phases, which indicates it was probably sourced from an established edifice magma system rather than a short-lived flank vent. The lava is unlikely to be from Tongariro because the orientation of field exposures extrapolates south-westwards back towards Ruapehu. Previous notions that the lava is >349 ka in age stem from observed bluffs of Whakamaru Group ignimbrite topographically above the lava's position in the Tongariro River and paleomagnetic results (Topping, 1974; Downs et al., 2014). This distal Ruapehu-sourced lava probably flowed down a paleo-river channel similar to the one existing today, which was already incised into older rocks. The >28 km runout distance of this lava is significantly greater than the ~18 km-long Rangataua Member on southern Ruapehu, previously inferred to be the longest-travelled andesite lava in the TVZ (Gamble et al., 2003; Price et al., 2012; Conway et al., 2016).

3.6. CONCLUSIONS

New field mapping, geochemical analyses and $^{40}Ar/^{39}Ar$ age determinations from edifice-forming eruptives on Tongariro have been used to establish the composite stratovolcano's growth history. A new eruptive stratigraphy is presented, which is composed of 12 formations, 32 constituent members and six undifferentiated units. The key findings of this study are as follows.

(1) An inlier of basaltic-andesite on Tongariro's NW flank, defined here as the Otamatereinga Formation [new], yielded a $^{40}Ar/^{39}Ar$ age determination of 512 ± 59 ka. This is the oldest dated *in situ* material from the Tongariro edifice. However, the provenance of this lava is unclear and it may not have been erupted from Tongariro.

(2) Hornblende-phyric andesite boulders, mapped as the Tupuna Formation [new], yield the oldest $^{40}Ar/^{39}Ar$ age determination for materials confidently attributed to Tongariro volcano. Tupuna Formation andesites are correlated with the Turakina Formation debris flows of Tost and Cronin (2015), which were deposited between 349-309 ka. In this study, the source is inferred to be Tongariro rather than Ruapehu, as proposed by Tost and Cronin (2015) and Tost et al. (2016). At the time when Turakina Formation debris flows were deposits, Ruapehu probably did not exist, certainly not in its current form.

(3) New $^{40}Ar/^{39}Ar$ and previous K/Ar age determinations on *in situ* edifice-forming materials show that Tongariro's edifice-building eruptive history has been (more or less) continuous since ~229 ka, including during glacial periods.

(4) Comparisons between new $^{40}Ar/^{39}Ar$ and previous K/Ar age determinations show that holocrystalline lava samples yield results that are consistently more accurate than glassy samples. K/Ar age determinations become systematically more accurate with increasing K_2O

concentrations, and within error of $^{40}Ar/^{39}Ar$ determinations above 1.8 wt% K_2O, irrespectively of whether the samples are glassy or holocrystalline. The percentage of phenocrysts (which can host melt inclusions with excess argon) does not correlate with the accuracy of whole-rock K/Ar age determinations.

(5) Tongariro's total edifice volume of ~90 km^3 was calculated against a base datum that separates volcanic materials and underlying sediments, which occurs at ~750 m a.s.l. The total ring plain volume surrounding the Tongariro edifice contains ~60 km^3 of material. The total volume of mapped units on Tongariro sums to 19 km^3, which is 21 % of the total edifice. The volume of moraines and glacial deposits is no more than 1 km^3.

(6) During periods of major ice coverage, edifice-building rates on Tongariro are only 17-21 % of edifice-building rates during warmer climatic periods. These shifts in edifice-building rates do not coincide with changes in erupted compositions, which indicates that differences are due to a preservation bias rather than effusion rates. It is inferred that materials erupted during periods of major ice coverage were emplaced onto ice masses and conveyed to the ring plain as debris, which accounts for reduced edifice-building rates during cool climatic periods. Edifice-building rates thus do not represent actual eruptive rates. Available data from Tongariro implies that deglaciation does not cause an increase in eruptive rates.

(7) Steep increases in whole-rock MgO concentrations to ~5-9 wt% are observed in Tongariro eruptives at ~230, ~160, ~117, ~88, ~56 ka and in the Holocene. This is in addition to the appearance of mafic flank vents at ~35 ka (Pukeonake Formation) and ~17.5 ka (Makahikatoa Formation). These abrupt increases in MgO concentrations are followed by gradual declines in erupted MgO concentrations and occur on irregular ~10-70 kyr cycles, which suggests that they reflect episodes of enhanced mafic replenishment.

(8) Explosive output (~6.2 km^3) was ~3 times greater than effusive output (~2.0 km^3) during the Holocene at Tongariro. If the 12-11 ka Pahoka-Mangamate explosive eruptions are excluded, then Holocene effusive versus explosive output is about equal.

(9) A voluminous lava flow that is intermittently exposed in the Tongariro River, east of both volcanoes by ~15 km (or 1-2 km east of State Highway 1), was sourced from Ruapehu, rather than Tongariro as previously supposed. This conclusion is drawn from a tentative $^{40}Ar/^{39}Ar$ age determination between 60-70 ka, field exposures that trace back towards Ruapehu, and compositions that are more similar to Ruapehu Wahianoa Formation and early Mangawhero Formation eruptives than any other known stratigraphic unit on Tongariro or Ruapehu. The age of this lava is within New Zealand peak Last Glacial advance and it was possibly emplaced supra-glacially near source (cf. Rangataua Member flow on Ruapehu: Conway et al.,

2016), beyond which it travelled at least 28 km down the paleo-Tongariro River valley, which has since been partially re-excavated.

(10) A new $^{40}Ar/^{39}Ar$ age determination on a summit lava flow on the Pihanga edifice indicates a minimum age of 180 ka, which implies that the volcano is much older than the ~123 ka K/Ar age reported by Stipp (1969).

Chapter 4

The geochemistry and petrogenesis of basaltic-andesite to dacite magmas at Tongariro volcano, New Zealand

"It's turtles all the way down"

R. J. Arculus (c. 2013)

4.1. INTRODUCTION

Intermediate-composition magmas are ubiquitous features at continental arc volcanoes (Gill, 1981), yet despite their prevalence, the processes controlling their genesis are still debated after almost a century of study (Bowen, 1928; Eichelberger, 1975; Taylor, 1980; Eichelberger et al., 2006; Lee and Bachmann, 2014). Simultaneous crystallisation-differentiation, crystal-melt fractionation, magma recharge, magma mixing and country rock assimilation can occur in contrasting proportions at any given volcano and at the same volcano through time (Eichelberger, 1975; Hildreth and Moorbath, 1988; Dungan et al., 2001; Eichelberger et al., 2006; Price et al., 2012; Jagoutz, 2014; Lee and Bachmann, 2014; Sisson et al., 2014). Comprehensive petrogenetic studies are therefore essential for constraining and refining models of andesite-series magma genesis. In pursuit of this goal, this study presents new major oxide, trace element and Sr-Nd-Pb isotope data from a comprehensive suite of Tongariro whole-rock samples, groundmass separates and metasedimentary xenoliths. These data are used to address fundamental questions relating to the generation of intermediate-composition magmas at continental arc volcanoes, as follows.

- What percentage of felsic country rock is assimilated into Tongariro magmas?
- Does the ratio of mass assimilation rate (M_a) over the mass fractional crystallisation rate (M_c)—a.k.a. the r-value in DePaolo (1981)—vary as magmas evolve?
- Do Sr-Nd-Pb isotope ratios in xenolithic fragments accurately reflect their (unaltered) protoliths?
- Do assimilant compositions reflect their bulk protoliths, or do assimilated materials primarily occur as partial melts with contrasting compositions to those of the bulk country rocks from which they were derived?

These questions are addressed with the results and discussion in this chapter. For a summary of the regional and local geological setting of Tongariro, see section 1.4.

4.1.1. Previous work

A large body of whole-rock major element data obtained via XRF already exists on edifice-forming Tongariro eruptives (i.e. lavas, agglutinates, lapilli tuff breccias, spatter), which also includes some trace elements (Cole, 1978, 1979; Wahyudin, 1993; Hobden, 1997). Other whole-rock trace element concentration data are less numerous and have been determined by both instrumental neutron activation analysis (INAA: Hobden, 1997; Gamble et al., 1993) and ICP-MS (Gamble et al., 1996; Shane et al., 2017). High-quality Sr-Nd-Pb isotope data are sparse. Graham et al. (1992) report Pb isotope data on selected Tongariro eruptives but the samples were not

leached and these analyses were corrected for fractionation externally. Analyses from this study on materials from the same stratigraphic units indicate large inaccuracies in the data of Graham et al. (1992). The same limitations apply to the Pb isotope data reported by Hobden (1997), although these samples were leached before digestion and analysis. However, Sr and Nd isotope ratio measurements reported by Hobden (1997) and Hobden et al. (1999, 2002) determined by TIMS on samples from the same stratigraphic units analysed here generally give results within analytical error, which indicates that they are accurate and appropriate for comparisons. The limited number of Sr-Nd isotope ratio measurements on Red Crater Formation eruptives, determined via MC-ICP-MS by Shane et al. (2017), are within analytical error of Sr-Nd TIMS analyses by Gamble et al. (1993) and by Hobden (1997). Pb isotope data also reported by Shane et al. (2017) are within analytical error of Pb isotope ratio analyses of the Te Ahititi Member (11-1.8 ka Red Crater Formation eruptives: section 3.3.2.12). The data reported by Shane et al. (2017) are also the first Pb isotope ratio data for the Te Rongo Member (1.8 ka to 1800 CE Red Crater Formation eruptives: section 3.3.2.12). Ten whole-rock samples reported by Hobden (1997) also have measured oxygen isotopic compositions.

Geochemical datasets for metasedimentary xenoliths, which represent country rock fragments entrained during magma assembly, are expanded substantially here. Previously reported geochemical data on metasedimentary xenoliths in Tongariro eruptives are from Graham (1987), Graham et al. (1988), Hobden (1997) and Price et al. (2010). These compilations include major oxide (XRF) and trace element concentrations (XRF, INAA and ICP-MS) and Sr-Nd isotope ratios (TIMS and MC-ICP-MS), although the Pb data from Hobden (1997) are not included in data interpretations here for the reasons outlined above.

Reference geochemical data for regional greywacke and argillite lithologies sampled from surface exposures from the Torlesse and Waipapa composite terranes are reported by Price et al. (2015). These data are preferred for comparisons to metasedimentary xenoliths for the same reasons outlined by Price et al. (2015), which include the scarcity and inferior-quality of Pb isotope data and lack of Sr and Nd isotope ratio measurements performed on digestions of the same samples. Major oxide and trace element data reported by Price et al. (2015) are representative of larger datasets that lack Sr-Nd-Pb isotope data (see references therein) and are therefore considered suitable for comparisons with xenolith data from this study.

4.1.2. Basement geology of the southern TVZ

Basement rocks beneath Tongariro are inferred to be Mesozoic greywackes, argillites and sandstones[1] (Beetham and Watters, 1985; Mortimer, 2004; Price et al., 2015; Townsend et al., 2017). These (meta)sediments have been proposed to rest on lower-crustal meta-igneous oceanic crust (Graham et al., 1990). Previous regional (Charlier et al., 2010; Price et al., 2015) and local (Beetham and Watters, 1985; Graham, 1987; Graham et al., 1988; Hobden, 1997; Price et al., 2012; Conway et al., 2018) investigations indicate that three greywacke and argillite terranes could possibly be present beneath Tongariro, as inferred by their representation in metasedimentary country rock xenoliths in Tongariro, Ruapehu and Taupō eruptives. From oldest to youngest depositional age, these greywacke lithologies are the Waipapa composite terrane (Jurassic), Kaweka terrane (Late Jurassic) and the Pahau terrane (Early Cretaceous). The youngest of these terranes (Kaweka plus Pahau) comprise the Torlesse composite terrane in New Zealand's North Island (Mortimer, 1994; Mortimer et al., 2014). At the surface, Kaweka terrane occurs ~15 km east of Tongariro in the Kaimanawa Mountains, while Waipapa greywacke occurs ~15 km northwest of Tongariro in an uplifted fault block and is capped by <200 m of Neogene Māui Supergroup sediments (Townsend et al., 2017). Waipapa greywacke has been intercepted at shallow depths (≤200 m) in basement rocks at a site ~10 km west of the Tongariro edifice, about ~5 km closer to Tongariro than the corresponding surface exposures (Beetham and Watters, 1985; Townsend et al., 2017). In contrast, the nearest surface exposure of Pahau terrane is hundreds of kilometres to the northeast, but is known to occur beneath the Taupō area as indicated by zircon provenance studies on a metasedimentary xenolith erupted with the ~27 ka Rubbish Tip dome (Sutton, 1995; Charlier et al., 2010). Miocene sediments with thicknesses of ≤1.5 km thick occur between southern TVZ Quaternary volcanic rocks and subjacent metasedimentary lithologies (Sissons and Dibble, 1981; Robertson and Davey, 2018) but are largely buried by ring plain sediments surrounding the volcanoes (Cronin and Neall, 1997; Townsend et al., 2017).

4.2. ANALYTICAL METHODS

Analytical protocols for determining major oxide and trace element concentrations and Sr-Nd-Pb isotope ratios are outlined here and described fully in Chapter 2. Briefly, bulk sample major oxide concentrations for whole-rock and xenolith samples were determined by XRF on powders prepared with an agate TEMA. All trace element analyses were determined by solution ICP-MS,

[1] Reference samples exposed at the surface, that represent possible basement (meta)sediments, are henceforth referred to as 'greywackes'.

including limited major element concentrations (Ti, Fe, Mn, Na, P) on xenoliths and groundmass separates, following conventional HF-HNO_3 digestion procedures. Reconnaissance EPMA analyses on orthopyroxene-hosted silicate melt inclusions informed choice of the most appropriate mineral/melt partition coefficients (Kd values) for modelling magma compositions. Kd values used from modelling and interpreting trace element data are from the compilations of Gill (1981), Rollinson (1993), Ersoy and Helvaci (2010) and references therein. All new Sr-Nd-Pb isotope ratios were determined by TIMS: Pb measurements employed the ^{207}Pb-^{204}Pb double-spike method after Thirlwall (2000). All radiogenic isotope ratios, from this study and elsewhere, were normalised to values of NBS987 $^{87}Sr/^{86}Sr = 0.710248$ (Thirlwall, 1991); JNdi-1 $^{143}Nd/^{144}Nd = 0.512115$ (Tanaka et al., 2000) which is equivalent to La Jolla $^{143}Nd/^{144}Nd = 0.511858$ (Lugmair and Carlson, 1978); NBS981 $^{206}Pb/^{204}Pb = 16.9409$, $^{207}Pb/^{204}Pb = 15.4956$, $^{208}Pb/^{204}Pb = 38.7228$, $^{207}Pb/^{206}Pb = 0.91469$, $^{208}Pb/^{206}Pb = 2.1677$ (Thirlwall, 2000). All geochemical data are reported with quadratically combined internal (2 s.e.) and external reproducibilities (2 s.d.) except where noted otherwise.

4.3. RESULTS

Geochemical data are presented here without context of their respective stratigraphic groups on Tongariro for the sake of solely examining petrogenetic processes. Results presented here include petrographic observations, major oxide concentrations, trace element concentrations and radiogenic Sr-Nd-Pb isotope ratios. Data were collected from lava whole-rock, lava groundmass and xenolith samples with the purpose of characterising the materials involved with magma assembly at Tongariro. These results are presented in context with data from previous studies on Tongariro xenoliths and lava whole-rock samples (Hobden, 1997), regional basalt reference samples in the TVZ-Kermadec arc (Gamble et al., 1993, 1996; Barker et al., 2015; Waight et al., 2017) and reference data for greywacke terranes that form the basement rocks beneath Tongariro (Price et al., 2015). Time-composition relationships of Tongariro magmas are presented in Chapter 5.

4.3.1. Whole-rock samples

4.3.1.1. Petrography

The crystal cargoes of most whole-rock samples contain plagioclase, orthopyroxene and clinopyroxene, with occasional olivine that often displays reaction rims of pyroxene. A more detailed summary of petrographic features for all edifice-forming materials on Tongariro according to stratigraphic groups refined in this study is given in Table 3.3. Trace amounts of apatite (≤0.5 vol%) occur in high-silica andesites and dacites. Hornblende is only observed as a significant phenocryst phase in Tupuna Formation andesites where it is the most abundant ferromagnesian mineral. Zircon is not observed as a phenocryst in any Tongariro eruptives. Fe-Ti oxides are present in most lavas although highly vesicular, glassy and pyroclastic materials typically have lower abundances.

4.3.1.2. Major oxides

Edifice-forming materials on Tongariro are dominantly medium-K andesites and less commonly basaltic-andesites and dacites (Fig. 4.1) (Gill, 1981). Whole-rock SiO_2-TiO_2 data form a scattered array with high TiO_2 concentrations (~1 wt%) that are more common in basaltic andesites and low TiO_2 concentrations (~0.5-0.6 wt%) that are more common in high-silica andesites (Fig. 4.1a). Al_2O_3 concentrations form a funnel-shaped array where values converge to 16-17 wt% Al_2O_3 at SiO_2 concentrations around 63 wt% but are otherwise scattered between ~14-19 wt% at lower SiO_2 concentrations (Fig. 4.1b). A similar funnel-shaped array for equivalent SiO_2-Al_2O_3 concentrations is observed at neighbouring Ruapehu volcano and was interpreted there to reflect varied modal abundances of plagioclase (high-Al_2O_3) and pyroxene (low-Al_2O_3) (Graham and Hackett, 1987; Price et al., 2012; Conway et al., 2018).

Similar to andesites globally (Gill, 1981), Tongariro Fe_2O_3* (representing all Fe as ferric henceforth), MgO and CaO concentrations decrease with increasing SiO_2 (Fig. 4.1c-e). Fe_2O_3* concentrations in regional basalts increase from ~8 to 10 wt% as SiO_2 increases from ~49 to 52 wt%, which leads to the Tongariro array wherein Fe_2O_3* decreases linearly from ~10 to 5 wt% as SiO_2 increases from ~53 to 66 wt%. MgO-SiO_2 data define two curvilinear arrays for high-MgO and normal-MgO andesites (Fig. 4.1d), which is also observed at Ruapehu (Conway et al., 2018). The high-MgO array begins at ~9 wt% MgO at ~55 wt% SiO_2 and converges with the normal-MgO array at ~60 wt% SiO_2 and ~4 wt% MgO. A large proportion of samples that follow the high-MgO andesite array are eruptives from flank vents (e.g. Pukeonake Formation) but also include upper edifice locations (e.g. the Waiaruhairiki and Mangahouhouiti members: Chapter 3). There is no significant relationship between whole-rock MgO concentrations and the

relative abundance of pyroxenes: orthopyroxene occurs both more and less abundantly than clinopyroxene in samples over all MgO concentrations (Table 3.3).

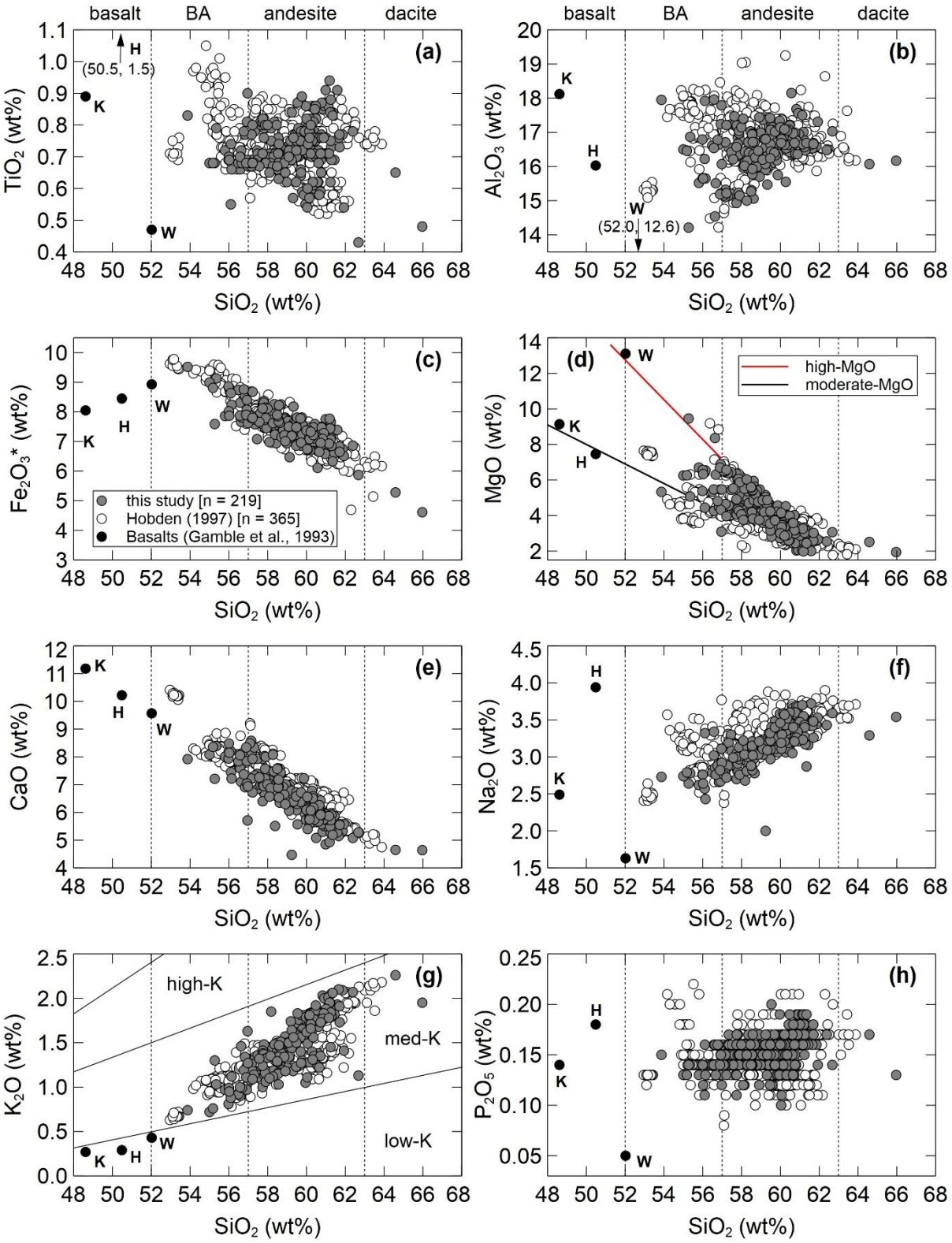

Figure 4.1. (Previous page.) Major oxides versus SiO_2 for Tongariro whole-rock samples (full data in Appendix 5). All data are normalised to 100 % anhydrous totals. Tongariro data are from this study (grey circles, n = 219) and Hobden (1997) (open circles, n = 365). Basalt samples (black) from the Havre Trough (H), Kakuki (K) and Waimarino (W) areas are from Gamble et al. (1993). Vertical dotted lines indicate the boundaries between the fields of basalt (left), basaltic-andesite (BA: mid-left), andesite (mid-right) and dacite (right). Greater Na_2O concentrations in some Hobden (1997) samples are from units not sampled in this study (e.g. Ngauruhoe/Te Pupu Formation). High, medium and low-K fields in (**g**) follow Gill (1981). 2 s.d. errors are approximately within symbols (section 2.4).

Na_2O, K_2O and P_2O_5 increase with increasing SiO_2, which probably reflect their incompatibilities in the common phenocryst phases, except for Na_2O in plagioclase (Fig. 4.1f-h). Simultaneous increases in Na_2O from ~2.5 to 4.0 wt% as SiO_2 concentrations increase from ~53 to 64 wt% indicate that although plagioclase is an abundant phenocryst phase, it may not be efficiently extracted from magmas after it crystallises. Alternatively, sodic plagioclase may be fractionated but not rapidly or efficiently enough to hold whole-rock Na_2O concentrations constant as SiO_2 increases. K_2O concentrations form a well-defined array that increases from ~0.7 to 2.3 wt% with increasing SiO_2 concentrations (~53 to 64 wt%) and cause the samples to plot in the medium-K field of Gill (1981) (Fig. 4.1g). Samples that define slower K_2O increases against increasing SiO_2 (similar to the low-K versus medium-K line of Gill, 1981: Fig. 4.1) are from the Lower Tama Member (~62.7 wt% SiO_2, ~1.1 wt% K_2O) which contains ~5 vol% pseudomorphs after amphibole and the Tupuna Formation (hornblende-phyric, ~60.0 wt% SiO_2, ~1.0 wt% K_2O), which suggest that petrogenetic processes leading to hornblende fractionation might be related to K_2O concentrations in early Tongariro magmas. In general, concentrations of P_2O_5 increase from ~0.1 to 0.2 wt% with SiO_2 (~55 to 63 wt%) but show increasing scatter in the area of greatest data-point density at $SiO_2 \geq 59$ wt% (Fig. 4.1h). Given that apatite is frequently observed in samples with >59 wt% SiO_2 (see Table 3.3), the scatter in P_2O_5 concentrations for more silicic samples implies varied amounts of apatite fractionation and/or accumulation in more evolved magmas (Fig. 4.1h).

4.3.1.3. Trace elements

Trace element variation diagrams for whole-rock samples show inflection points when plotted against major oxide concentrations (Fig. 4.2), which may indicate shifts in processes controlling magma evolution and/or changes in mineral assemblages. Data in Fig. 4.2 are interpreted to constrain the relative chronologies and proportions of each fractionating mineral, which are summarised in Table 4.1. Local and regional basalts are shown as an indication of possible end-member compositions: the Waimarino and Kakuki areas of the central TVZ and the Havre Trough (offshore north of the North Island)—the latter may reflect magmas derived from

mantle without substantial crustal or slab fluid modification (Gamble et al., 1993, 1996; Barker et al., 2015; Waight et al., 2017).

Data in Fig. 4.2a show a steep trend in Ni from ~300-100 ppm for MgO concentrations ≥8 wt%, which is interpreted as the presence or absence of olivine from evolving magmas. Below 8 wt% MgO, Ni loss compared with MgO occurs less rapidly, which suggests that the fractionation of ferromagnesian phases with lower Ni partition coefficients (i.e. not olivine) results in decreased MgO (e.g. Gill, 1981; Rollinson, 1993). Sc versus MgO data show the inverse relationship whereby Sc concentrations above 8 wt% MgO are invariant (~35 ppm) but begin declining from ~30-15 ppm at ≤8 wt% MgO (Fig. 4.2b). This inflection probably represents the onset of clinopyroxene (Kd_{Sc}^{cpx} = 17.0) and orthopyroxene (Kd_{Sc}^{opx} = 3.0) becoming significant fractionating phases at ≤8 wt% MgO, whereas above 8 wt% MgO the role of olivine probably drove decreases in MgO (Kd_{Sc} values from Gill, 1981 and Bacon and Druitt, 1988).

Table 4.1. Interpreted crystal fractionation order relative to major oxide concentrations in Tongariro whole-rock samples.

SiO_2 (wt%)	MgO (wt%)*	CaO (wt%)	Fractionating phases
≤53	≥8	≥7	ol > cpx + opx
55-53	8-7	10-7	cpx + opx + ol
59-55	7-4	9-6	cpx + opx + pl
66-59	4-2	7-3	cpx + opx + pl > ap

Note: * Due to scatter in major oxide arrays, specific MgO concentrations do not have unique equivalence to SiO_2 and CaO concentrations.

An inflection point in Rb/Sr versus CaO/Al_2O_3 ratios distinguishes between modes of clinopyroxene and plagioclase fractionation (Fig. 4.2c). Both clinopyroxene and plagioclase are calcic but only plagioclase incorporates significant amounts of Sr and Al_2O_3, which explains the inflection point at CaO/Al_2O_3 = 0.55. For CaO/Al_2O_3 ratios above ~0.55, Rb/Sr ratios are relatively constant (≤0.1) which implies that clinopyroxene fractionation decreases the CaO/Al_2O_3 ratios by preferentially removing CaO from magmas. Rb/Sr ratios increase for CaO/Al_2O_3 ratios below ~0.55, which was probably driven by an increased significance of plagioclase fractionation that simultaneously reduced magmatic Al_2O_3 and Sr concentrations. The axes in Fig. 4.2d show that CaO/Al_2O_3 = 0.55 equates to an MgO concentration of ~7 wt% for Tongariro samples, which approximates the onset of significant plagioclase fractionation.

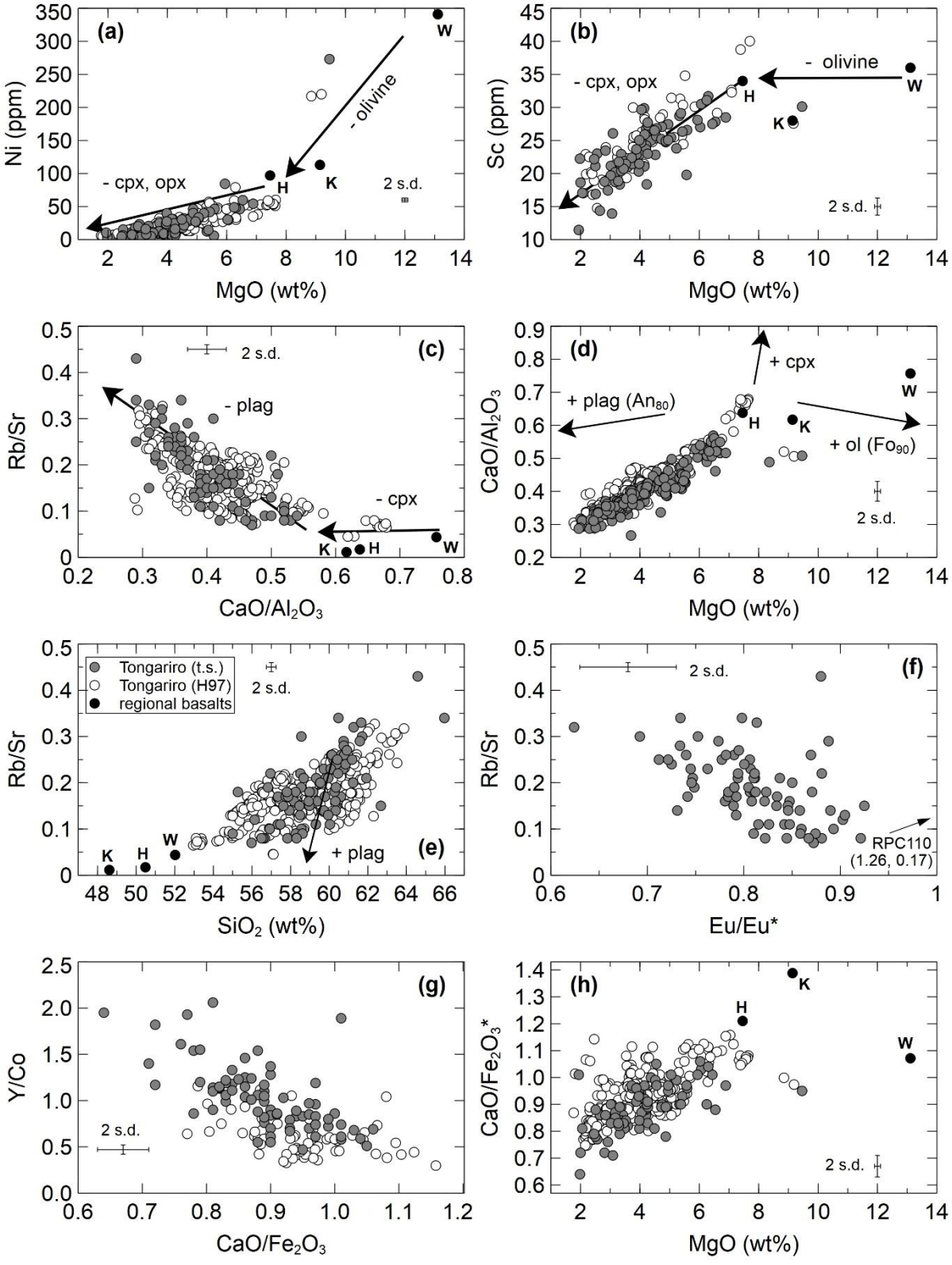

Figure 4.2. Trace elements in whole-rock Tongariro samples. Key in (**e**) applies to all panels. Basalt data are from the Havre Trough (H), Kakuki (K) and Waimarino (W) areas (Gamble et al., 1993). Tongariro trace element data are from this study ('t.s.': full data in Appendix 5) and Hobden (1997) ('H97'). H97 data are by XRF (Sr, Rb, Ni) and INAA (Sc, Co, Y, selected REEs only). Arrows and plus (+) and minus (-) symbols indicate crystal accumulation and fractionation of clinopyroxene (cpx), olivine (ol), plagioclase (plag) and orthopyroxene (opx). Trajectories in (**d**) reproduced from Gamble et al. (1990).

Trajectories in Fig. 4.2d show how the addition (+ symbols) of plagioclase (An_{80}), clinopyroxene and olivine (Fo_{90}) affect CaO/Al_2O_3 versus MgO systematics (adapted from Gamble et al., 1990). Compared with Tongariro and the basalt reference data (Gamble et al., 1993), the trajectories suggest that clinopyroxene and olivine fractionation are the primary drivers of decreases in CaO and MgO concentrations across the Tongariro array. The relatively steep gradient for the Tongariro array most closely matches the overall trajectory for clinopyroxene and olivine fractionation. However, for reasons outlined above (Fig. 4.2a-b; Table 4.1), olivine fractionation is unlikely to have a primary influence on removing MgO from magmas for concentrations below ~7 wt% (most Tongariro samples) and therefore decreases in MgO from ~7 down to 2 wt% are likely driven by orthopyroxene (similar trajectory to olivine) and clinopyroxene fractionation. The small number of samples (Pukeonake Formation) offset to higher MgO (~9 wt%) from the main array probably reflect olivine accumulation in these samples, consistent with petrographic observations (see Table 3.3). The trajectories in Fig. 4.2d also predict that fractionating large proportions of calcic plagioclase alone will drive Tongariro magmas towards higher MgO concentrations, which is not observed (Fig. 4.1d). In addition, although Rb/Sr ratios increase from ~0.1 to 0.4 with increasing SiO_2 (Fig. 4.2e), which indicates plagioclase fractionation and the incompatibility of Rb, other data presented here suggest that clinopyroxene and orthopyroxene are volumetrically dominant over plagioclase as fractionating minerals. In comparison, rhyolites erupted from Taupō volcano generally have Rb/Sr ratios >0.5 (Sutton et al., 1995, 2000; Charlier et al., 2005; Barker et al., 2015) that do not overlap with Tongariro values, consistent with significantly greater amounts of plagioclase fractionation in the rhyolites.

Rb/Sr systematics versus SiO_2 (Fig. 4.2e) and Eu/Eu* (Fig. 4.2f) show scatter in the main bodies of each array. Against SiO_2, Rb/Sr ratios increase nonlinearly from ~0.1 to 0.3 with a gently steepening gradient on the upper (high Rb/Sr) surface of the array that probably reflects increased proportions of fractionating plagioclase as magmas evolve. Conversely, the Rb/Sr versus SiO_2 array bows downwards (to Rb/Sr = ~0.1) between 56 and 62 wt% SiO_2 which is consistent with the incorporation of plagioclase (approximate trajectory shown with arrows). Rb/Sr ratios also increase as Eu anomalies[2] become more negative, from ~0.95 to 0.70, which is consistent with plagioclase fractionation (Fig. 4.2f). Scatter in the Rb/Sr versus Eu/Eu* ratios occurs perpendicular to the array (to high Rb/Sr and high Eu/Eu*) but has a relatively low data-point density: this feature indicates the net incorporation of a material enriched in Eu and

[2] Eu/Eu* was calculated as $Eu_N/(sqrt(Sm_N*Gd_N))$ after normalisation with the CI chondrite values of McDonough and Sun (1995).

Rb (or loss of a material depleted in Eu and Rb), which is unlikely to be a feldspar, but instead may represent the incorporation of crust enriched in incompatible elements (e.g. Price et al., 2015).

The relative proportions of clinopyroxene and orthopyroxene fractionation are difficult to assess because of their similar chemical affinities for most trace elements. Differences in partition coefficients for these minerals are noted for Y (Kd_Y^{cpx} ~1.5, Kd_Y^{opx} ~0.5) and Co (Kd_{Co}^{cpx} ~3.0, Kd_{Co}^{opx} ~6.0) that preferentially partition into clinopyroxene (Y) and orthopyroxene (Co) (Rollinson, 1993 and references therein). However, in Tongariro whole-rock samples, Y/Co ratios (~0.3-2.0) versus CaO/Fe_2O_3* ratios (~0.7-1.1) form a uniform array without inflection points which indicates that Y and Co are sequestered in fractionated minerals at equal rates to CaO and Fe_2O_3* (Fig. 4.2g). CaO/Fe_2O_3* versus MgO systematics define a uniform array that implies that there are no significant differences in the rates of clinopyroxene and orthopyroxene fractionation (Fig. 4.2h). Geochemical indications of contrasting pyroxene fractionation rates, if occurring in nature, are probably obscured by other factors such as plagioclase fractionation (CaO loss) and olivine fractionation (Co loss).

Chondrite-normalised rare earth element (REE) diagrams for whole-rock Tongariro samples show several systematic patterns (Fig. 4.3). All samples are LREE-enriched relative to MREE and HREE. As absolute REE concentrations increase, negative Eu anomalies become greater from Eu/Eu* ~0.95 to 0.70, which implies that the process(es) causing REE enrichment and negative Eu anomalies are coupled. Ce_N/Yb_N values vary from ~2 to 5 and do not correlate with Eu/Eu* values in whole-rock samples or groundmass separates (not shown). Negative Ce anomalies only occur in some high-silica andesites (e.g. LP051: Fig. 4.3a): negative Ce anomalies also occur in the groundmass separates of these same samples (Fig. 4.14). Although not illustrated, total REE concentrations in whole-rock samples do not correlate with SiO_2 concentrations. High-silica andesites and dacites of the Haumata and Mangahouhounui formations have relatively low REE concentrations compared with Taiko Formation eruptives, despite equivalent andesite-dacite SiO_2 concentrations (Fig. 4.3a). Furthermore, relatively primitive eruptives such as the Pukeonake Formation (~55 wt% SiO_2, ~9 wt% MgO: LP001 in Fig. 4.3b) have moderate REE concentrations that exceed those observed for most high-silica andesites of the Haumata Formation (e.g. LP109, MSR15018: Fig. 4.3a).

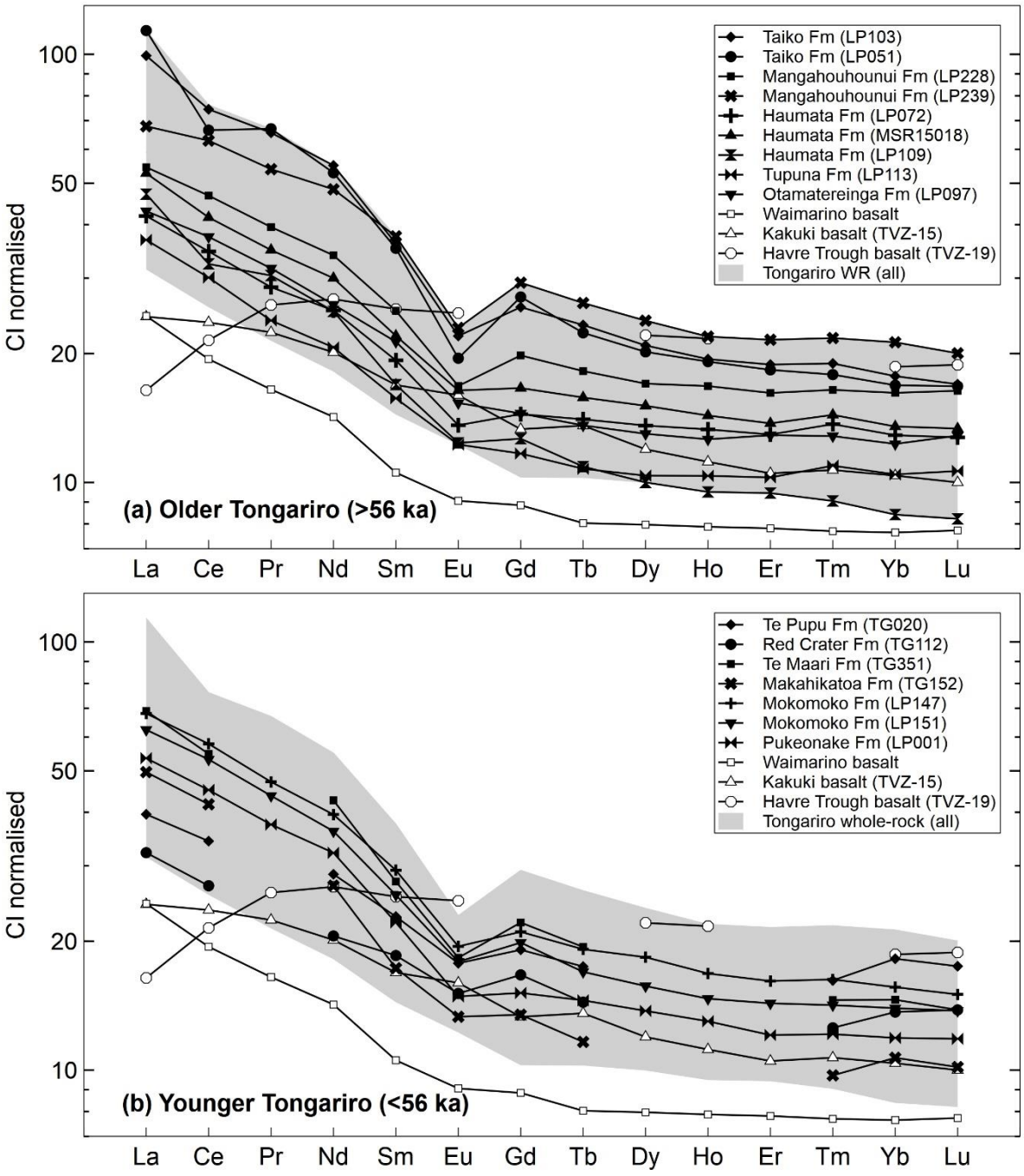

Figure 4.3. REE concentrations for whole-rock samples from Tongariro, normalised to the CI chondrite values from McDonough and Sun (1995). Tongariro data are from this study (all REEs: source data reported in Appendix 5) and incomplete REE data from young eruptives are from Hobden (1997) and were obtained by INAA. Basalt reference data are from Gamble et al. (1996) for Havre Trough, Barker et al. (2015) for Waimarino and Waight et al. (2017) for Kakuki, all by ICP-MS. (**a**) Whole-rock samples from older (>56 ka) Tongariro formations (Fm) that are not represented by presently-visible vent foci (see Chapter 3). The order of Tongariro samples in the key approximately follows a (bottoms-up) stratigraphic chronology. (**b**) Whole-rock samples from younger Tongariro formations (<56 ka) that were erupted from vent foci that are still presently-visible.

4.3.1.4. Sr-Nd-Pb isotopes

Tongariro whole-rock samples form coherent arrays in Sr-Nd-Pb isotope ratio space and are more crust-like than regional basalt samples (Fig. 4.4) (Gamble et al., 1993). In general, linear and curvilinear arrays are observed between all isotope ratios which indicates that processes leading to variation in Sr, Nd and Pb isotope compositions are generally linked. Moreover, the significant variations observed in Sr-Nd-Pb isotope ratios indicate that Tongariro magmas were assembled from multiple materials with distinct end-member isotopic characteristics.

$^{87}Sr/^{86}Sr$ versus $^{143}Nd/^{144}Nd$ data define an array which is scattered at low $^{87}Sr/^{86}Sr$ values of 0.7044-0.7049 and high $^{143}Nd/^{144}Nd$ values of 0.51276-0.51288. Towards higher $^{87}Sr/^{86}Sr$ (~0.706) and lower $^{143}Nd/^{144}Nd$ (~0.51265), the scatter decreases. Increases in the crust-like character of Tongariro whole-rock Sr-Nd-Pb isotope ratios occur simultaneously as shown by $^{206}Pb/^{204}Pb$ versus $^{87}Sr/^{86}Sr$ and $^{143}Nd/^{144}Nd$ ratios which form similar and coherent Sr-Pb (Fig. 4.4e) and Nd-Pb (Fig. 4.4f) arrays.

All Pb isotope ratios define arrays of contemporaneously increasing radiogenic character. Strong systematic correlations are observed between $^{206}Pb/^{204}Pb$ ratios (18.82-18.86) versus $^{207}Pb/^{204}Pb$ (15.62-15.64) and $^{208}Pb/^{204}Pb$ (38.70-38.79) (Fig. 4.4b-c). For Tongariro samples, Pb-Pb pseudochrons calculated with the method outlined in Faure and Mensing (2005) give a meaningless age of 3.79 Ga (not shown) which is probably the result of mixed mantle-derived magma and isotopically distinct metasedimentary basement material. The well-defined array between increasing $^{207}Pb/^{206}Pb$ ratios of 0.8291-0.8301 versus $^{208}Pb/^{206}Pb$ ratios of 2.0560-2.0572 (Fig. 4.4d) indicates that variations in $^{206}Pb/^{204}Pb$, $^{207}Pb/^{204}Pb$ and $^{208}Pb/^{204}Pb$ ratios (Fig. 4.4b-c) are at least partially determined by variations in the radiogenic Pb isotopes, and not solely from common ^{204}Pb. Therefore, the highly systematic variations in $^{206}Pb/^{204}Pb$ versus $^{207}Pb/^{204}Pb$ and $^{208}Pb/^{204}Pb$ ratios could be consistent with two-component mixing between reservoirs of contrasting radiogenic Pb isotopic compositions (Fig. 4.4b-c).

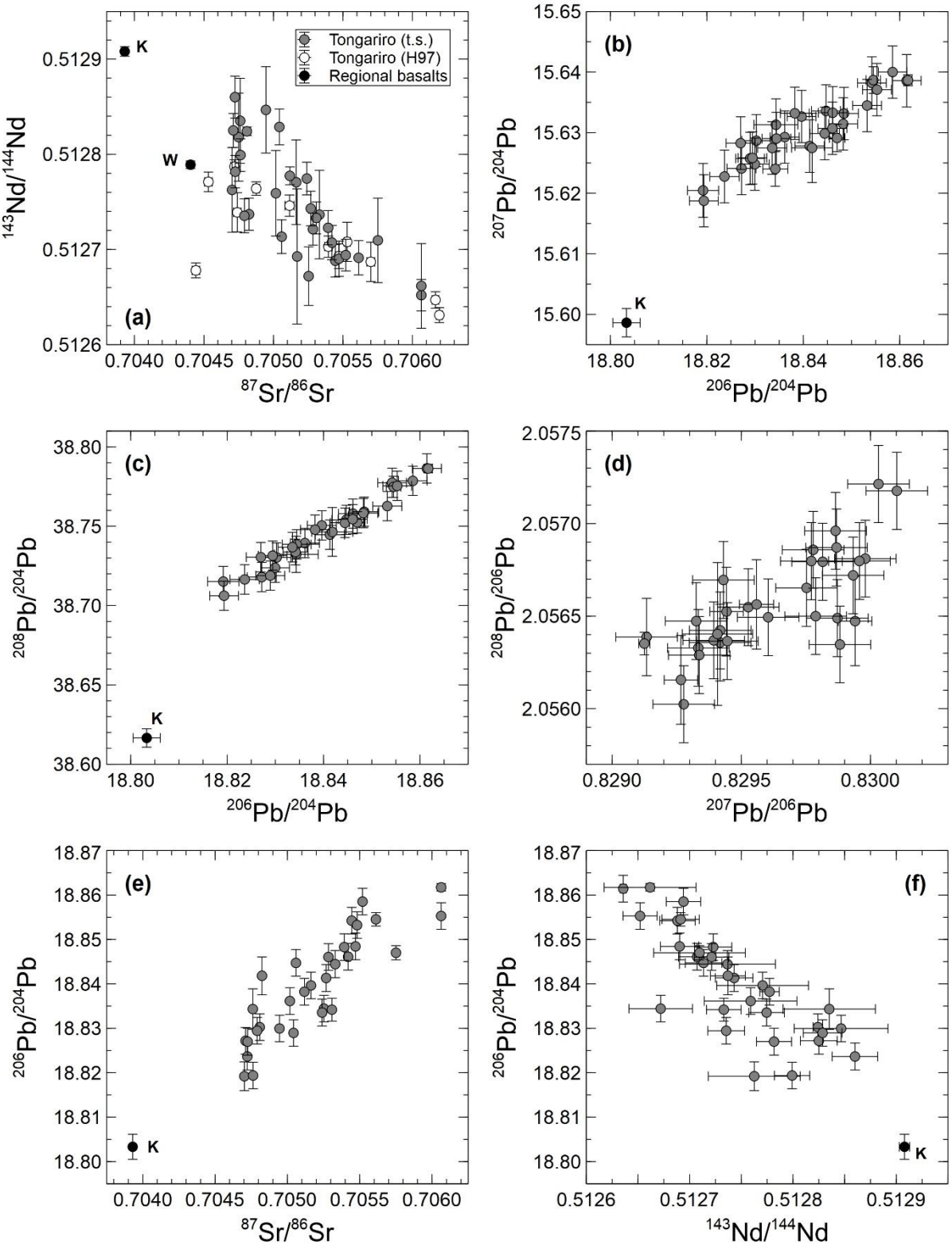

Figure 4.4. Sr-Nd-Pb isotope ratio diagrams from whole-rock Tongariro samples. Comparison data for the Waimarino (W) and Kakuki (K) basalts are shown where appropriate for scales (Gamble et al., 1993, 1996). Whole-rock Tongariro data is from this study ('t.s.': see Appendix 5) and Hobden (1997) ('H97'). Hobden (1997) Pb data is excluded (see section 4.1.1 for details). All errors are quadratically added internal precision (2 s.e.) and external reproducibility (2 s.d.) except for basalt data (internal 2 s.e. only).

4.3.2. Xenolithic materials

This section examines xenolith materials in Tongariro eruptives with a focus on inclusions of metasedimentary origin. These inclusions occur in all Tongariro formations and generally comprise ≤3 vol% of whole-rock samples. Characterising and identifying basement rocks is fundamental to quantifying the amount of crustal material that has been assimilated into Tongariro magmas. All other types of inclusions (magmatic enclaves, andesite lithics and cognate crystal clots) have overlapping compositions with whole-rock samples in major oxide and trace element concentrations and in isotope ratios, and therefore provide limited additional information about magma assembly processes.

4.3.2.1. Petrography

Most inclusions hosted in Tongariro eruptives are metasedimentary in origin and were derived from subjacent metasedimentary basement rocks (Graham, 1987; Graham et al., 1988). Metasedimentary xenoliths are petrographically distinguished from xenocrystic and antecrystic crystal clots, magmatic enclaves and andesite lithics by several features. First, crystals in metasedimentary xenoliths are unzoned whereas all other inclusion types show compositionally zoned crystals. Second, metasedimentary xenoliths are generally elongate with high aspect ratios (>3), which contrasts with the spherical clusters of zoned crystals and porphyritic magmatic enclaves and andesite lithics. Third, metasedimentary xenoliths preserve compositional layering in crystal sizes and mineralogy that contrasts with randomly orientated crystals of varying sizes in porphyritic enclaves and lithics. Petrographic observations are reported for most xenoliths that were analysed geochemically in Table 4.2.

In hand-specimen, metasedimentary xenoliths are represented by several types. Most commonly, they are gneissic or schistose and generally smaller than 1 cm across (Fig. 4.5). Less commonly, xenoliths are larger (to 10 cm long), as noted by Hobden (1997) for Te Pupu Formation (Ngauruhoe) eruptives. In some cases the xenoliths are pure quartz, such as LP063X (Table 4.2; Graham, 1987; Hobden, 1997; Price et al., 2010). On average, quartz-rich xenoliths are more common in eruptives with elevated MgO concentrations such as the Rangitaupahi Member (4.4-5.1 wt%), Pukeonake Formation (7.9-8.9 wt%), Toakakura Member (4.0-4.9 wt%) and the Matariki Member (4.2-5.4 wt% MgO). Quartz-rich xenoliths have also been reported by Hobden (1997) and Price et al. (2010) for Te Pupu Formation (Ngauruhoe) eruptives. However, feldspathic (schistose and gneissic) xenoliths co-occur with quartz-rich xenoliths in the same eruptives. The only exceptions are Pukeonake eruptives for which feldspar-dominated schistose and gneissic xenoliths have not been observed in this study. Some metasedimentary xenoliths

from across Tongariro possess frothy buchitic textures, as previously reported for Te Pupu Formation (Ngauruhoe) eruptives by Graham et al. (1988).

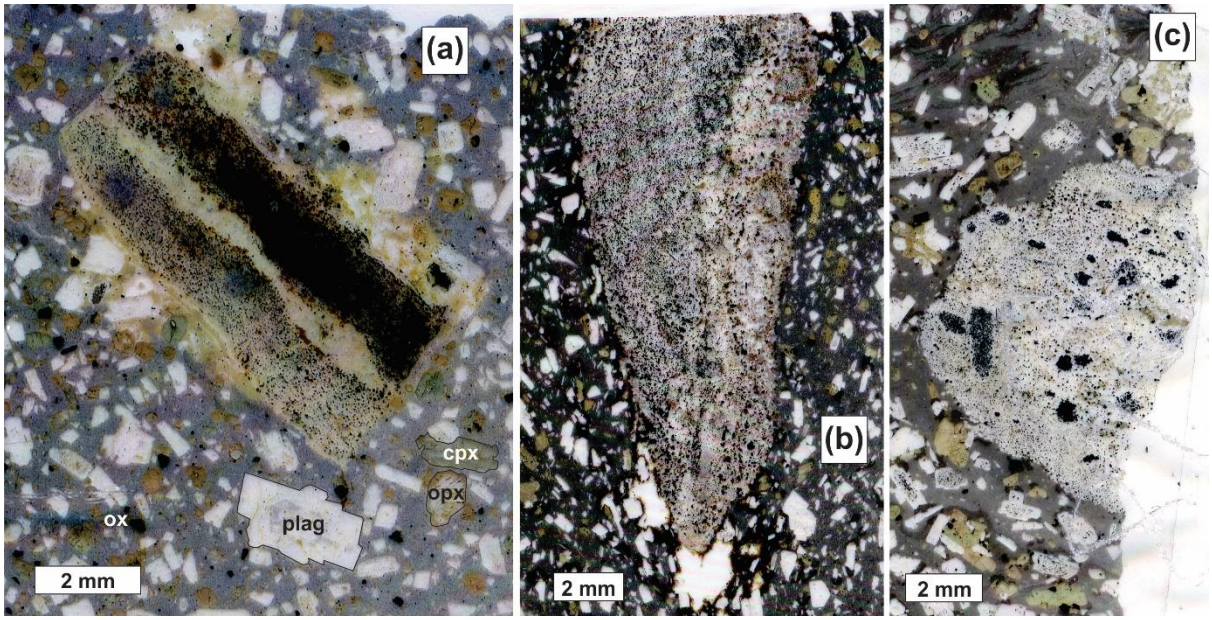

Figure 4.5. Flatbed scanner images from thin sections of metasedimentary xenoliths showing relationships with host lavas. Crystals in the host lavas are commonly clinopyroxene (cpx, green), plagioclase (plag, clear/white), orthopyroxene (opx, brown) and Fe-Ti oxides (ox, black). (**a**) LP034 (Toatoa Member). (**b**) LP022 (Te Porere Member). (**c**) LP018 (Otamangakau Member) (see Chapter 3 for stratigraphic units). Note the clusters of Fe-Ti oxides within the xenolith that commonly (but not always) align with the foliation.

In thin section, metasedimentary xenoliths reveal diverse mineralogies and textures that are summarised in Table 4.2. Internal layering in schistose and gneissic xenoliths occurs in 0.5-1.5 mm bands. Grain sizes range from <40-1500 μm and ~1 mm compositional layering is commonly represented by bands that are ~3-15 crystals thick for typical crystal sizes of 100-600 μm (Fig. 4.6a-b). The average grain sizes (<63-400 μm) of greywacke reference samples for the Kaweka, Pahau and Waipapa terranes reported by Price et al. (2015) are similar to the ranges reported for metasedimentary xenoliths in Table 4.2. However, the schistose and gneissic textures in the metasedimentary xenoliths observed in Tongariro eruptives were probably partially developed during amphibolite facies metamorphism before they were incorporated into magmas.

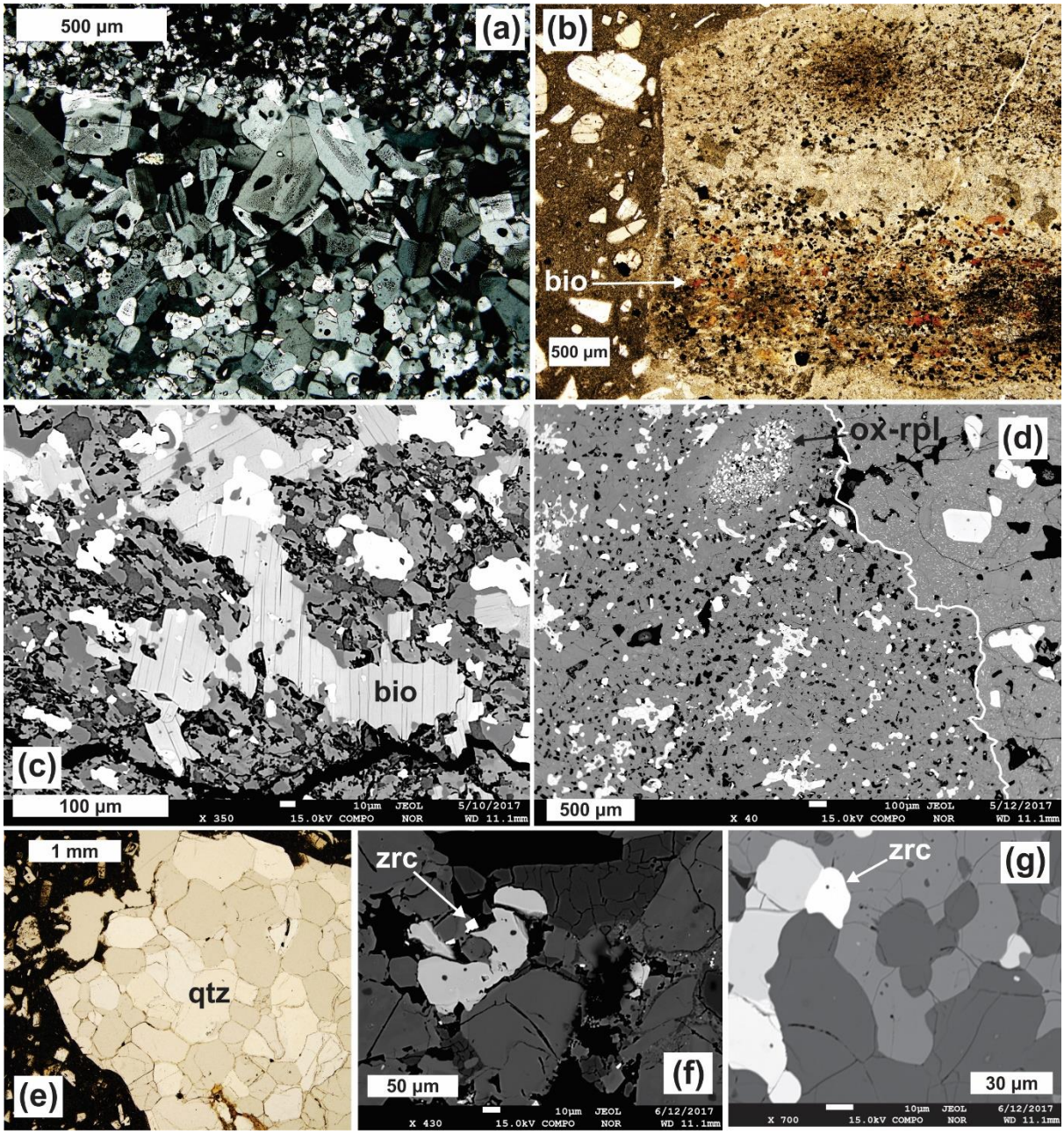

Figure 4.6. Petrographic features of metasedimentary xenoliths. (**a**) Microphotograph in XPL of LP147X (Te Wai Whakaata Member). Note the ~0.5-1.0 mm compositional layering. Contact with host lava is not visible. (**b**) Microphotograph in PPL of LP034 (Toatoa Member: see also Fig. 4.5a). Note the ~0.5-1.0 mm compositional layering and orange xenolith-hosted biotite (bio). The dark patches in the middle layer are grit trapped between the sample and glass slide. (**c**) SEM image of biotite from LP034 (Toatoa Member), which occurs interstitially between feldspars, pyroxenes, Fe-Ti oxides and rarer hercynite. (**d**) SEM image of a metasedimentary xenolith in LP032 (Otamangakau Member). Note the oval-shaped cluster of Fe-Ti oxides (denoted 'ox-rpl': Table 4.2) aligned with the foliation direction. The white line shows the approximate xenolith-host boundary (**e**) A xenolith comprised of quartz (qtz) in LP030 (Otamangakau Member). (**f**) SEM image showing a zircon (zrn) crystal with angular edges (no evidence for dissolution) in LP134X (Te Wai Whakaata Member). (**g**) SEM image showing a zircon crystal with rounded edges that indicate partial dissolution in LP147X (Te Wai Whakaata Member). See Chapter 3 for details of the stratigraphic units.

Xenolith crystal shapes are almost universally equant (aspect ratios of ~1) and have anhedral crystal surfaces that are shared with neighbouring crystals (Fig. 4.6). Grains commonly have slightly rounded edges and less commonly trap selvedges of brown glass between crystal surfaces. This is consistent with studies of textural maturity and surface energy minimisation in metamorphic and igneous systems (e.g. Holness and Siklos, 2000; Holness et al., 2011). Textural maturity and surface energy minimisation are expected to obtain equilibrium within ~1 week for crystal-crystal interstices at scales of ~10-100 μm for typical magma temperatures (Holness and Siklos, 2000). Xenolith crystals with higher aspect ratios indicate less advanced recrystallisation (e.g. Fig. 4.6a-b).

Plagioclase occurs in all metasedimentary xenoliths where it is always the most abundant mineral except for pure-quartz xenoliths (e.g. LP063X: Table 4.2; cf. Graham, 1987; Hobden, 1997; Price et al., 2010). Alkali feldspars occur in some xenoliths but are difficult to identify because most xenoliths have undergone recrystallisation and partial melting (common brown glass selvedges). Fe-Ti oxides also occur universally in feldspathic metasedimentary xenoliths: magnetite always occurs, but ilmenite is also commonly present too. Pyroxene is a common phase in metasedimentary xenoliths and is usually more abundant than Fe-Ti oxides. However, pyroxene grains are more heterogeneously distributed within a given xenolith which contrasts with Fe-Ti oxides that are generally distributed more evenly.

Some xenoliths contain oval-shaped clusters of isotropic minerals (denoted 'ox-rpl' in Table 4.2) that occur at a density of ~50-90 vol% within each cluster and are overall about ≤700 μm across (Fig. 4.6d). These isotropic minerals are magnetite, ilmenite and an unidentified opaque mineral (possibly a spinel) of a distinct shade of grey that differs from magnetite and ilmenite. All of these isotropic minerals occur in varied proportions from cluster to cluster (Figs. 4.5c, 4.6d). Where the aspect ratios of clusters are high, their long axes are generally aligned with the direction of xenolith foliation. These clusters probably represent areas of crystal breakdown and replacement for minerals that contained Fe and Ti, such as garnet, titanite or amphibole.

Less common minerals occur in xenoliths that show considerable textural variety in grain size between layers. Of these, biotite is the most frequently observed phase along with rarer occurrences of zoisite, tourmaline and corundum. One sample, not analysed geochemically (LP034X), possesses well-developed foliation and contains biotite that spatially coincides with hercynite (Al-spinel: Fig. 4.6b-c). Another xenolith (LP234X) that was not analysed geochemically is listed in Table 4.2 for completeness because it contains tourmaline and corundum which have not been identified in other xenoliths.

Two xenoliths examined with SEM imaging (LP134X and LP147X) contain apatite (more abundant: ≤50 μm) and zircon (less abundant: ≤20 μm). Comprehensive searching for apatite and zircon was not undertaken via SEM in other xenoliths but these minerals are probably ubiquitous in all feldspathic metasedimentary xenoliths (e.g. Cawood et al., 1999; Adams et al., 2009; Charlier et al., 2010). Despite this, apatite has not been identified using a petrographic microscope in these two samples or in other xenoliths, which contrasts with larger (≤200 μm) and more obvious phenocrystic apatite observed in thin section for whole-rock samples (Table 3.3). Differences are observed in zircon crystals shapes between LP134X (angular: Fig. 4.6f) and LP147X (rounded: Fig. 4.6g), which reflect different amounts of dissolution.

Graham et al. (1988) report quartz-wollastonite assemblages from Tongariro and interpret them as high-temperature products of calcite vein breakdown. Geochemical data for these xenoliths are shown alongside samples from this study when appropriate for the scales on geochemical plots (Fig. 4.7), but are sometimes absent because some elements were not measured in the previous work (e.g. Cs, some REEs). Geochemical data are also reported for three quartz-dominated (~60-90 vol%) metasedimentary xenoliths by Hobden (1997). They contain (in order of decreasing abundance) minor amounts of wollastonite, calcic plagioclase and diopside. These xenoliths preserve highly radiogenic Sr isotope ratios despite the low proportions of Sr-compatible minerals ($^{87}Sr/^{86}Sr$ = 0.70757 to 0.70817), which indicates that radiogenic isotope signatures can be preserved in refractory xenoliths.

Table 4.2. Petrographic summary for xenoliths analysed geochemically, in addition to LP234X (contains rare minerals and is shown for completeness).

Sample number	Xenolith provenance[1]	Total mass (g)	Phase proportions[2]	Crystal sizes (μm)	Texture[3]	Petrographic features[2]
LP063X	MS	3.5	qtz	200-1200	-	anhedral crystals w/ curvilinear surfaces; uncommon fractures at edges
LP130X	CC	0.4	pl > cpx > opx > ox	200-1500	C	randomly orientated phenocrysts in ball-shaped cluster; no ol or ap
LP134X	MS	11.2	pl > (alb?) > ox > px	<40-300	F	fsps have two populations: pristine vs. partially internally dissolved
LP147X	MS	8.6	pl > alb > ox > px > ox-rpl	50-500	F	crystal sizes in layers vary between 50-200 μm and 100-500 μm
LP155X	MS	7.1	pl > (alb?) > px ~ ox	50-600	F	recrystallisation has reset most previous mineral elongation w/ foliation
LP168X	I?	4.7	original: pl > ox > px	<40-200	G	v. altered; yellow selvedges w/ amorphous mineral(s) that are possibly clays
LP181X	MS	1.6	zst > pl > ox	100-700	G	zst replacing pl which probably occurred before incorporated into magma
LP182X	MS	1.3	n.t.s.	-	-	-
LP186X	MS	1.5	n.t.s.	-	-	-
LP187X	MS	1.4	pl > px > ox > ox-rpl	100-600	G	anhedral crystal surfaces are slightly rounded; ox-rpls have ovular shapes
LP191M	CC	45	n.t.s.	-	-	-
LP193X	L	0.7	pl > opx > cpx	200-800	P	~20 vol% crystals in GM; no ol or ap; sharp contact w/ host material
LP201L	L	19.0	n.t.s.	-	-	-
LP202X	MS	0.3	pl > (alb?) > ox > gls	100-1200	F	gls between anhedral pl crystals that have isometric/equant geometries
LP204X	MS	3.1	pl > (alb?) > ox > px > gls > bio	80-600	F	~1 mm layering; ox-rpl generally coincides with bio; gls MIs in alb
LP205X	MS	0.10	px ~ pl ~ ox	50-200	F	up to ≤1 mm ox-rpls orientated parallel to foliation direction
LP214X	MS	3.0	pl > ox > px	100-500	F	~1 mm layering, ~700 μm ox-rpls; crystals isometric w/ rounded surfaces
LP215X	MS	13.0	pl > alb > ox > px > bio	100-1000	F	~1 mm layering, crystals more rounded on xenolith edges; bio in interior
LP224X	EN	27.5	pl > opx > cpx > ox	150-1200	P	more crystalline GM than host; transitional boundary to host
LP226X	L	1.9	pl > cpx > opx	100-1200	P	similar GM crystallinity to host; boundary w/ host is sharp and subangular
LP233X	MS	0.6	pl > (alb?) > ox > gls > px	100-500	F	~1-2 mm compositional and crystal size layering; 100-400 μm ox-rpls
LP234X	MS	-	pl > alb > px > ox > bio > cdm + tml	100-900	F	layering poorly defined but foliated; px species is opx; trace cdm and tml
LP242X	MS	0.3	pl > (alb?) > px > ox	<40-500	F, G	px generally larger (100-400 μm) than fsp (<40-100 μm)
LP243X	L	1.1	pl > opx > cpx	80-1000	P, G	sharp subangular boundary w/ host; more holocrystalline GM than host
LP245X	MS	0.6	pl > (alb?) > ox > gls > ox	100-500	F	~1 mm layers; generally equant crystals; ≤1.5 mm ox-rpls parallel to foliation
LP247X	EN	5.6	pl ~ px	≤40	G	extremely fine but not glassy: interpreted as quickly quenched melt
TG088X	MS	0.1	n.t.s.	-	-	-

[1] MS = metasedimentary, CC = crystal clot, L = andesite lithic, EN = magmatic enclave, I = meta-igneous with non-arc magma type chemistry.

[2] qtz = quartz, fsp = feldspar, pl = plagioclase, alb = albite, px = pyroxene, opx = orthopyroxene, cpx = clinopyroxene, ox = Fe-Ti oxides, ox-rpl = Fe-Ti oxide replacement of pre-existing mineral, zst = zoisite, bio = biotite, gls = brown glass, cdm = corundum, tml = tourmaline, n.t.s. = no thin section available for this sample, GM = groundmass, ol = olivine, ap = apatite, w/ = with, MI = melt inclusion.

[3] N = none, G = gritty (fine <10 μm pockets of internally dissolved material in minerals that give a dull appearance), C = clustered, F = foliated, P = porphyritic.

4.3.2.2. Major oxides

Most metasedimentary xenoliths have major oxide compositions that are offset from reference data for surficial greywacke materials (Fig. 4.7) (Price et al., 2015). All xenoliths from this study (excepting LP134X) have SiO_2 concentrations below 55 wt% and higher Al_2O_3 and CaO concentrations than in greywacke reference samples (Fig. 4.7b, e) (Price et al., 2015). This observation is consistent with plagioclase-rich mineralogies and recrystallised textures (crystals with equant dimensions) in most xenoliths (Table 4.2) (e.g. Holness et al., 2011). Relative to reference greywacke compositions, TiO_2, Fe_2O_3 and MgO are also elevated in metasedimentary xenoliths, which is consistent with the universal occurrence of Fe-Ti oxides and commonly observed pyroxene in the xenoliths, which probably act as reservoirs that retain these major oxides during partial melting (Table 4.2; Fig. 4.7).

Greywacke reference samples have similar concentrations of Na_2O and P_2O_5 to xenoliths but K_2O is relatively depleted in metasedimentary xenoliths (Fig. 4.7f-h). Similar Na_2O concentrations are consistent with the presence of feldspars in all xenoliths (Tables 4.2, 4.3). Similar P_2O_5 values indicate that phosphates are present, which is consistent with the identification of apatite in both samples that were examined via SEM (LP134X and LP147X). Lower K_2O concentrations in xenoliths relative to greywacke samples suggests that K-bearing phases commonly break down when metasedimentary fragments are assimilated into magmas, which is supported by the less common occurrence of biotite (Table 4.2). Reconnaissance EPMA analyses indicate that the associated pockets of interstitial brown glass contain 1-7 wt% K_2O, compared with only 0-1.5 wt% in bulk metasedimentary xenoliths (Fig. 4.7g).

Whether or not the metasedimentary countryrock beneath Tongariro experienced partial melting or metasomatism before being assimilated into magmas is addressed by the discovery of LP134X (Table 4.3; Figs. 4.5, 4.6). This xenolith sample has 63 wt% SiO_2 and has only minor offsets in other major oxide concentrations relative to greywacke reference samples when compared to other xenoliths (Fig. 4.7). The close overlap between the major oxide concentrations of LP134X and greywacke reference samples provides evidence that negligible partial melting and/or metasomatism of metasedimentary basement rocks occurred before entrainment. Similar conclusions were drawn from examinations of the R623 xenolith from Rubbish Tip Dome (Taupō), which was partially melted, but the associated zircon age spectrum showed that this melting event had to have been of Cretaceous age (Charlier et al., 2010).

Major oxide systematics in metasedimentary xenoliths reported by Hobden (1997) contrast with those of xenoliths reported here. In general, the Hobden (1997) samples have higher SiO_2 and lower concentrations of other major oxides than greywacke reference samples

(Price et al., 2015) and metasedimentary xenoliths from this study. The exceptions are for elevated CaO concentrations and one sample with elevated P_2O_5, consistent with their quartz-wollastonite-plagioclase-diopside mineralogies. These xenoliths probably represent meta-carbonates (i.e. veins of calcite) as implied in other reports of quartz-wollastonite-calcic plagioclase xenoliths in Tongariro eruptives (Graham et al., 1988). Note that all Hobden (1997) xenoliths were collected from the 1975 CE pyroclastic flow erupted from Ngauruhoe, which represents <1 % of Tongariro's lifespan. In contrast, xenoliths analysed in this study were hosted in eruptives with ages that range from the Holocene (e.g. TG088X) to 130-189 ka (e.g. LP233X, LP242X, LP245X).

Table 4.3. Major oxide concentrations in metasedimentary xenoliths.

Oxide	LP134X	LP147X	LP168X	LP181X	LP182X	LP186X	LP187X	LP204X	LP214X	LP215X
SiO_2	63.24	48.17	49.33	49.89	49.40	50.73	49.32	52.06	50.23	49.82
TiO_2	0.36	1.53	1.29	1.57	0.91	0.75	1.33	1.23	1.17	1.06
Al_2O_3	19.61	25.07	19.97	20.15	25.46	15.10	25.35	22.31	26.56	23.94
Fe_2O_3*	3.19	8.92	10.59	10.96	7.80	10.65	7.83	9.23	8.83	8.61
MnO	0.07	0.11	0.19	0.15	0.09	0.22	0.09	0.07	0.12	0.10
MgO	1.04	3.15	2.59	3.74	2.84	5.28	2.17	3.18	2.48	2.77
CaO	6.53	8.86	10.50	7.47	8.39	11.12	9.65	6.48	4.77	8.02
Na_2O	3.90	3.69	2.53	3.78	3.95	2.33	3.43	4.69	3.63	3.81
K_2O	1.18	0.34	0.30	0.79	0.47	1.06	0.37	0.68	1.15	0.73
P_2O_5	0.19	0.23	0.28	0.55	0.24	0.11	0.14	0.25	0.29	0.23
LOI	0.20	-0.34	1.64	-0.35	0.11	2.97	0.71	0.27	1.29	0.23
Total	99.68	100.16	99.32	99.17	99.75	100.39	100.48	100.69	100.64	99.42

Data are raw totals. Where plotted in Fig. 4.7, the data are normalised to 100 % anhydrous totals.

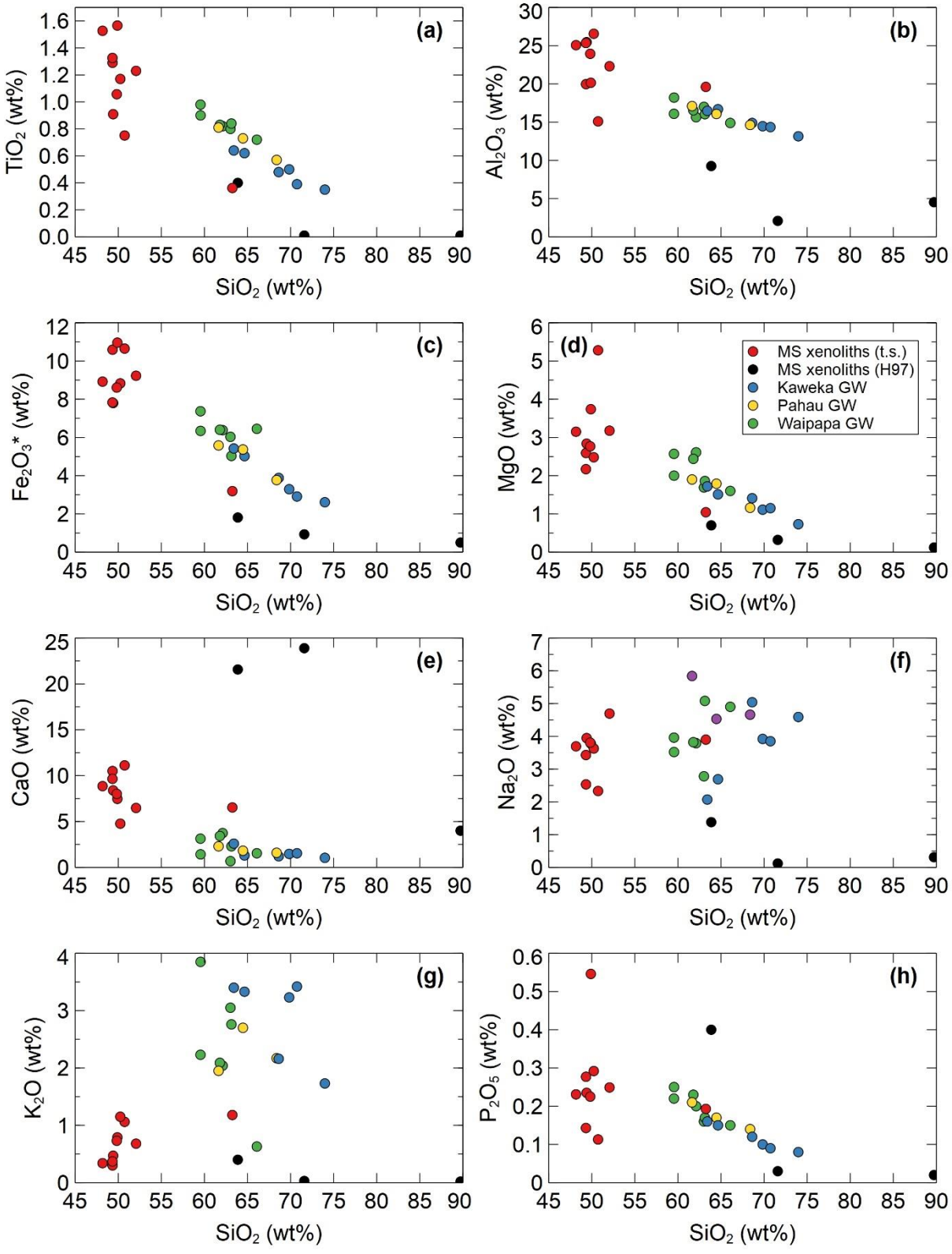

Figure 4.7. Major oxide variation diagrams for metasedimentary (MS) xenoliths from Tongariro: data from this study ('t.s.') (red) and Hobden (1997) ('H97') (black). All H97 MS xenolith samples are from the 1975 CE pyroclastic flow deposits from Ngauruhoe, which are mapped into the Matariki Member (Chapter 3). Reference data for possible correlative basement greywacke (GW) rocks are from Price et al. (2015). Key in panel (**d**) applies to all panels. All oxides are normalised to 100 % anhydrous totals. 2 s.d. uncertainties are approximately contained within symbols (see XRF methods in section 2.4).

4.3.2.3. Trace elements

Trace element systematics in the xenoliths are compared with greywacke reference samples for the Waipapa, Kaweka and Pahau terranes (Price et al., 2015) and three quartzite-wollastonite metasedimentary xenoliths from Tongariro (Hobden, 1997). Comparisons focus on elements that are expected to occur in typical xenolith assemblages (Table 4.2) of plagioclase, alkali feldspar, pyroxene, Fe-Ti oxides and biotite, as indicated by Kd values in Gill (1981), Rollinson (1993), Ersoy and Helvaci (2010) and references therein. These comparisons are organised in order to assess whether parent-daughter fractionation occurred in Sr-Nd-Pb isotope systems, which has the potential to alter bulk xenolith isotope ratios from their protolith values.

Metasedimentary xenoliths have lower Rb (5-38 ppm) and higher Sr (236-880 ppm) concentrations than Rb (24-171 ppm) and Sr (159-723 ppm) in the reference samples (Price et al., 2015) (Fig. 4.8a; Table 4.4). Greater differences between xenolith and greywacke Rb concentrations than for Sr concentrations show that Rb/Sr variations are primarily caused by Rb variation. Almost no overlap occurs between the Rb/Sr ratios of xenoliths (generally <0.1) and greywacke reference samples (generally >0.1-0.8) (Fig. 4.8b-d). Trajectories (arrows) in Rb/Sr versus CaO/Na_2O space indicate how xenolith compositions will be modified when plagioclase or alkali feldspar are dissolved (Fig. 4.8b). Xenolith compositions are offset to lower Rb/Sr (generally <0.1) and higher CaO/Na_2O (~1-5) relative to the reference samples, which more closely follows the trajectory for alkali feldspar loss than plagioclase loss. This is because the extraction of melts derived from alkali-feldspar breakdown will cause overall loss of Na and Rb relative to Ca and Sr, and vice versa for plagioclase breakdown. Despite this, xenolith CaO/Na_2O ratios are generally decoupled from Rb/Sr variation because Rb/Sr ratios are already at their minima (~0-0.1) when CaO/Na_2O ratios increase from ~1 to 5. Comparable decoupling is also observed in Rb/Sr versus Ba systematics (Fig. 4.8c). In contrast with scattered Rb/Sr versus Ba data, Rb/Sr ratios and Cs concentrations are correlated and show continuity between xenolith, greywacke, lava groundmass and lava whole-rock arrays (Fig. 4.8d). Greywacke Rb/Sr ratios (~0.1-0.8) and elevated Cs concentrations of 1.6 to 10.9 ppm (Price et al., 2015) contrast with xenolith Rb/Sr ratios (generally <0.1) and Cs concentrations (generally 0.3 to 1.7 ppm).

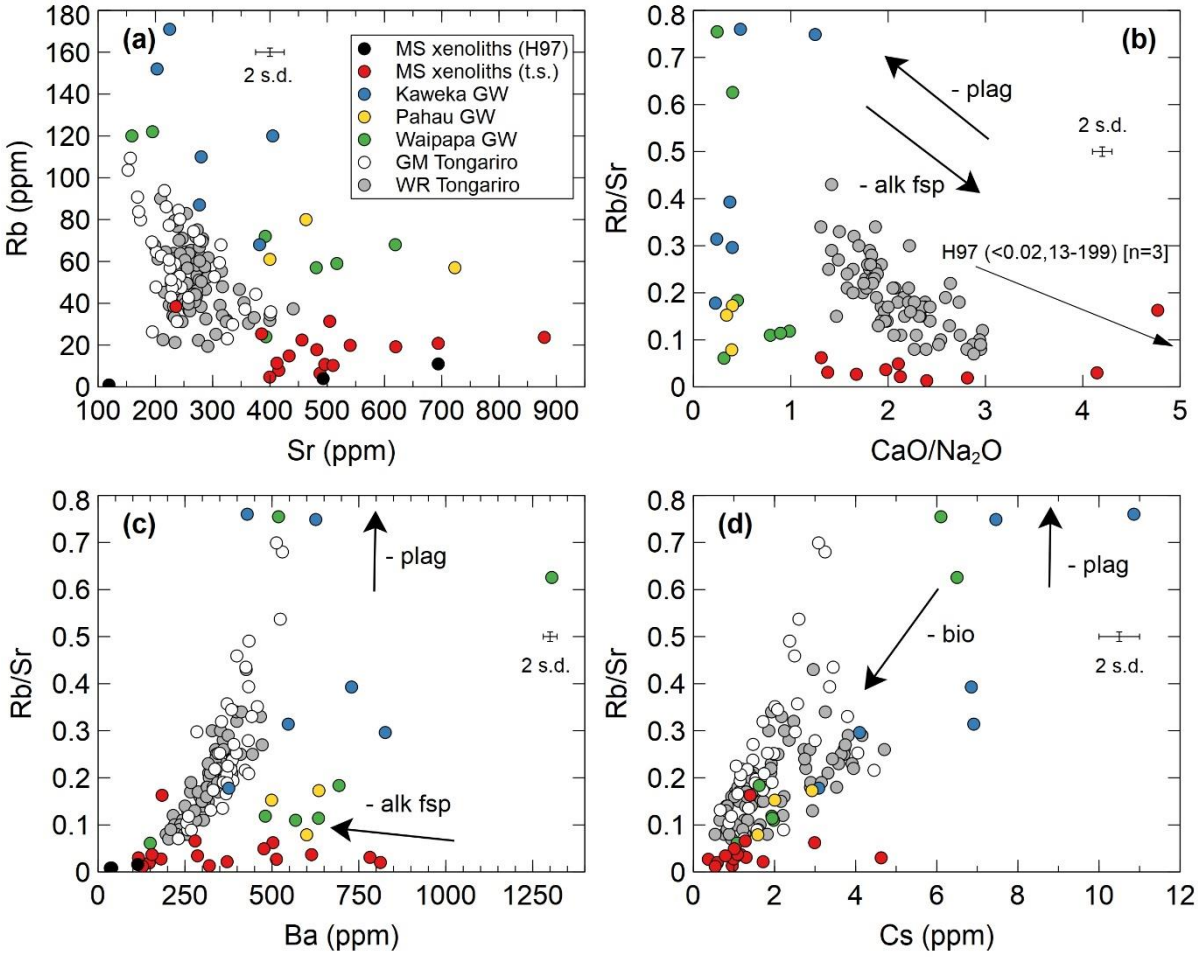

Figure 4.8. Trace element variation diagrams for greywacke (GW) reference samples (Price et al., 2015) and (MS) xenoliths from this study ('t.s.') and Hobden (1997) ('H97'). Tongariro groundmass separates (GM) and whole-rock (WR) samples from this study only. Symbology in (a) is the same for all panels. In (b), three H97 samples have coordinates outside of the CaO/Na_2O axis range. Trajectories show the direction of xenolith compositional change expected for the loss (-) of plagioclase (plag), alkali feldspar (alk fsp) and biotite (bio). Typical 2 s.d. errors are shown (for details see section 2.9 and Table 2.4). WR data in Appendix 5; GM data in Appendix 6.

The concentrations of REEs in metasedimentary xenoliths vary systematically between samples. LREE and HREE concentrations are coupled which increase or decrease simultaneously, maintaining La_N/Yb_N values ~5-15, except for Eu which is relatively invariant regardless of other REE concentrations (Fig. 4.9). LP168X is unusual and is discussed in section 4.3.2.5, below. Covariant REE concentrations are also shown by comparisons of Sm and Nd concentrations that form a single uniform array for all sample types (Fig. 4.10a). Five xenoliths (LP186X, LP187X, LP202X, LP205X and LP242X) have lower Sm (1-3 ppm) and Nd (6-14 ppm) concentrations than the Sm (4-10 ppm) and Nd (17-46 ppm) in greywacke samples (Price et al., 2015), whereas all other xenoliths overlap with greywacke concentrations (Fig. 4.10a; Table 4.4). Four of these five xenoliths plus another xenolith (LP187X, LP202X, LP205X,

LP233X and LP242X), also have strong positive Eu anomalies, as shown by Eu/Eu* values between 1.3-2.3 (Fig. 4.10b; Table 4.4). Arrays defined by Nd concentrations versus Eu/Eu* values form patterns of exponential decrease for xenolith and greywacke samples (Fig. 4.10b). Chondrite-normalised REE plots also show that absolute Eu concentrations are relatively similar (0.8-2.1 ppm) between most metasedimentary xenoliths despite large variations in LREE and HREE (Fig. 4.9; Table 4.4). Together, these features suggest that negative xenolith Eu anomalies in xenoliths develop when other REEs are lost (Fig. 4.10b). However, the process(es) controlling variations in LREE and HREE appear not to affect xenolith Sm/Nd ratios (Table 4.4; Fig. 4.10a). Sm/Nd ratios of xenoliths (0.18-0.28) and greywacke samples (0.16-0.24) overlap and do not correlate with variations in their Eu/Eu* values or P concentrations (Fig. 4.10c-d). These features indicate that phosphate stability and the breakdown of non-feldspar minerals do not affect the REE systematics in xenoliths.

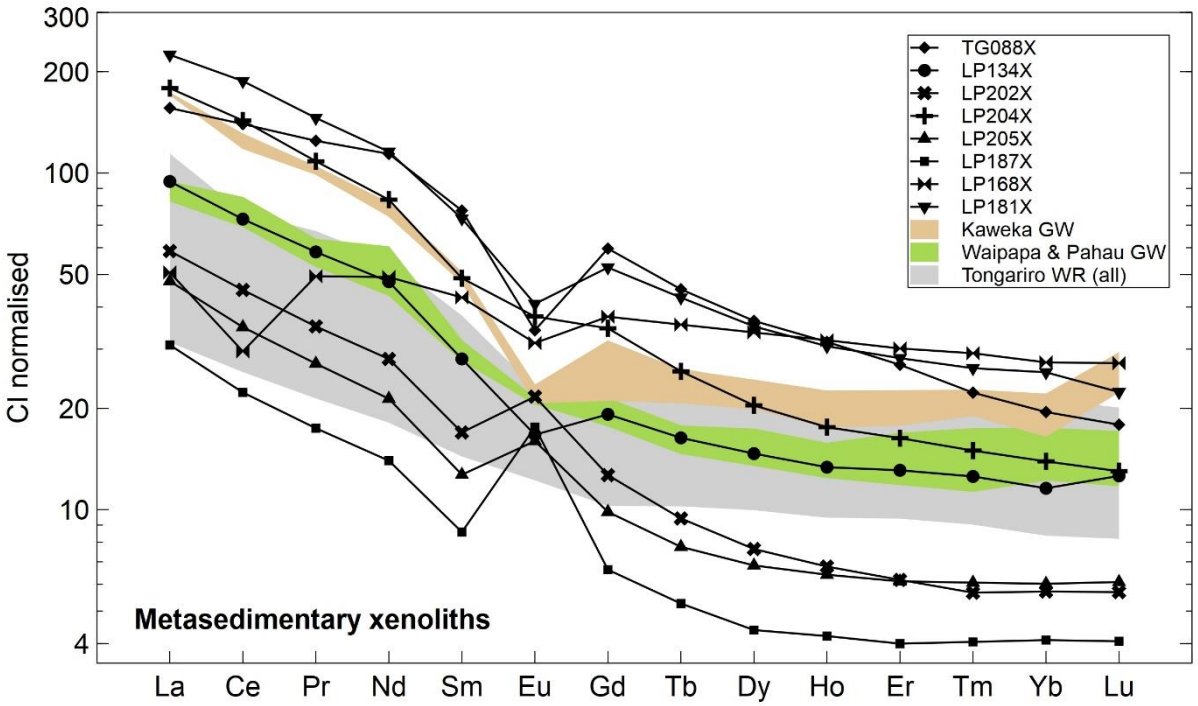

Figure 4.9. Metasedimentary xenolith REE diagram. Concentrations normalised to the CI chondrite values of McDonough and Sun (1995). The Tongariro whole-rock (WR) field is defined from data in this study. Greywacke (GW) reference data are from Price et al. (2015) for the Kaweka, Pahau and Waipapa terranes. Pahau and Waipapa REE concentrations overlap so are not distinguished. One xenolith sample (LP168X) may not be metasedimentary (see section 4.3.2.5) and is the only xenolith sample with a Ce anomaly.

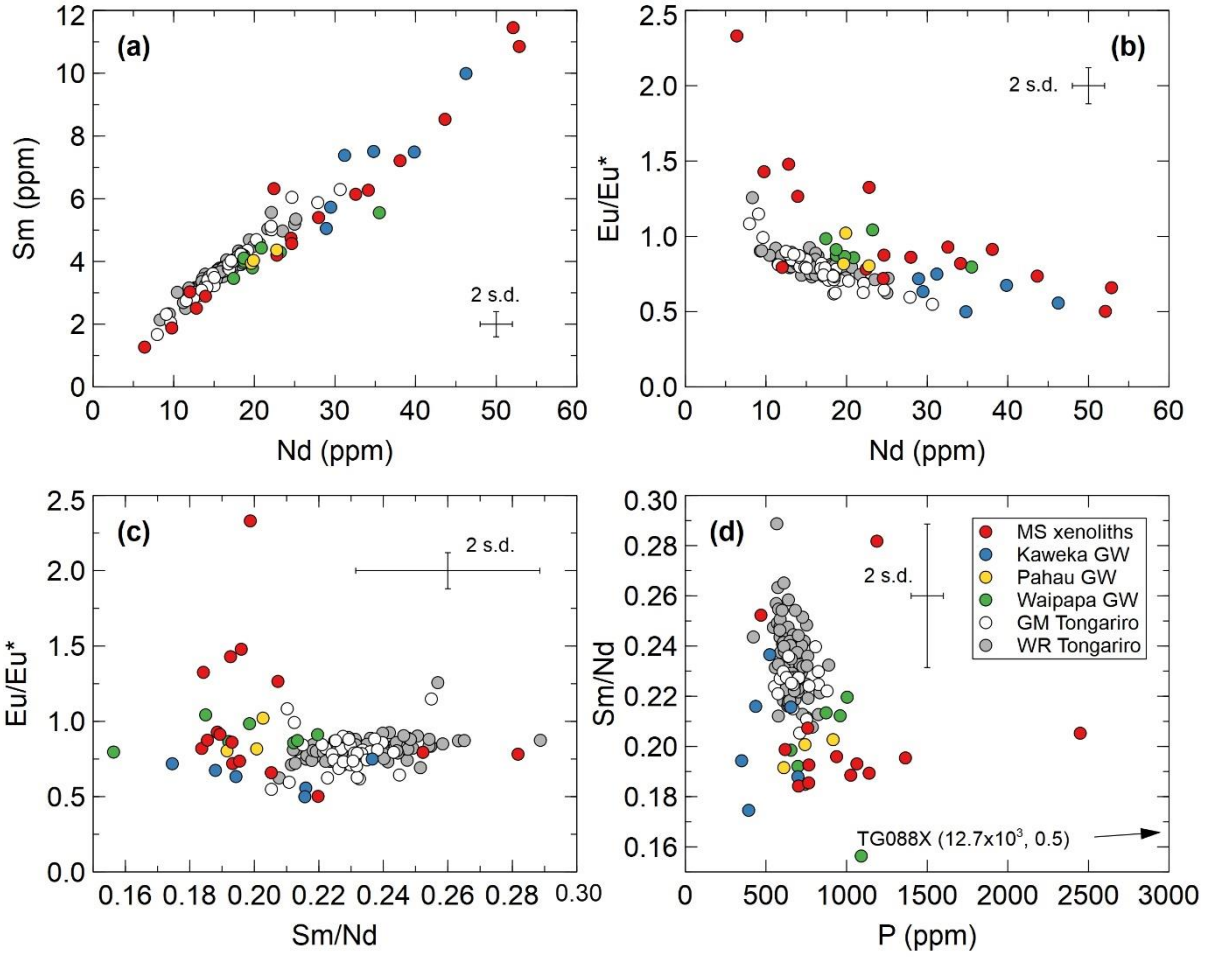

Figure 4.10. Trace element variation diagrams for metasedimentary (MS) xenoliths, greywacke (GW) reference samples and Tongariro groundmass separates (GM) and whole-rock (WR) samples. Symbology in (**d**) is the same for all panels. In (d), one sample (TG088X) has an unusually high P concentration which plots outside of the shown axis range. Greywacke reference data from Price et al. (2015). 2 s.d. errors are approximately 5-11 % of absolute concentrations (section 2.9; Table 2.4). WR data in Appendix 5; GM data in Appendix 6. WR data in Appendix 5; GM data in Appendix 6.

Data for xenoliths, greywacke reference samples, lava groundmass separates and lava whole-rock samples define scattered arrays of increasing U, Th and Pb (Fig. 4.11a-b). Xenolith concentrations of U (0.2-3.0 ppm) and Pb (generally 4.2-19.2 ppm) are generally lower than U (1.4-4.6 ppm) and Pb (13-32 ppm) in greywacke samples (Price et al., 2015) (Table 4.4; Fig. 4.11a). In contrast, Th concentrations in xenoliths (0.2-19.5 ppm) are similar to but more diverse than in greywacke samples (5.6-19.4 ppm). Comparisons between xenolith and greywacke Th/U ratios and Pb concentrations demonstrate this relationship further (Fig. 4.11c). Xenolith Th/U ratios define a vertical array with values generally between ~6 and 17 that occur within a low and narrow range of Pb concentrations (~5-10 ppm). This vertical array is perpendicular to the horizontal array defined by greywacke samples, lava groundmass separates and lava whole-rock samples for Th/U ratios of ~3 to 6 and diverse Pb concentrations (~3-33 ppm). The

orthogonal and offset arrays suggest that processes leading to Th/U and Pb variations in xenoliths are decoupled (Table 4.4; Fig. 4.11c) and that Th/U variations are probably driven by U variations (Fig. 4.11a-b).

Strong correlations are observed between Zr and Hf concentrations in all sample types (Fig. 4.11e). Greywacke reference samples (Price et al., 2015), xenoliths, lava groundmass separates and lava whole-rock samples form a single uniform array with a Hf/Zr slope of ~0.03. Of the samples shown, xenoliths have the lowest concentrations of Zr (26-88 ppm) and Hf (0.9-2.7 ppm) while the greywacke reference samples have the highest concentrations (Zr = 137-260 ppm, Hf = 3.5-8.3 ppm: Price et al., 2015). The concentrations of Zr (99-225 ppm) and Hf (2.5-5.8 ppm) in lava groundmass separates have minimum values that are close to maximum xenolith concentrations, hence forming segmented halves of the same linear trend.

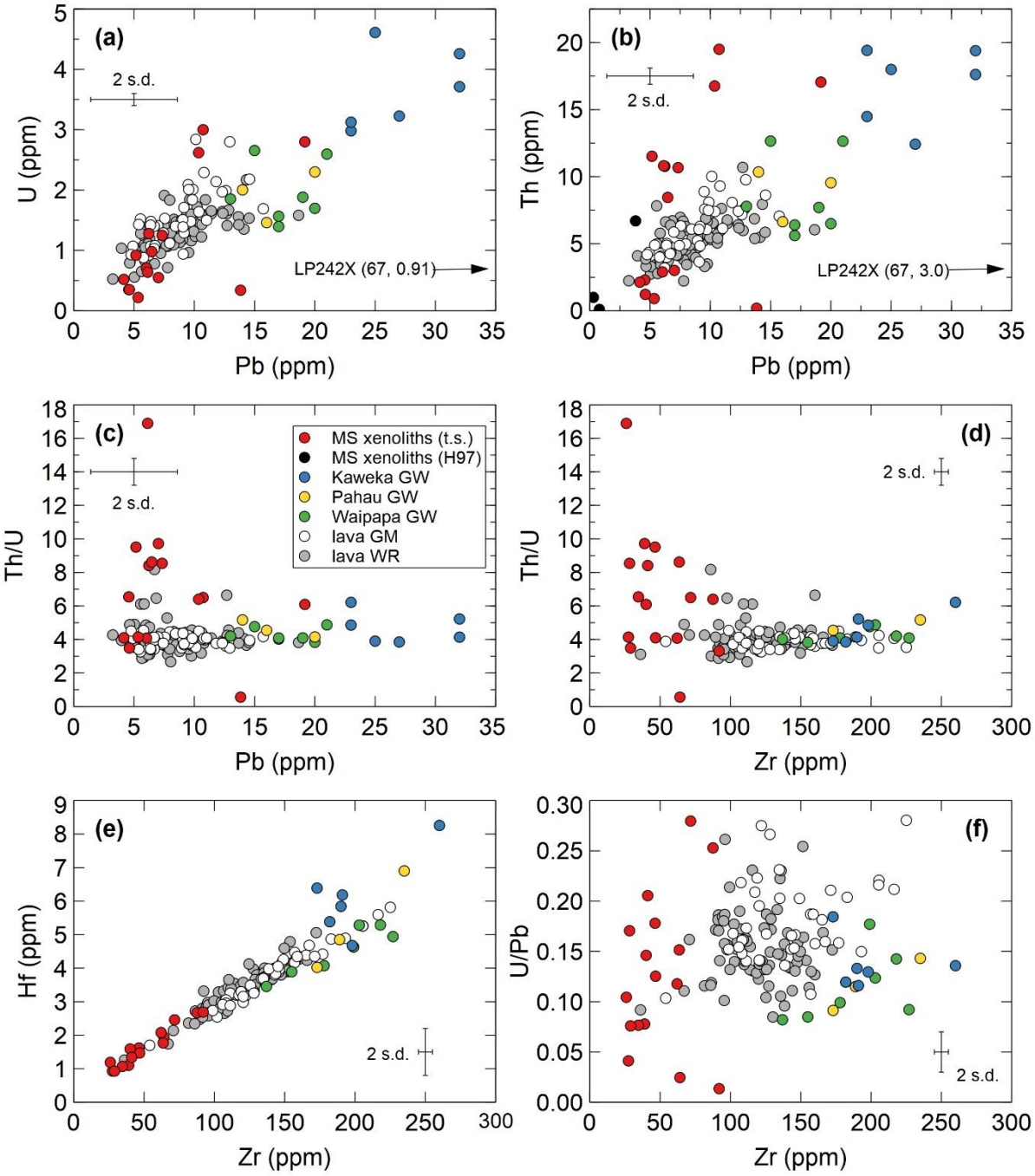

Figure 4.11. Trace element variation diagrams for metasedimentary (MS) xenoliths primarily from this study ('t.s.': red). Greywacke (GW) reference samples from Price et al. (2015). Tongariro lava groundmass separates (GM) and whole-rock (WR) samples from this study. Symbology in (**c**) is the same for all panels. Other MS xenolith data from Hobden (1997) ('H97': black) do not include U and Hf. One sample (LP242X) has an unusually high Pb concentration that plots outside of the shown axis ranges in (a) and (b). WR data in Appendix 5; GM data in Appendix 6.

Table 4.4. Trace element data for metasedimentary xenoliths in Tongariro eruptives.

Element	LP134X	LP147X	LP168X	LP181X	LP182X	LP186X	LP187X	LP202X
Rb	23.7	6.5	20.8	19.9	10.8	38.4	7.9	11.4
Sr	879	488	694	540	496	236	416	412
Y	27.0	20.9	51.2	46.4	22.4	25.8	6.5	10.3
Zr	39.0	46.4	64.1	71.7	28.3	62.1	27.5	34.6
Nb	5.12	19.27	2.37	20.25	10.86	2.59	5.33	5.7
Mo	0.20	0.48	1.50	0.59	0.41	0.74	0.30	0.29
Cd	0.03	0.06	0.11	0.06	0.03	0.14	0.04	0.03
In	0.01	0.03	0.05	0.04	0.02	0.05	0.02	0.02
Sn	0.2	0.4	1.3	1.1	0.8	1.4	0.7	0.6
Cs	0.4	1.0	4.6	1.2	1.7	1.4	0.6	1.0
Ba	513	320	116	614	371	184	147	181
La	24.2	40.0	12.0	53.2	37.6	11.0	7.3	13.9
Ce	49.9	80.5	18.1	115.0	77.5	22.0	13.7	27.6
Pr	5.96	8.81	4.58	13.53	8.83	2.84	1.62	3.25
Nd	24.5	34.1	22.4	52.9	32.6	12.0	6.4	12.8
Sm	4.74	6.27	6.32	10.85	6.14	3.03	1.27	2.51
Eu	1.15	1.71	1.76	2.30	1.82	0.84	0.99	1.22
Gd	4.53	5.75	7.45	10.43	5.82	3.43	1.32	2.52
Tb	0.68	0.78	1.28	1.54	0.77	0.58	0.19	0.34
Dy	4.03	4.21	8.27	8.62	4.12	3.81	1.08	1.88
Ho	0.85	0.80	1.74	1.67	0.78	0.82	0.23	0.37
Er	2.32	2.18	4.82	4.51	2.11	2.37	0.64	0.99
Tm	0.34	0.30	0.72	0.65	0.29	0.38	0.10	0.14
Yb	2.14	1.84	4.41	4.12	1.68	2.44	0.66	0.92
Lu	0.31	0.27	0.67	0.55	0.24	0.39	0.10	0.14
Hf	1.10	1.62	1.94	2.46	0.93	2.08	0.93	1.07
Ta	0.4	1.6	0.2	1.7	1.0	0.3	0.5	0.4
Tl	0.1	0.1	0.1	0.1	0.1	0.2	0.3	0.1
Pb	7.0	5.2	14.0	11.0	7.3	6.0	5.3	4.6
Th	3.01	11.5	0.19	19.5	10.7	2.90	0.91	2.29
U	0.55	0.92	0.34	3.00	1.25	0.71	0.22	0.35
Sc	6.86	22.1	41.8	31.8	13.3	36.9	11.0	12.6
V	53.1	218	312	248	149	322	289	202
Cr	3.15	103	695	102	57.6	154	91.7	55.1
Co	5.53	22.7	46.5	23.1	15.6	31.2	21.3	21.6
Ni	1.91	22.5	99.6	26.2	12.9	20.8	13.7	13.0
Cu	0.7	4.94	133	6.64	6.44	37.9	15.5	6.41
Zn	31.1	160	211	153	135	101	113	179
Ga	21.9	39.3	19.0	26.4	33.1	15.5	31.8	31.7
Sm/Nd	0.193	0.184	0.282	0.205	0.189	0.252	0.199	0.196
Rb/Sr	0.027	0.013	0.030	0.037	0.022	0.163	0.019	0.028
Th/U	5.516	12.539	0.559	6.500	8.536	4.085	4.136	6.543
Eu/Eu*	0.72	0.82	0.78	0.66	0.93	0.79	2.33	1.48
Ce/Ce*	0.98	1.02	0.59	1.04	1.03	0.95	0.96	0.99

Eu/Eu* was calculated as $Eu_N/(sqrt(Sm_N*Gd_N))$; Ce/Ce* was calculated as $Ce_N/(sqrt(La_N*Pr_N))$ after normalisation with the CI chondrite values of McDonough and Sun (1995).

Table 4.4. Continued.

Element	LP204X	LP205X	LP214X	LP215X	LP233X	LP242X	LP245X	TG088X
Rb	19.2	17.8	31.4	22.4	10.3	25.4	14.9	4.7
Sr	620	482	505	456	510	386	434	400
Y	27.2	10.0	38.2	20.9	12.3	16.2	16.6	47.7
Zr	87.6	46.8	40.1	41.2	26.0	92.0	63.6	29.0
Nb	15.52	1.97	16.99	13.41	12.84	6.29	9.2	4.64
Mo	1.50	0.28	0.77	0.76	0.33	2.90	0.43	0.27
Cd	0.05	0.04	0.07	0.04	0.03	0.1	0.04	0.04
In	0.03	0.02	0.01	0.02	0.02	0.04	0.02	0.03
Sn	0.8	0.9	0.9	0.8	0.5	1.6	1.0	0.7
Cs	1.3	1.1	3.0	1.0	0.6	1.3	0.8	0.5
Ba	782	155	503	477	812	279	286	128
La	42.4	11.3	47.4	31.8	24.2	14.4	27.5	37.0
Ce	87.8	21.4	98.0	62.4	50.9	28.2	55.3	85.7
Pr	10.06	2.52	11.50	7.38	6.03	3.49	6.45	11.57
Nd	38.1	9.8	43.7	28.0	22.8	13.9	24.6	52.1
Sm	7.21	1.88	8.53	5.40	4.20	2.89	4.57	11.45
Eu	2.11	0.90	2.02	1.50	1.73	1.22	1.28	1.92
Gd	6.88	1.96	8.21	5.22	3.77	2.99	4.35	11.87
Tb	0.93	0.28	1.15	0.71	0.46	0.45	0.57	1.63
Dy	5.02	1.68	6.40	3.84	2.31	2.80	3.09	8.95
Ho	0.96	0.35	1.27	0.74	0.44	0.59	0.60	1.72
Er	2.61	0.98	3.43	1.99	1.21	1.68	1.63	4.31
Tm	0.37	0.15	0.48	0.27	0.17	0.27	0.23	0.55
Yb	2.24	0.97	2.78	1.65	1.08	1.77	1.44	3.14
Lu	0.32	0.15	0.40	0.24	0.16	0.29	0.22	0.44
Hf	2.67	1.47	1.59	1.34	1.19	2.69	1.77	0.93
Ta	0.9	0.2	1.1	0.9	1.0	0.4	0.7	0.4
Tl	0.1	0.1	0.3	0.1	0.1	0.1	0.1	0.1
Pb	10.0	4.2	19.0	6.2	6.1	67.0	6.5	4.6
Th	16.8	2.13	17.1	10.8	10.8	3.01	8.45	1.22
U	2.62	0.52	2.80	1.28	0.64	0.91	0.98	0.35
Sc	22.5	12	20.4	17.47	13.22	22.9	12.09	23.55
V	195	231	211	191	165	180	174	302
Cr	61.6	61.1	81.7	68.8	52.6	45.3	65.9	114
Co	17.5	23.2	26.3	22.8	16.0	19.1	18.4	27.2
Ni	21.2	31.3	32.8	26.4	13.4	20.4	10.7	17.1
Cu	25.1	29.7	30.7	24.1	7.21	1094	11.3	7.58
Zn	168	99.4	183	164	86.6	134	144	100
Ga	32.6	31.3	37.8	36.9	34.5	19.9	29.4	26.0
Sm/Nd	0.189	0.193	0.195	0.193	0.184	0.207	0.185	0.220
Rb/Sr	0.031	0.037	0.062	0.049	0.020	0.066	0.034	0.012
Th/U	6.40	4.10	6.09	8.41	16.9	3.31	8.62	3.49
Eu/Eu*	0.91	1.43	0.74	0.86	1.33	1.27	0.88	0.50
Ce/Ce*	1.03	0.97	1.02	0.98	1.02	0.96	1.01	1.00

4.3.2.4. Sr-Nd-Pb isotopes

Radiogenic Sr-Nd-Pb isotope ratios are compared with greywacke reference samples from the Waipapa, Kaweka and Pahau terranes (Price et al., 2015) that probably comprise the basement rocks beneath Tongariro. Sr and Nd isotope data are available for three metasedimentary xenoliths from Hobden (1997), which are also shown. However, xenolith Pb isotope data from Hobden (1997) are not considered for the reasons outlined in section 4.2, above.

Metasedimentary xenoliths analysed in this study have $^{87}Sr/^{86}Sr$ ratios ranging from 0.70538 to 0.70851 (Fig. 4.12a; Table 4.5). These values encompass the narrower range of 0.70757 to 0.70817 for metasedimentary xenolith $^{87}Sr/^{86}Sr$ ratios (n = 3) reported by Hobden (1997). Similarly, $^{143}Nd/^{144}Nd$ isotope ratios in xenoliths span the complete range of values observed in greywacke reference samples (Fig. 4.12a). Xenolith $^{143}Nd/^{144}Nd$ ratios determined in this study vary from 0.51243 to 0.51284 and overlap with Kaweka terrane $^{143}Nd/^{144}Nd$ ratios that range from 0.51240 to 0.51248 (Fig. 4.12a; Table 4.5). Less crustal xenolith $^{143}Nd/^{144}Nd$ ratios that are greater than 0.51250 overlap with Waipapa (0.51258-0.51278) and Pahau terrane (0.51269-0.51277) ratios. Xenolith $^{143}Nd/^{144}Nd$ ratios determined by Hobden (1997) range from 0.51240 to 0.51253 and are consistent with the results reported here. Whilst the array defined by xenoliths in $^{87}Sr/^{86}Sr$ versus $^{143}Nd/^{144}Nd$ space overlaps with the fields defined by each greywacke terrane, there is a general offset wherein xenolith $^{87}Sr/^{86}Sr$ ratios are about 0.002 less greywacke data (Fig. 4.12a).

Xenolith $^{207}Pb/^{204}Pb$ ratios range from 15.61 to 15.65 (Table 4.5) and form an array between Kaweka values (15.64-15.65) and less radiogenic Waipapa (15.61-15.63) and Pahau (15.61-15.62) values (Price et al., 2015). Similar relationships exist between xenoliths and greywacke samples for $^{206}Pb/^{204}Pb$, $^{208}Pb/^{204}Pb$ and $^{207}Pb/^{206}Pb$ ratios. Xenolith $^{206}Pb/^{204}Pb$ ratios (18.81-18.89) are more similar to those ratios of Kaweka (18.85-18.96) and Pahau (18.77-18.89) terranes than the Waipapa terrane (18.74-18.84) (Fig. 4.12b; Table 4.5) (Price et al., 2015). Xenolith $^{208}Pb/^{204}Pb$ ratios (38.72-38.83) generally overlap most closely with Kaweka ratios (38.72-38.84), relative to Pahau (38.60-38.79) and Waipapa ratios (38.57-38.75) (Fig. 4.12c; Table 4.5) (Price et al., 2015). Xenolith $^{207}Pb/^{206}Pb$ ratios (generally 0.8288-0.8302) also overlap with values from the Kaweka, Pahau and Waipapa terranes. In contrast, xenolith $^{208}Pb/^{206}Pb$ ratios (generally 2.055-2.058) only overlap with Waipapa (~2.057-2.060) and Pahau ratios (~2.053-2.057 (Fig. 4.12d; Table 4.5) (Price et al., 2015). One outlier in $^{207}Pb/^{206}Pb$-$^{208}Pb/^{206}Pb$ space (LP168X), which has unusually radiogenic isotopic compositions is discussed in section 4.3.2.5.

Table 4.5. Radiogenic Sr-Nd-Pb isotope ratios for metasedimentary xenoliths in Tongariro lavas.

Isotope ratio	LP134X	LP147X	LP168X	LP181X	LP182X	LP186X
$^{87}Sr/^{86}Sr$	0.707199±23	0.706825±23	0.707761±23	0.708062±23	0.707823±23	0.705449±23
$^{143}Nd/^{144}Nd$	0.512748±9	0.512488±9	0.512835±8	0.512470±9	0.512427±10	0.512722±9
$^{206}Pb/^{204}Pb$	18.8303±17	18.8702±33	18.8085±15	18.8855±16	18.8760±30	18.8460±30
$^{207}Pb/^{204}Pb$	15.6285±23	15.6428±45	15.6544±22	15.6531±23	15.6473±44	15.6309±43
$^{208}Pb/^{204}Pb$	38.7396±68	38.7865±97	38.7965±66	38.8305±69	38.8017±94	38.7539±92
$^{207}Pb/^{206}Pb$	0.82997±6	0.82897±12	0.83231±6	0.82885±7	0.82895±12	0.82940±12
$^{208}Pb/^{206}Pb$	2.05730±24	2.05543±21	2.06271±24	2.05610±24	2.05561±22	2.05634±21

Isotope ratio	LP187X	LP202X	LP204X	LP205X	LP214X	LP215X
$^{87}Sr/^{86}Sr$	0.705549±4	0.706155±23	0.706367±23	0.705379±23	0.708505±37	0.705893±23
$^{143}Nd/^{144}Nd$	0.512702±9	0.512559±9	0.512558±9	0.512678±9	0.512431±10	0.512515±8
$^{206}Pb/^{204}Pb$	18.8466±31	18.8522±16	18.8632±15	18.8318±155	18.8615±15	18.8513±30
$^{207}Pb/^{204}Pb$	15.6322±44	15.6325±22	15.6447±22	15.6332±139	15.6468±22	15.6361±43
$^{208}Pb/^{204}Pb$	38.7536±94	38.7546±68	38.8053±67	38.7429±363	38.8067±67	38.7660±92
$^{207}Pb/^{206}Pb$	0.82945±12	0.82921±6	0.82938±6	0.83015±17	0.82956±6	0.82945±12
$^{208}Pb/^{206}Pb$	2.05627±21	2.05571±24	2.05720±24	2.05732±54	2.05745±24	2.05641±21

Isotope ratio	LP233X	LP242X	LP245X	TG088X
$^{87}Sr/^{86}Sr$	0.706794±23	0.706845±23	0.706475±23	0.705629±23
$^{143}Nd/^{144}Nd$	0.512496±9	0.512611±12	0.512528±10	0.512564±9
$^{206}Pb/^{204}Pb$	18.8653±30	18.8448±16	18.8548±30	18.8339±21
$^{207}Pb/^{204}Pb$	15.6405±43	15.6297±22	15.6339±43	15.6180±27
$^{208}Pb/^{204}Pb$	38.7867±92	38.7537±67	38.7668±92	38.7177±80
$^{207}Pb/^{206}Pb$	0.82906±12	0.82939±6	0.82918±12	0.82925±7
$^{208}Pb/^{206}Pb$	2.05598±21	2.05647±24	2.05607±21	2.05574±26

$^{87}Sr/^{86}Sr$ data normalised to NBS987 = 0.710248 after Thirlwall (1991).

$^{143}Nd/^{144}Nd$ data normalised to JNdi-1 = 0.512115 (Tanaka et al., 2000) which is equivalent to La Jolla = 0.511858 after Langmuir and Carlson (1978).

Pb isotope data normalised to NBS981 values of Thirlwall (2000): $^{206}Pb/^{204}Pb$ = 16.9409, $^{207}Pb/^{204}Pb$ = 15.4956, $^{208}Pb/^{204}Pb$ = 36.7228, $^{207}Pb/^{206}Pb$ = 0.91469 and $^{208}Pb/^{206}Pb$ = 2.1677.

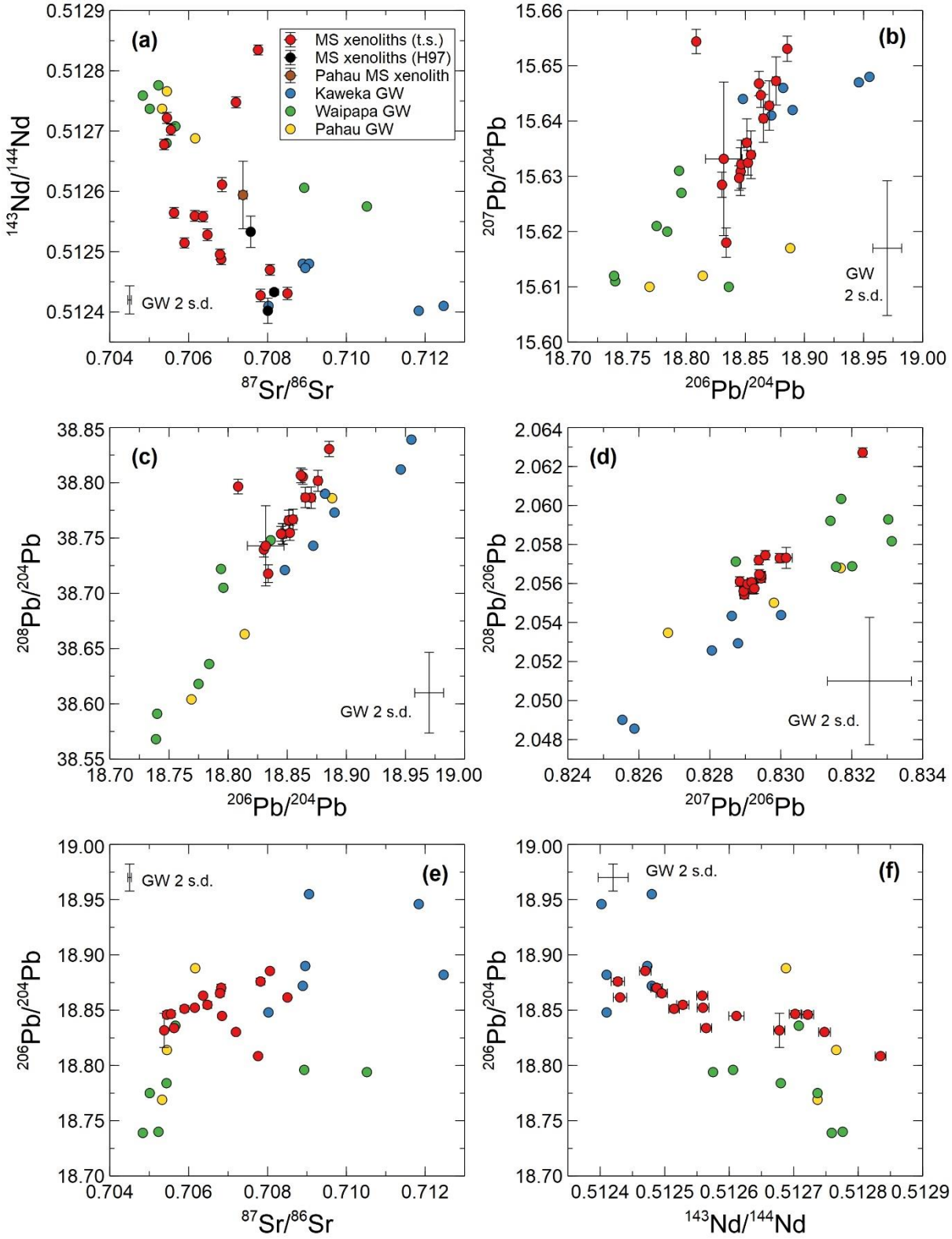

Figure 4.12. Sr-Nd-Pb isotope ratios for metasedimentary (MS) xenoliths. Data from this study (red) are shown with 2 s.d. errors, which are sometimes smaller than the symbols. Greywacke (GW) reference data from Price et al. (2015) for which uncertainties are indicated in panel corners. Symbology as in (**a**) for all panels. Metasedimentary xenolith data are from this study ('t.s.') and Hobden (1997) ('H97'). The Pahau terrane xenolith is sample R623 from Rubbish Tip Dome at Taupō volcano: data from Sutton (1995).

4.3.2.5. Unusual xenolith samples

Three metasedimentary xenolith samples examined in this study (LP063X, LP134X, LP168X) are unusual in their petrographic, major oxide, trace element and/or isotopic characteristics relative to other xenoliths. LP063X is a quartzite metasedimentary xenolith. Insufficient material was available for XRF major oxide analysis but trace elements were analysed by solution ICP-MS and all concentrations were within error of zero. This is consistent with the absence of minerals other than quartz observed petrographically.

LP134X is the potentially the most pristine metasedimentary xenolith as shown by relatively similar major oxide concentrations to greywacke reference samples (Fig. 4.7). SEM images of LP134X also show zircons are well faceted compared with LP147X which contains highly rounded zircons (Fig. 4.6f-g). However, Zr (39 ppm), Hf (1.1 ppm) and Cs (0.4 ppm) concentrations in LP134X are similar to other xenoliths which indicates that processes controlling Zr, Hf and Cs concentrations probably affected LP134X equally to other xenoliths (Fig. 4.11e; Table 4.4). These elements are likely hosted in zircon (Hf, Zr) and biotite (Cs), which would indicate a similar amount of zircon and biotite breakdown to other xenoliths, provided that their starting concentrations were similar. In consideration with petrographic observations and major oxide systematics, LP134X may not accurately reflect its source protolith in absolute element concentrations or in mineralogy.

The third unusual xenolith is LP168X, which is possibly not metasedimentary but is shown alongside other metasedimentary xenoliths for comparative purposes (Tables 4.2-4.5; Figs. 4.7-4.12). Major oxide concentrations in LP168X are similar to these other xenoliths, however the petrographic, trace element and isotopic characteristics of LP168X are distinct. LP168X is fine-grained (<10 μm), lacks compositional layering (Table 4.2) and is comprised of texturally-homogeneous but unidentified material. 'Small' grain sizes could be dissolution zones or represent separate minerals, although they are too small for EPMA analysis because of ~20 μm diameter excitation areas. LP168X is also cut by veinlets of an unidentified fibrous mineral that comprises ~15 vol% of the xenolith. For these reasons bulk analysis by XRF analysis potentially provides representative major oxide concentrations (Table 4.3).

LP168X has a negative Ce anomaly[3] (Ce/Ce* = 0.59), higher HREE concentrations (Fig. 4.9), a very low Th/U ratio of 0.56 (other xenoliths have Th/U = 3.3-16.9) and a deficit of ^{206}Pb relative to other Pb isotopes. The deficit in ^{206}Pb is shown by unusually high $^{207}Pb/^{206}Pb$ (0.8323) and $^{208}Pb/^{206}Pb$ (2.063) ratios which are reflected in a lower $^{206}Pb/^{204}Pb$ ratio

[3] Ce/Ce* was calculated as $Ce_N/(sqrt(La_N*Pr_N))$ after normalisation with the CI chondrite values of McDonough and Sun (1995).

(18.809) relative to other xenoliths (Fig. 4.12c-d; Table 4.5). Cs, Sc, Cr, Co, Ni and Zn are also more concentrated in LP168X relative to other metasedimentary xenoliths by ~10-450 % (Table 4.4). These elements are on average more compatible in amphibole than most other minerals and might indicate a contrasting protolith for LP168X compared with other xenoliths (Rollinson, 1993 and references therein). LP168X has an $^{87}Sr/^{86}Sr$ ratio of 0.707761±23 that is significantly more radiogenic than any whole-rock $^{87}Sr/^{86}Sr$ value reported for a Tongariro lava (max of 0.706165±22: Hobden, 1997). These data indicate that the xenolith is not an andesite lithic, crystal clot or magmatic enclave associated with magmatism at Tongariro, and is more likely a fragment of basement country rock but possibly from a non-metasedimentary protolith. The possible protolithic material(s) of LP168X are discussed further in section 4.4.2.2, below.

4.3.3. Groundmass separates from Tongariro lavas

4.3.3.1. Petrography

Groundmass separates were analysed in this study because they effectively represent melt compositions that can be compared against 'integrated' whole-rock samples, which are combinations of melt and crystal cargoes. Groundmass textures are generally >90 % (micro)crystalline for all analysed samples and were collected in tandem with aliquots prepared for $^{40}Ar/^{39}Ar$ geochronology. Groundmass mineral assemblages consist of feldspar (>95 % plagioclase), Fe-Ti oxides, glass and trace amounts of pyroxene. The negligible concentration of possible phenocryst fragments in groundmass separates is indicated by $^{40}Ar/^{39}Ar$ age determinations that generally yield step heating spectra with well-defined age plateaux (Chapter 3; Appendix 1).

4.3.3.2. Major oxides

Major oxide concentrations were not determined for groundmass separates by XRF although some major element concentrations were determined by ICP-MS on selected samples. Poor calibration curves, high blanks and isobaric interferences for Si, Al, Mg, Ca and K commonly prevented accurate measurements of these major elements by ICP-MS. For similar reasons, Ti, Fe, Mn, Na and P concentrations are only reported for some groundmass samples. These data are reported in comparison with xenoliths (this study; Hobden, 1997), greywacke reference samples (Price et al., 2015) and lava whole-rock samples from Tongariro (this study) in Fig. 4.13.

The compositions of groundmass separates have similar relationships to xenoliths, greywacke samples and lava whole-rock samples for most major oxides (Fig. 4.13). In general, groundmass concentrations of TiO_2, Fe_2O_3*, MnO and P_2O_5 are similar to greywacke samples

but are lower than in xenoliths, except for the three xenoliths of Hobden (1997). Na_2O in groundmass, greywacke reference samples (Price et al., 2015), xenoliths and whole-rock samples are similar, generally clustered around ~3 wt%. TiO_2. Fe_2O_3*, MnO and P_2O_5 systematics suggest that if partial melts are derived from assimilated greywacke, they are generally retained in the magmatic melt phase (i.e. groundmass). Groundmass concentrations of TiO_2, Na_2O, MnO and P_2O_5 are similar to whole-rock concentrations, which indicates that these elements are not separated from Tongariro magmas by crystal fractionation processes at the compositional range of analysis. In contrast, Fe_2O_3* concentrations are greater in whole-rock samples (4.6-9.0 wt%) than in groundmass separates (3.6-5.5 wt%), which likely reflects the sequestration of Fe into pyroxene and Fe-Ti oxide phenocrysts in whole-rock samples (Fig. 4.13c).

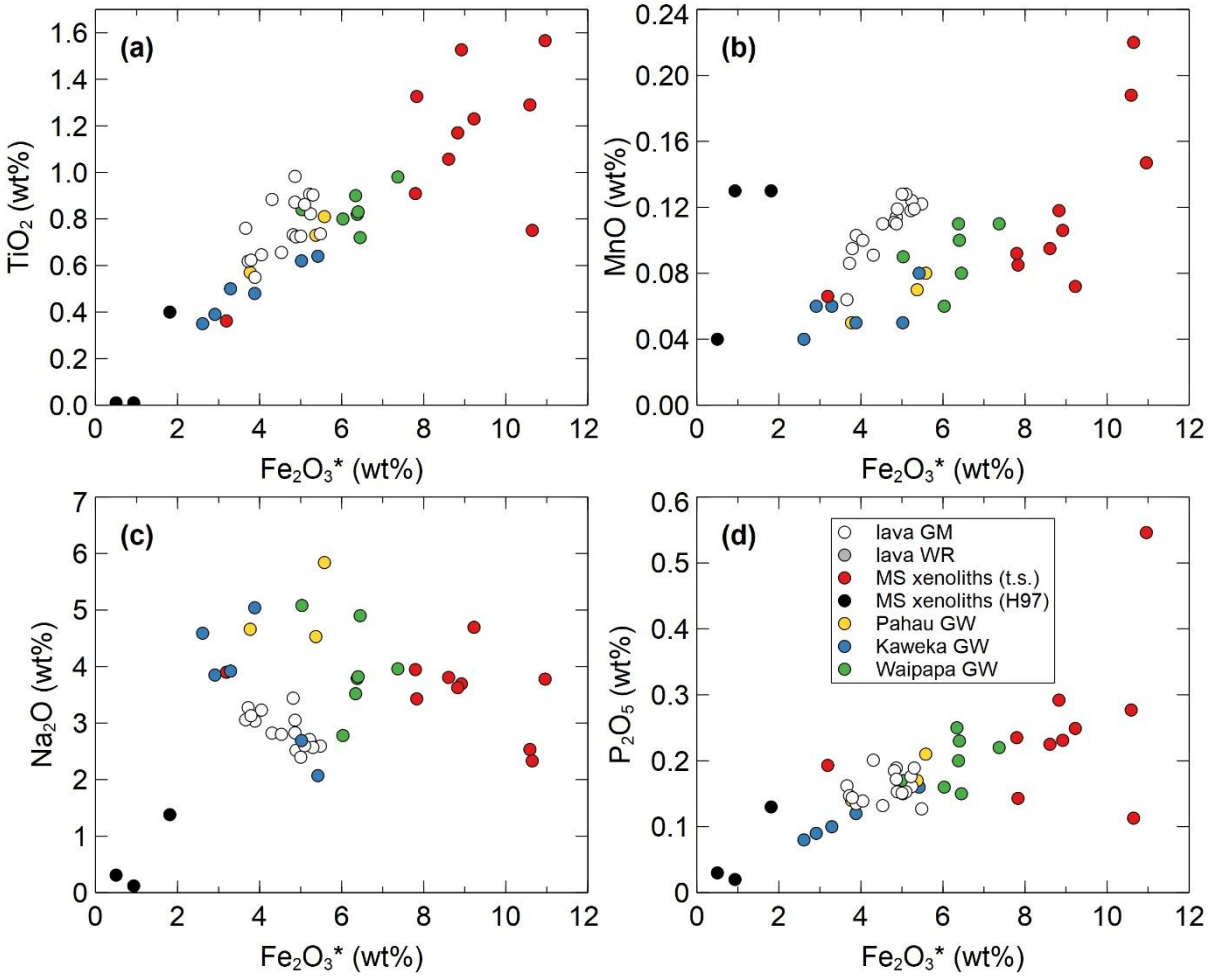

Figure 4.13. Major oxide variation diagrams from lava groundmass (GM) separates and whole-rock (WR) samples. Data from metasedimentary (MS) xenoliths from this study ('t.s.') and Hobden (1997) ('H97') are shown for comparison alongside greywacke (GW) reference data from Price et al. (2015). Key in (**d**) applies to all panels. Major oxides are plotted against Fe_2O_3* in each diagram because SiO_2 data is unavailable for groundmass separates and, in its absence, Fe_2O_3* is alternative proxy for magma evolution (e.g. Fig. 4.1c), wherein Fe_2O_3* concentrations decrease as magmas evolve. WR data in Appendix 5; GM data in Appendix 6.

4.3.3.3. Trace elements

Some trace element data for groundmass separates were presented and discussed above in section 4.3.2 because they provide important context for xenoliths (Figs. 4.6, 4.8 and 4.9). These groundmass trace element data are reported again here for completeness. First, total trace element arrays for groundmass and whole-rock are compared, then second, paired groundmass and whole-rock data from the same samples are compared.

The total data arrays for groundmass separates overlap with whole-rock samples (not paired samples) for most incompatible trace elements: Ba (~200-500 ppm) and Cs (~0.3-4.3 ppm: Fig. 4.8c-d), Sm (~2-6 ppm) and Nd (~7-31 ppm: Fig. 4.10a), and Pb (~3-19 ppm), U (~0.5-2.5 ppm), Th (~2-11 ppm), Zr (~25-200 ppm) and Hf (~1-5 ppm) (Fig. 4.11). Rb/Sr ratios are on average 0.2 higher in groundmass than whole-rock samples, although this is influenced by absolute Sr concentrations that are greater in whole-rock samples (Fig. 4.8). REE concentrations and Eu anomalies are similar and show strong overlap between groundmass and whole-rock samples (Fig. 4.14). However, groundmass separates possess stronger (negative) Ce/Ce* in samples with higher REE concentrations (e.g. LP051GM: Fig. 4.14). Groundmass separates also have more diverse REE concentrations than whole-rock samples, to both lower and higher concentrations (Fig. 4.14).

Paired groundmass separates and whole-rock compositions show significant differences in incompatible and compatible element concentrations. In general, groundmass samples have similar or slightly greater (by 8-17 % on average) REE concentrations (Fig. 4.14). On average, whole-rock concentrations of Sr are 13 % greater, whereas Rb, Cs and Ba are 20-31 % lower. High field strength elements (HFSEs: Zr, Nb, Hf, Ta, Th and U) are also 28-51 % more concentrated in the groundmass. These features show that elemental partitioning between phenocrysts and groundmass in Tongariro magmas is consistent with predictions from Kd values. Some of the observed whole-rock versus groundmass differences may reflect a 'diluting' influence of the phenocryst cargo in whole-rock samples. Groundmass separates with lower REE concentrations than whole-rock values correspond to samples that contain either hornblende (LP113) or abundant (~5 vol%) pseudomorphs after amphibole (LP109) (Fig. 4.14). These samples also have low K_2O (~1 wt%) for their relative to other Tongariro andesites (section 4.3.1.2; Fig. 4.1g). The groundmass separates for samples LP113GM and LP109GM do not contain hornblende or pseudomorphs after amphibole and have lower HREE concentrations than their whole-rock equivalents, which suggests that phenocrystic amphibole in whole-rock samples probably has elevated HREE concentrations.

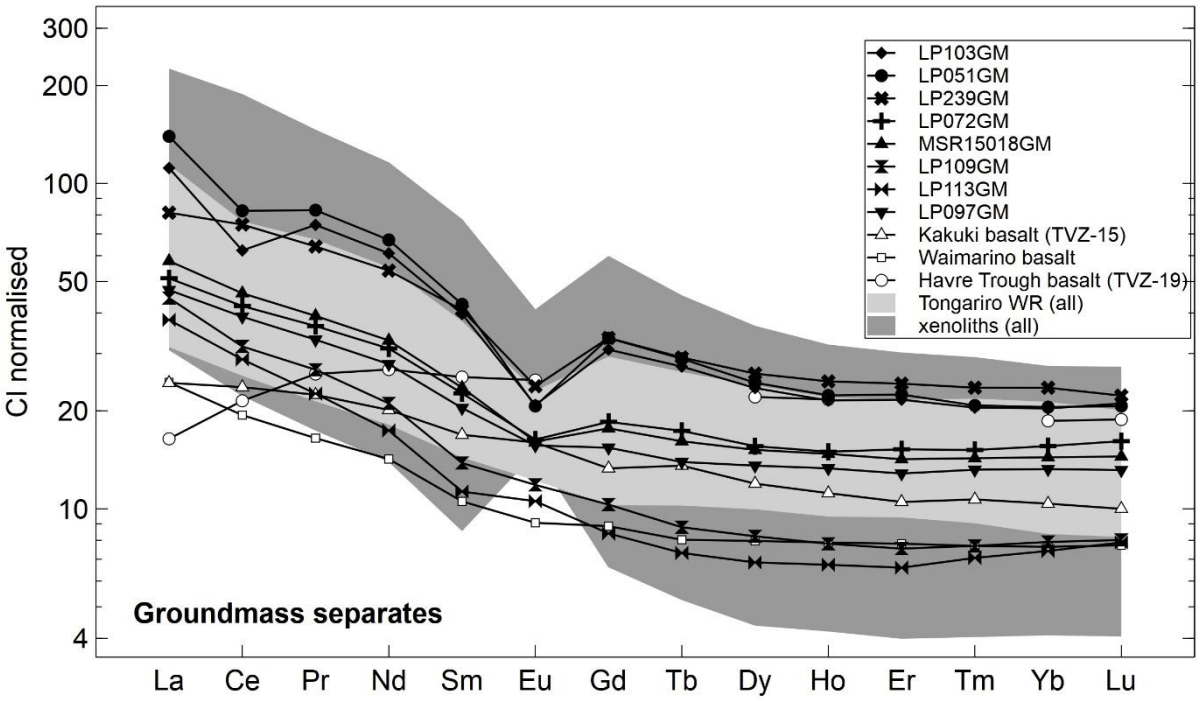

Figure 4.14. Lava groundmass REE concentrations normalised to the CI chondrite values of McDonough and Sun (1995). Light and dark grey fields show the total variation in lava whole-rock samples and metasedimentary xenoliths. Basalt reference samples are from Gamble et al. (1996) for Havre Trough, Barker et al. (2015) for Waimarino and Waight et al. (2017) for Kakuki. Note the negative Ce anomalies of LP051GM and LP103GM, which also occur (but are less pronounced) in whole-rock samples LP051 and LP103. WR data in Appendix 5; GM data in Appendix 6.

4.3.3.4. Sr-Nd-Pb isotopes

Radiogenic Sr-Nd-Pb isotope ratios in groundmass separates are similar to whole-rock values for the same samples, but with small differences (Fig. 4.15). Strong correlations are observed between whole-rock and groundmass isotope ratios for $^{87}Sr/^{86}Sr$ (Fig. 4.15a) and $^{143}Nd/^{144}Nd$ ratios (Fig. 4.15b) whereas Pb isotope ratios show features of general increase ($^{206}Pb/^{204}Pb$: Fig. 4.15c), or scatter ($^{207}Pb/^{204}Pb$: Fig. 4.15d), or both ($^{208}Pb/^{204}Pb$ and $^{208}Pb/^{206}Pb$: Fig. 4.15e-f). Groundmass and whole-rock $^{87}Sr/^{86}Sr$ ratios are approximately equal for the total diversity of whole-rock values (0.7047-0.7061). Offsets between groundmass and whole-rock $^{87}Sr/^{86}Sr$ ratios are at most 0.0004. The regression slope (thick line in Fig. 4.15a) suggests that groundmass and whole-rock $^{87}Sr/^{86}Sr$ ratios are approximately equal for high values (0.7060) whereas whole-rock samples are on average more radiogenic by 0.0001 than groundmass separates in less radiogenic samples ($^{87}Sr/^{86}Sr = 0.7045$), which implies either contamination with radiogenic crystal cargos or contamination with non-radiogenic melts.

Similar to Sr isotope systematics (Fig. 4.15a), paired groundmass and whole-rock $^{143}Nd/^{144}Nd$ ratios are within analytical error for effectively the entire range of Nd isotope ratios observed in Tongariro whole-rock samples (0.51264-0.51286: Fig. 4.15b). Note, however, that

the sample regression and equal-value lines have distinctly different slopes and intersect at 0.51276. The divergence suggests potential differences between average isotope ratios in groundmass versus whole-rock samples. $^{143}Nd/^{144}Nd$ ratios above 0.51276 are primarily typified by less crustal groundmass separates than their whole-rock counterparts by 0.00002. This contrasts with more crustal $^{143}Nd/^{144}Nd$ ratios in groundmass than whole-rock ratios by 0.00004 for $^{143}Nd/^{144}Nd$ below 0.51276. This is consistent with Sr isotope systematics wherein groundmass separates have less crustal $^{87}Sr/^{86}Sr$ ratios than their whole-rock counterparts in less radiogenic samples (Fig. 4.15a).

Pb isotope ratios in groundmass separates and their whole-rock counterparts form scattered arrays (Fig. 4.15c-f) which differ from Sr and Nd isotope systematics. Groundmass and whole-rock Pb isotope ratios are similar and are commonly within error of equal-value lines. Differences between groundmass and whole-rock Pb isotope are up to ~0.01 ($^{206}Pb/^{204}Pb$, $^{207}Pb/^{204}Pb$), ~0.03 ($^{208}Pb/^{204}Pb$) and ~0.001 ($^{208}Pb/^{206}Pb$). Unlike the Sr and Nd isotope systems (Fig. 4.16a, e-f), groundmass and whole-rock Pb isotope ratios overlap with Pb isotope ratios in metasedimentary xenoliths (Fig. 4.16b-d).

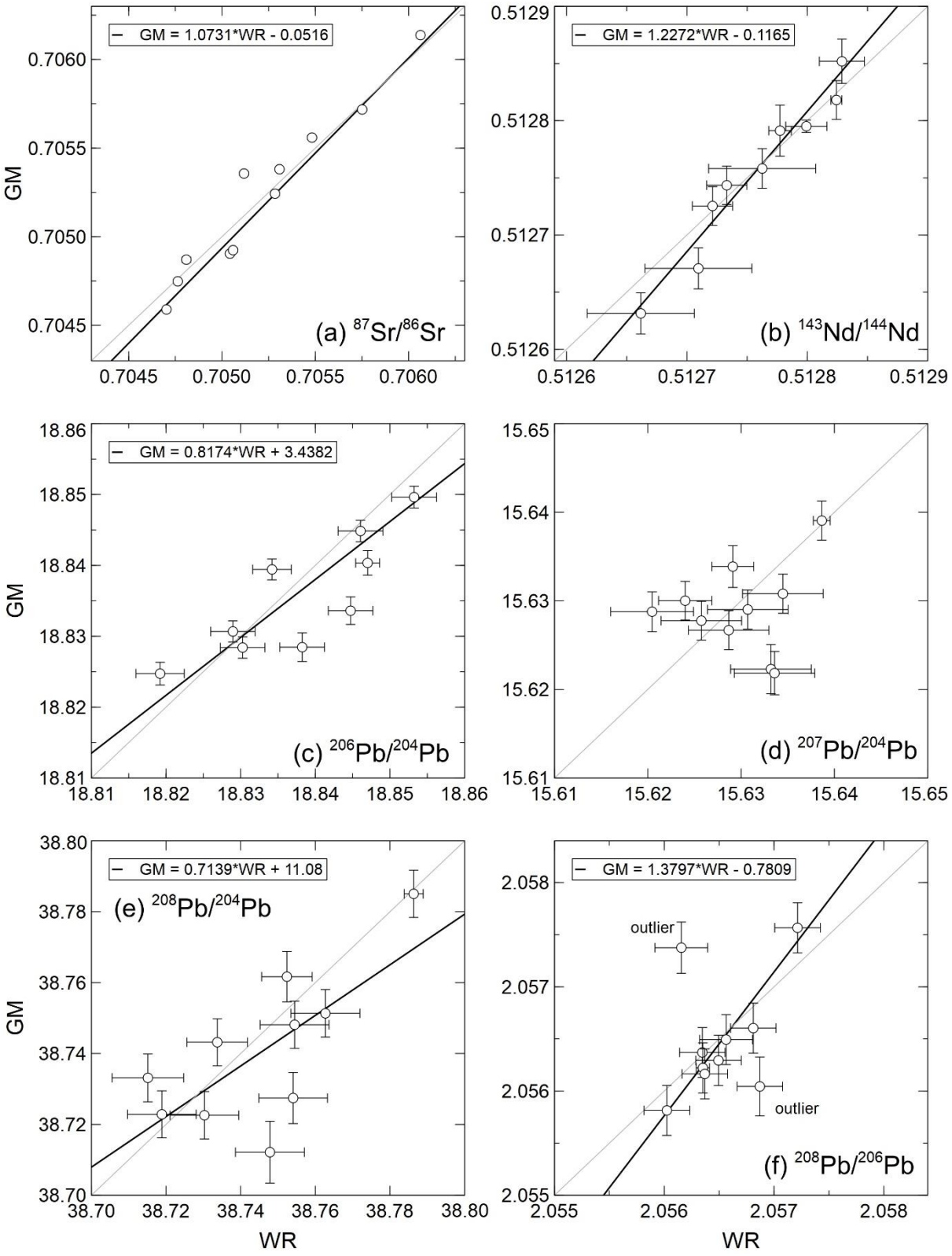

Figure 4.15. Radiogenic Sr-Nd-Pb isotope ratio comparisons between lava groundmass (GM: full data in Appendix 6) separates (vertical axes) and whole-rock (WR: full data in Appendix 5) samples (horizontal axes). GM samples were selected for analysis based on WR values that spanned the full range of Tongariro Sr and Nd isotope ratios. Thin grey lines reflect equal values. Dark lines reflect linear best fit lines with equations shown in each panel. Two outliers are excluded from the $^{208}Pb/^{206}Pb$ regression in (**f**) and are annotated. Error-bars show quadratically added internal (2 s.e.) and external (2 s.d.) uncertainties.

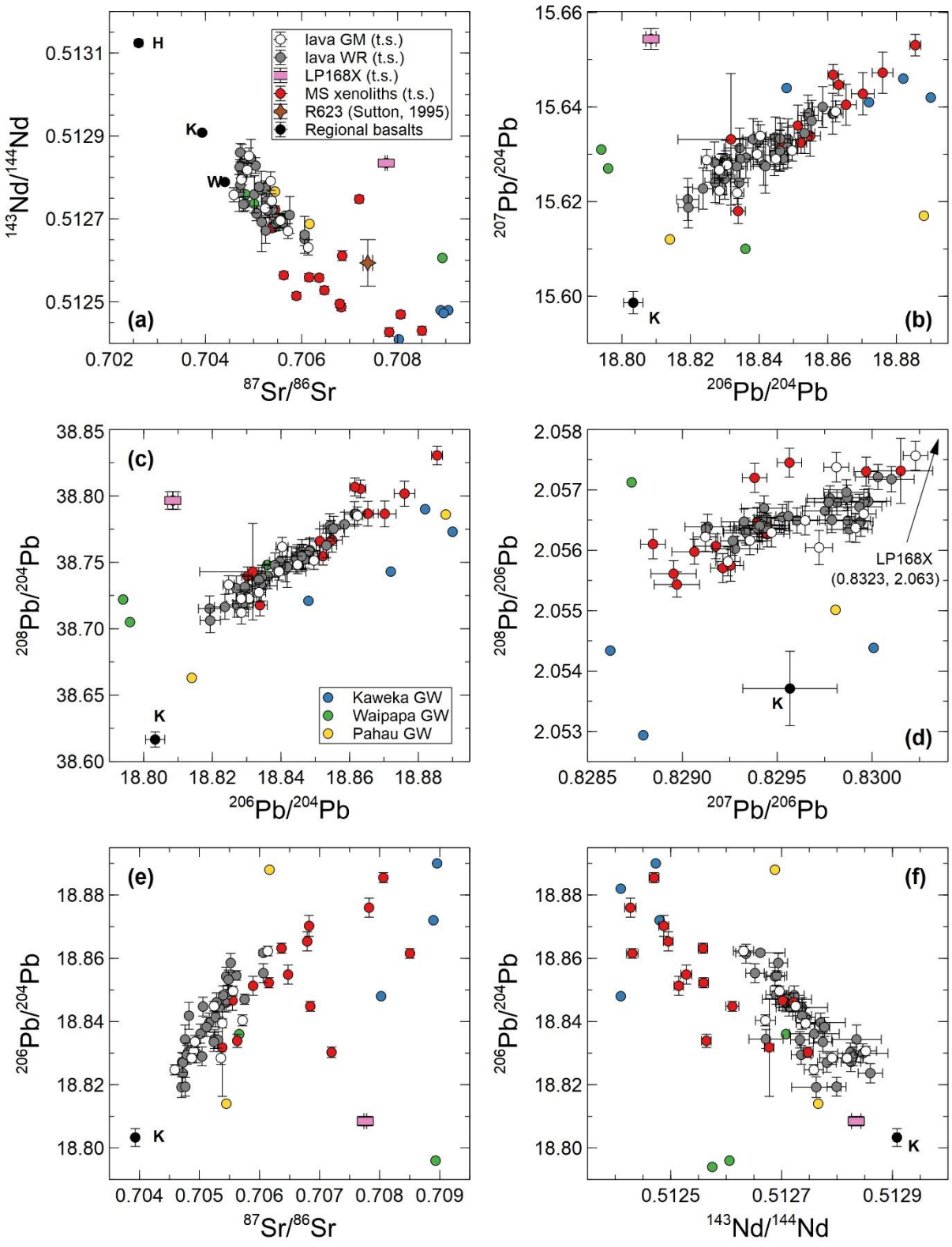

Figure 4.16. Sr-Nd-Pb isotope ratio diagrams for lava groundmass (GM) separates, lava whole-rock (WR) samples, metasedimentary (MS) xenoliths and regional basalts. Havre Trough (H), Kakuki (K) and Waimarino (W) basalt data from Gamble et al. (1993, 1996). Key for all panels is split between (**a**) and (**c**). Error-bars show quadratically added internal (2 s.e.) and external (2 s.d.) uncertainties except for the published basalt data (internal 2 s.d. precision only). Greywacke (GW) data from Price et al. (2015): see Fig. 4.12 for GW uncertainties. R623 data Sutton (1995) which is Pahau terrane (Charlier et al., 2010).

4.4. DISCUSSION

4.4.1. Crystallisation, differentiation and fractionation

The joint consideration of whole-rock major oxide and trace element systematics and petrographic observations indicates which minerals have crystallised and fractionated from Tongariro magmas. Following inferences drawn in section 4.3.1 and summarised in Table 4.1, the crystallising minerals in Tongariro eruptives were predominantly plagioclase, orthopyroxene and clinopyroxene ± olivine and Fe-Ti oxides. A distinction is emphasised between crystallising phases versus fractionating phases, which are similar but occur in different proportions. Despite the predominance of plagioclase as the most common phenocryst phase in Tongariro eruptives (Table 3.3), geochemical data indicate that a greater mass of pyroxene than plagioclase has fractionated from Tongariro magmas (Fig. 4.2). Geochemical data relevant to interpreting the order of crystallisation and crystal fractionation are presented in their anticipated evolutionary order, as follows.

Olivine was probably the dominant crystallising phase in basaltic magmas that replenished Tongariro's magma system, but these primitive magmas are not well represented at the surface. Of the basalt reference data shown (Gamble et al., 1993, 1996; Barker et al., 2015; Waight et al., 2017), Waimarino basalt is a plausible choice of primitive end-member for Tongariro eruptives because it has REE concentrations that are consistently lower than in Tongariro samples (Fig. 4.3). In contrast, relatively high MREE concentrations in the Havre Trough basalt suggest that it is probably dissimilar to the primitive magmas feeding Tongariro's magma system. The Kakuki basalt has slightly higher but similar REE concentrations to the Waimarino basalt, and which are similar to the lowest REE concentrations observed for Tongariro samples (e.g. LP109: Fig. 4.5a). Therefore, Kakuki basalt may also be compositionally similar to the primitive magmas that recharge Tongariro's magma system.

Basaltic-andesites are the least evolved magma types represented by Tongariro eruptives (Fig. 4.1). They have significantly lower Ni concentrations (~10-50 ppm: Fig. 4.2) than regional basalts (~100-350 ppm: e.g. Gamble et al., 1993) which indicates that olivine was the most abundant fractionating mineral in the initial stages of magma evolution, as implied by Kd values in Gill (1981), Rollinson (1993) and references therein (e.g. Table 4.1).

For basaltic-andesite and andesite magmas, geochemical data indicate that clinopyroxene and orthopyroxene were fractionated in greater proportions than plagioclase (Fig. 4.2). Ni-MgO relationships indicate that pyroxene fractionation occurred from 8 to 7 wt% MgO (Fig. 4.2a). As MgO concentrations further decrease from ~7 to 2 wt%, Sc concentrations decrease from ~35 to 15 ppm, which is consistent with continued pyroxene fractionation (Fig. 4.2b). In contrast,

increases in Rb/Sr ratios (primarily driven by plagioclase fractionation) from ~0.1 to 0.4 are observed at CaO/Al_2O_3 ratios of <0.55 that equate to an MgO concentration of ~7 wt% or less, therefore indicating that plagioclase fractionation began after pyroxene fractionation (Fig. 4.2c-d). Given that MgO versus CaO/Al_2O_3 arrays cannot be explained by plagioclase-dominated crystal fractionation (Fig. 4.2d), and that olivine is not a dominant fractionating phase below ~8 wt% MgO (Table 4.1), it is most likely that Mg-bearing orthopyroxene and clinopyroxene comprise a greater mass proportion of fractionating mineral cargoes in Tongariro magmas. Therefore, for modelling purposes, fractionating proportions of plagioclase (~30 wt%), orthopyroxene (~35 wt%) and clinopyroxene (~35 wt%) are adopted to represent magma evolution from basaltic-andesites to dacites. Non-systematic variations in Rb/Sr ratios occur as SiO_2 increases from ~53 to 65 wt%, which probably reflects the recycling of (high-Sr) plagioclase antecrysts during magma evolution which may contain variable melt-inclusion cargoes (Fig. 4.2e). This interpretation is consistent with scattered Eu/Eu* versus Rb/Sr ratios that indicate simultaneous magma mixing, the recycling of plagioclase crystals and country rock assimilation during magma evolution (Fig. 4.2f).

Increasing scatter in P_2O_5 concentrations between ~0.1 and 0.2 wt% is observed as SiO_2 concentrations increase above ~59 wt%, which indicates apatite fractionation and accumulation (e.g. Fig. 4.1). Some high-silica andesites and dacites possess subtle negative Ce anomalies in whole-rock samples but these are more pronounced in groundmass separates (Figs. 4.3, 4.15), also consistent with apatite fractionation (Rollinson, 1993 and references therein). Recycling or inefficient fractionation of apatite is shown petrographically by the occurrence of apatite-pyroxene and apatite-pyroxene-plagioclase crystal clots in some eruptive units (Table 3.3). For modelling purposes, apatite fractionation in more evolved Tongariro magmas is estimated to occur at proportions of ≤0.5 wt% of the overall fractionating assemblage. In contrast, Zr and Hf systematics between metasedimentary xenoliths, greywacke reference samples (Price et al., 2015), lava groundmass separates and lava whole-rock samples, as described above (Fig. 4.11e; section 4.3.2.3) provide strong evidence that zircon has not crystallised in Tongariro magmas, as also indicated by the lack of petrographic evidence of zircon.

Apatite crystallisation and fractionation from Tongariro magmas, without zircon crystallisation, shows that interstitial dacitic and rhyolitic melts in Tongariro andesites do not fractionate and probably remain too hot for zircon crystallisation for their Zr concentrations of 99-225 ppm (Fig. 4.11e). The model of Watson and Harrison (1983) predicts that for the most silicic melt inclusion analysed in this study (~74 wt% SiO_2: Appendix 5) zircon will not crystallise in Tongariro magmas if temperatures exceed 735-805 °C, which they do almost universally

according to estimates of 800-1220 °C by Hobden (1997) and Arpa et al. (2017). Lee and Bachmann (2014) suggested that P_2O_5-Zr-SiO_2 systematics like those in Tongariro andesites (Figs. 4.1h, 4.11e) arise from fractional crystallisation, partially because rhyolite-basalt mixing cannot produce P_2O_5-Zr-SiO_2 relationships commonly observed in andesites globally. However, this model assumes that rhyolitic interstitial melt in andesite magmas efficiently separates during differentiation, which may not be the case for andesite-dominated volcanoes (e.g. Reubi and Blundy, 2009). The absence of rhyodacitic and rhyolitic eruptives at Tongariro (this study; Hobden, 1997), despite the ubiquitous occurrence of dacitic-rhyolitic melt inclusions (Appendix 8), indicates that crystal-melt separation during differentiation has been consistently ineffective over Tongariro's lifespan.

Comparisons between Sr-Nd-Pb isotope ratios from lava groundmass and whole-rock pairs indicate a relatively consistent balance between fractional crystallisation and assimilation in most Tongariro magmas (section 4.3.3.4). Highly systematic variation between whole-rock and groundmass $^{87}Sr/^{86}Sr$ and $^{143}Nd/^{144}Nd$ ratios indicates that crystal cargoes in whole-rock samples have approximately identical isotope ratios to their interstitial melts (i.e. groundmass). Given that the percentages of crystals in separate whole-rock samples strongly overlap between ~25-50 vol% (Table 3.3), Sr and Nd isotopic differences between each whole-rock and groundmass pair cannot be solely attributed to processes of crystal loss or gain. Groundmass and whole-rock Sr and Nd concentrations for the same samples (n = 35) show that Sr concentrations are on average (± 2 s.d.) greater by 13 ± 20 % (-34 ppm to +113 ppm total range) in whole-rock samples whereas Nd concentrations are on average (± 2 s.d.) greater by 13 ± 20 % (-0.8 ppm to +6.5 ppm total range) in groundmass separates. The opposing preferences for Sr in crystals (i.e. plagioclase) versus Nd in melts appears to have a limited effect on the overall array of covariant Sr and Nd isotope ratios in groundmass and whole-rock pairs (Fig. 4.15). The data indicate that the addition of country rock into magmas and the extraction of phenocrysts occurs at relatively balanced rates for all Tongariro magmas, which is likely reinforced by repeated mixing between evolved and replenishing magmas which encourages homogeneity in isotopic evolutionary trends (Fig. 4.15, 4.16).

4.4.2. Crustal lithologies

4.4.2.1. Metasedimentary basement

The basement rocks beneath Tongariro are represented as xenolithic inclusions in Tongariro eruptives. Whilst these inclusions include andesite lithics, magmatic enclaves and cognate crystal clots, only metasedimentary xenoliths demonstrably represent fragments of pre-existing country

rock that is non-magmatic. Following the distinctions drawn between inclusion types in section 4.3.2.1, above, this subsection examines the relationship between metasedimentary xenoliths and their specific metasedimentary protoliths. Sr-Nd-Pb isotope ratios and trace element data indicate that metasedimentary xenoliths in Tongariro magmas represent at least two greywacke terranes. One of these is the Kaweka terrane; the other(s) may be the Pahau or Waipapa terrane (or both). Before xenolith provenance can be established, it is necessary to determine whether measured xenolith Sr-Nd-Pb isotope compositions reflect their metasedimentary protoliths, or whether incongruent mineral dissolution has modified bulk xenolith isotope ratios (e.g. Knesel and Davidson, 1996, 1999).

4.4.2.1.1. Relationships between isotope ratios in xenoliths versus protoliths

4.4.2.1.1.1. Strontium

For Sr isotopes, evidence for biotite and alkali feldspar breakdown indicates that radiogenic ingrowths of ^{87}Sr (contained mainly in Rb-bearing host minerals) were potentially lost into partial melts then mixed into surrounding magma. The variation in xenolith Ba concentrations versus Rb/Sr ratios is similar to the trajectory for alkali feldspar loss (Fig. 4.8c). These features are consistent with the initial loss of high Rb/Sr minerals that was followed by alkali feldspar breakdown. This interpretation is supported by variable proportions of alkali feldspar in metasedimentary xenoliths (Table 4.2) and Al_2O_3-CaO-Na_2O-K_2O versus SiO_2 systematics that imply the loss of K-bearing minerals whereas Al-Ca-Na-bearing minerals do not break down, as indicated by higher Al-Ca-Na concentrations in xenoliths than greywacke references samples (Fig. 4.7; Price et al., 2015). This relationship can be simply explained by mass balance following mineral breakdown and melt extraction wherein Al-Ca-Na-bearing phases are preferentially retained (Fig. 4.1). The offset between Cs concentrations in greywacke and xenolith arrays matches the trajectory for biotite breakdown which is a viable mechanism for explaining differences in Cs concentrations and Rb/Sr ratios (Fig. 4.8d) (e.g. partition coefficients in Rollinson, 1993 and references therein). Biotite breakdown is also indicated by low percentages (≤5 vol%) of biotite in xenoliths (Table 4.2) and lower K_2O concentrations in xenoliths (0.3-1.2 wt%) relative to greywacke samples (0.6-3.8 wt%) (Fig. 4.7g). It is likely that biotite dissolution primarily controls xenolith Rb/Sr ratios and Cs concentrations whereas alkali feldspar dissolution controls Ba concentrations but is generally less advanced.

Given that xenolith Rb/Sr ratios have been modified relative to their protoliths, it is expected that Sr isotope ratios in xenoliths will not exactly reflect their original values prior to incorporation into magmas. This prediction fits with the observed offset between xenolith

$^{87}Sr/^{86}Sr$ ratios (-0.002) relative to more radiogenic Waipapa, Kaweka and Pahau greywacke samples (Fig. 4.12a) (Price et al., 2015). Biotite possibly composed ~25 vol% or more of some xenoliths before any dissolution occurred, as indicated by contrasting Cs concentrations that are ~2-5 times lower in xenoliths than greywacke samples (Fig. 4.8d) and the surviving modal abundances of biotite in some xenoliths (~5 vol%: Table 4.2) (cf. 45 vol% biotite in R623 xenolith at Taupō: Sutton, 1995; Charlier et al., 2010). Radiogenic ingrowth of ^{87}Sr in biotite from 200 to 100 Ma, which is when the Waipapa, Kaweka and Pahau terranes were accreted, is likely to develop $^{87}Sr/^{86}Sr$ ratios of ~0.716-0.728 for 300 ppm Rb and 100 ppm Sr in biotite with an initial $^{87}Sr/^{86}Sr$ ratio of 0.705. (Rb and Sr concentrations are approximated from mass balance considerations of the R623 xenolith.) Mass balance mixing with 25 % of this biotite added to Tongariro metasedimentary xenoliths will increase xenolith $^{87}Sr/^{86}Sr$ ratios by 0.0007-0.0014 on average. If the modal proportions of biotite in xenoliths were initially greater (up to ~45 %), then xenolith $^{87}Sr/^{86}Sr$ ratios will increase by 0.003 when restored. These values are comparable to the general $^{87}Sr/^{86}Sr$ ratio offset of 0.002 observed between xenolith and greywacke reference samples (Fig. 4.12a). Alkali feldspar breakdown may have also contributed to shifts in bulk xenolith $^{87}Sr/^{86}Sr$ ratios, but this effect has not been quantified because trace element systematics indicate that alkali feldspar breakdown was more varied and less advanced than for biotite, as discussed above (Fig. 4.8). Therefore, original bulk xenolith $^{87}Sr/^{86}Sr$ ratios were probably more radiogenic before they were incorporated into magmas.

The quartz-wollastonite xenoliths reported by Hobden (1997) have elevated radiogenic $^{87}Sr/^{86}Sr$ ratios of 0.70757-0.70817 but may represent metamorphosed quartz and calcite veins, as implied by other xenolith studies from Tongariro (Graham et al., 1988). An alternative but less likely explanation is that these xenoliths represent highly refractory restites of feldspathic protoliths, which is compatible with (but does not uniquely constrain) their low Rb (1-11 ppm) concentrations and similar Sr concentrations (119-694 ppm) relative to other metasedimentary xenoliths and greywacke reference samples (Price et al., 2015).

4.4.2.1.1.2. Neodymium

No geochemical evidence suggests that Sm and Nd have fractionated from each other in xenoliths relative to greywacke samples (Figs. 4.9, 4.10), which suggests that bulk xenolith $^{43}Nd/^{144}Nd$ ratios should reflect their protolithic values. Even xenolith samples with strong positive Eu anomalies ($Eu/Eu^* = 1.3$-2.3), which are interpreted to be more refractory than other xenoliths, have overlapping Sm and Nd concentrations and Sm/Nd ratios (0.18-0.28) to Waipapa (Sm/Nd = 0.16-0.22), Kaweka (Sm/Nd = 0.17-0.24) and Pahau (Sm/Nd = 0.19-0.20)

greywacke samples (Price et al., 2015). The preferential dissolution of minerals with contrasting Sm/Nd ratios is not indicated by geochemical data and therefore contrasting $^{143}Nd/^{144}Nd$ ratios that were potentially developed via radiogenic ingrowth in some minerals have not resulted in systematic changes to bulk xenolith $^{143}Nd/^{144}Nd$ ratios. This is consistent with the general observation that minerals that typically occur in arc magmas and their sedimentary derivatives do not have high Sm/Nd ratios (e.g. Gill, 1981; Rollinson, 1993 and references therein).

4.4.2.1.1.3. Lead

HFSE and Pb systematics indicate that bulk xenolith Pb isotope ratios, except $^{208}Pb/^{206}Pb$, probably reflect their protolithic values (section 4.3.2.3; Fig. 4.11). It is likely that xenoliths initially possessed Zr and Hf concentrations similar to those of greywacke reference samples (Zr = 137-260 ppm, Hf = 3.5-8.3 ppm: Price et al., 2015), which subsequently decreased to Zr = 26-88 ppm and Hf = 0.9-2.7 ppm when the xenoliths were incorporated into magmas (Fig. 4.11e). Intermediate concentrations of Zr (99-225) and Hf (2.5-5.8) in groundmass separates (whole-rock values are similar) bridge the compositional space between refractory xenoliths and 'pristine' protoliths (i.e. greywacke reference samples: Price et al., 2015). The loss of Zr and Hf in xenoliths can be explained by a Hf-Zr-bearing mineral that dissolved and liberated its Zr and Hf cargo into the surrounding melt (groundmass). This mineral is probably zircon because of the high (>100) Kd values for Zr and Hf into zircon (Rollinson, 1993 and references therein; Reid et al., 2011) and because relict zircon is observed in metasedimentary xenoliths (Fig. 4.6f-g).

If xenolith-hosted zircons dissolve when their protoliths are entrained into Tongariro magmas, then U, Th and Pb might be expected to correlate with Zr variation. However, this hypothesis is not supported by comparisons of Th/U and U/Pb versus Zr (Fig. 4.11d, f). Th/U ratios appear decoupled in the same manner as for Pb (Fig. 4.11c), wherein varied Zr concentrations (137-260 ppm) define a horizontal array that is perpendicular to a vertical xenolith array at lower Zr (26-88 ppm) and variable Th/U ratios (~6-17) (Table 4.4; Fig. 4.11d). Even greater scatter is observed in U/Pb ratios versus Zr concentrations: the U/Pb ratios of xenoliths (~0-0.3) are more diverse than for greywacke samples (~0.05-0.2) (Fig. 4.11f).

Despite the geochemical evidence for zircon dissolution (Fig. 4.11e), U and Pb concentrations have not been significantly fractionated during xenolith partial melting, and bulk isotopic characteristics probably remain representative of their sources. Incongruent melting processes are unlikely to have modified bulk xenolith $^{206}Pb/^{204}Pb$, $^{207}Pb/^{204}Pb$, $^{208}Pb/^{204}Pb$ and $^{207}Pb/^{206}Pb$ ratios because U/Pb (Fig. 4.11f) and Th/Pb ratios (not shown) in xenoliths do not differ from those in greywacke reference data (Price et al., 2015). However, Th/U fractionation,

driven by U loss from xenoliths relative to greywacke samples (section 4.3.2.3; Fig. 4.11a-c), predicts that $^{208}Pb/^{206}Pb$ ratios will differ between xenoliths and protoliths. This is because the simultaneous loss of co-hosted U and daughter ^{206}Pb (in the same mineral reservoir(s)) during incongruent melting will produce systematic shifts to greater $^{208}Pb/^{206}Pb$ ratios, because Th and daughter ^{208}Pb are preferentially retained. For the same reason, bulk xenolith $^{208}Pb/^{207}Pb$ ratios will also likely differ from their protolithic values, although these values are not conventionally presented. Apatite and alkali feldspar are capable of hosting significant cargoes of U and Th (apatite) and Pb (feldspar), as indicated by favourable Kd values (Rollinson, 1993 and references therein). However, it is unlikely that apatite and alkali feldspar breakdown in xenoliths modified their Pb isotope ratios because U/Pb does not correlate with Ba or P and Th/Pb does not correlate with P (not plotted).

Anticipated offsets to higher $^{208}Pb/^{206}Pb$ ratios in xenoliths relative to greywacke protoliths, as predicted from observed Th versus U fractionation, are consistent with Pb isotope data in Fig. 4.12d. Xenolith $^{208}Pb/^{206}Pb$ ratios have much less overlap with the Kaweka array than for other Pb isotope ratios. Back-tracing xenolith $^{208}Pb/^{206}Pb$ ratios to Kaweka-like values implies that Th versus U fractionation could have modified $^{208}Pb/^{206}Pb$ ratios by about +0.004 in xenoliths relative to greywacke protoliths (Fig. 4.12d).

The robustness of all radiogenic Pb isotope ratios except $^{208}Pb/^{206}Pb$ for accurately representing xenolith provenance is illustrated further by comparing Pb isotope ratios with Th/U ratios (Fig. 4.17). Trajectories in the diagram show the anticipated direction of bulk xenolith evolution for progressive U loss relative to Th, and the losses of radiogenic Pb ingrowth associated with these elements. In all panels, greywacke samples form vertical arrays because of their relatively invariant Th/U ratios relative to xenoliths. Th versus U fractionation is not expected to modify xenolith $^{206}Pb/^{204}Pb$, $^{207}Pb/^{204}Pb$ or $^{207}Pb/^{206}Pb$ ratios because these isotope ratios do not depend on ^{208}Pb produced by ^{232}Th decay. $^{208}Pb/^{204}Pb$ is also not expected to be modified by Th versus U fractionation because $^{208}Pb/^{204}Pb$ is unaffected by ^{238}U and ^{235}U decay, and that Th and Pb variation is decoupled in xenoliths (Fig. 4.11b). It is only within $^{208}Pb/^{206}Pb$ data that xenolith samples plot away from the Kaweka array, whereas Kaweka and xenolith samples have more closely overlapping $^{206}Pb/^{204}Pb$, $^{207}Pb/^{204}Pb$, $^{208}Pb/^{204}Pb$ and $^{207}Pb/^{206}Pb$ ratios (Fig. 4.17a-c). Moreover, in each Th/U versus Pb isotope ratio comparison (Fig. 4.17), the direction of offset matches predictions from Th versus U fractionation.

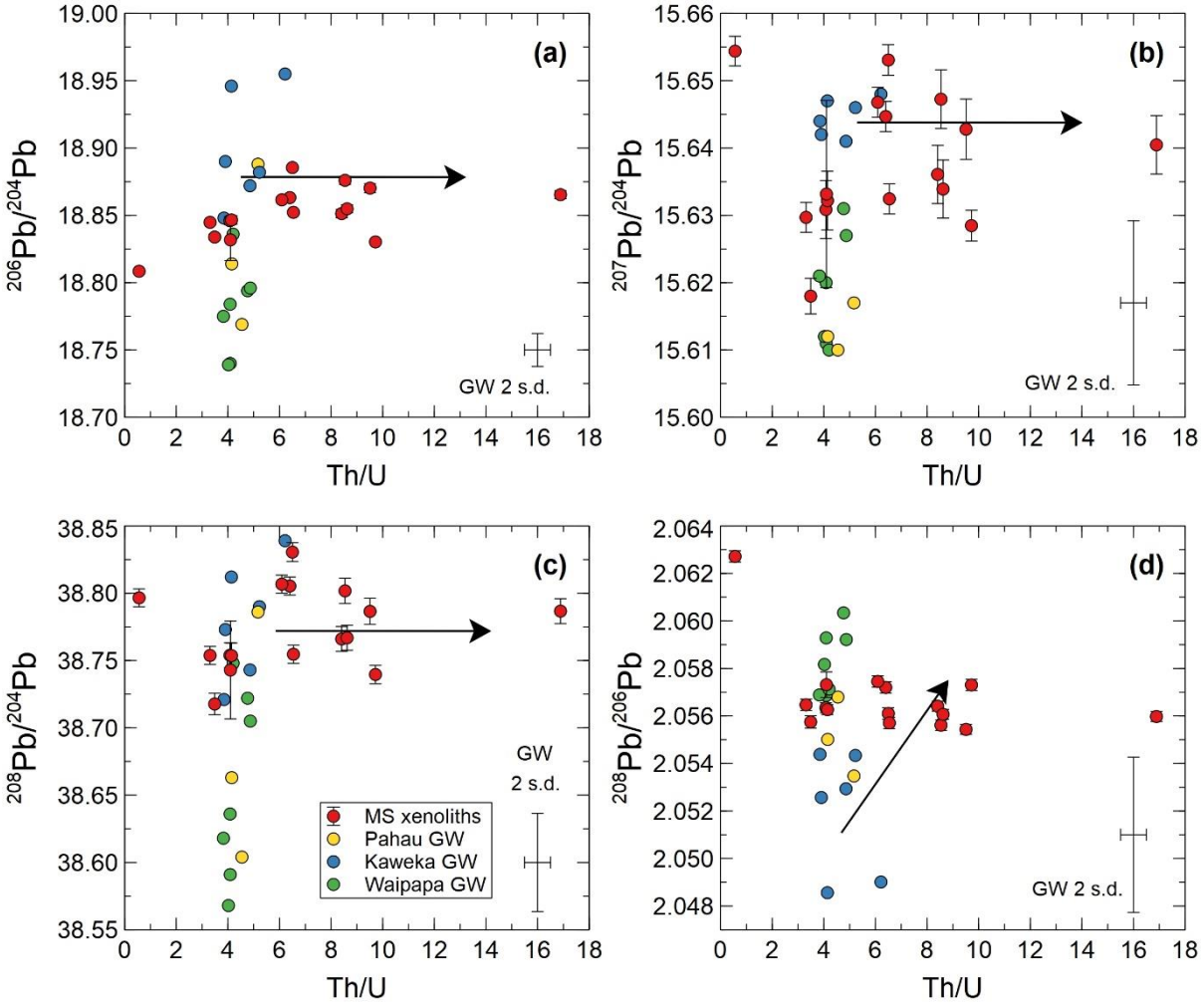

Figure 4.17. Pb isotope ratios versus Th/U ratios in metasedimentary (MS) xenoliths and greywacke (GW) reference samples. GW data from Price et al. (2015) with uncertainties shown in panel corners. Arrows point in the approximate directions of isotopic and compositional evolution for loss of U, ^{206}Pb and ^{207}Pb relative to Th and ^{208}Pb.

4.4.2.1.2. Interpretation of metasedimentary basement terrane(s)

In general, trace element systematics are consistent with Nd and Pb isotope ratios in xenoliths, reflecting their metasedimentary protoliths from before they were incorporated into magmas (section 4.3.2.3, above). Whilst $^{87}Sr/^{86}Sr$ isotope ratios probably shifted to less radiogenic values due to loss of radiogenic Sr during biotite breakdown, it is possible to constrain which regional greywacke terranes are represented by xenoliths by using Nd and Pb isotope data alone. Greywacke (Price et al., 2015) and xenolith (this study; Hobden, 1997) Nd and Pb isotope ratios indicate that metasedimentary xenoliths in Tongariro eruptives represent the Kaweka and at least one of the Pahau and Waipapa terranes. Considerable overlap occurs between xenolith $^{143}Nd/^{144}Nd$, $^{206}Pb/^{204}Pb$, $^{207}Pb/^{204}Pb$, $^{208}Pb/^{204}Pb$ and $^{207}Pb/^{206}Pb$ ratios and Kaweka samples (Fig. 4.16), but less so for Pahau and Waipapa samples, indicating that Tongariro xenoliths chiefly

represent a Kaweka metasedimentary source. However, because no known Kaweka samples have $^{143}Nd/^{144}Nd$ ratios higher than ~0.5125 (Price et al., 2015), the range of xenolith $^{143}Nd/^{144}Nd$ ratios (0.51243 to 0.51284) indicates that Pahau or Waipapa metasedimentary (or both) must also be represented (Figs. 4.12 and 4.16).

Equivalent arguments can be made for $^{206}Pb/^{204}Pb$, $^{207}Pb/^{204}Pb$, $^{208}Pb/^{204}Pb$ and $^{207}Pb/^{206}Pb$ ratios, for which xenolith versus greywacke terrane similarities are described in section 4.3.2.4, above. Pb isotope data show that metasedimentary xenoliths in Tongariro eruptives are more similar to Kaweka than Pahau or Waipapa greywacke (Figs. 4.12 and 4.16), consistent with inferences drawn from Nd isotope data. The presence of a second (and possibly third) greywacke terrane other than Kaweka beneath Tongariro has not previously been reported. The existence of multiple greywacke terranes beneath Tongariro indicates complexities in basement structure. Whether other metasedimentary basement rocks are represented by the Waipapa or Pahau terranes (or both) is not possible to determine with available with available Sr-Nd-Pb isotope data because of overlap between their isotope ratios.

4.4.2.2. Crustal structure beneath Tongariro

Evidence for multiple Mesozoic basement lithologies beneath Tongariro provides new constrains on crustal structure. Other constraints on crustal structure are provided by geophysical surveys of crustal velocity structure from which the depths of compositionally-distinct materials can be inferred (Sissons and Dibble, 1981; Harrison and White, 2006; Stern and Benson, 2011; Robertson and Davey, 2018). Observations from both geophysical and xenolith studies are used to define a model for the crustal structure beneath Tongariro (Fig. 4.18). The general features of the model are summarised first then justified below.

- A crust-mantle boundary ("Moho") between ~25 to 35 km depth (Harrison and White, 2006; Stern and Benson, 2011; Dimech et al., 2017).
- Mid-crustal Mesozoic metasediments that were accreted from east to west, wherein younger greywacke terranes were underplated beneath older terranes (Mortimer, 2004; Jiao et al., 2014; Mortimer et al., 2014), and occur to depths of probably ~15 km (Harrison and White, 2006; Stern and Benson, 2011; Arpa et al., 2017).
- Miocene sediments beneath Tongariro and Ruapehu that are about ≤1.5 km thick (Sissons and Dibble, 1981; Robertson and Davey, 2018), which separate underlying Mesozoic basement rocks from overlying Quaternary volcanic and sedimentary deposits.

Arguments for meta-igneous oceanic crust that underplates basement metasedimentary, first proposed by Graham et al. (1990), are considered at the end of this subsection.

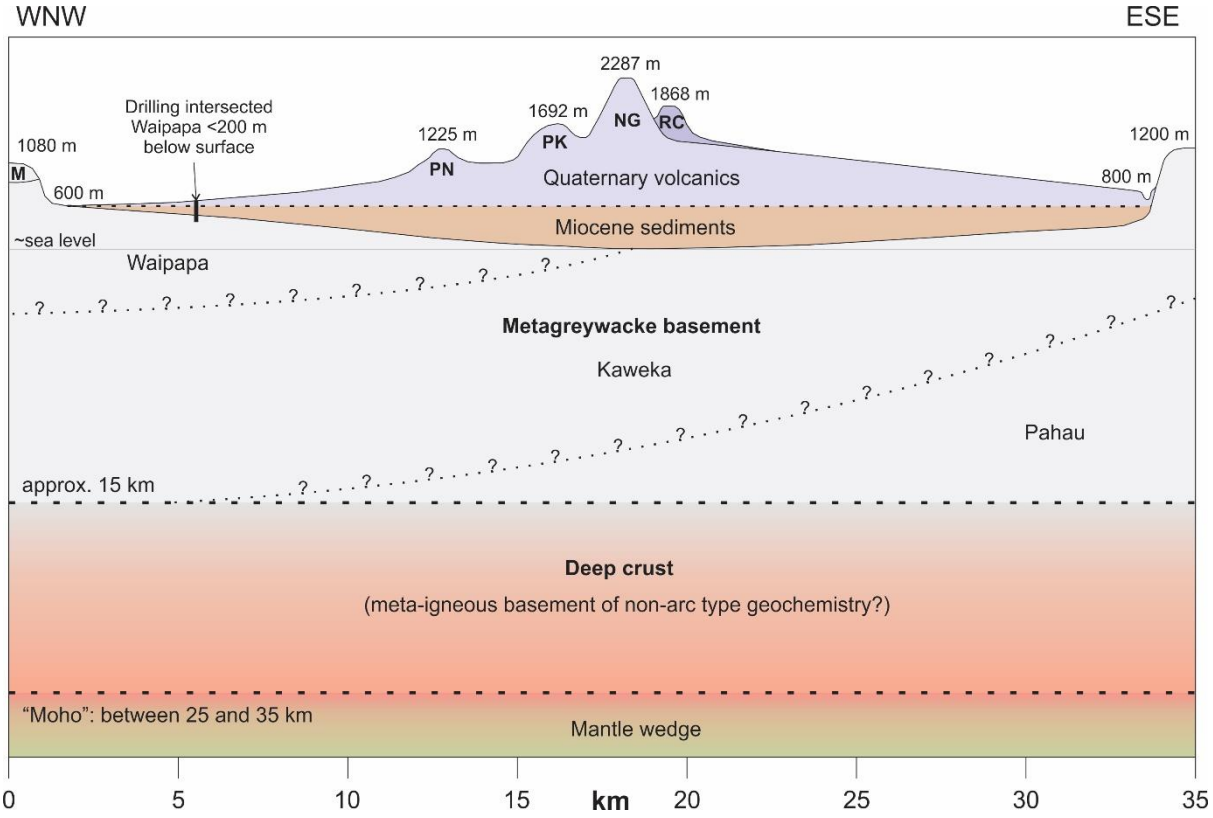

Figure 4.18. Suggested crustal structure beneath Tongariro volcano constrained by regional geophysical surveys and xenolith investigations. Not-to-scale vertical axis is compressed, except for above sea level line. Suggested orientation and ordering of basement greywacke terranes are discussed in text. Abbreviations are: M = Māui Supergroup and Te Tuiti Group sediments (Neogene and Oligocene depositional ages), PN = Pukeonake, PK = Pukekaikiore, NG = Ngauruhoe, RC = Red Crater. Topographic features are annotated with elevations in metres above sea level. It unclear whether the Miocene sediments inferred beneath Tongariro, following Robertson and Davey (2018), are from the aforementioned Māui Supergroup and Te Tuiti Group because their presence has not been directly identified or inferred from xenolith studies. Annotation to WNW side shows the approximate position where Waipapa terrane was intersected during drilling <200 m depth below surface (Beetham and Watters, 1985).

The boundary between the mantle and crust ("Moho"), which is likely gradual in a petrological sense, probably exists between ~25 and 35 km depth (Fig. 4.18). Seismic imaging north of Taupō volcano shows that mantle-like P wave velocities occur at a depth of 32 ± 1 km, but may persist to shallower depths of ~25 km (Harrison and White, 2006; Stern and Benson, 2011). Earthquake locations at latitudes equivalent to the southern TVZ indicate a crust-mantle boundary between 25 to 35 km depth (Dimech et al., 2017). Geobarometry estimates for nucleation depths of plagioclase and pyroxene, reported for Holocene Tongariro eruptives, are consistent with but do not offer improved constraints on a crust-mantle boundary between 25 to 35 km depth (Arpa et al., 2017).

Seismic imaging data show that metasedimentary lithologies probably continue to ~15 km depth north of Taupō volcano (Harrison and White, 2006; Stern and Benson, 2011) and it is plausible that similar crustal structures occur beneath Tongariro. Petrological evidence from 25.4 ka Oruanui deposits also suggests that metasediments occur to depths of at least ~8-12 km. Xenocrystic feldspars derived from the metasedimentary basement (Charlier et al., 2008), that were erupted as part of the Oruanui eruption from Taupō, were probably incorporated from a depth of at least ~8-12 km which is the estimated depth of the mush zone (Barker et al., 2015). The scarcity of multiple conjoined feldspar xenocrysts in Oruanui eruptives (Charlier et al., 2008), which are ubiquitous in southern TVZ eruptives as multi-crystal 1-100 mm xenoliths, implies that any hypothetical metasedimentary xenoliths entrained into Oruanui magmas were partially melted, reacted and disaggregated on incorporation into the ~8-12 km depth mush zone before the melt-dominant body was extracted then erupted (Allan et al., 2017). The xenocrystic feldspars in Oruanui deposits occur as single crystals which contrast with the ~10-15 cm across intact gneissic metasedimentary xenolith (R623: Sutton, 1995; Charlier et al., 2010) erupted with the Rubbish Tip Dome ~10 km northeast of Taupō, potentially outside of the sub-caldera mush zone. This relationship suggests that large (>1 cm) xenolithic country rock material may be disaggregated and filtered in mush zones which are known to occur at ~8-12 km depth. Using these observations, the base of the greywacke basement is at least ~15 km deep, but could potentially be deeper depending on how the percentage of magmatic intrusions in deeper crust affects seismic properties (e.g. Harrison and White, 2006; Stern and Benson, 2011).

The geometry of boundaries between distinct metasedimentary terranes beneath Tongariro is unclear based on current geophysical data. However, the depositional ages, timings of accretion and geochemical characteristics of Waipapa, Kaweka and Pahau terranes provide useful constraints on basement structure. The occurrences of the Waipapa terrane west of Tongariro and the Kaweka terrane east of Tongariro indicate successive accretion and juxtapositioning of these terranes in a westward direction, following their deposition during the Jurassic and Early Cretaceous periods (Mortimer, 2004; Mortimer et al., 2012; Ring et al., 2019). Accretion in this direction is most consistent with underplating wherein the younger Kaweka terrane was wedged beneath the older Waipapa terrane (Mortimer et al., 2012; Jiao et al., 2014; Price et al., 2015). Burial and accretion of the Waipapa and Kaweka terranes occurred in the Early Cretaceous when Pahau terrane was deposited as indicated by fission track and (U-Th-Sm)/He ages in exhumed Kaweka greywacke east of Tongariro (Jiao et al., 2014) versus detrital zircon regional ages in the Waipapa, Kaweka and Pahau terranes (Cawood et al., 1999; Adams et al., 2009). Detrital zircon ages of 110-140 Ma (~65 % of zircons) in the R623 xenolith link it to a

Pahau terrane protolith and suggests that Pahau terrane underplates Kaweka terrane in some areas within the central TVZ (Charlier et al., 2010). It is therefore plausible that similar crustal structure exists beneath the southern TVZ (Fig. 4.18)

Sr-Nd-Pb isotope ratios of metasedimentary xenoliths in Tongariro eruptives show that alongside a minor proportion of Pahau and/or Waipapa metasedimentary, the Kaweka terrane occurs as the most common end-member composition of the southern TVZ metasedimentary basement to interact with Tongariro magmas (sections 4.3.2.4, 4.4.2.1; Figs. 4.12, 4.18). The inferred vent locations of Tongariro's eruptive units are generally orientated in a NNE direction (Chapter 3) and thus unlikely to intercept any E-W differences in basement lithology across the volcano. The entrainment depths of individual xenoliths are poorly constrained, and xenolith provenance is varied within the same eruptive units. For example, the Te Wai Whakaata Member contains xenolith samples LP134X, LP147X and LP181X, which effectively span the entire range of xenolith major oxide, trace element and Sr-Nd-Pb isotope compositions and represent at least two distinct metasedimentary protoliths. However, this observation does suggest some degree of sub-horizontal layering between greywacke terranes, because if the terrane boundaries were vertical, it would be unlikely for individual eruptive units to contain multiple types of greywacke. The frequent occurrence of non-Kaweka-type xenoliths in Tongariro eruptives suggests that a significant thickness of Pahau or Waipapa terrane material exists beneath the volcano (Fig. 4.12; Table 4.5). This is consistent with the suggestions of Price et al. (2015) that the boundaries between greywacke terranes under the TVZ volcanoes dip towards the west.

Shallow crustal material beneath Tongariro is composed of Miocene sediments, which have unknown geochemical characteristics, but are likely represented by some xenoliths in Tongariro eruptives. Seismic refraction (Sissons and Dibble, 1981) and gravity data (Robertson and Davey, 2018) indicate that basement Miocene sediments have asymmetric E-W profiles in cross-section, and are at most ~1.5 km thick. Drill-cores collected to the northwest and southeast of Tongariro show that Waipapa and Kaweka terranes occur respectively as basement rocks at depths of ≤200 m (Beetham and Watters, 1985). The Waipapa greywacke intersected during drilling occurs ~5 km closer to Tongariro than surficial exposures of Waipapa greywacke, which potentially indicates its existence in the basement beneath western Tongariro (Fig. 4.18).

Attempts at constraining pressures and temperatures of metasedimentary crust, before their incorporation into magmas, are hampered by ubiquitous post-entrainment mineral breakdown in xenoliths (e.g. Figs. 4.7, 4.8, 4.11). Petrographic textures (Figs. 4.5, 4.6; Table 4.2) indicate that the surviving minerals in metasedimentary xenoliths also underwent recrystallisation in hot magmas (section 4.3.2.1; e.g. Holness and Siklos, 2000). Metasedimentary xenoliths in Te

Pupu Formation (Ngauruhoe) eruptives experienced temperatures of >800 °C at depths possibly shallower than 5 km, as indicated by experimental phase relations (Graham et al, 1988). Results from two-pyroxene geothermometry indicate that xenoliths in Ruapehu volcano eruptives experienced temperatures between ~800 and 910 °C (Graham et al., 1990). Even higher temperatures are indicated by titanomagnetite-ilmenite thermometry of 900-980 °C (Graham, 1987) for Tongariro and Ruapehu eruptives. These high temperatures approach typical andesite eruption temperatures of about 900-1000 °C (e.g. Gill, 1981) and provide evidence that xenoliths re-equilibrated according to the pressure and temperature conditions of their host magmas. Pseudosections drawn by Vry et al. (2008, 2009) for greywacke compositions (Grapes et al., 1982) that are compositionally similar to data reported by Price et al. (2015), indicate pre-incorporation temperatures of ~450-600 °C, but possibly lower, for pressures of ≤4 kbar (up to ~15 km depth: Robertson and Davey, 2018). Therefore, the minimum geotherm in 15 km of metasedimentary basement that comprises the upper crust is ~30 °C/km but is probably greater.

Arguments were presented by Graham et al. (1990) for a meta-igneous oceanic crust basement below the mid-crustal metasedimentary. The authors suggested that xenoliths with $^{87}Sr/^{86}Sr$ ratios of 0.7051-0.7087 and $^{143}Nd/^{144}Nd$ ratios of 0.5127-0.5130 in southern TVZ eruptives represented a meta-oceanic crust lithology in the deep crust, partially because $^{143}Nd/^{144}Nd$ ratios conflicted with the previous notion that all metasedimentary xenoliths in southern TVZ volcanics were derived from the Kaweka terrane. A second argument presented for a non-greywacke protolith was that xenolith Zr concentrations were lower than typical greywacke values (e.g. Price et al., 2015). However, this argument is potentially invalid because Zr concentrations in this study are ~2-3 times lower in metasedimentary xenoliths due to zircon dissolution (Fig. 4.11e; section 4.3.2.3). The absence of olivine in xenoliths is also cited as evidence for a deep crustal origin from pressures ≥7-9 kbar, based on phase equilibria (Graham et al., 1990). However, this argument is invalid because the protolith is unknown and may not have originally contained olivine. Compositional layering in xenoliths examined by Graham et al. (1990) occurs on a scale of ~1 mm and has striking petrographic resemblance to the textures reported for metasedimentary xenoliths in previous work (Graham, 1987) and in this work (Fig. 4.6). Given the comparable $^{87}Sr/^{86}Sr$ ratios of 0.70538 to 0.70851 and $^{143}Nd/^{144}Nd$ ratios of 0.51243 to 0.51285 determined for xenoliths in this study (Table 4.5), it is more likely that the more mantle-like Sr-Nd isotope ratios reported for "meta-igneous" xenoliths by Graham et al. (1990) instead represent a non-Torlesse (Kaweka) metasedimentary basement lithology such as the Pahau or Waipapa terrane. However, the enigmatic xenolith (LP168X) reported in this study (section 4.3.2.5; Table 4.2; Figs. 4.9, 4.12) is potentially a meta-igneous basement lithology that

has a distinct geochemical signature from typical arc magmatic/volcanic rocks beneath the southern TVZ (i.e. not metasediments derived from arc volcanics or plutonics: e.g. Ewart and Stipp, 1968). It is considered plausible that deep crustal basement rocks beneath Tongariro contain igneous material with non-arc type chemical signatures, probably at depths greater than ~15 km (e.g Harrison and White, 2006; Stern and Benson, 2011), but that such lithologies may not be accurately represented by xenoliths reported by Graham et al. (1990).

4.4.2.3. A metasedimentary basement composition for modelling

A hypothetical metasedimentary basement composition is proposed here for modelling assimilation processes in Tongariro magmas. Given the dominance of Kaweka-like Nd-Pb isotope ratios relative to Pahau-like and Waipapa-like Nd-Pb isotope ratios in xenoliths (e.g. Fig. 4.12), an average metasedimentary assimilant composition is estimated (Table 4.6) from 60 % Kaweka, 20 % Pahau and 20 % Waipapa, using the average terrane compositions suggested by Price et al. (2015).

4.4.3. Fractional crystallisation and assimilation

Chemical and thermodynamic models of assimilation-fractional crystallisation (AFC) processes have been proposed to explain the partial fusion and incorporation of country rock that occurs simultaneously with magma crystallisation (DePaolo, 1981; Bohrson and Spera, 2001, 2007; Spera and Bohrson, 2004). A salient feature of such models is the need to constrain the relative amounts of country rock assimilation versus ongoing magmatic crystallisation. The heat costs of country rock fusion are balanced by latent heat liberated during magma crystallisation (Bowen, 1928; Taylor, 1980; DePaolo, 1981). AFC models account for this process by scaling the mass assimilation rate (M_a) against the mass crystallisation rate (M_c) with a ratio known as the r-value (= M_a/M_c: DePaolo, 1981). In some models the r-value is thermodynamically restricted with the energy needed for mineral fusion and crystallisation (Bohrson and Spera, 2001; Spera and Bohrson, 2004; Bohrson and Spera, 2007). In their common application, r-values are chosen arbitrarily, despite their fundamental representation of assimilation and crystallisation rates, which often precludes AFC modelling as an avenue for determining the relative amounts of assimilation versus crystallisation, because of circularity. Geochemical and petrographic data presented above are used here to infer the percentages of assimilated crust in Tongariro magmas.

4.4.3.1. Assimilation: bulk or partial protolith incorporation?

In studying typical arc settings, micro-scale investigations on natural and experimental materials have indicated that magma-country rock interactions typically produce partial melts rather than wholesale melting of country rock (e.g. Knesel and Davidson, 1996; Tommasini and Davies, 1997; Knesel and Davidson, 1999). These processes have been modelled numerically (Zeng et al., 2005; Farina and Stevens, 2011) and demonstrated by outcrop-scale studies of intrusive and plutonic rocks (White and Chappell, 1977; Petcovic and Grunder, 2003; Farina et al., 2014; Wolf et al., 2019). However, the salient question here is whether assimilant compositions are more closely represented by partial melts derived from country rock (with contrasting compositions to the bulk protolith) or the bulk country rock composition itself. The incomplete fusion of country rock may result in either of these situations. In the first case, partial melts may be derived from wall-rocks without incorporating associated restites and will likely possess contrasting compositions to their bulk protolith (Knesel and Davidson, 1996; 1999). In the second case, the partial fusion of country rock adjacent to hot magma may facilitate stoping by reducing the cohesion between internal grain boundaries in wall-rock material, which may encourage shearing and fragmentation induced by the friction of ascending magma. In the latter case, the partial fusion of country rock results in the joint assimilation of partial melts and their associated restites which have a net composition equal to their bulk protolithic source (e.g. White and Chappell, 1977). The abundance of metasedimentary restites that have re-equilibrated at temperatures typical of andesite magmas (~800-1100 °C) provide strong evidence that this is the dominant assimilation process that occurs in Tongariro magmas (Graham, 1987; Graham et al., 1988).

Strong similarities between Sr-Nd isotope ratios in groundmass and whole-rock pairs imply that radiogenic contamination by country rock at Tongariro is a bulk incorporation process (Fig. 4.15). Alternatively, if country rock-derived partial melts are the primary radiogenic contaminants of Tongariro magmas, then magmas must ascend through equally fertile crust to explain the highly systematic Sr and Nd isotope ratio variation in whole-rock and groundmass pairs. If magma ascent pathways are reused, then contamination will be less efficient with time because adjacent wall-rock will become increasingly depleted in 'fertile' minerals near temperatures typical of andesite magmas. However, if instead country rock assimilation occurs as a bulk process, then equally radiogenic crust will contaminate each magma batch.

4.4.3.2. A two-stage scenario for estimating crustal inputs into Tongariro magmas

The mass assimilation rate (M_a) and mass crystal fractionation rate (M_c) were estimated for two stages of magma evolution at Tongariro. Stage 1 represents AFC magma evolution for compositions that are more primitive than observed on Tongariro's edifice. In practice this equates to primitive end-member magmas that intrude the deep crust and replenish Tongariro's magma system, and magmas that evolve from these end-members into the most primitive materials (lowest SiO_2 concentration) preserved on Tongariro's edifice. The latter is represented by the Red Crater 'basalt' (actually a basaltic-andesite: Gamble et al., 1993), and is henceforth referred to as the Te Rongo basaltic-andesite, following the definitions in Chapter 3. The primitive end-member chosen for stage 1 is Kakuki basalt because its composition is similar to those of Tongariro magmas that are extrapolated to primitive compositions (e.g. Figs. 4.1-4.4). Specifically, Kakuki basalt has REE concentrations that are similar to the lower concentrations observed in Tongariro whole-rock samples (Fig. 4.3) and Kakuki basalt also has less evolved Sr-Nd-Pb isotope compositions that more closely align with the Tongariro array extrapolated to less crustal values than the Waimarino or Havre basalts (Fig. 4.4) (Gamble et al., 1993, 1996; Waight et al., 2017). Stage 2 covers the entire array of Tongariro magma compositions represented in edifice-forming eruptives and is modelled from a Te Rongo basaltic-andesite starting composition to continue on from the first stage. Stages 1 and 2 are considered separately for two reasons. First, major and trace element arrays (Figs. 4.1, 4.2; section 4.3.1.3) indicate that olivine is the dominant fractionating phase in samples with >8 wt% MgO (i.e. stage 1), which contrasts with a clinopyroxene + orthopyroxene + plagioclase fractionating assemblage in stage 2 (Table 4.1; sections 4.3.1.3, 4.4.1). Second, the mafic compositional end-member in stage 2 is well-constrained whereas the Kakuki-like primitive end-member in stage 1 is only inferred and would introduce inaccuracies if used to model the entire Tongariro array.

The mass proportions of assimilated crust and fractionated material in stage 1 were estimated from $^{87}Sr/^{86}Sr$ ratios and SiO_2 concentrations. Petrographic and geochemical observations provide no compelling evidence for significant plagioclase fractionation in magmas with <55 wt% SiO_2 (Figs. 4.1-4.2; Table 4.1), which is the only viable option for removing significant amounts of Sr from mafic magmas. Assimilation of radiogenic country rock should therefore modify $^{87}Sr/^{86}Sr$ ratios according to simple mixing. Despite a higher Sr concentration in Kakuki basalt (~350 ppm) relative to Te Rongo basaltic-andesite (278 ppm: Gamble et al., 1993), other Tongariro basaltic-andesites have up to ~640 ppm Sr (Hobden, 1997) and do not present evidence for plagioclase fractionation (Makahikatoa Formation: Chapter 3). Therefore, for mass balance calculations, end-member (Kakuki) and final (Te Rongo) magma Sr concentrations are

considered to be equal. The Sr concentration in the hypothetical metasedimentary assimilant (359 ppm: section 4.4.2.3) is also similar to Kakuki and Te Rongo magmas. In this case, a simple two-component mixing model can be used to model the isotopic data. In contrast, metasedimentary basement rocks have higher Nd (20-35 ppm) and Pb (18-27 ppm) concentrations (Price et al., 2015) than in Kakuki and Te Rongo magmas (~10 ppm Nd; ~2 ppm Pb), and therefore such simplified mixing models are not applicable (Gamble et al., 1993; Price et al., 2015). The mixing calculations below estimate the proportions of assimilated crust versus Kakuki-like basalt in a Te Rongo-type basaltic-andesite magma from $^{87}Sr/^{86}Sr$ ratios, which are assumed to be unaffected by fractional crystallisation.

Equation 4.1 describes the concentration (C) of an element in the Te Rongo basaltic-andesite (TR subscript) as a function of fractions (f) of assimilant (A subscript), Kakuki basalt (K subscript) and fractionating crystals (X subscript):

$$C_{TR} = C_A f_A + C_K f_K - C_X f_X \quad . \tag{4.1}$$

Accurate models will satisfy the relationship in equation 4.2.

$$1 = f_A + f_M + f_X \quad . \tag{4.2}$$

Whether the fractions of assimilated crust, retained magma and fractionated crystals sum to 1 depends on the choice of geochemical data. However, because input geochemical data were independently collected on a variety of natural samples, is it unlikely that equation 4.2 will be exactly satisfied. In the case of Sr isotope ratios, no Sr should be removed from an evolving Kakuki-type magma because plagioclase fractionation is negligible and therefore $f_X = 0$ in equation 4.2. This allows f_A to be expressed as a function of f_K (for the $^{87}Sr/^{86}Sr$ case only), thus:

$$f_{A(\frac{87Sr}{86Sr})} = 1 - f_{K(\frac{87Sr}{86Sr})} \quad . \tag{4.3}$$

From here, it is possible to express equation 1 with respect to $^{87}Sr/^{86}Sr$ ratios according equation 4.3. When rearranged for f_K, the relationship in equation 4.4 is obtained:

$$f_A = \frac{C_{K(\frac{87Sr}{86Sr})} - C_{TR(\frac{87Sr}{86Sr})}}{C_{K(\frac{87Sr}{86Sr})} - C_{A(\frac{87Sr}{86SR})}} \quad . \tag{4.4}$$

Evaluating equation 4.4 with the $^{87}Sr/^{86}Sr$ ratios in Table 4.6 gives $f_A = 0.18$, or 18 % assimilated crust needed to achieve a Te Rongo basaltic-andesite $^{87}Sr/^{86}Sr$ ratio via mixing with the hypothetical metasediment composition given in Table 4.6. However, equation 4.2 first needs to be satisfied to determine whether this idealised model accurately represents nature with the geochemical data used for computations here. To do this, it is necessary to compute the fraction of melt with a Kakuki basalt composition (f_K) and the fraction of crystallised material removed from the magma (f_X). This is achieved by considering SiO_2 concentrations, which are modified by

loss of an olivine + clinopyroxene + orthopyroxene assemblage. Equation 4.1 is expressed for this situation (technically an alternative AFC model) with equation 4.5:

$$C_{TR(SiO2)} = C_{A(SiO2)}f_{A(SiO2)} + C_{K(SiO2)}f_{K(SiO2)} - C_{X(SiO2)}f_{X(SiO2)} \quad . \qquad (4.5)$$

In an assimilation scenario, the relationship in equation 4.6 will hold when absolute Sr concentrations are equal in the parental Kakuki basalt and hypothetical metasedimentary assimilant, which is assumed for stage 1 (Table 4.6).

$$\frac{f_{A(SiO2)}}{f_{A(SiO2)}+f_{K(SiO2)}} = \frac{f_{A(\frac{87Sr}{86Sr})}}{f_{A(\frac{87Sr}{86Sr})}+f_{K(\frac{87Sr}{86Sr})}} \quad . \qquad (4.6)$$

Substitution of equation 4.3 into equation 4.6 allows $f_{K(SiO2)}$ to be formulated in terms of other determinable variables, as in equation 4.7:

$$f_{K(SiO2)} = f_{A(SiO2)}\frac{f_{K(\frac{87Sr}{86Sr})}}{f_{A(\frac{87Sr}{86Sr})}} = f_{A(SiO2)}\frac{(1-f_{A(\frac{87Sr}{86Sr})})}{f_{A(\frac{87Sr}{86Sr})}} \quad . \qquad (4.7)$$

Table 4.6. Geochemical data for AFC and mixing model calculations.

Variable for models	Kakuki B	Te Rongo BA	Hypothetical MS
SiO_2 (wt%) e.g. C_K, C_{TR}, C_A (C_X = 45)	49.1	53.1	67.7
Rb (ppm)	4	20	100
Sr (ppm)	350	278	359
Zr (ppm)	79	68	197
Nd (ppm)	12.7	9.9	29.7
Rb/Sr	0.0114	0.0719	0.2777
La/Yb	3.581	3.827	12.415
$^{87}Sr/^{86}Sr$	0.703931	0.704609	0.707637
$^{143}Nd/^{143}Nd$	0.512908	0.512830	0.512517
Data source*	1	1	via 2

* 1 = Gamble et al. (1993), 2 = hypothetical metasediment values are from 60 % Kaweka, 20 % Pahau and 20 % Waipapa terrane average values of Price et al. (2015).
C_X = 45 wt% SiO_2 from 60 % olivine, 20 % clinopyroxene and 20 % orthopyroxene based on average EPMA results of Hobden (1997). B = basalt, BA = basaltic-andesite, MS = metasediment.

The expression in equation 4.7 can be substituted into equation 4.2 (for the SiO_2 case) and solved for $f_{X(SiO2)}$, which yields equation 4.8:

$$f_{X(SiO2)} = f_{A(SiO2)}\left(1 + \frac{1-f_{A(\frac{87Sr}{86Sr})}}{f_{A(\frac{87Sr}{86Sr})}}\right) - 1 \quad . \qquad (4.8)$$

Equation 5 can then be solved for $f_{A(SiO2)}$ by substituting the formulation in equation 4.8 to yield equation 9:

$$f_{A(SiO2)} = \frac{C_{TR(SiO2)} - C_{X(SiO2)}}{C_{A(SiO2)} + C_{K(SiO2)}\left(\frac{1}{f_{A(\frac{87Sr}{86Sr})}} - 1\right) - \frac{C_{X(SiO2)}}{f_{A(SiO2)}}} \quad . \qquad (4.9)$$

Equation 4.9 can be evaluated with the values given in Table 4.6. Of these, $C_{X(SiO2)}$ has a value of ~45 wt% SiO_2 which is the bulk SiO_2 concentration of a fractionating assemblage of 60 % olivine, 20 % clinopyroxene and 20 % orthopyroxene, based on average SiO_2 concentrations reported for these minerals in Tongariro eruptives by Hobden (1997). Evaluating $f_{A(SiO2)}$ in equation 4.9 yields ~0.20 (20 %), which is the proportion of SiO_2 in the Te Rongo basaltic-andesite obtained from assimilated model metasediment. Evaluating $f_{K(SiO2)}$ in equation 4.7 gives 0.88 (88 %), which is the proportion of Kakuki-like magma retained in the Te Rongo basaltic-andesite. Note however that these values sum to 108 %, which allows no leftover proportion for fractionating crystals. In this case, the requirement of equation 2 is not closely satisfied, thus reflecting the uncertainties that arise from making precise computations from a variety of measured and estimated geochemical values from independent samples.

Issues with estimating the percentage of fractionated crystals can be circumvented by rearranging equation 4.5 and evaluating for $f_{X(SiO2)}$ which gives ~0.08 (8 %). Reapplying equation 4.2 for the SiO_2 case gives a total of 1.16 instead of 1, where 0.16 (~16%) can be taken as a quantitative metric of this model's inaccuracy. Normalising $f_{A(SiO2)}$, $f_{K(SiO2)}$ and $f_{X(SiO2)}$ gives the respective mass percentages of assimilated countryrock (17 %), residual Kakuki-type magma (76 %) and fractionated olivine, clinopyroxene and orthopyroxene (7 %) needed to evolve from a Kakuki basalt composition to a Te Rongo basaltic-andesite composition. The value of 17 % assimilated crust estimated for stage 1 represents a minimum amount of assimilated crust in Tongariro magmas. AFC evolution continues in stage 2, as indicated by Sr-Nd-Pb isotope ratios in Tongariro magmas that are generally more crust-like (Fig. 4.4) than Te Rongo-type isotope ratios (e.g. $^{87}Sr/^{86}Sr = 0.70461$, $^{143}Nd/^{144}Nd = 0.51283$: Table 4.6).

The associated r-value for stage 1 is ~2.5. If the ~16 % inaccuracy of model calculations are propagated for minimum and maximum r-values, the range obtained is 1.8-3.5. Although uncertainties surround the actual compositions of assimilants, fractionating assemblages and primitive deep crustal magmas, the calculations here indicate that mass assimilation rates (M_a) are greater than mass crystal fractionation rates (M_c) in the early stages of magma assembly beneath Tongariro.

The total amount of assimilated crust in Tongariro magmas, considered in stage 2, is obtained by considering $\delta^{18}O$ data for Tongariro eruptives versus assimilant metasedimentary and primitive mafic magmas that intrude the deep crust beneath Tongariro. Hobden (1997) report $\delta^{18}O_{(SMOW)}$[4] values of 6.16-6.59 ‰ for Tongariro eruptives whereas probable mafic end-member values (Beier et al., 2017) for ~Fo_{90} olivines from the Pukeonake Formation are 4.98-5.25 ‰,

[4] All $\delta^{18}O$ values henceforth are reported against SMOW.

which overlap with mantle-like values (Mattey et al., 1994). Additional confidence in primitive end-member values of ~5.1 ‰ is given by submarine TVZ and Kermadec Arc volcanic $\delta^{18}O$ values of 4.83-5.47 ‰ (Macpherson et al., 1998). If the meta-igneous xenoliths reported by Graham et al. (1990) are actually metasedimentary, as suggested above (section 4.4.2.2), then greywacke assimilants have $\delta^{18}O$ values of 8.2-11.7 ‰. Simple mixing calculations of average $\delta^{18}O_{(SMOW)}$ values for metasedimentary (10.0 ‰) and primitive magma (5.1 ‰) give between 22-31 % assimilated crust in the average Tongariro magma. This equates to the addition of a further 5-14 % of assimilated crust in stage 2 after stage 1. The proportions of crystal fractionation and country rock assimilation for stage 2 are evaluated using conventional AFC modelling with the original DePaolo (1981) formulation in section 4.4.3.4, below.

4.4.3.3. AFC and mixing model parameters

The second stage of magma evolution considers an AFC pathway beginning with a Te Rongo basaltic-andesite composition (section 4.4.3.2), with mixing calculations for comparison. AFC and mixing calculations use a hypothetical metasediment composition as an assimilant (Table 4.6). Trial-and-error modelling with average Waipapa versus Kaweka greywacke compositions reported by Price et al. (2015) versus the hypothetical metasediment do not show significant differences. Potential isotopic contrasts between the Pahau terrane versus the Kaweka and Waipapa terrane, suggested by the data of Price et al. (2015), are diminished when the $^{87}Sr/^{86}Sr$ ratio (=0.707378±100) and $^{143}Nd/^{144}Nd$ ratio (=0.512594±56) of R623 are considered (Fig. 4.12a; Sutton, 1995), which is the only demonstrably Pahau terrane xenolith erupted in the TVZ (Charlier et al., 2010). AFC curves are calculated for r-values between 0.1 and 0.9 using both intermediate and silicic melt Kd values supplied in the spreadsheet of Ersoy and Helvaci (2010) with the addition of Kd_{Sc}^{opx} and Kd_{Sc}^{cpx} values of 3.0 for intermediate composition melts (Gill, 1981). Interstitial melts in Tongariro magmas are dacitic to rhyolitic (~63-74 wt% SiO_2), as indicated by reconnaissance EPMA analyses of orthopyroxene-hosted melt inclusions (Appendix 8).

Figure 4.19. (Next page.) Results of AFC modelling (after DePaolo, 1981) and mixing modelling for a Te Rongo (Red Crater) 'basalt' (Gamble et al., 1993) assimilating model metasediment (see Table 4.6 for details). Tongariro whole-rock data from this study ('t.s.') and Hobden (1997) ('H97'). Basalt data for the Waimarino (W), Havre Trough (H) and Kakuki (K) basalts from Gamble et al. (1993). Lines with tick marks are mixing curves with percentages of mixed greywacke annotated. Key in (**d**) applies to all panels. AFC curves are for intermediate (red **X**s) and silicic (black **+**s) Kd values with fractions of remaining melt and r-values annotated. Full Tongariro whole-rock data in Appendix 5.

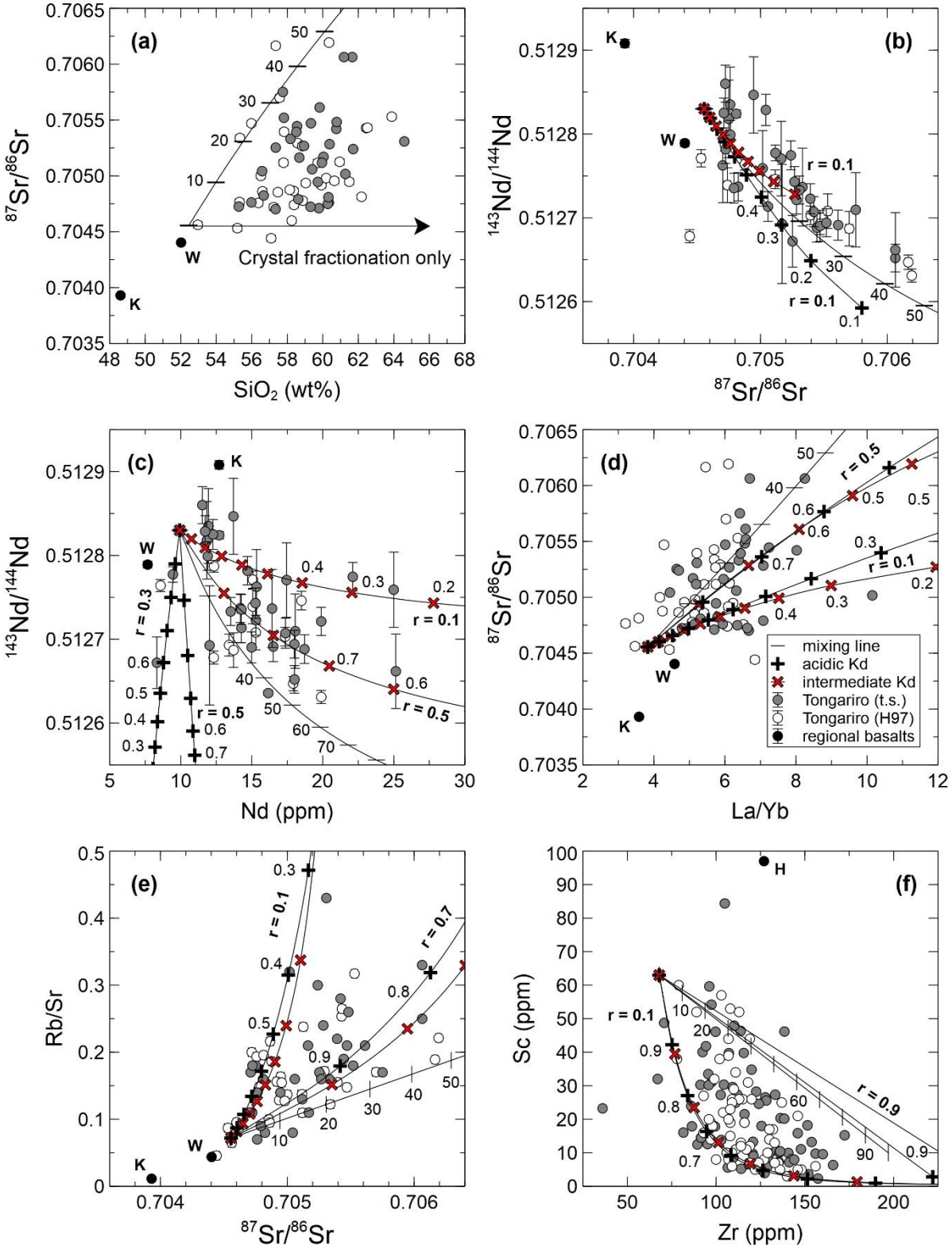
(a)
$^{87}Sr/^{86}Sr$
SiO_2 (wt%)
W
K
Crystal fractionation only
(b)
$^{143}Nd/^{144}Nd$
$^{87}Sr/^{86}Sr$
r = 0.1
(c)
$^{143}Nd/^{144}Nd$
Nd (ppm)
r = 0.3
r = 0.5
r = 0.1
(d)
$^{87}Sr/^{86}Sr$
La/Yb
r = 0.5
r = 0.1
mixing line
acidic Kd
intermediate Kd
Tongariro (t.s.)
Tongariro (H97)
regional basalts
(e)
Rb/Sr
$^{87}Sr/^{86}Sr$
r = 0.1
r = 0.7
(f)
H
Sc (ppm)
Zr (ppm)
r = 0.1
r = 0.9

4.4.3.4. AFC and mixing modelling results

Comparisons between whole-rock Tongariro samples and the results of AFC and mixing models are shown in Fig. 4.19. AFC models are generally successful at reproducing trajectories that are appropriate for Tongariro magma compositions, although a variety of r-values and Kd values are needed. Mixing and fractional crystallisation pathways for SiO_2 and $^{87}Sr/^{86}Sr$ ratios show that varied amounts of crystal fractionation and assimilation are needed to explain the compositional diversity of Tongariro's magmas (Fig. 4.19a). Whilst some Tongariro samples plot near the pure crystal fractionation line, their SiO_2 concentrations are restricted to ≤58 wt%, which implies that crustal contamination is inevitable during magma evolution. Some samples also plot on the mixing curve which indicates that crystal fractionation processes are sometimes inefficient and crystal cargoes are retained as magmas evolve, as noted previously (section 4.4.1). The positions of samples near the SiO_2-$^{87}Sr/^{86}Sr$ mixing curve imposes an upper limit of ~50 % assimilated greywacke in the most radiogenic Tongariro samples, which is seen at elevated (but not maximal) SiO_2 concentrations of ~60-62 wt%. In such circumstances, mass assimilation rates may exceed mass crystal fractionation rates (r >1).

In $^{87}Sr/^{86}Sr$-$^{143}Nd/^{144}Nd$ space, AFC curves converge on the mixing curve as r-values increase towards 1, but for clarity only r = 0.1 curves (as end-members) are shown (Fig. 4.19b). Tongariro's most radiogenic Sr and Nd isotope ratios cannot be explained by AFC processes when r-values = 0.1 for silicic or intermediate melt Kd values, because residual melt fractions reach 0.1 (90 % crystal fractionation) before $^{87}Sr/^{86}Sr$ reaches 0.70610 or $^{143}Nd/^{144}Nd$ reaches 0.51263. However, these maximal radiogenic Tongariro Sr and Nd isotope ratios can be reproduced when r-values are ≥0.3, which equates to roughly ≤55 % crystal fractionation (and ~20-30 % assimilated crust) from the Te Rongo basaltic-andesite starting composition. Mixing curves indicate that almost equal proportions of Te Rongo basaltic-andesite and model metasediment are needed to produce maximal whole-rock $^{87}Sr/^{86}Sr$ and $^{143}Nd/^{144}Nd$ ratios. However, lesser proportions of assimilated greywacke are needed to explain radiogenic isotope characteristics when assimilation and crystal fractionation occur simultaneously, because less crustal Sr and Nd can be removed with plagioclase, pyroxene and apatite fractionation.

Variation between whole-rock Nd concentrations and $^{143}Nd/^{144}Nd$ ratios are most closely reproduced by intermediate melt Kd values and r-values of ~0.5 (Fig. 4.19c). Most Tongariro samples plot between the mixing curve (r >1) and r = 0.1 AFC curve (intermediate melt composition), although a small number of samples are better explained by AFC evolution with a silicic melt composition for r-values between 0.3-0.5. Whilst some differences exist between AFC curves that use silicic versus intermediate mineral/melt partition coefficients (Fig. 4.19c), most

Tongariro compositions are reproduced equivalently with silicic and intermediate mineral/melt partition coefficients (Fig. 4.19d-f).

Other trace element and isotope ratio comparisons indicate similar proportions of crystal differentiation and assimilation. When compared with $^{87}Sr/^{86}Sr$ ratios, La/Yb (Fig. 4.19d) and Rb/Sr ratios (Fig. 4.19e) indicate that compositional diversity in Tongariro magmas requires AFC evolution with r-values of ~0.1-1. A similar result is obtained for AFC and mixing curves in Sc-Zr space (Fig. 4.19f), wherein r-values between ~0.1-0.9 are needed to reproduce the total compositional diversity in Tongariro samples. On average, AFC modelling results most closely reproduce Tongariro compositions with r-values of ~0.5 for intermediate and silicic melt Kd values (Fig. 4.19), which represents twice as much mass lost as fractionated crystals than mass added from assimilated country rock. This contrasts with the initial stages of magma evolution that are most likely represented by greater amounts of assimilated country rock than fractionated crystals (r >1), as concluded in section 4.4.3.2, above.

4.4.4. Magma assembly processes at Tongariro volcano

Tongariro's magmatic system is inferred to extend through the crust, probably as a plexus of interconnected dikes and sills. Although examples of jointly-exposed volcanic and magmatic components of the same system are rare, the deep crustal feeder zone beneath Tongariro may be typified by examples of exposed deep crustal root zones elsewhere in New Zealand, such as in Fiordland (e.g. Bhattacharya et al., 2018). Available data for the Tongariro area indicate a crustal thickness of ~25-35 km (Harrison and White, 2006; Stern and Benson, 2011; Arpa et al., 2017; Dimech et al., 2017), within which Tongariro's magma system has been established since at least ~300 kyr (Chapter 3). Sr-Nd-Pb isotope ratios from this study and elsewhere provide strong evidence for the assimilation of metasedimentary lithologies (Graham, 1987; Graham et al., 1988; Hobden, 1997; Hobden et al., 1999), which probably occur to depths of ~15 km but possibly deeper (Harrison and White, 2006; Stern and Benson, 2011). One enigmatic xenolith indicates that a meta-igneous lithology, with non-arc magma-type geochemical characteristics, may also be present in the deep crust (LP168X: Tables 4.2-4.5; Figs. 4.8-4.12; section 4.3.2.5).

Long-standing debates surround which of several petrogenetic processes are the most fundamental to producing andesite magmas at volcanic arcs (e.g. Bowen, 1928; Eichelberger, 1974; Gill, 1981; Hildreth and Moorbath, 1988; Eichelberger et al., 2006; Kent et al., 2010; Jagoutz, 2014; Sisson et al., 2014; Lee and Bachmann, 2014)—see also sections 1.2.3, 1.2.5. Observations from this study support a model wherein crystallisation, differentiation, fractionation and assimilation all contribute to andesite magma generation to varying degrees, but

with emphasis that each of these processes are expressed variably at different stages of magma evolution and vary according to the local circumstances specific to each magma. A salient consideration is that whilst crystallisation drives melt differentiation, these processes can operate in situ without crystal-melt fractionation, thereby limiting changes in bulk magma composition (Sisson et al., 2014).

Crystallisation-differentiation occurred ubiquitously in Tongariro magmas although crystal fractionation has been expressed variably. Initial crystal fractionation of olivine > clinopyroxene + orthopyroxene occurred in replenishing basalt magmas with MgO >8 wt% as they evolved to basaltic-andesite compositions (Figs. 4.1, 4.2; Table 4.1). Subsequent crystallisation in basaltic-andesites continued between MgO concentrations of ~8-7 wt% primarily with clinopyroxene and orthopyroxene crystallising, and which were then removed from the magmas. Plagioclase fractionation began by ~7 wt% MgO (from >55 wt% SiO_2) and was overall less efficient than pyroxene fractionation The fractionation of clinopyroxene, orthopyroxene and plagioclase probably occurred in subequal proportions between ~4 and 2 wt% MgO (~59-66 wt% SiO_2) and coincided with the beginning of apatite fractionation (Table 4.1).

The amount of assimilated country rock in Tongariro magmas is about 21-33 %, which compares with the 8-15 % figure in the average Mount Rainier magma (Sisson et al., 2014). Initially crustal assimilation at Tongariro occurred at a greater rate than fractional crystallisation in replenishing basalt magmas (as they evolved to basaltic-andesites) as indicated by r-values between ~1.8-3.5 (section 4.4.2.2), which corresponds to about 17 % assimilated crust. Approximately equal amounts of assimilation and crystal fractionation have been inferred from isotopic investigations on deep crustal cumulate xenoliths from eastern Australia, which suggests that this process is not limited to extrusive igneous rocks only (Rudnick et al., 1986). Subsequent evolution from basaltic-andesites to dacites is reflected by r-values of 0.1-1.0, averaging to ~0.5 (section 4.4.2.4; Fig. 4.19), which indicates that assimilation rates were equal to or outpaced by fractional crystallisation processes. By difference, 5-14 % assimilation of country rock is inferred to correspond to this second stage of magma evolution.

Highly systematic covariance in paired whole-rock and groundmass Sr-Nd isotope ratios indicates that crystal extraction and the additional of crustal material into magmas has occurred at balanced rates for all Tongariro magmas. A caveat is that at Tongariro bulk phenocryst cargoes in andesite whole-rock samples are effectively the same as their phenocryst cargoes and melts. This contrasts with microscale isotopic heterogeneities that have been widely observed (e.g. Charlier et al., 2007, 2008), including elsewhere at Tongariro (Hora, 2003). Given that isotopic homogeneity

on macroscales coincides with microscale isotopic heterogeneity supports the aforementioned model wherein crystallisation, differentiation, fractionation and assimilation occur repeatedly but in episodic events and are ostensibly recorded on sub-crystal scales (e.g. Hora, 2003; Charlier et al., 2008). The chemical clues of episodic chemical variation in magmas are apparently 'smoothed out' by repeated mixing and homogenisation of magmas in a complex plumbing system before they are finally erupted.

Initially high r-values (>1) that subsequently decreased (<1) as magmas evolved follow predictions from some isenthalpic (heat-balanced) AFC models. For basalts assimilating felsic crust, the model of Reiners et al. (1995) predicts r-values that are initially high (~2.0-2.7) which subsequently decrease to ~0.5-1.0 when magmas reach intermediate compositions. However, other energy-balanced AFC models have concluded the opposite result wherein r-values should be initially low in the deep crust (<0.1) then later increase to ~0.8 in the mid-shallow crust as magmas become more evolved (Bohrson and Spera, 2001). This inconsistency indicates that energy-constrained AFC models are highly sensitive to the choice of thermodynamic parameters. As pointed out by Sisson et al. (2014), r-values exceeding 1 do not violate the conservation of energy because ascending magmas can mix with previously melted country rock contained within other magmas. Latent heat carried by previously fused country rock reduces the need for replenishing magmas to crystallise, hence assimilation can occur without advanced crystallisation (or fractionation). This results in r-values >1 and approximates a mixing scenario between the model starting composition and the assimilant end-member. The initially high (~1.8-3.5) then decreased (~0.1-1.0) r-values determined for evolving Tongariro magmas indicate that AFC models will most accurately represent nature when applied to individual segments of compositional arrays, to reflect contrasting fractionating mineral assemblages and allow for variable r-values as magmas evolve.

4.5. CONCLUSIONS

New geochemical data combined with petrographic observations from Tongariro whole-rock samples, groundmass separates and metasedimentary inclusions reveal a complex interplay between magma assembly processes over Tongariro's lifespan. The key findings of this study follow.

1) Tongariro eruptives are medium-K basaltic-andesites, andesites and dacites that contain dacitic to rhyolitic interstitial melts with up to ~7 wt% K_2O.
2) Phenocryst cargoes in Tongariro magmas are most commonly plagioclase-dominated over orthopyroxene, clinopyroxene, olivine, hornblende (Tupuna Formation only), Fe-Ti oxides and apatite. In contrast, fractionating mineral assemblages typically contain greater proportions of pyroxene than plagioclase, and early crystallisation-differentiation (for basalt to basaltic-andesite compositions) is chiefly represented by olivine with lesser amounts of pyroxene. Differences in crystallising versus fractionating minerals indicate that crystal-melt separation is more efficient for olivine and pyroxene but less so for plagioclase, which suggests that AFC modelling with plagioclase-dominated fractionating assemblages (e.g. Price et al., 2012; Conway et al., 2018) should be applied with caution to andesitic magma systems. Overstated plagioclase fractionation will result in greater Sr removal from crystallising magmas, which will lead to accelerated (modelled) rates of $^{87}Sr/^{86}Sr$ increase to crustal values, and may not reflect nature.
3) Inclusions in Tongariro magmas represent cognate crystal clots of aggregated phenocrysts and antecrysts, andesite lithics, magmatic enclaves and, most commonly, metasedimentary xenoliths.
4) Metasedimentary xenoliths in Tongariro magmas were derived from at least two (or three) greywacke terranes that form the basement rocks to depths of at least 15 km beneath Tongariro. Nd-Pb isotope ratios indicate that assimilated metasedimentary country rock was primarily derived from the Kaweka terrane but the Pahau and/or Waipapa terrane were also involved. $^{87}Sr/^{86}Sr$ ratios in bulk metasedimentary xenoliths probably shifted to values ~0.002 lower than their protolith equivalents due to the disproportionate loss of radiogenic Sr hosted in biotite and alkali feldspar, which were preferentially melted when xenoliths were entrained into hot magmas.
5) Th/U fractionation occurred in metasedimentary xenoliths relative to their protoliths because of U loss that was likely associated with zircon dissolution. This Th/U fractionation has modified $^{208}Pb/^{206}Pb$ (and $^{208}Pb/^{207}Pb$) ratios to higher values, potentially by +0.004.

6) Assimilated country rock accounts for ~22-31 wt% of Tongariro magmas. The compositions of assimilated materials are equal to bulk country rock compositions, because both pure melts derived from dissolved minerals and unmolten restites are incorporated simultaneously (e.g. White and Chappell, 1977). This process probably occurs via wall-rock stoping that is facilitated by frictional stresses from ascending magmas and reduced grain-boundary cohesion that results from incongruent melting. Country rock melts were probably produced from dissolved biotite, alkali feldspar, zircon and phosphate minerals. Restites are composed of plagioclase, pyroxene, quartz, Fe-Ti oxides and in rarer occasions biotite, zoisite, corundum and tourmaline.
7) The ratio of mass assimilation rate (M_a) over mass fractional crystallisation rate (M_c)—a.k.a. the r-value of DePaolo (1981)—at Tongariro is initially high (1.8-3.5) for replenishing basalt magmas that evolve to basaltic-andesites via AFC processes, which primarily fractionate olivine. Subsequent evolution from basaltic-andesites to dacites is represented by r-values of ~0.1-1.0 (average of ~0.5), which indicates increased and varied amounts of crystal fractionation relative to country rock assimilation in the mid- to shallow-crust.
8) Radiogenic contamination of magmas with Sr-Nd-Pb isotopes derived from country rock(s) occurred to varied extents for each isotope system. In whole-rock and groundmass samples, Sr and Nd isotopic contrasts with metasedimentary xenoliths and their protolithic sources are retained. In contrast, Pb isotope equilibration is rapid and results in strong overlap between whole-rock, groundmass, metasedimentary xenolith and reference greywacke Pb isotope ratios.
9) Systematic covariance in Sr and Nd isotope ratios is observed in whole-rock and groundmass pairs (of the same sample). This result implies a consistent balance between rates of crystal fractionation and country rock assimilation because phenocrysts, whole-rock aliquots and interstitial melts (groundmass separates) have highly similar $^{87}Sr/^{86}Sr$ and $^{143}Nd/^{144}Nd$ isotope ratios. This situation contrasts with the much greater $^{87}Sr/^{86}Sr$ and $^{143}Nd/^{144}Nd$ isotope ratio differences between different samples.

Chapter 5

An integrated time-space-composition evolution of edifice-forming eruptives at Tongariro volcano, New Zealand

"Bulk chemical trends at arc volcanoes are not liquid lines of descent"

Eichelberger et al. (2006)

5.1. INTRODUCTION

Petrogenetic studies of erupted materials at arc volcanoes have evolved from traditional models that attempted to explain compositional diversity via crystal fractionation alone to models that incorporate significant contributions from assimilated crust (e.g. Gill, 1981). Subsequent evidence, particularly from crystal-specific studies, for open-system evolution at intermediate-composition arc volcanoes has further influnced models for andesite magma assembly (Eichelberger, 1975; Gamble et al., 1999; Izbekov et al., 2004; Humphreys et al., 2006a). These models emphasise that compositional trends at arc volcanoes are liable to be misinterpreted unless they are considered within a chronostratigraphic context (Eichelberger et al., 2006; Conway et al., 2018). Where arc volcanoes have been mapped in detail, time-composition trends in eruptive records provide sequential, long-term and potentially high-resolution records of how magma systems evolve compositionally through stratovolcano lifespans (Schmidt and Grunder, 2011; Hildreth and Fierstein, 2012; Price et al., 2012; Conway et al., 2018).

This study contributes a high-resolution temporal reconstruction of magma diversity over Tongariro's ~350 ka lifespan with the aim of identifying and interpreting patterns in time-composition relationships. The eruptive stratigraphy presented for edifice-forming products of Tongariro in Chapter 3 and the geochemical data presented in Chapter 4 form the basis of time-composition relationships investigated here. Geochemical data are arranged chronologically to examine relationships between major oxide, trace element and Sr-Nd-Pb isotope compositions in individual samples with $^{40}Ar/^{39}Ar$ age determinations and their assigned stratigraphic units. These investigations focus on whether time-composition trends demonstrate cyclicity, whether composition-volume relationships can provide novel context into petrogenetic processes and also offer a new dataset for assessing petrogenetic models for arc volcanoes (cf. Hildreth and Moorbath, 1988; Annen et al., 2006; Eichelberger et al., 2006).

5.2. METHODS AND DATASETS

All analytical procedures are described in full in Chapter 2. The petrographic and geochemical data in this chapter were presented in chapters 3 and 4 and appendices 5 and 6, but with limited stratigraphic context. Modal phenocryst concentrations were estimated on ~230 samples with the charts of Terry and Chilingar (1955), which yield concentrations precise to ≤5 vol%. Where geochemical data are presented for stratigraphic units, as opposed to individual samples, the range is shown with the adopted ages and the total ranges in mean geochemical values of individual samples: these are represented as crosses in the diagrams of this chapter. The ranges of major oxide concentrations in stratigraphic units were defined with XRF data from this study and

Hobden (1997), and were supplemented with the XRF data of Cole (1978, 1979) for the Mangatetipua and Heretoa members of the Te Maari area. One sample from Cole et al. (2018) has previously reported major oxide concentrations and a $^{40}Ar/^{39}Ar$ age determination (RPC110); in addition, trace elements and isotopic compositions were measured in this study. For trace element and Sr-Nd-Pb isotope compilations, all ICP-MS and TIMS data collected in this study (Chapter 4) were combined with TIMS and INAA data from Hobden (1997). Exceptions are for the Mangatetipua and Heretoa members, for which only XRF trace element data from Cole (1978, 1979) were available, and Sr-Nd-Pb isotope data for the Te Rongo Member (Red Crater Formation) which is from Shane et al. (2017). The 189-130 ka Te Pakiraki Member is subdivided into 189-152 ka and 150-130 ka groups, because of the Waiaruhairiki Member that was erupted between 152-150 ka (Chapter 3; Appendix 2).

5.3. RESULTS

Data presented here show how Tongariro eruptive compositions vary over the volcano's lifespan. Bulk modal phenocryst mineral abundances, major oxide and trace element concentrations and Sr-Nd-Pb isotopic ratios are examined for the period since 350 ka. Where possible, lava whole-rock samples and lava groundmass separates are shown in the same diagrams. Groundmass separates that were analysed geochemically (n = 37) were prepared in tandem with aliquots for $^{40}Ar/^{39}Ar$ geochronology, and therefore have specific age determinations. However, eleven of these separates do not have determined ages because they were either withheld from analysis, or yielded meaningless ages, or were deemed to be inaccurate after analysis because of unsuitably high proportions of glass.

Time-composition comparisons consider both the individual samples and their assigned stratigraphic units. The latter represents the total compositional range of all samples in that stratigraphic grouping and may encompass several samples with individual $^{40}Ar/^{39}Ar$ age determinations: elsewhere, ages were inferred from field relationships (see Chapter 3). The field-defined relative age constraints on stratigraphic units allow more samples without individual $^{40}Ar/^{39}Ar$ age determinations to be placed in eruptive chronology. Exposures and consequent sampling of pre-230 ka eruptives are limited and thus potentially unrepresentative of time-composition variation in the 350-240 ka period: discussion and interpretation of these data are less detailed than for ≤230 ka eruptives.

5.3.1. Petrography versus time

The total phenocryst concentrations in Tongariro eruptives have minor systematic variation through time (Fig. 5.1). Total concentrations range from ~5-50 vol% (Table 3.3) and are most commonly between 25-40 vol%. Two periods of systematic decline from ~40 to 25 vol% are observed between 125 and 110 ka and between 100 and 50 ka. The latter is a stronger relationship because it is constrained by seven successive stratigraphic units and represents a 50 kyr interval whereas the former is only defined by three units and a 15 kyr interval. The modal proportions of phenocrysts are not compared with time because observations are generally qualitative (Table 3.3).

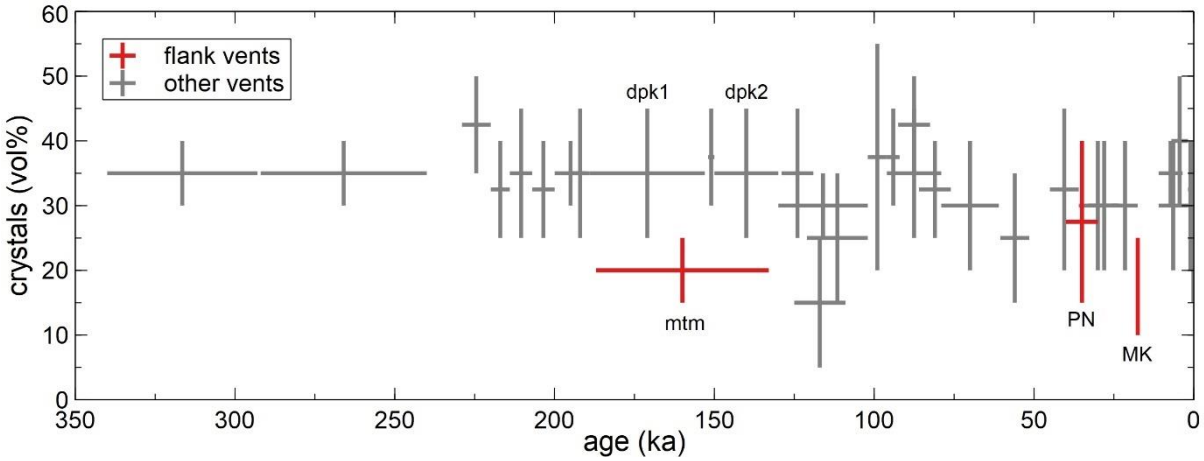

Figure 5.1. Total crystal concentrations versus time for the Tongariro eruptive units considered in this thesis. The crosses show the possible age ranges of each stratigraphic unit (= width: see Chapter 3) and the total range in observed crystal contents for that unit (= height: Table 3.3), plus an additional uncertainty of ± 5 vol% which accounts for the precision associated with hand-specimen estimates using the charts of Terry and Chilingar (1955). The 189-130 ka Te Pakiraki Member is subdivided into pre- and post-Waiaruhairiki Member groups (either side of 152-150 ka), labelled dpk1 and dpk2, respectively. Flank vents, from oldest to youngest, are the Tātaramoa Member (~160 ka: mtm), Pukeonake Formation (~35 ka: PN) and Makahikatoa Formation (~17.5 ka: MK).

5.3.2. Major oxides versus time

Variations in major oxide concentrations show minor systematic variation through time (Fig. 5.2), except for MgO-time relations (Fig. 5.2c), as previously considered in section 3.5.4 (Fig. 3.14). Time-composition patterns displayed by individual samples are similar to the time-composition patterns displayed by total compositional ranges in their associated stratigraphic units, as is generally assumed in most time-composition studies of stratovolcanoes (e.g. Schmidt and Grunder, 2011; Fierstein et al., 2011; Jicha et al., 2012; Calvert et al., 2018; Conway et al., 2018). Time-SiO_2 relationships from ~300 ka are scattered for individual samples and their parental stratigraphic units (Fig. 5.2a). SiO_2 concentrations appear to cluster around ~60 wt% at ~200 ka,

~59 wt% at ~100 ka and ~58 wt% in the Holocene, thereby defining a generalised trend of decreasing SiO_2 over Tongariro's lifespan, albeit with large amounts of scatter. This trend is reflected in a greater frequency of >61 wt% SiO_2 concentrations in ~300-150 ka eruptive units relative to a greater frequency of <57 wt% SiO_2 concentrations in eruptive units since ~50 ka.

Time-MgO relationships show ~10-70 kyr cycles of steeper MgO increases to ≥5-9 wt% followed by more gradual declines that begin by ~230 ka and at ~160, ~88, ~56 ka and during the Holocene (Fig. 5.2c). Patterns of MgO increase and decrease are more systematic in stratigraphic unit ranges than for individual samples. Potentially two parallel arrays occur in the ~150-100 ka interval, which begin from elevated MgO concentrations defined by the ~160 ka Tātaramoa (5.3 wt%) and ~117 ka Mangahouhounui (6.1 wt%) members. The regression line shown in Fig. 5.2c occurs between these parallel arrays and was determined for all stratigraphic unit data in the 160-100 ka interval. Two flank vents display elevated MgO concentrations of ~8.9 wt% at ~35 ka (Pukeonake Formation) and ~7.0 wt% at ~17.5 ka (Makahikatoa Formation) and are offset from the main array. Similar patterns of sharper increases then more gradual decreases, with the nodes at similar time spacings, are observed for Al_2O_3 which increases to ~18 wt% at ~230, ~160, ~110, ~30 ka and in the Holocene (Fig. 5.2b). CaO increases to ~8 wt% at ~230 and ~117 ka but data are generally more scattered (Fig. 5.2d). Variation in time versus K_2O concentrations (Fig. 5.2e) is scattered but is synchronised with variations in SiO_2 concentrations (Fig. 5.2a) and Rb/Sr ratios, as described in section 5.3.3 (Fig. 5.3a).

Figure 5.2. (Next page.) Major oxide versus time for Tongariro eruptives. Stratigraphic units (grey crosses) show the total range of determined compositions and ages defined by $^{40}Ar/^{39}Ar$ age results and field relationships. Individual samples (black filled circles) are plotted with their individual $^{40}Ar/^{39}Ar$ age determinations and 2 s.d. age errors. Flanks vents (red crosses) are the Tātaramoa Member (~160 ka: mtm), Pukeonake (~35 ka: PN) and Makahikatoa (~17.5 ka: MK) formations which are symbolised as stratigraphic units. Key in (**a**) applies to all panels. Major oxide data are from this study, Hobden (1997), Cole (1978, 1979) and Cole et al. (2018): ages are as presented in Chapter 3. Regression lines for data between interpreted pivot points are shown for MgO (**c**), following Fig. 3.14 (Chapter 3): pivot points are as in Table 5.1 and Fig. 5.5.

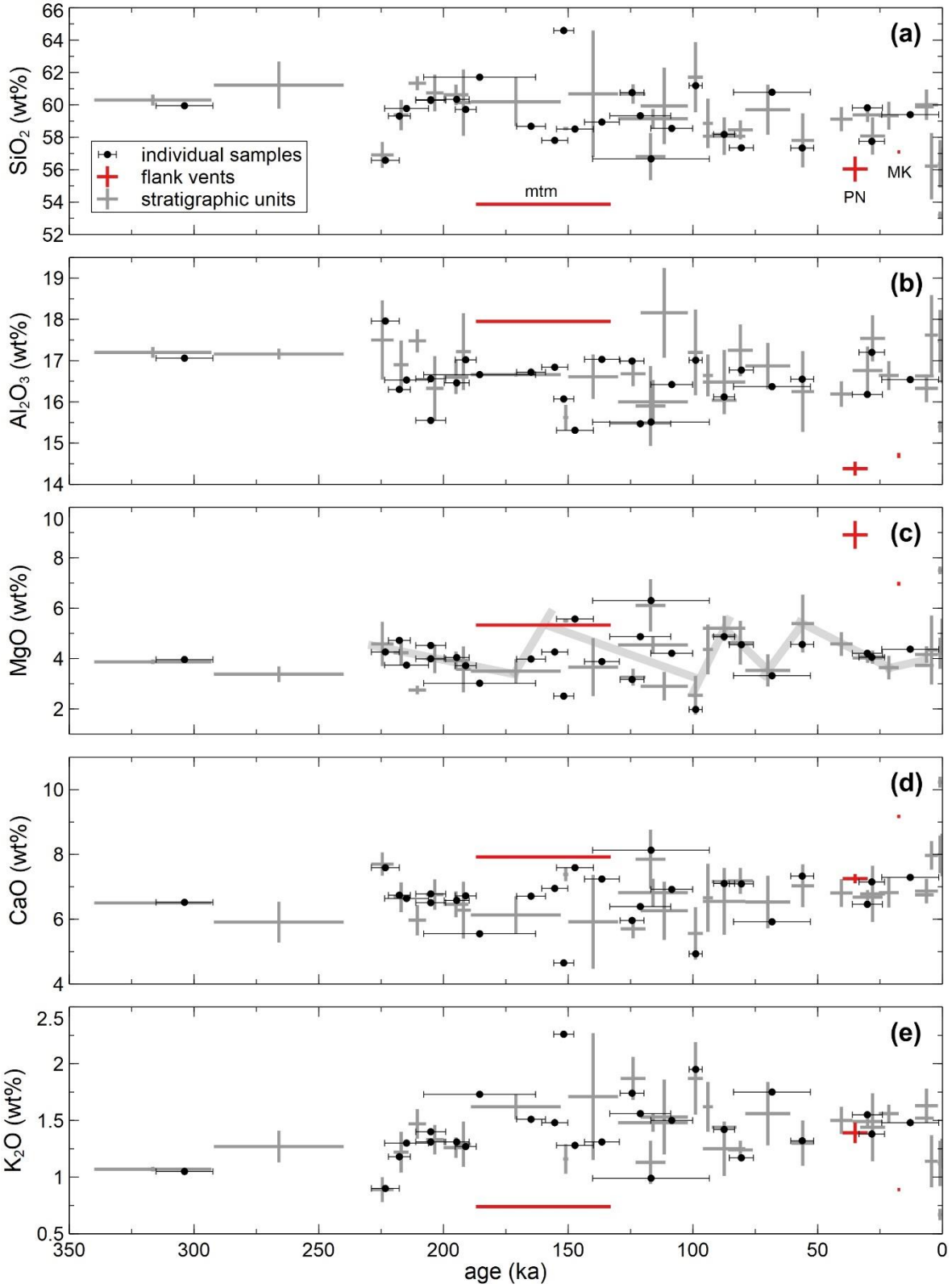
(a)
(b)
(c)
(d)
(e)
SiO2 (wt%)
Al2O3 (wt%)
MgO (wt%)
CaO (wt%)
K2O (wt%)
individual samples
flank vents
stratigraphic units
mtm
MK
PN
age (ka)

5.3.3. Trace elements versus time

Trace element concentrations and ratios show systematic and synchronised variations through time (Fig. 5.3). Similar patterns are observed for individual whole-rock and groundmass pairs and their encompassing stratigraphic units. Offsets between paired groundmass separates and whole-rock values indicate the direction of magma evolution, wherein groundmass separates have higher Rb/Sr ratios by ~0.1, higher Zr concentrations by ~10-30 ppm, lower Eu/Eu* ratios by ~0.1 and lower Sm/Nd ratios by ~0.01 but have similar Ba/La ratios to their whole-rock counterparts.

The Rb/Sr ratios and Zr concentrations of stratigraphic units and individual samples show regular versus scattered variations between values of ~0.1-0.5 and ~70-170 ppm, respectively (Fig. 5.3a-b). Note that patterns in absolute Rb concentrations versus time are effectively identical to Rb/Sr versus time patterns (not shown). The timings of Rb/Sr and Zr variation are similar to SiO_2 and K_2O variations (Fig. 5.2a, e), which suggest that these compositional indices are controlled by synchronised or shared magma processes. Between ~230-210 ka, stratigraphic unit and individual whole-rock Rb/Sr ratios increase from ~0.1 to 0.2 and Zr concentrations increase from ~85 to 105 ppm. From ~200 ka to present, stratigraphic unit Rb/Sr ratios and Zr concentrations become scattered, although both show similar patterns with maxima up to Rb/Sr ~0.3 and ~150 ppm Zr at ~170, ~125, ~100 and ~70 ka. Minima are observed down to Rb/Sr ~0.05-0.1 and ~75-90 ppm Zr at ~195, ~150, ~117, ~88-81, ~56 ka and in the Holocene, with similarly low Rb/Sr and Zr for ~17.5 ka Makahikatoa Formation flank vent eruptives.

Figure 5.3. (Next page.) Selected trace elements versus time for Tongariro whole-rock (WR: filled circles) and groundmass (GM: open circles) samples and stratigraphic unit ranges (grey crosses). Flank vents shown by red crosses. Key in (**a**) applies to all panels. Data are from this study (ICP-MS), Hobden (1997) (INAA and XRF) and Cole (1978, 1979) (XRF). Outliers are indicated with arrows in (**a**: LP051) and (**c**: RPC110). Age data for RPC110 were reported previously by Cole et al. (2018). The height of crosses represents the range of mean values in each stratigraphic unit (or flank vent) with inferred age ranges as defined as in Chapter 3 (horizontal width of crosses). Flank vents depicted are the ~35 ka Pukeonake and ~17.5 ka Makahikatoa formations (red).

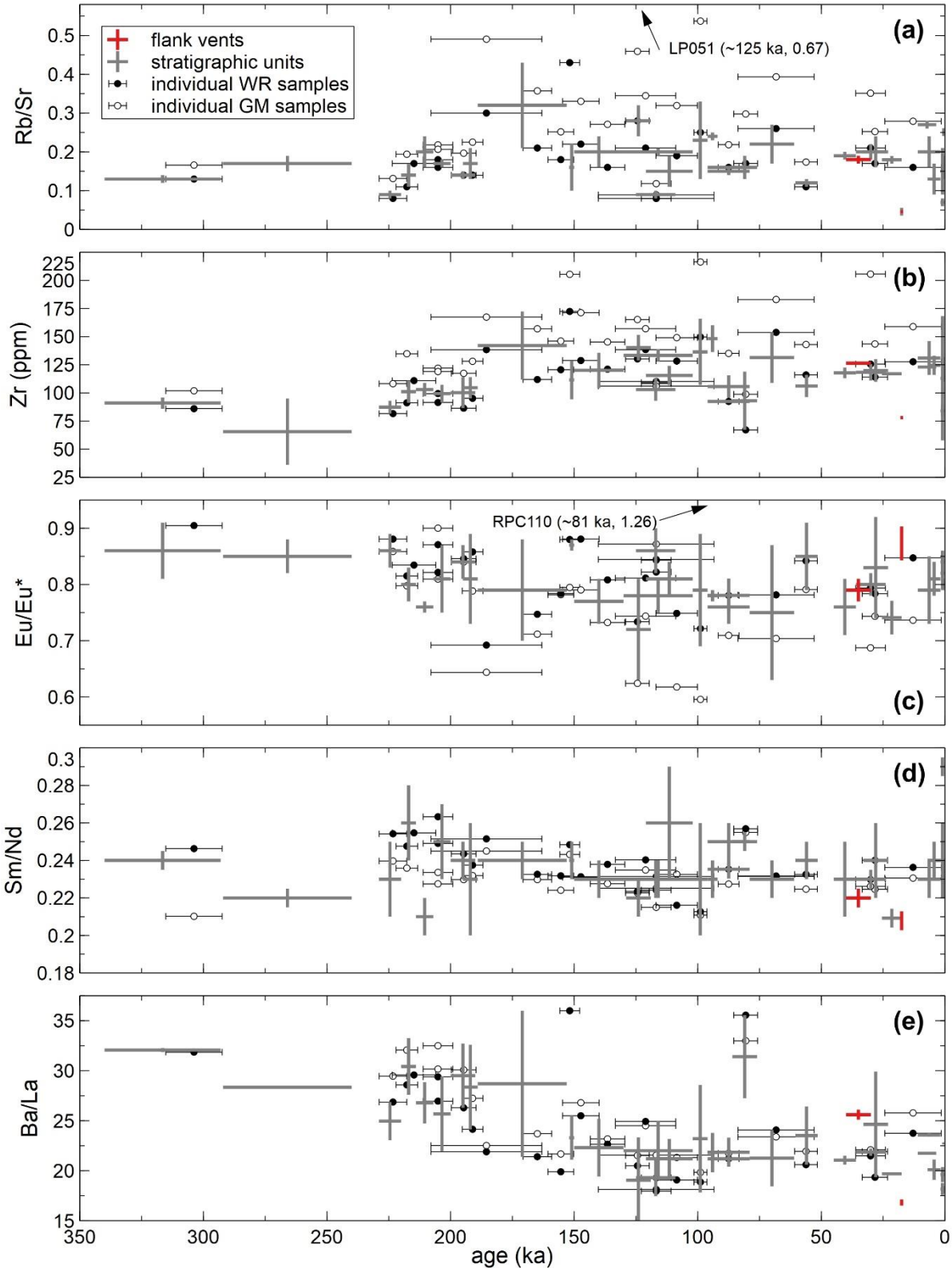
flank vents
stratigraphic units
individual WR samples
individual GM samples
LP051 (~125 ka, 0.67)
RPC110 (~81 ka, 1.26)
(a)
(b)
(c)
(d)
(e)
Rb/Sr
Zr (ppm)
Eu/Eu*
Sm/Nd
Ba/La
age (ka)

Rb/Sr and Zr versus time patterns are similar to other incompatible element concentrations (not shown) and are mirrored by time-Eu/Eu* variation (Fig. 5.3c). Eu/Eu* ratios decrease from ~0.87-0.75 between ~230-210 ka which is followed by maxima of ~0.85-0.90 at ~195, ~150, ~117, ~100, ~88, ~56, ~28 ka and during the Holocene, with similarly high Eu/Eu* for ~17.5 ka Makahikatoa Formation flank vent eruptives. Eu/Eu* minima of ~0.65-0.75 are observed at ~170, ~125, ~100, ~70, ~40 and ~20 ka. Synchronised Rb/Sr, Zr and Eu/Eu* variations are consistent with Rb and Zr enrichments and Sr and Eu losses, which likely involved the fractionation of plagioclase because of Kd values >3 for Sr and Eu^{2+} into plagioclase (Rollinson, 1993 and references therein).

Time-composition patterns observed for Sm/Nd and Ba/La ratios are synchronised and are similar to Eu/Eu* variations (Fig. 5.3c-e). From ~230-100 ka, Sm/Nd ratios decrease from ~0.27 to 0.21 as do Ba/La ratios from ~33 to 20, and are followed by increases to Sm/Nd ~0.23-0.26 and Ba/La ~28-35 between ~100-80 ka. Subsequent decreases to Sm/Nd ~0.21 and Ba/La ~20 occur gradually from ~80-20 ka. These successive periods of gradual decline in Sm/Nd and Ba/La ratios may reflect greater incompatibilities of Nd relative to Sm and La relative to Ba for fractionating assemblages. However, this hypothesis is not supported by the presence of basaltic-andesite flank vent eruptives that have Sm/Nd ratios of ~0.22-0.25 and Ba/La ratios of ~20-26 that are similar to most other eruptives and are lower than maxima of Sm/Nd ~0.28 and Ba/La ~35. These observations suggest that Sm/Nd and Ba/La ratios are more strongly controlled by a process other than crystal fractionation.

Figure 5.4. (Next page.) Sr-Nd-Pb isotope ratios versus time for Tongariro whole-rock (WR: filled circle) and groundmass (GM: open circles) samples and stratigraphic unit ranges (grey crosses). Flank vents (red crosses) are the Pukeonake (PN, ~35 ka) and Makahikatoa (MK, ~17.5 ka) formations. Pb data are unavailable for the Makahikatoa Formation. Key in (**a**) applies to all panels. Data are from this study, Hobden (1997) and Cole et al. (2018). The height of crosses represents the range of mean values in each stratigraphic unit (or flank vent) with inferred age ranges from Chapter 3 (width of crosses). All data determined via TIMS.

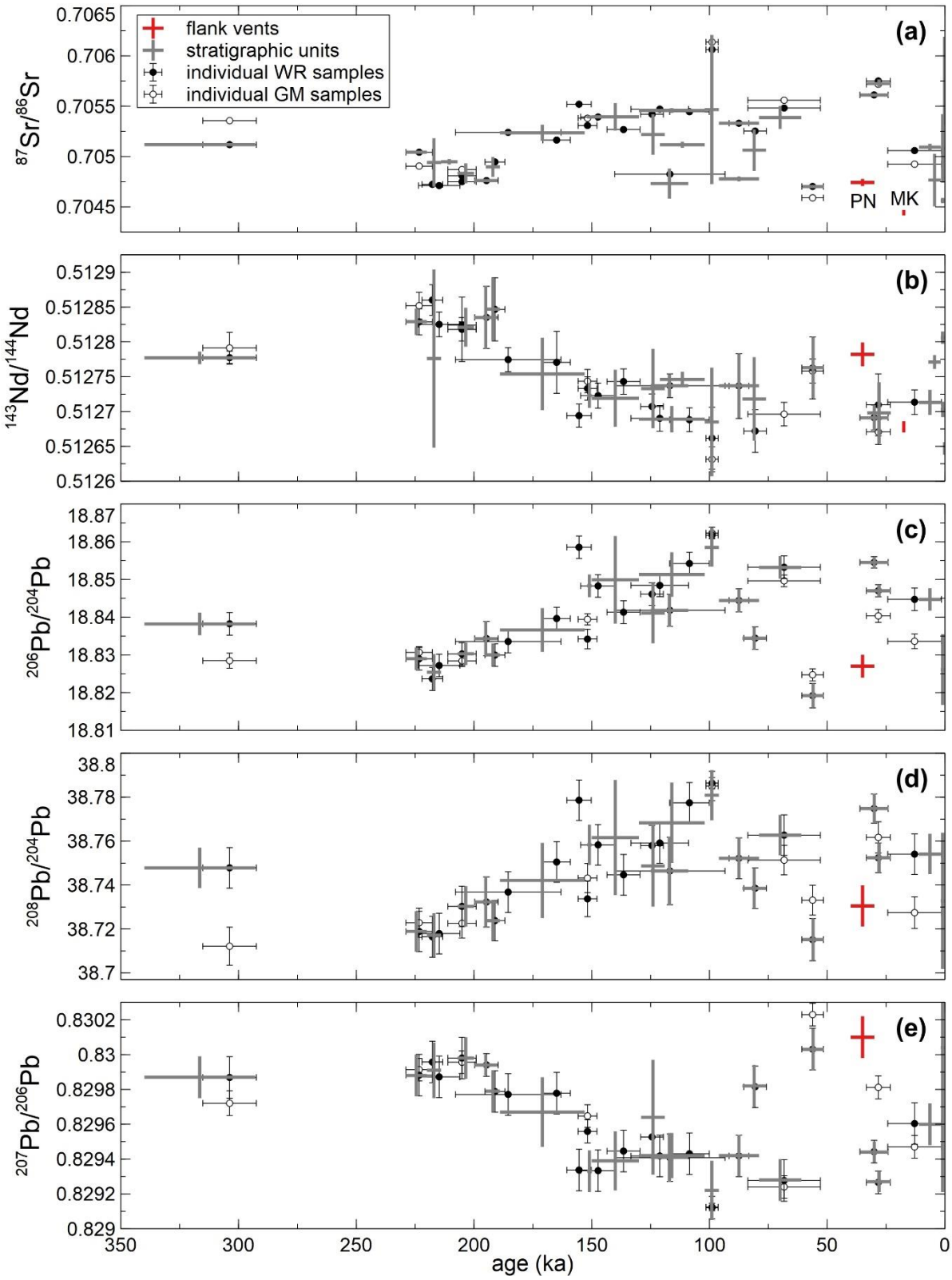
flank vents
stratigraphic units
individual WR samples
individual GM samples
(a)
(b)
(c)
(d)
(e)
PN
MK
$^{87}Sr/^{86}Sr$
$^{143}Nd/^{144}Nd$
$^{206}Pb/^{204}Pb$
$^{208}Pb/^{204}Pb$
$^{207}Pb/^{206}Pb$
0.7065
0.706
0.7055
0.705
0.7045
0.5129
0.51285
0.5128
0.51275
0.5127
0.51265
0.5126
18.87
18.86
18.85
18.84
18.83
18.82
18.81
38.8
38.78
38.76
38.74
38.72
38.7
0.8302
0.83
0.8298
0.8296
0.8294
0.8292
0.829
350
300
250
200
150
100
50
0
age (ka)

5.3.4. Sr-Nd-Pb isotopes versus time

Time-composition relationships for Sr-Nd-Pb isotope ratios (incorporating some Sr and Nd isotope data from Hobden, 1997) show synchronised and systematic trends of increasing $^{87}Sr/^{86}Sr$, $^{206}Pb/^{204}Pb$ and $^{208}Pb/^{204}Pb$ with decreasing $^{143}Nd/^{144}Nd$ and $^{207}Pb/^{206}Pb$, and therefore display some of the clearest evidence for composition variations versus time at Tongariro volcano (Fig. 5.4). Between ~230 and 100 ka, $^{87}Sr/^{86}Sr$ ratios increase from ~0.7047 to ~0.7060, $^{143}Nd/^{144}Nd$ ratios decrease from ~0.51285 to ~0.51265, $^{206}Pb/^{204}Pb$ ratios increase from ~18.82 to ~18.86, $^{208}Pb/^{204}Pb$ ratios increase from ~38.71 to ~38.78 and $^{207}Pb/^{206}Pb$ ratios decrease from ~0.8300 to ~0.8291, which reflect contemporaneously increasing crustal isotopic character. In contrast, time-isotope ratio trends for the ~100-0 ka interval are scattered, most notably for $^{87}Sr/^{86}Sr$ ratios that vary between ~0.7045 and ~0.7061. During this period, flank vents from the Pukeonake and Makahikatoa formations define minima of ~0.7044-0.7047, while other eruptives define a maximum of ~0.7057 at ~30 ka (Fig. 5.2a; Hobden, 1997). $^{143}Nd/^{144}Nd$ ratios are less scattered as shown by an increase from ~0.51265 to ~0.51275 between ~100 to ~56 ka, a decline to ~0.5127 at ~30 ka, then scatter between ~0.51265-0.51275 leading into and throughout the Holocene (Fig. 5.2b; Hobden, 1997). Within this interval, the ~35 ka Pukeonake Formation displays $^{143}Nd/^{144}Nd$ ratios of 0.51278. In general, these trends are mirrored by time-Pb isotope ratio variations for the same intervals at ~100-56 ka, ~56-30 ka and ~30-0 ka (Fig. 5.2c-e). Compared with isotope ratio variation since 230 ka, Sr-Nd-Pb isotope ratios for the 349-293 ka Tupuna Formation are similar to median and average values of all other younger Tongariro eruptives, although isotope ratio variations in the ~290-230 ka window are not well sampled with available data and therefore compositional variations during this interval are unclear.

5.4. DISCUSSION

5.4.1. Summary of time-composition relationships

Time-composition relationships for major oxides, trace elements and radiogenic isotopes commonly display contemporaneous variations that suggest that they are controlled by coupled or shared magmatic processes. Amongst other representative compositional parameters, systematic time-composition variations are observed for MgO, Rb/Sr, $^{143}Nd/^{144}Nd$ and $^{206}Pb/^{204}Pb$ (Fig. 5.5) relative to other compositional parameters such as SiO_2, CaO, Eu/Eu* and $^{87}Sr/^{86}Sr$, which display more irregular time-compositional variations (Figs. 5.2-5.4). MgO, Rb/Sr, $^{143}Nd/^{144}Nd$ and $^{206}Pb/^{204}Pb$ time-composition data for each stratigraphic unit are presented with linear regressions between the pivot-points that define ~10-70 kyr sub-trends, as summarised in

section 5.3. These time-composition arrays illustrate the long-term evolution of Tongariro's magma system, as follows.

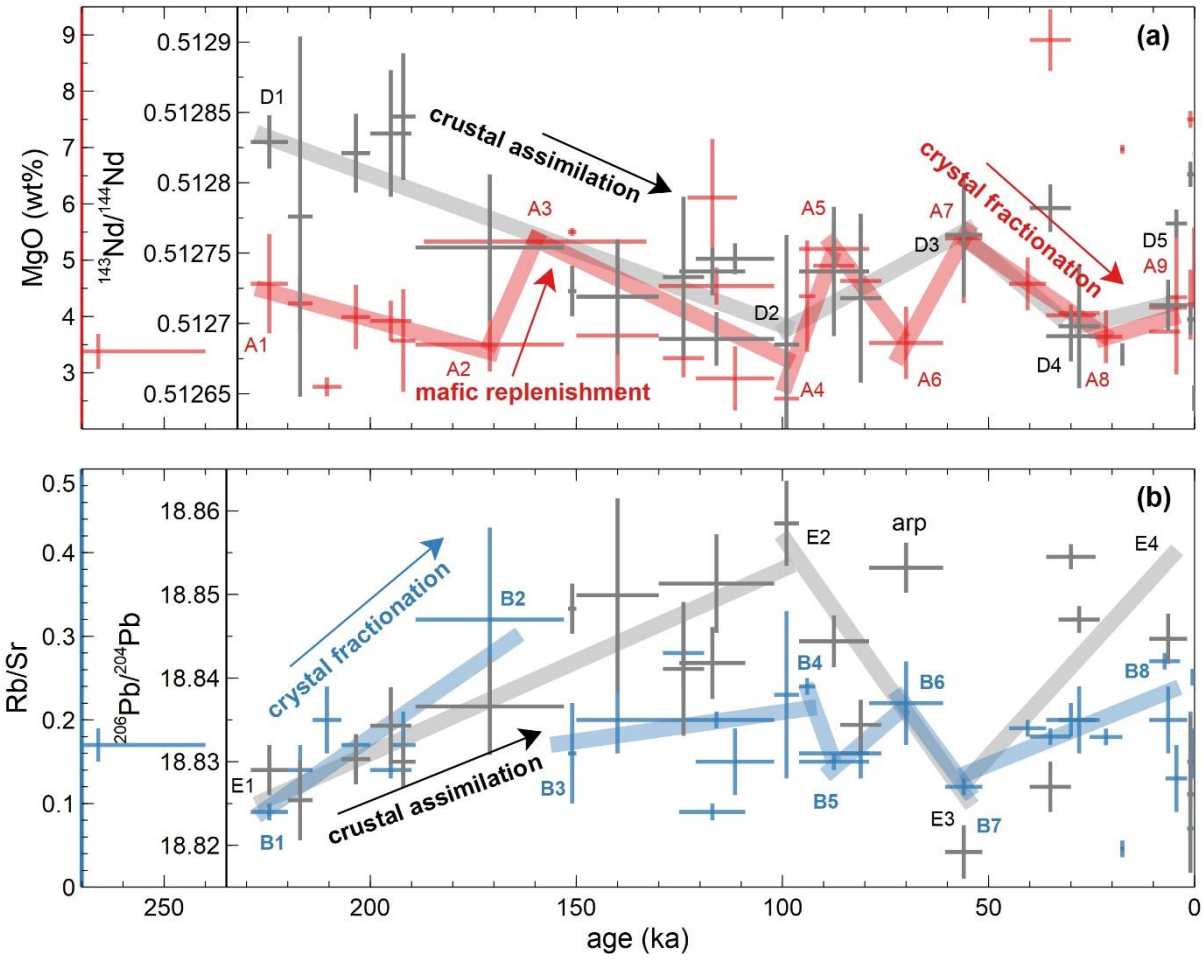

Figure 5.5. Selected composition versus time relationships for stratigraphic units (crosses). Annotations, data, regression lines and axes are coloured differently for each compositional parameter. **(a)** red = MgO, black/grey = $^{143}Nd/^{144}Nd$ ratios; **(b)** blue = Rb/Sr, black/grey = $^{206}Pb/^{204}Pb$. The Rotopaunga Member (arp) is labelled in (**b**). Regression lines were calculated for all data between pivot points A_1-A_9, B_1-B_8, D_1-D_5 and E_1-E_4 except for the ~210 ka Upper Tama Member (outlier), ~35 ka Pukeonake Formation (flank vent),~17.5 ka Makahikatoa Formation (flank vent) and Te Pupu Formation (late Holocene materials swayed by small-volume [<0.01 km^3] eruptions). Pivot points and regression equations are reported in Table 5.1.

Central edifice eruptives at Tongariro display elevated MgO concentrations of ≥5-9 wt% peaking at ~230, ~160, ~117, ~88, ~56 ka and during the Holocene, which are interpreted to represent periods of enhanced mafic replenishment (Fig. 5.5a). MgO-rich lavas at ~35 ka (Pukeonake Formation) and ~17.5 ka (Makahikatoa Formation) also indicate mafic replenishment, although these are excluded from time-composition regressions because they were erupted from flank vents. Field observations are unable to demonstrate whether or not the

~117 ka Mangahouhouiti Member was erupted from a flank vent (Chapter 3), and therefore this unit is included in the time-composition regression for the ~160-100 ka interval. Mafic replenishment events and the intervening periods of sequential magma evolution are separated by ~10-70 kyr which show that although mafic magma supply rates and crustal residence durations are cyclic, they are spaced at irregular intervals.

Rb/Sr variations are broadly synchronised with variations in MgO concentrations and Nd-Pb isotope ratios (Fig. 5.5). Intervals of decreasing MgO concentrations from ≥5 wt% to ~3 wt% coincide with intervals of increasing Rb/Sr ratios to ≥0.2, which suggests that mafic replenishment events reset Rb/Sr ratios to values of ≤0.1 and temporarily reduce crystal fractionation rates for periods of ~10 kyr. Overlap between Rb/Sr ratios in whole-rock (~0.1-0.3) and basement reference samples (~0.1-0.8: Price et al., 2015) indicates that Rb/Sr variation is controlled by crystal fractionation processes more strongly than by crustal assimilation processes (Fig. 5.5b), relative to Rb/Sr ≤0.05 in regional basalts (Gamble et al., 1993). On the other hand, trace element ratios such as Sm/Nd (Fig. 5.3d) mirror the variations observed in Nd-Pb isotope ratios (Fig. 5.4) and more likely reflect crustal assimilation because of contrasts between Sm/Nd ratios in whole-rock samples (generally 0.21-0.28) versus greywacke reference samples (generally 0.16-0.22: Price et al., 2015) and metasedimentary xenoliths (generally 0.18-0.22).

Tongariro eruptives display Ba/La versus time trends that are parallel to evolution towards more crustal Nd-Pb isotope ratios, suggesting that Ba/La ratios decrease with enhanced crustal contamination. Comparisons of Ba/La ratios in metasedimentary xenoliths (generally 10-20) and greywacke reference samples (10-20 for the Kaweka terrane and generally 10-30 for Pahau and Waipapa terranes: Price et al., 2015) relative to Tongariro whole-rock samples (Fig. 5.3e) indicate that Kaweka-type material is the dominant metasedimentary contaminant of Tongariro magmas. Moreover, the decreases in Tongariro whole-rock Ba/La ratios with ongoing evolution contrast with a study of central (Taupō) and northern (Okataina) TVZ rhyolitic eruptives and their adjacent mafic eruptives, wherein Ba/La ratios are inferred to increase with magma evolution (Rooney and Deering, 2014). In northern and central TVZ eruptives, Ba/La ratios are suggested to reflect heterogeneous mantle-derived inputs that are largely controlled by water concentrations in mantle-source regions (Rooney and Deering, 2014). In this model, Tongariro eruptives are more similar to the 'wet' northern TVZ basalts and rhyolites because mafic eruptives at Tongariro have Ba/La ratios of ~30-35 (Fig. 5.3), which are probably similar to their mantle-derived parental basalts.

Nd and Pb isotope ratios are generally less radiogenic when MgO concentrations are ≥5 wt%, and vice versa, except for the ~170-160 ka interval when MgO increases to ~5.5 wt% (which is, however, associated with a decrease in Rb/Sr ratios from ~0.32 to ~0.12: Fig. 5.5). These features indicate that the more crustal isotopic ratios in erupted magmas increase continuously until mixed with replenishing mafic magmas. Comparisons of Pb isotopic compositions in Tongariro whole-rock and groundmass samples, greywacke reference samples (Price et al., 2015) and metasedimentary xenoliths indicate that most Pb isotopic diversity in Tongariro magmas is created via contamination with Kaweka-type metasediments (Fig. 4.16).

Table 5.1. Regression equations for linear segments in MgO, Rb/Sr, $^{143}Nd/^{144}Nd$ and $^{206}Pb/^{204}Pb$ time-composition arrays shown in Figs. 5.5 and 5.6.

Stratigraphic unit (and pivot points)[1]	**Age range midpoint ± range (ka)**	**MgO midpoint ± range (wt%)**	**MgO regression equation**	**Rb/Sr midpoint ± range[2]**	**Rb/Sr regression equation**
mtu (A_1, B_1, D_1, E_1)	224.5 ± 4.5	4.58 ± 0.88	y = 0.020x – 0.0523 r^2 = 0.883	0.09 ± 0.01	y = -0.0034x + 0.859 r^2 = 0.700
atp	217 ± 3	4.23 ± 0.49		0.14 ± 0.03	
ato	203.5 ± 3.5	3.99 ± 0.57		0.17 ± 0.01	
apk	195 ± 5	3.92 ± 0.36		0.14 ± 0.01	
awp	192 ± 3	3.57 ± 0.91		0.17 ± 0.04	
dpk1 (A_2, B_2)	171 ± 18	3.50 ± 0.48		0.32 ± 0.11	
			y = -0.166x – 31.887 (r^2 = 1)		N/A
mtm (A_3)	160 ± 27	5.30		n.d.	
			y = 0.035x – 0.2262 r^2 = 0.306		
awh (B_3)	151 ± 1	5.50 ± 0.07		0.16 ± 0.06	y = -0.0007x + 0.2794 r^2 = 0.052
dpk2	140 ± 10	3.66 ± 1.15		0.20 ± 0.04	
arh	124 ± 5	3.26 ± 0.34		0.28 ± 0.04	
mhi	117 ± 6	6.11 ± 1.04		0.09 ± 0.01	
amp	116 ± 14	4.54 ± 0.33		0.20 ± 0.01	
apg	111.5 ± 9.5	2.90 ± 0.57		0.15 ± 0.04	
dtp (A_4)	99 ± 3	2.54 ± 0.77		0.23 ± 0.10	
			y = -0.203x + 22.928 r^2 = 0.9021		y = -0.0135x – 1.0311 r^2 = 0.985
aok (B_4)	94 ± 2	4.36 ± 0.99		0.24 ± 0.01	
atr	87.5 ± 5	4.90 ± 0.05		0.16	
awu (A_5, B_5)	87.5 ± 8.5	5.20 ± 0.50		0.15 ± 0.01	
			y = 0.096x – 3.1768 r^2 = 0.999		y = -0.0042x + 0.5104 r^2 = 0.944
ati	81 ± 5	4.63 ± 0.87		0.16 ± 0.03	
arp (A_6, B_6)	70 ± 9	3.53 ± 0.64		0.22 ± 0.05	
			y = -0.1331x + 12.844 (r^2 = 1)		y = -0.0067x – 0.253 (r^2 = 1)
att (A_7, B_7)	56 ± 4.5	5.39 ± 1.15		0.12 ± 0.01	
			y = 0.0502x + 2.5719 r^2 = 0.994		y = -0.0020x + 0.2465 r^2 = 0.6544
ari	40.5 ± 4.5	4.58 ± 0.47		0.19 ± 0.01	
amt	30 ± 6	4.02 ± 0.19		0.20 ± 0.02	
aww	28 ± 5	4.06 ± 0.26		0.20 ± 0.04	
api (A_8)	21.5 ± 4	3.64 ± 0.47		0.18 ± 0.01	
			y = -0.0221x + 4.0991 r^2 = 0.458		
aht	7.25 ± 3.75	3.73		0.27 ± 0.01	
ahi (A_9, B_8)	6.4 ± 4.6	4.16 ± 0.33		0.20 ± 0.04	

Table 5.1. Continued.

Stratigraphic unit	Age range midpoint ± range (ka)	$^{143}Nd/^{144}Nd$ midpoint ± range	$^{143}Nd/^{144}Nd$ regression equation	$^{206}Pb/^{204}Pb$ midpoint ± range	$^{206}Pb/^{204}Pb$ regression equation
mtu (D_1, E_1)	224.5 ± 4.5	0.512829±19	y = 0.00000107x + 0.5125917 r^2 = 0.716	18.8290±30	y = -0.00022x + 18.8750 r^2 = 0.810
atp	217 ± 3	0.512776±128		18.8254±48	
ato	203.5 ± 3.5	0.512821±28		18.8303±30	
apk	195 ± 5	0.512835±45		18.8343±46	
awp	192 ± 3	0.512847±45		18.8300±30	
dpk1	171 ± 18	0.512754±52		18.8366±58	
mtm	160 ± 27	n.d.		n.d.	
awh	151 ± 1	0.512723±18		18.8483±30	
dpk2	140 ± 10	0.512719±41		18.8499±116	
arh	124 ± 5	0.512733±57		18.8411±80	
mhi	117 ± 6	0.512737±17		18.8418±43	
amp	116 ± 14	0.512689±19		18.8513±59	
apg	111.5 ± 9.5	0.512746±11		n.d.	
dtp (D_2, E_2)	99 ± 3	0.512685±78		18.8585±51	y = 0.00070x + 18.7870 r^2 = 0.540
aok	94 ± 2	n.d.	y = -0.00000160x + 0.512855 r^2 = 0.792	n.d.	
atr	87.5 ± 5	0.512737±46		18.8444±31	
awu	87.5 ± 8.5	n.d.		n.d.	
ati	81 ± 5	0.512718±60		18.8344±30	
arp	70 ± 9	n.d.		18.8532±30	
att (D_3, E_3)	56 ± 4.5	0.512763±44		18.8192±32	y = -0.00054x + 18.8576 r^2 = 0.508
ari	40.5 ± 4.5	n.d.	y = 0.00000249x + 0.512623 r^2 = 0.977	n.d.	
amt	30 ± 6	0.512691±18		18.8545±15	
aww (D_4)	28 ± 5	0.512698±44		18.8470±16	
api	21.5 ± 4	n.d.	y = -0.00000070x + 0.512718 r^2 = 1	n.d.	
aht	7.25 ± 3.75	n.d.		n.d.	
ahi (D_5, E_4)	6.4 ± 4.6	0.512713±18		18.8447±30	

Stratigraphic unit ranges were calculated from data in this study, Hobden (1997) and Cole (1978, 1979). Pivot point define the stratigraphic units between which regressions are calculated and were chosen interpretively following consideration of whole-rock, groundmass and stratigraphic unit time-composition variations reported in section 5.3. The pivot points are denoted A_1…A_9 etc. are as annotated in corresponding Figs. 5.5 and 5.6, with A corresponding to MgO, B corresponding to Rb/Sr, D corresponding to $^{143}Nd/^{144}Nd$ and E corresponding to $^{206}Pb/^{204}Pb$. Regressions were calculated through the midpoints of compositional and age ranges for each stratigraphic unit, as shown in this table.

[1] dpk1 and dpk2 refer to 189-130 ka Te Pakiraki Member eruptives that occur before and after the intervening 152-150 ka Waiaruhairiki Member.

[2] Rb/Sr regression between B_1-B_2 calculated with the Upper Tama Member (aut: 210.5 ± 3.5 ka, Rb/Sr = 0.20 ± 0.04).

At Tongariro, coupled increases in Rb/Sr ratios and in radiogenic Nd and Pb isotope ratios indicate that crystal fractionation and crustal assimilation commonly occur contemporaneously (Fig. 5.5). Crystal fractionation proceeded to more advanced stages during intervals of prolonged crustal residence between ~230-170, ~160-100, ~88-70 and ~56-30 ka, which were intermittently reduced (or halted) when replenishing mafic magmas intruded and

mixed with pre-existing magmas at ~230, ~160, ~117, ~88, ~56 ka and during the Holocene, with concomitant decreases in the crustal isotopic character of magmas at these times (Fig. 5.5). In contrast, Oruanui and post-Oruanui eruptives at Taupō potentially show the reverse scenario wherein magma replenishment was possibly coupled with increased crustal Sr isotopic compositions (Sutton et al., 1995, 2000; Barker et al., 2015). However, the larger volumes and potentially more integrated crystal mush magma systems at voluminous rhyolitic volcanoes (e.g. Hildreth and Moorbath, 1988) possibly make such comparisons inapplicable, because of surface/area volume contrasts (see section 5.4.2, below) and the contrasting temperatures of andesitic and rhyolitic systems.

The processes driving decreasing bulk crystal abundances from ~100 ka (~40 vol%) to ~50 ka (~25 vol%: Fig. 5.1), appear to be coupled with increasing rates of mafic replenishment (Figs. 5.2c, 5.4a). Decreasing crystal concentrations through time may reflect shorter magma residence durations in the crust or thermochemical shifts in magmas influenced by mafic replenishment that inhibit or reduce crystallisation rates. However, this interpretation is not supported by the relatively radiogenic Sr-Nd-Pb isotope ratios observed for the ~70 ka Rotopaunga Member, which should display shifts to less radiogenic isotope ratios because of mixing with mafic magma, unless the mafic magma is enriched itself. Alternatively, the cause of reduced crystal concentrations may sometimes be thermal in origin, without chemical contamination (Figs. 5.4-5.5).

The observation of irregular cyclicity in time-composition variation for MgO, Rb/Sr, $^{143}Nd/^{144}Nd$ and $^{206}Pb/^{204}Pb$ (and other compositional parameters: see Figs. 5.2-5.4) implies non-uniform rates of mafic replenishment on timescales of >10 kyr, which contrasts with unidirectional thermal models for crustal evolution proposed elsewhere (cf. Annen et al., 2006). Instead, ~10-70 kyr intervals display compositional variations that exceed any long-term (≥150 kyr) compositional variations, which suggests that processes other than steady-state crustal heating have a greater influence on long-term compositional trends at Tongariro. An alternative process such as tectonics associated with southern TVZ rifting could influence the timing of mafic replenishment events and control the timescales of magma residence in the crust, via alternating crustal stress states (e.g. Lanphere and Sisson, 2003; Allan et al., 2012). This concept is developed further in section 5.4.5, below.

5.4.2. Composition-volume relationships

Volumes are commonly the most overlooked variable in petrogenetic processes, probably because they are challenging to estimate comprehensively and accurately. Further complexities are likely because the volumes of erupted magma may be detached from volumes involved with petrogenetic processes at depth. Discussions of elemental and isotopic concentrations in magmas commonly lack the context of their respective erupted volumes, which essentially reflect the surficial petrogenetic significance of such magmas. Some studies of arc volcanoes have drawn connections between erupted magma volumes and their compositions (e.g. Chen et al., 1993) whereas others have disputed them (e.g. Lanphere and Sisson, 2003).

Accurately estimating erupted volumes is challenging, if not impossible, for most previously-glaciated stratovolcanoes because systematic biases favour preservation during periods of reduced ice coverage (Hildreth and Fierstein, 2012; Conway et al., 2016) and of effusive, rather than explosive, eruptive products (e.g., Watt et al., 2013; Sisson et al., 2014; Vallance and Sisson, 2017). Such challenges may prevent meaningful investigations of erupted magma compositions and their respective volumes. This situation likely applies to Tongariro because of the preservation biases inferred from time-volume reconstructions relative to climate proxies (Chapter 3). Despite this, some examples have been used to show that edifice-building rates are greater during glacial periods (e.g. North Sister, Oregon Cascades: Schmidt and Grunder, 2009; Middle Sister, Oregon Cascades: Calvert et al., 2018) or have no relationship to the state of climate or to erupted magma compositions (Mount Rainier, Washington Cascades: Lanphere and Sisson, 2003; T. W. Sisson, pers. comm., 2018).

In contrast, Holocene eruptive volumes at Unzen volcano (Japan) are sometimes greater when Nd isotopic signatures are more mantle-like, although it is unclear whether this relationship has been sustained over Unzen's ~275 ka lifespan (Chen et al., 1993). Conversely, the most radiogenic $^{87}Sr/^{86}Sr$ ratio of 0.706165±14 determined on any Tongariro eruptive is from the 1975 CE Ngauruhoe pyroclastic avalanche deposit (Hobden et al., 1999; within the Matariki Member defined in this work), which is one of the smallest volume eruptive units known (0.002 km^3: Hobden et al., 2002). Eruptions of similar volume are likely to have occurred throughout Tongariro's lifespan, but their small volumes (and potentially unconsolidated pyroclastic constituents) would have been highly vulnerable to erosion and/or burial, hence their under-representation in the edifice record and the sampling in this study.

The volume of a magma may influence its composition because of thermodynamic consequences that result from contrasting surface area/volume ratios, wherein smaller magma volumes are exposed to greater areas of country-rock and therefore have a greater potential to

become contaminated. One example is the 0.002 km^3 1975 CE Ngauruhoe pyroclastic avalanche deposits because they are composed of basaltic-andesite, despite the high associated $^{87}Sr/^{86}Sr$ ratio, which suggests that the surface area/volume ratio during crustal storage may have influenced the amount of assimilated crust (towards more radiogenic isotope ratios) involved during magma assembly. However, other historical eruptions from Ngauruhoe also have small volumes (<0.008 km^3: Hobden et al., 2002) but have distinctly lower $^{87}Sr/^{86}Sr$ ratios of 0.70531-0.70569 (Hobden et al., 1999), which correlate with neither residence time nor crystal fractionation rates as indicated by U-series disequilibria measurements (Price et al., 2010). Idiosyncrasies in the local storage conditions of each magma body may therefore exert a greater influence on magma compositions than residence time (up to ~2 kyr: Price et al., 2010) or surface area/volume ratios for erupted magma volumes of <0.01 km^3. However, crustal residence time and surface area/volume ratios may result in significant contrasts in magma compositions where there are large differences (e.g. by ≥2 orders of magnitude) in crustal residence times and/or volumes.

Composition-volume relationships are therefore difficult to examine for meaningful periods of time (i.e. ≥100 kyr, not just the Holocene: cf. Hobden et al., 1999, 2002) or are hampered by incomplete eruption records for periods ≥100 kyr because of preservation biases relating to ice coverage (Chapter 3) or unequal vulnerability to erosion (i.e. lavas versus unconsolidated pyroclastic deposits). At both Tongariro and Ruapehu, the entire diversity of magma compositions over the lifespans of each volcano have been observed in eruptions since European arrival in New Zealand, effectively since ~1800 CE (Gamble et al., 1999; Nakagawa et al., 1999; Hobden et al., 1999, 2002). This is at odds with the long-term compositional trends observed for both Tongariro, as discussed above, and for Ruapehu by Price et al. (2012) and Conway et al. (2016, 2018). Therefore, it seems to be the smaller the volume window that is examined that the larger the diversity, and that the modern situation may in fact represent the smaller-scale 'background' activity that has been present through much of the lifetime of both Tongariro and Ruapehu. The historic record is represented by material that is small in volume, dominantly pyroclastic and most of which will not pass into the geological record. As a counterpoint, longer-term edifice records (i.e. ≥100 kyr) represent a smoothed running mean assessment of the compositions that are volumetrically dominant and overwhelmingly effusive at the volcano.

5.4.3. Tongariro versus Ruapehu time-composition relationships

Tongariro and Ruapehu, along with their magma systems, are separated by ~20 km along the NNE-SSW trending line of the TVZ arc and have been established through similar basement rocks. Both volcanoes have erupted basaltic-andesite to dacite magmas over their lifespans with the exposed Tongariro edifice being ~100 kyr older than that of Ruapehu (Chapter 3; Gamble et al., 2003; Conway et al., 2016). The general processes contributing to magma generation and assembly at each volcano are probably similar and thus provide a novel opportunity for comparing time-composition relationships at two adjacent natural 'magma factories'. Such comparisons can potentially demonstrate how the idiosyncrasies of each volcano—such as age, edifice structure, local rifting rate and previous glaciation—may have affected petrogenetic processes, despite other similarities.

Time-composition trends for Tongariro and Ruapehu are broadly similar for $^{87}Sr/^{86}Sr$ and $^{143}Nd/^{144}Nd$ ratios but less so for MgO and Rb/Sr (Fig. 5.6). MgO concentrations at Ruapehu decrease from ~8 to ~2 wt% between ~45 and 40 ka and are mirrored by increased Rb/Sr ratios from ~0.2 to ~0.6 (Gamble et al., 2003; Price et al., 2012; Conway et al., 2016, 2018), which is not observed in Tongariro time-composition arrays. However, at other times Ruapehu MgO concentrations display general similarity with Tongariro eruptives. Ruapehu MgO concentrations of ~5-7 wt% in 200-150 ka Te Herenga Formation eruptives are followed by a decline to ~3-6 wt% in 166-80 ka Wahianoa Formation eruptives (Gamble et al., 2003; Price et al., 2012; Conway et al., 2016, 2018). This pattern parallels that of Tongariro data that show a decrease from ~5-6 wt% MgO in older ~190-150 ka Mangahouhounui Formation eruptives to generally ~2-5 wt% MgO in younger ~150-100 ka Mangahouhounui and Taiko formation eruptives. In contrast, Rb/Sr ratios of ~0.1-0.2 for Ruapehu's 200-150 ka Te Herenga and 166-80 ka Wahianoa formations are generally lower than Rb/Sr ratio of ~0.1-0.4 in similar-age 290-189 ka Haumata, 189-130 ka Mangahouhounui and 133-52 ka Taiko formation eruptives at Tongariro.

Contemporaneous time-composition variations are observed for $^{87}Sr/^{86}Sr$ and $^{143}Nd/^{144}Nd$ ratios in Tongariro and Ruapehu eruptives (Fig. 5.6). Pb isotope data from Ruapehu are not compared because external fractionation corrections used for the Ruapehu data yield uncertainties of ≥0.097 % for all Pb isotope ratios, which is equivalent to the inter-sample variations measured by double-spike methods in this study for Tongariro (Price et al., 1999, 2012; Chapter 4). Ruapehu's 200-150 ka Te Herenga Formation (Conway et al., 2016) has $^{87}Sr/^{86}Sr$ ratios of ~0.7048-0.7053 (Price et al., 2012) that essentially form a bridge between older ~230-190 ka Tongariro Haumata Formation $^{87}Sr/^{86}Sr$ ratios of ~0.7047-0.7052 and younger 189-130 ka Tongariro Mangahouhounui Formation $^{87}Sr/^{86}Sr$ ratios of ~0.7051-0.7055 (Fig. 5.6c).

Overlapping $^{87}Sr/^{86}Sr$ ratios centred at ~0.7055 are observed for the similar-age 166-80 ka Ruapehu Wahianoa Formation and Tongariro Mangahouhounui and Taiko formations. $^{87}Sr/^{86}Sr$ ratios in Mangawhero Formation eruptives at Ruapehu increase from ~0.7050 to 0.7062 between ~45 to 40 ka then steadily decline to ~0.7052 into the Holocene (Gamble et al., 2003; Price et al., 2012; Conway et al., 2016, 2018). This coincides with a similar pattern at Tongariro wherein $^{87}Sr/^{86}Sr$ ratios increase from ~0.7047 for the ~56 ka Te Tatau Member to ~0.7056-0.7058 for ~36-23 ka Mokomoko Formation eruptives (North Crater and Blue Lake vents), setting aside the ~35 ka Pukeonake Formation flank vent eruptives ($^{87}Sr/^{86}Sr$ ~0.7047). Subsequently Tongariro $^{87}Sr/^{86}Sr$ ratios decrease to ~0.7051 in 11.0-1.8 ka Te Ahititi Member eruptives (Red Crater Formation), not including the ~17.5 ka Makahikatoa Formation flank vent ($^{87}Sr/^{86}Sr$ ~0.7044: Hobden, 1997).

$^{143}Nd/^{144}Nd$ versus time relationships at Tongariro and Ruapehu (Fig. 5.6d) show similar patterns to $^{87}Sr/^{86}Sr$ data with excursions to crustal isotopic compositions at the same times (Fig. 5.6c). The general decrease in Tongariro $^{143}Nd/^{144}Nd$ ratios from ~0.51285 to ~0.51265 between ~230-100 ka parallels less radiogenic $^{143}Nd/^{144}Nd$ ratios for Ruapehu 200-150 ka Te Herenga Formation eruptives (~0.51290) but similar $^{143}Nd/^{144}Nd$ ratios for 166-80 ka Wahianoa Formation eruptives (~0.51270-0.51280) (Gamble et al., 2003; Price et al., 2012; Conway et al., 2016, 2018). Ruapehu Mangawhero Formation eruptives have initially high $^{143}Nd/^{144}Nd$ ratios of ~0.512677-0.51275 at ~45-40 ka that become more crrustal (~0.51264-0.51273) at ~25-15 ka, which closely overlaps with Tongariro $^{143}Nd/^{144}Nd$ ratios for the same period. In general, both Tongariro and Ruapehu $^{143}Nd/^{144}Nd$ ratios become less crustal into the Holocene as shown by values clustered around ~0.51270-0.51275. Available data therefore indicate that relatively similar variation in Tongariro and Ruapehu $^{43}Nd/^{144}Nd$ ratios has occurred contemporaneously since ~170 ka and persisted into the Holocene.

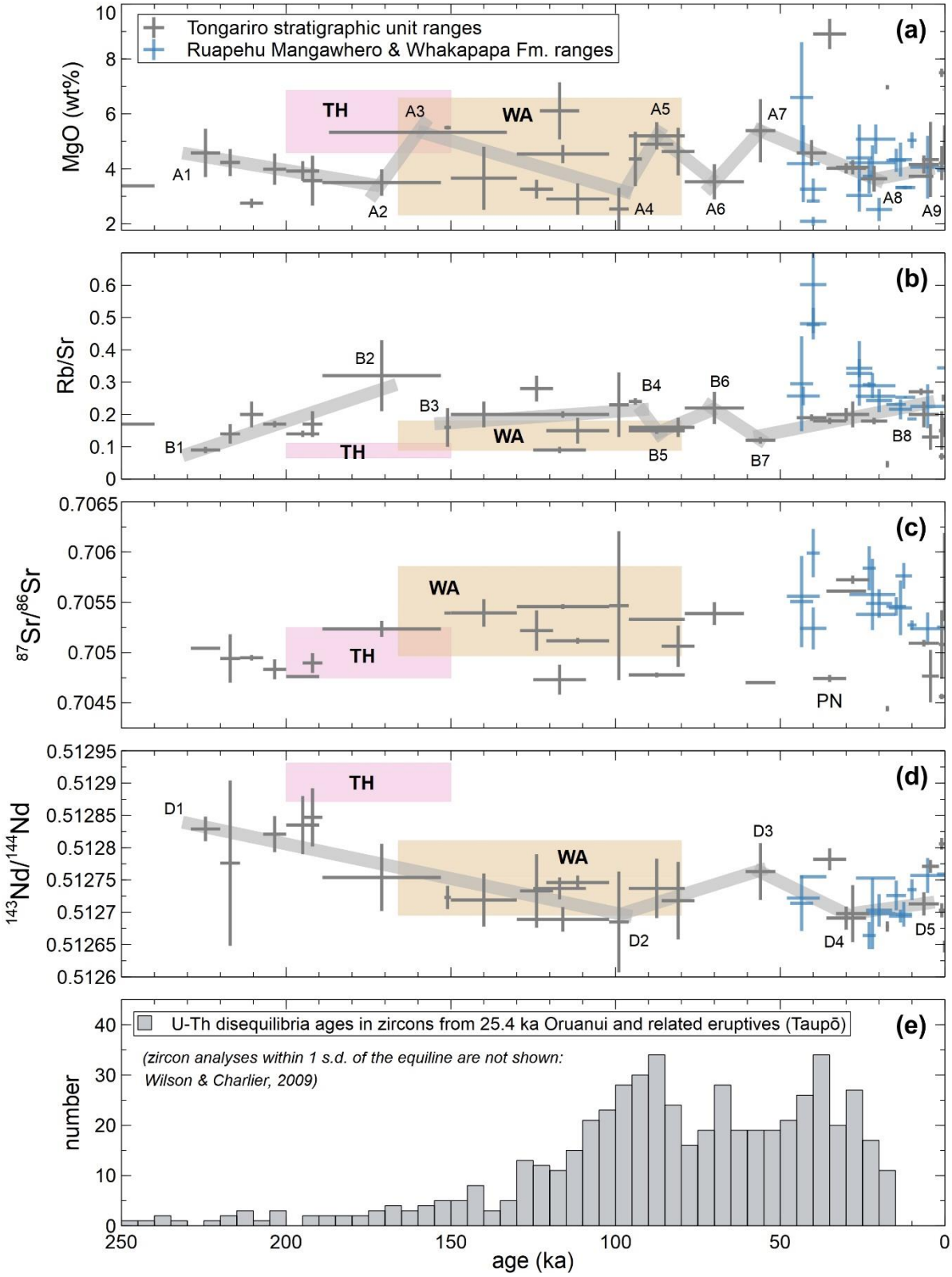
Tongariro stratigraphic unit ranges
Ruapehu Mangawhero & Whakapapa Fm. ranges
(a)
MgO (wt%)
TH
WA
A1
A2
A3
A4
A5
A6
A7
A8
A9
(b)
Rb/Sr
B1
B2
B3
B4
B5
B6
B7
B8
(c)
$^{87}Sr/^{86}Sr$
PN
(d)
$^{143}Nd/^{144}Nd$
D1
D2
D3
D4
D5
(e)
U-Th disequilibria ages in zircons from 25.4 ka Oruanui and related eruptives (Taupō)
(zircon analyses within 1 s.d. of the equiline are not shown:
Wilson & Charlier, 2009)
number
age (ka)

Figure 5.6. (Previous page.) Time-composition data for Tongariro and Ruapehu stratigraphic units (ranges and midpoints shown by crosses: **a**-**d**) alongside U-Th disequilibrium zircon model ages for 25.4 ka Oruanui and related deposits (**e**) (Wilson and Charlier, 2009). Key in panel (**a**) applies to (**a**-**d**). Ruapehu major oxide and trace element data from Conway et al. (2018). Ruapehu Sr-Nd isotope data from Price et al. (2012) and references therein. TH and WA refer to Te Herenga and Wahianoa formations at Ruapehu, which are shown as boxed because paired $^{40}Ar/^{39}Ar$ age determinations are sparse. Tongariro data are from this study and Hobden (1997) and Cole (1978, 1979). Linear regressions (shaded lines) were determined for all data between the pivot-points labelled A_1-A_9 (**a**), B_1-B_8 (**b**) and D_1-D_5 (**d**) except for the ~210 ka Upper Tama Member, ~35 ka Pukeonake Formation (PN in (**c**)), ~17.5 ka Makahikatoa Formation and Te Pupu Formation (Holocene). Typical r^2-values are 0.5-0.9 (see Table 5.1).

Time-composition variation at Tongariro and Ruapehu are generally contemporaneous for MgO concentrations and Rb/Sr, $^{87}Sr/^{86}Sr$ and $^{143}Nd/^{144}Nd$ ratios which indicates that the timings of mafic replenishment and the intervals of prolonged magma residence in the crust are at the same times. For the two physically-separated volcanoes, synchronised compositional variation on 10-100 kyr timescales indicates that either their magmatic systems are interconnected and shared, or that external processes control mafic replenishment rates and the durations of magmatic residence in the crust. The former case is considered unlikely because abundant evidence for multiple coexisting magmas is observed for both volcanoes throughout their lifespans, which indicates that numerous independent magma bodies coexisted at any one time at each volcano (Chapter 4; Gamble et al., 1999, 2003; Hobden et al., 1999; Nakagawa et al., 1999; Price et al., 2012; Conway et al., 2016, 2018). Sustained intra-volcanic magma diversity indicates that large and unified magma reservoirs are rare, if not totally absent, features at Tongariro and Ruapehu. Contemporaneous explosive eruptions during the Pahoka-Mangamate tephra sequence from Tongariro and Ruapehu show distinct compositions that are attributed separately to each volcano (Nairn et al., 1998; Nakagawa et al., 1998). It is therefore unlikely that sub-volcanic magmatic systems laterally interact across the ~20 km that separate Tongariro and Ruapehu. The second scenario, wherein an external force (i.e. tectonics) influences magmatic processes at each volcano simultaneously is considered more likely, and is discussed below in section 5.4.6.

5.4.4. The petrogenesis of early Tongariro and Ruapehu magmas

5.4.4.1. Tongariro: Tupuna Formation (between 349 and 293 ka)

The oldest eruptives confidently related to Tongariro volcano are from the Tupuna Formation, which was erupted between 349 and 293 ka (section 3.3.2.2). Tupuna Formation eruptives are distinguished from other Tongariro eruptives because they contain intact hornblende phenocrysts up to 3 mm long, which are the dominant ferromagnesian phase (also noted by Hobden, 1997).

Compared with other Tongariro eruptives, Tupuna Formation andesites have relatively low K_2O concentrations (~1 wt%) that were previously interpreted to reflect hornblende fractionation (section 4.3.1.2). In contrast, hornblende fractionation appears not to have occurred to significant extents in other Tongariro eruptives as indicated by the absence of phenocrystic hornblende (Table 3.3) and the higher K_2O concentrations observed for equivalent SiO_2 concentrations (Fig. 4.1). Tupuna Formation andesites have similar trace element characteristics (Fig. 5.3) and Sr-Nd-Pb isotope compositions (Fig. 5.4) to other Tongariro eruptives. However, REE concentrations in Tupuna Formation andesites plot towards the lower values observed for Tongariro eruptives (Fig. 4.3) which is consistent with hornblende fractionation. Groundmass separates from the Tupuna Formation also display a positive Eu anomaly[1] (Eu/Eu* = 1.08) (Fig. 4.14) which indicates plagioclase accumulation.

The stability of amphibole in arc magmas is strongly dependent on temperature, pressure and water concentrations (Rutherford and Devine, 1988; Blundy and Cashman, 2001; Annen et al., 2006). 'Cryptic' amphibole fractionation has also been proposed for numerous andesite volcanoes globally based on REE patterns (e.g. Davidson et al., 2007a). At Tongariro, the transition from hornblende as the dominant ferromagnesian phase to pyroxene was apparently gradual, because pseudomorphs (~5 vol%) of reacted amphiboles are observed in the 290-242 ka Lower Tama Member, which is the next youngest stratigraphic unit erupted after the 349-293 ka Tupuna Formation (Table 3.3; section 3.3.2.3.1). The next youngest units, such as the 229-220 ka Tutangatahiro Member, also contain reacted amphibole pseudomorphs (≤2 vol%), but in progressively lower proportions (Table 3.3; section 3.3.2.3.2).

Why early Tongariro eruptives contained hornblende, but have not subsequently, probably indicates changes in storage conditions with regard to temperature, pressure and/or water concentration (e.g. Rutherford and Devine, 1988; Blundy and Cashman, 2001). Such parameters are not well-constrained for Tupuna Formation versus subsequent eruptives. However, the positive Eu anomaly observed in Tupuna Formation groundmass (Eu/Eu* = 1.08) (Fig. 4.14) suggests that the plagioclase was potentially unstable at the time of eruption, which may provide additional clues on storage conditions. The plagioclase crystals in Tupuna Formation whole-rock samples are equant, 0.5-3.0 mm, contain highly reacted core regions with sieved textures (100 % of crystals) that are surrounded by a 100-200 μm overgrowth rim and occur in equal modal proportions to hornblende crystals. These textures are also represented by 50-100 % of plagioclase crystals in Haumata Formation eruptives (ages between 290 and 189 ka), which may imply a xenocrystic origin for the majority of plagioclase crystals in the Tupuna and

[1] Eu/Eu* calculated as $Eu_N/(sqrt(Sm_N*Gd_N))$ after normalisation with the values of McDonough and Sun (1995).

Haumata formations. EPMA analyses of plagioclase cores in the Tupuna Formation have anorthite (An) concentrations of 74-89 %, which is consistent with a xenocrystic source from basement metasediments (frequency node at An_{80-95}: Price et al., 2012). The majority of plagioclase crystals in the Ruapehu Te Herenga Formation also contain highly reacted core regions with sieved textures that are surrounded by <0.5 mm overgrowths, which may also be xenocrystic (Graham, 1985; Price et al., 2005, 2012). Note that elsewhere, Tongariro and Ruapehu plagioclase compositions are typically 60 % anorthite (Hobden, 1997; Price et al., 2012; Coote and Shane, 2016; Shane et al., 2019).

The phase diagram presented by Annen et al. (2006: their Fig. 16), which is based on data from Mount St Helens dacites (Blundy and Cashman, 2001), indicates that coinciding plagioclase instability and amphibole stability occur at depths of >1 GPa, which indicates storage at depths of >30 km. Whether or not such storage depths at Tongariro are within the crust or extend into the mantle (cf. section4.4.2.2; Harrison and White, 2006; Stern and Benson, 2011; Dimech et al., 2017), the inferences above imply that early Tongariro eruptives from the Tupuna Formation (and less so, the Haumata Formation) may have been stored in deeper crust than Tongariro eruptives younger than ~190 ka (i.e. the Mangahouhounui, Taiko and younger formations), provided that amphibole crystallised before plagioclase. However, a significant proportion of the radiogenic isotope contamination in early Tongariro eruptives may be represented by non-molten xenocrystic components, such as the cores of plagioclase crystals in the 349-293 ka Tupuna Formation, which would imply that amphibole crystallised before plagioclase.

5.4.4.2. Ruapehu: Te Herenga Formation (between 200 and 150 ka)

The oldest edifice-forming unit on Ruapehu is the 200-150 ka Te Herenga Formation (Hackett, 1985; Gamble et al., 2003; Price et al., 2012; Conway et al., 2016). This formation is petrographically distinguished from other Ruapehu formation by clinopyroxene (up to 12 mm), which is the dominant phenocryst phase over plagioclase and orthopyroxene. It has also been noted that $^{143}Nd/^{144}Nd$ ratios of 0.51285-0.51295 in Te Herenga Formation eruptives trend towards mantle-like values relative to their $^{87}Sr/^{86}Sr$ ratios of 0.7048-0.7053 that are similar to Sr isotope ratios in other Ruapehu and Tongariro eruptives (Fig. 5.7; Price et al., 2005, 2012; Conway et al., 2016, 2018).

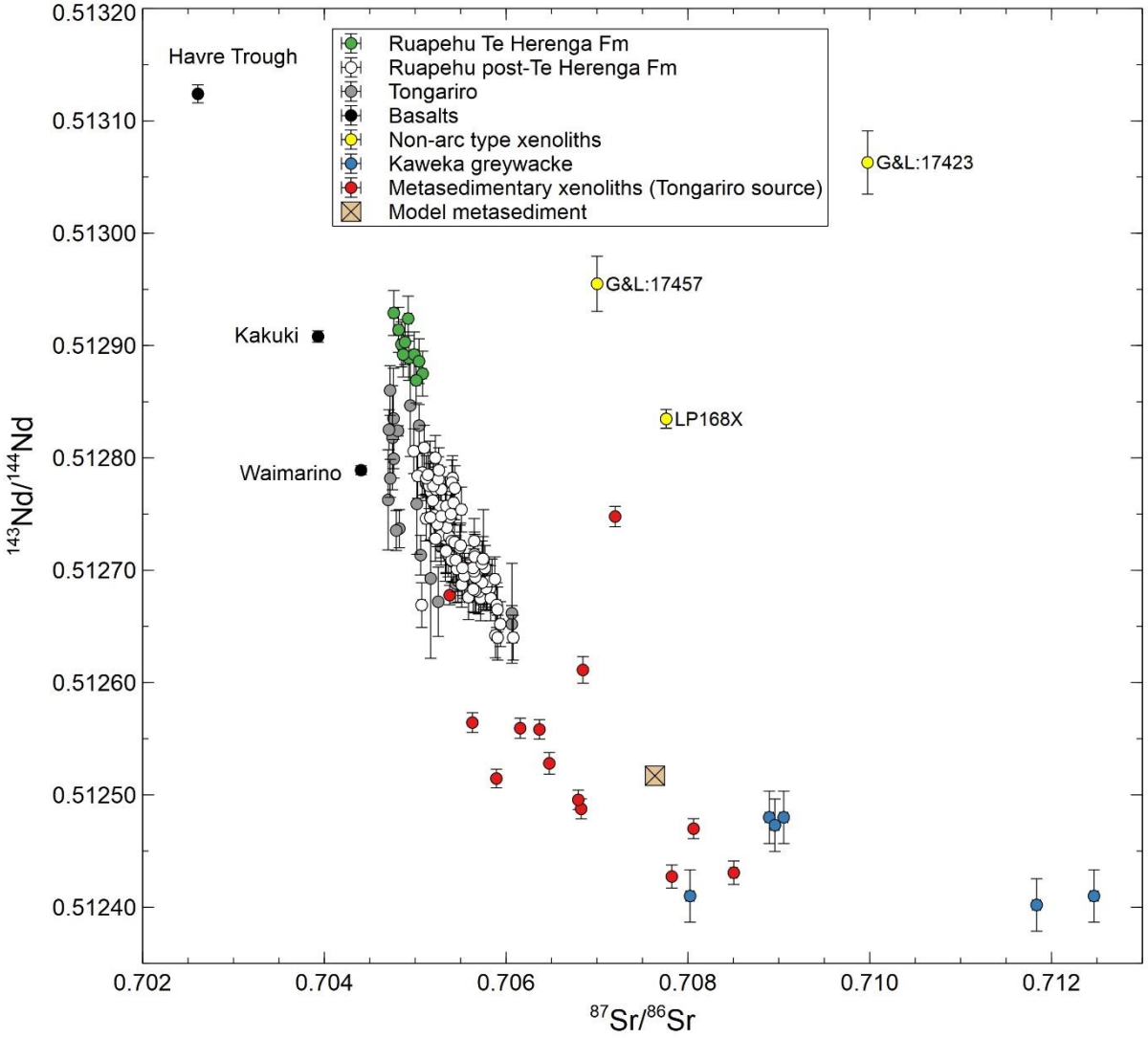

Figure 5.7. Sr-Nd isotope comparison of Ruapehu Te Herenga Formation eruptives relative to other Ruapehu eruptives (Price et al., 2012 and references therein), Tongariro eruptives from this study (data in Appendix 5) and unusual xenoliths from Graham (1985) and Lee (2008), prefixed G&L, and this study (LP168X: Table 4.5). Other data for regional basalts from Gamble et al. (1993) and metasedimentary xenolith data are from this study in Tongariro eruptives (Table 4.5). Greywacke reference samples are from the Kaweka terrane (Price et al., 2015). The model metasedimentary assimilant previously used for AFC modelling (section 4.3.3; Table 4.6) is also shown. Errors are all quadratically combined internal 2 s.e. and external 2 s.d. uncertainties, except for basalt data which are only internal 2 s.e.

Explanations for why Te Herenga Formation eruptives have unusually mantle-like Nd isotope compositions (Fig. 5.7) have been offered by Price et al. (2005), Lee (2008), Cameron et al. (2010) and Price et al. (2012). Each of these explanations involve the contamination of a primitive TVZ arc basalt (e.g. Kakuki: Gamble et al., 1993) by a deep-crustal lithology with contrasting isotopic compositions to shallower metasedimentary basement rocks (Price et al., 2005; Lee, 2008; Price et al., 2012). These explanations are scrutinised here and are found to be generally accurate. However, inconsistencies are identified in the characterisation of 'meta-

igneous' versus 'meta-sedimentary' xenoliths, which appear to have misguided petrogenetic modelling (cf. Graham et al., 1987, 1990). New xenolith trace element and isotopic data in this study, and the re-examination of data reported by Lee (2008) who analysed xenoliths collected by Graham (1985, 1987) and Graham et al. (1990), provide evidence that some meta-igneous basement lithologies beneath the southern TVZ have non-arc type chemical signatures (section 4.4.2.2).

To address issues of circularity, in that sediments are ultimately derived from igneous sources, the geochemical data reported by Lee (2008) and in this study (Chapter 4) are used to devise a new classification scheme for 'meta-igneous' xenoliths. In the context of the southern TVZ, it is suggested that the phraseology 'metasedimentary' should refer to metamorphosed sedimentary rocks that are comprised predominantly of clastic materials derived from arc volcanic and plutonic rocks. In contrast, the phraseology 'meta-igneous' should be used with the terms 'arc' or 'non-arc' to distinguish between the dominant lithological constituents in higher-grade metamorphic basement rocks. This classification scheme is summarised in section 5.4.4.3, below.

Te Herenga Formation eruptives have similar REE systematics to unusual xenolith samples collected by Graham (1985) and analysed by Lee (2008), and xenolith LP168X reported in this study (Fig. 5.8). These xenoliths have non-arc type compositions (section 5.4.4.3) that are similar to the LREE-depleted Havre Trough basalt, which is not an arc basalt (Fig. 5.8; Gamble et al., 1996). In contrast, the Kakuki basalt—which is an arc basalt erupted between Tongariro and the central TVZ—displays LREE enrichment relative to depleted HREE, which is typical of arc magmas (Gamble et al., 1993, 1996; Waight et al., 2017). REE patterns in Te Herenga Formation eruptives (Conway et al., 2018) display negative Ce anomalies, Eu anomalies and relatively low La_N/Yb_N ratios of ~1-2, which is similar to the unusual xenoliths (Fig. 5.8). These features indicate that the unusual xenoliths may not be metasedimentary in origin because they lack arc type compositions, and that Te Herenga Formation magmas at Ruapehu have been contaminated with the basement materials represented by these unusual xenoliths.

Sr and Nd isotope systematics further distinguish the unusual xenoliths from other metasedimentary xenoliths reported in this study (Fig. 5.7) and elsewhere (e.g. Graham, 1987; Graham et al., 1990; Hobden, 1997). Despite having similar $^{87}Sr/^{86}Sr$ ratios of ~0.707-0.710 to metasedimentary xenoliths and greywacke reference samples (Price et al., 2015), the unusual xenoliths have higher $^{143}Nd/^{144}Nd$ values of 0.5128-0.5130 (Fig. 5.7). This relationship parallels Sr-Nd isotope systematics in Te Herenga Formation eruptives relative to other Ruapehu eruptives (Price et al., 2012). Te Herenga Formation eruptives display $^{143}Nd/^{144}Nd$ ratios of

0.51285-0.51295 that are consistently higher than other Ruapehu eruptives for similar $^{87}Sr/^{86}Sr$ ratios around 0.705 (Fig. 5.7; Price et al., 2012). The Sr-Nd isotopic arrays for Ruapehu and xenolith samples therefore indicate that Te Herenga Formation eruptives contain greater proportions of a basement contaminant with isotopic (and trace element: Fig. 5.8) properties similar to the unusual xenolith samples (Fig. 5.7).

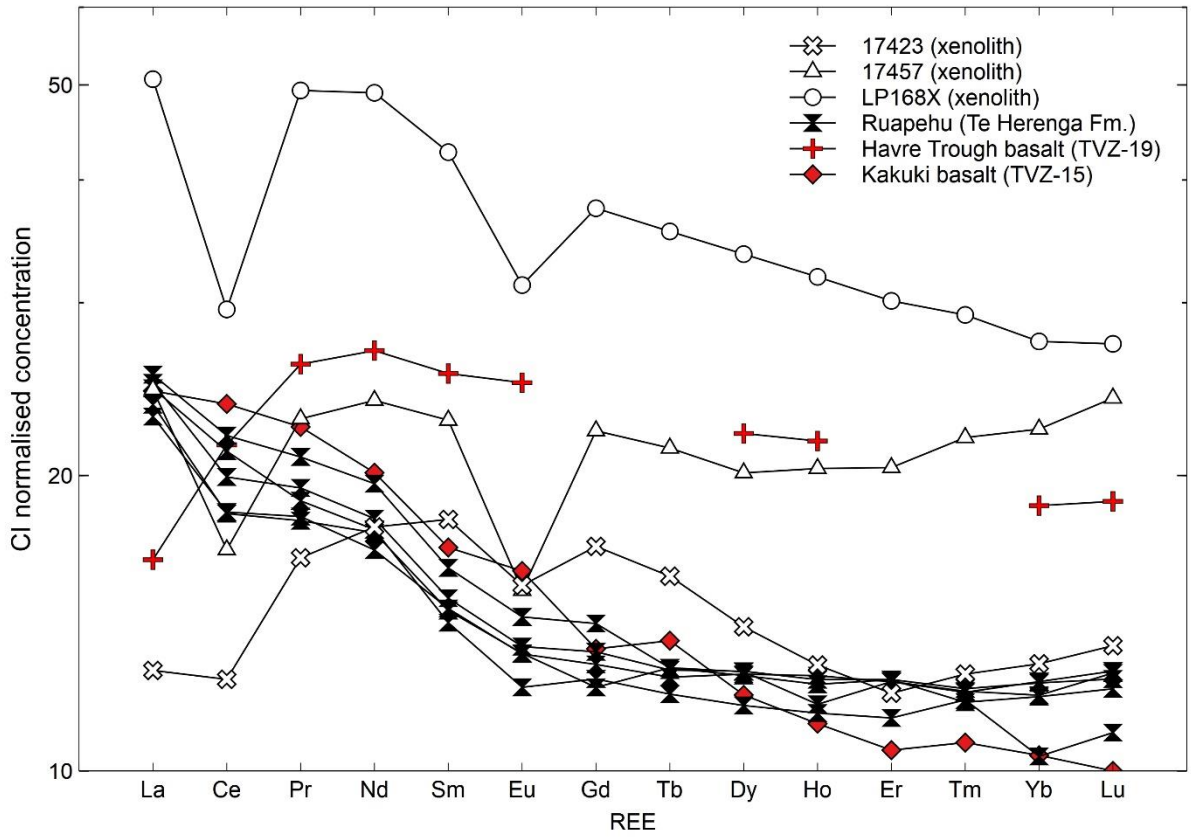

Figure 5.8. REE diagram for representative selection of (n = 5) Ruapehu Te Herenga Formation lavas and unusual xenoliths. Te Herenga Formation data are from (Conway et al., 2018). Unusual xenoliths are from Tongariro (LP168X: this study—see also Tables 4.2-4.5; section 4.3.2.5, 4.4.2.2) and Graham (1985: 17423 and 17457) which were analysed by Lee (2008). Basalts comparison data are from an arc setting (Kakuki) and non-arc setting (Havre Trough) from Gamble et al. (1996) and Waight et al. (2017), respectively. REE normalisation uses the CI chondrite values of McDonough and Sun (1995).

The basement rocks represented by unusual xenolith samples have non-arc type compositions (Figs. 5.7, 5.8) and may reflect a high-grade meta-igneous lithology such as metamorphosed oceanic crust. Alternatively, accreted fragments of oceanic crust may be dispersed throughout metasedimentary-dominated basement material (e.g. Mortimer, 2004) which have disproportionately contaminated Te Herenga Formation magmas relative to other Ruapehu (or Tongariro) eruptives. It is unclear if basement lithologies with non-arc compositions occur in the deep crust relative to shallower metasedimentary rocks (e.g. Harrison and White, 2006; Stern and Benson, 2011), so on this basis interpretations of storage depth of Te Herenga

Formation magmas cannot be made. If, however, Te Herenga Formation magmas were stored at greater crustal depths than younger Ruapehu magmas, then magma reservoirs at both Tongariro and Ruapehu may have undergone shallowing in their early histories, which could be potentially be related to the TVZ rift propagating southwards with time (e.g. Villamor and Berryman, 2006).

5.4.4.3. Classification scheme for basement rocks

Distinctions between arc-like and non-arc chemical signatures in the xenoliths reported by Graham (1987) and Graham et al. (1990) were originally hampered by the lack of trace element and Sr-Nd-Pb isotopic data. Subsequently, the original definitions by Graham (1987) and Graham et al. (1990) have not been revised, despite the re-analysis of the original xenolith collection of Graham (1985) for most trace elements and Sr-Nd-Pb-Hf isotopes by Lee (2008). Re-examination of the trace element data for 'metasedimentary' and 'meta-igneous' xenoliths collected by Graham (1985, 1987) and Graham et al. (1990), and analysed by Lee (2008), show only two samples (17423 and 17457) with geochemical features similar to sample LP168X (Figs. 5.7, 5.8), which was the only xenolith collected in this study to be interpreted as having a non-arc composition (section 4.3.2.5). Ironically, the samples 17423 and 17457 were originally categorised by Graham (1985) as metasedimentary rather than meta-igneous in origin, which has persisted in the literature and caused the unintentional averaging of metasedimentary and meta-igneous compositions for modelling purposes (e.g. Price et al., 2005, 2012).

This section attempts to clarify distinctions between basement lithologies in the southern TVZ based on overview of improved compositional and isotopic datasets for xenolith samples (Lee, 2008; this study: Chapter 4). Non-arc type chemical signatures shared by LP168X, 17423 and 17457 (Graham, 1985; Lee, 2008) are summarised here and suggested as a tentative checklist for distinguishing between non-arc type meta-igneous xenoliths versus arc type metasedimentary xenoliths, as a revision of previous definitions (cf. Graham, 1987; Graham et al., 1990), as follows.

- Negative Ce anomalies (Fig. 5.8), which are absent in metasedimentary xenoliths (Fig. 4.9).
- Similar LREE and HREE concentrations, with La_N/Yb_N ~1-2 (Fig. 5.8), normalised to CI chondrite values from McDonough and Sun (1995). In contrast, metasedimentary xenoliths have $La_N/Yb_N \geq 2$, typically ~4-10 (cf. Fig. 4.9).
- $^{87}Sr/^{86}Sr$ ratios that are above 0.7062 (which is the most radiogenic whole-rock value reported for Tongariro and Ruapehu eruptives: Hobden, 1997; Price et al., 2012 and

references therein) and $^{143}Nd/^{144}Nd$ ratios >0.5128 (Lee, 2008). Metasedimentary xenoliths overlap with this range but differ in other aspects listed here.

- $^{207}Pb/^{206}Pb$ ratios of ≥0.8314 and $^{208}Pb/^{206}Pb$ ratios of ≥2.059 (Table 4.5; Fig. 4.12) (Lee, 2008). In contrast, metasedimentary xenoliths have $^{207}Pb/^{206}Pb$ ratios of ≤0.8314 and $^{208}Pb/^{206}Pb$ ratios of ≤2.059 (Fig. 4.12).

None of the xenoliths reported by Graham (1987) and Graham et al. (1990) as metasedimentary or meta-igneous possess all of the features listed above. The two aforementioned samples (17423 and 17457) used to define the criteria were collected during doctoral research by Graham (1985) but were not reported in subsequent peer-reviewed publications (cf. Graham, 1987; Graham et al., 1990). Relatively high MgO concentrations in 'meta-igneous' xenoliths reported by Graham et al. (1990) can be explained by similar modal proportions of pyroxene and feldspar, whereas metasedimentary xenoliths generally have greater amounts of feldspar (e.g. Graham et al., 1987; section 4.3.2.1). Varied clastic inputs of ferromagnesian versus feldspathic minerals into sedimentary deposits can arise from arc volcanic and plutonic sources, which will equally preserve arc type REE and Sr-Nd-Pb chemical signatures as distinct from other magmatic settings (e.g. mid-oceanic ridges or intra-plate volcanism: cf. Fig. 5.8).

5.4.5. Links between regional andesitic and rhyolitic activity in the TVZ

New observations from this study are presented in context with and are consistent with previous arguments for external (i.e. tectonic) influences on eruptive activity at Tongariro, Ruapehu and Taupō which are the most active volcanoes in the southernmost ~100 km of the TVZ arc. Uncanny contemporaneity has been suggested for relatively large eruptions (Nakagawa et al., 1998; Nairn et al., 1998) and contemporaneous compositional variation (Kohn and Topping, 1978; Hodder, 1983) between each of these volcanoes during the Holocene. To build on this, new results from Tongariro (this study) and a recently improved chronostratigraphic framework for Ruapehu (Conway et al., 2016; Townsend et al., 2017) are used to examine evidence for potentially synchronised magmatism for a greater interval from ~230 ka to present.

One of the first studies to present evidence supporting synchronised magmatism between Taupō volcano and southern TVZ andesite volcanoes was by Kohn and Topping (1978). Based largely on interfingered tephra deposits on the ringplain, they reported contrasting transition metal concentrations in titanomagnetite crystals that distinguished ~12 ka versus late Holocene tephras erupted from Tongariro, Ruapehu and Taupō. Within these tephras, contemporaneous shifts in compositions of similar magnitudes and directions occurred at each of these volcanoes, which provoked the idea that magmatic variation between separate volcanoes could be

synchronised by an external, common influence. The results reported by Kohn and Topping (1978) are summarised below because they are relevant to interpretations of magmatic contemporaneity in the ~230-0 ka interval.

Titanomagnetites in the 11.8 ka Okupata Tephra (Lowe et al., 2013) have greater concentrations of V (~5000-12000 ppm), Cr (2000-6000 ppm), Ni (~300-500 ppm) and Co (~170-300 ppm) relative to the 11.3 ka Te Rato Lapilli (Hitchcock and Cole, 2007) and <1.8 ka Ngauruhoe Formation tephras (Topping, 1973; Froggatt and Lowe, 1990; Hogg et al., 2012). The titanomagnetites in these younger tephras have V, Cr, Ni and Co concentrations that are approximately half of the earlier values (Kohn and Topping, 1978). Similarly, titanomagnetites in the 11.5 ka Unit B (Karapiti) and 10.0 ka Unit E (Opepe) (Wilson, 1993; Lowe et al., 2013) deposits from Taupō possess V/Cr ratios of ~20-30 and Ni and Co concentrations of ~100-150 ppm which contrast with the younger Taupō-sourced ~4.5 ka rhyolites of subgroup 2 (Froggatt and Lowe, 1990; Sutton et al., 1995, 2000; Barker et al., 2015) and 1.8 ka Taupō eruption deposits (Hogg et al., 2012). Titanomagnetites in these younger Taupō tephras have lower V/Cr ratios of ~5-10 and Ni and Co concentrations of ~10-100 ppm (Kohn and Topping, 1978). A separate study by Hodder (1983) showed that titanomagnetite Co/Mn ratios decreased from ~0.080 to ~0.040 (Tongariro and/or Ruapehu) and from ~0.020 to ~0.005 (Taupō) between the corresponding early and late Holocene periods.

Compositional shifts in rhyolite-hosted versus andesite-hosted titanomagnetites show that andesite-hosted titanomagnetites became V-Cr-Ni-Co-depleted by ~11.3 ka. In contrast, the compositional shift observed in Taupō rhyolites occurred between subgroup 1 (units B to E: ~11.8-10.0 ka) to subgroup 2 rhyolites (units F to W: ~7.1-2.8 ka), following the stratigraphy of Wilson (1993) and revised ages of Lowe et al. (2013). What this delay represents depends on the process(es) driving compositional changes in titanomagnetites, which are interpreted here using data from experimental studies of transition metal partitioning in andesitic and dacitic melts. Elevated oxygen fugacities (less reducing), which typically occur in more evolved arc magmas (e.g. Fudali, 1965), favour greater concentrations of V, Ni, Mn and Co in titanomagnetites (Sievwright et al., 2017). This relationship predicts that transition metal concentrations in titanomagnetite will decrease when magma compositions become more reducing, which is consistent with the input of mafic magma or reducing supercritical fluids into Tongariro and Ruapehu magmas between 11.8-11.3 ka and into Taupō magmas between 10.0-4.5 ka (e.g. Fig. 5.9), as indicated by geothermometry results reported by Barker et al. (2015).

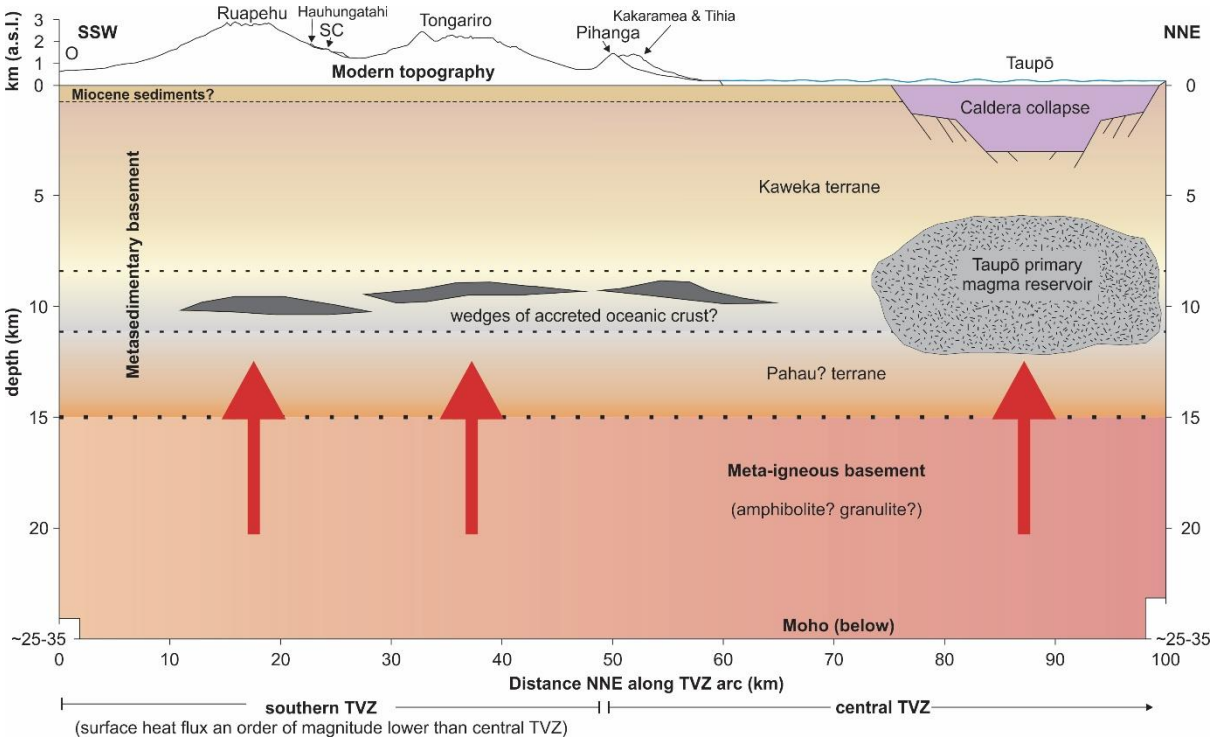

Figure 5.9. Schematic NNE cross-section along the TVZ arc from Ruapehu to Taupō volcanoes. Sill and dikes complexes comprise a fundamental part of basement structure beneath the TVZ but are not illustrated because their locations and spatial densities are not well constrained (e.g. Barker et al., 2015). Abbreviations are O = Ohakune Craters and SC = Saddle Cone. Taupō magma reservoir depth and geometry after Barker et al. (2015). Presence of Pahau terrane beneath Taupō inferred from Cretaceous ages in detrital zircons from xenolith R623 in the Rubbish Tip Dome (Sutton, 1995; Charlier et al., 2010). Continuity of Pahau terrane beneath the southern TVZ follows interpretations of xenolith data presented in Chapter 4. Miocene sediments depth after geophysical surveys of Miller and Williams-Jones (2016) and Robertson and Davey (2018). Meta-igneous basement inferred from xenoliths LP168X (Chapter 4) and 17423 and 17457 (Graham, 1985, 1987; Graham et al., 1990; Lee, 2008). Depth of metasedimentary basement and Moho after Harrison and White (2006), Stern and Benson (2011) and Dimech et al. (2017) which is consistent with the geobarometry results of Arpa et al. (2017). Depth relationships between the Pahau and Kaweka terranes are largely unknown, but potentially coincide with wedges of oceanic crust that were accreted during underplating, as is observed within Jurassic-Cretaceous greywacke and argillite of New Zealand (e.g. Mortimer, 2004). Note that the surface heat flux beneath the central TVZ is an order of magnitude greater than in the southern TVZ (Wilson and Rowland, 2016 and references therein).

At Taupō, similar conclusions are drawn from studies of phenocrystic zircons (Barker et al., 2014). Zircon crystallisation model ages for Holocene Taupō eruptives are most frequently ~10-15 ka and become less numerous after ~10 ka (Charlier et al., 2005; Barker et al., 2014). Zircon-saturation modelling in these studies shows that magma temperatures probably controlled whether or not zircons precipitated or survived in their host magmas, which is compatible with a mafic replenishment event at Taupō after ~10 ka (Charlier et al., 2005; Barker et al., 2014). At the same time, a general shift to basaltic-andesite compositions is observed in <7 ka effusive eruptives at Tongariro, relative to early Holocene and pre-Holocene andesitic eruptives

(Chapter 4; Hobden, 1997; Townsend et al., 2017). These basaltic-andesite magmas were erupted from three distinct vent foci at Tongariro (Ngauruhoe, Red Crater and Upper Te Maari Crater), which are spaced ~7 km apart NNE across the volcano (Fig. 3.8). These observations suggest the presence of a volcano-wide mafic replenishment event in the early Holocene, consistent with the systematic variations in titanomagnetite compositions discussed above and which likely was tectonically-synchronised (Fig. 5.9). Mafic replenishment between ~10 and 5 ka follows a series of voluminous andesitic explosive eruptions between ~12-10 ka from Tongariro and Ruapehu (Nakagawa et al., 1998; Nairn et al., 1998) that coincided with the 11.5 ka Unit B (Karapiti) and 11.2 ka Unit C (Poronui) rhyolitic explosive eruptions from Taupō, which have been interpreted to reflect a period of tectonically-synchronised eruptive activity (Kohn and Topping, 1978).

The model ages of zircons in 25.4 ka Oruanui eruption deposits from Taupō, and similar-age related eruptives (Charlier et al., 2005; Wilson and Charlier, 2009) record magma assembly processes for the same period as the high-resolution time-composition records for Tongariro (this study) and Ruapehu (Conway et al., 2016, 2018) eruptives (Fig. 5.6). These records are compared here to examine whether pre-Holocene synchronised magmatism may have occurred at these volcanoes, following the arguments outlined above. Time-composition patterns for $^{143}Nd/^{144}Nd$ ratios in Tongariro eruptives show gradually decreasing ratios that attain their most crustal isotopic ratios of ~0.51265 at ~100 ka and ~30 ka, which coincide with the ~95 ka and ~35 ka peaks in zircon residence model-age observed in Oruanui and related eruptive deposits (Fig. 5.6d-e) (Charlier et al., 2005; Wilson and Charlier, 2009). Similar peaks of radiogenic Sr and Pb isotope ratios also occur at ~100 ka and ~30 ka at Tongariro (Figs. 5.4-5.5). Isotopic variations at Ruapehu broadly mirror those of Tongariro, wherein Sr-Nd isotope ratios are most radiogenic during the ~40-20 ka interval. These contemporaneous periods of accelerated zircon crystallisation in rhyolitic Taupō magmas and increasingly radiogenic and evolved andesitic Ruapehu and Tongariro intermediate magmas at ~100-95 ka and ~35-30 ka imply preceding corresponding periods of prolonged crustal residence and cooling.

A limited number (<10) of U-Th isotope ratio analyses on Ruapehu eruptives are consistent with this interpretation (Hughes, 1999). The sole Ruapehu sample erupted within the ~95-35 ka period that has been analysed for U-Th isotopes gives a U-Th disequilibrium age of 81 +13/-12 ka (Hughes, 1999) which is within error of the eruption age of 74 ± 37 ka ($^{40}Ar/^{39}Ar$ age determination: Gamble et al., 2003). These overlapping ages imply a relatively short residence time within the crust that is likely to be ~10-20 kyr or less, given the U-Th and $^{40}Ar/^{39}Ar$ age uncertainties. Younger Ruapehu eruptives with $^{40}Ar/^{39}Ar$ age determinations between ~22 and 0 ka (Gamble et al., 2003; Conway et al., 2016) have U-Th disequilibria ages of 72 +23/-19 ka

and 62 +18/-15 ka (Hughes, 1999) that imply longer crustal times of ~40-50 kyr. Protracted crustal residence will allow more time for crustal assimilation with ongoing crystal fractionation, consistent with the more radiogenic Sr-Nd isotope ratios in ~30-20 ka Ruapehu eruptives. However, this view is somewhat contradicted by Sr-Nd isotope ratios that become less radiogenic into the Holocene (Fig. 5.6) (Price et al., 2012). The U-Th and $^{40}Ar/^{39}Ar$ data therefore provide some support for a model wherein crustal residence is short (i.e. <10 kyr) for magmas erupted between ~95-35 ka at Ruapehu relative to longer crustal residence times (i.e. ~40-50 kyr) for younger ~30-20 ka eruptives. Given their similar U-Th disequilibria ages but contrasting eruption ages, it is plausible that these Ruapehu eruptives were derived from similar-age magmas (Hughes, 1999).

The lesser abundances of zircon model ages between ~95 and 35 ka for Oruanui and related eruptives from Taupō (Charlier et al., 2005; Wilson and Charlier, 2009) coincides with excursions to less radiogenic $^{143}Nd/^{144}Nd$ ratios of ~0.51277 (Fig. 5.6c-e) and $^{206}Pb/^{204}Pb$ ratios of ~18.82 (Fig. 5.5b) in Tongariro eruptives. Elevated Tongariro MgO concentrations during this period indicate that pre-existing magmas were replenished and mixed with mafic magma (Fig. 5.5), which may have coincided with periods of mafic replenishment into Taupō magmatic system also. Zircon saturation modelling for Taupō eruptives by Charlier et al. (2005, using the model of Watson and Harrison, 1983) indicates that temperature was a primary influence on the crystallisation and/or survival of zircons in these Taupō magmas. Hence the modelling predictions are consistent with elevated mafic replenishment between ~95-35 ka that led to lower degrees of zircon crystallisation because of unfavourable melt compositions or elevated temperatures (or both). In addition to evidence for mafic replenishment at Tongariro at ~88 ka and ~56 ka, as shown by increased MgO concentrations to ≥5 wt%, Ruapehu eruptives also display increased MgO concentrations up to 8 wt% between ~50-40 ka, which is consistent with regional mafic replenishment during the ~95-35 ka interval. Stratigraphically-ordered Sr-Nd-Pb isotope data and MgO concentrations (Tongariro and Ruapehu: this study; Price et al., 2012 and references therein; Conway et al., 2016, 2018), alongside U-Th disequilibrium ages from Ruapehu eruptives (Hughes, 1999) and in zircons from 25.4 ka Oruanui and most related and younger eruptives from Taupō (Charlier et al., 2005; Wilson and Charlier, 2009; Barker et al., 2014), therefore indicate intervals of prolonged crustal residence preceding ~100-95 ka and ~40-20 ka with an intervening period of shorter crustal residence times and enhanced replenishment rates of mafic magma at Tongariro, Ruapehu and Taupō volcanoes. The recognition of contemporaneous magmatism at these volcanoes between ~230 and 20 ka corroborates previously highlighted contemporaneous activity from ~12 ka to the late Holocene, as discussed above, which indicates

that an external forcing such as tectonics may have modulated magmatism and the expression of volcanism over ~100 km of the TVZ arc over this time period.

Previous arguments for tectonically-controlled volcanism were presented by Lanphere and Sisson (2003), who proposed the term "tectonic throttling" to explain how time-varied edifice-building rates at Mount Rainier (Cascade arc) did not correlate with the state of climate or eruptive compositions. In contrast to Tongariro (Chapter 3), it appears that edifice growth rates somewhat reflect eruption rates because time-volume relationships show alternating ~100 kyr intervals of elevated then decreased rates (Vallance and Sisson, 2017) that do not correlate with climate proxies such as marine $\delta^{18}O$ records (Lanphere and Sisson, 2003). Further elaboration on the "tectonic throttling" concept is provided by personal correspondence from T. W. Sisson (2018):

> *"The tectonic throttling idea came from trying to understand why volcanoes like Rainier can have periods of ca. 10^5 years duration over which the eruptive rate is 3-10 fold greater or lesser. At Rainier, these are not associated, in so far as I can see, with shifts to more or less primitive magmas. It's as though a valve were more or less spun open, but with the same spectrum of stuff coming out. Within these extended periods of higher or lower volcanic flux are much briefer changes in the trace element geochemistry that I think are more representative of the residence times of magmas in the system."*

Similar findings are reported by Calvert et al. (2018) for Middle Sister (Cascade arc), where time-volume relationships show elevated rates during peak glacial periods relative to interglacial periods, which is the reverse to what lava-ice interaction models (Lescinsky and Sisson, 1998) and preservation bias models would predict (Chapter 3). The study of Calvert et al. (2018) shows that another process must influence eruptive output because the volcanic record is already biased towards lower preservation during glacial periods.

In New Zealand and the United States, inferred stop-start behaviour in voluminous caldera-forming eruptions has been recognised, which cannot be reconciled by models where eruptions are purely driven by internal magmatic processes. The 2.08 Ma, ~2500 km^3 Huckleberry Ridge Tuff (Yellowstone) begins with fall deposits that took some weeks to episodically erupt (Myers et al., 2016), then three ignimbrite units that were separated by periods of weeks to months and years to decades, respectively (Swallow et al., 2019). Deposits from the ~530 km^3 Oruanui eruption (25.4 ka) from Taupō display field evidence that initial eruptive phases were separated by months and resumed eruptive activity coincided with the lateral migration of a foreign biotite-bearing magma from a NE vent system into the main Oruanui magma system (Wilson, 2001; Allan et al., 2012). Both examples demonstrate that large silicic eruptions can be stopped and started by an external process (i.e. tectonics) because gas-saturated

magmas in volumes >500 km^3 are unlikely to stop erupting once they begin, according to traditional hypotheses of internally-driven explosive eruptions (Blake, 1984; Cassidy et al., 2019). Independent support for this hypothesis is given by fault slip rates constrained by regional and local tephras since ~50 ka in the southern TVZ, with regard to the Oruanui eruption (Gómez-Vasconcelos et al., 2016). Fault slip rates (extensional) increase to as much as 1.5 mm/yr, against a background rate of 0.5 mm/yr, leading up to and after the 25.4 ka Oruanui eruption. Note, however, that such fault slip rate variations may be very uneven, and partly syn-eruptive because of associated caldera collapse and localised changes in crustal stress regimes (Wilson, 2001).

If magmatism and volcanism at volcanic arcs are influenced by tectonics, this association appears to be globally under-recognised. This is potentially because of the relatively few examples of high-resolution chronostratigraphic frameworks from adjacent volcanoes and accompanying geochemical data that are needed to interrogate such relationships. Where "tectonic throttling" or equivalent mechanisms have been suggested to explain time-varied stratovolcano behaviour, it is usually deduced by elimination, in that no measured or considered variables correlate with the observed time-composition or time-volume variation at the volcano(es) in question (e.g., Lanphere and Sisson, 2003; Conway et al., 2016; Calvert et al., 2018). It is possible that evidence supporting tectonically throttled volcanism and magmatism has been misinterpreted and associated with an alternative process. A potential example of previously unrecognised tectonic throttling is in southern Chile where volume-time-composition variations in tephras from Mocho-Choshuenco volcano were interpreted to occur in response to deglaciation that affected the crustal local stress regime (Rawson et al., 2016). Note however that tephra dispersal and accumulation may be biased by wind directions, which were not discussed in that study, and strong concerns over the completeness of southern Chilean tephra records have been expressed and demonstrated by others (Watt et al., 2013; Weller et al., 2015). Despite these concerns, if eruptive compositions or volumes varied in response to crustal stress regimes at Mocho-Choshuenco, it is equally—if not more—likely that crustal stress regimes could have varied in response to external tectonic processes, rather than varied stress regimes arising from deglaciation, as has been suggested elsewhere (cf. Maclennan et al., 2002).

5.4.6 Implications for popular petrogenetic models

Many studies of arc magma petrogenesis have adopted long-term, unidirectional crustal heating models (e.g. Annen et al., 2006; Jagoutz, 2014) wherein crust is heated to a critical pivot point, because of repeated injections of mafic magma, and experiences rapid and irreversible depletion of fertile and radiogenic materials at which point the "lower crust becomes an infertile residue"

(Smith et al., 2003). These models are similar to the melting, assimilation, storage and homogenisation (MASH) model of Hildreth and Moorbath (1988), but with the distinction that the MASH model does not impose requirements of long-term crustal heating, nor does it imply a uniform rate of mafic replenishment. This contrasts with the deep crustal hot zone (DCHZ) model of Annen et al. (2006) which does imply gradual and relatively uniform heating. The DCHZ model has been applied to explain the evolution of Ruapehu's magma system (Lee, 2008; Price et al., 2012), although this view was not emphasised in more recent petrogenetic investigations of magma assembly at Ruapehu (Conway et al., 2018). Whether such models are appropriate for explaining time-composition trends at Tongariro are evaluated here.

Time-composition relationships for Tongariro eruptives show repeated excursions to MgO concentrations of ≥5 wt% at ~230, ~160, ~117, ~88, ~56, ~35, ~17 ka and during the Holocene, which demonstrates that mafic replenishment is cyclic. At least two excursions to maximally radiogenic magma compositions at ~100 ka and ~30 ka (Figs. 5.5-5.6) indicates that radiogenic enrichment of Tongariro magmas is not represented by a single and irreversible depletion event wherein all radiogenically fertile materials are exhausted. Small-volume basaltic-andesite eruptions since 1870 CE also show huge diversity in $^{87}Sr/^{86}Sr$ ratios, including the most radiogenic value determined on a Tongariro eruptive (0.706165±14), which shows that sub-edifice basement remains highly fertile in radiogenic material (Hobden et al., 1999, 2002). This effectively precludes application of magma assembly models wherein repeated injections of mafic magma occur at a constant rate, and where long-term crustal heating is the primary process that controls time-composition variation in magmas, such as implied by the DCHZ model of Annen et al. (2006). Whilst it is true that long-term thermal conditioning of the crust beneath Tongariro must have occurred because of repeated injections of mafic magma, otherwise the conservation of energy would be violated, it is first important to consider the magnitude of crustal heating that was likely experienced.

The heating modelled by Annen et al. (2006) for Tongariro's ~300 ka to present lifespan is ~160 °C for intrusion depths of 20-30 km at intrusion rates of 5 mm/yr, which equates to ≤5 % melt produced from intruded amphibolite country rock. However, country rock heating is potentially less than implied by this one-dimensional model because sill intrusions are unlikely to be laterally infinite, and cooling from adjacent country rock will probably be at greater rates than suggested by the model. The model of Annen et al. (2006) predicts that in the 10 kyr following the intrusion of a single 50 m basalt sill at 1285 °C, adjacent country rock will heat by ≤25 °C (or 200 °C after 0.6 kyr). Such heating is unlikely to induce pervasive modification of surrounding country rock unless: (1) the same intrusion pathway is reused and (2) wall-rock material is

not stoped, thereby causing the same wall-rock to be repeatedly exposed to high temperature magmas (Annen et al., 2006). However, the abundance of refractory metasedimentary xenoliths in Tongariro eruptives indicates that wall-rock stoping is the primary mechanism for crustal assimilation (Chapter 4), which is expected to repeatedly expose cooler country-rock material that minimises long-term conductive heating from prolonged exposure to ascending mafic magmas. Repeated excursions to crustal Sr-Nd-Pb isotopic compositions in Tongariro eruptives (Figs. 5.4-5.6) indicate that long-term thermal conditioning of the crust is not the strongest process controlling 1-100 kyr variation in magma compositions. Instead, time-composition variations in Tongariro and Ruapehu magmas are more likely controlled by non-uniform rates of mafic replenishment and varied crustal residence times (section 5.4.5; cf. Hughes, 1999). This study supports the notion that thorough examinations of magma assembly processes fundamentally require high-resolution chronostratigraphic frameworks, such as those produced in this work (Chapter 3), for Ruapehu (Gamble et al., 2003; Price et al., 2012; Conway et al., 2016) and elsewhere (e.g. Dungan et al., 2001; Fierstein et al., 2011; Hildreth and Fierstein, 2012; Calvert et al., 2018).

5.5. CONCLUSIONS

New $^{40}Ar/^{39}Ar$ age determinations, detailed field mapping (Chapter 3) and comprehensive whole-rock geochemistry (Chapter 4) of the edifice-forming chronostratigraphic units on Tongariro have been integrated to examine time-composition relationships from ~350 ka to present. These results were examined in the context of pre-existing data for time-compositional variation at Ruapehu volcano, 20 km south of Tongariro, and with zircon model ages (from U-Th disequilibria) from Taupō volcano, ~50 km north of Tongariro, for the ~230-0 ka interval, which is represented by 34 distinct chronostratigraphic units on Tongariro. Summaries and interpretations from these investigations are as follows.

1) Edifice-forming eruptives on Tongariro indicate that magma compositions have varied from basaltic-andesite to dacite compositions repeatedly. Late Holocene eruptive records show equivalent compositional diversity to Tongariro's entire ~350 ka eruptive history, although these are represented by small volume (<0.01 km^3) eruptions that unlikely to pass into the geological record. These late Holocene eruptives indicate that the smaller the volume window that is examined that the larger the diversity, and that the modern situation may in fact represent smaller-scale 'background' activity through much of the lifetime of Tongariro. Similar interpretations have been made for neighbouring Ruapehu volcano (Nakagawa et al., 1999).
2) MgO concentrations in Tongariro's stratigraphic units with ages between 230 and 0 ka display successive and irregular cyclicity that occurs over ~10-70 kyr intervals. During these cycles, relatively rapid (≤10 kyr) increases in MgO concentrations to ≥5-9 wt% are followed by gradual declines to ~2-5 wt%, which occur from ~230, ~160, ~117, ~88, ~56 ka and during the Holocene. These periods of increasing MgO values are interpreted as events of enhanced mafic replenishment. Flank vent eruptives from the ~35 ka Pukeonake and ~17.5 ka Makahikatoa formations display elevated MgO concentrations of ~9 wt% and ~7 wt%, respectively, that are offset from the main time-composition array but also demonstrate events of mafic replenishment, and are relatively unmodified by interactions in the magmatic complex beneath the main part of Tongariro.
3) Long-term (i.e. >200 kyr), unidirectional time-compositional variations are not observed in Tongariro magmas. This record contrasts with predictions from "MASH" and "deep/lower crustal hot zone" models (cf. Hildreth and Moorbath, 1988; Annen et al., 2006) wherein the crust is thermally conditioned via the repeated injection of mafic magmas. The large variations in MgO concentrations (2-9 wt%, see point 1) that occur repeatedly on ~10-70 kyr intervals, and at least two excursions to crust-like radiogenic Sr-Nd-Pb isotope ratios, indicate

that time-composition variations are driven by cyclic—rather than unidirectional—modification of magma systems and hosting country-rock. Similarly, models that invoke the irreversible exhaustion of fertile radiogenic phases in a single "depletion" event (cf. Smith et al., 2003) are not supported by repeated excursions to relatively radiogenic $^{87}Sr/^{86}Sr$ ratios of ~0.7057-0.7061, $^{143}Nd/^{144}Nd$ ratios of ~0.51265, $^{206}Pb/^{204}Pb$ of ~18.86, $^{208}Pb/^{206}Pb$ of ~38.78 and $^{207}Pb/^{206}Pb$ of ~0.8291-0.8292 in Tongariro magmas. Whilst the model proposed by Annen et al. (2006) is useful from a thermal crustal evolution perspective, it is less able to describe 1-100 kyr compositional variations at typical intermediate-composition arc volcanoes than other processes. Time-variable mafic replenishment rates and crustal residence durations appear to have more significant effects on time-composition variation in arc magmas than long-term (>200 kyr) crustal heating.

4) Composition-volume relationships are a rarely harnessed avenue for providing additional context to petrogenetic studies. However, biases favour the preservation of (1) effusive products relative to explosive products and (2) the preservation of materials erupted during ice-free periods. These biases essentially preclude truly representative pre-Holocene composition-volume investigations at most Quaternary stratovolcanoes. Despite this, the examination of composition-volume relationships in Tongariro's Holocene eruptives indicate that surface/area volume ratios could result in contrasting magma evolution pathways in situations where erupted magma volumes differ by ≥2 orders of magnitude.
5) Comparisons between Ruapehu and Tongariro eruptives show parallel variations in time-composition patterns for MgO concentrations and Sr-Nd isotope ratios, but less so for Rb/Sr ratios, except for Ruapehu's 200-150 ka Te Herenga Formation (Gamble et al., 2003; Price et al., 2012; Conway et al., 2016: see next point). Contemporaneous time-composition variation at Tongariro and Ruapehu does not indicate shared or laterally-connected magma systems, but instead indicate that an external process has regulated the timings of mafic replenishment and prolonged crustal residence, which is likely to be regional tectonics.
6) Meta-igneous xenoliths derived from basement rocks beneath the southern TVZ are redefined here, in contrast with the definitions of Graham (1985) and Graham et al. (1987, 1990). It is suggested that meta-igneous xenoliths, as previously defined, should be further distinguished with trace element and Sr-Nd-Pb isotope compositions into 'arc type' and 'non-arc type' compositional groups. Comparisons of three unusual xenoliths from Tongariro (LP168X: this study, section 4.3.2.5) and Ruapehu (samples 17423 and 17457: Graham, 1985; Lee, 2008), display the following similarities, which are suggested as a checklist for identifying non-arc type meta-igneous xenoliths in the southern TVZ.

a. Negative Ce anomalies (Fig. 5.8), which are absent in metasedimentary xenoliths (Fig. 4.9).
b. Similar LREE and HREE concentrations, with La_N/Yb_N ~1-2 (Fig. 5.8), normalised to CI chondrite values from McDonough and Sun (1995). In contrast, metasedimentary xenoliths have La_N/Yb_N ≥2, typically ~4-10 (cf. Fig. 4.9).
c. $^{87}Sr/^{86}Sr$ ratios that are above 0.7062 (which is the most radiogenic whole-rock value reported for Tongariro and Ruapehu eruptives: Hobden, 1997; Price et al., 2012 and references therein) and $^{143}Nd/^{144}Nd$ ratios >0.5128 (Lee, 2008).
d. $^{207}Pb/^{206}Pb$ ratios of ≥0.8314 and $^{208}Pb/^{206}Pb$ ratios of ≥2.059 (Table 4.5; Fig. 4.12) (Lee, 2008).

7) Synchronised variations in Tongariro and Ruapehu magma compositions, which coincide with reported zircon model-ages in Taupō magmas, are observed for the ~230-0 ka period. This contemporaneity is interpreted as representing a form of "tectonic throttling" (cf. Lanphere and Sisson, 2003), wherein tectonic processes have externally modulated and synchronised the timings of pulses of mafic replenishment and periods of prolonged crustal residence at each of these volcanoes.

Chapter 6

Synthesis and conclusions

6.1. INTRODUCTION

This chapter organises the collective results and conclusions from chapters 3-5, then integrates them with those of previous studies to demonstrate their global significance. Results and conclusions that are pertinent to the 'outstanding questions in the study of stratovolcanoes and intermediate composition arc magmas' (introduced in section 1.2) are summarised first (section 6.2). These questions are used as a framework for organising the results and conclusions of this study. Other results and conclusions that arose during the course of the thesis that go beyond the questions posed in section 1.2 are summarised second (section 6.3). Finally, there are suggestions for future studies in section 6.4.

6.2. ANSWERING THE OUTSTANDING QUESTIONS

6.2.1. Stratovolcano geomorphology

Why do some stratovolcano landforms possess simple 'cone' geometries, such as that of the Ngauruhoe cone on Tongariro volcano, whereas others possess irregular or "ice-ravaged" geometries?

The morphology of Quaternary stratovolcanoes in arc settings is strongly determined by whether or not edifice growth occurred in the presence of ice. This model has been proposed in numerous detailed studies of glaciated stratovolcanoes, such as those by Lescinsky and Sisson (1998), Schmidt and Grunder (2009), Conway et al. (2015, 2016) and Calvert et al. (2018). In contrast to syn-glacial growth models are others that invoke discrete periods of edifice growth that alternate with periods of quiescence wherein glacial erosion produces valleys and other "ice-ravaged" (e.g. Hildreth and Lanphere, 1994) landforms, as proposed by Singer et al. (1997, 2008), Dungan et al. (2001) and Jicha et al. (2012). Similar to studies of neighbouring Ruapehu volcano (Spörli and Rowland, 2006; Conway et al., 2015, 2016), the findings from this study show that the morphology of Tongariro's edifice is best explained with a syn-glacial growth model as demonstrated by the following results.

- New $^{40}Ar/^{39}Ar$ age determinations (this study) and previous K/Ar age determinations (Stipp, 1969; Hobden et al., 1996) on *in situ* edifice-forming materials show that Tongariro has been persistently active since ~230 ka, including during glacial periods. Sustained edifice growth in the presence of ice has been reported at other mid-latitude stratovolcanoes, such as in the Cascades (e.g. Hildreth and Lanphere, 1994; Schmidt and Grunder, 2009; Calvert et al., 2018) and the Andes (e.g. Dungan et al., 2001; Klemetti and Grunder, 2008; Singer et al., 2008). Large valley-filling glaciers have been persistent on most of Tongariro, excluding volcanic deposits from filling those valleys. However, a large part of the northwestern to northern

edifice was able to build itself in the Last Glacial period and maintain an ice-free morphology into the Holocene, with no signs of moraine.

- Inferred moraine volumes on Tongariro (≤1 km^3) are small compared with:
    - The total edifice volume (~90 km^3);
    - Exposed edifice-forming materials that are >90 % effusive volcanic products (19 km^3); and
    - The ringplain volume (~60 km^3) for an area equal to Tongariro's edifice (~200 km^2).
- The timings of glaciation and deglaciation, as inferred from the locations and thicknesses of preserved Tongariro lavas, are in strong agreement with climatic changes inferred from cosmogenic exposure dating on moraines at Tongariro (Eaves et al., 2016a) and from speleothem records in southern New Zealand (Williams et al., 2015).
- During periods of major ice coverage, edifice-building rates on Tongariro were only 17-21 % of those during warmer climatic periods (Fig. 6.1a). These shifts in edifice-building rates do not coincide with the cyclicity in erupted compositions (Fig. 6.1c-d; Chapter 5), which indicates that the differences are primarily due to a preservation bias. Many of the materials erupted during periods of major ice coverage were therefore emplaced onto or into ice masses and conveyed to the ringplain as debris, which accounts for reduced edifice-building rates during cool climatic periods (Fig. 6.1).

Figure 6.1. (Next page. Reproduced from Chapter 3, Fig. 3.14.) **(a)** Cumulative preserved volumes of map units. Width of crosses reflects the adopted age range of each stratigraphic unit (section 3.3.2). One exception is the Te Pakiraki Member (**dpk**), which is subdivided into pre-152 and post-150 ka (Waiaruhairiki Member) ages (see section 3.3.2.4 for further details). Red and blue lines are regressions calculated from midpoints of adopted age ranges (section 3.3.2) and average volumes (Table 3.5) for five intervals of distinct edifice-building rates, which correspond to warm and cool climatic periods, respectively. **(b)** Benthic $\delta^{18}O$ record and MIS intervals after Lisiecki and Raymo (2005). Blue-shaded areas reflect major periods of ice coverage on Tongariro, as inferred from field relationships at Tongariro (this study: section 3.5.3), cosmogenic exposure dating of moraines on Tongariro (Eaves et al., 2016a), climate proxies records in New Zealand speleothems (Williams et al., 2015) and the aforementioned global $\delta^{18}O$ record (Lisiecki and Raymo, 2005). **(c)** Time-composition systematics for SiO_2 concentrations in each stratigraphic unit (whole-rock samples), shown as crosses. Te Pakiraki Member subdivided as in (a). Cross heights represent the range of mean values for all samples of that unit. Red symbols are flank vents: 189-130 ka Tātaramoa Member (mtm), 40-30 ka Pukeonake Formation (PN), ~17.5 ka Makahikatoa Formation (MK). **(d)** Time-composition systematics for MgO concentrations in all stratigraphic units, symbolised as in (c). Regression lines calculated between interpreted vertices A_1-A_9 are reported in Table 5.1. Typical r^2 values are 0.50-0.98. There is no correlation between changes in ice volume and compositional ranges, or equivalently, no correlation between compositional changes and preserved volumes. This indicates that deglaciation does not trigger increased eruptive rates and that variation in preserved cumulative volume trends reflect a preservation bias, because they corelate with changes in ice volumes on Tongariro as represented by the $\delta^{18}O$ time-series.

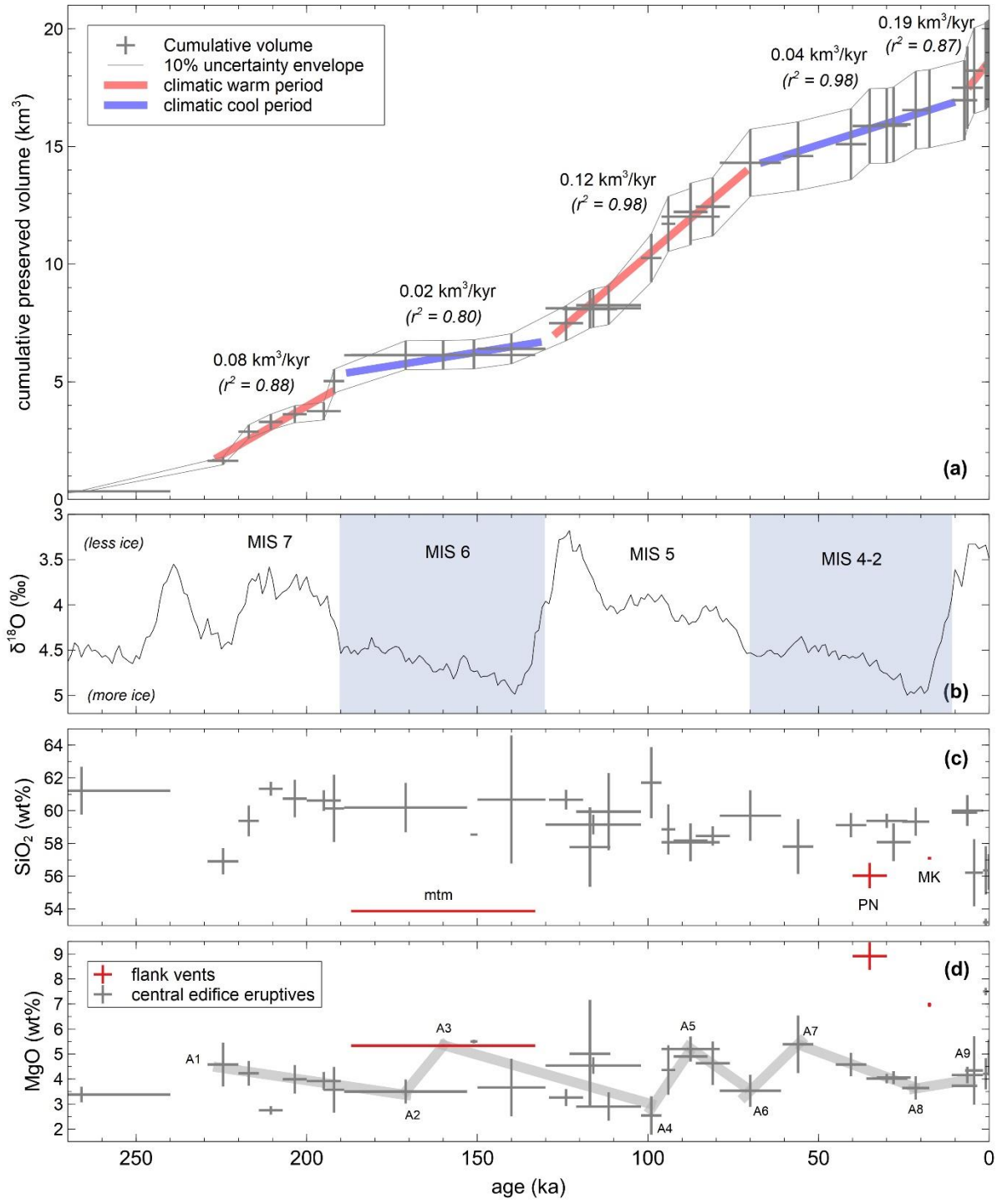
Cumulative volume
10% uncertainty envelope
climatic warm period
climatic cool period
cumulative preserved volume (km³)
0.08 km³/kyr
(r² = 0.88)
0.02 km³/kyr
(r² = 0.80)
0.12 km³/kyr
(r² = 0.98)
0.04 km³/kyr
(r² = 0.98)
0.19 km³/kyr
(r² = 0.87)
(a)
(less ice)
(more ice)
MIS 7
MIS 6
MIS 5
MIS 4-2
δ¹⁸O (‰)
(b)
SiO₂ (wt%)
mtm
PN
MK
(c)
flank vents
central edifice eruptives
MgO (wt%)
A1
A2
A3
A4
A5
A6
A7
A8
A9
(d)
age (ka)

6.2.2. Magmatism, volcanism and tectonics

What is the relationship between magmatism, its expression (i.e. volcanism) and external but related processes such as tectonics?

Tectonic processes are intimately related to magmatism and its expression in volcanic eruptions. Over stratovolcano lifespans, long-term trends (i.e. ≥10-100 kyr) in eruptive output and compositional variation in magmas are fundamentally influenced by tectonic processes. Episodic variations in crustal stress regimes related to volcanism have been observed (Gerst and Savage, 2004) and inferred in many studies (Lanphere and Sisson, 2003; Allan et al., 2012; Geshi and Teruki, 2016; Rawson et al., 2016; Swallow et al., 2019). Interrelated behaviour between rifting and magmatism are known in arc settings such as in the TVZ where rifting is assisted by thermally-assisted crustal weakening, and vice versa, which can result in positive feedbacks (Rowland et al., 2010; Allan et al., 2013; Ellis et al., 2014). In the crust, time-variable changes in magma storage durations versus mafic magma replenishment rates are probably regulated by tectonic processes, such as episodic variations in crustal stress regimes. These influences of tectonics on magmatism and volcanism go beyond the genetic relationships between volcanic arcs and proximity to subduction systems (e.g. Gill, 1981; Tatsumi and Takahashi, 2006). New support for these interpretations from this study are summarised as follows.

- MgO concentrations in Tongariro stratigraphic units with ages between 230 and 0 ka display successive and irregular cyclicity that occurs over ~10-70 kyr intervals (Fig. 6.2). During these cycles, more rapid (≤10 kyr) increases in MgO concentrations to ≥5-9 wt% are followed by gradual declines to ~2-5 wt%, with maxima at ~230, ~160, ~117, ~88, ~56 ka and during the Holocene. The periods of increasing MgO values are interpreted to reflect episodes of enhanced mafic magma replenishment, as is also demonstrated by flank vent eruptives at ~160 ka (~6 wt% MgO: Tātaramoa Member), ~35 ka (~9 wt% MgO: Pukeonake Formation) and ~17.5 ka (~7 wt% MgO: Makahikatoa Formation). High-MgO flank vent eruptives may also represent periods of enhanced mafic replenishment but also provide additional evidence for relaxed crustal stress regimes (i.e. extensional), because they were erupted from flank vents rather than central edifice regions. Holocene basaltic-andesites erupted from separate vents (Mangatetipua Member [Upper Te Maari Crater], Te Rongo Member [Red Crater] and Te Pupu Formation [Ngauruhoe]) mark a transition from earlier andesite-dominated volcanism to more mafic eruptives, and potentially signal a recent volcano-wide mafic replenishment episode (e.g. Fig. 6.2a).
- Comparisons between Ruapehu (Gamble et al., 2003; Price et al., 2012; Conway et al., 2016) and Tongariro eruptives show contemporaneous variations in time-composition patterns for

MgO concentrations and Sr-Nd isotope ratios for the ~200 ka to Holocene interval (Fig. 6.2). Parallel time-composition variations at Tongariro and Ruapehu do not indicate shared or laterally-connected magma systems (the geochemistries of eruption products remain distinct), but instead indicate that an external process (probably tectonics) has regulated the timings of mafic replenishment versus prolonged crustal residence. The inferred timings of prolonged crustal duration are consistent with a small number (<10) of U-Th isotopic residence model-ages reported for Ruapehu eruptives by Hughes (1999).

- Contemporaneous variations in Tongariro and Ruapehu magma compositions are observed for the ~230-0 ka period and these variations coincide with reported zircon growth model-ages in Taupō magmas (Fig. 6.2: Charlier et al., 2005; Wilson and Charlier, 2009). This contemporaneity is interpreted as representing a form of "tectonic throttling" (e.g. Lanphere and Sisson, 2003), wherein regional tectonic processes have externally regulated and synchronised the timings of elevated mafic replenishment episodes versus periods of prolonged crustal residence at each of these volcanoes. In general, longer crustal residence durations at Taupō are indicated by greater abundances of zircons, whereas at Tongariro and Ruapehu greater crustal residence durations are indicated by time-composition trends towards more crustal Sr-Nd-Pb isotope ratios. The reverse situation, wherein mafic replenishment rates are enhanced and crustal residence intervals are shorter, is demonstrated by rapid increases in whole-rock MgO concentrations, which are generally contemporaneous with time versus Sr-Nd-Pb isotope composition variation (Fig. 6.2), which indicate that the two processes are broadly coupled.

These findings corroborate previously reported contemporaneity between the Tongariro-Ruapehu-Taupō area that led to suggestions that tectonics may have synchronised activity at these volcanoes, as inferred from voluminous interfingered andesitic and rhyolitic tephras erupted in the early Holocene (Kohn and Topping, 1978; Hodder, 1983; Nairn et al., 1998; Nakagawa et al., 1998).

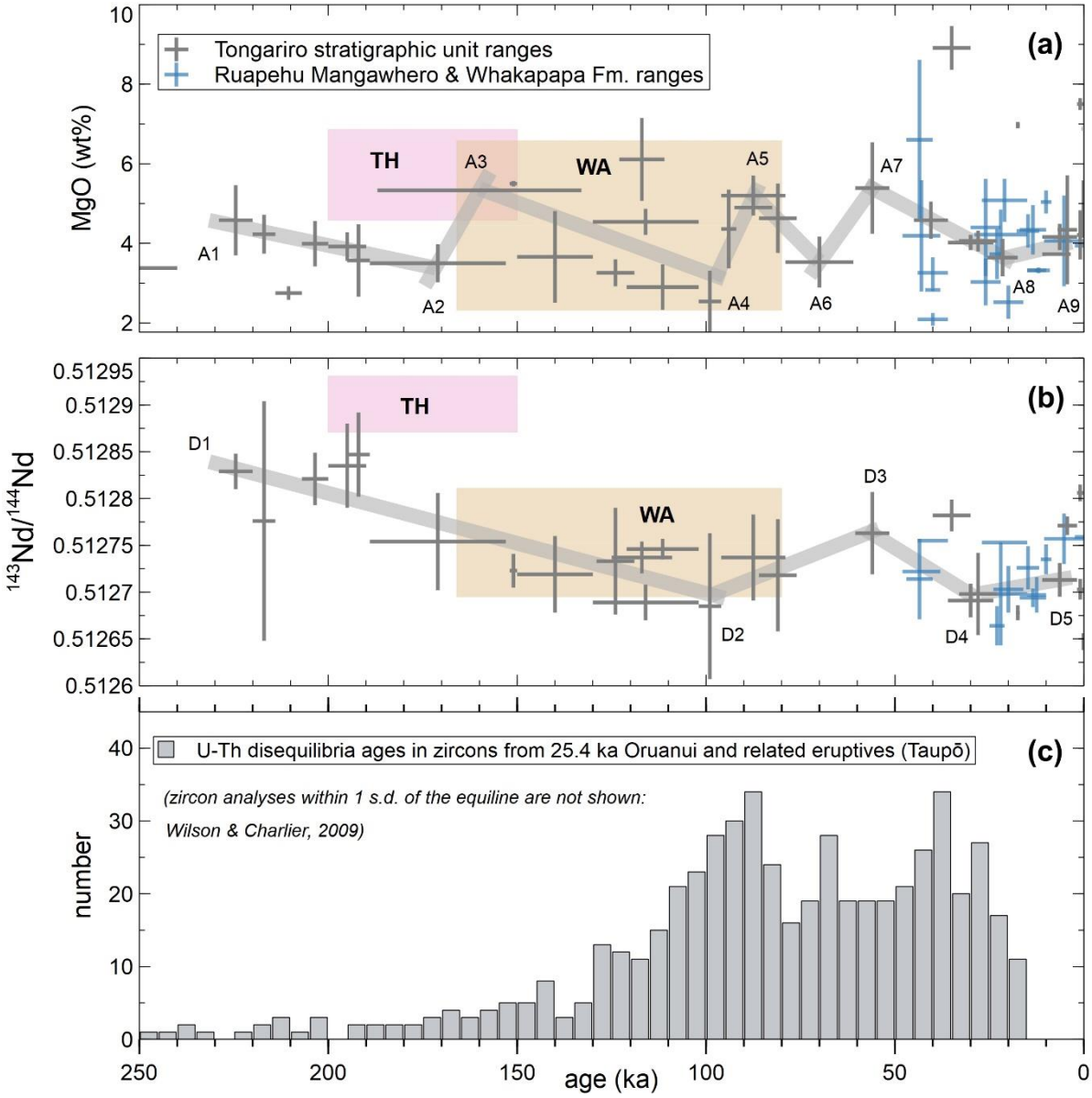

Figure 6.2. (Reproduced from Chapter 5, Fig. 5.6.) **(a)** Time-composition data for Tongariro and Ruapehu stratigraphic units as ranges and midpoints shown by crosses for MgO. **(b)** As (a) but for $^{143}Nd/^{144}Nd$ ratios. **(c)** U-Th zircon model-ages for the 25.4 ka Oruanui and related deposits (Charlier et al., 2005; Wilson and Charlier, 2009). Key in panel (a) applies to (b). Ruapehu major oxide data from Conway et al. (2018). Ruapehu Nd isotope data from Price et al. (2012) and references therein. TH and WA refer to Te Herenga and Wahianoa formations on Ruapehu. Tongariro data are from this study and Hobden (1997) and Cole (1978, 1979). Linear regressions (grey lines) were determined for all data between the pivot-points labelled A_1-A_9 (a) and D_1-D_5 (b) except for the ~210 ka Upper Tama Member, ~35 ka Pukeonake Formation, ~17.5 ka Makahikatoa Formation and Te Pupu Formation (Holocene). Typical r^2-values are 0.5-0.9 (see Table 5.1).

6.2.3. Compositional diversity of intermediate composition arc magmas

How are andesite magmas assembled and what controls their diversity?

Whilst intermediate composition arc magmas display large amounts of compositional diversity, including over short timescales at single volcanoes (i.e. $<10^2$ yrs: Gamble et al., 1999; Hobden et al., 1999; Bergal-Kuvikas et al., 2017), the diversity that they exhibit conforms to predictable patterns. Basaltic-andesite to dacite magmas in arc systems are overwhelmingly comprised of phenocryst assemblages of plagioclase + clinopyroxene + orthopyroxene ± olivine ± apatite ± hornblende ± Fe-Ti oxide, relative to other minerals (Gill, 1981). In arc settings, the ratio of FeO*/MgO is typically limited to ≤2.5 for basaltic-andesite to dacite compositions (i.e. "calc-alkaline": Miyashiro, 1974; cf. Arculus, 2003). Replenishing mantle-derived basaltic magmas are hydrous (Sisson and Layne, 1993) with an average of ~4 wt% H_2O (Plank et al., 2013). Studies of historical eruption deposits from arc type stratovolcanoes show that discrete pockets or batches of coexisting and interacting magma are ubiquitous features of intermediate composition stratovolcanoes (e.g. Unzen volcano, Japan: Nakamura, 1995; Ruapehu: Gamble et al., 1999; Nakagawa et al., 1999). Hence, the seemingly chaotic compositional variations in arc magmas arise from the range of materials and their varied proportions that are involved with magma assembly. Such compositional diversity ultimately develops when magmas and their cargoes (phenocrysts, antecrysts, xenocrysts, xenoliths) are mixed or mingled and evolve according to the idiosyncrasies of each volcano's plumbing system (e.g. Nakamura, 1995; Gamble et al., 1999; Humphreys et al., 2006a; Allan et al., 2017). Pressure and temperature conditions, the host country-rock composition(s), replenishing mafic magma composition(s), crustal residence duration and degree of mixing each contribute to compositional diversity in erupted magmas. The expression of these processes is known to create compositional variation that occurs at all temporal resolutions observable in the eruptive record, from $<10^2$ yrs (e.g. Nakamura, 1995; Gamble et al., 1999; Hobden et al., 1999; Nakagawa et al., 1999; Bergal-Kuvikas et al., 2017) to $>10^5$ yrs (e.g. Fierstein et al., 2011; Schmidt and Grunder, 2011; Jicha et al., 2012; Conway et al., 2016; this study). However, for typical arc magmas, the extent to which these processes create compositional diversity is limited by thermodynamics and the physical dimensions of magma reservoirs in andesite- and dacite-dominated arc magma systems. New observations from Tongariro further reveal the uniformity of processes, and exceptions, that control intermediate composition magma assembly in arc settings. These findings are relevant to models of andesite petrogenesis globally and are summarised as follows.

- Differences in crystallising versus fractionating minerals indicate that crystal-melt separation is more efficient for olivine but less so for pyroxene and plagioclase. This suggests that AFC

modelling with plagioclase-dominated fractionating assemblage, instead of subequal with both clinopyroxene and orthopyroxene, should be carefully considered before being applied to andesitic magma systems (e.g. Price et al., 2012; Conway et al., 2018).

- Long-term (i.e. >200 kyr), unidirectional time-compositional variations are not observed in Tongariro magmas. This record contrasts with predictions from "deep/lower crustal hot zone" models (cf. Annen et al., 2006) wherein the crust is thermally conditioned via the repeated injection of mafic magmas. The large variations in MgO concentrations (2-9 wt%) that occur repeatedly on ~10-70 kyr intervals, and at least two excursions to radiogenic Sr-Nd-Pb isotope ratios at ~100-95 ka and 35-30 ka, indicate that time-composition variations are driven by cyclic—rather than unidirectional—modification of magma systems and their hosting country-rock. Similarly, models that invoke the irreversible exhaustion of fertile radiogenic phases in a single "depletion" event (cf. Smith et al., 2003) are not supported by repeated excursions to relatively crustal $^{87}Sr/^{86}Sr$ ratios of ~0.7057-0.7061, $^{143}Nd/^{144}Nd$ ratios of ~0.51265, $^{206}Pb/^{204}Pb$ of ~18.86, $^{208}Pb/^{206}Pb$ of ~38.78 and $^{207}Pb/^{206}Pb$ of ~0.8291-0.8292 in Tongariro magmas (Fig. 6.2).
- Sr-Nd-Pb isotope ratios in paired whole-rock and groundmass separates from the same sample are strongly correlated (Fig. 6.3). For the entire range of $^{87}Sr/^{86}Sr$ (0.7047-0.7062) and $^{143}Nd/^{144}Nd$ (0.51265-0.51285) ratios observed in Tongariro eruptives, paired whole-rock and groundmass $^{87}Sr/^{86}Sr$ ratios display strong similarities and paired whole-rock and groundmass $^{143}Nd/^{143}Nd$ ratios are entirely within analytical error. Similar relationships are implied by paired whole-rock, groundmass and plagioclase crystal $^{87}Sr/^{86}Sr$ ratios in andesitic eruptives from Ruapehu, although isotopic heterogeneities exist on intra-crystal scales, as shown by micromilling of plagioclase crystals from Tongariro (Hora, 2003; Davidson et al., 2007b, Ruapehu (Price et al., 2012) and Taupō (Charlier et al., 2008). These observations demonstrate that contemporaneous crystal fractionation and assimilation occur in approximately equal balance for essentially all Tongariro magmas. This is despite intra-crystal isotopic heterogeneities within a given crystal cargo that likely reflect episodes of enhanced crustal input to magmas, which are evidently averaged out on the scale of whole-rock and groundmass compositions. Like Sr and Nd, similar Pb isotopic compositions are also observed in paired whole-rock and groundmass samples, and therefore also support this conclusion (Fig. 6.3).

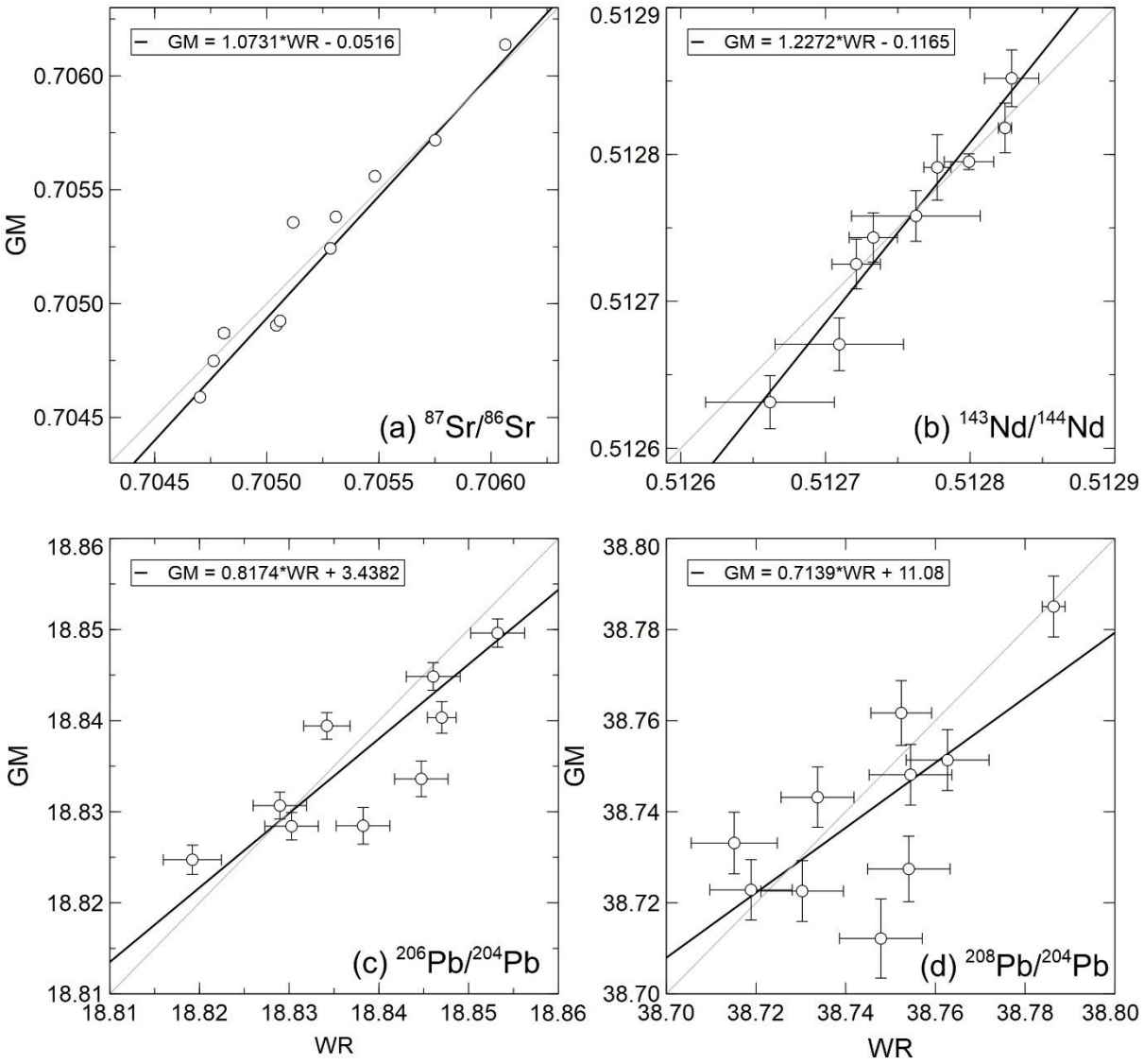

Figure 6.3. (Reproduced from Chapter 4, Fig. 4.15.) Sr-Nd-Pb isotope compositions of paired whole-rock (WR: horizontal axes) and groundmass (GM: vertical axes) separates of the same samples. GM samples were selected for analysis based on WR values that spanned the full range of Tongariro Sr and Nd isotope ratios. Thin grey lines reflect a 1:1 ratio. Dark lines reflect linear best fit lines with equations shown in each panel. Error-bars show quadratically added internal (2 s.e.) and external (2 s.d.) uncertainties. All panels show that Sr-Nd-Pb isotope compositions are similar in paired whole-rock and groundmass samples, and often within analytical error. The data therefore indicate that bulk magmas, their phenocryst cargoes and interstitial melts (groundmass) have effectively the same isotopic compositions at Tongariro.

6.2.4. Crustal versus mantle inputs into magmas

What are the relative proportions of mantle-derived and crust-derived materials in intermediate composition arc magmas?

Assimilated country-rock represents about one quarter of Tongariro magmas which is similar to estimates for predominantly andesitic arc stratovolcanoes elsewhere (e.g Mount Rainier: Sisson et al., 2014). At Tongariro, the remaining three quarters are represented by mantle-derived material. These crustal versus mantle proportions may be typical for arc magmas elsewhere, but at the least, Tongariro estimates provide a new case example for comparisons and contrasts with other petrological studies of stratovolcanoes. The ratio of mass assimilation rate (M_a) over mass fractional crystallisation rate (M_c) (the r-value of DePaolo,1981) is also inferred to be initially high (>1.0) then to subsequently decrease (to ≤1.0) as arc magmas evolve, as has been suggested elsewhere (e.g. Reiners et al., 1995). In equivalent terms, this indicates that crustal assimilation becomes less efficient as magmas evolve to more silicic compositions with their associated lower temperatures. Investigations of crustal assimilation in Tongariro magmas from this study are summarised as follows.

- Assimilated country rock accounts for 22-31 wt% of the average Tongariro magma. Initial evolution from a hypothetical Kakuki basalt-type end-member to a Tongariro Te Rongo Member basaltic-andesite reflects the addition of 17 % assimilated average metasedimentary basement material (r-value ~1.8-3.5). Subsequently, AFC evolution from a Te Rongo Member basaltic-andesite to other Tongariro eruptive compositions represents 5-14 % more assimilated crust (r-values ~0.1-1.0). At Mount Rainier, where the primary crustal assimilants are also metasedimentary basement rocks with strong isotopic contrasts to the mantle-derived magmas, the estimates of assimilated crust are 8-15 % in average andesite magmas (Sisson et al., 2014). The Tongariro and Rainier estimates provide comparison points for similar studies of crustal assimilation in arc andesites elsewhere.
- Wall-rock stoping is likely to be a primary process of crustal assimilation in arc magma systems. This conclusion contrasts with those of other models that suggest assimilation primarily occurs in the form of pure melts derived from country-rock, without the incorporation of restite materials (e.g. Knesel and Davidson, 1996, 1999; Wolf et al., 2019). At Tongariro, evidence for the bulk assimilation of country-rock protoliths is given by the ubiquitous occurrence of refractory metasedimentary xenoliths. These xenoliths display petrographic and geochemical evidence (major oxides, trace elements and isotope ratios) for the pervasive breakdown of fertile minerals (i.e. biotite, alkali feldspar, zircon and phosphate minerals) in country-rock fragments when they were incorporated into magmas. Similar

explanations have been proposed elsewhere from the perspective of plutonic rocks (e.g. White and Chappell, 1977). Intensely sieve-textured plagioclase crystals and positive Eu anomalies (in groundmass separates) in early Tongariro eruptives represented by the 349-293 ka Tupuna Formation suggest that the crystal cargoes in early Tongariro eruptives may contain significant proportions of xenocrysts. Similar plagioclase textures are observed in the clinopyroxene-rich early Ruapehu eruptives of the 200-150 ka Te Herenga Formation (Hackett, 1985; Price et al., 2012), and these might also reflect a xenocrystic origin. This is a novel suggestion for the early-stage petrogenetic evolution of Tongariro and Ruapehu eruptives that warrants further investigation.

- Incorporation of materials with more-radiogenic Sr-Nd-Pb isotopes from country rock into magmas occurred to varied extents in each isotope system. In whole-rock and groundmass samples, Sr and Nd isotopic contrasts against metasedimentary xenoliths and their protolithic sources are retained. In contrast, Pb isotope contamination is rapid and results in strong overlap in Pb isotope ratios between whole-rock, groundmass, metasedimentary xenoliths (this study: Chapter 4) and reference greywackes (Price et al., 2015).

6.2.5. Relationships between arc andesite and rhyolite magmas

Do genetic relationships exist between andesite and rhyolite magmas in arc settings?

In New Zealand, available observations demonstrate that a genetic relationship between andesite and rhyolite magmas is possible (Price et al., 2005), but local circumstances such as crustal heat flux (as indicated by surface heat flux) may be better indicators of whether such andesite-to-rhyolite progression will occur with time (Wilson et al., 1995; Rowland et al., 2010; Wilson and Rowland, 2016). Recent geophysical studies in the central TVZ have shown contrasts between mantle, lower-crustal and shallow-crustal properties that correlate with local rifting rates (Illsley-Kemp et al., 2019; Eberhart-Phillips et al., 2019). As previously pointed out, high rifting rates do not predict the occurrence of rhyolite volcanism, as is shown by White Island/Whakaari volcano which is situated in the Bay of Plenty, where rifting rates exceed those of the central TVZ (Gamble et al., 1993; Wallace et al., 2004; Villamor and Berryman, 2006). The genetic development of rhyolite and andesite magma systems is discussed as follows, informed by the results and inferences of previous chapters.

Globally, equivalent propositions have been made which state that arc rhyolites are ultimately derived from interstitial melts in andesites, following crystal-melt separation (Bachmann and Bergantz, 2004; Lee and Bachmann, 2014). In New Zealand, this suggestion is consistent with available geochemical data, although petrographic data are generally unable to test

this hypothesis because crystal-poor rhyolite magmas may continue to crystallise after episodes of crystal-melt separation (cf. variable crystal concentrations from <5-50 vol% in TVZ rhyolites: Ewart, 1965; Sutton et al., 1995; Brown et al., 1998; Sutton et al., 2000; Cooper and Wilson, 2014). As pointed out by Price et al. (2005), similarities exist between interstitial melt in TVZ andesites and bulk rhyolite compositions. This view is consistent with new EPMA analyses of melt inclusions (Appendix 8) and trace element analyses of groundmass separates in Tongariro eruptives (Chapter 4). Typical melt inclusions have 63-74 wt% SiO_2 and 1.9-6.5 wt% K_2O (normalised to 100% anhydrous totals), which are similar to values reported for Ruapehu melt inclusions and groundmass glasses (Price et al., 2005; Pardo et al., 2014; Conway et al., 2018). The maximum $^{87}Sr/^{86}Sr$ ratios (~0.7062) and $^{143}Nd/^{144}Nd$ ratios (~0.5126) observed in intermediate composition Tongariro and Ruapehu eruptives for whole-rock samples and groundmass separates (Hobden, 1997; Price et al., 2012; sections 4.3.2.4 and 4.3.3.4) are essentially equal to maximum whole-rock $^{87}Sr/^{86}Sr$ ratios (~0.7062) and $^{143}Nd/^{144}Nd$ ratios (~0.5126) in rhyolites from Taupō, excluding the strongly crustally influenced ~100-300 ka SE domes (Sutton et al., 1995, 2000). This similarly in isotope ratios for rhyolites and andesites is potentially revealing: if country rock assimilants affecting rhyolite and andesite magmas are similar, Sr-Nd isotopic similarity may imply that assimilation becomes greatly reduced in rhyolites because of reduced thermal contrasts with fertile country-rock. Alternatively, it may indicate the development of spatially extensive magma systems, wherein a high concentration of sills and dikes become effectively integrated to produce a magma reservoir system with a decreased surface area/volume ratio that limits interaction with fertile country-rock (adjacent to the magma system) but whilst still being modified by replenishing mafic magmas. A caveat, however, is that if rhyolite magmas represent interstitial melts derived from intermediate magmas (e.g. Bachmann and Bergantz, 2004; Price et al., 2005; Reubi and Blundy, 2009; Lee and Bachmann, 2014), then rhyolites should contain about the same amount of assimilated crust as andesites (i.e. ~20-30 % based on estimates from Tongariro andesites), which is consistent with the aforementioned isotope data.

One outstanding observation that has not been satisfactorily addressed is why andesitic melt inclusions are rare in arc volcanic rocks with intermediate bulk compositions, as observed in global datasets (Reubi and Blundy, 2009; Fig. 6.4b, below). In their study, Reubi and Blundy (2009) suggest that andesites are primarily the product of basalt mixing with dacite-rhyolite magmas, although this has been disputed by others because andesite melts do exist, even if they are not abundant (Lee and Bachmann, 2014; Rooyakkers et al., 2018). Mixing of basalt magmas and dacite-rhyolite melts to produce andesite magmas should ideally require rhyolites to be produced from a process that does not involve andesites, to avoid circularity. In an attempt to

understand why andesitic melt inclusions are rare in arc volcanic rocks (Reubi and Blundy, 2009), this study offers the following novel explanation.

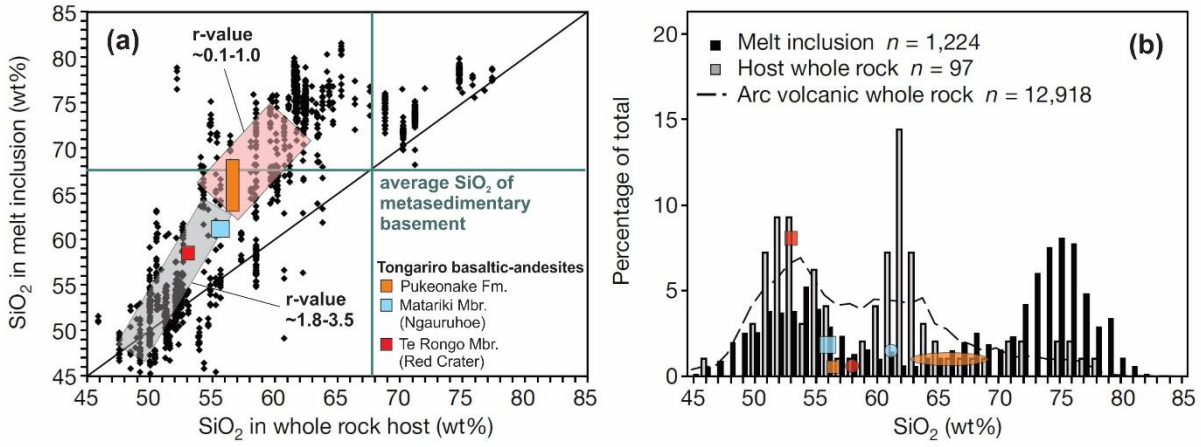

Figure 6.4. (Reproduced from Fig. 1c-d of Reubi and Blundy, 2009.) (**a**) Comparison of SiO_2 in melt inclusions and corresponding host whole-rocks. Green lines show the average composition of the metasedimentary basement beneath Tongariro (see section 4.3). Pukeonake Formation data from this study (Appendix 8) and Beier et al. (2017); Matariki Member (Ngauruhoe) data from Hobden et al. (1999) and Moebis et al. (2011); Te Rongo Member (Red Crater) data from Hobden (1997) and Moebis et al. (2011). (**b**) Frequency histograms for SiO_2 concentrations of whole-rock and paired melt inclusions. Colours for Tongariro basaltic-andesite data are as in (**a**) with rectangles showing whole-rock data and ellipses showing melt inclusion or interstitial melt data.

The scarcity of andesitic melt inclusions in intermediate composition volcanic rocks is proposed here to be a consequence of rapid AFC evolution from replenishing mantle-derived basalt magmas to basaltic-andesites, which is typified by high r-values (more assimilation relative to crystal fractionation). Subsequent magma evolution via AFC processes from basaltic-andesite compositions to andesites and dacites occurs at lower r-values and with reduced SiO_2 contrasts between evolving magmas and country-rock assimilants. Both of these factors act to reduce the rate of SiO_2 increase in whole-rock and corresponding interstitial melts (as preserved in melt inclusions). The dearth of andesitic melt inclusions in intermediate composition volcanic rocks may therefore represent the rapidity of the evolution of basaltic melts to dacitic compositions, which reduces the probability that andesitic melt inclusions will be trapped and preserved during crystal growth.

At Tongariro the primary crustal assimilant has an average SiO_2 concentration of ~68 wt% (section 4.3) and therefore as magmas evolve, the contrast between magmatic and country-rock SiO_2 concentrations will diminish. If r-values are initially high for basalts evolving to basaltic-andesites, as is estimated for Tongariro (r-value ~1.8-3.5: sections 4.3-4.4), then the rapid assimilation of approximately dacitic country-rock must have coincided with equivalently

rapid increases in interstitial melt SiO_2 concentrations. Available data for melt inclusions and interstitial glasses in Tongariro basaltic-andesites indicate corresponding melt compositions of ~58 wt% SiO_2 (Te Rongo Member [Red Crater]: Moebis et al., 2011), ~61 wt% SiO_2 (Matariki Member [Ngauruhoe]: Moebis et al., 2011) and ~63-68 wt% SiO_2 (Pukeonake Formation: Beier et al., 2017; Appendix 8 in this study): these are plotted in Fig. 6.4. On average, Tongariro basaltic-andesite hosted melts have ~63 wt% SiO_2 for corresponding whole-rock host SiO_2 concentrations of ~53-57 wt% (Hobden, 1997; Hobden et al., 1999; Beier et al., 2017), which correspond well to the global data arrays presented by Reubi and Blundy (2009; Fig. 6.4). This shows that elevated r-values (~1.8-3.5) characterise the interval of melt evolution from basaltic to dacitic compositions—which is rapid—and contrasts with slower evolution from dacitic to rhyolitic melt composition at r-values that are ~0.1-1.0, for Tongariro eruptives.

The data presented by Reubi and Blundy (2009) are consistent with this model and show overlapping arrays (Fig. 6.4a). Given that the average composition of the continental crust is andesitic-dacitic (Rudnick and Gao, 2003), it is probable that other arc magma systems may be characterised by initially rapid evolution from basaltic to dacitic melt compositions. Initially high r-values (~2.0-2.7) in arc magma evolution, that later decrease to ~0.5-1.0 as magmas evolve, have been predicted from thermodynamically-balanced AFC modelling (Reiniers et al., 1995), despite the opposite result being reported by energy-balanced AFC modelling elsewhere (Bohrson and Spera, 2001, 2007; Spera and Bohrson, 2004). With regard to the existence of andesitic melt inclusions in arc volcanic rocks, the dataset presented by Reubi and Blundy (2009: their Fig. 1c) shows that continuity exists between basaltic to rhyolitic melt inclusions. SiO_2-P_2O_5-Zr relationships reported for other global datasets also show that andesitic melt inclusions observed in arc volcanic rocks cannot be reproduced from mixing basaltic and rhyolitic melts (Lee and Bachmann, 2014), which indicates that whilst andesitic melts exist, they are under-represented in melt inclusion records. Paired whole-rock (host) and melt inclusion data show departure from equal SiO_2 concentrations at ~53 wt% (Fig. 6.4a: Reubi and Blundy, 2009). This is reflected by a decreased frequency in whole-rock compositions from basalt to basaltic-andesite that corresponds to relatively scarce melt inclusion concentrations of andesitic composition. The relative abundance of melt inclusions begins increasing from dacitic compositions, which approximately corresponds to the shift in r-values from ~1.8-3.5 to ~0.1-1.0 and the effective elimination of contrasting melt versus country-rock SiO_2 concentrations.

6.3. OTHER RESULTS AND CONCLUSIONS

6.3.1. Results and conclusions for the southern TVZ area

This subsection summarises the results and conclusions that are specifically relevant to the southern TVZ. These include new chronostratigraphic age constraints on southern TVZ eruptives, petrogenetic interpretations relating to magma assembly processes at Tongariro and Ruapehu, and the interpretations of basement structure based on xenolith geochemistry.

- An inlier of basaltic-andesite on Tongariro's NW flank, defined here as the Otamatereinga Formation (new), yielded a $^{40}Ar/^{39}Ar$ age determination of 512 ± 59 ka. This is the oldest *in situ* material on the Tongariro edifice. However, the provenance of this lava is unclear and it may not have been erupted from Tongariro but instead be from an almost-entirely buried volcano, analogous to (or directly flowed from) Maungaku or Maungakatote to the NNW (Fig. 1.1).
- Hornblende-phyric andesite boulders, mapped within the Tupuna Formation (new), yield the oldest $^{40}Ar/^{39}Ar$ age determination for materials confidently attributed to Tongariro. Tupuna andesites are correlated here with the Turakina Formation debris flows of Tost and Cronin (2015), deposited between 349-309 ka. The source of these debris flows is thus inferred to be an early Tongariro edifice, rather than Ruapehu as proposed by previous workers. At the time when the Turakina debris flows were deposited, Ruapehu did not exist, at least not in its current form.
- A new $^{40}Ar/^{39}Ar$ age determination for a summit lava flow from the Pihanga edifice indicates a minimum age of 180 ka, significantly older than the ~123 ka K/Ar date that was reported previously by Stipp (1969).
- A voluminous lava flow that is intermittently exposed in the Tongariro River, east of both volcanoes by ~15 km (or 1-2 km east of State Highway 1), was sourced from Ruapehu, rather than Tongariro as previously supposed (cf. Grindley, 1960). This conclusion is drawn from step heating $^{40}Ar/^{39}Ar$ data that may give an age between 60 and 70 ka, field exposures that trace back towards Ruapehu, and compositions that are more similar to Ruapehu's Wahianoa Formation and early Mangawhero Formation eruptives than any known stratigraphic unit on Tongariro or Ruapehu. The age of this lava is within New Zealand's Last Glacial period and it was possibly emplaced supra-glacially near source (e.g. Rangataua Member flow on Ruapehu: Conway et al., 2016), beyond which it travelled at least 28 km down the paleo-Tongariro River valley, which has since been partially re-excavated.
- Nd-Pb isotope systematics in metasedimentary xenoliths indicate that the majority of Tongariro magmas have been contaminated by at least two (but possibly three) greywacke

terranes that form the basement rocks to depths of at least 15 km beneath Tongariro. $^{87}Sr/^{86}Sr$ ratios in bulk metasedimentary xenoliths probably shifted to values 0.002 lower than their protolithic equivalents due to the disproportionate loss of radiogenic Sr hosted in biotite and alkali feldspar, which were preferentially melted when xenoliths were entrained into hot magmas.

- Th/U fractionation occurred in Tongariro metasedimentary xenoliths relative to their protoliths because of U loss that was likely associated with zircon dissolution. This Th/U fractionation has modified $^{208}Pb/^{206}Pb$ (and $^{208}Pb/^{207}Pb$) ratios to higher values, potentially by +0.004.
- Meta-igneous xenoliths derived from basement rocks beneath the southern TVZ are redefined here, in contrast with the definitions of Graham (1985) and Graham et al. (1987, 1990). It is suggested that meta-igneous xenoliths, as previously defined, should be further distinguished with trace element and Sr-Nd-Pb isotope compositions into 'arc type' and 'non-arc type' compositional groups. Comparisons of three unusual xenoliths from Tongariro (LP168X: this study, section 4.3.2.5) and Ruapehu (samples 17423 and 17457: Graham, 1985; Lee, 2008), display the following similarities, which are suggested as a checklist for identifying non-arc type meta-igneous xenoliths in the southern TVZ.
    - Negative Ce anomalies, which are absent in metasedimentary xenoliths.
    - Similar LREE and HREE concentrations, with La_N/Yb_N ~1-2. In contrast, metasedimentary xenoliths have $La_N/Yb_N \geq 2$, typically ~4-10 (CI chondrite values from McDonough and Sun, 1995).
    - $^{143}Nd/^{144}Nd$ ratios higher than >0.5128.
    - $^{87}Sr/^{86}Sr$ ratios ≥0.7062.
    - $^{207}Pb/^{206}Pb$ ratios of ≥0.8314 and $^{208}Pb/^{206}Pb$ ratios of ≥2.059.

6.3.2. Analytical and methodological findings

This subsection summarises the findings from investigations and experimentation with analytical methods used in this study, as follows.

- Comparisons between new $^{40}Ar/^{39}Ar$ and previous K/Ar age determinations show that holocrystalline samples yield results that are consistently more accurate than glassy samples. K/Ar age determinations become systematically more accurate with increasing K_2O concentrations and are within error of $^{40}Ar/^{39}Ar$ determinations on materials with >1.8 wt% K_2O, irrespective of whether the samples are glassy or holocrystalline. The percentage of

phenocrysts (which can host melt inclusions with excess argon) does not correlate with the accuracy of whole-rock K/Ar age determinations.

- Pb leaching experiments on basaltic-andesite, andesite and dacite samples—that span Pb concentrations of 4-14 ppm—demonstrate that between 16-35 % of Pb is lost during leaching. The leaching method used 4 mL 6M HCl at 100 °C for 45-60 mins, which follows conventional procedures (e.g. Todd et al., 2015). The results may help future studies achieve desired ng yields of Pb for TIMS analysis by compensating for anticipated loss in the leaching step.

6.4. SUGGESTIONS FOR FUTURE STUDIES

The successes and insights provided by this project advocate for further detailed field studies of stratovolcanoes, especially for studies of multiple adjacent volcanoes in the same volcanic arc wherever possible. Presently, the armoury of available geochronological techniques ($^{40}Ar/^{39}Ar$, ^{238}U-^{230}Th disequilibria, radiocarbon, cosmogenic nuclides) and robust geochemical techniques (i.e. XRF, EPMA, ICP-MS, TIMS) permits investigations (and may warrant re-investigation) of volcanic and magmatic processes that are effectively limited only by the resolution of field examination. Even for Quaternary stratovolcanoes with ≥200 kyr lifespans, sequential reconstructions of magmatic evolution and volcanic behaviour are now possible at resolutions approaching ~1 kyr. Hence, following Rumsfeldian logic (e.g. Rumsfeld, 2002, via Wilson, 2017), detailed and comprehensive field studies—which do not have circular dependence on models for results and interpretations—are potentially of the greatest use for identifying previously unknown or under-acknowledged volcanological and petrogenetic processes. In this view, the following recommendations are made for future studies of arc magma systems in both New Zealand and globally, in no particular order.

- The northernmost volcanoes in the southern TVZ, which effectively separate andesitic Tongariro and Ruapehu from the rhyolitic central TVZ (e.g. Taupō and Okataina), have received limited examination. These volcanoes are Maungaku, Maungakatote, Kakaramea, Tihia, Pihanga and Rotopounamu (Fig. 1.1). Geochemical studies of these volcanoes by Cashman (1979) and Cole et al. (1983) have identified that geochemical diversity is present, comparable to that of Tongariro and Ruapehu (cf. Cole, 1978; Hobden, 1997; Price et al., 2012; Conway et al., 2018; this study), despite the smaller volumes of the associated edifices. Currently, the understanding of southern TVZ petrogenesis and volcanism—and the relationship to the rhyolite-dominated central TVZ—is hampered by a lack of examination at these volcanoes.

- The geochemical study of olivine-hosted melt inclusions offers a simple avenue for examining whether contemporaneous basaltic-andesite volcanism at Tongariro was fuelled by a common mafic source. Holocene basaltic-andesites erupted from separate vents (Mangatetipua Member [Upper Te Maari Crater], Te Rongo Member [Red Crater] and Te Pupu Formation [Ngauruhoe]) mark a transition from earlier andesite-dominated volcanism to more mafic eruptives, and potentially signal a volcano-wide mafic replenishment episode (e.g. Fig. 6.2). The presence of this episode could be tested for by geochemically fingerprinting olivine-hosted melt inclusions to examine whether the sources of these basaltic-andesites are related.
- Studies of zircon provenance in metasedimentary xenoliths in southern TVZ eruptives would provide further constraints on basement structure and terrane geometry. Zr versus Hf relationships and petrographic observations (Chapter 4) provide compelling evidence for zircon dissolution in recovered metasedimentary xenoliths. It is unclear whether the population of surviving zircons would be biased towards particular ages, or even if there are enough zircons to make such studies statistically viable.
- Recently improved chronostratigraphic frameworks for Tongariro (Chapter 3) and Ruapehu (Conway et al., 2016; Townsend et al., 2017) provide new opportunities for examining ring plain deposits. These chronostratigraphies provide high-resolution age context for geochemical data which make studies of clast provenance in ring plain deposits feasible. In some cases, specific compositions are restricted to distinct time intervals, and therefore geochemical investigations of clasts in debris flow and sector collapse deposits may provide robust constraints on their maximum depositional ages. Such studies would likely guide new edifice-focussed investigations in cases where unrecognised clastic components are discovered, which may reveal aspects of southern TVZ volcanic history that are not well represented in edifice records.
- To date, no representative studies of crystal-scale isotopic variability have been undertaken at Tongariro (cf. Hora, 2003; Shane et al., 2019), nor Ruapehu (cf. Price et al., 2012). Advances in instrumental sensitivity now enable precise measurements of ≤10 ng load for Sr-Nd-Pb isotope ratios via TIMS (e.g. Charlier et al., 2006, 2007; Davidson et al., 2007b). This effectively permits studies of isotopic heterogeneity in minerals other than feldspar and for Nd and Pb isotope systems. Two other suggestions are Pb in feldspars (e.g. Kd values of ~1.0-2.5 for dacitic-rhyolitic melts: Rollinson, 1993 and references therein) and Nd in pyroxenes and amphiboles (e.g. Kd values of ~0.1-4.3 in basaltic to rhyolitic melts: Rollinson, 1993 and references therein). These minerals are present in most arc magmas which indicates

that this is a fruitful area for future work. Such studies would provide high resolution records of crustal contamination episodes on spatial scales (mm) relevant to crystal growth, and allow comparisons of how different isotope systems and minerals are effected during discrete magma-building events.

Within the frameworks of recently improved chronostratigraphies for Tongariro (Chapter 3) and Ruapehu (Conway et al., 2016; Townsend et al., 2017), there are now new opportunities to examine magma assembly processes from isotopic perspectives at crystal-scales for samples that are representative of whole volcano lifecycles. The unusually large (up to 8-9 mm) plagioclase and clinopyroxene phenocrysts observed in Mangahouhounui Formation eruptives from Tongariro would make good candidates for micromilling isotopic studies because of their large sizes and potentially continuous records of isotopic variations as their host magmas were assembled. Why such large crystals developed in these magmas, relative to other Tongariro eruptives is unclear. A crystal-specific study that compares Mangahouhounui Formation eruptives versus other Tongariro eruptives is potentially of value. Furthermore, plagioclase textures and groundmass Eu anomalies in early Tongariro eruptives, represented by the Tupuna Formation, suggest that a significant portion of early Tongariro eruptives may be xenocrystic, which could be investigated with trace element and isotopic studies at inter- and intra-crystal scales.

- A general recommendation for petrogenetic studies of all magma systems is that r-values may vary at different stages of magma evolution and should potentially be modelled separately.

The successes and insights of this project have arisen from the integrated use of field data, radioisotopic geochronology and targeted geochemical investigations. These observations comprise detailed, integrated and high-quality datasets that offer insights that would otherwise remain hidden or would be inadequately supported by lower-quality datasets of limited breadth. The rate and clarity with which scientific knowledge will advance therefore depends on whether scientific investigations take shortcuts or adopt a 'no half measures' approach, the latter being advocated for here.

References

Adams, C. J., Mortimer, N., Campbell, H. J., and Griffin, W. L. (2009). Age and isotopic characterisation of metasedimentary rocks from the Torlesse Supergroup and Waipapa Group in the central North Island, New Zealand, New Zealand Journal of Geology and Geophysics, 52, 149-170.

Allan, A. S. R., Wilson, C. J. N., Millet, M.-A., and Wysoczanski, R. J. (2012). The invisible hand: Tectonic triggering and modulation of a rhyolitic supereruption. Geology, 40, 563-566.

Allan, A. S. R., Morgan, D. J., Wilson, C. J. N., and Millet, M.-A. (2013). From mush to eruption in centuries: assembly of the super-sized Oruanui magma body. Contributions to Mineralogy and Petrology, 166, 143-164.

Allan, A. S. R., Barker, S. J., Millet, M.-A., Morgan, D. J., Rooyakkers, S. M., Schipper, C. I., and Wilson, C. J. N. (2017). A cascade of magmatic events during the assembly and eruption of a super-sized magma body. Contributions to Mineralogy and Petrology, 172, 49.

Annen, C., Blundy, J. D., and Sparks, R. S. J. (2006). The Genesis of Intermediate and Silicic Magmas in Deep Crustal Hot Zones. Journal of Petrology, 47, 505-539.

Arculus, R. J. (2003). Use and Abuse of the Terms Calcalkaline and Calcalkakic. Journal of Petrology, 44, 929-935.

Arculus, R. J., and Wills, K. J. (1980). The Petrology of Plutonic Blocks and Inclusions from the Lesser Antilles Island Arc. Journal of Petrology, 21, 743-799.

Arpa, M. C., Zellmer, G., Christenson, B., Lube, G., and Shellnutt, G. (2017). Variable magma reservoir depths for Tongariro Volcanic Complex eruptive deposits from 10,000 years to present. Bulletin of Volcanology, 79, 56.

Bachmann, O., and Bergantz, G. (2004). On the Origin of Crystal-poor Rhyolites: Extracted from Batholithic Crystal Mushes. Journal of Petrology, 45, 1565-1582.

Bacon, C. R. (1985). Implications of Silicic Vent Patterns for the Presence of Large Crustal Magma Chambers. Journal of Geophysical Research, 90, 11243-11252.

Bacon, C. R., and Druitt, T. H. (1988). Compositional evolution of the zoned calcalkaline magma chamber of Mount Mazama, Crater Lake, Oregon. Contributions to Mineralogy and Petrology, 98, 224-256.

Bacon, C. R., and Duffield, W. A. (1981). Late Cenozoic rhyolites from the Kern Plateau, southern Sierra Nevada, California. American Journal of Science, 281, 1-34.

Baker, J., Peate, D., Waight, T., and Meyzen, C. (2004). Pb isotopic analysis of standards and samples using a $^{207}Pb/^{204}Pb$ double spike and thallium to correct for mass bias with a double-focusing MC-ICP-MS. Chemical Geology, 211, 275-303.

Barker, S. J., Wilson, C. J. N., Smith, E. G. C., Charlier, B. L. A., Wooden, J. L., Hiess, J., and Ireland, T. R. (2014). Post-supereruption Magmatic Reconstruction of Taupo Volcano (New Zealand) as Reflected by Zircon Ages and Trace Elements. Journal of Petrology, 55, 1511-1533.

Barker, S. J., Wilson, C. J. N., Allan, A. S. R. and Schipper, C. I. (2015). Fine-scale temporal recovery, reconstruction and evolution of a post-supereruption magmatic system. Contributions to Mineralogy and Petrology, 170:5.

Barley, M. E. (1987). Origin and evolution of mid-Cretaceous, garnet-bearing, intermediate and silicic volcanics from Canterbury, New Zealand. Journal of Volcanology and Geothermal Research, 32, 247-267.

Barrell, D. J. A. (2011). Quaternary glaciers of New Zealand. In: Ehlers, J., Gibbard, P.L., and Hughes, P.D. (Eds.), Developments in Quaternary Science. 15, Elsevier, Amsterdam, 1047–1064.

Barton, S. J. (2011). Crystal forensics of historical lava flows from Mt Ngauruhoe. Unpublished MSc thesis, Victoria University of Wellington, 132 pp.

Battey, M. H. (1949). The recent eruption of Ngauruhoe. Records of the Auckland Institute and Museum, 3, 387-395.

Bayly, T. F., and Quinlan, L. (1965). Tokaanu – Poutu Canal: core number j130. In: Tongariro Power Development Core Log, 8 pp.

Beavan, J., Wallace, L. M., Palmer, N., Denys, P., Ellis, S., Fournier, N., Hreinsdottir, S., Pearson, C., Denham, M. (2016). New Zealand GPS velocity field: 1995–2013. New Zealand Journal of Geology and Geophysics, 59, 5-14.

Beetham, R. D., and Watters, A. D. (1985). Geology of Torlesse and Waipapa terrane basement rocks encountered during the Tongariro Power Development project, North Island, New Zealand. New Zealand Journal of Geology and Geophysics, 28, 575-594.

Beier, C., Haase, K., Brandl, P. A., and Krumm, S. (2017). Primitive andesites from the Taupo Volcanic Zone formed by magma mixing. Contributions to Mineralogy and Petrology, 172, 33.

Bergal-Kuvikas, O., Nakagawa, M., Kuritani, T., Muravyev, Y., Malik, N., Klimenko, E., Amma-Miyasaka, M., Matsumoto, A., and Shimada, S. (2017). A petrological and geochemical study on time-series samples from Klyuchevskoy volcano, Kamchatka arc. Contributions to Mineralogy and Petrology, 172, 35.

Berryman, K. (1992). A stratigraphic age of Rotoehu Ash and late Pleistocene climate interpretation based on marine terrace chronology, Mahia Peninsula, North Island, New Zealand. New Zealand Journal of Geology and Geophysics, 35, 1-7.

Bhattacharya, S., Kemp, A. I. S., and Collins, W. J. (2018). Response of zircon melting to melting and metamorphism in deep arc crust, Fiordland (New Zealand): implications for zircon inheritance in cordilleran granites. Contributions to Mineralogy and Petrology, 173, 28.

Blake, S. (1984). Volatile oversaturation during the evolution of silicic magma chambers as an eruption trigger. Journal of Geophysical Research 89, 8237-8244.

Blundy, J., and Cashman, K. (2001). Ascent-driven crystallisation of dacite magmas at Mount St Helens, 1980-1986. Contributions to Mineralogy and Petrology, 140, 631-650.

Bohrson, W. A., and Spera, F. J. (2001). Energy-Constrained Open-System Magmatic Processes II: Application of Energy-Constrained Assimilation-Fractional Crystallisation (EC-AFC) Model to Magmatic Systems. Journal of Petrology, 42, 1019-1041.

Bohrson, W. A., and Spera, F. J. (2004). Energy-Constrained Recharge, Assimilation, and Fractional Crystallization (EC-E'RA$_X$FC): A Visual Basic computer code for calculating trace element and isotopic variations of open-system magmatic systems. Geochemistry, Geophysics, Geosystems, 8, Q11003.

Bova, S. (2010). What lies beneath: deciphering magma chamber dynamics at Ngauruhoe volcano. Unpublished BSc thesis, University of Canterbury, Christchurch, 14 pp.

Bowen, N. L. (1928). The Evolution of the Igneous Rocks. Princeton University Press, New Jersey, 334 pp.

Brown, S. J. A., Wilson, C. J. N., Cole, J. W., and Wooden, J. (1998). The Whakamaru group ignimbrites, Taupo Volcanic Zone, New Zealand: evidence for reverse tapping of a zoned silicic magmatic system. Journal of Volcanology and Geothermal Research, 84, 1-37.

Calvert, A. T., Fierstein, J., and Hildreth, W. (2018). Eruptive history of Middle Sister, Oregon Cascades, USA—product of a late Pleistocene eruptive episode. Geosphere, 14, 2118-2139.

Cameron, E., Gamble, J., Price, R., Smith, I., McIntosh, W., and Gardner, M. (2010). The petrology, geochronology and geochemistry of Hauhungatahi volcano, S.W. Taupo Volcanic Zone. Journal of Volcanology and Geothermal Research, 190, 179-191.

Capra, L. (2006). Abrupt climatic changes as triggering mechanisms of massive sector collapses. Journal of Volcanology and Geothermal Research, 155, 329-333.

Cashman, K. V. (1979). Evolution of Kakaramea and Maungakatote volcanoes, Tongariro Volcanic Centre, New Zealand. Unpublished MSc thesis, Victoria University of Wellington, Wellington, 152 pp.

Cassidy, J., Ingham, M., Locke, C. A., and Bibby, H. (2009). Subsurface structure across the axis of the Tongariro Volcanic Centre, New Zealand. Journal of Volcanology and Geothermal Research, 179, 233-240.

Cassidy, M., Ebmeier, S. K., Helo, C., Watt, S., Caudron, C., Odell, A., Spaans, K., Kristianto, P., Triastuty, H., Gunawan, H., and Castro, J. M. (2019). Explosive eruptions with little warning: experimental petrology and volcano monitoring observations from the 2014 eruption of Kelud, Indonesia. Geochemistry, Geophysics, Geosystems 20, 4218-4247.

Cawood, P. A., Nemchin, A. A., Leverenz, A., Saeed, A., and Ballance, P. F. (1999). U/Pb dating of detrital zircons: implications for the provenance record of Gondwana margin terranes. Geological Society of America Bulletin, 111, 1107-1119.

Chappell, J. (2002). Sea level changes forced ice breakouts in the Last Glacial cycle: new results from coral terraces. Quaternary Science Reviews, 21, 1229-1240.

Charlier, B. L. A., Wilson, C. J. N., Lowenstern, J. B., Blake, S., van Calsteren, P. W., and Davidson, J. P. (2005). Magma Generation at a Large, Hyperactive Silicic Volcano (Taupo, New Zealand) Revealed by U-Th and U-Pb Systematics in Zircons. Journal of Petrology, 46, 3-32.

Charlier, B. L. A., Ginibre, C., Morgan, D., Nowell, G. M., Pearson, D. G., Davidson, J. P., and Ottley, C. J. (2006). Methods for the microsampling and high-precision analysis of strontium and rubidium isotopes at single-crystal scale for petrological and geochronological applications. Chemical Geology, 232, 114-133.

Charlier, B. L. A., Bachmann, O., Davidson, J. P., Dungan, M. A., and Morgan, D. J. (2007). The Upper Crustal Evolution of a Large Silicic Magma Body: Evidence from Crystal-scale Rb-Sr Isotopic Heterogeneities in the Fish Canyon Magmatic System, Colorado. Journal of Petrology, 48, 1875-1894.

Charlier, B. L. A., Wilson, C. J. N., and Davidson, J. P. (2008). Rapid open-system assembly of a large silicic magma body: time-resolved evidence from cored plagioclase crystals in the Oruanui eruptions deposits, New Zealand. Contributions to Mineralogy and Petrology, 156, 799-813.

Charlier, B. L. A., Wilson, C. J. N., and Mortimer, N. (2010). Evidence from zircon U-Pb age spectra for crustal structure and felsic magma genesis at Taupo volcano, New Zealand. Geology, 38, 915-918.

Chen, C.-H., DePaolo, D. J., Nakada, S., and Shieh, Y.-N. (1993). Relationship between eruption volume and neodymium isotopic composition at Unzen volcano. Nature, 362, 831-834.

Cole, J. W. (1978). Andesites of the Tongariro Volcanic Centre, North Island, New Zealand. Journal of Volcanology and Geothermal Research, 3, 121-153.

Cole, J. W. (1979). Chemical analyses of lavas and ignimbrites of the Taupo Volcanic Zone. Department of Geology, Victoria University of Wellington, 13.

Cole, J.W., and Lewis, K.B. (1981). Evolution of the Taupo-Hikurangi subduction system. Tectonophysics, 72, 1-21.

Cole, J. W., Kashman, C. V., and Rankin, P. C. (1983). Rare-earth element geochemistry and the origin of andesites and basalts of the Taupo Volcanic Zone, New Zealand. Chemical Geology, 38, 255-274.

Cole, R. P. (2019). Andesitic glaciovolcanic interactions at Tongariro and Ruapehu volcanoes, New Zealand. Unpublished PhD thesis, University of Otago, Dunedin, 208 pp.

Cole, R. P., White, J. D. L., Conway, C. E., Leonard, G. S., Townsend, D. B., and Pure, L. R. (2018). The glaciovolcanic evolution of an andesitic edifice, South Crater, Tongariro volcano, New Zealand. Journal of Volcanology and Geothermal Research, 352, 55-77.

Cole, R. P., Ohneiser, C., White, J. D. L., Townsend, D. B., and Leonard, G. S. (2019). Paleomagnetic evidence for cold emplacement of eruption-fed density current deposits beneath an ancient summit glacier, Tongariro volcano, New Zealand. Earth and Planetary Science Letters, 522, 155-165.

Conway, C. E. (2016). Studies on the glaciovolcanic and magmatic history of Ruapehu volcano, New Zealand. Unpublished PhD thesis, Victoria University of Wellington, Wellington, 207 pp.

Conway, C. E., Townsend, D. B., Leonard, G. S., Wilson, C. J. N., Calvert, A. T., and Gamble, J. A. (2015). Lava-ice interaction on a large composite volcano: a case study from Ruapehu, New Zealand. Bulletin of Volcanology, 77, 21.

Conway, C. E., Leonard, G. S., Townsend, D. B., Calvert, A. T., Wilson, C. J., Gamble, J. A., and Eaves, S. R. (2016). A high-resolution $^{40}Ar/^{39}Ar$ lava chronology and edifice construction history for Ruapehu volcano, New Zealand. Journal of Volcanology and Geothermal Research, 327, 152-179.

Conway, C. E., Gamble, J. A., Wilson, C. J. N., Leonard, G. S., Townsend, D. B., and Calvert, A. T. (2018). New petrological, geochemical, and geochronological perspectives on andesite-dacite magma genesis at Ruapehu volcano, New Zealand. American Mineralogist, 103, 565-581.

Cooper, G. F., and Wilson, C. J. N. (2014). Development, mobilisation and eruption of a large crystal-rich rhyolite: the Ongatiti ignimbrite, New Zealand. Lithos, 198-199, 38-57.

Coote, A. C., and Shane, P. (2016). Crystal origins and magmatic system beneath Ngauruhoe volcano (New Zealand) revealed by plagioclase textures and compositions. Lithos, 260, 107-119.

Cronin, S. J. (1996). Late Quaternary volcanic stratigraphy within a portion of the northeastern Tongariro Volcanic Centre. Unpublished PhD thesis, Massey University, Palmerston North, 181 pp.

Cronin, S. J., and Neall, V. E. (1997). A late Quaternary stratigraphic framework for the northeastern Ruapehu and eastern Tongariro ring plains, New Zealand. New Zealand Journal of Geology and Geophysics, 40, 185-197.

Cussen, L. (1891). Report on the Topographical Survey of Tongariro mountains. Appendix to the Journals of the House Representatives (Session II, C1A), New Zealand, 36-38.

Dalrymple, G. B. (1989). The GLM continuous laser system for $^{40}Ar/^{39}Ar$ dating: description and performance characteristics. In New Frontiers in Stable Isotopic Research, Shanks, W.C., and Criss, R.E. (Eds.), U. S. Geological Survey Bulletin 1890, 89-96.

Dalrymple, G. B., Alexander E. C. Jr., Lanphere, M. A., and Kraker, G. P. (1981). Irradiation of samples for $^{40}Ar/^{39}Ar$ dating using the Geological Survey TRIGA reactor. U. S. Geological Survey Professional Paper 1176.

Danišík, M., Shane, P., Schmitt, A. K., Hogg, A., Santos, G. M., Storm, S. Evans, N. J., Fifield, L. K., and Lindsay, J. M. (2012). Re-anchoring the late Pleistocene tephrochronology of New Zealand on concordant radiocarbon ages and combined $^{238}U/^{230Th}$ disequilibrium and (U-Th)/He zircon ages. Earth and Planetary Science Letters, 249-250, 240-250.

Davidson, J., Turner, S., Handley, H., Macpherson, C., and Dosseto, A. (2007a). Amphibole "sponge" in arc crust?. Geology, 35, 787-790.

Davidson, J. P., Morgan, D. J., Charlier, B. L. A., Harlou, R., and Hora, J. M. (2007b). Microsampling and isotopic analysis of igneous rocks: implications for the study of magmatic systems. Annual Reviews of Earth and Planetary Science, 35, 273-311.

DeMets, C., Gordon, R. G., and Argus, D. F. (2010). Geologically current plate motions. Geophysical Journal International, 181, 1-80.

DePaolo, D. J. (1981). Trace element and isotopic effects of combined wallrock assimilation and fractional crystallization. Earth and Planetary Science Letters, 53, 189-202.

Dimech, J.-L., Stern, T., and Lamb, S. (2017). Mantle earthquakes, crustal structure, and gravitational instability beneath western North Island, New Zealand. Geology, 45, 155-158.

Donoghue, S. L., and Neall, V. E. (1996). Tephrostratigraphic studies at Tongariro Volcanic Centre, New Zealand: an overview. Quaternary International, 34-36, 13-20.

Donoghue, S. L., and Neall, V. E. (2001). Late Quaternary constructional history of the southeastern Ruapehu ringplain, New Zealand. New Zealand Journal of Geology and Geophysics, 44, 439-466.

Donoghue, S. L., Neall, V. E., Palmer, A. S. (1995a). Stratigraphy and chronology of late Quaternary andesitic tephra deposits, Tongariro Volcanic Centre, New Zealand. Journal of the Royal Society of New Zealand, 25, 115-206.

Donoghue, S. L., Gamble, J. A., Palmer, A. S., and Stewart, R. B. (1995b). Magma mingling in an andesite pyroclastic flow of the Pourahu Member, Ruapehu volcano, New Zealand. Journal of Volcanology and Geothermal Research, 68, 177-191.

Downs, D. T., Wilson, C. J. N., Cole, J. W., Rowland, J. V., Calvert, A. T., Leonard, G. S., and Keall, J. M. (2014). Age and eruptive center of the Paeroa Subgroup ignimbrites (Whakamaru Group) within the Taupo Volcanic Zone of New Zealand. Geological Society of America Bulletin, 126, 1131-1144.

Dungan, M. A., Wulff, W., and Thompson, R. (2001). Eruptive Stratigraphy of the Tatara-San Pedro Complex, 36°S, Southern Volcanic Zone, Chilean Andes: Reconstruction Method and Implications at Long-lived Arc Volcanic Centers. Journal of Petrology, 42, 555-626.

Eaves, S. R. (2015). The glacial history of Tongariro and Ruapehu volcanoes, New Zealand. Unpublished PhD thesis, Victoria University of Wellington, Wellington, 253 pp.

Eaves, S. R., Mackintosh, A. N., Winckler, G., Schaefer, J. M., Alloway, B. V., and Townsend, D. B. (2016a). A cosmogenic ^{3}He chronology of late Quaternary glacier fluctuations in North Island, New Zealand (39°S). Quaternary Science Reviews, 132, 40-56.

Eaves, S. R., Anderson, B. M., Mackintosh, A. N., Doughty, A. M., Townsend, D. B., Conway, C. E., Winckler, G., Schaefer, J. M., Leonard, G. S., and Calvert, A. T. (2016b). The Last Glacial Maximum in central North Island, New Zealand: paleoclimate inferences from 2D glacier modelling. Climate of the Past, 12, 943-960.

Eberhart-Phillips, D., Bannister, S., and Reyners, M. (2019). Attenuation in the mantle wedge beneath super-volcanoes of the Taupo Volcanic Zone, New Zealand. Geophysical Journal International, 220, 703-723.

Edwards, B. R., Gudmundsson, M. T., and Russell, J. K. (2015). Glaciovolcanism. In: Sigurdsson, H., Houghton, B., Rymer, H., Stix, J., and McNutt, S. (Eds.), Encyclopedia of Volcanoes, Elsevier, Academic Press, London, 377-393.

Eichelberger, J. C. (1975). Origin of andesite and dacite: evidence of mixing at Glass Mountain in California and at other circum-Pacific volcanoes. Geological Society of America Bulletin, 86, 1381-1391.

Eichelberger, J. C., Izbekov, P. E., and Browne, B. L. (2006). Bulk chemical trends at arc volcanoes are not liquid lines of descent. Lithos, 87, 135-154.

Ellis, S. Heise, W., Kissling, W., Villamor, P., and Schreurs, G. (2014). The effect of crustal melt on rift dynamics: case study of the Taupo Volcanic Zone. New Zealand Journal of Geology and Geophysics, 57, 453-458.

Ersoy, Y., and Helvaci, C. (2010). FC-AFC-FCA and mixing modeler: A Microsoft® Excel© spreadsheet program for modelling geochemical differentiation of magma by crystal fractionation, crustal assimilation and mixing. Computers & Geosciences, 36, 383-390.

Esser, R. P., McIntosh, W. C., Heizler, M. T., and Kyle, P. R. (1997). Excess argon in melt inclusions in zero-age anorthoclase feldspar from Mt. Erebus, Antarctica, as revealed by the ^{40}Ar/^{39}Ar method. Geochimica et Cosmochimica Acta, 61, 3789-3801.

Ewart, A. (1965). Mineralogy and Petrogenesis of the Whakamaru Ignimbrite in the Maraetai area of the Taupo volcanic zone, New Zealand. New Zealand Journal of Geology and Geophysics, 8, 611-679.

Farina, F., and Stevens, G. (2011). Source controlled ^{87}Sr/^{86}Sr isotope variability in granitic magmas: The inevitable consequence of mineral-scale isotopic disequilibrium in the protolith. Lithos, 122, 189-200.

Farina, F., Dini, A., Rocchi, S., and Stevens, G. (2014). Extreme mineral-scale Sr isotope heterogeneity in granites by disequilibrium melting of the crust. Earth and Planetary Science Letters, 399, 103-115.

Faure, G., and Mensing, T. M. (2005). Isotopes: principles and applications. John Wiley & Sons, Inc., New Jersey, 897 pp.

Fierstein, J., Hildreth, W., and Calvert, A. T. (2011). Eruptive history of South Sister, Oregon Cascades. Journal of Volcanology and Geothermal Research, 207, 145-179.

Fleck, R. J., Calvert, A. T., Coble, M. A., Wooden, J. L., Hodges, K., Hayden, L. A., van Soest, M. C., du Bray, E. A., and John, D. A. (2019). Characterization of the rhyolite of Bodie Hills and ^{40}Ar/^{39}Ar intercalibration with Ar mineral standards. Chemical Geology, 525, 282-302.

Flude, S., and Storey, M. (2016). $^{40}Ar/^{39}Ar$ age of the Rotoiti Breccia and Rotoehu Ash, Okataina Volcanic Complex, New Zealand, and identification of heterogeneously distributed excess ^{40}Ar in supercooled crystals. Quaternary Geochronology, 33, 12-23.

Frey, H. M., Lange, R. A., Hall, C. M., and Delgado-Granados, H. (2004). Magma eruptions rates constrained by $^{40}Ar/^{39}Ar$ chronology and GIS for the Ceboruco-San Pedro volcanic field, western Mexico. Geological Society of America Bulletin, 116, 259-276.

Froggart, P. C., and Lowe, D. J. (1990). A review of late Quaternary silicic and some other tephra formations from New Zealand: Their stratigraphy, nomenclature, distribution, volume and age. New Zealand Journal of Geology and Geophysics, 33, 89-109.

Fudali, R. F. (1965). Oxygen fugacities of basaltic and andesitic magmas. Geochimica et Cosmochimica Acta, 29, 1063-1075.

Galer, S. J. G., and Abouchami, W. (1998). Practical application of lead triple spiking for correction of instrumental mass discrimination. Mineralogical Magazine, 62A, 491-492.

Gamble, J. A., Smith, I. E. M., Graham, I. J., Kokelaar, B. P., Cole, J. W., Houghton, B. F., and Wilson, C. J. N. (1990). The petrology, phase relations and tectonic setting of basalts from the Taupo Volcanic Zone, New Zealand and the Kermadec Island Arc – Havre Trough, New Zealand. Journal of Volcanology and Geothermal Research, 43, 253-270.

Gamble, J. A., Smith, I. E. M., McCulloch, M. T., Graham, I. J., and Kokelaar, B. P. (1993). The geochemistry and petrogenesis of basalts from the Taupo Volcanic Zone and Kermadec Island Arc, S.W. Pacific. Journal of Volcanology and Geothermal Research, 54, 265-290.

Gamble, J. A., Woodhead, J., Wright, I., and Smith, I. (1996). Basalt and Sediment Geochemistry and Magma Petrogenesis in a Transect from Oceanic Island arc to Rifted Continental Margin Arc: the Kermadec-Hikurangi Margin, SW Pacific. Journal of Petrology, 37, 1523-1546.

Gamble, J. A., Wood, C. P., Price, R. C., Smith, I. E. M., Stewart, R. B., and Waight, T. (1999). A fifty year perspective of magmatic evolution on Ruapehu Volcano, New Zealand: verification of open system behaviour in an arc volcano. Earth and Science Planetary Letters, 170, 301-314.

Gamble, J. A., Price, R. C., Smith, I. E. M., McIntosh, W. C., and Dunbar, N. W. (2003). $^{40}Ar/^{39}Ar$ geochronology of magmatic activity, magma flux and hazards at Ruapehu Volcano, Taupo volcanic zone, New Zealand. Journal of Volcanology and Geothermal Research, 120, 271-287.

Gerst, A., and Savage, M. K. (2004). Seismic Anisotropy Beneath Ruapehu Volcano: A Possible Eruption Forecasting Tool. Science, 306, 1543-1547.

Gerstenberger, H., and Haase, G. (1997). A highly effective emitter substance for mass spectrometric Pb isotope ratio determinations. Chemical Geology, 136, 309-312.

Geshi, N., and Teruki, O. (2016). Orientation of the Eruption Fissures Controlled by a Shallow Magma Chamber in Miyakejima. Frontiers in Earth Science, 4, 99.

Gill, J. (1981). Orogenic Andesites and Plate Tectonics. Springer-Verlag, New York, 390 pp.

Girina, O. A. (2013). Chronology of Bezymianny volcano activity, 1956-2010. Journal of Volcanology and Geothermal Research, 263, 22-41.

Gómez-Vasconcelos, M. G. (2017). Paleoseismology, seismic hazard and volcano-tectonic interactions in the Tongariro Volcanic Centre, New Zealand. Unpublished PhD thesis, Massey University, Palmerston North, 241 pp.

Gómez-Vasconcelos, M. G., Villamor, P., Cronin, S. J., Procter, J., Kereszturi, G., Palmer, A., Townsend, D., Leonard, G., Berryman, K., and Ashraf, S. (2016). Earthquake history at the eastern boundary of the South Taupo Volcanic Zone, New Zealand. New Zealand Journal of Geology and Geophysics, 59, 522-543.

Gómez-Vasconcelos, M. G., Villamor, P., Cronin, S., Proctor, J., Palmer, A., Townsend, D., and Leonard, G. (2017). Crustal extension in the Tongariro graben, New Zealand: Insights into volcano-tectonic interactions and active deformation in a young continental rift. Geological Society of America Bulletin, 129, 1085-1099.

Graham, I. J. (1985). Petrochemical and Sr-isotopic studies of lavas and xenoliths from Tongariro Volcanic Centre—Implications for crustal contamination of calc-alkaline magmas. Unpublished PhD thesis, Victoria University of Wellington, Wellington, 345 pp.

Graham, I. J. (1987). Petrography and origin of metasedimentary xenoliths in lavas from Tongariro Volcanic Centre. New Zealand Journal of Geology and Geophysics, 30, 139-157.

Graham, I. J., and Hackett, W. (1987). Petrology of Calc-alkaline Lavas from Ruapehu Volcano and Related Vents, Taupo Volcanic Zone, New Zealand. Journal of Petrology, 28, 531-567.

Graham, I. J., Grapes, R. H., and Kifle, K. (1988). Buchitic metagreywacke xenoliths from Mount Ngauruhoe, Taupo Volcanic Zone, New Zealand. Journal of Volcanology and Geothermal Research, 35, 205-216.

Graham, I. J., Blattner, P., and McCulloch, M. T., 1990. Meta-igneous granulite xenoliths from Mount Ruapehu, New Zealand: fragments of altered oceanic crust? Contributions to Mineralogy and Petrology, 105, 650-661.

Graham, I. J., Gulson, B. L., Hedenquist, J. W., and Mizon, K. (1992). Petrogenesis of Late Cenozoic volcanic rocks from the Taupo Volcanic Zone, New Zealand, in the light of new lead isotope data. Geochimica et Cosmochimica Acta, 56, 2797-2819.

Grapes, R., Watanabe, T., and Palmer, K. (1982). XRF analyses of quartzo-feldspathic schists and metacherts, Franz Josef-Fox Glacier area, Southern Alps of New Zealand. Department of Geology, Victoria University of Wellington, 25.

Gregg, D. R. (1956). Eruption of Ngauruhoe 1954-1955. New Zealand Journal of Science and Technology, 37, 675-688.

Gregg, D. R. (1960). The Geology of Tongariro Subdivision. New Zealand Geological Survey Bulletin, 40, New Zealand Department of Scientific and Industrial Research, Wellington.

Greve, A., Turner, G. M., Conway, C. E., Townsend, D. B., Gamble, J. A., and Leonard, G. S. (2016). Palaeomagnetic refinement of the eruption ages of Holocene lava flows, and implications for the eruptive history of the Tongariro Volcanic Centre, New Zealand. Geophysical Journal International, 207, 702-718.

Gruender, K., Stewart, R. B., and Foley, S. (2010). Xenoliths from the sub-volcanic lithosphere of Mt. Taranaki, New Zealand. Journal of Volcanology and Geothermal Research, 190, 192-202.

Hackett, W. R. (1985). Geology and petrology of Ruapehu and related vents. Unpublished PhD thesis, Victoria University of Wellington, Wellington, 312 pp.

Harrison, A., and White, R. S. (2006). Lithospheric structure of an active backarc basin: the Taupo Volcanic Zone, New Zealand. Geophys. J. Int., 167, 968-990.

Hildreth, W. (1996). Kulshan caldera: A Quaternary subglacial caldera in the North Cascades, Washington. Geological Society of America Bulletin, 108, 786-793.

Hildreth, W. (2001). Longevity and Dynamics of Rhyolitic Magma Systems. Presentation at Penrose Conference, 2001 June 7-12, Mammoth.

Hildreth, W., and Fierstein, J. (2012). Eruptive history of Mount Katmai, Alaska. Geosphere, 8, 1527-1567.

Hildreth, W., and Lanphere, M. A. (1994). Potassium-argon geochronology of a basalt-andesite-dacite arc system: The Mount Adams volcanic field, Cascade Range of southern Washington. Geological Society of America Bulletin, 106, 1413-1429.

Hildreth, W., and Moorbath, S. (1988). Crustal contributions to arc magmatism in the Andes of Central Chile. Contributions to Mineralogy and Petrology, 98, 455-489.

Hitchcock, D. W., and Cole, J. W. (2007). Potential impacts of a widespread subplinian andesitic eruption from Tongariro volcano, based on a study of the Poutu Lapilli. New Zealand Journal of Geology and Geophysics, 50, 53-66.

Hobden, B. J. (1997). Modelling magmatic trends in space and time: eruptive and magmatic history of the Tongariro volcanic complex. Unpublished PhD thesis, University of Canterbury, Christchurch, 508 pp.

Hobden, B. J., Houghton, B. F., Lanphere, M. A., and Nairn, I. A. (1996). Growth of the Tongariro volcanic complex: new evidence from K-Ar age determinations. New Zealand Journal of Geology and Geophysics, 39, 151-154.

Hobden, B. J., Houghton, B. F., Davidson, J. P., and Weaver, S. (1999). Small and short-lived magma batches at composite volcanoes: time windows at Tongariro volcano, New Zealand. Journal of the Geological Society of London, 156, 865-868.

Hobden, B. J., Houghton, B. F., and Nairn, I. A. (2002). Growth of a young, frequently active composite cone: Ngauruhoe volcano, New Zealand. Bulletin of Volcanology, 64, 392-409.

Hochstein, M. P., and Ballance, P. F. (1993). Hauraki Rift: a young, active, intra-continental rift in a back-arc setting. In Balance, P. F. (Ed.), South Pacific sedimentary basins, Sedimentary basins of the world 2, Elsevier, Amsterdam, 295-305.

Hochstetter. F. von, (1864). Geologie von Neu Seeland. (Novara Expedition, Geological Part l(1)): 274 pp. (English translation by C. A. Fleming, Government Printer, Wellington, 1959).

Hodder, P. (1983). Diapiric replenishment of magma chambers and triggering of volcanism in the Taupo Volcanic Zone, New Zealand. Chemical Geology, 38, 275-285.

Hogg, A., Lowe, D., Palmer, J., Boswijk, G., and Ramsey, C. B. (2012). Revised calendar date for the Taupo eruption derived by ^{14}C wiggle-matching using a New Zealand ^{14}C calibration data set. The Holocene, 22, 439-449.

Holness, M. B., and Siklos, S. T. C. (2000). The rates and extent of textural equilibration in high-temperature fluid-bearing systems. Chemical Geology, 162, 137-153.

Holness, M. B., Cesare, B., and Sawyer, E. W. (2011). Melted rocks under the microscope: microstructures and their interpretation. Elements, 7, 247-252.

Hora, J. M. (2003). Magmatic differentiation processes at Ngauruhoe Volcano, New Zealand: constraints from chemical, isotopic and textural analysis of plagioclase crystal zoning. Unpublished MSc thesis, University of California, Los Angeles.

Hughes, R. D. (1999). The timescales of andesite generation at Mount Ruapehu, New Zealand. Unpublished PhD thesis, The Open University, Milton Keynes, 332 pp.

Humphreys, M. C. S., Blundy, J. D., and Sparks, R. S. J. (2006a). Magma Evolution and Open System Processes at Shiveluch Volcano: Insights from Phenocryst Zoning. Journal of Petrology, 47, 2303-2334.

Humphreys, M. C. S., Kearns, S. L., and Blundy, J. D. (2006b). SIMS investigation of electron-beam damage to hydrous, rhyolitic glasses: implications for melt inclusion analysis. American Mineralogist, 91, 667-679.

Illsley-Kemp, F., Savage, M. A., Wilson, C. J. N., and Bannister, S. (2019). Mapping Stress and Structure From Subducting Slab to Magmatic Rift: Crustal Seismic Anisotropy of the North Island. Geochemistry, Geophysics, Geosystems, 20, https://doi.org/10.1029/2019GC008529.

Izbekov, P. E., Eichelberger, J. C., and Ivanov, B. V. (2004). The 1996 Eruption of Karymsky Volcano, Kamchatka: Historical Record of Basaltic Replenishment of an Andesite Reservoir. Journal of Petrology, 45, 2325-2345.

Jagoutz, O. (2014). Arc crustal differentiation mechanisms. Earth and Planetary Science Letters, 396, 267-277.

Jiao, R., Seward, D., Little, T. A., and Kohn, B. P. (2014). Thermal history and exhumation of basement rocks from Mesozoic to Cenozoic subduction cycles, central North Island, New Zealand. Tectonics, 33, 1920-1935.

Jicha, B. R., Coombs, M. L., Calvert, A. T., and Singer, B. S. (2012). Geology and $^{40}Ar/^{39}Ar$ geochronology of the medium- to high-K Tanaga volcanic cluster, western Aleutians. Geological Society of America Bulletin, 124, 842-856.

Jochum, K. P., Weis, U., Schwagger, B., Stoll, B., Wilson, S. A., Haug, G. H., Andreae, M. O., and Enzweiler, J. (2016). Reference values following ISO guidelines for frequently requested rock reference materials. Geostandards and Geoanalytical Research, 40, 333-350.

Kempton, P. D. (1995). Common Pb chemical procedures for silicate rocks and minerals, methods of data correction and an assessment of data quality at the NERC Isotope Geosciences Laboratory. NIGL Report, 78, 26 pp., NERC Isotope Geoscience Laboratory, Keyworth.

Kent, A. J. R. (2013). Preferential eruption of andesitic magmas: implications for volcanic magma fluxes at convergent margins. In: Gomez-Tuena, A., Straub, S. M., Zellmer G. F. (Eds.), Orogenic Andesites and Crustal Growth, Geological Society of London, Special Publications, 385, 257-280.

Kent, A. J. R., Darr, C., Koleszar, A. M., Salisbury, M. J., and Cooper, K. M. (2010). Preferential eruption of andesitic magma through recharge filtering. Nature Geoscience, 3, 631-636.

Kohn, B. P., and Topping, W. W. (1978). Time-space relationships between late Quaternary rhyolitic and andesitic volcanism in the southern Taupo Volcanic Zone, New Zealand. Geological Society of America Bulletin, 89, 1265-1271.

Klemetti, E. K., and Grunder, A. L. (2008). Volcanic evolution of Volcán Aucanquilcha: a long-lived dacite volcano in the Central Andes of northern Chile. Bulletin of Volcanology, 70, 633-650.

Knesel, K. M., and Davidson, J. P. (1996). Isotopic disequilibrium during melting of granite and implications for crustal contamination of magmas. Geology, 24, 243-246.

Knesel, K. M., and Davidson, J. P. (1999). Sr isotope systematics during melt generation by intrusion of basalt into continental crust. Contributions to Mineralogy and Petrology, 136, 285-295.

Krippner, J. B. (2009). Ngauruhoe inner crater processes of the 1954-1955 and 1974-1975 eruptions. Unpublished MSc thesis, University of Waikato, Hamilton, 149 pp.

Lanphere, M. A., and Sisson, T. W. (2003). Episodic growth at Mt. Rainier, Washington: a product of tectonic throttling? Geological Society of America Annual Meeting, 2003 November 2-5, Seattle, 35, 644.

Lecointre, J. A., Neall, V. E., Wallace, R. C., and Prebble, W. M. (2002). The 55- to 60-ka Te Whaiau Formation: a catastrophic, avalanche-induced, cohesive debris-flow deposit from proto-Tongariro volcano, New Zealand. Bulletin of Volcanology, 63, 509-525.

Lecointre, J. A., Neall, V. E., Wallace, R. C., Elliot, M. B., and Sparks, R. (2004). Late Quaternary evolution of the Rotoaira Basin, northern Tongariro ring plain, New Zealand. New Zealand Journal of Geology and Geophysics, 47, 549-565.

Lee, T. R. (2008). The thermal evolution of subduction zone lithosphere: evidence from the chemical development of Mt. Ruapehu and surrounding vents, New Zealand. Unpublished PhD thesis, Durham University, Durham, 238 pp.

Lee, C.-T.A., and Bachmann, O. (2014). How important is the role of crystal fractionation in making intermediate magmas? Insights from Zr and P systematics. Earth and Planetary Science Letters, 393, 266-274.

Lee, J. M., Bland, K. J., Townsend, D. B., and Kamp, P. J. J. (compilers) (2011). Geology of the Hawkes Bay area [map]. Lower Hutt (NZ), Institute of Geological and Nuclear Sciences. 1 sheet + 93 pp., scale 1:250,000. (Institute of Geological & Nuclear Sciences 1:250,000 map; 8).

Lescinsky, D. T., and Fink, J. H. (2000). Lava and Ice Interaction at Stratovolcanoes: Use of Characteristic Features to Determine Past Glacial Extents and Future Volcanic Hazards. Journal of Geophysical Research, 105, 23711-23726.

Lescinsky, D. T., and Sisson, T. W. (1998). Ridge-forming, ice-bounded lava flows at Mount Rainier, Washington. Geology, 26, 351-354.

Lisiecki, L. E., and Raymo, M. E. (2005). A Pliocene-Pleistocene stack of 57 globally distributed benthic $\delta^{18}O$ records. Paleoceanography, 20, PA1003.

Lowe, D. J., Blaauw, M., Hogg, A. G., and Newnham, R. M. (2013). Ages of 24 widespread tephras erupted since 30,000 years ago in New Zealand, with re-evaluation of the timing and palaeoclimatic implications of the Lateglacial cool episode recorded at Kaipo bog. Quaternary Science Reviews, 74, 170-194.

Lugmair, G. W., and Carlson, R. W. (1978). The Sm-Nd history of KREEP. Proceedings of the 9th Lunar and Planetary Science Conference, Houston, 689-704.

Luyendyk, B. P. (1995). Hypothesis for Cretaceous rifting of east Gondwana caused by subducted slab capture. Geology, 23, 373-376.

Maclennan, J., Jull, M., McKenzie, D., Slater, L., and Grönvold, K. (2002). The link between volcanism and deglaciation in Iceland. Geochemistry, Geophysics, Geosystems, 3, 1062-1087.

Macpherson, C. G., Gamble, J. A., and Mattey, D. P. (1998). Oxygen isotope geochemistry of lavas from an oceanic to continental arc transition, Kermadec-Hikurangi margin, SW Pacific. Earth and Planetary Science Letters, 160, 609-621.

Makishima, A., Tanaka, R., and Nakamura, E. (2009). Precise elemental and isotopic analyses in silicate samples employing ICP-MS: application of hydrofluoric acid solution and analytical techniques. Analytical Sciences, 25, 1181-1187.

Mathews, W. H. (1952). Ice-damned lavas from Clinker Mountain, southwestern British Columbia. American Journal of Science, 250, 553-565.

Mattey, D., Lowry, D., and Macpherson, C. (1994). Oxygen isotope composition of mantle peridotite. Earth and Planetary Science Letters, 128, 231-241.

McArthur, J. L., and Shepherd, M. J. (1990). Late Quaternary glaciation of Mt. Ruapehu, North Island, New Zealand. Journal of the Royal Society of New Zealand, 20, 287-296.

McDonough, W. F., and Sun, S.-s. (1995). The composition of the Earth. Chemical Geology, 120, 223-253.

McDougall, I., and Wellman, P. (2011). Calibration of GA1550 biotite standard for K/Ar and $^{40}Ar/^{39}Ar$ dating, Chemical Geology, 280, 19-25.

Miller, C. A., and Williams-Jones, G. (2016). Internal structure and volcanic hazard potential of Mt. Tongariro, New Zealand, from 3D gravity and magnetic models. Journal of Volcanology and Geothermal Research, 319, 12-28.

Miller, T. P., and Smith, R. L. (1987). Late Quaternary caldera-forming eruptions in the earth Aleutian arc, Alaska. Geology, 15, 434-438.

Miyashiro, A. (1974). Volcanic rock series in island arcs and active continental margins. American Journal of Science, 274, 321-355.

Moebis, A., Cronin, S. J., Neall, V. E., and Smith, I. E. M. (2011). Unravelling a complex volcanic history from fine-grained, intricate Holocene ash sequences at the Tongariro Volcanic Centre, New Zealand. Quaternary International, 246, 352-363.

Morris, J. D., Leeman, W. P., and Tera, F. (1990). The subducted component in island arc lavas: constraints from Be isotopes and B-Be systematics. Nature, 344, 31-66.

Mortimer, N. (1994). Origin of the Torlesse and coeval rocks, North Island, New Zealand. International Geology Review, 36, 891-910.

Mortimer, N. (2004). New Zealand's geological foundations. Gondwana Research, 7, 261-272.

Mortimer, N., Gans, P. B., Palin, J. M., Meffre, S., Herzer, R. H., and Skinner, D. N. B. (2010). Location and migration of Miocene-Quaternary volcanic arcs in the SW Pacific region. Journal of Volcanology and Geothermal Research, 190, 1-10.

Mortimer, N., McLaren, S., and Dunlap, W. J. (2012). Ar-Ar dating of K-feldspar in low grade metamorphic rocks: Example of an exhumed Mesozoic accretionary wedge and forearc, South Island, New Zealand. Tectonics, 31, TC3020.

Mortimer, N., Rattenbury, M. S., King, P. R., Bland, K. J., Barrell, D. J. A., Bache, F., Begg, J. G., Campbell, H. J., Cox, S. C., Crampton, J. S., Edbrooke, S. W., Forsyth, P. J., Johnston, M. R., Jongens, R., Lee, J. M., Leonard, G. S., Raine, J. I., Skinner, D. N. B., Timm, C., Townsend, D. B., Tulloch, A. J., Turnbull, I. M., and Turnbull, R. E. (2014). High-level stratigraphic scheme for New Zealand rocks. New Zealand Journal of Geology and Geophysics, 57, 402-419.

Myers, M. L., Wallace, P. J., Wilson, C. J. N., Morter, B. K., and Swallow, E. J. (2016). Prolonged ascent and episodic venting of discrete magma batches at the onset of the Huckleberry Ridge supereruption, Yellowstone. Earth and Planetary Science Letters, 451, 285-297.

Nairn, I. A. (1996). The geology of the Tongariro area [2 unpublished maps]. Located at: GNS Science, Lower Hutt, NZ, Mapping Section vertical file T19.

Nairn, I. A., Kobayashi, T., and Nakagawa, M. (1998). The ~10 ka multiple vent pyroclastic eruption sequence at Tongariro Volcanic Centre, Taupo Volcanic Zone, New Zealand:

Part 1. Eruptive processes during regional extension. Journal of Volcanology and Geothermal Research, 86, 19-44.

Nakagawa, M., Nairn, I. A., and Kobayashi, T. (1998). The ~10 ka multiple vent pyroclastic eruption sequence at Tongariro Volcanic Centre, Taupo Volcanic Zone, New Zealand: Part 2. Petrological insights into magma storage and transport during regional extension. Journal of Volcanology Geothermal Research, 86, 45-65.

Nakagawa, M., Wada, K., Thordarson, T., Wood, C. P., and Gamble, J. A. (1999). Petrologic investigations of the 1995 and 1996 eruptions of Ruapehu volcano, New Zealand: formation of discrete and small magma pockets and their intermittent discharge. Bulletin of Volcanology, 61, 15-31.

Nakamura, M. (1995). Continuous mixing of crystal mush and replenished magma in the ongoing Unzen eruption. Geology, 23, 807-810.

Nicol, A., Mazengarb, C., Chanier, F., Rait, G., Uruski, C., and Wallace, L. (2007). Tectonic evolution of the active Hikurangi subduction margin, New Zealand, since the Oligocene. Tectonics, 26, TC4002.

Niespolo, E. M., Rutte, D., Deino, A. L. and Renne, P. R. (2017). Intercalibration and age of the Alder Creek sanidine $^{40}Ar/^{39}Ar$ standard. Quaternary Geochronology, 39, 205-213.

O'Nions, R. K., Hamilton, P. J., Evensen, N. M. (1977). Variations in $^{143}Nd/^{144}Nd$ and $^{87}Sr/^{86}Sr$ ratios in oceanic basalts. Earth and Planetary Science Letters, 34, 13-22.

Palmer, B. A., and Neall. V. E. (1989). The Murimotu Formation–9500 year old deposits of a debris avalanche and associated lahars, Mount Ruapehu, North Island, New Zealand. New Zealand Journal of Geology and Geophysics, 32, 477-486.

Pardo, N., Cronin, S. J., Wright, H. M. N., Schipper, C. I., Smith, I., and Stewart, B. (2014). Pyroclast textural variation as an indicator of eruption column steadiness in andesitic Plinian eruptions from Mt. Ruapehu. Bulletin of Volcanology, 76, 822.

Patterson, D. B., and Graham, I. J. (1988). Petrogenesis of andesitic lavas from Mangatepopo valley and Upper Tama Lake, Tongariro volcanic centre, New Zealand. Journal of Volcanology and Geothermal Research, 35, 17-29.

Petcovic, H. L., and Grunder, A. L. (2003). Textural and Thermal History of Partial Melting in Tonalitic Wallrock at the Margin of a Basaltic Dike, Wallowa Mountains, Oregon. Journal of Petrology, 44, 2287-2312.

Pillans, B. (1983). Upper Quaternary marine terrace chronology and deformation, South Taranaki, New Zealand. Geology, 11, 292-297.

Pin, C., Gannoun, A., and Dupont, A. (2014). Rapid, simultaneous separation of Sr, Pb and Nd by extraction chromatography prior to isotope ratios determination by TIMS and MC-ICP-MS. Journal of Analytical Atomic Spectrometry, 29, 1858-1870.

Plank, T., Kelley, K., Zimmer, M., Hauri, E. H., and Wallace, P. J. (2013). Why do mafic arc magmas contain ~4 wt% water on average? Earth and Planetary Science Letters, 364, 168-179.

Prebble, W. M. (1995). Landslides in New Zealand. In: Bell, D. H. Landslides: Proceedings of the Sixth International Symposium, 1992 Feb 10-14, Christchurch, 3, 2101-2123.

Price, R. C., Stewart, R. B., Woodhead, J. D., and Smith, I. E. M. (1999). Petrogenesis of High-K Arc Magmas: Evidence from Egmont Volcano, North Island, New Zealand. Journal of Petrology, 40, 167-197.

Price, R. C., Gamble, J. A., Smith, I. E. M., Stewart, R. B., Eggins, S., and Wright, I. C. (2005). An integrated model for the temporal evolution of andesites and rhyolites and crustal development in New Zealand's North Island: Journal of Volcanology and Geothermal Research, 140, 1-24.

Price, R. C., Turner, S., Cook, C., Hobden, B., Smith, I. E. M., Gamble, J. A., Handley, H., Maas, R., and Möbis, A. (2010). Crustal and mantle influences and U-Th-Ra disequilibrium in andesitic lavas of Ngauruhoe volcano, New Zealand. Chemical Geology, 277, 355-373.

Price, R. C., Gamble, J. A., Smith, I. E. M., Maas, R., Waight, T., Stewart, R. B., and Woodhead, J. (2012). The Anatomy of an Andesite Volcano: a Time–Stratigraphic Study of Andesite Petrogenesis and Crustal Evolution at Ruapehu Volcano, New Zealand. Journal of Petrology, 53, 2139-2189.

Price, R. C., Mortimer, N., Smith, I. E. M., and Maas, R. (2015). Whole-rock geochemical reference data for Torlesse and Waipapa terranes, North Island, New Zealand. New Zealand Journal of Geology and Geophysics, 58, 213-228.

Pringle, P. (2008). Roadside geology of Mount Rainier National Park and vicinity. Washington Division of Geology and Earth Resources, Information Circular 107, 19 pp.

Raczek, I., Jochum, K. P., and Hofmann, A. W. (2003). Neodymium and strontium isotope data for USGS reference materials BCR-1, BCR-2, BHVO-1, BHVO-2, AGV-1, AGV-2, GSP-1, GSP-2- and eight MPI-DING reference glasses. Geostandards Newsletter, 27, 173-179.

Rawson, H., Pyle, D. M., Mather, T. A., Smith, V. S., Fontijn, K., Lachowycz, S. M., and Naranjo, J. A. (2016). The magmatic and eruptive response of arc volcanoes to deglaciation: insights from southern Chile. Geology, 44, 251-254.

Reid, M. E., Sisson, T. W., and Brien, D. L. (2001). Volcano collapse promoted by hydrothermal alteration and edifice shape, Mount Rainier, Washington. Geology, 29, 779-782.

Reid, M. R., Vazquez, J. A., and Schmitt, A. K. (2011). Zircon-scale insights into the history of a supervolcano, Bishop Tuff, Long Valley, California, with implications for the Ti-in-zircon geothermometer. Contributions to Mineralogy and Petrology, 161, 293-311.

Reiners, P. W., Nelson, B. K., and Ghiorso, M. S. (1995). Assimilation of felsic crust by basaltic magma: thermal limits and extents of crustal contamination of mantle-derived magmas. Geology, 23, 563-566.

Reubi, O., and Blundy, J. (2009). A dearth of intermediate melts at subduction zone volcanoes and the petrogenesis of arc andesites. Nature, 461, 1269-1274.

Ring, U., Mortimer, N., and Deckert, H. (2019). Critical-wedge theory and the Mesozoic accretionary wedge of New Zealand. Journal of Structural Geology, 122, 1-10.

Robertson, E. I., and Davey, F. J. (2018). The basement morphology under Tongariro National Park, southern Taupo Volcanic Zone. New Zealand Journal of Geology and Geophysics, 61, 570-577.

Rogan, W., and Blake, S. (1994). Trace element zonation of phenocrysts from Ngauruhoe Volcano, New Zealand: Constraints on magmatic processes. Mineralogical Magazine, 58A, 783-784.

Rollinson, H. R. (1993). Using geochemical data: evaluation, presentation, interpretation. John Wiley & Sons, New York, 352 pp.

Rooyakkers, S. M., Wilson, C. J. N., Schipper, C. I., Barker, S. J., and Allan, A. S. R. (2018). Textural and micro-analytical insights into mafic-felsic interactions during the Oruanui eruption, Taupo. Contributions to Mineralogy and Petrology, 173, 35.

Rosman, K. J. R., and Taylor, P. D. P. (1997). Isotopic compositions of the elements 1997. Pure and Applied Chemistry, 70, 217-235.

Rowland, J. V., Wilson, C. J. N., and Gravley, D. M. (2010). Spatial and temporal variations in magma-assisted rifting, Taupo Volcanic Zone, New Zealand. Journal of Volcanology and Geothermal Research, 190, 89-108.

Rudnick, R.L., and Gao, S., 2003, Composition of the continental crust. In: Rudnick, R.L. (Ed.) The Crust. In: Holland, H. D., and Turekian, K. K. (Eds.), Treatise on Geochemistry, Elsevier, Oxford, 3, 1-64.

Rudnick, R. L., McDonough, W. F., McCulloch, and Taylor, S. R. (1986). Lower crustal xenoliths from Queensland, Australia: evidence for deep crustal assimilation and fractionation of continental basalts. Geochimica et Cosmochimica Acta, 50, 1099-1115.

Rumsfeld, D. (2002). Quotation excerpted from a U. S. Department of Defense news briefing on February 12, 2002. http://archive.defense.gov/Transcripts/Transcript.aspx?TranscriptID=2636.

Rutherford, M. J., and Devine, J. D. (1988). The May 18, 1980, Eruption of Mount St. Helens. 3. Stability and Chemistry of Amphibole in the Magma Chamber. Journal of Geophysical Research, 93, 11949-11959.

Sanders, F. (2010). Rheology and flow emplacement processes of the 1954 lavas, Mount Ngauruhoe. Unpublished MSc thesis, University of Waikato, Hamilton, 237 pp.

Schmidt, M. E., and Grunder A. L. (2009). The evolution of North Sister: A volcano shaped by extension and ice in the central Oregon Cascade Arc. Geological Society of America Bulletin, 121, 643-662.

Schmidt. M. E., and Grunder, A. L. (2011). Deep Mafic Roots to Arc Volcanoes: Mafic Recharge and Differentiation of Basaltic Andesite at North Sister Volcano, Oregon Cascades. Journal of Petrology, 52, 603-641.

Scott, B. J., and Potter, S. H. (2014). Aspects of historical eruptive activity and volcanic unrest at Mt. Tongariro, New Zealand: 1846-2013. Journal of Volcanology and Geothermal Research, 286, 263-276.

Seebeck, H., Nicol, A., Giba, M., Pettinga, J., and Walsh, J. (2014). Geometry of the subducting Pacific plate since 20 Ma, Hikurangi margin, New Zealand. Journal of the Geological Society, London, 171, 131-143.

Shane, P., Doyle, L. R., and Narin, I. A. (2008). Heterogeneous andesite-dacite ejecta in 26-16.6 ka pyroclastic deposits of Tongariro volcano, New Zealand: the product of multiple magma-mixing events. Bulletin of Volcanology, 70, 517-536.

Shane, P., Maas, R., and Lindsay, J. (2017). History of Red Crater volcano, Tongariro Volcanic Centre (New Zealand): abrupt shift in magmatism following recharge and contrasting evolution between neighbouring volcanoes. Journal of Volcanology and Geothermal Research, 340, 1-15.

Shane, P., Cocker, K., Coote, A., Stirling, C. H., and Reid, M. (2019). The prevalence of plagioclase antecrysts and xenocrysts in andesite magma, exemplified by lavas of the Tongariro volcanic complex, New Zealand. Contributions to Mineralogy and Petrology, 174, 89.

Sigurdsson, H., Houghton, B. F., McNutt, S., Rymer, H., and Stix, J. (2015). The Encyclopedia of Volcanoes. Elsevier, Academic Press, London, 1456 pp.

Sievwright, R. H., Wilkinson, J. J., O'Neill, H. St. C., and Berry, A. J. (2017). Thermodynamic controls on element partitioning between titanomagnetite and andesitic-dacitic silicate melts. Contributions to Mineralogy and Petrology, 172, 62.

Singer, B. S., Thompson, R. A., Dungan, M. A., Feeley, T. C., Nelson, S. T., Pickens, J. C., Brown, L. L., Wulff, A. A., Davidson, J. P., and Metzger, J. (1997). Volcanism and erosion during the past 930 ky at the Tatara–San Pedro complex, Chilean Andes. Geological Society of America Bulletin, 109, 127-142.

Singer, B. S., Jicha, B. R., Harper, M. A., Naranjo, J. A., Lara, L. E., and Moreano-Roa, H. (2008). Eruptive history, geochronology, and magmatic evolution of the Puyehue-Cordón-Caulle volcanic complex, Chile. Geological Society of America Bulletin, 120, 599-618.

Sinton, J., Grönvold, K., and Sæmundsson, K. (2005). Postglacial eruptive history of the Western Volcanic Zone, Iceland. Geochemistry, Geophysics, Geosystems, 6, Q12009.

Sisson, T. W., and Layne, D. (1993). H_2O in basalt and basaltic andesite glass inclusions from four subduction-related volcanoes. Earth and Planetary Science Letters, 117, 619-635.

Sisson, T. W., Vallance, J. W., and Pringle, P. T. (2001). Progress Made in Understanding Mount Rainier's Hazards. EOS Transactions, 82, 113-124.

Sisson, T. W., Salters, V. J. M., and Larson, P. B. (2014). Petrogenesis of Mount Rainier andesite: magma flux and geologic controls on the contrasting differentiation styles at stratovolcanoes of the southern Washington Cascades. Geological Society of America Bulletin, 126, 122-144.

Sissons, B.A., and Dibble, R. R. (1981), A seismic refraction experiment southeast of Ruapehu volcano. New Zealand Journal of Geology and Geophysics, 24, 31-38.

Smith, I. E. M., and Price, R. C. (2006). The Tonga-Kermadec arc and Havre-Lau back-arc system: Their role in the development of tectonic and magmatic models for the western Pacific. Journal of Volcanology and Geothermal Research, 156, 315-331.

Smith, I. E. M., Worthington, T. J., Stewart, R. B., Price, R. C., and Gamble, J. A. (2003). Felsic volcanism in the Kermadec arc, SW Pacific: crustal recycling in an oceanic setting. Journal of the Geological Society of London, Special Publications, 219, 99-118.

Spera, F. J., and Bohrson, W. A. (2004). Open-System Magma Chamber Evolution: an Energy-constrained Geochemical Model Incorporating the Effects of Concurrent Eruption, Recharge, Variable Assimilation and Fractional Crystallisation (EC-E'RA$_X$FC). Journal of Petrology, 45, 2459-2480.

Spörli, K. B., and Rowland, J. V. (2006). 'Column on column' structures as indicators of lava/ice interaction, Ruapehu andesite volcano, New Zealand. Journal of Volcanology and Geothermal Research, 157, 294-310.

Steiger, R. H., and Jaeger, E. (1977). Subcommission on geochronology: convention on the use of decay constants on geo- and cosmochronology. Earth and Planetary Science Letters, 36, 359-362.

Stern, T., and Benson, A. (2011). Wide-angle imaging beneath an andesitic arc: Central North Island, New Zealand. Journal of Geophysical Research, 116, B09308.

Stevens, N. F. (2002). Emplacement of the large andesite lava flow in the Oturere Stream valley, Tongariro Volcano, from airborne interferometric radar. New Zealand Journal of Geology and Geophysics, 45, 387-394.

Stipp, J. J. (1969). The geochronology and petrogenesis of the Cenozoic volcanics of the North Island, New Zealand. Unpublished PhD thesis, Australian National University, Canberra, 438 pp.

Strelow, F. W. E., and Toerien, F. von S. (1966). Separation of Lead(II) from Bismuth(III), Thallium(III), Cadmium(II), Mercury(II), Gold(II), Platinum(IV), Palladium(II), and Other Elements by Anion Exchange Chromatography. Analytical Chemistry, 38, 545-548.

Sutton, A. N. (1995). Evolution of a large silicic magma system: Taupo volcanic centre, New Zealand. Unpublished PhD thesis, The Open University, Milton Keynes, 416 pp.

Sutton, A. N., Blake, S., and Wilson, C. J. N. (1995). An outline geochemistry of rhyolite eruptives from Taupo volcanic centre, New Zealand. Journal of Volcanology and Geothermal Research, 68, 153-175.

Sutton, A. N., Blake, S., and Wilson, C. J. N., and Charlier, B. L. A. (2000). Late Quaternary evolution of a hyperactive rhyolite magmatic system: Taupo volcanic centre, New Zealand. Journal of the Geological Society of London, 157, 537-552.

Swallow, E. J. (2018). Aspects of the petrology and geochemistry of the Huckleberry Ridge Tuff, Yellowstone. Unpublished PhD thesis, Victoria University of Wellington, Wellington, 333 pp.

Swallow, E. J., Wilson, C. J. N., Charlier, B. L. A., and Gamble, J. A. (2019). The Huckleberry Ridge Tuff, Yellowstone: evacuation of multiple magmatic systems in a complex episodic eruption. Journal of Petrology, 60, 1371-1426.

Tanaka, T., Togashi, S., Kamioka, H., Amakawa, H., Kagami, H., Hamamoto, T., Yuhara, M., Orihashi, Y., Yoneda, S., Shimizu, H., Kunimaru, T., Takahashi, K., Yanagi, T., Nakano, T., Fujimaki, H., Shinjo, R., Asahara, Y., Tanimizu, M., and Dragusanu, C. (2000). JNDi-1: a neodymium isotopic reference in consistency with LaJolla neodymium. Chemical Geology, 168, 279-281.

Tatsumi, Y., and Takahashi, T. (2006). Operation of subduction factory and production of andesite. Journal of Mineralogical and Petrological Sciences, 101, 145-153.

Taylor, H. P. Jr. (1980). The effects of assimilation of country rocks my magmas on $^{18}O/^{16}O$ and $^{87}Sr/^{86}Sr$ systematics in igneous rocks. Earth and Planetary Science Letters, 47, 243-254.

Terry, R. D., and Chilingar, G. V. (1955). Summary of "concerning some additional aids in studying sedimentary formations" by M. S. Shvetsov. Journal of Sedimentary Petrology, 25, 229-234.

Thirlwall, M. F. (1991). Long-term reproducibility of multicollector Sr and Nd isotope ratio analysis. Chemical Geology, 94, 85-104.

Thirlwall, M. F. (2000). Inter-laboratory and other errors in Pb isotope analyses investigated using a ^{207}Pb-^{204}Pb double spike. Chemical Geology, 163, 299-322.

Todd, E., Stracke, A., and Scherer, E. E. (2015). Effects of simple acid leaching of crushed and powdered geological materials on high-precision Pb isotope analyses. Geochemistry, Geophysics and Geosystems, 16, 2276-2302.

Tollan, P. M. E., Dale, C. W., Hermann, J., Davidson, J. P., and Arculus, R. J. (2017). Generation and Modification of the Mantle Wedge and Lithosphere beneath the West Bismarck Island Arc: Melting, Metasomatism and Thermal History of Peridotite Xenoliths from Ritter Island. Journal of Petrology, 58, 1475-1510.

Tommasini, S., and Davies, G. R. (1997). Isotope disequilibrium during anatexis: a case study of contact melting, Sierra Nevada, California. Earth and Planetary Science Letters, 148, 273-285.

Topping, W.W. (1973). Tephrostratigraphy and chronology of late Quaternary eruptives from the Tongariro Volcanic Centre, New Zealand. New Zealand Journal of Geology and Geophysics, 16, 397-423.

Topping, W. W. (1974). Some aspects of Quaternary history of Tongariro Volcanic Centre. Unpublished Ph.D. thesis, Victoria University of Wellington, New Zealand, 245 pp.

Tost, M., and Cronin, S. J. (2015). Linking distal volcaniclastic sedimentation and stratigraphy with the development of Ruapehu volcano, New Zealand. Bulletin of Volcanology, 77, 94.

Tost, M., Price, R. C., Cronin, S. J., and Smith, I. E. M. (2016). New insights into the evolution of the magmatic system of a composite andesite volcano revealed by clasts from distal mass-flow deposits: Ruapehu volcano, New Zealand. Bulletin of Volcanology, 78, 38.

Townsend, D. B., Leonard, G. S., Conway, C. E., Eaves, S. R., and Wilson, C. J. N. (2017). Geology of the Tongariro National Park area [map]. Lower Hutt (NZ): GNS Science. 1 sheet + 109 pp., scale 1:60,000. (GNS Science geological map; 4).

Vallance, J. W., and Scott, K. M. (1997). The Osceola Mudflow from Mount Rainier: Sedimentology and hazard implications of a huge clay-rich debris flow. Geological Society of America Bulletin, 109, 143-163.

Vallance, J. W., and Sisson, T. W. (2017). Geologic Field-Trip Guide to Volcanism and its Interaction with Snow and Ice at Mount Rainier, Washington. Draft report for IAVCEI 2017 Meeting, Portland, 2017 August 14-18. U. S. Department of the Interior and U. S. Geological Survey, 101 pp.

Vandergoes, M. J., Hogg, A. G., Lowe, D. J., Newnham, R. M., Denton, G. H., Southon, J., Barrell, D. J. A., Wilson, C. J. N., McGlone, M. S., Allan, A. S. R., Almond, P. C., Petchey, F., Dabell, K., Dieffenbacher-Krall, A. C., and Blaauw, M. (2013). A revised age for the Kawakawa/Oruanui tephra, a key marker for the Last Glacial Maximum in New Zealand. Quaternary Science Reviews, 74, 195-201.

Villamor, P., and Berryman, K. (2006). Evolution of the southern termination of the Taupo Rift, New Zealand. New Zealand Journal of Geology and Geophysics, 49, 23-37.

Villamor, P., Berryman, K. R., Ellis, S. M., Schreurs, G., Wallace, L. M., Leonard, G. S., Langridge, R. M., Ries, W. F. (2017). Rapid Evolution of Subduction-Related Continental Intraarc Rifts: The Taupo Rift, New Zealand. Tectonics, 36, 2250-2272.

Vry, J. K., Powell, R., and Williams, J. (2008). Establishing the P-T path for Alpine Schist, Southern Alps near Hokitika, New Zealand. Journal of Metamorphic Geology, 26, 81-97.

Vry, J., Powell, R., Golden, K. M., and Petersen, K. (2009). The role of exhumation in metamorphic dehydration and fluid production. Nature Geoscience, 3, 31-35.

Wadsworth, F. B., Kennedy, B. M., Branney, M. J., von Aulock, F. W., Lavallée, Y., and Menendez, A. (2015). Exhumed conduit records magma ascent and drain-back during a Strombolian eruption at Tongariro volcano, New Zealand. Bulletin of Volcanology, 77, 71.

Wahyudin, D. (1993). Volcanology and petrology of the Tama Lakes area, Tongariro Volcanic Centre, New Zealand. Unpublished MSc thesis, Victoria University of Wellington, Wellington, 153 pp.

Waight, T. E., Troll, V. R., Gamble, J. A., Price, R. C., and Chadwick, J. P. (2017). Hf isotope evidence for variable slab input and crustal addition in basalts and andesites of the Taupo Volcanic Zone, New Zealand. Lithos, 284-285, 222-236.

Wallace, L. M., Beavan, J., McCaffrey, R., and Darby, D. J. (2004). Subduction zone coupling and tectonic block rotations in the North Island, New Zealand. Journal of Geophysical Research, 109, B12406.

Watson, E. B., and Harrison, T. M. (1983). Zircon saturation revisited: temperature and composition effects in a variety of crustal magma types. Earth and Planetary Science Letters 64, 295-304.

Watt, S. F. L., Pyle, D. M., and Mather, T. A. (2013). The volcanic response to deglaciation: Evidence from glaciated arcs and a reassessment of global eruption records. Earth-Science Reviews, 122, 77-102.

Weller, D. J., Miranda, C. G., Moreno, P. I., Villa-Martínez, R., and Stern, C. R. (2015). Tephrochronology of the southernmost Andean Southern Volcanic Zone, Chile. Bulletin of Volcanology, 77, 107.

White, A. J. R., and Chappell, B. W. (1977). Ultrametamorphism and granitoid genesis. Tectonophysics, 43, 7-22.

Williams, P. W., McGlone, M., Neil, H., and Zhao, J.-X. (2015). A review of New Zealand palaeoclimate from the Last Interglacial to the global Last Glacial Maximum. Quaternary Science Reviews, 110, 92-106.

Wilson, C. J. N. (1993). Stratigraphy, chronology, styles and dynamics of late Quaternary eruptions from Taupo volcano, New Zealand. Philosophical Transactions of the Royal Society of London, Series A, 343, 205-306.

Wilson, C. J. N. (2001). The 26.5 ka Oruanui eruption, New Zealand: an introduction and overview. Journal of Volcanology and Geothermal Research, 112, 113-174.

Wilson, C. J. N. (2017). Volcanoes: Characteristics, Tipping Points, and those Pesky Unknown Unknowns. Elements, 13, 41-46.

Wilson, C. J. N., and Charlier, B. L. A. (2009). Rapid Rates of Magma Generation at Contemporaneous Magma Systems, Taupo Volcano, New Zealand: Insights from U-Th Model-age Spectra in Zircons. Journal of Petrology, 50, 875-907.

Wilson, C. J. N., and Rowland, J. V. (2016). The volcanic, magmatic and tectonic setting of the Taupo Volcanic Zone, New Zealand, reviewed from a geothermal perspective. Geothermics, 59, 168-187.

Wilson, C. J. N., Houghton, B. F., McWilliams, M. O., Lanphere, M. A., Weaver, S. D., and Briggs, R. M. (1995). Volcanic and structural evolution of Taupo Volcanic Zone, New Zealand: a review. Journal of Volcanology and Geothermal Research, 68, 1-28.

Wolf, W., Romer, R. L., and Glodny, J. (2019). Isotope disequilibrium during partial melting of metasedimentary rocks. Geochimica et Cosmochimica Acta, 257, 163-183.

Yamamoto, T., Kudo, T., and Isizuka, O. (2018). Temporal variations in volumetric magma eruption rates of Quaternary volcanoes in Japan. Earth, Planets and Space, 70, 65.

Zeng, L., Asimow, P. D., and Saleeby, J. (2005). Coupling of anatectic reactions and dissolution of accessory phases and the Sr and Nd isotope systematics of anatectic melts from a metasedimentary source. Geochimica et Cosmochimica Acta, 69, 3671-3682.

Appendix 1

$^{40}Ar/^{39}Ar$ step heating age analysis data

A1.1. INTRODUCTION

$^{40}Ar/^{39}Ar$ age determinations on Tongariro lavas were performed at the United States Geological Survey geochronological facility in Menlo Park by A. T. Calvert, G. S. Leonard and D. T. Downs between 2016-2019. Data from these age analyses are presented below, as step heating results in alphabetical order which are plotted with 1 s.d. analytical uncertainties (Fig. A1). All data presented in Chapter 3 are reproduced in Table A1.1 for completeness. A full description of analytical procedures was provided in Chapter 2.

A1.2. AGE DETERMINATIONS

A number of $^{40}Ar/^{39}Ar$ age determinations of the total 39, mentioned above, are not reported because of unsuitable proportions of groundmass glass (15-25 vol%) to have confidence in the accuracy of determined ages (LP033, LP051, LP109, LP187, MSR15020A, MSR15023). Some samples (LP051, LP126) have non-ideal proportions of groundmass glass (up to 15 vol%) but yield ages that appear to be accurate as indicated by other age determinations and field relationships, so are reported here (but not in Chapter 3). Other samples reported here but not in in Chapter 3 yield $^{40}Ar/^{39}Ar$ age results that cannot be quantified in terms of specific mean age values and standard deviations, but do however allow semi-quantitative statements to be made about their ages (CC351, LP001, LP007).

LP001 is from the Pukeonake Formation, and the red-coloured step heating results (below) indicate an age that could be around 40 to 30 ka, consistent with 25.4 ka Oruanui deposits that overlie Pukeonake Formation lava in the prominent cone at the end of the Mangatepopo valley (Oruanui age from Vandergoes et al., 2013). Age determinations performed on non-Tongariro samples are for LP007 and CC351. LP007 is sampled form the lava that fills the Tongariro River, ~15 km east of Tongariro and Ruapehu, or ~1 km east of State Highway 1. This lava probably erupted from Ruapehu because its geochemistry is similar to early Mangawhero Formation eruptives (Ruapehu) and the interpreted $^{40}Ar/^{39}Ar$ age result for LP007 of about 60 to 70 ka occurs within the 80 to 50 ka eruptive 'hiatus' highlighted in the detail chronostratigraphic study of Ruapehu edifice materials by Conway et al. (2016), following Gamble et al. (2003)—see section 3.5.7. CC351 was sampled from a summit lava on Pihanga and the $^{40}Ar/^{39}Ar$ data presented below indicate an age of >180 ka, based on the low temperature (550-700 °C) heating steps that form a plateau around ~180 ka. This result contrasts with K/Ar age determination by Stipp (1969) of 123 ± 10 ka, revised with the decay constants of Steiger and Jaeger (1977), which was determined on a plagioclase-phyric boulder in the Poutu Canal area south of Pihanga, but may have been sourced from an edifice other than Pihanga. Note that

CC351, the Pihanga sample analysed here, has a clinopyroxene-dominated phenocryst cargo with plagioclase only occurring as a microphenocrystic groundmass phase.

Table A1. (Previously shown as Table 3.1.) Summary of new $^{40}Ar/^{39}Ar$ age determinations for Tongariro lavas.

Sample	Formation – Member (member abbreviation)[1]	Plateau age[2]				Isochron age[2]				Total gas age
		n/N	$\%^{39}Ar$	MSWD	(ka ± 2 s.d.)	$\%^{39}Ar$	MSWD	(ka ± 2 s.d.)	$^{40}Ar/^{36}Ar_i$ (± 2 s.d.)	(ka ± 2 s.d.)
TG088	RC – Te Ahititi (**ahi**)	6/10	77.8	2.07	**12.9 ± 11.8**	77.8	2.40	8.3 ± 25.4	301.4 ± 22.4	21.8 ± 10.2
LP147	MM – Te Wai Whakaata (**aww**)	11/11	100.0	0.46	**28.3 ± 5.2**	100.0	0.50	29.3 ± 7.6	298.0 ± 3.5	27.2 ± 6.0
LP151	MM – Mangatapate (**amt**)	5/10	69.3	0.41	**30.1 ± 6.0**	69.3	0.49	26.8 ± 14.8	305.0 ± 33.7	51.6 ± 6.2
GL2223	TA – Te Tatau (**att**)	11/11	100.0	1.31	**56.2 ± 4.6**	100.0	1.05	59.5 ± 5.4	296.3 ± 2.8	54.8 ± 4.8
LP211	TA – Rotopaunga (**arp**)	9/10	98.9	3.47	86.4 ± 12.4	**98.9**	**1.60**	**68.3 ± 15.4**	319.3 ± 18.4	96.0 ± 7.6
GL2007	TA – Rotopaunga (**arp**)	9/10	97.4	0.44	**76.1 ± 3.5**	97.4	0.38	78.4 ± 5.9	291.2 ± 10.1	73.3 ± 4.1
RPC110	TA – Te Wakarikiariki (**ati**)	4/11	63.6	0.98	**80.6 ± 4.8**	63.6	1.13	74.8 ± 15.2	304.0 ± 15.7	82.9 ± 6.0
LP062	undifferentiated Otukou lava (**uol**)	10/10	100.0	0.87	**85.0 ± 6.0**	100.0	0.86	89.7 ± 11.6	296.7 ± 4.4	83.8 ± 6.6
LP023	TA – Te Rurunga (**atr**)	6/11	58.7	1.07	**87.5 ± 4.2**	58.7	0.79	84.2 ± 6.2	304.0 ± 9.0	96.0 ± 4.0
LP103	TA – Te Porere (**dtp**)	4/10	71.2	0.69	**98.9 ± 2.6**	71.2	0.96	101.1 ± 14.2	290.7 ± 55.7	98.5 ± 3.0
LP010	TA – Mangatepopo (**amp**)	8/10	96.4	1.80	**108.5 ± 8.4**	96.4	1.73	102.9 ± 15.6	305.1 ± 21.2	119.1 ± 7.2
MSR15019	TA – Mangahouhouiti (**mhi**)	10/11	99.2	0.89	**116.8 ± 23.4**	99.2	0.88	141.4 ± 56.2	297.3 ± 3.1	108.0 ± 25.4
LP250	TA – Mangatepopo (**amp**)	7/10	70.5	2.12	**121.1 ± 12.2**	70.5	1.83	114.3 ± 14.6	307.0 ± 21.4	169.2 ± 9.0
LP214	TA – Rahuituki (**arh**)	7/10	75.9	0.77	**124.4 ± 4.8**	75.9	0.78	124.2 ± 5.4	297.4 ± 6.2	135.0 ± 5.6
TG084	MH – Te Pakiraki (**dpk**)	8/10	90.5	0.84	**136.5 ± 7.0**	90.5	0.79	130.8 ± 11.8	304.2 ± 12.6	153.3 ± 7.6
LP245	MH – Waiaruhairiki (**awh**)	7/10	81.8	0.30	**147.3 ± 7.4**	81.8	0.35	148.9 ± 17.4	296.9 ± 17.2	174.9 ± 7.6
LP234	MH – Te Pakiraki (**dpk**)	8/10	96.0	0.92	**151.8 ± 4.0**	96.0	0.62	146.7 ± 7.4	310.5 ± 18.0	158.9 ± 4.6
LP118	MH – Te Pakiraki (**dpk**)	8/10	88.2	1.35	**155.4 ± 5.2**	88.2	1.48	157.1 ± 13.4	297.0 ± 11.3	152.6 ± 5.0
LP129	MH – Te Pakiraki (**dpk**)	10/10	100.0	1.13	**164.9 ± 5.8**	100.0	1.23	166.2 ± 12.2	296.8 ± 11.5	164.9 ± 5.8
LP239	MH – Te Pakiraki (**dpk**)	3/10	58.2	2.43	203.8 ± 9.6	**58.2**	**1.12**	**185.5 ± 22.4**	319.1 ± 28.2	296.9 ± 8.6
MSR15018	HA – Waipoa (**awp**)	6/11	74.0	1.19	**191.1 ± 4.4**	74.0	0.72	195.8 ± 7.0	292.2 ± 8.5	196.4 ± 4.2
LP039	HA – Pukekaikiore (**apk**)	7/10	95.1	0.38	**194.7 ± 5.0**	95.1	0.40	197.7 ± 12.6	296.1 ± 11.0	192.6 ± 5.8
LP036	HA – Toatoa (**ato**)	8/10	**96.3**	**Recoil**	**205.1 ± 6.0**	100.0	7.97	208.9 ± 7.4	293.0 ± 17.7	208.8 ± 4.2
LP149	HA – Toatoa (**ato**)	4/10	67.2	1.72	**205.1 ± 6.0**	67.2	1.48	191.3 ± 23.4	311.0 ± 24.4	225.6 ± 5.0
GL2132	HA – Upper Tama (**aut**)	6/11	85.2	0.74	**209.1 ± 4.9**	85.2	0.84	211.8 ± 17.9	290.9 ± 31.0	201.9 ± 5.7
LP072	HA – Tawhairauiki (**atw**)	10/10	100.0	0.72	**217.7 ± 4.4**	100.0	0.76	219.0 ± 6.6	296.6 ± 7.2	215.6 ± 5.6
LP074	HA – Tutangatahiro (**mtu**)	6/10	89.0	0.66	**223.3 ± 5.6**	89.0	0.45	214.1 ± 16.2	305.5 ± 13.9	221.2 ± 6.6
LP113	TU	5/10	67.0	1.85	**304.4 ± 11.4**	67.0	1.06	285.5 ± 58.8	342.9 ± 109.5	376.4 ± 10.6
LP097	OT	3/11	62.2	0.51	**512.0 ± 59.4**	62.2	0.52	631.1 ± 338.4	294.6 ± 12.6	931.1 ± 57.4

[1] Formation abbreviations: OT = Otamatereinga, TU = Tupuna, MH = Mangahouhounui, HA = Haumata, TA = Taiko, MM = Mokomoko, RC = Red Crater.
[2] n/N = number [n] of heating steps used for plateau age calculation out of total [N] steps in age analysis. $\%^{39}Ar$ is the percentage of radiogenic argon released over the selected plateau steps of the total radiogenic argon. Recoil ages are noted where used instead of plateau ages—see Appendix 1 for heating step data. $^{40}Ar/^{36}Ar_i$ = denotes the isochron intercept value. Preferred ages appear in bold typeface. Details of heating step experiments, $^{40}Ar/^{36}Ar$ intercepts, isochrons and plateau spectra are provided in Appendix 1.

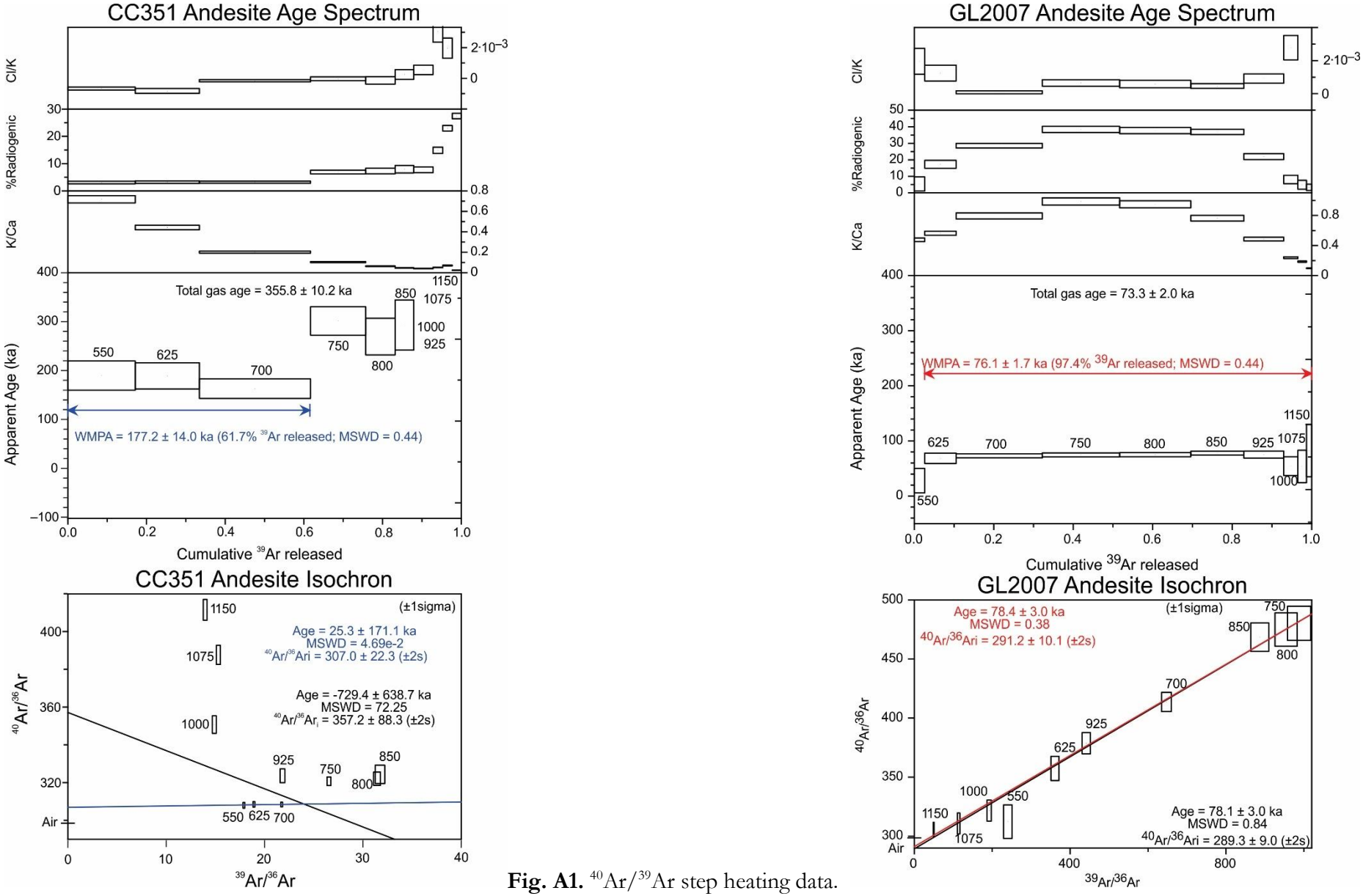

Fig. A1. $^{40}Ar/^{39}Ar$ step heating data.

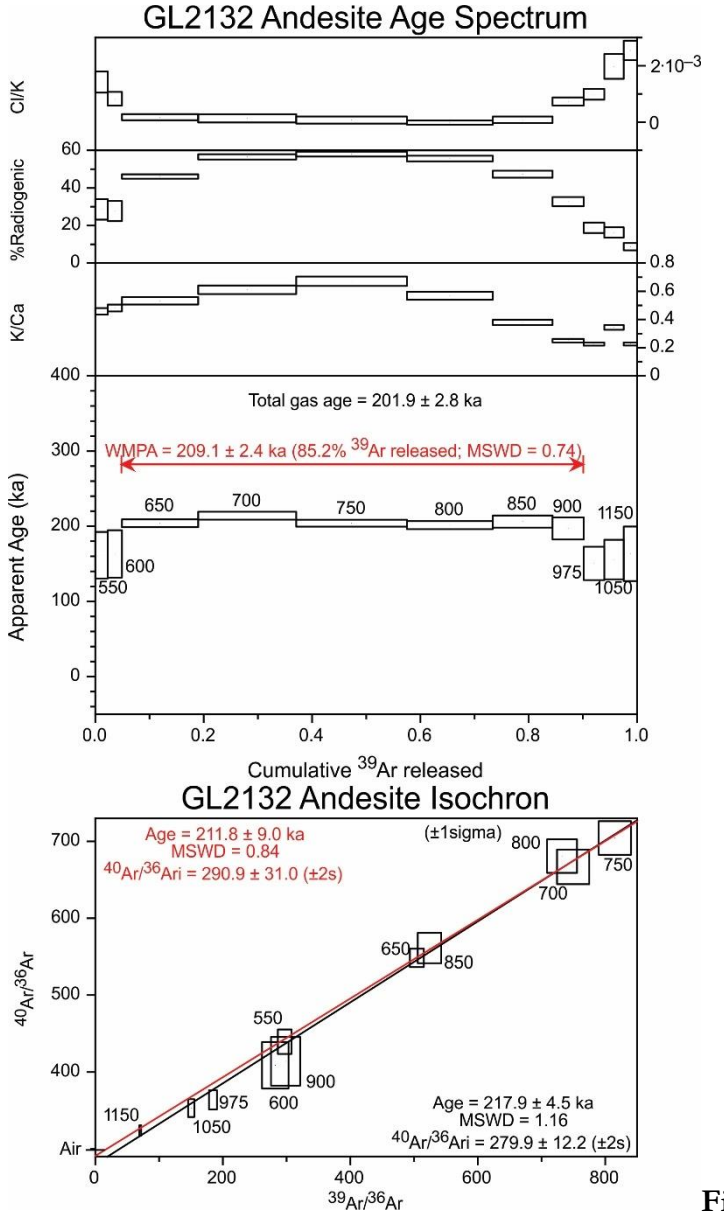

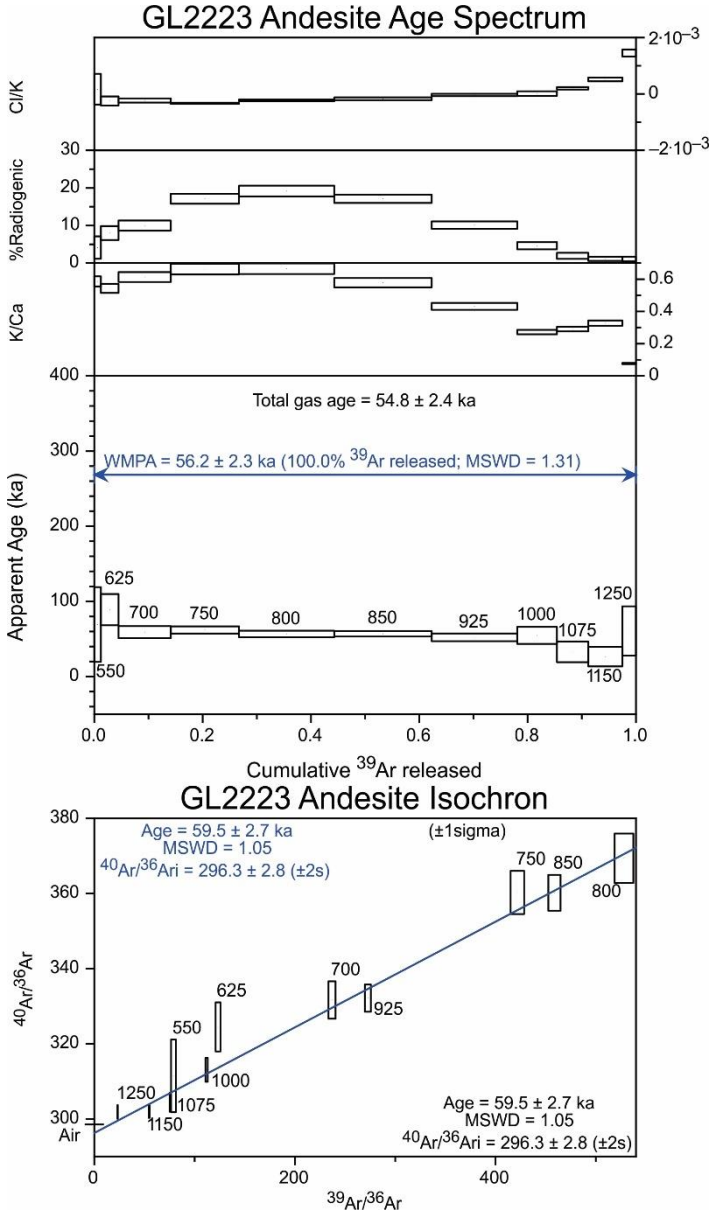

Fig. A1. Continued.

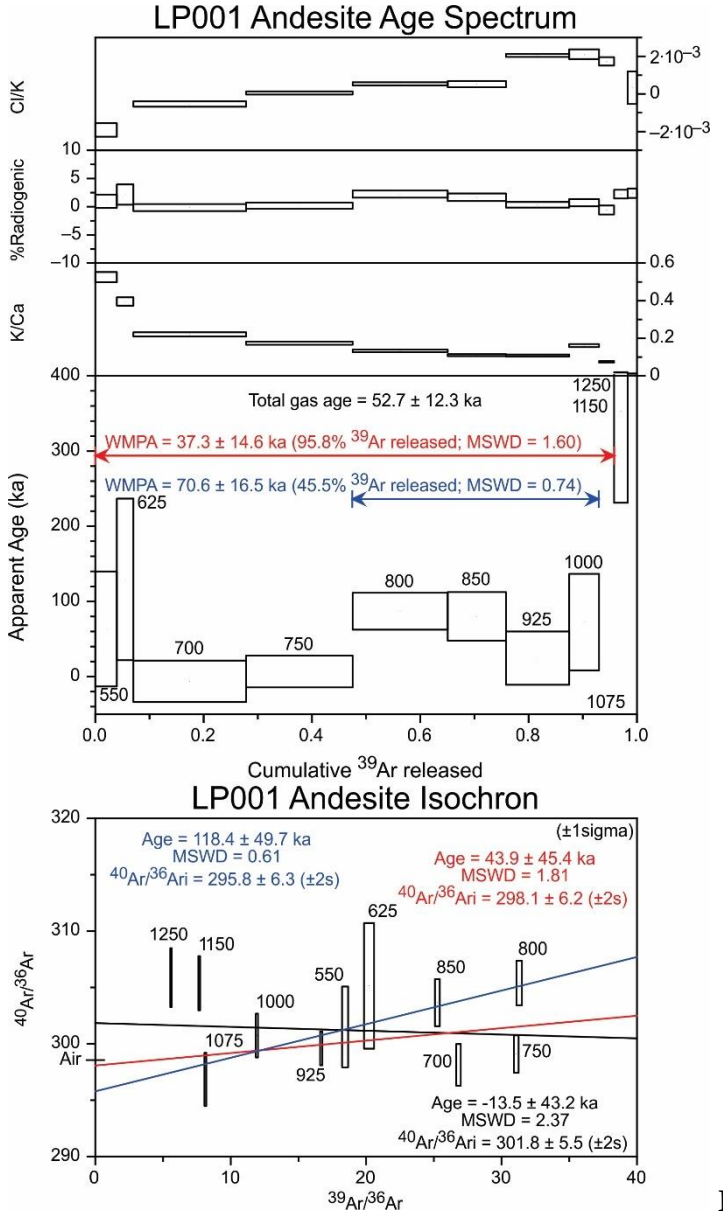

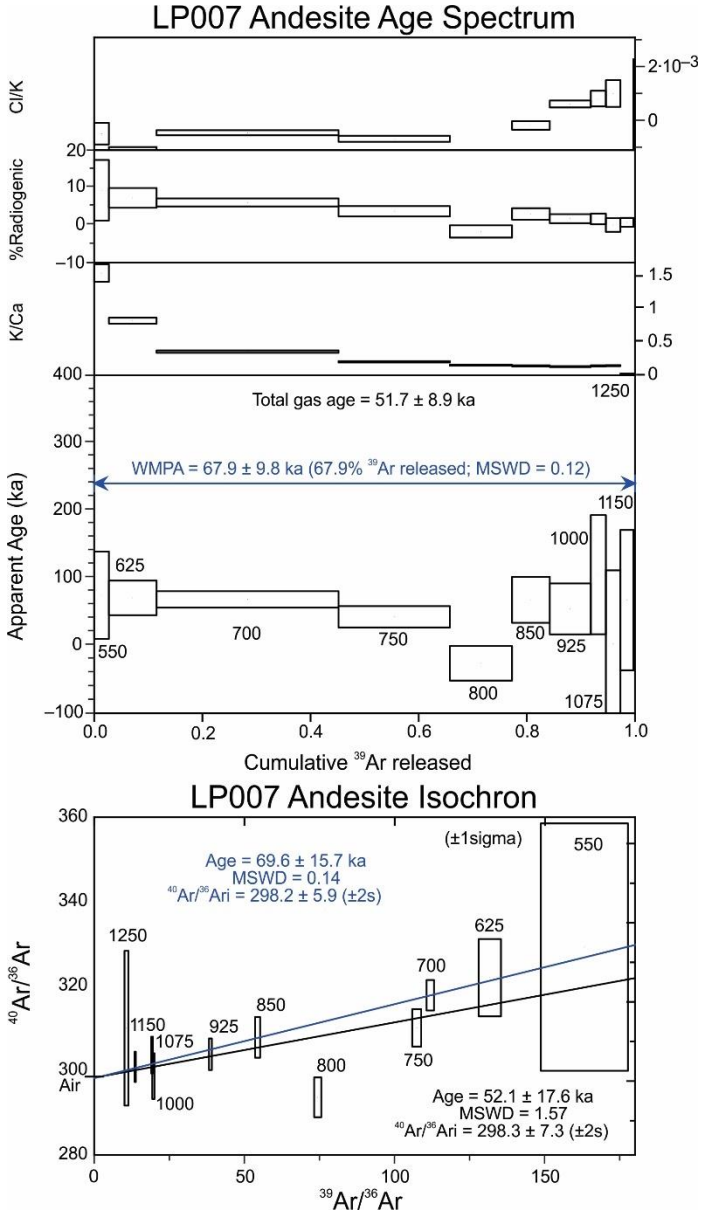

Fig. A1. Continued.

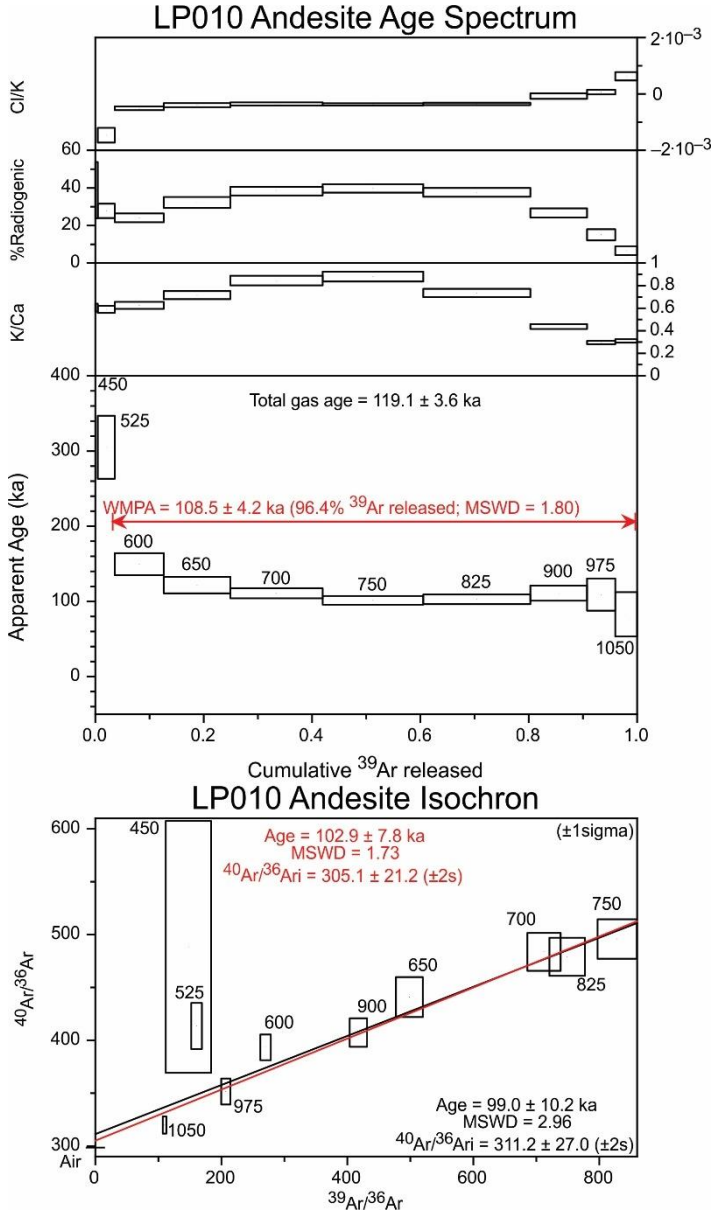

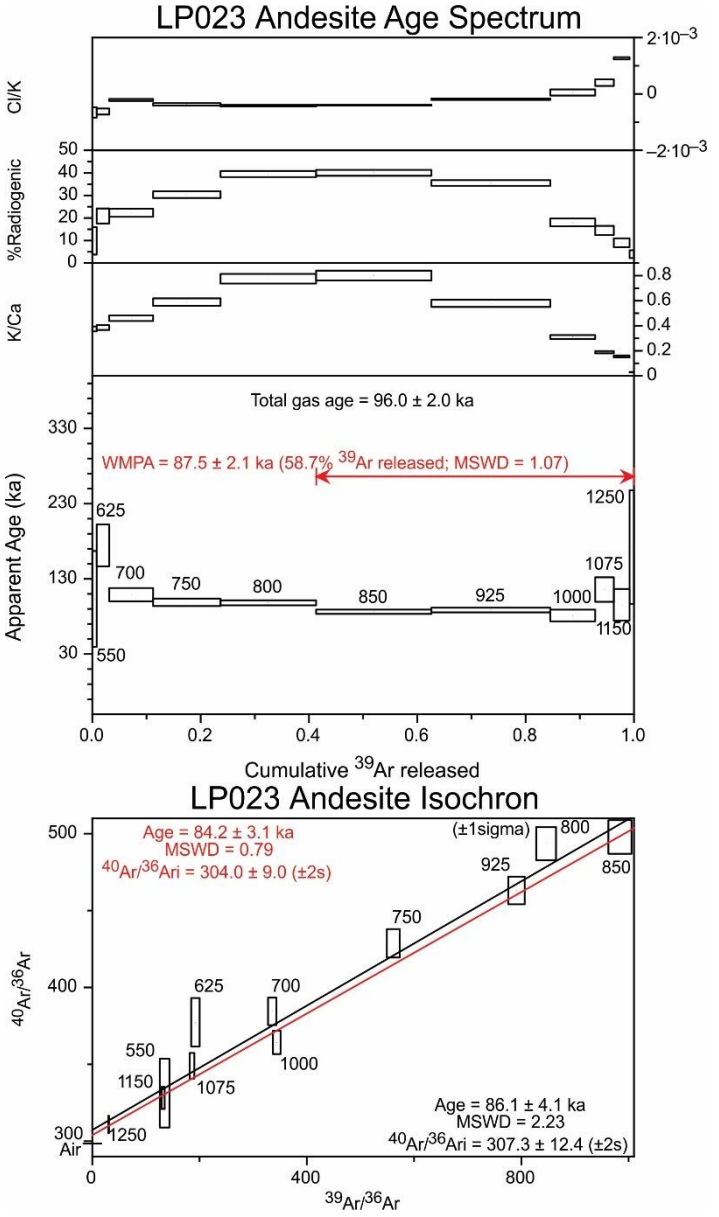

Fig. A1. Continued.

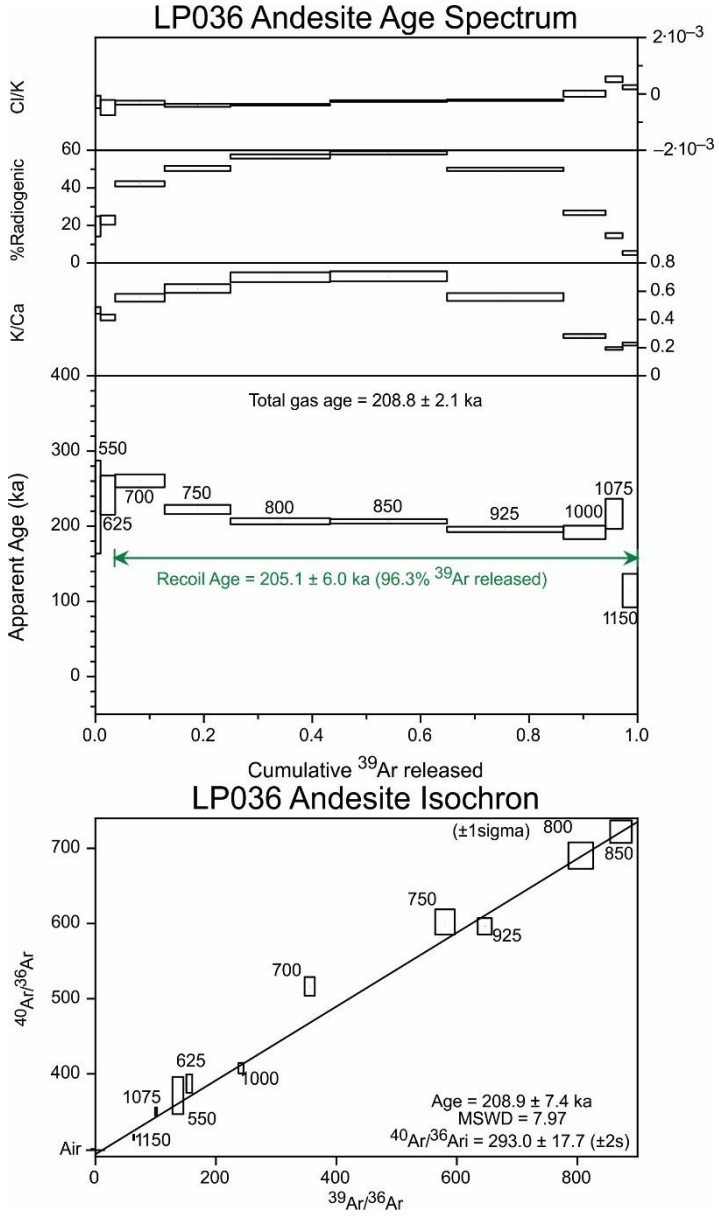

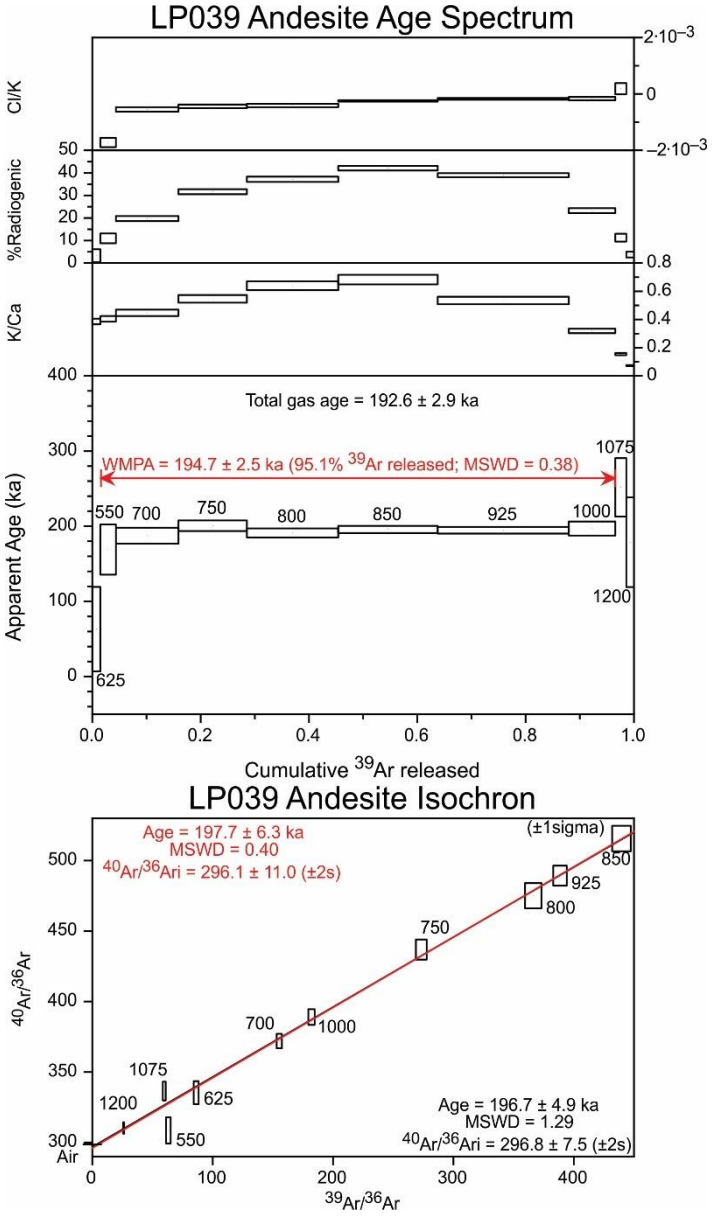

Fig. A1. Continued.

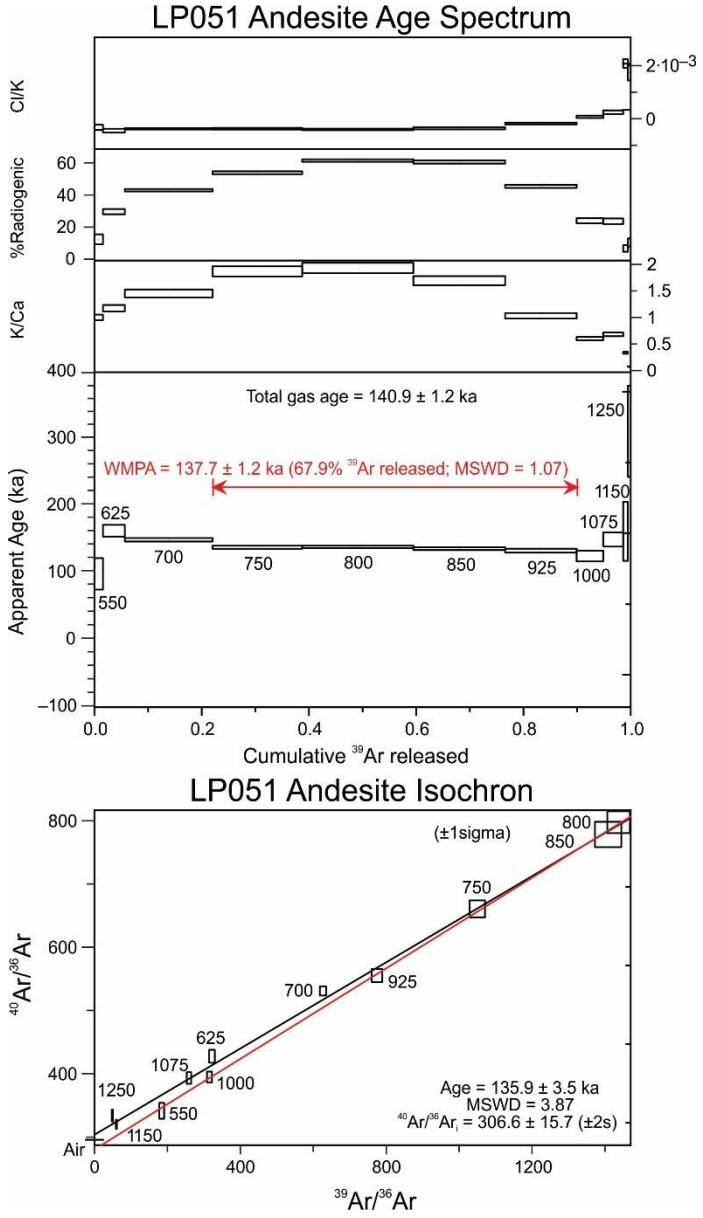

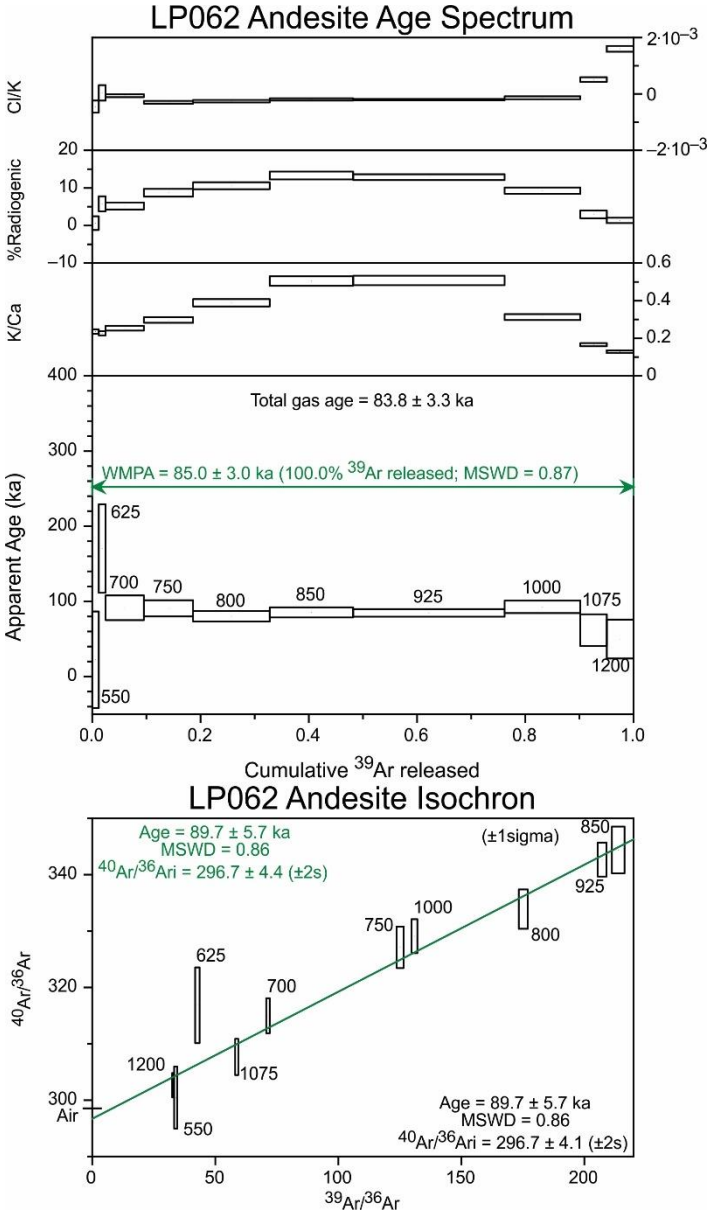

Fig. A1. Continued.

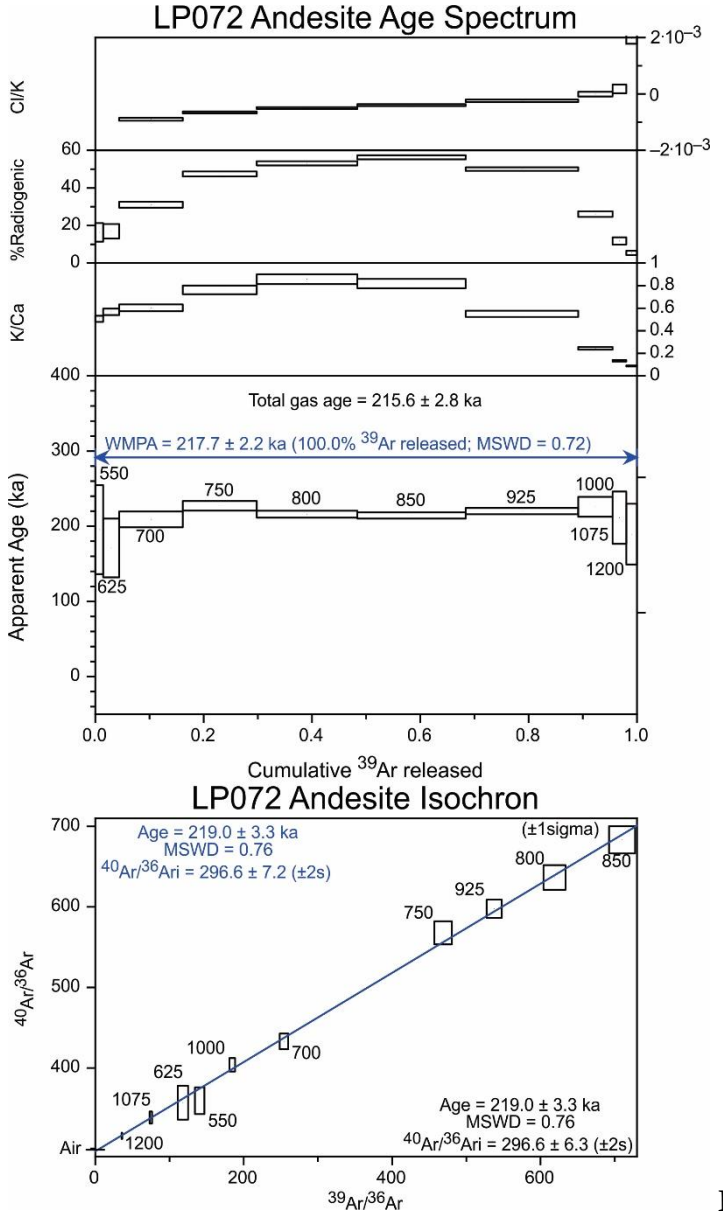

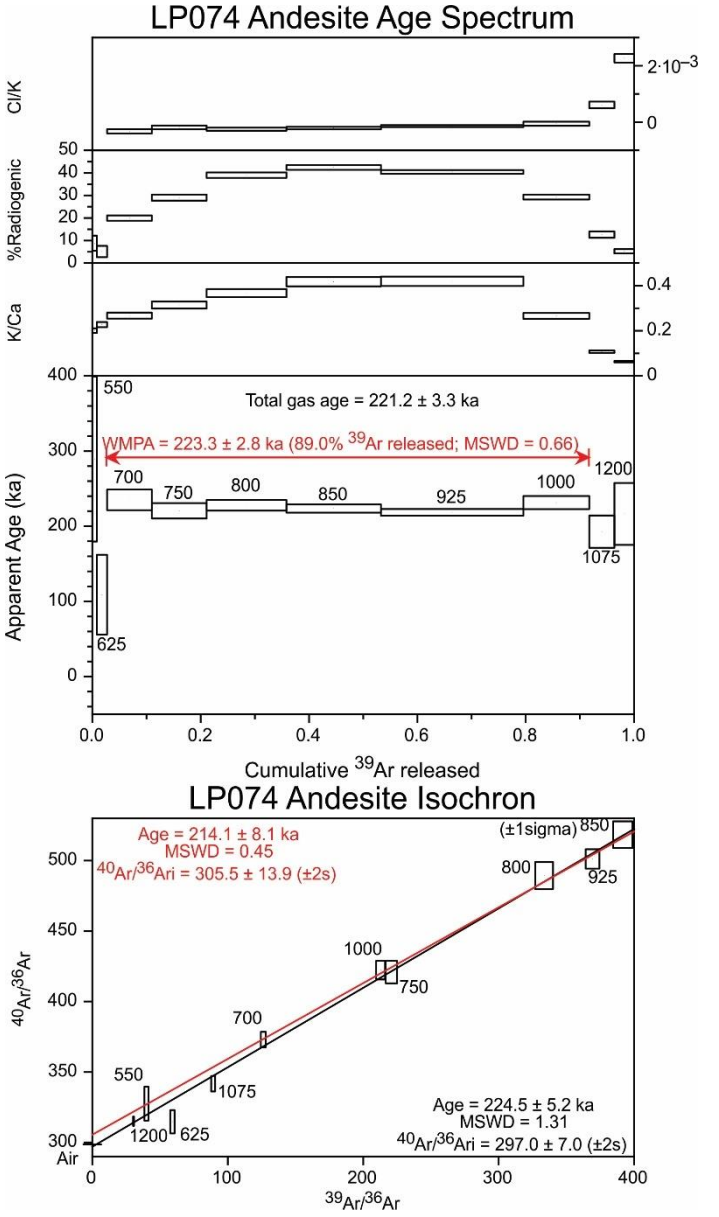

Fig. A1. Continued.

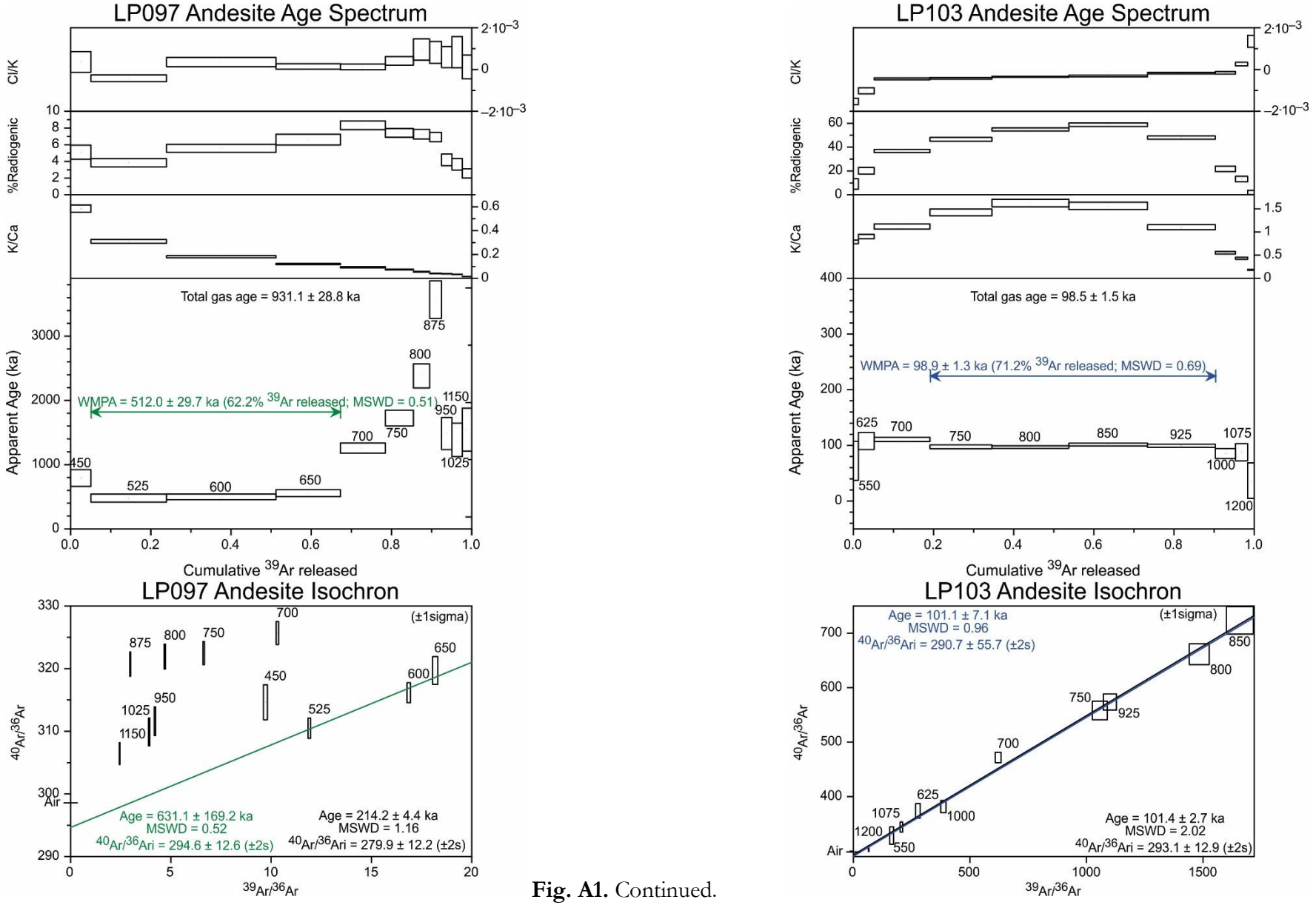

Fig. A1. Continued.

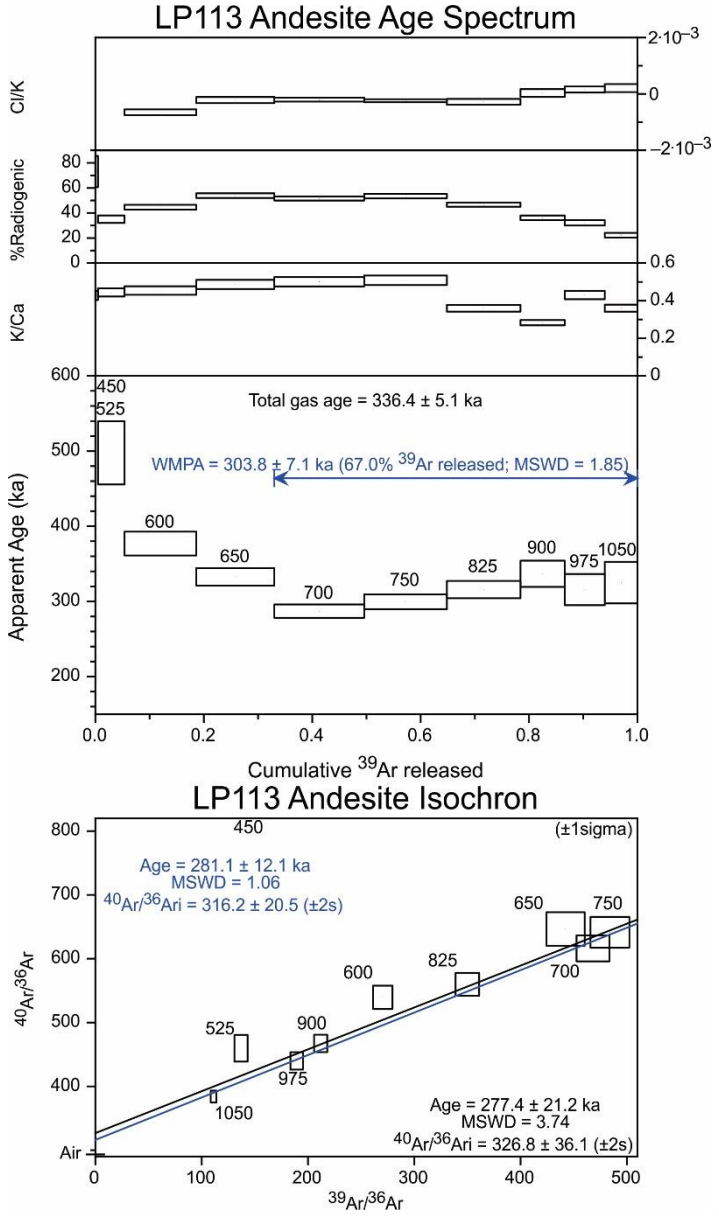

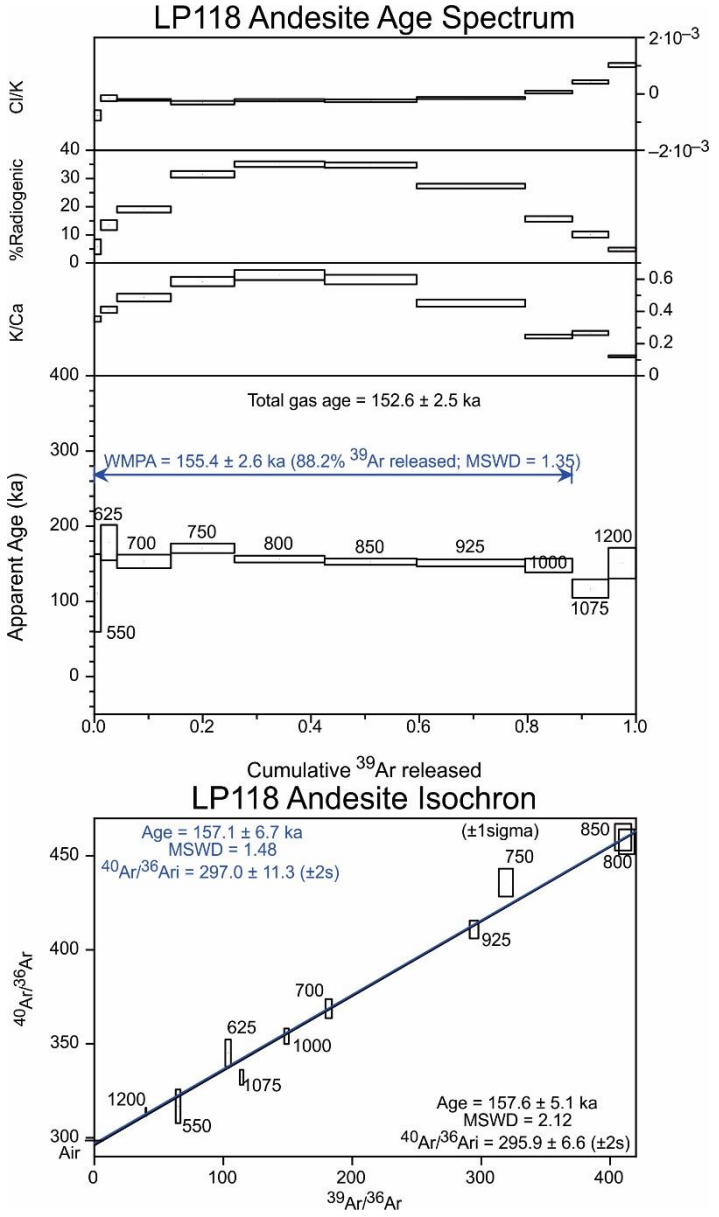

Fig. A1. Continued.

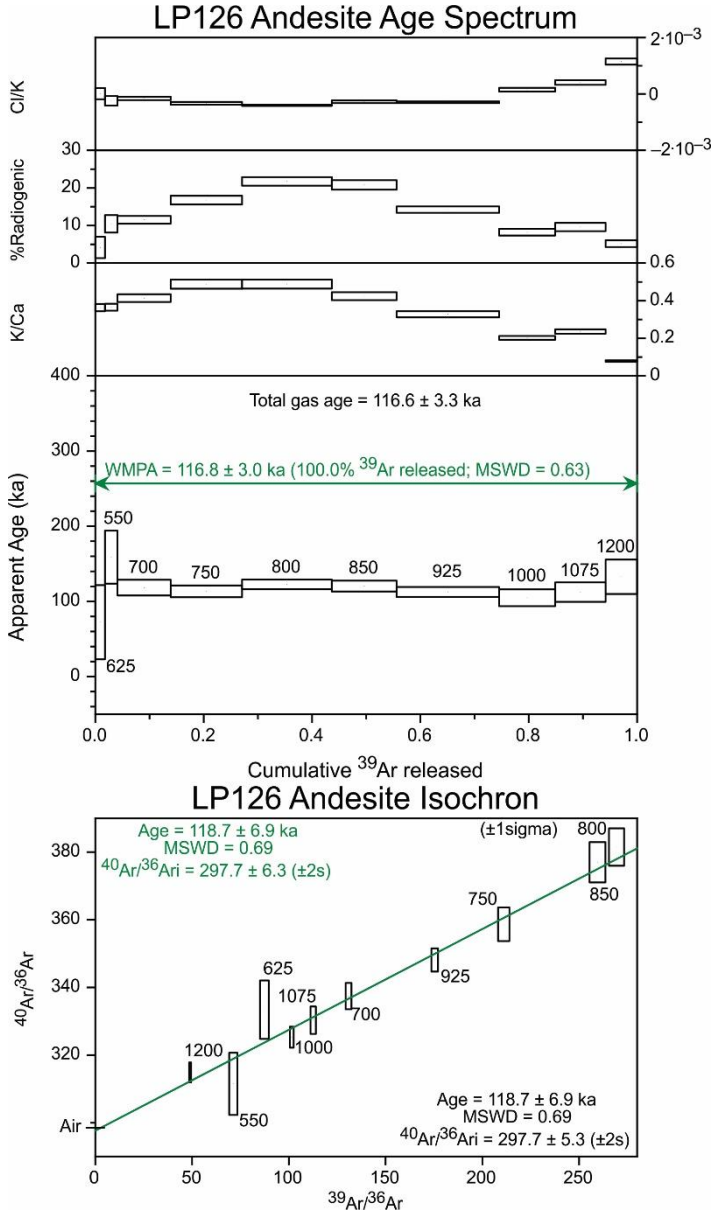

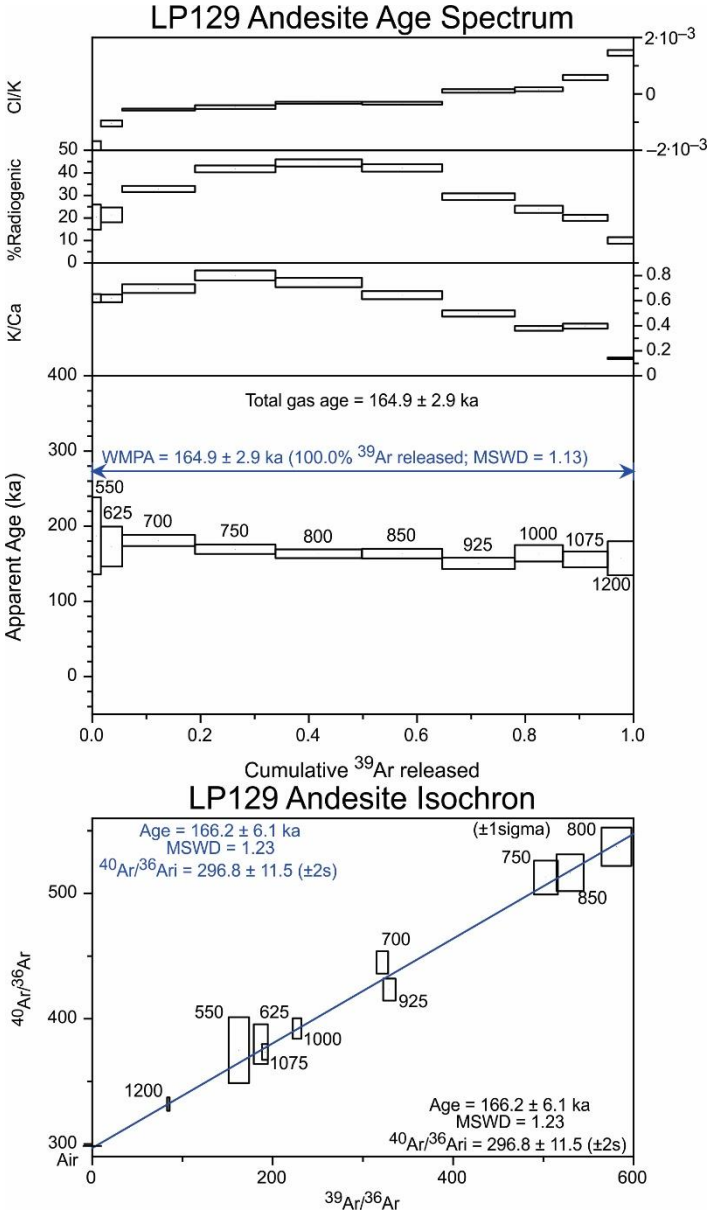

Fig. A1. Continued.

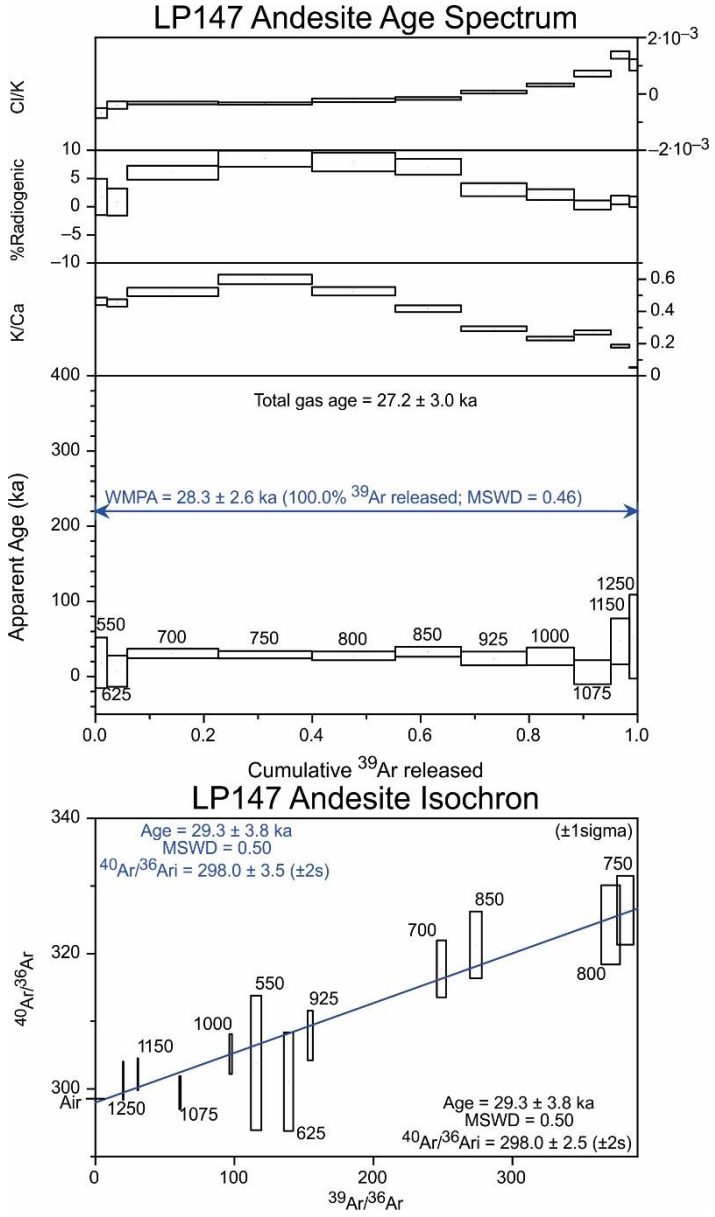

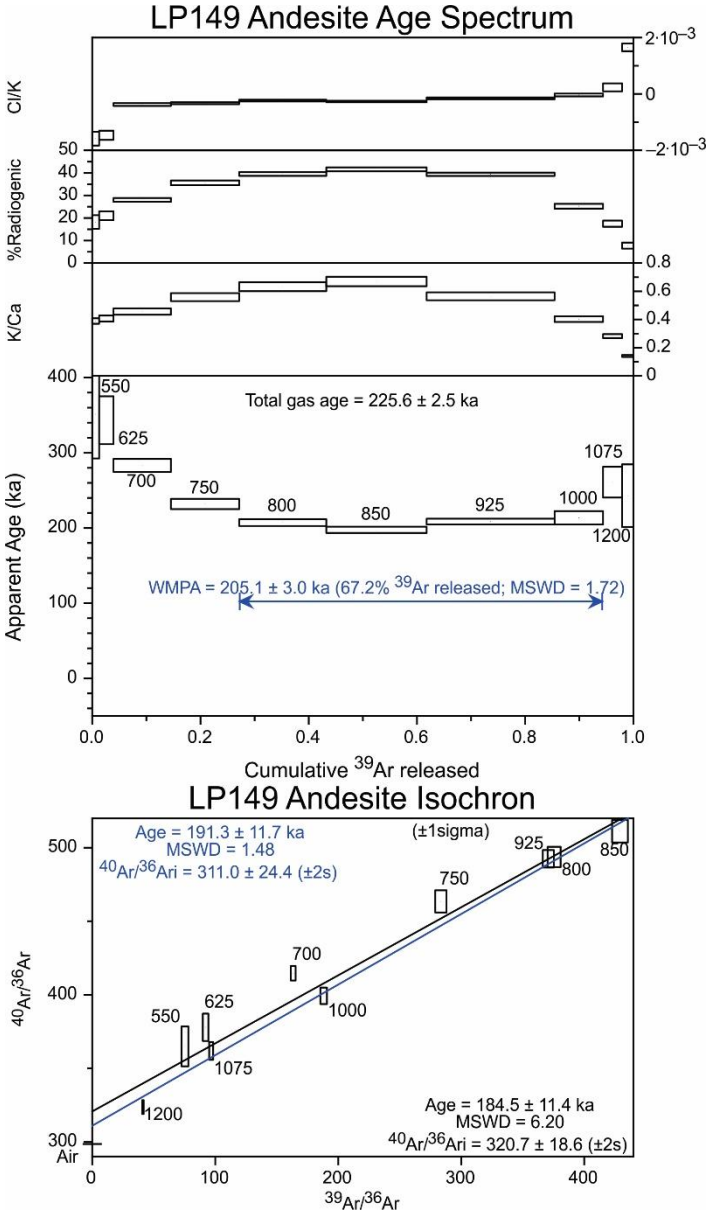

Fig. A1. Continued.

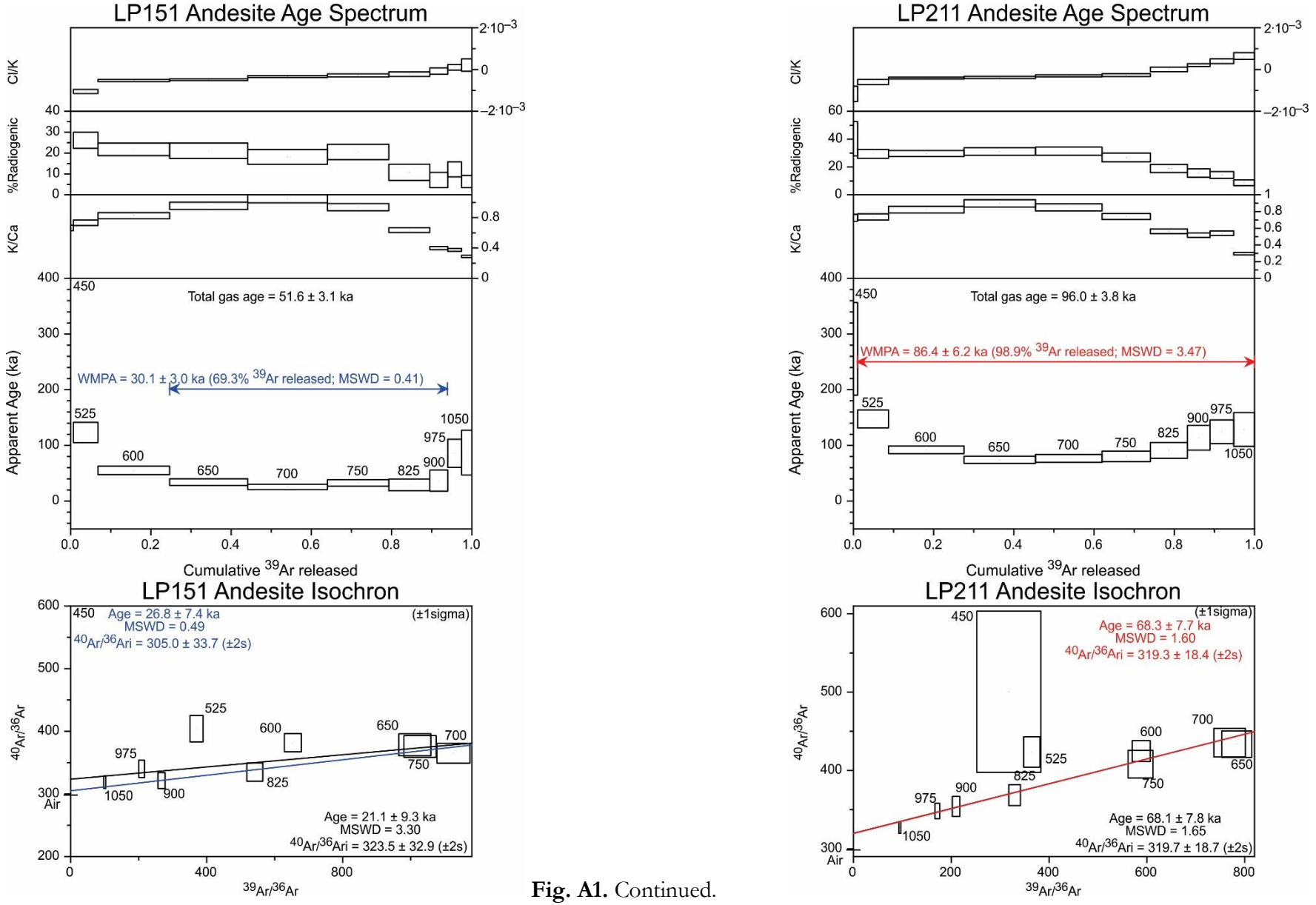

Fig. A1. Continued.

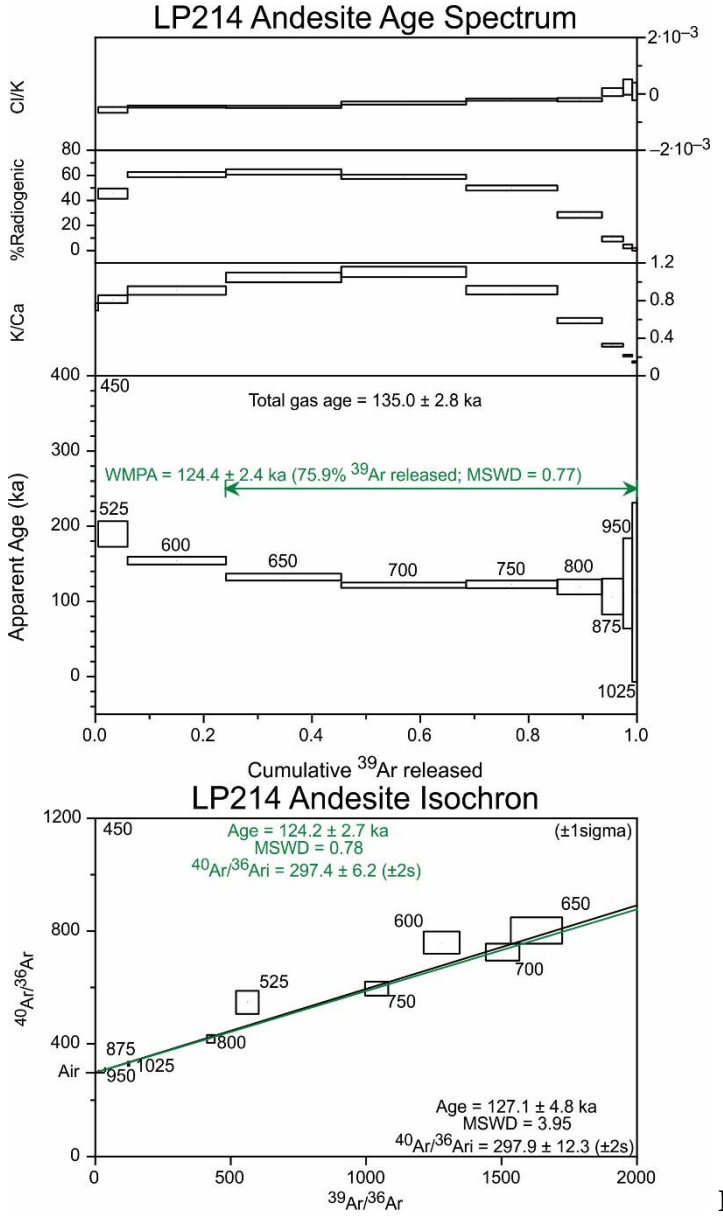

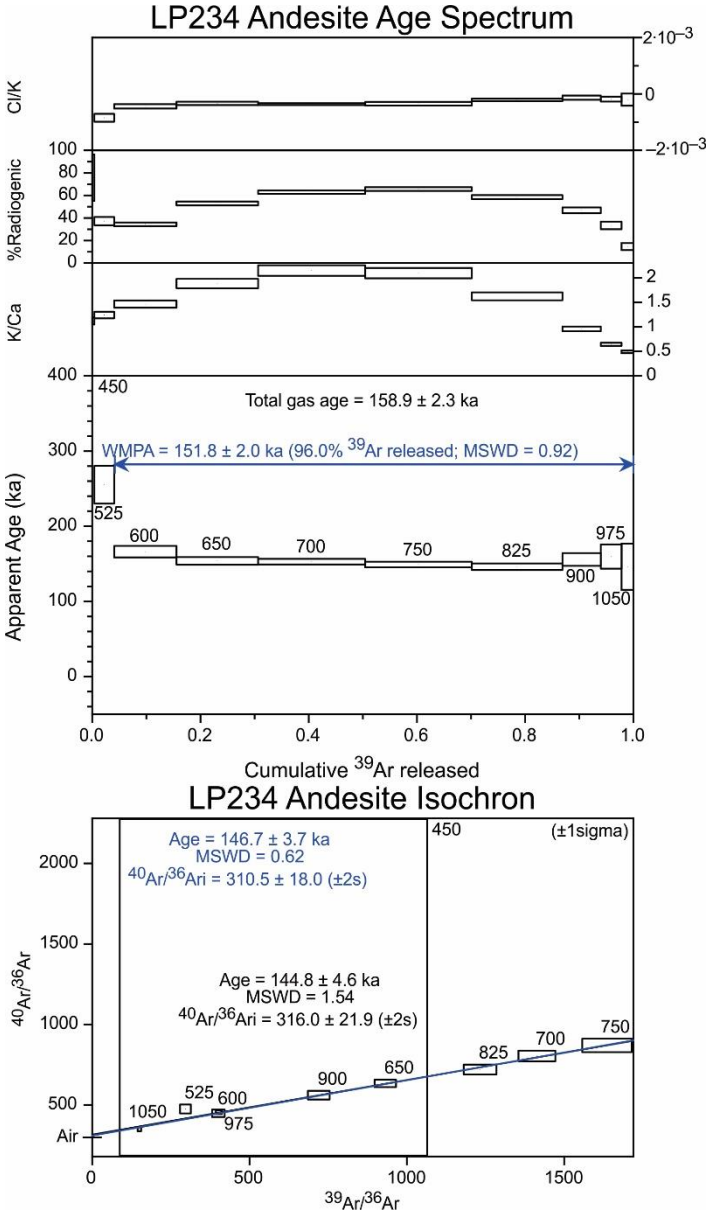

Fig. A1. Continued.

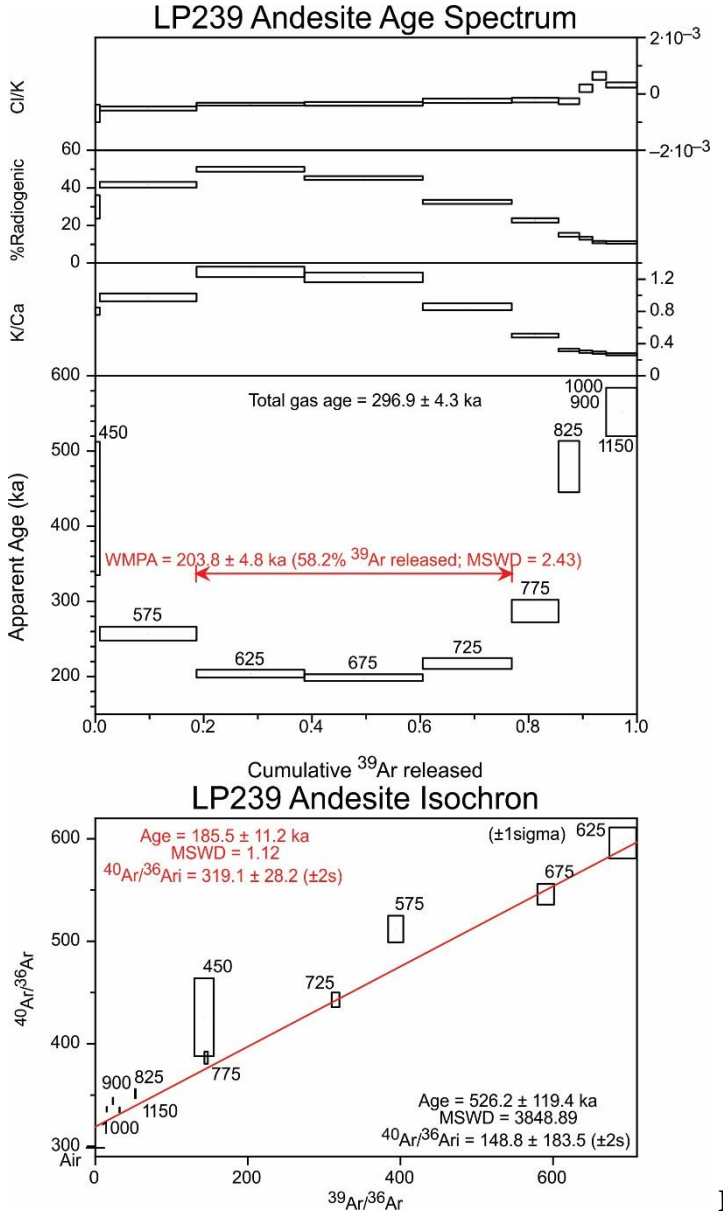

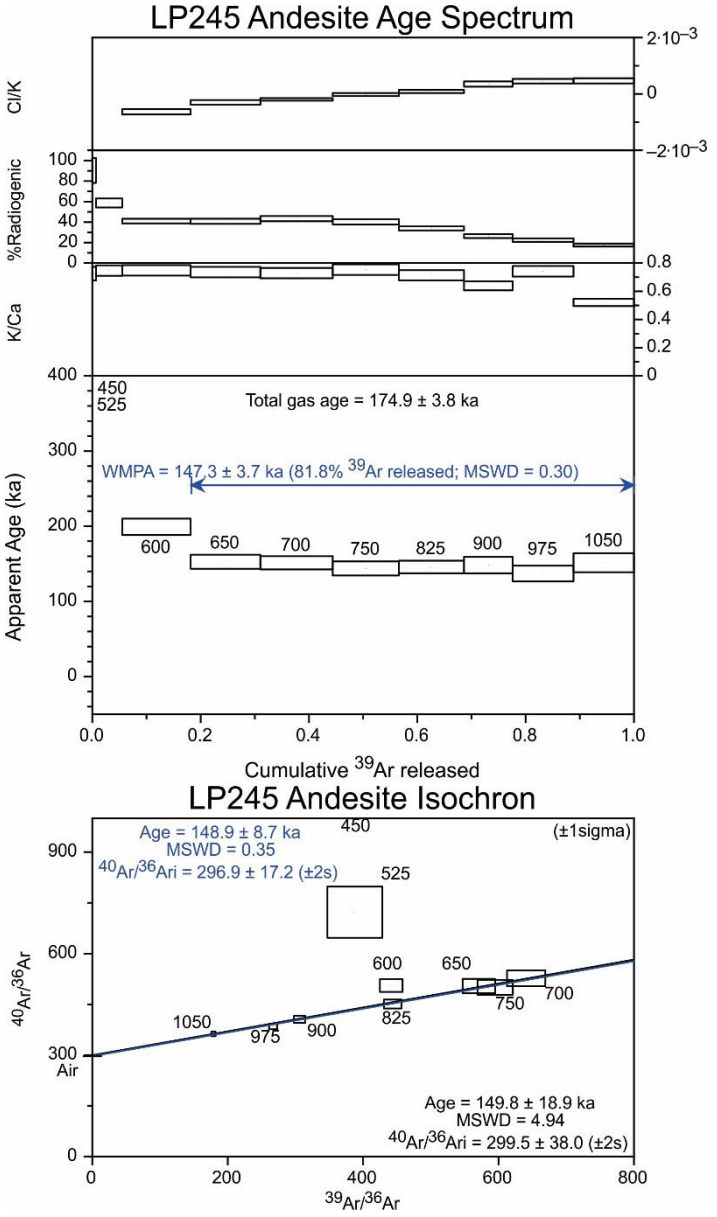

Fig. A1. Continued.

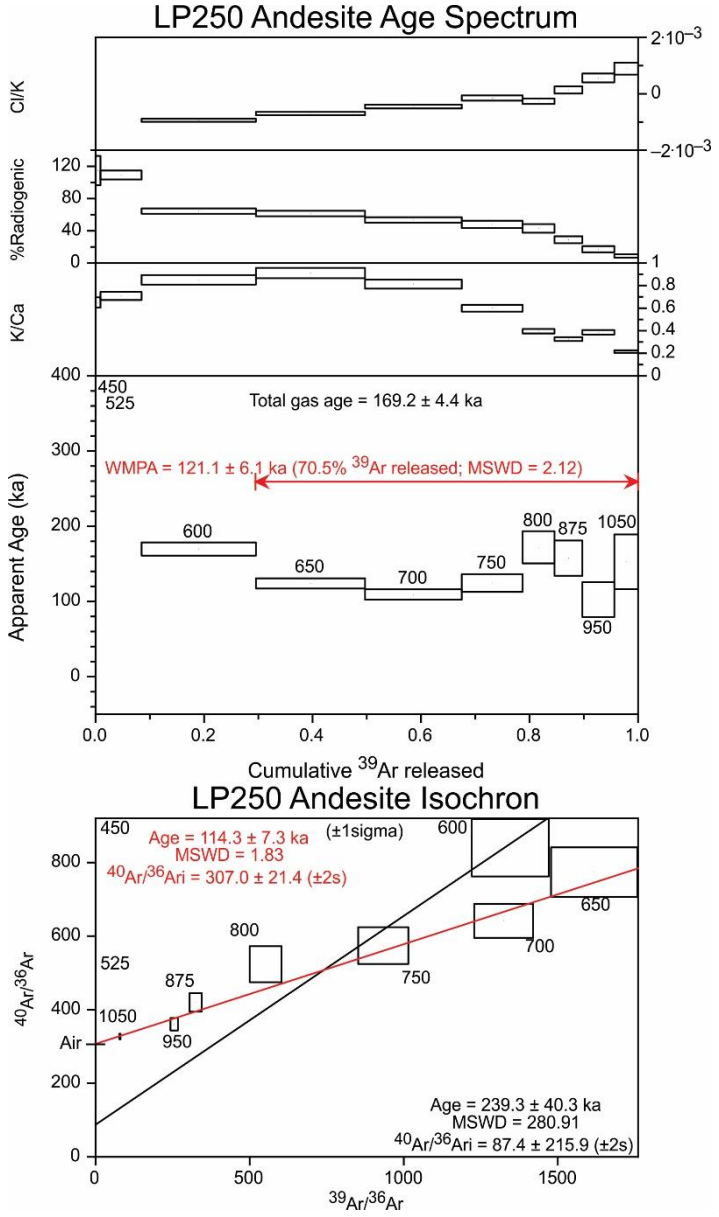

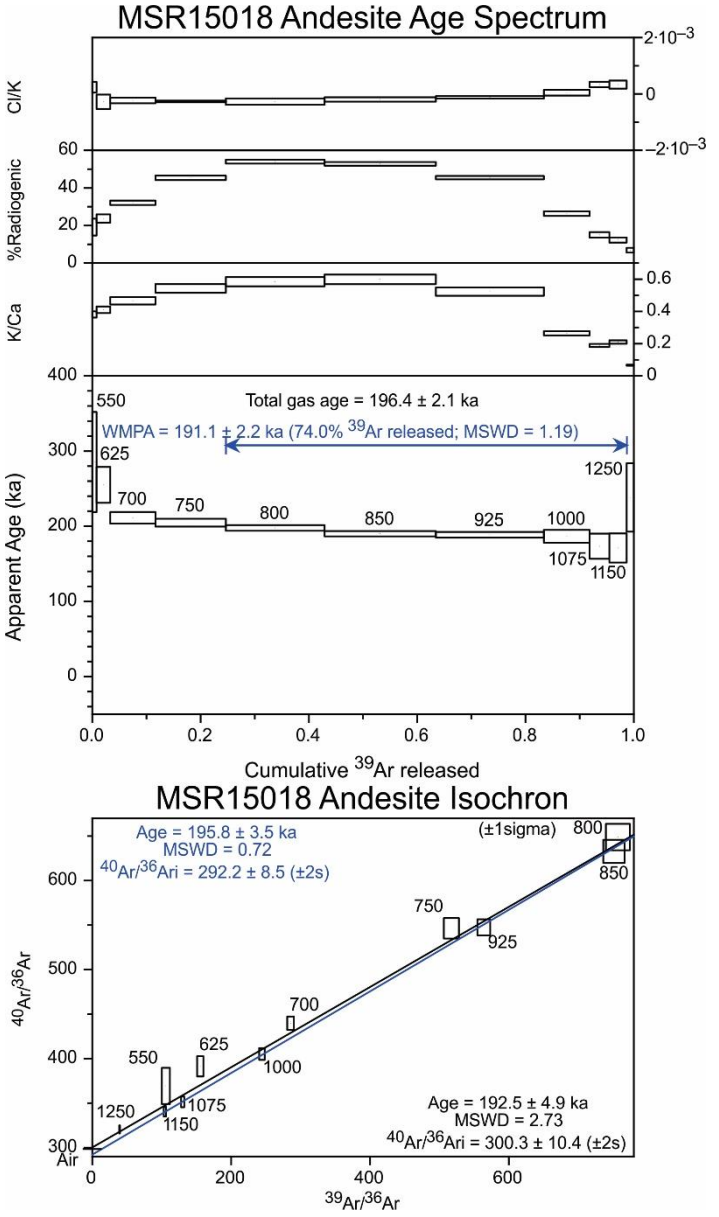

Fig. A1. Continued.

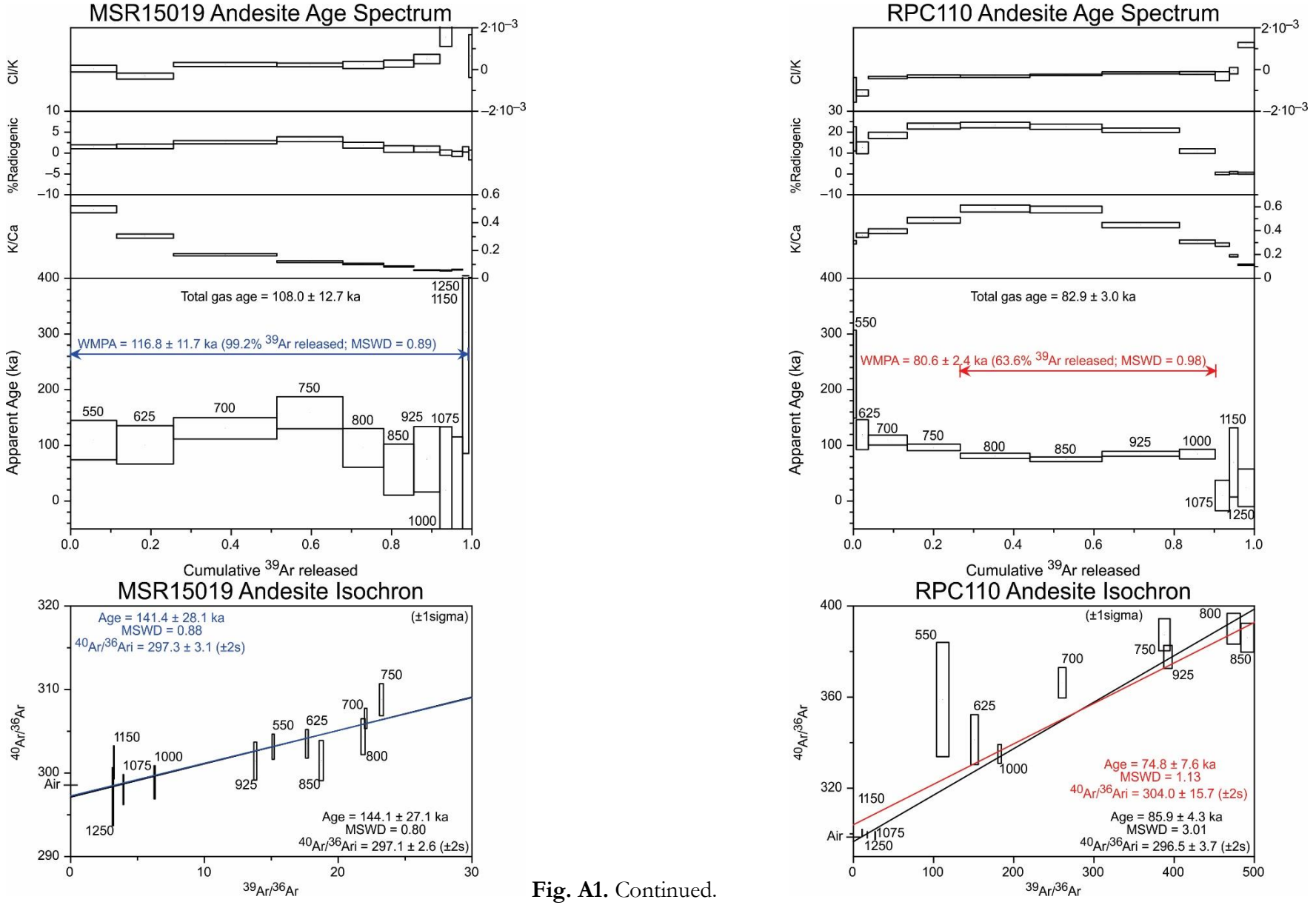

Fig. A1. Continued.

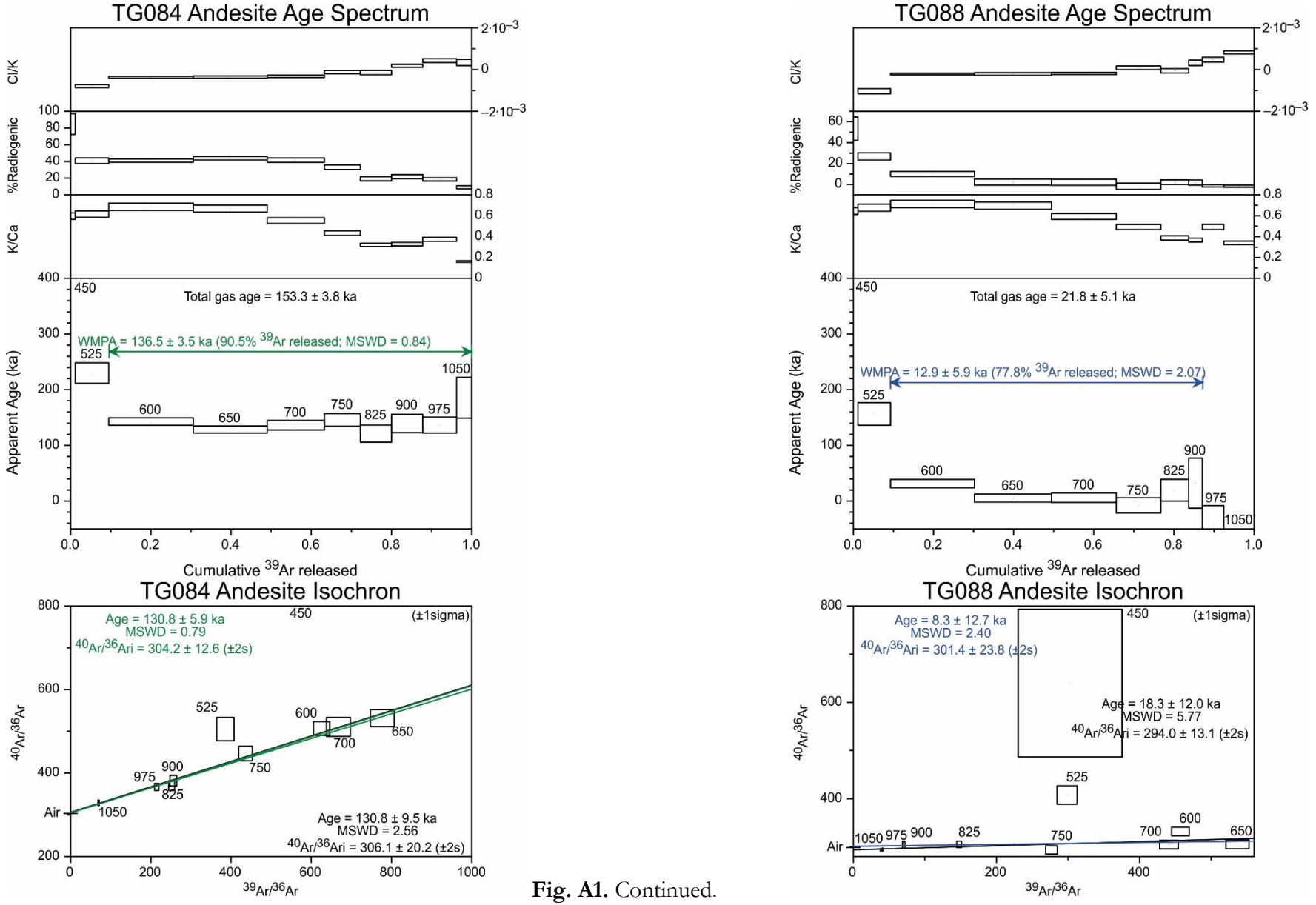

Fig. A1. Continued.

Appendix 2

Features used to define and discriminate members and formations on Tongariro volcano

A2.1. INTRODUCTION

The coding here follows that of Table 3.2 in Chapter 3. The descriptions here explain the distinctions between separate map units of this study.

C – compositional. This relates to major and trace element concentrations and petrographic differences.

F – field relations. This relates to contacts with other map units observed at field localities.

G – geochronological. This relates to age differences between map units as established by $^{40}Ar/^{39}Ar$ and K/Ar age determinations.

S – spatial. This relates to the spatial separation between map units or their inferred source vent locations, typically for distances exceeding 5 km.

L – lithological. This relates to differences in the lithologies of separate map units. It is most often used to distinguish units that were erupted subaerially versus subglacially.

A – adopted ages. This heading provides a case-by-case consideration of age control information for each map unit are, from which ages are proposed and adopted.

A2.2. SYSTEMATIC DESCRIPTIONS

A2.2.1. Otamatereinga Formation (between 571 and 453 ka) – OT

C: The Otamatereinga Formation is entirely basaltic-andesite, which contrasts with the next-youngest Formation exposed on Tongariro's edifice, the 340-293 ka Tupuna Formation.

F: Otamatereinga Formation basaltic-andesite is an inlier within 102-96 ka Te Porere Member lava to the east and <53 ka Pukeonake Formation lava to the SW. These field contacts are adjacent and inferred, and are the only contacts with the Otamatereinga Formation. However, no direct contacts are observed between the Otamatereinga Formation and younger Tongariro eruptives.

G: The Otamatereinga Formation has a minimum age at least 200 kyr older than any other dated material on Tongariro. The $^{40}Ar/^{39}Ar$ age determination (weighted mean plateau age) of LP097 is 512 ± 59 ka. If alternative combinations of heating steps are chosen (which have poorer isochron $^{40}Ar/^{36}Ar$ intercept values), the mean plateau age values are older. Isochron ages and total gas ages are also older than 512 ± 59 ka. See Appendix 2 for $^{40}Ar/^{39}Ar$ age analysis data.

S: This formation is separated from the next oldest volcanic product (Tupuna Formation) on Tongariro by 12 km.

A: The adopted age for the Otamatereinga Formation is the 2 s.d. range from the $^{40}Ar/^{39}Ar$ age determination on LP097, which is between 571 and 453 ka.

A2.2.2. Tupuna Formation (between 349 and 293 ka) – TU

C: Tupuna Formation lavas are characterised by distinctive ≤3 mm phenocrystic hornblendes, which are the dominant ferromagnesian mineral (Hobden, 1997). This feature distinguishes Tupuna Formation andesites from any other *in situ* products on Tongariro and Ruapehu. In addition to the distinctive petrography of the Tupuna Formation, the 290-242 ka Lower Tama

Member of the Haumata Formation has lower MgO (3.0-3.1 wt%) and higher SiO_2 (61.2-62.7 wt%) than the Tupuna Formation.

F: The Tupuna Formation occurs as lava boulders up to 0.4 m in diameter found predominantly on the ridge east of Lower Tama lake. The inferred *in situ* location for this formation is beneath Lower Tama lake and the boulders are thought to have been excavated during the ~11 ka Wharepu eruption (Nairn et al., 1998). The Tupuna Formation is therefore inferred to underlie the Lower Tama Member of the Haumata Formation.

G: A new $^{40}Ar/^{39}Ar$ age determination on a Tupuna Formation boulder of 304 ± 11 ka does not overlap within error of age determinations (K/Ar and $^{40}Ar/^{39}Ar$) for other Tongariro map units. This $^{40}Ar/^{39}Ar$ age determination has mixed agreement with previous K/Ar age determinations on Tupuna Formation lava boulders. Initial K/Ar dating by Stipp (1969) of 259 ± 6 ka was revised with the decay constants of Steiger and Jager (1977) by Hobden et al. (1996) to give 266 ± 6 ka who also re-dated (by K/Ar methods) the same unit for a result of 273 ± 44 ka. Of these, the $^{40}Ar/^{39}Ar$ age result is only analytical within error of Hobden et al.'s (1996) K/Ar result.

A: The adopted ages of Tupuna Formation eruptives are between ~349 and 293 ka. The maximum age boundary value of ~349 ka is suggested by compositional correlations between Tupuna Formation andesite boulders found in the Tama lakes area of Tongariro and hornblende-phyric clasts in the Turakina Formation debris flow deposits. These debris flows reached the distal Turakina River which drains into the Wanganui Basin, which is ~100 km SSW of Tongariro (Tost and Cronin, 2015). The Turakina Formation debris flows have maximum depositional ages of ~349 ka because they overlie marine terraces correlated in time with the 349 ka Whakamaru supereruption (Pillans, 1983; age from Downs et al., 2014). The correlation between the Tupuna Formation and clasts in the Turakina Formation is discussed section 4.2 in Chapter 3. The adopted minimum age value of 293 ka is the minimum value of the sole $^{40}Ar/^{39}Ar$ age determination on the Tupuna Formation at 2 s.d. (304 ± 11 ka: LP113).

A2.2.3. Haumata Formation (between 290 and 189 ka)

A2.2.3.1. Lower Tama Member (between 290 and 242 ka) – alt

C: Lower Tama Member andesites have lower MgO (3.0-3.1 wt%) and higher SiO_2 (61.2-62.7 wt%) than the Tupuna Formation. Lower Tama Member andesites also contain abundant Fe-Ti oxide pseudomorphs after amphibole, which suggests a shared lineage with the older hornblende-phyric Tupuna Formation. Amphibole pseudomorphs occur in other >189 ka Tongariro lavas (≤2 vol%) but are most abundant in Lower Tama Member lavas (~5 vol%).

F: Lower Tama Member lavas have an inferred contact overlying Tupuna Formation andesites.

G: The K/Ar age determination of 266 ± 24 ka (N89: Hobden et al., 1996) is outside of analytical error of all $^{40}Ar/^{39}Ar$ determinations on Tongariro. However, there is overlap within analytical error of other K/Ar age determinations because of the poorer precision on age determinations by the K/Ar method relative to the $^{40}Ar/^{39}Ar$ method (e.g. Stipp, 1969; Hobden et al., 1996).

A: The adopted ages of Lower Tama Member eruptives are between 290 and 242 ka. The minimum and maximum possible ages of the Lower Tama Member are defined by the values at 2 s.d. for the K/Ar age determination of 266 ± 24 ka (N89: Hobden et al., 1996). No contact is observed directly between the Lower Tama Member and the underlying 340-293 ka Tupuna Formation.

A2.2.3.2. Tutangatahiro Member (between 229 and 220 ka) – mtu

C: Basaltic-andesite lavas of the Tutangatahiro Member are characterised by ≤6 mm euhedral clinopyroxenes, making them unique when compared with other >190 ka volcanic products on Tongariro. The additional presence of Fe-Ti oxide pseudomorphs after amphibole (≤3 vol%) also suggests a lineage with the Tupuna Formation and Lower Tama Member.

F, G & A: The adopted age of Tutangatahiro Member lavas are between 229 and 220 ka. The maximum value of 229 ka corresponds with the maximum value at 2 s.d. for the sole $^{40}Ar/^{39}Ar$ age determination on the Tutangatahiro Member (223 ± 6 ka: LP074). The minimum value of 220 ka is a midpoint between the $^{40}Ar/^{39}Ar$ age determinations of LP074 (Tutangatahiro Member) and LP072 (Tawhairauiki Member, direct overlying contact). LP072 is dated at 218 ± 4 ka, hence the preferred midpoint of 220 ka as the upper age of the Tutangatahiro Member. This adopted 229-220 ka age range is consistent with a single K/Ar determination on Tutangatahiro Member lava of 207 ± 36 ka (TG300: Hobden et al., 1996).

A2.2.3.3. Tawhairauiki Member (between 220 and 214 ka) – atp

C: Tawhairauiki Member andesites are the oldest Tongariro eruptives observed containing apatite. Andesitic SiO_2 concentrations and apatite distinguish Tawhairauiki Member lavas from underlying Tutangatahiro Member basaltic-andesites. Compared with older Haumata Formation andesites, Tawhairauiki Member andesites are the most magnesian (>3.8 wt%). Tawhairauiki Member lavas also contain Fe-Ti oxide pseudomorphs after amphibole, but they are less abundant (≤2 vol%) than other >190 ka eruptives.

F, G & A: Field relations and $^{40}Ar/^{39}Ar$ age determinations indicate that Tawhairauiki Member andesites were emplaced between 220 ka (for explanation see 1.2.3.2, Appendix 1: Tutangatahiro Member) and 214 ka. The younger age boundary value of 214 ka is the minimum value at 2 s.d. of the Tawhairauiki Member's sole $^{40}Ar/^{39}Ar$ age determination (218 ± 4 ka: LP072).

A2.2.3.4. Upper Tama Member (between 214 and 207 ka) – aut

C: Lower MgO concentrations (<3 wt%) distinguish Upper Tama Member andesites from all other Haumata Formation materials (>3 wt%).

F: The Upper Tama Member overlies the 229-220 ka Tutangatahiro Member and 220-214 ka Tawhairauiki members.

G: The sole $^{40}Ar/^{39}Ar$ age determination for the Upper Tama Member (209 ± 5 ka: GL2132, G. S. Leonard, pers. comm., 2016) has no age overlap within analytical error of $^{40}Ar/^{39}Ar$ age determinations for the Tawhairauiki or Tutangatahiro members.

A: Upper Tama Member lavas have adopted ages between 214 and 207 ka. The upper limit of 214 ka is obtained from the maximum value of the Upper Tama Member's sole $^{40}Ar/^{39}Ar$ age determination at 2 s.d. (209 ± 5 ka: GL2132). This is consistent with relations with the underlying 220-214 ka Tawhairauiki Member, which has an independently-constrained minimum age boundary value of 214 ka. The Upper Tama Member's minimum age boundary value of 207 ka is a midpoint between the mean age values of GL2132 (209 ± 5 ka, Upper Tama Member) and the two similar $^{40}Ar/^{39}Ar$ age determinations for the Toatoa Member (both 205 ± 6 ka: LP036 and LP149).

A2.2.3.5. Toatoa Member (between 207 and 200 ka) – ato

C: MgO concentrations above 3 wt% distinguish Toatoa Member andesites from underlying Upper Tama Member andesites (<3 wt% MgO).

F: The Toatoa Member overlies the Tawhairauiki and Upper Tama members and underlies the Pukekaikiore Member. Forming the Pukekaikiore landform, the Toatoa and Pukekaikiore members are separated by a horizontal contact where agglutinated material caps the Toatoa Member bluff and underlies the hackly base of the Pukekaikiore Member's bluff.

G: Distinct $^{40}Ar/^{39}Ar$ age determinations for the Toatoa Member (both 205 ± 6 ka: LP036 and LP149) and underlying Tawhairauiki Member (218 ± 4 ka: LP072) do not overlap within analytical uncertainty.

A: The ages of Toatoa Member andesites are likely between 207 and 200 ka. For justification of the older 207 ka age boundary value, see discussion in section 1.3.4 (Appendix 1: Upper Tama Member). The Toatoa Member's younger age boundary of 200 ka is the midpoint between $^{40}Ar/^{39}Ar$ age determinations of the overlying Pukekaikiore Member (195 ± 5 ka, LP039) and the Toatoa Member (both 205 ± 6 ka: LP036 and LP149), which overlap by 1 kyr within 2 s.d. analytical uncertainty. The two $^{40}Ar/^{39}Ar$ age determinations for the Toatoa Member that are both 205 ± 6 ka have mixed agreement with K/Ar age determinations of 204 ± 30, 204 ± 26, 190 ± 18, and 158 ± 28 ka by Hobden et al. (1996). In particular, the 205 ± 6 ka (LP149, $^{40}Ar/^{39}Ar$) and 158 ± 28 ka (TG265, K/Ar) age determinations, which are from the same outcrop, do not overlap within analytical error.

A2.2.3.6. Pukekaikiore Member (between 200 and 190 ka) – apk

C: Unlike Toatoa Member andesites, Pukekaikiore Member andesites contain olivine and no apatite (this study; Hobden, 1997).

F: A time-break between the eruption of Toatoa Member and Pukekaikiore Member andesites is indicated by distinct terracing in the southern Mangatepopo valley (for details see section 1.2.3.5, Appendix 1). No field contact is observed between the Pukekaikiore Member and 195-189 ka Waipoa Member.

G: The Pukekaikiore Member's single $^{40}Ar/^{39}Ar$ age determination (195 ± 5 ka, LP039) has a mean value 10 kyr younger than the mean values of Toatoa Member's $^{40}Ar/^{39}Ar$ age determinations (both 205 ± 6 ka: LP036 and LP149).

A: The adopted ages of Pukekaikiore Member eruptives are between 200 and 190 ka. Justification for the older age boundary is given in section 1.3.5 (Appendix 1: Toatoa Member). The younger age boundary value of 190 ka adopted here is the minimum value of the Pukekaikiore Member's $^{40}Ar/^{39}Ar$ age determination at 2 s.d. (195 ± 5 ka, LP039). This $^{40}Ar/^{39}Ar$ age determination is incompatible with the K/Ar age determination of 121 ± 46 ka (TG151: Hobden et al., 1996) from a sample collected 500 m away from LP039.

A2.2.3.7. Waipoa Member (between 195 and 189 ka) – awp

C: Andesite lavas comprising the Waipoa Member are distinguished from older Haumata Formation eruptives partially by trace amounts of serpentinised olivine xenocrysts that have not been observed in other Haumata Formation eruptives.

S: Andesite lavas comprising the Waipoa Member are distinguished from older Haumata Formation eruptives primarily on spatial separation. Up to five conformable Waipoa Member lavas totalling up to 100 m thick occur in the NE Oturere valley wall, with trajectories pointing back towards the present-day position of Central Crater. The presence of other Waipoa Member lavas in the Mangatawai Stream and the SW Mangahouhounui valley further supports this interpretation of the vent location. The Waipoa Member contrasts as such with all other Haumata Formation eruptives which appear to triangulate back to a vent focus beneath present-day Ngauruhoe. Compositionally, Waipoa Member andesites are indistinguishable within analytical uncertainties of the Pukekaikiore Member for major and trace elements, although minor petrographic contrasts are observed. Trace amounts of serpentinised olivine are observed in Waipoa Member andesites but have not yet been observed in the Pukekaikiore Member (Hobden, 1997; this study). However, Fe-Ti oxide pseudomorphs after amphibole are observed in Waipoa Member lavas, the presence of which suggest a lineage with other Haumata Formation eruptives.

(G) & A: Waipoa Member andesites have adopted ages between 195 and 189 ka. The older age boundary of 195 ka is defined by the maximum value of MSR15018's $^{40}Ar/^{39}Ar$ age determination of 191 ± 4 ka at 2 s.d.. The younger age boundary of 198 ka is a midpoint between $^{40}Ar/^{39}Ar$ age determinations of the Waipoa and overlying Te Pakiraki Members. The oldest $^{40}Ar/^{39}Ar$ age determination of the Te Pakiraki Member is 186 ± 22 ka (LP239). Considering the better analytical precision (and therefore also the probability density) of MSR15018's age determination (191 ± 4 ka), the midpoint of 198 ka between Waipoa Member and Te Pakiraki Member eruptives is chosen to be closer to MSR15018's mean age value. The single $^{40}Ar/^{39}Ar$ age determination for the Waipoa Member of 191 ± 4 ka contrasts with K/Ar determinations by Hobden et al. (1996) of 247 ± 20 ka (TG048), 229 ± 22 ka (TG111) and 173 ± 20 ka (TG098). These K/Ar determinations are all from outcrops at similar stratigraphic levels in the NE Oturere valley that are inherently unlikely to span >70 kyr of eruptive activity, as suggested by the spread of their mean ages. This suggests that some of these K/Ar age determinations are inaccurate. The Waipoa Member's sole $^{40}Ar/^{39}Ar$ age determination (191 ± 4 ka) has a younger mean value (although within analytical error) than that for the Pukekaikiore Member (195 ± 5 ka). But no field contact is observed between these members.

A2.2.3.8. Undifferentiated Haumata Formation eruptives – uhm

F: The landscape-forming lithology in the upper NE Oturere valley is comprised of volcanic products with poor exposure and are heavily covered in fan deposits. These units are mapped as undifferentiated Haumata Formation products. Field relations imply that these units underlie the Waipoa Member and therefore must be products of the Haumata Formation (or, but less likely, the Tupuna Formation or Otamatereinga Formation).

A2.2.4. Mangahouhounui Formation – MH

A2.2.4.1. Te Pakiraki Member (between 189 and 130 ka) – dpk

C: Te Pakiraki Member eruptives are characterised by their (generally) andesitic to dacitic compositions (Table 3: thesis chapter 3) and large plagioclase (up to 9 mm) and clinopyroxene (up to 8 mm) phenocrysts. This feature distinguishes Te Pakiraki Member eruptives from all other older volcanic products on Tongariro.

F & S: Field relations show that Te Pakiraki Member products were erupted contemporaneously with the Waiaruhairiki Member (for details see section 1.4.2 below). The inferred vent location for Te Pakiraki Member eruptives is at a northern focus, near present-day Central Crater, which contrasts with all older Tongariro eruptives (except the Waipoa Member) that were erupted from a southern vent location beneath present-day Ngauruhoe.

G & A: The adopted ages of Te Pakiraki Member eruptives are between 189 and 130 ka. The older age boundary of 189 ka is the midpoint between the only Waipoa Member and oldest Te Pakiraki Member $^{40}Ar/^{39}Ar$ age determinations (for details see section 1.3.7, Appendix 1), because Te Pakiraki Member eruptives directly overlie Waipoa Member andesites in the Mangahouhounui and Oturere valleys. The younger age boundary of 130 ka is defined by the minimum age at 2 s.d. for Te Pakiraki Member's youngest $^{40}Ar/^{39}Ar$ age determination of 137 ± 7 ka. This $^{40}Ar/^{39}Ar$ age determination was performed on TG084, which is a sample from the collection of Hobden (1997) that has a K/Ar age determination of 97 ± 20 ka (Hobden et al., 1996). The $^{40}Ar/^{39}Ar$ and K/Ar age results for this sample do not overlap within analytical uncertainty.

A2.2.4.2. Waiaruhairiki Member (between 152 and 150 ka) – awh

C: Greater MgO concentrations (5.4-6.2 wt%) distinguish Waiaruhairiki Member eruptives from the Te Pakiraki Member eruptives (2.5-4.8 wt% MgO). Waiaruhairiki Member eruptives are also on average less silicic than Te Pakiraki Member eruptives. Despite this, field relations and geochronological results indicate the two Members were erupted contemporaneously.

F: The Waiaruhairiki Member bisects Te Pakiraki Member eruptives in the NE wall and headwall of the Mangahouhounui valley and is found as an inlier on the NE Mangahouhounui planeze. Like Te Pakiraki Member eruptives, Waiaruhairiki Member lavas contain large plagioclase (up to 9 mm) and clinopyroxene (up to 8 mm) phenocrysts, which suggests a common magmatic source. Waiaruhairiki Member outcrops in the NE wall and headwall of the Mangahouhounui valley are compositionally correlated to an inlier of lava (LP245) on the NE Mangahouhounui planeze. However, the phenocrysts in sample LP245 are only up to 5 mm across, which is smaller

than in other Mangahouhounui Formation eruptives. In each location where they occur, Waiaruhairiki Member eruptives only bisect Te Pakiraki Member eruptives once as singular occurrences: they do not sandwich Te Pakiraki Member eruptives.

A: The adopted age of Waiaruhairiki Member eruptives is between 152 and 150 ka. The older age boundary of 152 ka is chosen as a midpoint between Te Pakiraki Member and Waiaruhairiki Member $^{40}Ar/^{39}Ar$ age determinations. Te Pakiraki Member lava overlying Waiaruhairiki Member eruptives in the NE Mangahouhounui valley has a $^{40}Ar/^{39}Ar$ age determination of 155 ± 5 ka (LP118). This determination has an older mean value than the single Waiaruhairiki Member $^{40}Ar/^{39}Ar$ age determination of 147 ± 7 ka (LP245) from a separate location ~800 m to the northeast, where Te Pakiraki Member eruptives are not exposed (see **F**, above). These comparative age determinations have some conflict with field relations because the younger mean age occurs in the underlying unit. However, field relations and $^{40}Ar/^{39}Ar$ age determinations can be reconciled within analytical uncertainties. Adjusting each age determination by ~1.5 s.d. in opposite directions indicates alternative ages to mean $^{40}Ar/^{39}Ar$ values of ~152 ka (LP245, Waiaruhairiki Member) and ~151 ka (LP118, Te Pakiraki Member), which indicate a maximum age boundary of 152 ka for the Waiaruhairiki Member. Whilst it is possible that the compositional correlation between LP245 and other Waiaruhairiki Member eruptives is inaccurate, this is the simplest interpretation that considers all available compositional data, field relations and geochronological results within their analytical uncertainties. Another $^{40}Ar/^{39}Ar$ age determination from Te Pakiraki Member lava underlying Waiaruhairiki Member eruptives in the NE Mangahouhounui valley (same cliff section as Te Pakiraki Member sample LP118) of 186 ± 22 ka (LP239) is consistent with an adopted maximum age boundary of 152 ka for the Waiaruhairiki Member. The minimum age boundary of 150 ka is required by the adjusted mean age values as discussed above, where Te Pakiraki Member eruptives overlying Waiaruhairiki Member lava can be no older than 150 ka without exceeding 2 s.d. age uncertainties on LP118 (Te Pakiraki Member sample). A minimum age of 150 ka for the Waiaruhairiki Member is also compatible with field relations in the head of the Mangahouhounui valley where a Waiaruhairiki Member lava underlies a Te Pakiraki Member lava (inferred adjacent contact). A single $^{40}Ar/^{39}Ar$ age determination on this Te Pakiraki Member outcrop was adversely affected by glassy groundmass, but yields an age of about 145 ka (LP187: Appendix 1).

A2.2.4.3. Tātaramoa Member (between 189 and 130 ka) – mtm

S: An isolated outcrop (<300 m of streambed outcrop) of basaltic-andesite in the Tahurangi Stream on NE Tongariro is the sole representative of the Tātaramoa Member. Large (up to 9 mm) plagioclase and clinopyroxene phenocrysts in this unit associate it with other Mangahouhounui Formation eruptives.

C: Tātaramoa Member's low SiO_2 concentration (53.9 wt%) distinguishes it from other Mangahouhounui Formation eruptives (>56 wt% SiO_2).

A: Field relations with the overlying Rotopaunga Member indicate that Tātaramoa Member basaltic-andesite must pre-date 68 ± 15 ka (LP211, locally), which is the only field relationship that provides age control. No direct geochronological results exist for the Tātaramoa Member basaltic-andesite. In the absence of precise stratigraphic age-control for the Tātaramoa Member,

the compositional association with other Mangahouhounui Formation eruptives is preferred as an indicator of age. The compositional association between the Tātaramoa Member and other Mangahouhounui Formation eruptives is based on large plagioclase and clinopyroxene phenocrysts (up to 9 mm) that occur in all of these eruptives. Given the ages of other Mangahouhounui Formation eruptives, the Tātaramoa Member was probably erupted between 189 and 130 ka.

A2.2.4.4. Undifferentiated Mangahouhounui Formation products – uma

F: Landscape-forming materials in the lower Mangahouhounui valley's headwall are poorly exposed, covered in fan deposits, and have not been sampled. Extrapolating Te Pakiraki Member and Waiaruhairiki Member outcrops from north of the headwall of the Mangahouhounui valley (uphill of Te Maari Craters) into the area of this undifferentiated material suggests that the deposits are likely Mangahouhounui Formation eruptives and they are thus mapped here as undifferentiated Mangahouhounui Formation. However, it is also possible that they are older Haumata Formation eruptives.

A2.2.5. Taiko Formation (between 133 and 52 ka) – TA

A2.2.5.1. Rahuituki Member (between 129 and 119 ka) – arh

C: Rahuituki Member andesites are distinguished from older Mangahouhounui Formation eruptives by phenocryst sizes ≤5 mm and the lack of apatite. Lower TiO_2 (<0.75 wt%) and Sr (~190-260 ppm) concentrations distinguish Rahuituhi andesites from 130-102 ka Pungarara Member andesites (0.78-0.89 wt% TiO_2; 268-326 ppm Sr).

F: Rahuituki Member eruptives have no field contacts with Mangahouhounui Formation eruptives. Rahuituki Member eruptives have generally splayed geomorphologies with greater runout distances than Mangahouhounui Formation eruptives which suggests that they were erupted in an ice-poorer environment than Mangahouhounui Formation eruptives.

G & A: Rahuituki Member andesites were likely erupted between 129 and 119 ka, which are the minimum and maximum values of their sole $^{40}Ar/^{39}Ar$ age determination (124 ± 5 ka: LP214) at 2 s.d.. This age determination is younger than the youngest Te Pakiraki Member age determination which do not overlap within error (137 ± 7 ka: TG084 re-date from this study). The oldest Tongariro eruptive overlying the Rahuituki Member is the Te Porere Member, which has a maximum adopted age of 102 ka, therefore consistent with field relations.

A2.2.5.2. Pungarara Member (between 130 and 102 ka) – apg

C: Pungarara Member andesites are distinguished from other Tongariro eruptives by their distinctive compositions, with high TiO_2 (0.78-0.89 wt%), moderate Ba (290-353 ppm) and high Sr (268-326 ppm) (Hobden, 1997). These compositions contrast with lower values in the Rahuituki Member (<0.75 wt% TiO_2; ~190-260 ppm Sr) and Te Pakiraki Member (<0.75 wt% TiO_2) members. Pungarara Member lavas have K_2O concentrations of 1.2-1.7 wt% which distinguishes them from overlying Te Porere Member lavas (1.6-2.2 wt%). Pungarara Member

andesites also contain traces of Fe-Ti oxide pseudomorphs after amphibole, which Rahuituki Member lavas do not.

F: Pungarara Member andesites also underlie the 102-96 ka Te Porere Member and no other direct field contacts are observed. Pungarara Member lavas are inferred to overlie young Te Pakiraki Member lava.

A: Field relations indicate that Pungarara Member andesites were erupted between 130 and 102 ka. Pungarara Member andesites overlie a Te Pakiraki Member lava re-dated with $^{40}Ar/^{39}Ar$ in this study at 137 ± 7 ka (TG084; inferred contact, locally). The minimum value of this $^{40}Ar/^{39}Ar$ age determination at 2 s.d. provides the maximum age boundary value for the Pungarara Member. The minimum age boundary value of 102 ka is adopted because the Pungarara Member underlies the 102-96 ka Te Porere Member. This adopted age range has mixed agreement with K/Ar age determinations by Hobden et al. (1996). The two K/Ar ages relevant to the Pungarara Member of 103 ± 24 ka (TG171) and 77 ± 28 ka (TG077) are considered inaccurate due to sample alteration (TG171), glassiness (TG171 and TG077; see Appendix 4 in Hobden, 1997) and low radiogenic argon yield (TG077: Hobden et al., 1996). Because of these concerns, field relations provide the preferred age constraints here.

S: Pungarara Member andesites occur on SE Tongariro which is more than 5 km from outcrops of the 129-119 ka Rahuituki Member that occur on Tongariro's NE and NW flanks.

A2.2.5.3. Mangahouhouiti Member (between 130 and 96 ka) – mhi

C: High MgO concentrations (5.5-7.1 wt%) in combination with an olivine- and clinopyroxene-dominated mineralogy (over plagioclase) distinguish Mangahouhouiti Member basaltic-andesites from all older Tongariro eruptives.

F: Direct field contacts show that the Mangahouhouiti Member overlies the 189-130 ka Te Pakiraki Member and underlies the 96-79 ka Waitakatorua Member. All of these (three) units have distinctive compositions in SiO_2-MgO space (Table 3, Chapter 3). The field relations distinguish Mangahouhouiti Member basaltic-andesites from other Tongariro eruptives.

G: Field relations are consistent with $^{40}Ar/^{39}Ar$ age determinations on Mangahouhouiti Member lavas. Two $^{40}Ar/^{39}Ar$ age age determinations have been attempted on lavas from the Mangahouhouiti Member. Of these, that for sample LP126 was adversely affected by glass in the groundmass material and is reported only in Appendix 2 (mean age of ~117 ka). LP126's mean value matches the second $^{40}Ar/^{39}Ar$ age determination of 117 ± 23 ka (MSR15019) for the Manghouhouiti Member, which is the preferred radiometric age constraint. The 117 ± 23 ka $^{40}Ar/^{39}Ar$ age result has mixed agreement with previous K/Ar determinations of 202 ± 46 and 123 ± 32 ka (Hobden et al., 1996). The older K/Ar age has a low yield of radiogenic argon (3.5%; TG400) whereas the younger age's yield is greater (7.1 %; TG109) and agrees within error to the $^{40}Ar/^{39}Ar$ age estimate here. Age results for MSR15019 and TG109 are consistent with field relations of Mangahouhouiti Member eruptives overlying a Te Pakiraki Member dacite lava (152 ± 4 ka at this location: LP234).

A: The adopted age of Mangahouhouiti Member eruptives is between 130 and 96 ka. The older age boundary value is constrained by field relations that show Mangahouhouiti Member eruptives

overlying 189-130 ka Te Pakiraki Member eruptives. The minimum age boundary for the Mangahouhouiti Member of 96 ka is the maximum age of the 96-79 ka Waitakatorua Member, which overlies the Mangahouhouiti Member (see section 1.5.7, below). The Mangahouhouiti Member's adopted minimum age of 96 ka is close to the minimum age (94 ka) at 2 s.d. for MSR15019's $^{40}Ar/^{39}Ar$ age determination of 117 ± 23 ka.

A2.2.5.4. Mangatepopo Member (between 133 and 102 ka) – amp

C: The Mangatepopo Member lavas have greater MgO concentrations (4.2-4.9 wt%) than the similar-age Rahuituki (2.9-3.4 wt%) and Pungarara Member (2.5-3.9 wt%) members. Mangatepopo Member andesites also contain traces of olivine, which Rahuituki and Pungarara Members do not.

F: The lower boundary of the Mangatepopo Member is not observed at any known field localities. Mangatepopo Member andesites underlie 102-96 ka Te Porere Member eruptives in the northern Mangatepopo valley. The distribution of Mangatepopo Member lavas in topographic lows, such as the floor of the Mangatepopo valley, suggests emplacement in an ice-free environment, in similar fashion to Rahuituki Member lavas.

G: $^{40}Ar/^{39}Ar$ ages determined for the Mangatepopo Member are 109 ± 8 ka (LP010) and 121 ± 12 ka (LP250), which are compatible with K/Ar age determinations for overlying Te Porere Member lavas, which range from 107 ± 20 ka to 91 ± 14 ka (Stipp, 1969; Hobden et al., 1996).

A: The adopted ages of Mangatepopo Member andesites are between 133 and 102 ka. The older age boundary value of 133 ka is the maximum age of LP250 (121 ± 12 ka) at 2 s.d.. The minimum age boundary value of 102 ka is implied by direct field contact with the Mangatepopo Member underlying the Te Porere Member. This is similar to the minimum value (101 ka) of LP010's $^{40}Ar/^{39}Ar$ age determination at 2 s.d. (109 ± 8 ka).

A2.2.5.5. Te Porere Member (between 102 and 96 ka) – dtp

C: Te Porere Member andesites and dacites have high average incompatible element concentrations (e.g. K_2O ~2 wt%; Ba ~400 ppm: Hobden, 1997). Greater TiO_2 concentrations distinguish Te Porere Member eruptives (0.74-0.94 wt%) from Rahuituki Member andesites (0.65-0.73 wt%). Te Porere Member eruptives are MgO-poorer (1.7-3.1 wt%) than Mangatepopo Member andesites (4.2-4.9 wt%). Te Porere Member eruptives cluster towards higher Ba (317-515 ppm) and lower Sr (214-296 ppm) than Pungarara Member andesites (290-353 ppm Ba; 268-326 ppm Sr). Apatite also occurs in Te Porere Member eruptives, which is absent in Pungarara Member andesites. However, the minor compositional overlap between Te Porere Member and Pungarara Member eruptives is compatible with a common magmatic lineage. This is supported by Te Porere Member eruptives overlying Pungarara Member andesites in the SW Oturere valley.

F: Te Porere Member eruptives overlie the 130-102 ka Mangatepopo Member, from which they are geochemically distinct (**C**, above).

L: In addition to lavas and agglutinates, Te Porere Member eruptives include hyaloclastites, lapilli tuffs and lapilli tuff breccias (labelled ERh, ERltb, ERc, PLT and PCB in Cole et al., 2018). These lithologies have not been observed in older Tongariro materials.

G: A single $^{40}Ar/^{39}Ar$ age determination on a Te Porere Member lava of 99 ± 3 ka is within error of most previous K/Ar determinations for this member of 110 ± 12, 97 ± 20, 95 ± 20, 95 ± 20, 91 ± 18, 81 ± 34, 68 ± 22 ka (Hobden et al., 1996) and 107 ± 20 ka (Stipp, 1969). Compared with other Tongariro $^{40}Ar/^{39}Ar$ age determinations, the Te Porere Member result has minimal error overlap with results for the Mangahouhouiti and Mangatepopo members of 117 ± 23 ka and 109 ± 8 ka, respectively.

A: The adopted age of Te Porere Member eruptives is between 102 and 96 ka, which are the minimum and maximum ages of the Te Porere Member $^{40}Ar/^{39}Ar$ age determination at 2 s.d. (99 ± 3 ka: LP103).

A2.2.5.6. Otamangakau Member (between 96 and 92 ka) – aok

C: The Otamangakau Member is characterised by higher MgO concentrations (3.4-3.9 wt%) than the 102-96 ka Te Porere Member (1.7-3.1 wt%) but is otherwise compositionally similar and also contains apatite. These features suggest a shared magmatic lineage.

F & A: All occurrences of the Otamangakau Member overlie the 102-96 ka Te Porere Member. Otamangakau Member lavas also underlie eruptives of the 92-84 ka Te Rurunga Member and the 61-23 ka Mokomoko Formation. These field relations indicate that the Otamangakau Member was erupted between 96 and 92 ka, due to its stratigraphic position between the Te Porere and Te Rurunga members.

A2.2.5.7. Waitakatorua Member (between 96 and 79 ka) – awu

C: Higher MgO concentrations (4.8-5.8 wt%) distinguish the Waitakatorua Member from the 102-96 ka Te Porere (1.7-3.1 wt%), 96-92 ka Otamangakau (3.4-3.9 wt%), 86-79 ka Te Wakarikiariki (3.8-4.6 wt%) and 79-61 ka Rotopaunga (3.0-4.2 wt%) members. Sr concentrations of 307-396 ppm distinguish Waitakatorua Member eruptives from Te Rurunga Member eruptives (246-275 ppm) (Hobden, 1997).

F: Visible contacts separate the Waitakatorua Member from the overlying Rotopaunga Member and underlying Mangahouhouiti and Te Porere members.

L: The Waitakatorua Member contains lapilli tuff breccias that are sometimes reworked and are intercalated with coherent lavas. This is similar to some Rotopaunga Member materials. However, these lithological features distinguish Waitakatorua Member eruptives from other similar-age members that do not contain lapilli tuffs or lapilli tuff breccias: the 92-84 ka Te Rurunga, 86-79 ka Te Wakarikiariki and 61-52 ka Te Tatau members.

A: The adopted ages for Waitakatorua Member eruptives are between 96 and 79 ka. The maximum age boundary value of 96 ka is inferred by field contacts with underlying 102-96 ka Te Porere Member eruptives. The minimum age value of 79 ka is assigned because the Waitakatorua Member underlies the 79-61 ka Rotopaunga Member (see section 1.5.10, below). This adopted

age window is consistent within analytical error with only the younger of two previous K/Ar determinations by Hobden et al. (1996) of 128 ± 24 ka (TG123) and 104 ± 26 ka (TG227) for lavas mapped into the Waitakatorua Member.

A2.2.5.8. Te Rurunga Member (between 92 and 84 ka) – atr

C: Te Rurunga Member eruptives have lower SiO_2 (58.1-58.3 wt%) and higher MgO (4.9-5.0 wt%) concentrations than the older Otamangakau Member (59.4-61.7 wt% SiO_2; 3.4-3.9 wt% MgO) and Te Porere Member (59.4-63.9 wt% SiO_2; 1.7-3.1 wt% MgO) eruptives.

F: Te Rurunga Member andesites overlie older Otamangakau Member and 102-96 ka Te Porere Member eruptives which are compositionally distinct (**C**, above).

G: A single $^{40}Ar/^{39}Ar$ age determination of 88 ± 4 ka (LP023) was determined on a boulder within 1 km of in situ Te Rurunga Member andesites. This boulder is compositionally correlated to other *in situ* Te Rurunga Member products that were texturally unsuitable for dating due to high proportions of glassy matrix. This age result has minimum error overlap with only one other Tongariro $^{40}Ar/^{39}Ar$ age determination of 81 ± 5 ka from the younger Te Wakarikiariki Member, which is compositionally distinct from the Te Rurunga Member.

A: Te Rurunga Member eruptives have an adopted age between 92 and 84 ka. These age boundaries are the maximum and minimum values at 2 s.d. for LP023's $^{40}Ar/^{39}Ar$ age determination of 88 ± 4 ka.

A2.2.5.9. Te Wakarikiariki Member (between 86 and 79 ka) – ati

C: MgO concentrations (3.8-4.6 wt%) distinguish Te Wakarikiariki Member lavas from similar-age 92-84 ka Te Rurunga Member (4.9-5.0 wt%) and older 102-96 ka Te Porere Member (1.7-3.1 wt%) and 96-92 ka Otamangakau Member (3.4-3.9 wt%) eruptives. One Te Wakarikiariki Member lava (LP161) contains plagioclase crystals up to 7 mm, which suggests a possible magmatic lineage with the earlier Mangahouhounui Formation eruptives.

G & F: A single $^{40}Ar/^{39}Ar$ age determination of 81 ± 5 ka for Te Wakarikiariki Member lava was previously reported by Cole et al. (2018). This $^{40}Ar/^{39}Ar$ age result is consistent with field relations that show Te Wakarikiariki Member lavas overlying eruptives of the 102-96 ka Te Porere Member and underlying eruptives of the 79-61 ka Rotopaunga Member and 61-52 ka Te Tatau Member.

A: Te Wakarikiariki Member eruptives have adopted ages between 86 and 79 ka. The upper age boundary is the maximum value at 2 s.d. for RPC110's $^{40}Ar/^{39}Ar$ age determination of 81 ± 5 ka (Cole et al., 2018). The minimum age boundary is a midpoint between the mean $^{40}Ar/^{39}Ar$ age values for RPC110 (Te Wakarikiariki Member) and GL2007, which is the sample with the oldest $^{40}Ar/^{39}Ar$ age determination for the Rotopaunga Member of 76 ± 4 ka (GL2132, G. S. Leonard, pers. comm., 2016).

A2.2.5.10. Rotopaunga Member (between 79 and 61 ka) – arp

C: MgO concentrations distinguish Rotopaunga Member eruptives (3.0-4.2 wt%) from older 92-84 ka Te Rurunga Member (4.9-5.0 wt%) eruptives. Rotopaunga Member eruptives also have generally lower MgO and higher SiO_2 (57.6-61.3 wt%) concentrations than older Te Wakarikiariki Member lavas (4.0-4.6 wt% MgO; 58.9-59.1 wt% SiO_2). Rotopaunga Member eruptives also contain apatite in crystal clots whereas apatite has not been observed in Te Rurunga Member and Te Wakarikiariki Member eruptives.

L: In addition to lavas and agglutinates, the Rotopaunga Member includes hyaloclastites and lapilli tuff breccias on upper Tongariro and correspond to units named ERh and ERltb, respectively, in Cole et al. (2018). These lithologies are not observed in the similar-age 86-79 ka Te Wakarikiariki or 92-84 ka Te Rurunga members.

F & G: Field relations and radiometric age data distinguish Rotopaunga Member eruptives from Te Porere Member eruptives. Two $^{40}Ar/^{39}Ar$ ages determined for Rotopaunga Member lavas add to three previous K/Ar determinations. An inlier of lava partially buried by Ngauruhoe (Te Pupu Formation) eruptives yielded a $^{40}Ar/^{39}Ar$ result of 76 ± 4 ka (G.S. Leonard, pers. comm., 2016: GL2007, Table 1). This result compares well with a previous K/Ar age from the same inlier of 79 ± 18 ka (Hobden et al., 1996). A second $^{40}Ar/^{39}Ar$ age determination on a lava exposed in Tahurangi Stream (NE Tongariro) gives 68 ± 15 ka. These results are indistinguishable within uncertainty of the two other Rotopaunga Member K/Ar determinations of 87 ± 20 ka (TG051) and 64 ± 22 ka (TG330; Hobden et al., 1996). The $^{40}Ar/^{39}Ar$ age results are consistent with field relations elsewhere showing Rotopaunga Member eruptives overlying the 102-96 ka Te Porere Member (upper Tongariro) and a 86-79 ka Te Wakarikiariki Member lava (NE Mangahouhounui valley).

A: Rotopaunga Member eruptives have adopted ages between 79 and 61 ka. Justification for the maximum age value is given in (**A**) for the Te Wakarikiariki Member—see section 1.5.9, above. The minimum age value of 61 ka is the maximum value at 2 s.d. of 56 ± 5 ka, which is the Te Tatau Member's sole $^{40}Ar/^{39}Ar$ age determination (GL2223).

A2.2.5.11. Te Tatau Member (between 61 and 52 ka) – att

C: Te Tatau Member eruptives are low-silica andesites (57.4-59.5 wt% SiO_2), that have high MgO (4.2-6.5 wt%; Table 3) and contain trace amounts of olivine. Some compositional similarity with Waitakatorua Member lavas and lapilli tuff breccias indicates they were sourced from a related magma and are possibly of similar age.

F: The Te Tatau Member overlies the 79-61 ka Rotopaunga, 86-79 ka Te Wakarikiariki and 96-92 ka Otamangakau members.

G: A single $^{40}Ar/^{39}Ar$ age determination of 56 ± 5 ka for the Te Tatau Member is younger outside of error than $^{40}Ar/^{39}Ar$ age determinations of the Te Wakarikiariki Member (81 ± 5 ka: RPC110).

L: The Te Tatau Member is comprised by scoria, agglutinates and lavas exposed north of the Mangahouhounui valley. These lithologies present no evidence for syn-glacial eruptive activity

which distinguishes them from the earlier 96-79 ka Waitakatorua Member, 86-79 ka Te Wakarikiariki Member and 79-61 ka Rotopaunga Member eruptives.

A: The ages of Te Tatau Member eruptives are between 61 and 52 ka, which are the maximum and minimum age values at 2 s.d. for the sole $^{40}Ar/^{39}Ar$ age determination of this member (56 ± 5 ka: GL2223—or 56.2 ± 4.6 ka at 1 decimal place).

A2.2.6. Undifferentiated Otukou lava (between 91 and 79 ka) – uol

C: The Otukou lava's low crystal content (7 vol%) distinguishes it from all eruptives on Tongariro, except the Mangahouhouiti Member. However, the Mangahouhouiti Member is generally olivine- and clinopyroxene-dominant, in contrast to the plagioclase-dominant Otukou lava.

G: A single $^{40}Ar/^{39}Ar$ age determination for the Otukou lava of 85 ± 6 ka (LP062) is identical to Stipp's (1969) K/Ar age determination of 85 ± 6 ka (sample 3258). These age results distinguish the Otukou lava from the older 130-96 ka Mangahouhouiti Member, with which the Otukou lava is petrographically similar.

S: The Otukou lava has no known field contact with any Tongariro eruptives observed in outcrop due to its location on Tongariro's distal northern flank.

A: The adopted age for the Otukou lava is between the minimum and maximum values at 2 s.d. for the $^{40}Ar/^{39}Ar$ age determination of 85 ± 6 ka (LP062), which gives between 91 and 79 ka.

A2.2.7. Te Whaiau Formation (between 50 and 45 ka) – TW

L: The Te Whaiau Formation is a series of debris flows that are lithologically distinct from all other map units presented in this study, which are primary volcanic products.

A: The Te Whaiau Formation has an adopted age between 50 and 45 ka. It overlies the Rotoehu Ash (Lecointre et al., 2002), which has a debated age that provides the maximum possible age of the Te Whaiau Formation (54 ka). The adopted maximum age of the Te Whaiau Formation is about 50 ka which accounts for ~2 m of sediment that accumulated between the Rotoehu Ash and the Te Whaiau Formation. The preferred age value of the Rotoehu Ash is the heating-stepped $^{40}Ar/^{39}Ar$ isochron age of Flude and Storey (2016) of 54 ± 6 ka (5 K-feldspars and 1 biotite). This value is preferred because it is in good agreement with an estimate of 54 ± 7 ka determined from marine terrace chronology, after Berryman (1992). The mean value of 54 ka is revised from Berryman's (1992) original figure of 52 ka by using more recent age estimates for the relevant correlative marine terraces on the Huon Peninsula, Papua New Guinea (Chappell, 2002). The minimum possible age of the Te Whaiau Formation is likely around 45 ka. Lecointre et al. (2002) report ~45 ka Tihoi and Tahuna (Wilson and Charlier, 2009) and 25.4 ka Oruanui fall deposits overlying the Te Whaiau Formation. Depending on the locality, the Oruanui and Te Whaiau Formation deposits are separated by erosion horizons and then either 1 m of sand or 1.5 m of paleosols and poorly-identified tephras. These erosion and sediment horizons probably represent an equivalent or longer time period (≥5 kyr) than between the Rotoehu Ash and overlying Te Whaiau Formation. Although Tihoi fall deposits are unlikely to be easily identified

in the Tongariro area, the accompanying horizon of Tahuna fall deposits is larger-volume and likely to be corrected identified, as reported by Lecointre et al. (2002). An erosional contact between the Te Whaiau Formation and overlying soils and Tihoi fall deposits support a >45 ka age for the Te Whaiau Formation. The Te Whaiau Formation also underlies the Pukeonake Formation of Tongariro that itself underlies Oruanui fall deposits with paleosols in between, which is described further in section 1.8, below. Based on these field relations, a minimum age possible age of the Te Whaiau Formation of 45 ka is adopted. This adopted age conflicts with the 60-55 ka age adopted by Lecointre et al. (2002) who suggest the range of 60-55 ka based on a single radiocarbon age where the measured ^{14}C signal is within error of background.

A2.2.8. Pukeonake Formation (between 40 and 30 ka) – PN

C: Pukeonake Formation eruptives are more magnesian (7.9-8.9 wt% MgO) than all other eruptives from Tongariro. They also have pyroxene-dominated phenocryst assemblages that include forsteritic olivines (Hobden, 1997; Beier et al., 2017) which are rarely observed in Tongariro's eruptives.

F & S: Pukeonake Formation eruptives were vented from the Pukeonake cone, and possibly two ~20 m-high mounds that are probably smaller but related cones found 800 m and 1100 m to the north of the main cone. These distinct vent locations distinguish Pukeonake Formation eruptives from all other eruptives on Tongariro.

A: The adopted age of the Pukeonake Formation is between 40 and 30 ka. Pukeonake Formation eruptives overlie the Te Whaiau Formation debris flows, which has a minimum adopted age of 40 ka (see section 1.7, above). In Pukeonake's main cone, a paleosol underlies 25.4 ka Oruanui fall deposit. This soil probably took at least several hundred years to accumulate, possibly longer, indicating a minimum age of about 30 ka for Pukeonake Formation eruptives (Topping, 1974; Townsend et al., 2017). This compares well with the age of the Ohakune Craters eruptives located to the SW of Ruapehu, which are also have a pyroxene-dominated mineralogy (over olivine and plagioclase) like Pukeonake Formation eruptives (e.g. Cole, 1978), and probably represent a period of related peripheral vent magmatism. Ohakune Craters eruptives are dated at 35.4 ± 0.6 ka (Froggatt and Lowe, 1990, via OxCal reprocessing by Townsend et al., 2017). The adopted age between 40 and 30 ka for the Pukeonake Formation is consistent with a $^{40}Ar/^{39}Ar$ age determination that was adversely affected by glassy material in the groundmass. The age analysis data are presented in Appendix 2 (LP001) and a mean age value that is consistent with field relations (after the 54 ± 6 ka Rotoehu Ash and ~45 ka Tihoi and Tahuna fall deposits: Berryman, 1992; Wilson and Charlier, 2009; Flude and Storey, 2016) suggests an age of ~37 ka (red weighted mean plateau age) for the Pukeonake Formation. Note that in the heating step results for LP001, the influence of degassing glass is likely to occur at higher temperature steps than other andesites with $^{40}Ar/^{39}Ar$ age determinations in this study, because Pukeonake Formation eruptives are basaltic-andesites with dacitic groundmass and melt inclusions (Beier et al., 2017; EPMA data from this study), which contrasts with generally rhyolitic groundmass and melt inclusions in Tongariro and Ruapehu andesites (Price et al., 2012; Beier et al., 2017; Conway et al., 2018; this study).

A2.2.9. Mokomoko Formation (between 45 and 23 ka) – MK

A2.2.9.1. Rangitaupahi Member (between 45 and 36 ka) – ari

C: K_2O and Sr concentrations distinguish the Rangitaupahi Member (1.4-1.7 wt% K_2O, <300 ppm Sr) from the 61-52 ka Te Tatau Member (1.2-1.5 wt% K_2O; ~290-360 ppm Sr). Likewise, the Rangitaupahi Member has lower Sr concentrations than the 96-79 ka Waitakatorua Member (307-396 ppm). Compared with Rangitaupahi Member eruptives (4.2-6.5 wt% MgO), 79-61 ka Rotopaunga Member eruptives have lower MgO (3.0-4.2 wt%) for equal SiO_2 concentrations.

F: Rangitaupahi Member eruptives overlie the older 102-96 ka Te Porere, 96-92 ka Otamangakau, 92-84 ka Te Rurunga, 86-79 ka Te Wakarikiariki and 79-61 ka Rotopaunga members.

L: The Rangitaupahi Member is primarily comprised of lava and agglutinate but also contains smaller proportions of bedded lapilli tuffs on upper Tongariro (units LTa, LTac, LTb, LTc, LTd, LTo in Cole et al., 2018) at earlier stratigraphic positions of this member. Lapilli tuffs, breccias or reworked material is not observed in the 96-92 ka Otamangakau, 92-84 ka Te Rurunga or 86-79 ka Te Wakarikiariki members, which is a point of difference compared with the Rangitaupahi Member.

A: The adopted ages for the Rangitaupahi Member's eruptives are between 45 and 36 ka. The maximum age boundary value of 45 ka is the minimum adopted age of the Te Whaiau Formation debris flows, which must pre-date the Mokomoko Formation based on field relations. The minimum age boundary value of 36 ka is adopted from relations between the Rangitaupahi Member and the overlying 36-24 ka Mangatapate Member that collectively form North Crater. Note that the slight U-shaped concavity in the heating steps for the underlying Mangatapate Member's sole $^{40}Ar/^{39}Ar$ age determination (30 ± 6 ka: LP151) indicates excess ^{40}Ar (see LP151 in Appendix 2). The affect of excess ^{40}Ar on the determined age is the least pronounced where radiogenic ^{39}Ar proportions are the greatest (approximately the 700 °C step). A caveat of this feature is that the plateau age value is probably slightly older than the true eruption age. However, it is not possible to accurately quantify the effect of possible excess ^{40}Ar.

A2.2.9.2. Mangatapate Member (between 30 and 24 ka) – amt

C: Compared with the underlying Rangitaupahi Member (0.65-0.72 wt% TiO_2; 4.4-5.1 wt% MgO), Mangatapate Member eruptives do not contain olivine, have less orthopyroxene than clinopyroxene and have higher TiO_2 (0.74-0.80 wt%) and lower MgO (3.8-4.2 wt%). Mangatapate Member SiO_2 concentrations also cluster at higher values (~60 wt%) than Rangitaupahi Member SiO_2 concentrations (~59 wt%). Other compositional indices show similarities between Rangitaupahi Member and Mangatapate Member eruptives, which suggests that Mangatapate Member eruptives could be derived from a Rangitaupahi Member-type magma that has undergone small amounts of fractional crystallisation of olivine and pyroxene. This is consistent with field relations showing superimposed vent locations.

F: The Mangatapate Member includes agglutinates that clearly drape underlying the Rangitaupahi Member eruptives that form the outer rim of North Crater.

G: Based on geochronological results, the Mangatapate Member is younger than all eruptives from the Taiko Formation (and older formations) on Tongariro. A single $^{40}Ar/^{39}Ar$ age determination of 30 ± 6 ka (LP151) conflicts with suggestions that North Crater is entirely post-Oruanui in age (25.4 ka: Shane et al., 2008). Outside of the analytical error, this $^{40}Ar/^{39}Ar$ age determination is younger than all $^{40}Ar/^{39}Ar$ age determinations on eruptives from the 133-52 ka Taiko Formation.

S: The Mangatapate Member's vent source is the inner North Crater explosion pit. This vent source differs from that of the Te Wai Whakaata Member, which was vented from the area of Blue Lake.

A: The adopted ages for eruptives of the Mangatapate Member are between 36 and 24 ka, which are the maximum to minimum values of LP151's $^{40}Ar/^{39}Ar$ age determination (30 ± 6 ka) at 2 s.d.

A2.2.9.3. Te Wai Whakaata Member (between 33 and 23 ka) – aww

F: Te Wai Whakaata Member eruptives overlie 96-79 ka Waitakatorua Member deposits and abut against 79-61 ka Rotopaunga Member eruptives to the north.

G: A single $^{40}Ar/^{39}Ar$ age determination of 28 ± 5 ka (LP147) for the Te Wai Whakaata Member is outside of analytical error of all $^{40}Ar/^{39}Ar$ age determinations from the Taiko Formation.

S: The Te Wai Whakaata Member's distinct vent source from a focus at present-day Blue Lake distinguishes it from the Mangatapate Member that was vented from North Crater.

A: The adopted ages of the Te Wai Whakaata Member's eruptives are between 33 and 23 ka, which are the maximum and minimum age values of the Te Wai Whakaata Member's sole $^{40}Ar/^{39}Ar$ age determination (28 ± 5 ka: LP147) at 2 s.d..

A2.2.10. Te Maari Formation (older than 26 ka to present) – TM

A2.2.10.1. Undifferentiated pre-Oruanui Te Maari Formation lava (before 26 ka) – utm

F: Geomorphology suggests that this undifferentiated Te Maari Formation lava was probably erupted from a (now buried) vent located ~500 m east of Lower Te Maari Crater (Townsend et al., 2017). At roadcut outcrops on State Highway 46, the lava underlies the 25.4 ka Oruanui deposits (Cronin, 1996; Lecointre et al., 2004). These field relations distinguish this undifferentiated lava from other Te Maari Formation eruptives.

A: This undifferentiated Te Maari Formation lava was emplaced some time before the 25.4 ka Oruanui eruption, probably by several hundred years or more. Cronin (1996: section 83) and Lecointre et al. (2004: location S12) report 0.6-0.9 m of sand and tephra deposits between this undifferentiated Te Maari Formation lava and overlying Oruanui deposits. The major and trace element concentrations in the sole sample of the undifferentiated Te Maari Formation lava (JWC-81: Cole, 1979) are similar to eruptives of the Te Pakiraki, Pungarara, Rahuituki, Otamangakau and Rotopaunga members. There is a possibility therefore that the lava is much older and was not erupted from the vent location ~500 m east of Lower Te Maari Crater.

A2.2.10.2. Paungaiti Member (between 25.4 and 17.5 ka) – api

F: Andesite lavas comprising the Paungaiti Member have indistinguishable compositions to the undifferentiated Te Maari Formation lava, within analytical error. However, Paungaiti Member lavas do not underlie Oruanui fall deposits (Topping, 1974; Townsend et al., 2017). Paungaiti Member lavas can be traced geomorphologically back to a vent focus at the Lower Te Maari Crater.

A: Paungaiti Member lavas were erupted between 25.4 ka as inferred by the lack of overlying Oruanui deposits (Topping, 1974; Townsend et al., 2017) and before 17.5 ka, because they underlie the Rerewhakaaitu Tephra (Townsend et al., 2017). This relationship was noted by Lecointre et al. (2004) at their location S11.

A2.2.10.3. Heretoa Member (between 11.0 and 3.5 ka) – aht

F: The Heretoa Member consists of andesite lavas erupted from a vent located ~500 m NNE of Lower Te Maari Crater, which distinguishes these lavas from older Paungaiti Member eruptives that were vented from Lower Te Maari Crater. Unlike the Paungaiti Member, the 17.5 ka Rerewhakaaitu Tephra is not observed overlying the Heretoa Member.

A: The adopted ages of Heretoa Member andesites are between 11.0 and 3.5 ka. Deposits of the 12-11 ka Pahoka-Mangamate tephra sequence are observed overlying Paungaiti Member eruptives (Topping, 1974; Townsend et al., 2017) but these tephras do not overlie Heretoa Member lavas. Heretoa Member lavas have ages younger than the 11.0 ka Poutu Lapilli (youngest Pahoka-Mangamate unit: Nairn et al., 1998; Hitchcock and Cole, 2007). The minimum age boundary value of 3.5 ka for the Heretoa Member is constrained by the 3.5 ka Papakai Tephra (Donoghue et al., 1995) that overlies Heretoa Member lavas (Topping, 1974; Townsend et al., 2017).

A2.2.10.4. Mangatetipua Member (from 0.5 ka to 2012 CE) – mgt

C: The Mangatetipua Member is comprised of olivine-bearing basaltic-andesite lava which is compositionally distinct from older Te Maari Formation eruptives that are all andesitic (Cole, 1978; 1979; Hobden, 1997). Note that Mangatetipua Member lava contains 4.7 vol% olivine and 6.9 wt% MgO (Cole, 1978; sample 24266). In contrast, Hobden's (1997) sample TG282, which is reported to be from the same Mangatetipua Member lava, contains only trace amounts of olivine and is andesitic in composition with 3.6 wt% MgO. Comparisons between sample TG282 and other Te Maari Formation samples suggest that Hobden (1997) may have sampled an older Te Maari Formation lithic within the blocky 1528 CE lava.

F & S: The Mangatetipua Member was erupted from Upper Te Maari Crater, which distinguishes it from older Te Maari Formation eruptives that were erupted from separate vent locations.

A: The age of eruptives from Upper Te Maari Crater define the age boundaries of the Mangatetipua Member as from 0.5 ka to 2012 CE. Dendrochronology indicates that the basaltic-andesite lava that comprises the Mangatetipua Member was erupted at 1528 CE (Topping, 1974). A phreatic eruption at Upper Te Maari Crater was witnessed in 2012 CE but did not contain any

significant volumes of magmatic material (e.g. Scott and Potter, 2014). These two eruptive events define the current age boundaries of the Mangatetipua Member.

A2.2.11. Makahikatoa Formation (approximately 17.5 ka) – MK

C: The Makahikatoa Formation is comprised of high Sr (~630 ppm) basaltic-andesite lava, spatter and scoria. These compositions are distinct because they are not observed in any other eruptives from Tongariro. Makahikatoa Member eruptives also possess orthopyroxene- and clinopyroxene-dominated phenocryst assemblages (over plagioclase), which is are rare in Tongariro's eruptives.

F & S: The Makahikatoa Formation was erupted from a distinct vent on top of the Pukekaikiore landform. Field relations also indicate that the Makahikatoa Formation is 17.5 ka in age, which is a further point of distinction with other Tongariro eruptives (see **A**).

A: Scoria in the Makahikatoa Formation sandwiches deposits of the 17.5 ka Rerewhakaaitu Tephra (Topping, 1974; Lowe et al., 2013). Conformable field relations and the absence of erosion between vent-proximal lavas and scoria suggest that all Makahikatoa Member eruptives are of similar age (Topping, 1974). These field relationships are consistent with those that show Makahikatoa Member lava flowing around pre-existing last-glacial moraines (MIS 2) at the southwestern terminus of the Mangatepopo valley (Townsend et al., 2017). Glacial retreat that occurred after these moraines were deposited was underway by ~18 ka, as indicated by cosmogenic ^{3}He dating on moraine boulders (Eaves et al., 2016a).

A2.2.12. Red Crater Formation (between 11.0 and 0.1 ka) – RC

A2.2.12.1. Te Ahititi Member (between 11.0 and 1.8 ka) – ahi

C: The Te Ahititi Member is comprised of andesite lavas which are distinct from younger basaltic-andesite Te Rongo Member eruptives.

F: The 1.8 ka Taupo ignimbrite occurs between older Te Ahititi Member lavas and overlying Te Rongo Member lavas, and are therefore separated in time (Topping, 1974). Note however that both Te Ahititi and Te Rongo members were erupted from Red Crater, as indicated by their geomorphologies that are traced back to the vent.

G: The pre-1.8 ka age of Te Ahititi Member eruptives is consistent with an imprecise ^{40}Ar/^{39}Ar age determination for a Te Ahititi Member sample (re-date on sample TG088 from the collection of Hobden, 1997) of 12.9 ± 11.4 ka.

A: The absence of the 12-11 ka Mangamate Formation (age from Hitchcock and Cole, 2007) and the presence of overlying 1.8 ka Taupo ignimbrite (field relations from Topping, 1974 and Nairn et al., 1998; age from Hogg et al., 2012) indicates ages between 11.0 and 1.8 ka for the Te Ahititi Member. This is consistent with the lack of loess and surficial striations or till overlying Te Ahititi Member lavas (Topping, 1974).

A2.2.12.2. Te Rongo Member (1.8 – 0.15 ka) – mtr

C: The Te Rongo Member is comprised of basaltic-andesite lava, spatter and scoria. It is notable for its high MgO concentrations (6.3-7.7 wt%) and the presence of olivine. These features distinguish Te Rongo Member eruptives from older Te Ahititi Member eruptives.

F: Te Rongo Member eruptives overlie both the Te Ahititi Member and the 1.8 ka Taupo ignimbrite (Topping, 1974; Hobden, 1997; Townsend et al., 2017).

A: The ages of Te Rongo Member eruptives are between 1.8 ka and about 1800 CE, or 0.15 ka (to 1950 CE datum). The absence of 1.8 ka Taupo ignimbrite on top of Te Rongo Member eruptives indicates post-1.8 ka ages. No historical accounts of volcanic activity from Red Crater by European settlers report incandescence (1855 CE: Hochstetter, 1864; 1926 CE: Thompson, 1926), so whether eruptive activity actually occurred in 1855 and 1926 is unclear. However, paleomagnetic studies have inferred that the young Central Crater-filling lava flow from Red Crater (in the Te Rongo Member) was emplaced between 1500-1800 CE (Greve et al., 2016), which defines the minimum age boundary value of 1800 CE for the Te Rongo Member.

A2.2.13. Te Pupu Formation (7 ka? – 1975 CE) – TP

A2.2.13.1. Papamānuka Member (Holocene – 1.8 ka) – mpa

F & A: The Papamānuka Member is comprised of all 16 lava flows vented from Ngauruhoe that are observed underlying the 1.8 ka Taupo ignimbrite (Hogg et al., 2012). These lavas correspond to all nine of the Group 1, five of Group 2 and two of Group 3 lavas documented by Hobden et al. (2002). Collectively, these are approximately equivalent to the Pre-Taupo lava flows (ql_a) of Townsend et al. (2017). Papamānuka Member lavas are demonstrably Holocene because they are found in all key drainage areas around Ngauruhoe that were previously glaciated in MIS 2: Mangatepopo valley, Makahikatoa Stream and Waihohonu valley (Eaves et al., 2016a). These field relations indicate a Holocene to 1.8 ka age for the Papamānuka Member. This age range is more generalised than the range adopted by Townsend et al. (2017), which are based on the interpretations of Moebis et al. (2011). A proposed age of Ngauruhoe activity, as old as 7 ka, is discussed in section 4.2 in Chapter 3.

A2.2.13.2. Toakakura Member (1.8 – 0.08 ka) – mtk

F & A: Lavas and block and ash flows erupted after 1.8 ka (observed absence of overlying Taupo ignimbrite: age from Hogg et al., 2012) and before European arrival in New Zealand comprise the Toakakura Member. In relation to the groupings of Hobden et al. (2002), this member includes nine Group 2 lava flows but also an unknown number of unmapped flows that blanket the E and SE flanks of Ngauruhoe, with lesser representation also on the S and SW slopes.

A2.2.13.3. Undifferentiated Te Pupu Formation eruptives – utp

Products erupted from Ngauruhoe that (a) were not witnessed in eruption and (b) have an observed presence or absence of overlying Taupo ignimbrite are grouped into this undifferentiated Member. The eruptives in this member compositionally overlap with other Te

Pupu Formation eruptives. Because compositional types (cf., groups 1-5: Hobden et al., 2002) reappear before and after time-markers, compositions cannot be used to infer age. Undifferentiated Te Pupu Formation eruptives crudely approximate Hobden et al.'s (2002) Group 4 but do not map onto each other one-to-one. This undifferentiated unit also includes one Group 3 flow and three flows not grouped by Hobden et al. (2002) on Ngauruhoe's NE (2) and W (1) slopes. Collectively, these eruptives total ~17 subunits.

A2.2.13.4. Matariki Member (0.08 ka – 1975 CE) – mmt

All materials erupted from Ngauruhoe since European settlement are mapped into this member, including scoria within Ngauruhoe's summit crater (F & A), and will include any materials erupted from Ngauruhoe in the future. Detailed summaries of eruption year and type are given by Hobden et al. (2002) and Townsend et al. (2017). The Matariki Member encompasses 20 separate lava flows and block and ash flows with a total volume of ~0.1 km3. Eruptive events that produced lava flows or BAFs occurred in 1870 (2 lava flows: Hector, 1870; Townsend et al., 2017), 1949 (1 BAF and 1 lava flow: Battey, 1949; Hobden et al., 2002), 1954-5 (10 lava flows and 3 associated BAFs: Gregg, 1956; Hobden et al., 2002) and 1974-5 (3 BAFs: Nairn and Self, 1978; Hobden et al., 2002).

Appendix 3

Revised and new formations and members for the Te Hoata Group (Tongariro volcano)

A3.1. INTRODUCTION

New geochronological and compositional observations (geochemical and petrographic), and the recognition that syn-glacial eruptive activity has exerted a fundamental influence on Tongariro's edifice construction, along with sampling from under-examined NE and NW sectors, have necessitated a new stratigraphic framework to be devised for Tongariro volcano. Formal definitions of formations and members referred to throughout the thesis are presented here as follows. These definitions supersede those of Townsend et al. (2017) which were the most recent definitions available at the time of this work. Naming conventions for new units follow recent mapping work on Ruapehu volcano by Conway et al. (2016) which were formally defined by Townsend et al. (2017), as outlined in Chapter 3. Names are taken from nearby landmarks, flora or fauna in the Māori language. This process strongly benefited from discussions with T. 'Bubs' Smith from Ngati Tūwharetoa (pers. comm., 2019).

Edifice-forming eruptives from Tongariro volcano and its related vents are defined as the Te Hoata Group (Townsend et al., 2017). As a result of the updates arising from this study, existing formations within the Te Hoata Group are recommended to be reused where appropriate, demoted to 'member' status, or abandoned. The Pukeonake and Makahikatoa formations are not revised here. The adopted ages of each stratigraphic formation and member are presented with supporting discussion in Appendix 2 but duplicated here for completeness, as are relevant K/Ar age determinations by Hobden et al. (1996) and $^{40}Ar/^{39}Ar$ age determinations from this study and provided by G. S. Leonard (pers. comm., 2019). Most ages are weighted mean plateau ages (WPMA) as noted. Adopted age ranges include consideration of field relationships and known (dated) ages of other bounding units. The geochemical and petrographic compositions that define each stratigraphic unit are discussed in Appendix 2 wherein their distinguishing characteristics are fully explained. All age determinations are cited with 2 standard deviation uncertainties. All grid references are provided in the New Zealand Transverse Mercator projection (Easting, Northing).

A3.2. Formal formation and member definitions

A3.2.1. Otamatereinga Formation

Previous usage or definition: None.

Name: Named after the Otamatereinga Bush region on western Tongariro (T. 'Bubs' Smith, pers. comm., 2019).

Reference area and distribution: An inlier on northwestern Tongariro and as boulders in the Te Whaiau Formation debris flows. In situ outcrop occurs between flow lobes of Pukeonake Formation and Te Porere Member lava. Sample LP097 (E1823540, N5670030) shows typical petrological and geochemical characteristics of the unit and provides age control (see below).

Content: Olivine-bearing basaltic-andesite lava.

Source vent: Unclear, possibly not Tongariro and potentially Maungaku or Maungakatote volcano, located ~10-15 km NW of Tongariro's main edifice, or could be from a buried peripheral vent.

Age: $^{40}Ar/^{39}Ar$ age determination (WMPA) on sample LP097 gives 512.0 ± 59.4 ka. The adopted age range for this formation is between 571 and 453 ka.

A3.2.2. Tupuna Formation

Previous Usage or definition: none.

Name: Named after the Ngati Tūwharetoa word for 'ancestor' – Tupuna (T. 'Bubs' Smith, pers. comm., 2019).

Reference area and distribution: Occurs as boulders up to ~3 km east of Lower Tama Lake. Sample LP113 (E1825840, N5658660) shows typical petrological and geochemical characteristics of the unit and provides age control (see below).

Content: Hornblende-bearing andesite boulders that are inferred to be derived from subsurface lava beneath Lower Tama Lake. The boulders were ejected alongside juvenile components of the ~11 ka Wharepu eruption of the Pahoka-Mangamate eruptions (cf. Nairn et al., 1998; Nakagawa et al., 1998).

Source vent: Buried or eroded vent in the approximate position of the present-day Ngauruhoe cone.

Age: $^{40}Ar/^{39}Ar$ age determination (WMPA) on sample LP113 gives 303.8 ± 11.4 ka. The adopted age range for this formation is between 349 and 293 ka.

A3.2.3. Haumata Formation

Previous usage or definition: None with this naming, however the formation is broadly synonymous with the Tama Trig Formation of Townsend et al. (2017) and includes minor spatial overlap with the Tama Formation of Townsend et al. (2017). The formation is here subdivided into seven members (see below).

Name: Named after the Māori word for *Chionochloa rubra*, which is known as red tussock or snow grass, because this species is found in the Tama Lakes area of southern Tongariro at altitudes above 1000 m a.s.l. where this formation occurs.

Reference area and distribution: Much of southern, southwestern and southeastern Tongariro in the Tama Lakes area, including the Pukekaikiore landform (between the Mangatepopo Valley and

Makahikatoa Stream) and in the Oturere, Waihohonu and Mangahouhounui valleys. Type localities are given at the member level, as below.

Content: Basaltic-andesite and andesite lavas and andesite pyroclastic deposits.

Source vent: Buried or eroded vent in the approximate position of the present-day Ngauruhoe cone.

Age: The adopted age range for this formation is between 290 and 189 ka.

A3.2.3.1. Lower Tama Member

Previous usage or definition: None.

Name: Named after Lower Tama lake which is adjacent to the type locality outcrop.

Reference area and distribution: Variably fresh to altered *in situ* lavas surrounding Lower Tama lake. Sample LP109 (E1825100, N5658120) shows typical petrological and geochemical characteristics of the unit.

Content: Andesite lavas with ~5 vol% Fe-Ti oxide pseudomorphs after amphibole.

Source vent: Buried or eroded vent in the approximate position of the present-day Ngauruhoe cone.

Age: K/Ar age determination on sample N89 gives 266 ± 24 ka (Hobden et al., 1996). The adopted age range for this member is between 290 and 242 ka.

A3.2.3.2. Tutangatahiro Member

Previous usage or definition: None.

Name: Named after the Tutangatahiro Stream, located SE of Tongariro.

Reference area and distribution: Southeastern Tongariro in the walls and headwall of the Waihohonu Valley. Sample LP074 (E182980, N5660470) shows typical petrological and geochemical characteristics of this unit and provides age control (see below).

Content: Basaltic-andesite lavas that contains ≤6 mm euhedral clinopyroxenes and ≤3 vol% Fe-Ti oxide pseudomorphs after amphibole.

Source vent: Buried or eroded vent in the approximate position of the present-day Ngauruhoe cone.

Age: $^{40}Ar/^{39}Ar$ age determination (WMPA) on sample LP074 gives 223.3 ± 5.6 ka. The adopted age range for this member is between 229 and 220 ka.

A3.2.3.3. Tawhairauriki Member

Previous usage or definition: None.

Name: Named after the Māori word for *Nothofagus solandri*, which is known as mountain beech because this species is found in the Tama Lakes-Waihohonu area of southern Tongariro at altitudes above 800 m a.s.l. where this member occurs.

Reference area and distribution: Southern and southeastern Tongariro in the Tama Lakes area and in walls of the Waihohonu Valley. Sample LP072 (E1830440, N5659910) shows typical petrological and geochemical characteristics of this unit and provides age control (see below).

Content: Andesite lavas in the Tama-Waihohonu area that contain ≤2 vol% Fe-Ti oxide pseudomorphs after amphibole and has the earliest occurrence of phenocrystic apatite in known Tongariro eruptives.

Source vent: Buried or eroded vent in the approximate position of the present-day Ngauruhoe cone.

Age: $^{40}Ar/^{39}Ar$ age determination (WMPA) on sample LP072 gives 217.7 ± 4.4 ka. The adopted age range for this member is between 220 and 214 ka.

A3.2.3.4. Upper Tama Member

Previous usage or definition: None.

Name: Named after Upper Tama lake which is adjacent to the type locality outcrop.

Reference area and distribution: Southern Tongariro around Upper Tama lake and the ridgeline ~1 km east of Upper Tama lake. Sample TG376 (E1826540, N5660150) shows typical petrological and geochemical characteristics of this unit (Hobden, 1997).

Content: Andesite lavas and pumice-bearing pyroclastic deposits which have lower MgO concentrations (<3 wt%) than other Haumata Formation eruptives. Also contains <1 vol% of phenocrystic apatite and ≤2 vol% Fe-Ti oxide pseudomorphs after amphibole.

Source vent: Buried or eroded vent in the approximate position of the present-day Ngauruhoe cone.

Age: $^{40}Ar/^{39}Ar$ age determination (WMPA) on sample GL2132 gives 209.1 ± 4.9 ka (G. S. Leonard, pers. comm., 2019). The adopted age range for this member is between 214 and 207 ka.

A3.2.3.5. Toatoa Member

Previous usage or definition: None.

Name: Named after the Māori word for *Phyllocladus toatoa*, which is known as celery pine, because this species is found in the Tama Lakes area of southern Tongariro at altitudes above 1000 m a.s.l. where this member occurs.

Reference area and distribution: Southern and western Tongariro, including the Pukekaikiore landform, and in the Tama Lakes area. Sample LP149 (E1824640, N5663440) shows typical petrological and geochemical characteristics of this unit and provides age control.

Content: Andesite lavas that contain <1 vol% of phenocrystic apatite and ≤2 vol% Fe-Ti oxide pseudomorphs after amphibole.

Source vent: Buried or eroded vent in the approximate position of the present-day Ngauruhoe cone.

Age: $^{40}Ar/^{39}Ar$ age determinations on samples LP149 (WMPA) and LP036 (recoil) both give 205.1 ± 6.0 ka. The adopted age range for this member is between 207 and 200 ka.

A3.2.3.6. Pukekaikiore Member

Previous usage or definition: None.

Name: Named after the Pukekaikiore landform (hill) on western Tongariro.

Reference area and distribution: The upper of two ~100 m thick terraces of andesite lava which comprise the Pukekaikiore landform. Sample LP039 (E1825200, N5663320) shows typical petrological and geochemical characteristics of the unit.

Content: Andesite lavas that contain <1 vol% of phenocrystic apatite and ≤2 vol% Fe-Ti oxide pseudomorphs after amphibole.

Source vent: Buried or eroded vent in the approximate position of the present-day Ngauruhoe cone.

Age: $^{40}Ar/^{39}Ar$ age determination (WMPA) on sample LP039 gives 194.7 ± 5.0 ka. The adopted age range for this member is between 200 and 190 ka.

A3.2.3.7. Waipoa Member

Previous usage or definition: None.

Name: Named after the Waipoa Stream on eastern Tongariro.

Reference area and distribution: Southeastern and eastern Tongariro in the Oturere and Mangahouhounui valleys. Sample MSR15018 (E1833200, N5662120) shows typical petrological and geochemical characteristics of the unit and provides age control. However, the available thin section for MSR15018 does not contain serpentinised olivine (see below) whereas the thin section for sample LP123 does (E1832230, N5665640).

Content: Andesite lavas that contain trace amounts of serpentinised olivine xenocrysts, <1 vol% of phenocrystic apatite and ≤2 vol% Fe-Ti oxide pseudomorphs after amphibole.

Source vent: Buried or eroded vent in the approximate position of the present-day Ngauruhoe cone.

Age: $^{40}Ar/^{39}Ar$ age determination (WMPA) on sample MSR15018 gives 191.1 ± 4.4 ka. The adopted age range for this member is between 195 and 189 ka.

A3.2.4. Mangahouhounui Formation

Previous usage or definition: Synonymous and has general overlap (by about 60 %) with the Mangahouhounui Formation of Townsend et al. (2017). Three members are defined here (see below).

Name: Named after the Mangahouhounui valley wherein all members in the Mangahouhounui Formation eruptives are exposed.

Reference area and distribution: In the Mangahouhounui valley and between the Oturere and Waihohonu valleys. Type localities are given at the member level, as below.

Content: Basaltic-andesite to dacite composition lavas, agglutinates and breccias, which are notable for their large (up to 8-9 mm) plagioclase and clinopyroxene phenocrysts.

Source vent: Buried or eroded vent in the approximate position of the present-day Central Crater and a flank vent for the Tātaramoa Member (see below).

Age: The adopted age range for this formation is between 189 and 130 ka.

A3.2.4.1. Te Pakiraki Member

Previous usage or definition: None.

Name: Named after the Te Pakiraki Stream on northeastern Tongariro.

Reference area and distribution: In the Mangahouhounui valley and between the Oturere and Waihohonu valleys. Samples LP129 (E1832720, N566500), LP234 (E1831990, N5664960) and LP241 (E1832790, N5665810) show typical petrological and geochemical characteristics of the unit. Sample LP229 (E1831660, N5664740) displays chiselled horizontal column joints that are indicative of chilling when impounded by ice, which are some of the best-known examples of these features on Tongariro.

Content: Basaltic-andesite to dacite composition lavas, agglutinates and breccias, which are notable for their large (up to 8-9 mm) plagioclase and clinopyroxene phenocrysts.

Source vent: Buried or eroded vent in the approximate position of the present-day Central Crater.

Age: $^{40}Ar/^{39}Ar$ age determinations give 185.5 ± 22.4 ka (sample LP239: isochron), 164.9 ± 5.8 ka (sample LP129: WMPA), 155.4 ± 5.2 ka (sample LP118: WMPA), 151.8 ± 4.0 ka (sample LP234: WMPA) and 136.5 ± 7.0 ka (redate on sample TG084 collected by Hobden, 1997: WMPA). The adopted age range for this member is between 189 and 130 ka.

A3.2.4.2. Waiaruhairiki Member

Previous usage or definition: None.

Name: Named after the Waiaruhairiki Stream on northeastern Tongariro.

Reference area and distribution: In the headwall and northeastern wall of the Mangahouhounui valley, and as an inlier on the northeastern flank. Samples LP238 (E1832380, N5665930) and LP245 (E1833460, N5666280) show typical petrological and geochemical characteristics of the unit.

Content: Basaltic-andesite lavas and agglutinates, which are notable for their large (up to 8-9 mm) plagioclase and clinopyroxene crystals.

Source vent: Buried or eroded vent in the approximate position of the present-day Central Crater.

Age: $^{40}Ar/^{39}Ar$ age determination (WMPA) on sample LP245 gives 147.3 ± 7.4 ka. The adopted age range for this member is between 152 and 150 ka. The adopted age does not include the mean age value of 147.3 ka for sample LP245 because of field relationships with the Te Pakiraki Member. The older age boundary of 152 ka for the Waiaruhairiki Member is chosen as a midpoint between Te Pakiraki Member and Waiaruhairiki Member $^{40}Ar/^{39}Ar$ age determinations. Te Pakiraki lava overlying Waiaruhairiki eruptives in the NE Mangahouhounui Valley has a $^{40}Ar/^{39}Ar$ age determination of 155.4 ± 5.2 ka (sample LP118). This determination has an older mean value than the single Waiaruhairiki $^{40}Ar/^{39}Ar$ age determination of 147.3 ± 7.4 ka (sample LP245) from a separate location ~800 m to the northeast, where Te Pakiraki eruptives are not exposed (see Appendix 2). These comparative age determinations have some conflict with field relations because the younger mean age occurs in the underlying unit. However, field relations and $^{40}Ar/^{39}Ar$ age determinations can be reconciled within analytical uncertainties. Adjusting each age determination by ~1.5 s.d. in opposite directions indicates alternative ages to mean $^{40}Ar/^{39}Ar$ values of ~152 ka (sample LP245, Waiaruhairiki Member) and ~151 ka (sample LP118, Te Pakiraki Member), which indicate a maximum age boundary of 152 ka for the Waiaruhairiki Member. Whilst it is possible that the compositional correlation between sample LP245 and other Waiaruhairiki Member eruptives is inaccurate, this is the simplest interpretation that considers all available compositional data, field relations and geochronological results within their analytical uncertainties. Another $^{40}Ar/^{39}Ar$ age determination from Te Pakiraki Member lava underlying Waiaruhairiki Member eruptives in the NE Mangahouhounui Valley (same cliff section as Te Pakiraki Member sample LP118) of 185.5 ± 22.4 ka (LP239) is consistent with a suggested maximum age boundary of 152 ka for the Waiaruhairiki Member. The minimum age

boundary of 150 ka is required by the adjusted mean age values as discussed above, where Te Pakiraki Member eruptives overlying Waiaruhairiki lava can be no older than 150 ka without exceeding 2 s.d. age uncertainties on LP118 (Te Pakiraki sample).

A3.2.4.3. Tātarāmoa Member

Previous usage or definition: none.

Name: named after the Māori word for *Rubus cissoides, Rubus australis, Rubus squarrosus* and *Rubus schmidelioides*, which are also known as bush lawyer. These species are found in native forest on northern Tongariro where this unit occurs.

Reference area and distribution: as *in situ* lava in the bed of Tahurangi Stream on northern Tongariro. Sample LP209 (E1833940, N5668670) shows typical petrological and geochemical characteristics of the unit.

Content: basaltic-andesite lava and agglutinate, which contain large (up to 8-9 mm) plagioclase and clinopyroxene crystals.

Source vent: a buried vent, possibly beneath surficial material on the Te Tatau summit/hill between the Te Maari and northern Mangahouhounui regions on Tongariro, which is interpreted to be distinct from the Central Crater vent area for other Mangahouhounui Formation eruptives.

Age: The adopted age range for this member is between 189 and 130 ka on the basis of petrographic associations (with large plagioclase and clinopyroxene crystals) to other Mangahouhounui Formation eruptives which have well-defined ages.

A3.2.5. Taiko Formation

Previous usage or definition: none with this naming, however the formation is broadly synonymous with the undifferentiated central Tongariro deposits of Townsend et al. (2017).

Name: named after the Ngati Tūwharetoa word for 'mutton bird' – taiko (T. 'Bubs' Smith, pers. comm., 2019), which used to nest on Tongariro. The formation is subdivided into 11 members (see below).

Reference area and distribution: much of northwestern, northeastern, southeastern and central Tongariro. Exposed in the Mangatepopo, Mangahouhounui, Oturere and Waihohonu valleys. Type localities are given at the member level, as below.

Content: basaltic-andesite to dacite composition lavas, agglutinates, lapilli tuffs and lapilli tuff breccias, hyaloclastites and pyroclastic deposits.

Source vent: buried or eroded vent in the approximate position of the present-day Central Crater.

Age: The adopted age range for this formation is between 133 and 52 ka.

A3.2.5.1. Rahuituki Member

Previous usage or definition: none.

Name: named after the Rahuituki Stream on northeastern Tongariro.

Reference area and distribution: on the northeastern and northwestern flanks of Tongariro. Samples LP051 (E1826850, N5672330) and LP214 (E1835750, N5668690) show typical petrological and geochemical characteristics of the unit.

Content: Andesite lavas that display negative Ce anomalies in some samples.

Source vent: Buried or eroded vent in the approximate position of the present-day Central Crater.

Age: $^{40}Ar/^{39}Ar$ age determination (WMPA) on sample LP214 gives 124.4 ± 4.8 ka. The adopted age range for this member is between 129 and 119 ka. ($^{40}Ar/^{39}Ar$ age determination on sample LP051 was unsuccessful because of groundmass glass.)

A3.2.5.2. Pungarara Member

Previous usage or definition: None.

Name: Named after the Pungarara Stream on northeastern Tongariro. Common misspelling of "Pangarara" occurs on topographic maps but "Pungarara" is the correct spelling (T. 'Bubs' Smith, pers. comm., 2019).

Reference area and distribution: In the upper-valley area of southeastern Oturere valley. Sample TG077 (Hobden, 1997) (E1829940, N5663100) shows typical petrological and geochemical characteristics of the unit.

Content: Andesite lavas with <1 vol% of Fe-Ti oxide pseudomorphs after amphibole.

Source vent: Buried or eroded vent in the approximate position of the present-day Central Crater.

Age: The adopted age range for this member is between 130 and 102 ka.

A3.2.5.3. Mangahouhouiti Member

Previous usage or definition: None.

Name: Named after the Mangahouhouiti Stream on eastern Tongariro.

Reference area and distribution: On the planèze between the Mangahouhounui and Oturere valleys. Sample MSR15019 (E1834900, N5662560) shows typical petrological and geochemical characteristics of the unit.

Content: Basaltic-andesite and andesite lavas and agglutinates with greater modal abundances of olivine and clinopyroxene than plagioclase.

Source vent: Buried or eroded vent in the approximate position of the present-day Central Crater, or an indistinguishable flank vent in this area.

Age: $^{40}Ar/^{39}Ar$ age determination (WMPA) on sample MSR15019 gives 116.8 ± 23.4 ka. The adopted age range for this member is between 130 and 96 ka.

A3.2.5.4. Mangatepopo Member

Previous usage or definition: None.

Name: Named after the Mangatepopo valley on western Tongariro.

Reference area and distribution: Central edifice areas and on the western flank of Tongariro. Sample LP250 (E1824860, N5664130) shows typical petrological and geochemical characteristics of the unit.

Content: Andesite lavas with trace amounts of olivine.

Source vent: Buried or eroded vent in the approximate position of the present-day Central Crater.

Age: $^{40}Ar/^{39}Ar$ age determinations (WMPA) give 121.1 ± 12.2 ka (sample LP250: WMPA) and 108.5 ± 8.4 ka (sample LP010: WMPA). The adopted age range for this member is between 133 and 102 ka.

A3.2.5.5. Te Porere Member

Previous usage or definition: None.

Name: Named after the Te Porere Redoubt located northwest of Tongariro.

Reference area and distribution: Central edifice areas and on the western, northwestern, southeastern flanks of Tongariro and in the Mangatepopo, Oturere and Mangahouhounui valleys. Sample LP103 (E1823960, N5668560) shows typical petrological and geochemical characteristics of the unit.

Content: Widespread andesite and dacite lavas, agglutinates, lapilli tuffs, lapilli tuff breccias and hyaloclastites with trace amounts of apatite in some samples.

Source vent: Buried or eroded vent in the approximate position of the present-day Central Crater.

Age: $^{40}Ar/^{39}Ar$ age determination (WMPA) on sample LP103 gives 98.9 ± 2.6 ka. The adopted age range for this member is between 102 and 96 ka.

A3.2.5.6. Otamangakau Member

Previous usage or definition: None.

Name: Named after the Otamangakau Stream (and lake) located northwest of Tongariro.

Reference area and distribution: on the western and northern flanks of Tongariro and in the Mangahouhounui valley. Sample LP071 (E1827580, N5670010) shows typical petrological and geochemical characteristics of the unit.

Content: Andesite lavas and agglutinates with trace amounts of apatite and olivine.

Source vent: Buried or eroded vent in the approximate position of the present-day Central Crater.

Age: The adopted age range for this member is between 96 and 92 ka.

A3.2.5.7. Waitakatorua Member

Previous usage or definition: None.

Name: Named after the Waitakatorua Stream on eastern Tongariro.

Reference area and distribution: in the upper valley-areas of the Oturere and Mangahouhounui valleys. Sample LP141 (E1831340, N5665590) shows typical petrological and geochemical characteristics of the unit.

Content: Andesite lavas and lapilli tuff breccias with trace amounts of olivine.

Source vent: Buried or eroded vent in the approximate position of the present-day Central Crater.

Age: The adopted age range for this member is between 96 and 79 ka.

A3.2.5.8. Te Rurunga Member

Previous usage or definition: None.

Name: Named after the Te Rurunga area on western Tongariro (T. 'Bubs' Smith, pers. comm., 2019).

Reference area and distribution: On the upper western flank of Tongariro. Sample LP023 (not *in situ*: E1825800, N5666530) shows typical petrological and geochemical characteristics of the unit.

Content: Andesite lavas and agglutinates that contain olivine.

Source vent: Buried or eroded vent in the approximate position of the present-day Central Crater.

Age: $^{40}Ar/^{39}Ar$ age determination (WMPA) on sample LP023 gives 87.5 ± 4.2 ka. The adopted age range for this member is between 92 and 84 ka.

A3.2.5.9. Te Wakarikiariki Member

Previous usage or definition: None.

Name: Named after the Te Wakarikiariki Stream on northeastern Tongariro.

Reference area and distribution: Central edifice areas and in the Mangahouhounui valley. Sample RPC110/RPC090 (E1828200, N5665320) (R. P. Cole, pers. comm., 2017) shows typical petrological and geochemical characteristics of the unit.

Content: Andesite lavas that contain plagioclase crystals with widths up to 7 mm in some samples.

Source vent: Buried or eroded vent in the approximate position of the present-day Central Crater.

Age: $^{40}Ar/^{39}Ar$ age determination (WMPA) on sample RPC110 gives 80.6 ± 4.8 ka. The adopted age range for this member is between 86 and 79 ka.

A3.2.5.10. Rotopaunga Member

Previous usage or definition: Follows the Rotopaunga Formation of Townsend et al. (2017) but is demoted to 'member' status and incorporated into the Taiko Formation, defined here.

Name: Named after the Rotopaunga summit on upper northeastern Tongariro.

Reference area and distribution: On the western, northeastern and southeastern flanks of Tongariro and in the Mangahouhounui valley. Sample LP211 (E1833740, N5668580) shows typical petrological and geochemical characteristics of the unit.

Content: Andesite lavas, agglutinates, lapilli tuffs, lapilli tuff breccias and hyaloclastites that contain trace amounts of apatite.

Source vent: Buried or eroded vent in the approximate position of the present-day Central Crater.

Age: $^{40}Ar/^{39}Ar$ age determinations give 76.1 ± 3.5 ka (sample GL2007: WMPA) and 68.3 ± 15.4 ka (sample LP211: isochron). The adopted age range for this member is between 79 and 61 ka.

A3.2.5.11. Te Tatau Member

Previous usage or definition: Follows the Te Tatau Formation of Townsend et al. (2017) but is demoted to 'member' status and incorporated into the Taiko Formation, defined here.

Name: Named after the Te Tatau summit on upper northeastern Tongariro.

Reference area and distribution: On the northeastern area of Tongariro near the Te Tatau summit and north of the Mangahouhounui valley. Sample GL2223 (E1832030, N5667700) shows typical petrological and geochemical characteristics of the unit.

Content: Basaltic-andesite and andesite lavas, agglutinates and scoria that contain trace olivine.

Source vent: Buried or eroded vent in the approximate position of the present-day Central Crater.

Age: $^{40}Ar/^{39}Ar$ age determination (WMPA) on sample GL2223 gives 56.2 ± 4.6 ka. The adopted age range for this member is between 61 and 52 ka.

A3.2.6. Mokomoko Formation

Previous usage or definition: None with this naming. This formation combines the North Crater and Blue Lake formations of Townsend et al. (2017), redefined here as three new members (see below).

Name: Named after the Māori word for 'lizard' – mokomoko.

Reference area and distribution: Northwestern and upper central Tongariro, including minor representation in the head of the Mangahouhounui valley. Type localities are given at the member level, as below.

Content: Andesite lavas, agglutinates, bedded lapilli tuffs and spatter.

Source vent: Both North Crater and Blue Lake.

Age: The adopted age range for this formation is between 45 and 23 ka.

A3.2.6.1. Rangitaupahi Member

Previous usage or definition: None with this name. This member has general equivalence to many of the older subunits in the North Crater Formation of Townsend et al. (2017). However, some of the deposits previously mapped as North Crater Formation are here included within the Taiko Formation, defined above.

Name: Named after the Rangitaupahi area on western Tongariro (T. 'Bubs' Smith, pers. comm., 2019).

Reference area and distribution: On northwestern and upper Tongariro. Samples LP011 (E1827320, N5666960) and LP063 (E1828350, N5667550) show typical petrological and geochemical characteristics of the unit.

Content: Andesite lavas and agglutinates that contain trace olivine and apatite.

Source vent: The North Crater vent associated with the formation of the main outer crater.

Age: The adopted age range for this member is between 45 and 36 ka.

A3.2.6.2. Mangatapate Member

Previous usage or definition: None with this name. This member has general equivalence to the undifferentiated pyroclastic deposits mapped on the upper North Crater summit area by Townsend et al. (2017).

Name: Named after the Mangatapate area on western Tongariro (T. 'Bubs' Smith, pers. comm., 2019).

Reference area and distribution: On northwestern and upper Tongariro. Sample LP151 (E1828330, N5666750) shows typical petrological and geochemical characteristics of the unit.

Content: Andesite lavas, agglutinates and spatter.

Source vent: On upper North Crater, creating a ~400 m diameter explosion pit within the western floor of the main North Crater summit area.

Age: $^{40}Ar/^{39}Ar$ age determination (WMPA) on sample LP151 gives 30.1 ± 6.0 ka. The adopted age range for this member is between 36 and 24 ka.

A3.2.6.3. Te Wai Whakaata Member

Previous usage or definition: None with this name. This member is synonymous with the Blue Lake Formation of Townsend et al. (2017).

Name: Named after a Ngati Tūwharetoa word for the Blue Lake area of Tongariro – Te Wai Whakaata (T. 'Bubs' Smith, pers. comm., 2019).

Reference area and distribution: On northwestern and upper Tongariro. Sample LP147 (E1830850, N5666330) shows typical petrological and geochemical characteristics of the unit.

Content: Andesite lavas, agglutinates, spatter and scoria that contain trace amounts of apatite.

Source vent: The crater now occupied by Blue Lake.

Age: $^{40}Ar/^{39}Ar$ age determination (WMPA) on sample LP147 gives 28.3 ± 5.2 ka. The adopted age range for this member is between 33 and 23 ka.

A3.2.7. Te Maari Formation

Previous usage or definition: Synonymous with the Te Maari Formation of Townsend et al. (2017). Lavas within the Te Maari Formation that are pre-Oruanui (25.4 ka: age from Vandergoes et al., 2013) in age, but may be considerably older, are not formally defined here with member status. The only (probably) *in situ* sample from this unit is JWC-91/24265 (Cole, 1979). Other parts of the formation are subdivided here into three members (see below), broadly following the mapping of Townsend et al. (2017).

Name: Named after the Te Maari region on northern Tongariro.

Reference area and distribution: Northern Tongariro. Type localities are given at the member level, as below.

Content: Basaltic-andesite and andesite lavas, agglutinates, spatter and pyroclastic deposits.

Source vent: Upper Te Maari Crater, Lower Te Maari Crater and a vent to the north.

Age: The adopted age for this formation is from before 25.4 ka until the present-day (e.g. 2012 eruption).

A3.2.7.1. Paungaiti Member

Previous usage or definition: None with this name. This member is broadly equivalent to some of the middle-aged andesitic lavas in the Te Maari Formation as defined by Townsend et al. (2017).

Name: Named with the Ngati Tūwharetoa term for an emergent stream or river (= iti) from the ground in this area of northern Tongariro – Paungaiti (cf. "Rotopaunga" which is the compound

name for lake [= roto] at a summit point on northern Tongariro [= Paunga]) (T. 'Bubs' Smith, pers. comm., 2019).

Reference area and distribution: Lavas and agglutinates erupted from Lower Te Maari Crater on northern Tongariro. Sample TG349 (E1831640, N5668350), which was collected and analysed by Hobden (1997), shows typical petrological and geochemical characteristics of the unit.

Content: Andesite lavas and agglutinates.

Source vent: Lower Te Maari Crater.

Age: The adopted age range for this member is between 25.4 and 17.5 ka.

A3.2.7.2. Heretoa Member

Previous usage or definition: None with this name. This member is broadly equivalent to some of the middle-aged andesitic lavas in the Te Maari Formation as defined by Townsend et al. (2017).

Name: Named with the Ngati Tūwharetoa word for an area near the southwestern shores of Lake Rotoaira – Heretoa (T. 'Bubs' Smith, pers. comm., 2019).

Reference area and distribution: Lavas and agglutinates erupted from a vent system located ~500 m north of Lower Te Maari Crater on northern Tongariro, which is presently represented by a ~30 m-tall mound with three vents or pits spaced in a triangular geometry that are each ~100 m apart. Sample TG027 (E1832332, N5671850), which was collected and analysed by Hobden (1997), shows typical petrological and geochemical characteristics of the unit.

Content: Andesite lavas and agglutinates.

Source vent: A vent located ~500 m north of Lower Te Maari Crater.

Age: The adopted age range for this member is between 11.0 and 3.5 ka.

A3.2.7.3. Mangatetipua Member

Previous usage or definition: None with this name. This member is equivalent to youngest lava in the Te Maari Formation (Townsend et al. 2017).

Name: Named after the "Mangatipua Stream" on northern Tongariro. The correct spelling however, from which this member takes its name, is "Mangatetipua", despite the incorrect annotations on most local topographic maps. No streams near Tongariro are named "Mangatipua" (T. 'Bubs' Smith, pers. comm., 2019). Note that the Mangatipua Formation, as defined by Townsend et al. (2017), is a lahar deposit and is quite separate from the Mangatetipua Member, defined here.

Reference area and distribution: A lava flow with conspicuous levees emanating from Upper Te Maari Crater on northern Tongariro. Sample JWC-52 (E1830260, N5671100) shows typical petrological and geochemical characteristics of the unit.

Content: Basaltic-andesite lava.

Source vent: Upper Te Maari Crater.

Age: The adopted age for this member is from 1528 CE to present, including the 2012 CE eruption (Topping, 1974).

A3.2.8. Red Crater Formation

Previous usage or definition: Synonymous with the Red Crater Formation of Townsend et al. (2017). Subdivided here into two members (see below).

Name: Named after Red Crater on central/eastern Tongariro.

Reference area and distribution: Central and eastern Tongariro and on the Oturere valley floor. Type localities are given at the member level, as below.

Content: Basaltic-andesite and andesite lavas, agglutinates, spatter and pyroclastic deposits.

Source vent: Red Crater.

Age: The adopted age of this formation is between 11.0 to 0.1 ka.

A3.2.8.1. Te Ahititi Member

Previous usage or definition: None with this name. This member is equivalent to older andesitic lavas in the Red Crater Formation (Townsend et al., 2017).

Name: Named after a word associated with eastern Tongariro by the Ngati Tūwharetoa – Te Ahititi (T. 'Bubs' Smith, pers. comm., 2019).

Reference area and distribution: A long flow, or flows, forming the floor of the middle Oturere valley. Sample TG088 (E1832190, N5661250), which was collected and geochemically analysed by Hobden (1997), shows typical petrological and geochemical characteristics of the unit.

Content: Andesite lavas and agglutinates.

Source vent: Red Crater.

Age: $^{40}Ar/^{39}Ar$ age determination (WMPA) on sample TG088 (collected by Hobden, 1997) gave 12.9 ± 11.8 ka. The adopted age range for this member is between 11.0 and 1.8 ka.

A3.2.8.2. Te Rongo Member

Previous usage or definition: None with this name. This member is equivalent to the youngest basaltic-andesite eruptives in the Red Crater Formation (Townsend et al., 2017).

Name: Named after a shortened version of a name associated with eastern Tongariro by the Ngati Tūwharetoa – Te Rongo (T. 'Bubs' Smith, pers. comm., 2019).

Reference area and distribution: Distributed proximally around the Red Crater vent, with flows that flow west, north into Central Crater and east into the Oturere Valley. Sample TG126 (E1829490, N5665450), which was collected and analysed by Hobden (1997), shows typical petrological and geochemical characteristics of the unit.

Content: Basaltic-andesite lava, spatter, agglutinate and scoria that contain olivine.

Source vent: Red Crater.

Age: The adopted age range for this member is between 1.8 and 0.1 ka.

A3.2.9. Te Pupu Formation

Previous usage or definition: Te Pupu Formation was formally defined by Townsend et al. (2017). Three new members are defined within the formation (see below).

Name: Derived from Māori folklore. Te Pupu is the name of a spirit entity that brought fire to Ngātoroirangi during a blizzard on Tongariro (Townsend et al., 2017 and references therein).

Reference area and distribution: Around the Ngauruhoe vent of Tongariro, which includes lavas in the floors of the Mangatepopo valley, Waihohonu valley and Makahikatoa Stream, and the cone itself. Type localities are given at the member level, as below.

Content: Basaltic-andesite lavas, spatter, pyroclastic deposits and scoria that sometimes contain olivine.

Source vent: Ngauruhoe.

Age: The adopted age of this formation is between 7(?) ka to 1975 CE. Uncertainty in the older age boundary of Papamānuka Member eruptives precludes precise statements about the maximum age of the Ngauruhoe cone and Te Pupu Formation, which is explained in section A3.2.9.1, below.

A3.2.9.1. Papamānuka Member

Previous usage or definition: None with this name. As mapped here, the Papamānuka Member closely corresponds to the "Pre-Taupo lava flows" of Townsend et al. (2017).

Name: Named after a stream on western Tongariro - Papamānuka (T. 'Bubs' Smith, pers. comm., 2019).

Reference area and distribution: Around the Ngauruhoe vent of Tongariro, which includes lavas in the floors of the Mangatepopo valley, Waihohonu valley and Makahikatoa Stream. Samples TG156 (E1825540, N5662400), TG205 (E1829600, N5659540) and TG266 (E1824790, N5663600), which were collected and analysed by Hobden et al. (1999; 2002), show typical petrological and geochemical characteristics of the unit.

Content: Basaltic-andesite lavas.

Source vent: Ngauruhoe.

Age: The adopted age range for this member is between 7(?) and 1.8 ka. Uncertainty in the older age boundary of Papamānuka Member eruptives precludes precise statements about the maximum age of the Ngauruhoe cone and Te Pupu Formation. It has been suggested that Ngauruhoe's construction was underway by ~7 ka (Moebis et al., 2011). This age is consistent with field evidence for construction in an ice-free environment (Ngauruhoe is a perfect cone) and lava flows that fill drainage systems that were glaciated before the Holocene: Mangatepopo valley, Makahikatoa Stream and Waihohonu valley (Eaves et al., 2016a; Townsend et al., 2017). The older age boundary of ~7 ka was established by associating Ngauruhoe with tephra in Papakai Formation that underlies the ~6.9 ka Motutere rhyolitic tephra (Moebis et al., 2011). This association was established from similarities in glass compositions between Ngauruhoe's 1954 CE and 1975 CE eruptions and >6.9 ka tephra from the Papakai Formation, which contrast with tephra glass compositions in the Tufa Trig Formation of Ruapehu (between 1.8 ka and 1314 CE: Donoghue et al., 1995a; Donoghue and Neall, 1996; ages from Hogg et al., 2012 and Lowe et al., 2013) and Te Rongo Member scoria from Red Crater (between 1.8 ka and 1800 CE: Topping, 1973; Greve et al., 2016). However, in opposition to arguments put forward by Moebis et al. (2011), the available data indicates that Red Crater is a more likely source vent for >6.9 ka tephra in the Papakai Formation. Whole-rock compositions from Red Crater's Te Ahititi Member (between 11-1.8 ka) are more evolved than the Ngauruhoe-sourced Papamānuka Member (older than 1.8 ka), which is the reverse relation to Red Crater versus Ngauruhoe tephra glass compositions reported by Moebis et al. (2011). In contrast, Moebis et al. (2011) excluded Red Crater as a possible source vent for >6.9 ka tephra in the Papakai Formation because its

<1.8 ka compositions are more mafic than Ngauruhoe-sourced eruptives, although this argument is not applicable for materials older than 1.8 ka. Available isopach data for the Papakai Formation cannot distinguish between Ngauruhoe and Red Crater as source vents (Donoghue et al., 1995a), and also indicate a contribution of Ruapehu-sourced material to the Papakai Formation (Topping, 1973). Further detailed tephra provenance studies are required in order to constrain the timing of the onset of Ngauruhoe cone-building.

A3.2.9.2. Toakakura Member

Previous usage or definition: None with this name. As mapped here, the Toakakura Member closely corresponds to the "Post-Taupo lava and pyroclastic density current deposits" unit of Townsend et al. (2017).

Name: Named after the Toakakura Stream on western Tongariro.

Reference area and distribution: Around the Ngauruhoe vent of Tongariro, which includes lavas in the floors of the Mangatepopo valley, Waihohonu valley and Makahikatoa Stream. Sample TG020 (E1825940, N5663450), which was collected and analysed by Hobden et al. (1999; 2002), shows typical petrological and geochemical characteristics of the unit.

Content: Basaltic-andesite lavas and pyroclastic deposits that contain olivine in some samples.

Source vent: Ngauruhoe.

Age: The adopted age range for this member is between 232 and 1870 CE.

A3.2.9.3. Matariki Member

Previous usage or definition: None with this name. As mapped here, the Matariki Member closely corresponds to the "Historical lava, pyroclastic density current deposits, and scoria" unit of Townsend et al. (2017).

Name: Named after the Matariki Stream on western Tongariro, which is also the Māori name for 'new year'.

Reference area and distribution: Mainly on the northern to western quadrant of Ngauruhoe cone, Tongariro, which includes lavas and pyroclastics in the floor of the Mangatepopo valley. Samples TG001 (E1827090, N5664050) and TG010 (E1826740, N5663850), which were collected and analysed by Hobden et al. (1999; 2002), show typical petrological and geochemical characteristics of the unit.

Content: Basaltic-andesite lavas and pyroclastic deposits that contain olivine in some samples.

Source vent: Ngauruhoe.

Age: The adopted age range for this member is between 1870 and 1975 CE and would include any erupted material in the future.

Appendix 4

Sample list and analytical batch numbers

A4.1. INTRODUCTION

A summary of sample coordinates in New Zealand Transverse Mercator 2000 (NZTM2000) coordinates is presented here. The analytical batches corresponding to each sample for X-ray fluorescence (XRF), solution inductively couple plasma mass spectrometry (ICP-MS) and thermal ionisation mass spectrometry (TIMS) are provided here. Analytical batches for ICP-MS trace element data are prefixed 'T' whereas analytical batches for TIMS Sr-Nd-Pb data are prefixed 'I'.

The sample digestion batches corresponding to analytical ICP-MS batches are also indicated, because samples from three digestions (2, 3, 4) were analysed repeatedly until satisfactory results were obtained. Initial difficulties with obtaining reproducible data were overcome by experimenting with sample dilution factors. Two analytical sessions for ICP-MS data were performed at dilution factors of 10^{-3} (T4A) and 10^{-6} (T4B). Data from these sessions were combined for different elements to produce a complete trace element dataset. The sample concentrations of Cs, REEs, Hf, Th and Tl were obtained from T4A whereas all other elements were obtained from T4B. Additional details regarding data reduction and analytical protocols are provided in Chapter 2 (section 2.8).

Table A4. List of samples, coordinates, assigned stratigraphic units, year of $^{40}Ar/^{39}Ar$ age determinations and batch numbers for XRF, ICP-MS and TIMS analyses.

				XRF	$^{40}Ar/^{39}Ar$	ICP-MS batch		TIMS batch		
Sample	**E**	**N**	**unit**	**batch**	**year**	**digest**	**analysis**	**Sr**	**Nd**	**Pb**
CC351	1839661	5675104	PH	5	2017	4	T4A + T4B	I6	I6	I5
GL1951	1823360	5671213	dtp	10						
GL1957	1823579	5670392	OT?	10						
GL2007	1826896	5663982	arp		2014					
GL2132	1827579	5660057	aut		2014					
GL2139	1824716	5664547	arp	10						
GL2142	1824245	5665630	arp	10						
GL2145	1823965	5666864	dtp	10						
GL2148	1823917	5667288	dtp	10						
GL2218	1831305	5665594	awu	2						
GL2222	1832085	5667346	att	X						
GL2223	1832034	5667697	att	1	2016	3	T4A + T4B	I1	I1	I5
GL2224	1832711	5666015	dpk2	X						
GL2225	1833388	5664973	mhi	X						
GL2226	1831655	5666225	aww	X						
GL2229	1834803	5665968	arp	X						
GL2230	1836663	5666922	arh	X						
GL2231	1833999	5666462	arp	1						
GL2232	1836558	5664529	mhi	X						
GL2233	1835700	5664323	mhi	X						
GL2234	1834789	5664211	mhi	2						
LP001	1819612	5668420	PN	1	2017	1	T1	I3	I3	I5
LP002	1828323	5672925	arh	1		1	T1			
LP003	1832587	5672119	api	5						
LP004	1844045	5665122	RUG	1		1	T1			
LP005	1844075	5664946	RUG	1		1	T1			
LP006	1844127	5664908	?							
LP007	1842057	5660527	RUG	1	2017	1	T1			
LP008	1826825	5664687	dtp	1		1	T1			

E = easting and N = northings, which are in NZTM2000.

Units abbreviations in alphabetical order are: Te Ahititi Member (**ahi**), Heretoa Member (**aht**), Lower Tama Member (**alt**), Mangatepopo Member (**amp**), Mangatapate Member (**amt**), Otamangakau Member (**aok**), Pungarara Member (**apg**), Paungaiti Member (**api**), Pukekaikiore Member (**apk**), Rahuituki Member (**arh**), Rangitaupahi Member (**ari**), Rotopaunga Member (**arp**), Te Wakarikiariki Member (**ati**), Toatoa Member (**ato**), Te Rurunga Member (**atr**), Te Tatau Member (**att**), Tawhairauiki Member (**atw**), Upper Tama Member (**aut**), Waiaruhairiki Member (**awh**), Waipoa Member (**awp**), Waitakatorua Member (**awu**), Te Wai Whakaata Member (**aww**), the Te Pakiraki Member (**dpk**) is subdivided into pre-Waiaruhairiki Member age (**dpk1**) and post-Waiaruhairiki age (**dpk2**), Te Porere Member (**dtp**), Mangatetipua Member (**mgt**), Mangahouhouiti Member (**mhi**), Makahikatoa Formation (**MK**), Matariki Member (**mmt**), Papamānuka Member (**mpa**), Toakakura Member (**mtk**), Tātaramoa Member (**mtm**), Te Rongo Member (**mtr**), Tutangatahiro Member (**mtu**), Otamatereinga Formation (**OT**), Pihanga Formation (**PH**), Pukeonake Formation (**PN**), Ruapehu Group (**RUG**), Tupuna Formation (**TU**), Te Whaiau Formation [debris flows] (**TW**).

XRF batch refers to the sessions wherein sample-$BLiO_2$ flux mixtures were weighed and LOIs were determined. XRF analyses for several of these batches were performed together. These groupings were: 1, 2, 3, 4-5, 6, 7-11, 12, 13. X indicates that XRF data exists but was provided by other collaborators, which follow the sample prefixes: GL (G. S. Leonard, pers. comm., 2016), MSR (M. S. Rattenbury, pers. comm., 2016), RPC (R. P. Cole, pers. comm., 2016).

Table A4. Continued.

Sample	E	N	unit	XRF batch	$^{40}Ar/^{39}Ar$ year	ICP-MS batch		TIMS batch		
						digest	analysis	Sr	Nd	Pb
LP009A	1825244	5664270	dtp	1						
LP009B	1825244	5664270	dtp	1		1	T1	I6	I6	I5
LP010	1827029	5665491	amp	1	2018	1	T1	I3	I3	I5
LP011	1827320	5666955	atr	1		1	T1			
LP012	1827139	5667391	ari							
LP013	1826887	5667660	ari	6						
LP014	1826746	5667191	dtp	1		1	T1			
LP018	1826053	5666778	aok	1		1	T1			
LP019	1826210	5667166	dtp	1		1	T1			
LP020	1826297	5667739	dtp	1						
LP021	1826257	5667853	dtp	1						
LP022	1826145	5667188	dtp							
LP023	1825799	5666527	atr clast	1	2016	3	T4A + T4B	I1	I1	I5
LP024	1825282	5667158	dtp	1		6	T6		I6	I5
LP025	1825321	5666833	dtp	1						
LP026	1826658	5666432	atr	1						
LP027	1827089	5666438	atr	1						
LP028	1828550	5667795	ari	1						
LP029	1828461	5668417	ari	1						
LP030	1828239	5668711	aok	1						
LP031	1827968	5668236	ari	1						
LP032	1827394	5669025	aok	1						
LP033	1825842	5659715	atw	1	2016	4	T4A + T4B	I3	I3	I5
LP034	1826718	5661370	ato	1		4	T4A + T4B			
LP035	1826206	5661182	ato	1						
LP036	1825189	5661297	ato	1	2016	4	T4A + T4B	I1	I1	
LP037	1825199	5660461	atw	1						
LP038	1825556	5663261	apk	6						
LP039	1825202	5663324	apk	2	2017	3	T4A + T4B	I1	I1	I4
LP040	1825753	5662740	apk	6						
LP041	1839192	5656753	RUG	5						
LP042	1840016	5656323	RUG	5						
LP043	1825208	5673472	aok	6						
LP044	1825755	5672986	aok	2						
LP045	1827363	5667271	ari							
LP046A	1827690	5667295	ari	5						
LP046B	1827690	5667295	ari	5						
LP047	1827461	5667585	ari	6						
LP048	1826524	5668288	ari	4						
LP049	1826955	5668380	ari							
LP050	1821341	5667793	PN							
LP051	1826845	5672334	arh	2	2017	6	T6	I1	I1	I5
LP052	1826917	5672234	aok	12		10	T10			
LP053	1827955	5670913	dtp	4						
LP054	1828784	5659262	atw	6						
LP056	1824820	5673667	dtp	2						
LP057	1824700	5673397	dtp	6		6	T6			
LP058	1824750	5673056	dtp	4						
LP060	1825448	5671592	aok	2						
LP062	1829106	5675989	uol	2	2017	3	T4A + T4B	I3	I3	I5
LP063	1828350	5667547	ari	4		3	T4A + T4B			
LP064	1827713	5667937	ari	6						
LP065	1827713	5667937	ari							
LP066	1826738	5669208	aok	6						

Table A4. Continued.

Sample	E	N	unit	XRF batch	$^{40}Ar/^{39}Ar$ year	ICP-MS batch		TIMS batch		
						digest	analysis	Sr	Nd	Pb
LP067	1826409	5669514	aok	2						
LP070	1827048	5669741	aok	6						
LP071	1827579	5670009	aok	2		4	T4A + T4B			
LP072	1830438	5659913	atw	2	2017	3	T4A + T4B	I3	I3	I5
LP073	1829982	5660440	mtu	4						
LP074	1829821	5660463	mtu	2	2017	2	T4A + T4B	I3	I3	I5
LP075	1829843	5660485	?							
LP077	1825045	5671182	ari	5						
LP079	1825181	5670952	ari	6						
LP080	1825188	5670572	ari	6						
LP081	1824975	5670144	ari	2						
LP087	1823763	5670051	OT	6		6	T6			
LP088	1823855	5670040	dtp	6						
LP090	1824217	5669754	dtp	2						
LP091	1824415	5669598	dtp							
LP092	1824926	5668933	dtp							
LP093	1825214	5668645	dtp							
LP095	1825347	5668614	dtp	2						
LP096	1823571	5670384	PN	2						
LP097	1823538	5670030	OT	2	2019	4	T4A + T4B	I3	I3	I5
LP098	1823408	5669640	dtp	4						
LP099	1823449	5669377	dtp	4						
LP102	1823805	5668732	dtp							
LP103	1823956	5668561	dtp	2	2017	3	T4A + T4B	I1	I1	I1
LP107	1842019	5660531	RUG							
LP108H	1823466	5673714	TW clast	4		4	T4A + T4B			
LP108L	1823466	5673714	TW clast	4						
LP109	1825103	5658116	alt	5		4	T4A + T4B			
LP110	1825406	5657913	RUG	13						
LP113	1825837	5658660	TU	6	2018	4	T4A + T4B	I6	I2	I5
LP117	1832659	5665620	awp	4						
LP118	1832763	5665964	dpk2	2	2017	3	T4A + T4B	I3	I3	I5
LP119	1832790	5666029	att	4						
LP120	1832584	5666099	att	4						
LP122	1832345	5666116	dtp	5						
LP123	1832231	5665634	awp	4						
LP124	1832201	5665495	awp	4		4	T4A + T4B			
LP125	1832608	5663753	mhi	5		4	T4A + T4B			
LP126	1832926	5664819	mhi	2	2017	3	T4A + T4B			
LP128	1832661	5665088	awp	4		4	T4A + T4B			
LP129	1832720	5664995	dpk1	2	2017	2	T4A + T4B	I1	I1	I5
LP130	1832164	5662817	awp	5		3	T4A + T4B			
LP131	1832619	5662840	awp							
LP132	1833092	5662205	awp							
LP134	1830251	5665390	aww	5		3	T4A + T4B			
LP135	1830711	5665377	aww	6						
LP137	1831046	5665366	awu							
LP138	1831043	5665389	awu	5						
LP140	1831269	5665549	awu	6						
LP141	1831337	5665593	awu	4		4	T4A + T4B			
LP143	1831466	5665760	dtp	4		4	T4A + T4B			
LP145	1831289	5665941	awu	5		4	T4A + T4B			
LP147	1830848	5666330	aww	2	2017	3	T4A + T4B	I1	I1	I4
LP148	1830348	5666524	arp?							

Table A4. Continued.

Sample	E	N	unit	XRF batch	$^{40}Ar/^{39}Ar$ year	ICP-MS batch		TIMS batch		
						digest	analysis	Sr	Nd	Pb
LP149	1824643	5663438	ato	5	2017	4	T4A + T4B	I6	I6	I5
LP150	1828495	5666269	ari	7						
LP151	1828332	5666754	amt	7	2018	6	T6	I3	I3	I4
LP152	1828531	5667048	amt	7		6	T6			
LP155	1827714	5664501	arp	7						
LP156	1827207	5664735	dtp	7						
LP157	1831971	5666387	att	8						
LP158	1831979	5666280	arh	8						
LP159	1832027	5666254	dtp	11						
LP160	1832217	5666308	att	8						
LP161	1832188	5666246	ati	9						
LP163	1832454	5666088	arp	9						
LP164	1832456	5666079	arp	9						
LP165	1832452	5666073	arp	9						
LP166	1832463	5666050	dtp	10						
LP167	1832451	5666021	dtp	10						
LP168	1832474	5665970	dpk2	10		6	T6			
LP169	1832550	5665978	dpk2 clast	11						
LP170	1832560	5665934	dpk2	9						
LP171	1832619	5665965	dpk2	10						
LP172	1832702	5665883	dpk2	9						
LP173	1831651	5666532	aok	11						
LP174	1839169	5662530	mhi clast	10		6	T6			
LP175A	1836282	5655679	?	9		6	T6			
LP175B	1836282	5655679	RUG?	9		6	T6			
LP176	1836246	5655610	RUG							
LP177H	1835951	5648524	?	11						
LP177L	1835951	5648524	?	11						
LP179	1830773	5666078	aww	9						
LP180	1830800	5666091	aww	9						
LP181	1831075	5666220	aww	9		9	T9			
LP182	1830778	5666239	aww	11		9	T9			
LP183	1830494	5666525	dpk2	9						
LP184	1830470	5666589	awu	9						
LP185	1830458	5666569	aww	11						
LP186	1830745	5666921	dpk2	9						
LP187	1830747	5667011	dpk2	9		9	T9	I3	I3	I5
LP188	1830719	5667023	arp?							
LP189	1830736	5667033	arp?							
LP190	1830691	5667027	arp	9		6	T6			
LP191	1831144	5665321	awu	12						
LP192	1831222	5665346	awu	8						
LP193	1831426	5665406	awu	8						
LP194	1831495	5665384	awu	8						
LP197	1831324	5665050	awu	8						
LP198	1831358	5665120	awu	8						
LP199	1831378	5665143	awu	8						
LP200	1831567	5665033	awu	8						
LP201	1833716	5670340	?	10						
LP202	1833855	5669646	?	10		9	T9			
LP203	1835514	5670000	?	10						
LP204	1834663	5669129	?	8			T9			
LP205	1834471	5669018	?	10						
LP206	1834416	5668980	arp	7						

Table A4. Continued.

Sample	E	N	unit	XRF batch	$^{40}Ar/^{39}Ar$ year	ICP-MS batch		TIMS batch		
						digest	analysis	Sr	Nd	Pb
LP208	1834245	5668836	arp	7						
LP209	1833940	5668673	mtm	11						
LP211	1833741	5668576	arp	11	2018	9	T9	I3	I3	I5
LP212	1834120	5668619	arp	12						
LP213	1836621	5668206	?	7						
LP214	1835747	5668694	arh	12	2018	9	T9	I3	I3	I5
LP215	1835666	5668627	arh	9		9	T9			
LP217	1835491	5668428	arp	7						
LP219	1835430	5668389	arp	7						
LP220A	1834810	5667967	arh	7						
LP220B	1836634	5667987	arh	11						
LP221	1836739	5667628	arh	11						
LP222	1836365	5667101	arh	11		6	T6			
LP224	1836040	5666386	arh	8						
LP225	1831580	5664957	awu	8						
LP226	1831533	5664906	awu	11						
LP227	1831648	5664846	awu	8						
LP228	1831647	5664764	dpk2	8		6	T6			
LP229	1831657	5664737	dpk2	8						
LP231	1831809	5664880	mhi	7						
LP232	1831931	5664799	mhi	11		6	T6			
LP233	1831954	5664871	dpk2	11		9	T9			
LP234	1831986	5664962	dpk2	7	2018	9	T9	I3	I3	I4
LP235	1831880	5664961	dpk2	7						
LP236	1831691	5665555	awp	11						
LP237	1831641	5666024	dtp	8						
LP238	1832376	5665929	awh	7		9	T9			
LP239	1832557	5665753	dpk1	9	2019	9	T9	I3	I3	I5
LP240	1832772	5665775	dpk2	11						
LP241	1832785	5665805	dpk2	7						
LP242	1833404	5665725	dpk2	7		9	T9			
LP243	1833567	5666176	arp	12						
LP244	1833378	5666388	att	7						
LP245	1833459	5666275	awh	10	2018	6	T6	I3	I3	I5
LP247	1833134	5666718	awh	10		9	T9			
LP248	1832954	5666881	att	10						
LP249	1832853	5666861	att?	8		6	T6			
LP250	1824862	5664128	amp	7	2018	9	T9	I3	I3	I5
MSR15017A	1833061	5661833	awp	X						
MSR15018	1833196	5662123	awp	1	2016	3	T4A + T4B	I1	I1	I5
MSR15019	1834895	5662561	mhi	X	2017	10	T10	I3	I3	I5
MSR15020A	1834686	5661675	awp	X						
MSR15021	1835958	5660679	awp	X						
MSR15022	1835191	5659525	awp	X						
MSR15023	1834692	5658591	atw	X		4	T4A + T4B	I3	I3	
MSR15024	1833412	5658012	mtu?	1						
MSR15025	1833726	5658749	atw?	2		6	T6			
MSR15026	1833493	5659904	dpk2?	X						
MSR15027	1833522	5660731	dpk2?	2						
MSR15028	1832496	5663974	mhi	1						
MSR15029	1833097	5663966	mhi	2						
MSR15030	1833292	5664105	mhi	X						
MSR15031	1833549	5663982	mhi	2						
MSR15032	1833712	5663924	mhi	2						

Table A4. Continued.

Sample	E	N	unit	XRF batch	$^{40}Ar/^{39}Ar$ year	ICP-MS batch		TIMS batch		
						digest	analysis	Sr	Nd	Pb
MSR15033	1833822	5663753	mhi	2						
MSR15034	1834050	5663807	mhi	2						
MSR15035	1834286	5663671	mhi	X						
MSR15036	1834767	5663405	mhi							
MSR15037	1834946	5663061	mhi	X						
MSR15038	1835682	5663527	?	2						
RPC070	1828602	5665097	dtp	X						
RPC077	1828150	5664778	arp	X						
RPC078	1828216	5664767	arp	X						
RPC088C	1827855	5664986	dtp	X						
RPC090	1828203	5665318	ati	X						
RPC110	1828203	5665318	ati		2016	8	T8	I3	I3	I5
TG084	2741700	6222550	dpk2		2018	9	T9	I3	I3	I5
TG088	2742250	6222800	ahi		2018	9	T9	I3	I3	I5

Appendix 5

Whole-rock major oxide, trace element and Sr-Nd-Pb isotope compositions

A5.1. INTRODUCTION

All data presented in Table A5.1, below, were obtained in this study, except for the following exceptions.

- XRF major oxide data were provided by G. S. Leonard (pers. comm., 2016) for samples GL2222, GL2224, GL2225, GL2226, GL2229, GL2230, GL2232 and GL2233.
- XRF major oxide data were obtained for sample RPC090, by Cole et al. (2018), which are used here. RPC090 major oxide (and Ba and Sr) are paired with trace element data (via ICP-MS) and Sr-Nd-Pb isotope data (via TIMS) from this study, because RPC110 and RPC090 were collected by Cole et al. (2018) from the same outcrop.
- TG084 and TG084 XRF data are from Hobden (1997). Trace element and Sr-Nd-Pb isotope data for these samples are from this study and were performed on the same physical specimens collected by Hobden (1997).
- XRF major oxide data were provided by M. T. Rattenbury via D. B. Townsend (pers. comm., 2016) for samples MSR15017A, MSR15018, MSR15019, MSR15020A, MSR15021, MSR15022, MSR15023, MSR15024, MSR15026, MSR15035 and MSR15037.

Analytical methods were described in full previously (section 2.4). XRF analytical precision and accuracy were monitored with standards AGV-1, BCR-2, BHVO-2, OREAS, WS-E and an internal standard (LP009B). Analytical accuracy is within 5 % (1 r.s.d.) for each oxide concentration but generally ≤2.5 % (1 r.s.d.), as determined with rock standards compared with the recommended values of Jochum et al. (2016). Duplicate analyses of LP009B indicate an external precision (2 s.d.) better than 5 % for all major oxides and Sr, however Ba reproducibility is ~13 %. Quadratically combined sourced of error (internal precision, external reproducibility, weighing measurement uncertainities) indicate 5-11 % (2 s.d.) uncertainties for trace element data collected via solution ICP-MS. All Sr-Nd-Pb isotope data are reported with quadratically combined 2 s.e. internal analytical uncertainties and 2 s.d. external reproducibilities. Major oxide data is reported in wt% and trace element data is reported in ppm. Eu/Eu* values are calculated as $Eu_N/sqrt(Sm_N*Gd_N)$ after normalisation with the values of McDonough and Sun (1995). $^{87}Sr/^{86}Sr$ data are reported relative to NBS987 = 0.710248 (Thirlwall, 1991). $^{143}Nd/^{144}Nd$ data are reported relative to JNdi-1 = 0.512515 which is equivalent to La Jolla = 0.511858 (Lugmair and Carlson, 1978; Tanaka et al., 2000). Pb isotope data are reported relative to NBS981 values recommended by Thirlwall (2000) of $^{206}Pb/^{204}Pb$ = 16.9409, $^{207}Pb/^{204}Pb$ = 15.4956, $^{208}Pb/^{204}Pb$ = 38.7228, $^{207}Pb/^{206}Pb$ = 0.91469, $^{208}Pb/^{206}Pb$ = 2.16770.

Samples LP009BX, LP108L and LP130X are cognate crystal clots hosted in the samples LP009B, LP108H and LP130, respectively.

Table A5. Whole-rock major oxide, trace element and Sr-Nd-Pb isotopic compositions.

Sample	CC351	GL2139	GL2142	GL2145	GL2148	GL2218	GL2222	GL2223
SiO_2	55.59	62.39	60.20	61.46	60.74	59.04	57.70	57.90
TiO_2	0.63	0.78	0.73	0.84	0.82	0.69	0.72	0.79
Al_2O_3	16.44	16.48	16.48	16.58	17.29	16.28	17.31	16.71
Fe_2O_3 total	8.23	6.86	7.32	7.49	7.37	6.46	7.11	7.65
MnO	0.13	0.11	0.12	0.13	0.12	0.11	0.12	0.12
MgO	5.98	2.54	3.53	2.70	2.72	5.15	4.56	4.60
CaO	7.79	5.08	6.15	5.54	5.10	6.97	7.42	7.40
Na_2O	2.63	3.43	3.36	3.49	3.30	3.08	3.31	3.23
K_2O	0.95	2.07	1.63	1.80	1.84	1.48	1.11	1.33
P_2O_5	0.12	0.17	0.16	0.18	0.16	0.15	0.14	0.17
LOI	0.31	-0.03	0.13	-0.07	0.87	0.31	0.90	0.96
Total	98.92	100.00	99.90	100.29	100.40	99.85	100.44	100.97
Ba (XRF)	192	398	303	409	403	308		266
Sr (XRF)	450	232	232	260	239	306		319
Rb	27.3							40.3
Sr (ICP-MS)	416							355
Y	16.3							19.9
Zr	96.7							116.0
Nb	3.66							5.07
Mo	0.39							0.53
Cd	0.07							0.14
In	0.03							0.35
Sn	0.7							1.0
Cs	1.95							1.34
Ba (ICP-MS)	216							281
La	11.4							13.6
Ce	24.3							29.5
Pr	2.84							3.56
Nd	12.1							15.3
Sm	2.83							3.57
Eu	0.78							0.97
Gd	2.66							3.44
Tb	0.46							0.60
Dy	2.89							3.75
Ho	0.61							0.75
Er	1.72							2.13
Tm	0.26							0.33
Yb	1.66							2.05
Lu	0.27							0.30
Hf	2.58							3.19
Ta	0.3							0.4
Tl	0.1							0.2
Pb	4.7							9.0
Th	4.40							4.74
U	0.95							1.18
Sc	27.7							26.8
V	196							208
Cr	205							71.1
Co	32.2							23.9
Ni	67.5							21.5
Cu	60.2							21.1
Zn	73.1							69.1
Ga	18.3							17.0
Eu/Eu*	0.88							0.84
$^{87}Sr/^{86}Sr$	0.704979±10							0.704702±4
$^{143}Nd/^{144}Nd$	0.512615±9							0.512763±44
$^{206}Pb/^{204}Pb$	18.8450±30							18.8192±32
$^{207}Pb/^{204}Pb$	15.6334±43							15.6205±44
$^{208}Pb/^{204}Pb$	38.7600±93							38.7152±96
$^{207}Pb/^{206}Pb$	0.82958±12							0.83003±12
$^{208}Pb/^{206}Pb$	2.05678±21							2.05721±21

Major oxides in wt%, trace elements in ppm.

Table A5. Continued.

Sample	GL2224	GL2225	GL2226	GL2229	GL2230	GL2231	GL2232	GL2233
SiO_2	57.97	55.45	57.09	59.21	60.17	59.16	57.69	55.97
TiO_2	0.79	0.79	0.79	0.77	0.71	0.78	0.68	0.72
Al_2O_3	16.90	16.90	17.07	17.12	16.96	17.11	14.92	15.57
Fe_2O_3 total	8.17	9.15	7.76	7.25	6.86	7.33	7.58	7.88
MnO	0.13	0.15	0.14	0.12	0.12	0.12	0.14	0.14
MgO	4.17	5.08	4.15	3.47	3.19	3.10	6.34	6.72
CaO	6.70	8.41	7.18	6.40	5.85	6.26	7.93	8.03
Na_2O	2.93	2.79	2.98	3.31	3.18	3.38	2.70	2.63
K_2O	1.46	1.03	1.30	1.50	1.68	1.71	1.00	0.97
P_2O_5	0.14	0.14	0.13	0.14	0.14	0.16	0.13	0.13
LOI	0.87	0.26	0.37	0.35	1.27	0.11	0.75	1.48
Total	100.26	100.18	98.98	99.68	100.17	99.34	99.91	100.31
Ba (XRF)						345		
Sr (XRF)						259		
Rb								
Sr (ICP-MS)								
Y								
Zr								
Nb								
Mo								
Cd								
In								
Sn								
Cs								
Ba (ICP-MS)								
La								
Ce								
Pr								
Nd								
Sm								
Eu								
Gd								
Tb								
Dy								
Ho								
Er								
Tm								
Yb								
Lu								
Hf								
Ta								
Tl								
Pb								
Th								
U								
Sc								
V								
Cr								
Co								
Ni								
Cu								
Zn								
Ga								
Eu/Eu*								
$^{87}Sr/^{86}Sr$								
$^{143}Nd/^{144}Nd$								
$^{206}Pb/^{204}Pb$								
$^{207}Pb/^{204}Pb$								
$^{208}Pb/^{204}Pb$								
$^{207}Pb/^{206}Pb$								
$^{208}Pb/^{206}Pb$								

Major oxides in wt%, trace elements in ppm.

Table A5. Continued.

Sample	GL2234	LP001	LP002	LP003	LP008	LP009A	LP009B	LP009BX
SiO_2	57.08	55.35	61.00	59.52	60.65	62.08	62.09	57.28
TiO_2	0.69	0.68	0.69	0.74	0.86	0.77	0.76	0.91
Al_2O_3	15.30	14.23	16.45	16.21	16.97	16.65	16.64	17.89
Fe_2O_3 total	7.84	7.60	6.68	7.53	7.51	6.77	6.67	8.06
MnO	0.13	0.12	0.11	0.12	0.12	0.11	0.11	0.13
MgO	6.42	9.47	3.04	3.97	2.57	2.58	2.52	3.11
CaO	8.15	7.22	6.02	6.33	5.81	5.35	5.18	5.75
Na_2O	2.84	2.64	3.33	3.20	3.55	3.45	3.45	3.12
K_2O	1.15	1.30	1.83	1.64	1.84	2.10	2.11	1.64
P_2O_5	0.14	0.14	0.15	0.17	0.17	0.16	0.16	0.13
LOI	-0.09	1.27	0.97	-0.01	0.20	0.22	0.89	2.41
Total	99.85	100.15	100.41	99.54	100.37	100.35	100.69	100.57
Ba (XRF)	242	297	362	322	417	466	455	370
Sr (XRF)	303	264	235	301	268	251	236	253
Rb		55.3	71.1		70.9		82.9	
Sr (ICP-MS)		315	247		282		254	
Y		19.2	22.3		29.6		23.4	
Zr		125.8	140.7		152.0		165.9	
Nb		4.79	6.13		6.93		7.55	
Mo		0.91	0.96		0.59		0.58	
Cd		0.12	0.13		0.13		0.12	
In		0.03	0.03		0.03		0.04	
Sn		0.2	0.2		0.3		0.3	
Cs		3.53	4.16		1.99		2.18	
Ba (ICP-MS)		331	369		410		467	
La		12.7	15.8		23.0		16.4	
Ce		27.7	33.8		44.6		36.0	
Pr		3.48	4.09		5.72		4.39	
Nd		14.7	17.0		23.5		18.0	
Sm		3.27	3.68		4.97		4.02	
Eu		0.84	0.90		1.11		1.01	
Gd		3.01	3.38		4.55		3.57	
Tb		0.53	0.59		0.78		0.63	
Dy		3.38	3.74		4.87		4.11	
Ho		0.71	0.80		1.01		0.85	
Er		1.93	2.22		2.79		2.34	
Tm		0.30	0.35		0.43		0.38	
Yb		1.91	2.28		2.66		2.44	
Lu		0.29	0.35		0.41		0.37	
Hf		3.39	3.66		3.93		4.23	
Ta		0.4	0.5		0.5		0.6	
Tl		0.2	0.3		0.3		0.3	
Pb		10.0	10.2		9.7		10.9	
Th		5.45	6.54		6.64		7.63	
U		1.32	1.72		1.60		1.84	
Sc		30.1	21.2		23.0		21.1	
V		212	166		187		159	
Cr		654	22.8		6.64		10.9	
Co		41.1	17.4		15.4		15.1	
Ni		273.1	10.0		3.6		6.4	
Cu		86.9	10.9		8.0		12.3	
Zn		71.7	70.2		81.3		75.4	
Ga		17.4	17.9		19.9		19.3	
Eu/Eu*		0.81	0.77		0.71		0.81	
$^{87}Sr/^{86}Sr$		0.704725±11					0.706063±10	
$^{143}Nd/^{144}Nd$		0.512782±17					0.512652±16	
$^{206}Pb/^{204}Pb$		18.8270±30					18.8553±30	
$^{207}Pb/^{204}Pb$		15.6283±43					15.6371±43	
$^{208}Pb/^{204}Pb$		38.7305±93					38.7754±92	
$^{207}Pb/^{206}Pb$		0.83010±12					0.82933±12	
$^{208}Pb/^{206}Pb$		2.05718±21					2.05647±21	

Major oxides in wt%, trace elements in ppm.

Table A5. Continued.

Sample	LP010	LP011	LP013	LP014	LP018	LP019	LP020	LP021
SiO_2	58.80	58.49	58.52	61.05	60.28	60.23	60.78	60.92
TiO_2	0.76	0.71	0.72	0.86	0.74	0.81	0.86	0.86
Al_2O_3	16.49	16.13	15.77	16.86	16.59	17.01	16.89	16.89
Fe_2O_3 total	7.78	7.69	7.71	7.35	7.09	7.29	7.34	7.33
MnO	0.13	0.13	0.13	0.12	0.12	0.12	0.12	0.12
MgO	4.23	4.97	4.79	2.47	3.37	2.85	2.46	2.47
CaO	6.95	7.31	6.86	5.81	6.29	6.30	5.82	5.72
Na_2O	3.22	3.08	3.08	3.68	3.42	3.54	3.67	3.63
K_2O	1.51	1.44	1.48	1.82	1.72	1.68	1.81	1.81
P_2O_5	0.15	0.15	0.16	0.18	0.15	0.17	0.17	0.17
LOI	0.30	0.18	0.00	0.03	0.32	0.36	0.23	0.07
Total	100.42	100.39	99.30	100.34	100.23	100.46	100.24	100.11
Ba (XRF)	337	303	293	380	348	351	317	363
Sr (XRF)	259	275	265	270	244	275	255	249
Rb	53.0	52.5		66.9	64.6	61.8		
Sr (ICP-MS)	273	291		277	253	292		
Y	24.9	20.6		23.0	23.3	22.9		
Zr	128.3	120.0		147.4	136.3	141.2		
Nb	4.88	5.65		6.71	5.87	6.15		
Mo	0.34	0.63		0.70	0.88	0.74		
Cd	0.13	0.13		0.12	0.12	0.13		
In	0.03	0.03		0.03	0.03	0.04		
Sn	0.2	0.1		0.2	0.3	0.3		
Cs	1.39	2.89		3.43	3.71	3.32		
Ba (ICP-MS)	326	315		386	366	385		
La	17.1	14.7		16.7	15.4	16.4		
Ce	35.0	32.1		37.4	32.9	35.7		
Pr	4.50	3.89		4.49	4.06	4.36		
Nd	18.7	16.1		18.5	16.8	18.3		
Sm	4.04	3.52		4.06	3.72	3.90		
Eu	0.97	0.88		1.01	0.92	0.99		
Gd	3.82	3.17		3.65	3.42	3.58		
Tb	0.66	0.56		0.64	0.61	0.62		
Dy	4.22	3.58		4.07	3.92	3.98		
Ho	0.89	0.76		0.85	0.82	0.83		
Er	2.42	2.08		2.35	2.26	2.30		
Tm	0.37	0.33		0.36	0.36	0.36		
Yb	2.36	2.08		2.32	2.28	2.27		
Lu	0.36	0.32		0.35	0.35	0.35		
Hf	3.32	3.11		3.80	3.56	3.68		
Ta	0.3	0.4		0.5	0.5	0.5		
Tl	0.2	0.2		0.3	0.3	0.3		
Pb	8.4	10.1		10.9	9.7	10.6		
Th	5.16	5.30		6.01	5.80	5.74		
U	1.26	1.23		1.51	1.41	1.43		
Sc	26.8	27.4		22.2	22.9	23.5		
V	192	181		180	174	181		
Cr	98.6	140		5	33.5	6		
Co	22.5	24.9		14.8	19.9	15.7		
Ni	25.6	34.8		4.7	20.3	7.2		
Cu	43.3	36.9		7.7	16.2	6.1		
Zn	73.1	74.6		77.6	71.8	75.6		
Ga	18.1	17.2		19.1	18.1	18.6		
Eu/Eu*	0.75	0.81		0.80	0.79	0.81		
$^{87}Sr/^{86}Sr$	0.705445±11							
$^{143}Nd/^{144}Nd$	0.512688±17							
$^{206}Pb/^{204}Pb$	18.8542±30							
$^{207}Pb/^{204}Pb$	15.6382±43							
$^{208}Pb/^{204}Pb$	38.7774±93							
$^{207}Pb/^{206}Pb$	0.82943±12							
$^{208}Pb/^{206}Pb$	2.05670±21							

Major oxides in wt%, trace elements in ppm.

Table A5. Continued.

Sample	LP023	LP024	LP025	LP026	LP027	LP028	LP029	LP030
SiO_2	58.39	61.96	60.24	58.26	58.26	59.85	58.56	59.73
TiO_2	0.75	0.92	0.83	0.71	0.71	0.71	0.70	0.79
Al_2O_3	16.18	16.75	16.87	16.04	16.00	16.17	15.96	17.19
Fe_2O_3 total	7.99	7.43	7.22	7.73	7.70	7.35	7.56	7.00
MnO	0.13	0.12	0.12	0.13	0.13	0.13	0.13	0.12
MgO	4.89	2.01	2.64	4.87	4.96	4.42	4.94	3.42
CaO	7.13	5.32	5.85	7.17	7.06	6.68	6.92	6.45
Na_2O	3.10	3.74	3.54	3.05	3.05	3.21	3.06	3.34
K_2O	1.43	1.94	1.73	1.44	1.45	1.62	1.49	1.76
P_2O_5	0.14	0.18	0.17	0.15	0.15	0.15	0.15	0.16
LOI	0.14	0.14	0.80	0.60	0.68	0.11	0.73	0.15
Total	100.37	100.61	100.13	100.27	100.28	100.52	100.34	100.23
Ba (XRF)	272	418	347	296	317	335	278	408
Sr (XRF)	246	236	256	258	247	249	270	268
Rb	43.4	70.1						
Sr (ICP-MS)	272	241						
Y	22.0	22.8						
Zr	92.4	148.2						
Nb	4.88	6.51						
Mo	0.63	0.94						
Cd	0.17	0.08						
In	0.54	0.03						
Sn	0.9	1.7						
Cs	1.01	3.82						
Ba (ICP-MS)	308	374						
La	14.5	15.2						
Ce	31.8	32.8						
Pr	3.95	4.01						
Nd	16.4	16.2						
Sm	3.87	3.81						
Eu	0.96	1.11						
Gd	3.64	3.83						
Tb	0.64	0.62						
Dy	4.02	3.90						
Ho	0.85	0.83						
Er	2.33	2.41						
Tm	0.37	0.38						
Yb	2.27	2.38						
Lu	0.35	0.37						
Hf	3.32	4.18						
Ta	0.4	0.7						
Tl	0.2	0.4						
Pb	8.9	11.4						
Th	4.72	6.77						
U	1.26	1.66						
Sc	24.9	18.6						
V	202	165						
Cr	124	3						
Co	26.9	12.5						
Ni	40.0	4.0						
Cu	57.4	7.2						
Zn	73.1	78.5						
Ga	17.3	18.0						
Eu/Eu*	0.78	0.89						
$^{87}Sr/^{86}Sr$	0.705331±4							
$^{143}Nd/^{144}Nd$	0.512737±46	0.512636±3						
$^{206}Pb/^{204}Pb$	18.8444±31	18.8614±30						
$^{207}Pb/^{204}Pb$	15.6299±44	15.6386±43						
$^{208}Pb/^{204}Pb$	38.7522±93	38.7864±93						
$^{207}Pb/^{206}Pb$	0.82942±12	0.82913±12						
$^{208}Pb/^{206}Pb$	2.05642±21	2.05639±21						

Major oxides in wt%, trace elements in ppm.

Table A5. Continued.

Sample	LP031	LP032	LP033	LP034	LP035	LP036	LP037	LP038
SiO_2	58.86	59.65	60.08	60.99	60.07	60.46	59.89	59.93
TiO_2	0.71	0.76	0.59	0.59	0.59	0.59	0.64	0.60
Al_2O_3	15.95	16.67	16.61	16.43	15.80	15.60	16.67	16.62
Fe_2O_3 total	7.53	7.32	6.92	6.70	6.99	6.89	6.88	6.86
MnO	0.13	0.12	0.12	0.12	0.12	0.12	0.12	0.12
MgO	4.84	3.91	3.76	4.01	4.58	4.53	3.77	3.87
CaO	7.04	6.57	6.67	6.33	7.26	6.80	6.40	6.14
Na_2O	3.09	3.17	3.33	3.29	3.07	3.07	3.33	3.26
K_2O	1.52	1.75	1.31	1.39	1.27	1.40	1.40	1.34
P_2O_5	0.15	0.16	0.13	0.13	0.13	0.13	0.14	0.14
LOI	0.26	0.58	0.86	0.57	0.37	0.61	0.96	0.30
Total	100.21	100.78	100.50	100.63	100.33	100.31	100.32	99.24
Ba (XRF)	328	393	333	310	273	344	321	282
Sr (XRF)	285	252	216	220	247	239	274	263
Rb			38.5	39.2		43.6		
Sr (ICP-MS)			232	224		247		
Y			17.9	20.5		16.6		
Zr			110.9	107.2		99.4		
Nb			3.71	3.29		3.43		
Mo			1.00	0.55		0.24		
Cd			0.13	0.23		0.20		
In			0.04	0.04		0.03		
Sn			1.1	1.8		1.0		
Cs			1.14	1.04		1.10		
Ba (ICP-MS)			345	301		332		
La			11.7	11.4		11.3		
Ce			24.1	22.5		24.0		
Pr			3.05	3.48		3.05		
Nd			12.3	14.4		11.8		
Sm			3.13	3.57		3.12		
Eu			0.85	0.84		0.86		
Gd			3.08	3.33		2.91		
Tb			0.54	0.56		0.48		
Dy			3.44	3.62		3.06		
Ho			0.73	0.74		0.67		
Er			2.16	2.18		1.85		
Tm			0.34	0.34		0.29		
Yb			2.05	2.12		1.78		
Lu			0.36	0.33		0.30		
Hf			3.19	2.65		3.00		
Ta			0.3	0.2		0.3		
Tl			0.2	0.2		0.2		
Pb			7.7	6.0		5.8		
Th			6.68	5.02		3.64		
U			1.26	1.03		1.24		
Sc			21.4	20.8		22.8		
V			162	163		168		
Cr			75.7	268		100		
Co			20.9	22.9		22.9		
Ni			24.9	39.7		17.9		
Cu			32.7	60.4		30.4		
Zn			64.7	60.0		56.0		
Ga			16.3	17.0		15.8		
Eu/Eu*			0.83	0.74		0.87		
$^{87}Sr/^{86}Sr$			0.704711±11			0.704750±4		
$^{143}Nd/^{144}Nd$			0.512825±18			0.512818±46		
$^{206}Pb/^{204}Pb$			18.8272±30					
$^{207}Pb/^{204}Pb$			15.6241±43					
$^{208}Pb/^{204}Pb$			38.7179±92					
$^{207}Pb/^{206}Pb$			0.82987±12					
$^{208}Pb/^{206}Pb$			2.05649±21					

Major oxides in wt%, trace elements in ppm.

Table A5. Continued.

Sample	LP039	LP040	LP043	LP044	LP046A	LP046B	LP047	LP048
SiO_2	60.07	60.19	59.79	59.95	58.17	58.34	58.55	58.32
TiO_2	0.61	0.59	0.77	0.76	0.71	0.73	0.72	0.70
Al_2O_3	16.39	16.21	16.68	16.76	15.81	15.87	15.81	15.83
Fe_2O_3 total	6.98	6.85	7.08	7.21	7.78	7.74	7.71	7.70
MnO	0.12	0.12	0.12	0.12	0.13	0.13	0.13	0.13
MgO	4.02	3.99	3.36	3.48	5.03	4.65	4.78	4.90
CaO	6.55	6.38	5.93	6.06	6.53	6.34	6.88	6.98
Na_2O	3.29	3.25	3.27	3.25	2.96	3.07	3.09	3.04
K_2O	1.30	1.34	1.83	1.81	1.49	1.56	1.48	1.45
P_2O_5	0.13	0.13	0.17	0.17	0.16	0.17	0.16	0.16
LOI	-0.04	0.03	0.12	0.04	0.55	0.34	-0.07	0.02
Total	99.56	99.13	99.22	99.74	99.47	99.05	99.38	99.34
Ba (XRF)	270	292	373	389	308	306	319	338
Sr (XRF)	275	275	270	269	282	245	271	269
Rb	38.4							
Sr (ICP-MS)	280							
Y	17.8							
Zr	86.4							
Nb	3.84							
Mo	0.08							
Cd	0.13							
In	0.62							
Sn	0.5							
Cs	1.29							
Ba (ICP-MS)	300							
La	11.4							
Ce	22.3							
Pr	2.86							
Nd	12.0							
Sm	2.91							
Eu	0.80							
Gd	2.85							
Tb	0.50							
Dy	3.31							
Ho	0.69							
Er	1.94							
Tm	0.30							
Yb	1.92							
Lu	0.29							
Hf	2.72							
Ta	0.3							
Tl	0.2							
Pb	9.8							
Th	3.49							
U	1.16							
Sc	24.7							
V	176							
Cr	58.3							
Co	21.4							
Ni	17.9							
Cu	50.8							
Zn	67.5							
Ga	17.4							
Eu/Eu*	0.85							
$^{87}Sr/^{86}Sr$	0.704761±6							
$^{143}Nd/^{144}Nd$	0.512835±45							
$^{206}Pb/^{204}Pb$	18.8343±46							
$^{207}Pb/^{204}Pb$	15.6313±43							
$^{208}Pb/^{204}Pb$	38.7323±114							
$^{207}Pb/^{206}Pb$	0.82994±6							
$^{208}Pb/^{206}Pb$	2.05647±24							

Major oxides in wt%, trace elements in ppm.

Table A5. Continued.

Sample	LP051	LP052	LP053	LP054	LP056	LP057	LP058	LP060
SiO_2	61.14	59.37	60.80	58.78	60.64	60.57	60.98	59.81
TiO_2	0.73	0.77	0.91	0.62	0.87	0.85	0.86	0.78
Al_2O_3	16.51	16.80	16.84	16.93	17.62	17.46	17.46	16.70
Fe_2O_3 total	7.10	7.11	7.72	7.59	6.85	6.76	6.73	7.18
MnO	0.10	0.12	0.12	0.13	0.11	0.11	0.11	0.12
MgO	2.91	3.41	2.29	4.14	2.03	2.05	2.05	3.40
CaO	5.40	6.14	4.84	6.28	5.28	5.47	5.44	6.01
Na_2O	3.27	3.46	3.49	3.21	3.68	3.66	3.69	3.30
K_2O	2.05	1.80	1.98	1.22	2.02	1.99	2.01	1.82
P_2O_5	0.18	0.16	0.19	0.14	0.19	0.19	0.19	0.17
LOI	0.28	0.19	0.40	0.54	0.28	0.21	0.10	0.02
Total	99.78	99.42	99.70	99.65	99.69	99.43	99.76	99.44
Ba (XRF)	343	375	404	286	465	508	515	400
Sr (XRF)	222	270	230	201	267	277	273	271
Rb	76.7	61.5				75.1		
Sr (ICP-MS)	238	270				273		
Y	30.1	22.7				25.9		
Zr	151.5	156.0				157.4		
Nb	5.82	6.62				6.99		
Mo	1.03	0.87				1.12		
Cd	0.07	0.07				0.08		
In	0.03	0.02				0.03		
Sn	1.6	1.8				1.7		
Cs	2.47	3.91				3.74		
Ba (ICP-MS)	399	377				472		
La	27.0	17.4				19.7		
Ce	41.9	38.6				42.7		
Pr	6.10	4.67				5.13		
Nd	25.0	18.5				20.6		
Sm	5.19	4.04				4.57		
Eu	1.05	1.01				1.20		
Gd	5.08	4.06				4.63		
Tb	0.83	0.63				0.72		
Dy	5.16	3.87				4.38		
Ho	1.05	0.79				0.92		
Er	2.90	2.32				2.62		
Tm	0.44	0.36				0.40		
Yb	2.66	2.26				2.51		
Lu	0.40	0.33				0.39		
Hf	3.89	4.17				4.21		
Ta	0.5	0.6				0.5		
Tl	0.3	0.2				0.4		
Pb	7.5	13.7				12.8		
Th	6.97	6.86				7.61		
U	1.91	1.56				1.67		
Sc	17.4	21.3				17.1		
V	156	157				152		
Cr	26.9	30.7				10.7		
Co	18.7	18.2				12.6		
Ni	18.2	9.8				2.3		
Cu	40.3	13.5				8.7		
Zn	70.1	83.5				80.1		
Ga	16.8	17.5				18.9		
Eu/Eu*	0.62	0.76				0.79		
$^{87}Sr/^{86}Sr$	0.705017±4							
$^{143}Nd/^{144}Nd$	0.512759±45							
$^{206}Pb/^{204}Pb$	18.8361±30							
$^{207}Pb/^{204}Pb$	15.6293±43							
$^{208}Pb/^{204}Pb$	38.7394±93							
$^{207}Pb/^{206}Pb$	0.82975±12							
$^{208}Pb/^{206}Pb$	2.05665±21							

Major oxides in wt%, trace elements in ppm.

Table A5. Continued.

Sample	LP062	LP063	LP064	LP066	LP067	LP070	LP071	LP072
SiO_2	58.33	58.58	58.12	59.75	59.33	59.85	60.10	59.05
TiO_2	0.66	0.72	0.72	0.79	0.77	0.77	0.77	0.57
Al_2O_3	14.99	15.88	15.97	16.89	16.73	16.71	16.55	16.23
Fe_2O_3 total	7.48	7.62	7.73	7.18	7.16	7.16	7.21	7.50
MnO	0.12	0.13	0.13	0.12	0.12	0.12	0.12	0.13
MgO	5.91	4.71	4.67	3.50	3.44	3.44	3.44	4.70
CaO	7.53	6.83	6.95	5.97	5.91	5.96	5.92	6.71
Na_2O	2.99	3.08	3.04	3.24	3.25	3.27	3.27	3.15
K_2O	1.24	1.49	1.37	1.80	1.79	1.81	1.84	1.17
P_2O_5	0.15	0.16	0.16	0.17	0.17	0.17	0.17	0.13
LOI	-0.25	0.01	0.44	-0.03	0.24	0.14	0.00	0.11
Total	99.51	99.32	99.38	99.50	99.04	99.50	99.53	99.56
Ba (XRF)	250	337	335	428	391	382	395	257
Sr (XRF)	386	260	274	272	268	260	262	272
Rb	33.1	51.1					65.3	32.5
Sr (ICP-MS)	373	276					262	288
Y	17.1	20.0					20.7	18.8
Zr	104.9	122.6					160.1	91.2
Nb	4.10	5.38					6.36	3.34
Mo	0.02	0.93					1.07	0.17
Cd	0.16	0.21					0.26	0.18
In	0.51	0.32					0.08	0.72
Sn	0.7	1.2					1.4	0.7
Cs	0.83	2.95					3.71	0.85
Ba (ICP-MS)	262	319					385	284
La	13.2	15.5					19.4	9.9
Ce	28.6	33.5					43.5	21.2
Pr	3.45	4.00					4.88	2.65
Nd	14.3	16.9					19.4	11.5
Sm	3.24	3.75					4.69	2.85
Eu	0.84	0.97					1.13	0.77
Gd	3.06	3.55					4.18	2.87
Tb	0.52	0.60					0.65	0.51
Dy	3.25	3.83					4.23	3.34
Ho	0.69	0.81					0.85	0.73
Er	1.87	2.22					2.47	2.07
Tm	0.30	0.35					0.39	0.34
Yb	1.86	2.19					2.30	2.08
Lu	0.27	0.32					0.37	0.31
Hf	2.98	3.45					4.27	2.69
Ta	0.3	0.4					0.5	0.3
Tl	0.1	0.3					0.4	0.2
Pb	6.5	9.3					12.7	5.5
Th	3.72	5.76					10.69	3.45
U	1.04	1.30					1.61	0.99
Sc	28.1	27.1					21.7	25.2
V	183	178					160	177
Cr	194	126					33.6	111
Co	28.2	23.7					18.3	24.8
Ni	84.4	28.3					9.6	30.3
Cu	232.2	35.6					12.9	59.8
Zn	64.0	69.8					68.7	69.6
Ga	16.7	24.7					18.5	32.3
Eu/Eu*	0.81	0.81					0.78	0.82
$^{87}Sr/^{86}Sr$	0.704791±11							0.704723±11
$^{143}Nd/^{144}Nd$	0.512735±18							0.512860±22
$^{206}Pb/^{204}Pb$	18.8295±30							18.8237±31
$^{207}Pb/^{204}Pb$	15.6258±43							15.6228±43
$^{208}Pb/^{204}Pb$	38.7315±92							38.7165±93
$^{207}Pb/^{206}Pb$	0.82986±12							0.82996±12
$^{208}Pb/^{206}Pb$	2.05696±21							2.05680±21

Major oxides in wt%, trace elements in ppm.

Table A5. Continued.

Sample	LP073	LP074	LP077	LP079	LP080	LP081	LP087	LP088
SiO_2	55.55	56.14	58.63	58.39	58.58	58.54	56.04	60.45
TiO_2	0.73	0.66	0.72	0.71	0.72	0.72	0.67	0.86
Al_2O_3	17.74	17.82	15.87	15.84	15.84	15.74	16.48	16.76
Fe_2O_3 total	8.63	8.24	7.73	7.70	7.63	7.51	8.67	7.46
MnO	0.14	0.14	0.13	0.13	0.13	0.13	0.15	0.12
MgO	4.40	4.23	4.83	4.78	4.65	4.46	5.29	2.44
CaO	7.37	7.53	6.84	6.90	6.83	6.61	7.78	5.55
Na_2O	3.28	3.32	3.03	3.08	3.11	3.14	2.77	3.58
K_2O	0.90	0.89	1.47	1.47	1.49	1.54	0.91	1.77
P_2O_5	0.16	0.16	0.16	0.16	0.16	0.16	0.14	0.18
LOI	-0.10	-0.22	-0.12	-0.07	-0.03	-0.05	0.24	0.19
Total	99.00	99.21	99.53	99.24	99.22	98.68	99.20	99.46
Ba (XRF)	192	280	299	267	327	357	201	356
Sr (XRF)	258	260	273	269	266	240	297	255
Rb		22.3					25.2	
Sr (ICP-MS)		275					306	
Y		19.3					18.6	
Zr		81.6					89.5	
Nb		1.82					2.96	
Mo							0.68	
Cd		0.04					0.08	
In		0.24					0.03	
Sn							0.8	
Cs		0.54					1.27	
Ba (ICP-MS)		248					196	
La		9.2					9.7	
Ce		19.5					21.5	
Pr		2.59					2.67	
Nd		11.7					11.2	
Sm		2.98					2.69	
Eu		0.86					0.83	
Gd		2.95					2.82	
Tb		0.52					0.47	
Dy		3.44					3.07	
Ho		0.73					0.67	
Er		2.10					1.89	
Tm		0.34					0.30	
Yb		2.07					1.93	
Lu		0.31					0.29	
Hf		2.36					2.47	
Ta		0.2					0.2	
Tl		0.1					0.2	
Pb		5.6					4.7	
Th		2.78					3.31	
U		0.65					0.80	
Sc		23.0					28.7	
V		193					210	
Cr		26.6					89.5	
Co		22.5					26.6	
Ni		16.0					12.5	
Cu		33.3					44.3	
Zn		77.5					82.9	
Ga		17.6					16.7	
Eu/Eu*		0.88					0.92	
$^{87}Sr/^{86}Sr$		0.705043±11						
$^{143}Nd/^{144}Nd$		0.512829±19						
$^{206}Pb/^{204}Pb$		18.8290±30						
$^{207}Pb/^{204}Pb$		15.6257±43						
$^{208}Pb/^{204}Pb$		38.7189±92						
$^{207}Pb/^{206}Pb$		0.82988±12						
$^{208}Pb/^{206}Pb$		2.05635±21						

Major oxides in wt%, trace elements in ppm.

Table A5. Continued.

Sample	LP090	LP095	LP096	LP097	LP098	LP099	LP103	LP108H
SiO_2	60.83	60.82	56.15	55.54	59.66	60.27	60.89	54.65
TiO_2	0.87	0.84	0.71	0.68	0.85	0.86	0.94	0.67
Al_2O_3	16.55	16.46	14.42	16.66	17.25	17.14	16.93	16.40
Fe_2O_3 total	7.60	7.39	7.59	8.79	7.36	7.28	7.73	8.93
MnO	0.12	0.12	0.12	0.15	0.12	0.12	0.12	0.14
MgO	2.34	2.51	8.29	5.34	2.72	2.61	1.97	6.21
CaO	5.21	5.45	7.04	7.88	5.70	5.63	4.91	8.03
Na_2O	3.49	3.52	2.83	2.74	3.56	3.59	3.54	2.72
K_2O	1.88	1.94	1.45	0.80	1.78	1.85	1.94	0.72
P_2O_5	0.19	0.18	0.16	0.14	0.19	0.19	0.19	0.13
LOI	0.12	-0.19	0.29	0.40	0.18	-0.08	0.24	0.69
Total	99.32	99.34	99.15	99.22	99.49	99.65	99.51	99.37
Ba (XRF)	388	408	322	239	412	511	434	145
Sr (XRF)	254	253	269	293	285	297	260	218
Rb				19.4			69.6	21.3
Sr (ICP-MS)				292			282	234
Y				16.7			27.1	18.4
Zr				91.6			149.7	70.8
Nb				2.96			6.76	2.58
Mo				0.01			1.73	0.41
Cd				0.31			0.27	0.18
In				0.07			0.24	0.01
Sn				0.6			1.3	
Cs				0.94			2.09	1.22
Ba (ICP-MS)				203			444	209
La				10.2			23.5	7.9
Ce				23.0			45.6	17.6
Pr				2.93			6.09	2.35
Nd				11.9			25.1	10.4
Sm				3.15			5.35	3.02
Eu				0.86			1.24	0.85
Gd				2.88			5.11	2.91
Tb				0.49			0.84	0.51
Dy				3.20			5.14	3.56
Ho				0.69			1.06	0.77
Er				2.06			3.02	2.32
Tm				0.32			0.47	0.35
Yb				1.98			2.85	2.17
Lu				0.32			0.42	0.33
Hf				2.54			4.59	2.14
Ta				0.2			0.6	0.2
Tl				0.2			0.4	0.2
Pb				4.6			10.6	3.2
Th				3.86			5.05	2.24
U				0.79			1.58	0.52
Sc				29.1			22.2	31.1
V				208			173	233
Cr				81.3			23.1	142
Co				27.1			13.9	33.4
Ni				14.5			3.4	48.8
Cu				21.4			18.1	35.5
Zn				73.7			83.9	69.2
Ga				18.0			63.1	15.9
Eu/Eu*				0.87			0.72	0.87
$^{87}Sr/^{86}Sr$				0.704763±11			0.706063±4	
$^{143}Nd/^{144}Nd$				0.512799±17			0.512662±44	
$^{206}Pb/^{204}Pb$				18.8194±30			18.8617±8	
$^{207}Pb/^{204}Pb$				15.6187±43			15.6386±9	
$^{208}Pb/^{204}Pb$				38.7062±92			38.7863±26	
$^{207}Pb/^{206}Pb$				0.82993±12			0.82912±2	
$^{208}Pb/^{206}Pb$				2.05672±21			2.05635±6	

Major oxides in wt%, trace elements in ppm.

Table A5. Continued.

Sample	LP108L	LP109	LP113	LP117	LP118	LP119	LP120	LP122
SiO_2	54.80	62.46	59.41	60.34	57.46	57.65	56.90	60.75
TiO_2	0.67	0.43	0.54	0.62	0.82	0.69	0.71	0.76
Al_2O_3	16.35	16.97	16.91	18.08	16.74	16.29	16.25	16.74
Fe_2O_3 total	8.75	5.85	6.93	6.09	8.32	7.66	7.67	6.94
MnO	0.15	0.11	0.13	0.10	0.13	0.13	0.13	0.10
MgO	6.22	3.05	3.92	3.06	4.23	5.39	5.38	2.86
CaO	8.30	5.26	6.46	5.98	6.91	6.63	6.79	5.71
Na_2O	2.77	3.58	3.40	3.43	3.04	3.04	3.05	3.46
K_2O	0.75	1.13	1.04	1.24	1.47	1.39	1.35	1.87
P_2O_5	0.13	0.14	0.13	0.13	0.17	0.15	0.16	0.18
LOI	0.33	0.57	0.16	0.43	-0.17	0.45	0.49	0.09
Total	99.31	99.64	99.10	99.61	99.40	99.65	98.99	99.57
Ba (XRF)	196	279	324	301	340	326	310	394
Sr (XRF)	237	242	247	212	260	297	317	264
Rb		34.1	31.2		50.3			
Sr (ICP-MS)		231	246		280			
Y		13.5	13.6		23.4			
Zr		36.1	86.0		120.6			
Nb		2.99	2.76		5.04			
Mo		0.12	0.28		0.38			
Cd		0.16	0.08		0.24			
In		0.02	0.08		0.52			
Sn		0.1	0.3		0.9			
Cs		1.13	0.81		1.75			
Ba (ICP-MS)		317	278		314			
La		11.2	8.7		15.8			
Ce		19.9	18.4		32.6			
Pr		2.82	2.22		4.27			
Nd		11.5	9.4		18.0			
Sm		2.50	2.33		4.17			
Eu		0.70	0.69		1.05			
Gd		2.52	2.33		4.02			
Tb		0.39	0.39		0.67			
Dy		2.46	2.55		4.30			
Ho		0.52	0.57		0.89			
Er		1.51	1.64		2.52			
Tm		0.22	0.27		0.40			
Yb		1.35	1.68		2.40			
Lu		0.20	0.26		0.35			
Hf		1.26	2.34		3.57			
Ta		0.3	0.2		0.4			
Tl		0.1	0.2		0.2			
Pb		7.8	6.7		8.8			
Th		2.22	6.38		3.96			
U		0.71	0.78		1.20			
Sc		13.9	20.3		27.7			
V		134	161		207			
Cr		42.0	59.6		26.4			
Co		15.0	20.1		23.7			
Ni		23.2	24.0		9.7			
Cu		20.6	38.3		10.6			
Zn		67.3	65.3		72.8			
Ga		16.5	17.2		102.8			
Eu/Eu*		0.85	0.90		0.78			
$^{87}Sr/^{86}Sr$			0.705118±9		0.705520±11			
$^{143}Nd/^{144}Nd$			0.512777±9		0.512694±17			
$^{206}Pb/^{204}Pb$			18.8382±30		18.8585±30			
$^{207}Pb/^{204}Pb$			15.6332±43		15.6400±43			
$^{208}Pb/^{204}Pb$			38.7478±92		38.7786±92			
$^{207}Pb/^{206}Pb$			0.82987±12		0.82934±12			
$^{208}Pb/^{206}Pb$			2.05687±21		2.05629±21			

Major oxides in wt%, trace elements in ppm.

Table A5. Continued.

Sample	LP123	LP124	LP125	LP126	LP128	LP129	LP130	LP130X
SiO_2	60.11	61.08	57.24	57.50	61.68	58.34	59.35	55.73
TiO_2	0.57	0.62	0.68	0.68	0.54	0.73	0.65	0.54
Al_2O_3	16.93	16.72	15.14	15.14	17.24	16.62	16.96	16.11
Fe_2O_3 total	6.75	6.68	7.84	7.79	6.48	8.20	7.11	8.58
MnO	0.10	0.11	0.13	0.13	0.10	0.13	0.12	0.17
MgO	3.62	3.31	6.42	6.02	2.64	3.95	3.86	6.38
CaO	6.05	5.95	7.90	7.99	5.56	6.67	6.50	8.15
Na_2O	3.36	3.42	2.88	2.79	3.51	3.02	3.37	2.56
K_2O	1.28	1.45	1.11	1.12	1.40	1.50	1.24	0.87
P_2O_5	0.14	0.15	0.15	0.15	0.14	0.16	0.15	0.11
LOI	0.64	0.16	-0.28	-0.10	0.20	-0.06	-0.05	0.07
Total	99.93	99.74	99.60	99.41	99.59	99.43	99.41	99.35
Ba (XRF)	279	321	260	218	307	298	368	190
Sr (XRF)	222	234	334	413	220	229	251	222
Rb		46.3	34.1	31.8	45.3	49.4	36.6	
Sr (ICP-MS)		229	317	400	216	240	259	
Y		18.6	17.1	19.2	16.1	24.7	18.4	
Zr		102.9	99.7	109.3	106.6	111.9	96.0	
Nb		3.70	3.65	3.87	3.32	3.52	3.58	
Mo		0.19	0.34	0.67	0.18		0.16	
Cd		0.12	0.06	0.16	0.18	0.20	0.12	
In		0.07	0.05	0.50	0.03	0.29	0.25	
Sn				1.3			1.4	
Cs		1.48	0.66	0.76	1.38	1.91	0.81	
Ba (ICP-MS)		320	243	248	330	323	298	
La		11.9	13.9	13.8	11.3	15.1	11.2	
Ce		26.0	29.5	28.1	25.5	30.6	24.0	
Pr		3.17	3.67	3.71	3.09	4.03	2.97	
Nd		13.9	16.1	15.3	13.6	17.5	12.5	
Sm		3.59	3.79	3.43	3.45	4.06	3.09	
Eu		0.97	1.01	0.90	0.89	0.99	0.88	
Gd		3.37	3.50	3.23	3.03	4.02	2.96	
Tb		0.58	0.56	0.52	0.52	0.70	0.52	
Dy		3.77	3.50	3.33	3.29	4.38	3.46	
Ho		0.83	0.74	0.69	0.73	0.93	0.73	
Er		2.48	2.27	1.98	2.18	2.64	2.08	
Tm		0.38	0.33	0.31	0.32	0.41	0.33	
Yb		2.53	2.14	1.81	2.18	2.53	2.04	
Lu		0.38	0.31	0.27	0.31	0.37	0.31	
Hf		3.29	3.02	2.72	3.32	3.40	2.85	
Ta		0.4	0.3	0.3	0.3	0.4	0.3	
Tl		0.3	0.2	0.1	0.3	0.3	0.2	
Pb		8.5	7.2	5.8	6.3	8.0	5.8	
Th		4.19	4.15	5.78	3.74	3.44	3.98	
U		1.18	0.95	0.94	1.20	1.29	1.09	
Sc		18.3	27.5	30.5	14.4	25.0	22.9	
V		150	183	191	132	200	180	
Cr		47.5	213	198	17.9	51.4	31.3	
Co		18.8	29.5	28.0	13.9	22.4	21.6	
Ni		13.8	46.1	29.6	5.6	27.4	14.4	
Cu		29.7	42.6	58.3	21.3	35.2	19.7	
Zn		71.5	65.2	62.8	67.8	72.0	66.4	
Ga		16.6	15.8	16.1	18.0	16.6	16.2	
Eu/Eu*		0.85	0.85	0.82	0.84	0.75	0.89	
$^{87}Sr/^{86}Sr$						0.705163±5		
$^{143}Nd/^{144}Nd$						0.512771±44		
$^{206}Pb/^{204}Pb$						18.8396±30		
$^{207}Pb/^{204}Pb$						15.6327±43		
$^{208}Pb/^{204}Pb$						38.7505±92		
$^{207}Pb/^{206}Pb$						0.82978±12		
$^{208}Pb/^{206}Pb$						2.05686±21		

Major oxides in wt%, trace elements in ppm.

Table A5. Continued.

Sample	LP134	LP135	LP138	LP140	LP141	LP143	LP145	LP147
SiO_2	57.04	57.34	58.25	58.38	58.79	59.35	57.69	57.57
TiO_2	0.80	0.80	0.70	0.68	0.70	0.86	0.69	0.82
Al_2O_3	17.29	17.04	16.03	15.98	16.11	16.80	16.69	17.15
Fe_2O_3 total	7.89	8.20	6.92	7.30	6.92	7.68	7.42	8.17
MnO	0.14	0.14	0.12	0.12	0.11	0.19	0.12	0.14
MgO	4.10	4.17	5.51	5.12	5.21	2.80	5.02	4.04
CaO	6.92	6.96	6.82	6.90	6.82	5.56	7.48	7.13
Na_2O	2.97	3.02	3.04	3.10	3.14	3.39	3.08	3.04
K_2O	1.31	1.40	1.33	1.41	1.45	1.82	1.14	1.38
P_2O_5	0.15	0.16	0.15	0.15	0.15	0.20	0.14	0.17
LOI	0.26	-0.08	0.54	0.10	0.12	0.90	-0.10	-0.14
Total	98.97	99.32	99.68	99.38	99.67	99.68	99.57	99.69
Ba (XRF)	300	386	334	310	261	389	264	329
Sr (XRF)	258	254	321	348	332	295	230	257
Rb	40.8				47.9	57.5	33.3	46.0
Sr (ICP-MS)	269				317	286	233	272
Y	20.0				19.1	23.4	18.9	22.5
Zr	109.8				115.6	135.3	95.6	114.1
Nb	4.86				4.35	5.34	3.16	5.17
Mo	0.10				0.52	0.82	0.18	0.25
Cd	0.19				0.12	0.14	0.36	0.05
In	0.53				0.02	0.02		0.61
Sn	1.2							1.2
Cs	1.72				1.67	1.41	1.43	1.46
Ba (ICP-MS)	306				299	375	250	312
La	13.2				14.3	18.5	12.3	16.1
Ce	29.0				32.7	40.9	28.3	35.4
Pr	3.60				3.93	5.06	3.52	4.37
Nd	15.4				16.6	21.7	15.7	18.1
Sm	3.73				4.05	5.04	3.79	4.34
Eu	1.10				1.00	1.19	0.90	1.10
Gd	3.53				3.68	4.69	3.69	4.18
Tb	0.62				0.62	0.77	0.61	0.69
Dy	3.96				4.02	4.83	3.86	4.51
Ho	0.85				0.83	0.97	0.78	0.92
Er	2.35				2.47	2.77	2.31	2.58
Tm	0.37				0.36	0.42	0.34	0.40
Yb	2.33				2.37	2.62	2.26	2.51
Lu	0.34				0.35	0.38	0.33	0.37
Hf	3.43				3.46	3.86	2.90	3.55
Ta	0.4				0.4	0.5	0.3	0.4
Tl	0.2				0.2	0.4	0.4	0.4
Pb	7.8				5.6	6.3	9.5	8.0
Th	3.81				7.82	6.63	3.30	4.56
U	1.07				1.28	1.40	0.97	1.23
Sc	29.9				23.8	18.8	25.4	29.7
V	214				182	187	188	216
Cr	29.1				153	11.3	67.5	27.2
Co	22.7				24.0	20.1	25.7	22.2
Ni	8.6				39.8	7.3	33.5	5.2
Cu	10.4				44.6	23.5	319.8	13.4
Zn	86.5				72.3	120.9	76.3	78.4
Ga	18.8				18.0	18.4	18.0	19.1
Eu/Eu*	0.92				0.79	0.75	0.73	0.78
$^{87}Sr/^{86}Sr$								0.705751±4
$^{143}Nd/^{144}Nd$								0.512710±44
$^{206}Pb/^{204}Pb$								18.8470±16
$^{207}Pb/^{204}Pb$								15.6291±22
$^{208}Pb/^{204}Pb$								38.7524±68
$^{207}Pb/^{206}Pb$								0.82927±6
$^{208}Pb/^{206}Pb$								2.05616±24

Major oxides in wt%, trace elements in ppm.

Table A5. Continued.

Sample	LP149	LP150	LP151	LP152	LP155	LP156	LP157	LP158
SiO_2	59.98	59.93	59.88	59.19	57.82	60.45	58.82	61.13
TiO_2	0.62	0.74	0.74	0.75	0.86	0.85	0.66	0.71
Al_2O_3	16.47	16.39	16.20	16.81	15.80	17.09	15.79	17.00
Fe_2O_3 total	6.94	7.43	7.53	7.52	7.56	7.60	7.24	6.60
MnO	0.11	0.13	0.13	0.13	0.12	0.12	0.13	0.11
MgO	3.97	4.11	4.21	4.21	3.53	2.60	5.63	3.24
CaO	6.47	6.39	6.47	6.59	6.13	5.77	7.45	5.96
Na_2O	3.30	3.17	3.16	3.14	3.01	3.48	2.79	3.21
K_2O	1.30	1.57	1.55	1.44	1.57	1.74	1.20	1.77
P_2O_5	0.13	0.16	0.16	0.16	0.16	0.18	0.15	0.16
LOI	0.03	-0.02	-0.07	-0.02	0.12	0.07	0.33	0.30
Total	99.43	100.10	100.10	100.03	96.76	100.04	100.26	100.28
Ba (XRF)	277	312	351	287	342	454	260	379
Sr (XRF)	261	251	252	273	245	269	362	255
Rb	39.8		58.2	53.2				
Sr (ICP-MS)	252		272	291				
Y	15.8		22.8	21.1				
Zr	91.5		125.6	120.8				
Nb	3.45		5.34	5.83				
Mo	0.35		0.60	0.80				
Cd	0.02		0.07	0.07				
In			0.02	0.03				
Sn			0.2	1.4				
Cs	0.94		1.49	3.05				
Ba (ICP-MS)	293		318	313				
La	10.9		14.8	14.5				
Ce	23.7		32.6	31.6				
Pr	2.88		4.06	3.86				
Nd	12.7		16.5	15.7				
Sm	3.17		3.80	3.49				
Eu	0.83		1.01	0.96				
Gd	3.01		3.95	3.64				
Tb	0.51		0.61	0.57				
Dy	3.16		3.86	3.58				
Ho	0.70		0.80	0.75				
Er	1.96		2.29	2.19				
Tm	0.31		0.35	0.34				
Yb	2.05		2.25	2.11				
Lu	0.30		0.34	0.32				
Hf	2.80		3.37	3.20				
Ta	0.3		0.4	0.4				
Tl	0.2		0.2	0.3				
Pb	5.6		7.5	9.1				
Th	3.03		5.75	5.49				
U	1.05		1.40	1.25				
Sc	22.9		24.2	23.7				
V	171		185	186				
Cr	53.0		69.1	42.6				
Co	20.0		21.9	19.9				
Ni	14.5		18.0	13.3				
Cu	31.4		27.9	20.4				
Zn	63.6		76.4	74.2				
Ga	17.6		16.9	16.9				
Eu/Eu*	0.82		0.79	0.82				
$^{87}Sr/^{86}Sr$	0.704809±9		0.705612±11					
$^{143}Nd/^{144}Nd$	0.512824±4		0.512691±18					
$^{206}Pb/^{204}Pb$	18.8303±30		18.8545±15					
$^{207}Pb/^{204}Pb$	15.6287±43		15.6387±22					
$^{208}Pb/^{204}Pb$	38.7303±92		38.7748±67					
$^{207}Pb/^{206}Pb$	0.82998±12		0.82944±6					
$^{208}Pb/^{206}Pb$	2.05681±21		2.05652±24					

Major oxides in wt%, trace elements in ppm.

Table A5. Continued.

Sample	LP159	LP160	LP161	LP163	LP164	LP165	LP166	LP167
SiO_2	60.53	59.23	57.78	59.66	59.49	60.27	61.81	60.84
TiO_2	0.76	0.69	0.68	0.72	0.70	0.70	0.77	0.77
Al_2O_3	16.88	15.90	16.94	16.67	17.07	16.62	16.72	16.85
Fe_2O_3 total	7.26	7.33	7.72	7.22	6.90	7.06	6.84	7.17
MnO	0.13	0.13	0.13	0.12	0.11	0.12	0.10	0.11
MgO	3.08	5.15	4.44	3.41	3.15	3.23	2.59	2.99
CaO	5.84	6.78	7.56	6.24	6.36	6.15	5.59	5.95
Na_2O	3.35	3.10	3.13	3.21	2.97	3.31	3.48	3.40
K_2O	1.75	1.45	1.16	1.65	1.60	1.65	1.91	1.77
P_2O_5	0.17	0.16	0.14	0.16	0.15	0.16	0.18	0.17
LOI	0.21	-0.02	0.12	0.66	1.44	0.68	0.10	0.03
Total	100.05	100.00	99.84	99.79	100.00	100.01	100.18	100.12
Ba (XRF)	367	275	225	342	288	313	362	359
Sr (XRF)	278	317	223	229	238	237	265	273
Rb								
Sr (ICP-MS)								
Y								
Zr								
Nb								
Mo								
Cd								
In								
Sn								
Cs								
Ba (ICP-MS)								
La								
Ce								
Pr								
Nd								
Sm								
Eu								
Gd								
Tb								
Dy								
Ho								
Er								
Tm								
Yb								
Lu								
Hf								
Ta								
Tl								
Pb								
Th								
U								
Sc								
V								
Cr								
Co								
Ni								
Cu								
Zn								
Ga								
Eu/Eu*								
$^{87}Sr/^{86}Sr$								
$^{143}Nd/^{144}Nd$								
$^{206}Pb/^{204}Pb$								
$^{207}Pb/^{204}Pb$								
$^{208}Pb/^{204}Pb$								
$^{207}Pb/^{206}Pb$								
$^{208}Pb/^{206}Pb$								

Major oxides in wt%, trace elements in ppm.

Table A5. Continued.

Sample	LP168	LP169	LP170	LP171	LP172	LP173	LP174	LP175A
SiO_2	56.94	57.93	57.67	58.32	57.17	60.39	56.78	58.13
TiO_2	0.77	0.78	0.76	0.81	0.77	0.79	0.69	0.68
Al_2O_3	16.67	16.37	16.62	16.70	16.71	17.08	15.17	16.12
Fe_2O_3 total	8.55	7.94	8.29	8.25	8.69	6.73	8.05	7.69
MnO	0.13	0.14	0.14	0.13	0.14	0.12	0.14	0.13
MgO	4.50	4.28	4.35	4.17	4.65	3.61	6.87	4.94
CaO	6.92	6.76	6.94	6.84	7.22	5.63	7.83	7.45
Na_2O	2.67	2.67	2.90	3.01	2.87	3.24	2.67	3.12
K_2O	1.34	1.84	1.37	1.48	1.26	1.81	0.97	1.19
P_2O_5	0.16	0.16	0.15	0.17	0.15	0.17	0.15	0.15
LOI	1.48	0.62	0.54	-0.13	0.32	0.65	0.36	-0.26
Total	100.20	99.57	99.78	99.95	99.99	100.35	99.75	99.70
Ba (XRF)	257	306	309	323	288	419	238	281
Sr (XRF)	206	228	211	253	215	255	314	449
Rb	45.0						31.2	37.3
Sr (ICP-MS)	231						324	441
Y	24.6						18.3	18.8
Zr	104.4						97.4	102.6
Nb	4.21						3.98	4.01
Mo	0.81						0.57	0.60
Cd	0.08						0.06	0.06
In	0.03						0.02	0.02
Sn	1.2						0.9	0.9
Cs	2.89						1.64	0.88
Ba (ICP-MS)	267						237	258
La	11.9						11.6	12.4
Ce	25.2						24.9	26.4
Pr	3.39						3.20	3.31
Nd	14.4						13.2	13.7
Sm	3.52						3.02	3.10
Eu	0.96						0.90	0.90
Gd	3.78						3.15	3.19
Tb	0.62						0.50	0.51
Dy	4.08						3.11	3.19
Ho	0.87						0.66	0.67
Er	2.51						1.86	1.91
Tm	0.38						0.28	0.29
Yb	2.44						1.82	1.88
Lu	0.37						0.27	0.28
Hf	2.85						2.70	2.76
Ta	0.3						0.3	0.3
Tl	0.2						0.2	0.1
Pb	7.3						5.9	5.9
Th	4.12						3.80	4.08
U	1.11						0.93	1.05
Sc	26.5						28.5	25.1
V	221						191	190
Cr	59.7						255	61.4
Co	27.4						30.2	25.3
Ni	30.3						54.2	27.3
Cu	49.9						27.1	110.9
Zn	78.5						69.7	69.5
Ga	16.2						15.5	17.0
Eu/Eu*	0.80						0.89	0.87
$^{87}Sr/^{86}Sr$								
$^{143}Nd/^{144}Nd$								
$^{206}Pb/^{204}Pb$								
$^{207}Pb/^{204}Pb$								
$^{208}Pb/^{204}Pb$								
$^{207}Pb/^{206}Pb$								
$^{208}Pb/^{206}Pb$								

Major oxides in wt%, trace elements in ppm.

Table A5. Continued.

Sample	LP175B	LP179	LP180	LP181	LP182	LP183	LP184	LP185
SiO_2	60.56	56.93	57.36	58.46	57.89	61.47	58.77	57.93
TiO_2	0.70	0.81	0.81	0.80	0.80	0.69	0.71	0.80
Al_2O_3	16.44	17.24	17.25	17.03	17.04	16.61	16.51	17.13
Fe_2O_3 total	6.97	8.40	8.70	7.68	8.15	6.61	7.28	8.10
MnO	0.11	0.14	0.14	0.14	0.14	0.11	0.11	0.14
MgO	3.98	4.32	3.97	4.16	4.27	3.15	4.73	4.05
CaO	5.89	7.04	6.73	7.06	7.22	5.87	5.55	7.00
Na_2O	3.14	2.92	2.90	3.04	2.98	3.17	2.93	3.00
K_2O	1.92	1.24	1.18	1.39	1.32	1.82	1.31	1.33
P_2O_5	0.16	0.15	0.14	0.16	0.16	0.16	0.15	0.16
LOI	0.18	0.73	1.00	-0.06	-0.03	0.31	2.32	0.18
Total	100.13	100.01	100.24	100.00	100.03	100.04	100.67	99.89
Ba (XRF)	432	305	305	288	280	334	317	375
Sr (XRF)	210	258	250	258	256	248	306	259
Rb	79.4			39.7	44.4			
Sr (ICP-MS)	234			258	267			
Y	22.8			21.0	22.9			
Zr	133.3			118.6	124.6			
Nb	5.32			5.03	5.06			
Mo	0.70			0.44	0.86			
Cd	0.08			0.06	0.07			
In	0.03			0.02	0.02			
Sn	1.5			1.1	1.4			
Cs	3.25			2.16	1.30			
Ba (ICP-MS)	398			299	288			
La	15.9			13.5	13.6			
Ce	32.1			30.2	31.1			
Pr	4.22			3.74	3.89			
Nd	17.2			15.6	16.1			
Sm	3.81			3.60	3.81			
Eu	0.94			0.99	1.00			
Gd	3.98			3.60	3.89			
Tb	0.61			0.59	0.64			
Dy	3.76			3.73	3.98			
Ho	0.78			0.77	0.82			
Er	2.19			2.18	2.36			
Tm	0.33			0.33	0.36			
Yb	2.11			2.04	2.28			
Lu	0.32			0.29	0.34			
Hf	3.69			3.48	4.12			
Ta	0.4			0.5	0.6			
Tl	0.4			0.1	0.2			
Pb	9.6			8.8	8.3			
Th	6.88			4.93	4.89			
U	1.84			1.13	1.09			
Sc	21.5			25.9	27.3			
V	179			194	206			
Cr	76.8			25.1	26.5			
Co	20.5			20.4	21.7			
Ni	27.3			6.6	6.6			
Cu	40.1			11.3	11.0			
Zn	66.6			80.3	81.9			
Ga	16.7			17.0	17.4			
Eu/Eu*	0.73			0.83	0.79			
$^{87}Sr/^{86}Sr$								
$^{143}Nd/^{144}Nd$								
$^{206}Pb/^{204}Pb$								
$^{207}Pb/^{204}Pb$								
$^{208}Pb/^{204}Pb$								
$^{207}Pb/^{206}Pb$								
$^{208}Pb/^{206}Pb$								

Major oxides in wt%, trace elements in ppm.

Table A5. Continued.

Sample	LP186	LP187	LP190	LP191	LP192	LP193	LP194	LP197
SiO_2	61.28	60.49	60.27	58.05	58.96	58.84	59.24	57.88
TiO_2	0.69	0.72	0.79	0.68	0.69	0.68	0.69	0.72
Al_2O_3	16.47	16.98	16.97	16.16	15.71	16.00	16.07	16.61
Fe_2O_3 total	6.85	7.00	7.19	7.15	7.40	7.38	7.22	8.14
MnO	0.12	0.12	0.12	0.12	0.13	0.13	0.12	0.11
MgO	3.18	3.52	3.49	5.28	5.48	5.41	5.05	4.92
CaO	5.91	5.90	5.80	7.16	7.01	6.92	6.78	6.41
Na_2O	3.17	3.12	3.25	3.27	3.08	3.07	3.15	3.01
K_2O	1.80	1.67	1.79	1.35	1.38	1.37	1.44	1.24
P_2O_5	0.16	0.16	0.17	0.14	0.15	0.15	0.16	0.11
LOI	0.28	0.43	0.26	0.22	0.00	0.08	0.03	1.02
Total	99.99	100.18	100.21	99.65	100.06	100.08	100.02	100.24
Ba (XRF)	360	353	342	232	262	264	301	259
Sr (XRF)	230	246	265	308	306	344	327	307
Rb		60.6	71.7					
Sr (ICP-MS)		252	271					
Y		25.4	21.2					
Zr		135.7	147.8					
Nb		5.34	6.58					
Mo		1.99	0.77					
Cd		0.08	0.08					
In		0.02	0.03					
Sn		1.7	1.7					
Cs		2.74	4.71					
Ba (ICP-MS)		338	383					
La		17.4	16.3					
Ce		38.5	35.0					
Pr		4.82	4.15					
Nd		19.9	16.4					
Sm		4.48	3.70					
Eu		1.06	1.06					
Gd		4.46	3.71					
Tb		0.70	0.59					
Dy		4.33	3.62					
Ho		0.90	0.76					
Er		2.58	2.16					
Tm		0.39	0.34					
Yb		2.46	2.19					
Lu		0.36	0.33					
Hf		4.00	3.90					
Ta		0.6	0.5					
Tl		0.2	0.3					
Pb		14.5	9.8					
Th		5.85	7.07					
U		1.53	1.55					
Sc		21.4	21.8					
V		163	164					
Cr		21.1	33.1					
Co		19.1	18.5					
Ni		10.1	11.1					
Cu		16.3	42.6					
Zn		80.7	74.1					
Ga		16.6	17.7					
Eu/Eu*		0.73	0.87					
$^{87}Sr/^{86}Sr$		0.705284±11						
$^{143}Nd/^{144}Nd$		0.512721±17						
$^{206}Pb/^{204}Pb$		18.8460±30						
$^{207}Pb/^{204}Pb$		15.6307±43						
$^{208}Pb/^{204}Pb$		38.7544±92						
$^{207}Pb/^{206}Pb$		0.82939±12						
$^{208}Pb/^{206}Pb$		2.05637±21						

Major oxides in wt%, trace elements in ppm.

Table A5. Continued.

Sample	LP198	LP199	LP200	LP201	LP202	LP203	LP204	LP205
SiO_2	58.68	58.34	58.84	59.61	60.33	59.64	60.54	59.57
TiO_2	0.71	0.70	0.69	0.75	0.76	0.77	0.75	0.75
Al_2O_3	16.38	16.18	16.30	16.68	16.57	16.48	16.58	16.37
Fe_2O_3 total	7.64	7.63	7.16	7.70	7.48	7.82	7.15	7.77
MnO	0.12	0.12	0.13	0.14	0.13	0.13	0.12	0.13
MgO	4.89	5.37	5.20	3.62	3.29	3.74	3.27	3.77
CaO	6.36	6.66	6.67	6.10	6.10	6.32	5.91	6.37
Na_2O	2.97	3.00	3.05	3.11	3.26	3.22	3.37	3.25
K_2O	1.45	1.34	1.38	1.58	1.66	1.58	1.76	1.56
P_2O_5	0.15	0.14	0.15	0.16	0.16	0.17	0.17	0.17
LOI	0.69	0.51	0.57	0.68	0.14	0.28	0.42	0.02
Total	100.11	100.07	100.21	100.21	99.96	100.22	100.13	99.80
Ba (XRF)	255	283	308	344	359	268	331	318
Sr (XRF)	317	322	331	252	259	270	249	275
Rb					49.5		56.8	
Sr (ICP-MS)					255		256	
Y					20.4		21.6	
Zr					144.0		146.0	
Nb					5.99		5.83	
Mo					3.84		4.79	
Cd					0.08		0.08	
In					0.01		0.02	
Sn					1.7		2.1	
Cs					3.16		3.95	
Ba (ICP-MS)					344		346	
La					14.8		14.1	
Ce					33.3		31.4	
Pr					3.93		3.87	
Nd					16.3		15.8	
Sm					3.69		3.67	
Eu					0.96		0.96	
Gd					3.70		3.69	
Tb					0.60		0.58	
Dy					3.68		3.68	
Ho					0.75		0.77	
Er					2.17		2.26	
Tm					0.33		0.34	
Yb					2.09		2.19	
Lu					0.31		0.32	
Hf					4.02		3.89	
Ta					0.6		0.7	
Tl					0.2		0.2	
Pb					12.7		12.4	
Th					5.99		6.17	
U					1.41		1.62	
Sc					21.8		18.9	
V					174		151	
Cr					22.6		39.2	
Co					17.7		17.7	
Ni					8.0		15.8	
Cu					9.9		16.1	
Zn					77.2		74.5	
Ga					17.0		16.9	
Eu/Eu*					0.79		0.79	
$^{87}Sr/^{86}Sr$								
$^{143}Nd/^{144}Nd$								
$^{206}Pb/^{204}Pb$								
$^{207}Pb/^{204}Pb$								
$^{208}Pb/^{204}Pb$								
$^{207}Pb/^{206}Pb$								
$^{208}Pb/^{206}Pb$								

Major oxides in wt%, trace elements in ppm.

Table A5. Continued.

Sample	LP206	LP208	LP209	LP211	LP212	LP213	LP214	LP215
SiO_2	60.23	60.61	53.77	61.03	60.36	59.24	60.99	60.84
TiO_2	0.76	0.75	0.83	0.76	0.72	0.72	0.65	0.68
Al_2O_3	16.69	16.62	17.92	16.44	16.85	17.41	17.05	16.75
Fe_2O_3 total	7.14	7.23	9.50	7.50	7.22	7.48	6.91	7.23
MnO	0.12	0.12	0.16	0.13	0.12	0.13	0.12	0.12
MgO	3.19	3.32	5.32	3.34	3.32	3.60	3.18	3.61
CaO	5.79	5.82	7.91	5.94	6.16	6.08	5.99	5.93
Na_2O	3.35	3.37	2.72	3.27	3.44	3.04	3.28	3.07
K_2O	1.75	1.78	0.74	1.76	1.75	1.34	1.75	1.69
P_2O_5	0.17	0.17	0.15	0.16	0.15	0.16	0.14	0.15
LOI	0.00	0.66	0.74	-0.15	0.00	0.96	0.25	0.23
Total	99.27	100.52	99.81	100.40	100.17	100.23	100.38	100.37
Ba (XRF)	378	346	297	423	360	373	330	360
Sr (XRF)	251	247	258	233	246	218	225	228
Rb				63.7			63.8	61.5
Sr (ICP-MS)				244			232	234
Y				23.4			23.4	23.1
Zr				153.8			130.2	133.9
Nb				5.84			5.43	5.23
Mo				1.47			1.26	1.23
Cd				0.07			0.08	0.07
In				0.01			0.00	0.01
Sn				2.0			1.6	1.8
Cs				2.87			2.36	2.73
Ba (ICP-MS)				361			360	338
La				15.0			17.6	16.0
Ce				33.3			34.0	33.7
Pr				4.08			4.36	4.24
Nd				16.5			17.4	17.3
Sm				3.81			3.88	3.78
Eu				1.00			0.94	0.93
Gd				3.97			3.95	3.88
Tb				0.64			0.62	0.61
Dy				3.95			3.89	3.77
Ho				0.82			0.79	0.79
Er				2.41			2.30	2.30
Tm				0.37			0.35	0.35
Yb				2.28			2.19	2.22
Lu				0.35			0.33	0.32
Hf				4.79			3.80	3.67
Ta				0.6			0.6	0.6
Tl				0.2			0.3	0.1
Pb				11.4			18.6	10.8
Th				6.50			6.04	5.97
U				1.60			1.58	1.59
Sc				21.5			20.2	21.0
V				177			154	162
Cr				33.1			24.1	27.6
Co				19.5			18.8	20.2
Ni				13.2			9.8	10.8
Cu				19.8			20.8	22.2
Zn				75.8			66.7	71.5
Ga				17.2			16.6	16.7
Eu/Eu*				0.78			0.73	0.74
$^{87}Sr/^{86}Sr$				0.705482±11			0.705420±16	
$^{143}Nd/^{144}Nd$							0.512707±18	
$^{206}Pb/^{204}Pb$				18.8532±30			18.8461±30	
$^{207}Pb/^{204}Pb$				15.6345±43			15.6333±43	
$^{208}Pb/^{204}Pb$				38.7627±92			38.7579±92	
$^{207}Pb/^{206}Pb$				0.82928±12			0.82953±12	
$^{208}Pb/^{206}Pb$				2.05602±21			2.05655±21	

Major oxides in wt%, trace elements in ppm.

Table A5. Continued.

Sample	LP217	LP218	LP219	LP220	LP221	LP222	LP224	LP225
SiO_2	61.29	60.96	60.64	60.89	60.51	60.32	61.41	58.52
TiO_2	0.75	0.76	0.72	0.71	0.71	0.71	0.71	0.68
Al_2O_3	16.58	16.38	16.82	16.78	16.67	16.67	16.72	15.76
Fe_2O_3 total	7.08	7.29	7.12	7.10	7.11	7.14	6.96	7.70
MnO	0.11	0.12	0.12	0.12	0.12	0.12	0.12	0.13
MgO	3.03	3.41	3.33	3.31	3.30	3.38	3.28	5.38
CaO	5.72	5.76	5.67	5.91	5.75	6.00	5.90	7.15
Na_2O	3.40	3.35	3.21	3.26	3.20	3.22	3.25	3.07
K_2O	1.84	1.83	1.74	1.77	1.76	1.71	1.79	1.34
P_2O_5	0.17	0.17	0.17	0.17	0.16	0.17	0.16	0.15
LOI	-0.02	0.02	0.41	0.04	0.80	0.66	0.05	-0.07
Total	100.06	100.12	100.03	100.10	100.16	100.17	100.42	99.95
Ba (XRF)	354	358	395	328	371	366	385	296
Sr (XRF)	260	239	231	242	241	247	239	350
Rb						63.9		
Sr (ICP-MS)						259		
Y						22.4		
Zr						128.9		
Nb						5.35		
Mo						0.93		
Cd						0.07		
In						0.03		
Sn						1.6		
Cs						3.64		
Ba (ICP-MS)						340		
La						14.9		
Ce						31.7		
Pr						3.93		
Nd						16.0		
Sm						3.67		
Eu						0.98		
Gd						3.72		
Tb						0.59		
Dy						3.70		
Ho						0.78		
Er						2.21		
Tm						0.35		
Yb						2.21		
Lu						0.33		
Hf						3.66		
Ta						0.4		
Tl						0.3		
Pb						9.4		
Th						6.22		
U						1.61		
Sc						20.4		
V						167		
Cr						20.4		
Co						19.0		
Ni						8.2		
Cu						15.6		
Zn						72.6		
Ga						16.8		
Eu/Eu*						0.81		
$^{87}Sr/^{86}Sr$								
$^{143}Nd/^{144}Nd$								
$^{206}Pb/^{204}Pb$								
$^{207}Pb/^{204}Pb$								
$^{208}Pb/^{204}Pb$								
$^{207}Pb/^{206}Pb$								
$^{208}Pb/^{206}Pb$								

Major oxides in wt%, trace elements in ppm.

Table A5. Continued.

Sample	LP226	LP227	LP228	LP229	LP231	LP232	LP233	LP234
SiO_2	58.09	59.07	58.53	58.55	57.55	58.05	60.78	64.84
TiO_2	0.68	0.69	0.71	0.71	0.68	0.67	0.71	0.65
Al_2O_3	16.00	16.52	16.95	16.94	15.06	14.94	16.70	16.13
Fe_2O_3 total	7.72	7.24	7.73	7.70	7.75	7.59	6.95	5.30
MnO	0.12	0.12	0.12	0.12	0.14	0.14	0.12	0.09
MgO	5.49	4.79	4.23	4.20	5.84	6.01	3.17	2.52
CaO	6.87	6.66	6.92	6.90	7.96	8.05	5.91	4.67
Na_2O	3.03	3.04	3.12	3.15	2.74	2.80	3.21	3.30
K_2O	1.35	1.34	1.16	1.15	1.05	1.12	1.73	2.27
P_2O_5	0.12	0.15	0.15	0.15	0.15	0.15	0.16	0.17
LOI	0.33	0.68	0.28	0.39	0.41	0.03	0.57	0.37
Total	99.90	100.36	99.95	100.01	99.40	99.62	100.08	100.39
Ba (XRF)	282	305	259	255	233	224	339	435
Sr (XRF)	339	340	222	222	398	406	243	200
Rb			64.6			34.5	55.4	90.1
Sr (ICP-MS)			218			400	243	209
Y			26.8			18.2	21.1	22.2
Zr			124.1			95.8	142.6	172.4
Nb			5.05			3.83	5.64	6.43
Mo			0.85			0.54	1.24	1.20
Cd			0.06			0.06	0.07	0.08
In			0.07			0.02	0.01	0.02
Sn			2.1			1.0	1.8	2.2
Cs			1.86			1.60	3.58	2.96
Ba (ICP-MS)			328			233	356	426
La			12.9			12.2	14.6	11.8
Ce			28.7			26.5	31.6	26.1
Pr			3.66			3.38	3.96	3.30
Nd			15.5			13.9	16.2	13.5
Sm			3.73			3.17	3.69	3.36
Eu			0.95			0.90	0.90	0.96
Gd			3.94			3.19	3.70	3.31
Tb			0.66			0.50	0.58	0.56
Dy			4.18			3.11	3.66	3.64
Ho			0.92			0.64	0.75	0.76
Er			2.59			1.80	2.18	2.23
Tm			0.41			0.28	0.33	0.36
Yb			2.61			1.76	2.13	2.27
Lu			0.40			0.27	0.32	0.35
Hf			3.44			2.58	4.00	5.06
Ta			0.4			0.3	0.7	0.7
Tl			0.5			0.1	0.3	0.4
Pb			8.5			5.8	12.3	14.3
Th			5.42			3.73	6.41	7.94
U			1.47			0.92	1.64	2.17
Sc			18.4			27.0	18.7	16.9
V			157			191	160	132
Cr			32.0			183	17.7	41.6
Co			19.6			26.3	17.2	14.4
Ni			24.6			30.2	8.1	15.2
Cu			21.1			54.7	15.1	23.6
Zn			72.5			67.9	66.3	65.9
Ga			16.1			15.6	16.6	16.2
Eu/Eu*			0.75			0.86	0.74	0.88
$^{87}Sr/^{86}Sr$								0.705308±11
$^{143}Nd/^{144}Nd$								0.512733±17
$^{206}Pb/^{204}Pb$								18.8342±26
$^{207}Pb/^{204}Pb$								15.6240±28
$^{208}Pb/^{204}Pb$								38.7337±81
$^{207}Pb/^{206}Pb$								0.82956±7
$^{208}Pb/^{206}Pb$								2.05656±24

Major oxides in wt%, trace elements in ppm.

Table A5. Continued.

Sample	LP235	LP236	LP237	LP238	LP239	LP240	LP241	LP242
SiO_2	58.45	60.76	61.55	58.64	61.89	58.61	56.64	59.72
TiO_2	0.83	0.58	0.83	0.64	0.73	0.75	0.77	0.74
Al_2O_3	16.58	17.00	16.74	15.95	16.71	16.73	16.74	16.83
Fe_2O_3 total	7.10	6.66	6.36	7.69	6.67	8.23	8.74	7.36
MnO	0.11	0.09	0.10	0.13	0.10	0.13	0.14	0.12
MgO	3.65	3.58	2.44	5.44	3.03	3.82	4.80	3.43
CaO	4.42	6.27	5.20	7.19	5.56	6.54	7.35	6.09
Na_2O	1.98	3.41	2.88	2.82	3.27	3.02	2.88	3.28
K_2O	1.62	1.22	2.07	1.03	1.74	1.47	1.19	1.61
P_2O_5	0.17	0.14	0.19	0.14	0.17	0.17	0.16	0.16
LOI	3.72	0.40	1.64	0.37	0.33	0.50	0.29	0.00
Total	98.67	100.17	100.33	100.14	100.30	100.04	99.78	99.40
Ba (XRF)	351	258	453	196	366	324	300	297
Sr (XRF)	128	220	270	326	189	239	225	224
Rb				31.9	61.1			54.4
Sr (ICP-MS)				325	205			237
Y				20.6	33.3			21.3
Zr				94.3	138.4			125.3
Nb				3.68	5.21			5.01
Mo				1.05	1.48			0.91
Cd				0.06	0.06			0.06
In				0.01	0.01			0.01
Sn				1.1	1.8			1.7
Cs				1.06	2.25			1.92
Ba (ICP-MS)				220	352			317
La				10.4	16.1			12.6
Ce				23.3	38.5			28.2
Pr				3.06	5.00			3.51
Nd				13.2	22.1			14.5
Sm				3.22	5.56			3.45
Eu				0.93	1.29			0.93
Gd				3.37	5.83			3.56
Tb				0.57	0.95			0.56
Dy				3.53	5.87			3.63
Ho				0.73	1.20			0.75
Er				2.16	3.45			2.20
Tm				0.32	0.54			0.33
Yb				2.13	3.42			2.11
Lu				0.32	0.49			0.32
Hf				2.85	3.87			3.36
Ta				0.5	0.5			0.5
Tl				0.1	0.2			0.2
Pb				5.1	9.8			13.7
Th				3.29	5.60			5.38
U				0.94	1.54			1.43
Sc				26.3	19.7			20.7
V				200	183			173
Cr				149	32.6			10.9
Co				29.3	27.9			20.1
Ni				41.8	20.2			5.0
Cu				60.5	37.3			9.9
Zn				85.1	118.6			69.3
Ga				15.3	16.7			17.2
Eu/Eu*				0.86	0.69			0.81
$^{87}Sr/^{86}Sr$					0.705240±11			
$^{143}Nd/^{144}Nd$					0.512774±17			
$^{206}Pb/^{204}Pb$					18.8335±30			
$^{207}Pb/^{204}Pb$					15.6275±43			
$^{208}Pb/^{204}Pb$					38.7368±93			
$^{207}Pb/^{206}Pb$					0.82977±12			
$^{208}Pb/^{206}Pb$					2.05680±21			

Major oxides in wt%, trace elements in ppm.

Table A5. Continued.

Sample	LP243	LP244	LP245	LP247	LP248	LP249	LP250
SiO_2	60.45	59.10	58.39	58.37	59.37	56.25	59.41
TiO_2	0.77	0.70	0.66	0.67	0.72	0.66	0.76
Al_2O_3	16.94	16.20	15.28	15.24	16.21	15.68	15.49
Fe_2O_3 total	7.11	7.50	7.83	7.88	7.46	8.26	8.19
MnO	0.12	0.13	0.13	0.13	0.13	0.14	0.13
MgO	2.91	4.86	5.56	5.58	4.23	6.56	4.88
CaO	5.78	6.38	7.57	7.55	6.71	7.23	6.40
Na_2O	3.61	3.11	2.87	2.88	3.21	2.44	3.09
K_2O	1.82	1.50	1.28	1.29	1.50	1.12	1.56
P_2O_5	0.17	0.15	0.14	0.14	0.16	0.14	0.15
LOI	0.71	0.31	-0.08	-0.12	0.04	1.55	-0.04
Total	100.48	100.01	99.79	99.80	99.81	100.20	100.13
Ba (XRF)	383	310	251	244	317	222	303
Sr (XRF)	256	290	357	358	255	314	226
Rb			62.2	46.6		39.0	51.1
Sr (ICP-MS)			280	347		313	246
Y			21.3	19.1		16.0	22.3
Zr			128.8	113.9		96.2	138.5
Nb			5.51	4.52		3.99	5.60
Mo			0.74	0.83		0.65	0.48
Cd			0.08	0.05		0.05	0.06
In			0.03	0.01		0.02	0.02
Sn			1.4	1.6		1.7	1.7
Cs			2.77	2.94		2.21	1.77
Ba (ICP-MS)			355	258		216	333
La			13.9	11.7		8.2	13.3
Ce			30.0	26.0		18.1	29.3
Pr			3.74	3.19		2.21	3.67
Nd			15.3	12.9		9.3	15.0
Sm			3.54	3.11		2.33	3.60
Eu			1.03	0.81		0.70	0.97
Gd			3.58	3.13		2.41	3.67
Tb			0.57	0.51		0.41	0.60
Dy			3.55	3.24		2.70	3.79
Ho			0.75	0.69		0.59	0.80
Er			2.13	1.99		1.67	2.37
Tm			0.33	0.30		0.26	0.35
Yb			2.16	1.89		1.73	2.22
Lu			0.33	0.28		0.26	0.34
Hf			3.50	3.46		2.77	3.73
Ta			0.4	0.6		0.3	0.5
Tl			0.3	0.1		0.1	0.3
Pb			8.3	8.8		4.0	14.1
Th			5.92	4.65		4.09	5.48
U			1.52	1.16		1.04	1.35
Sc			19.8	26.6		27.8	24.7
V			176	189		188	194
Cr			13.0	178		259	155
Co			17.8	27.3		29.0	26.0
Ni			5.8	46.4		59.7	46.2
Cu			7.9	64.9		53.7	43.3
Zn			73.6	70.8		64.1	77.6
Ga			17.6	16.2		15.6	17.0
Eu/Eu*			0.88	0.79		0.90	0.81
$^{87}Sr/^{86}Sr$			0.705393±11				0.705471±11
$^{143}Nd/^{144}Nd$			0.512723±18				0.512690±19
$^{206}Pb/^{204}Pb$			18.8483±30				18.8484±30
$^{207}Pb/^{204}Pb$			15.6314±43				15.6332±43
$^{208}Pb/^{204}Pb$			38.7583±92				38.7591±92
$^{207}Pb/^{206}Pb$			0.82933±12				0.82942±12
$^{208}Pb/^{206}Pb$			2.05633±21				2.05636±21

Major oxides in wt%, trace elements in ppm.

Table A5. Continued.

Sample	MSR15017A	MSR15018	MSR15019	MSR15020A	MSR15021	MSR15022	MSR15023
SiO_2	59.52	59.99	56.77	58.70	57.94	60.10	60.29
TiO_2	0.62	0.65	0.68	0.65	0.65	0.60	0.54
Al_2O_3	17.43	17.10	15.54	17.38	17.36	16.81	16.76
Fe_2O_3 total	6.87	6.99	7.82	6.99	6.96	6.72	6.77
MnO	0.11	0.12	0.14	0.12	0.12	0.12	0.12
MgO	3.54	3.74	6.31	3.74	3.74	3.35	4.17
CaO	6.59	6.75	8.14	6.28	6.55	5.40	6.58
Na_2O	3.32	3.42	2.76	3.20	3.21	3.11	3.20
K_2O	1.23	1.28	0.99	1.18	1.10	1.49	1.11
P_2O_5	0.12	0.14	0.13	0.12	0.12	0.12	0.10
LOI	0.70	0.19	0.86	1.26	1.97	2.19	0.72
Total	100.08	100.46	100.18	99.65	99.75	100.07	100.41
Ba (XRF)		307					
Sr (XRF)		233					
Rb		36.4	30.5				22.6
Sr (ICP-MS)		260	363				213
Y		19.5	19.4				16.2
Zr		95.2	110.2				97.6
Nb		3.46	3.76				3.27
Mo			0.94				0.83
Cd		0.11	0.19				
In		0.66	0.05				0.00
Sn		1.6	1.0				
Cs		0.84	1.82				1.26
Ba (ICP-MS)		302	226				303
La		12.5	12.5				11.0
Ce		25.5	26.7				22.6
Pr		3.24	3.27				2.86
Nd		13.7	14.2				12.0
Sm		3.26	3.29				2.93
Eu		0.92	0.93				0.79
Gd		3.30	3.45				2.87
Tb		0.57	0.58				0.51
Dy		3.72	3.40				3.17
Ho		0.78	0.72				0.68
Er		2.20	2.23				2.01
Tm		0.36	0.34				0.31
Yb		2.18	2.15				2.15
Lu		0.33	0.33				0.31
Hf		2.97	3.66				2.78
Ta		0.3	0.3				0.3
Tl		0.2	0.3				0.2
Pb		6.2	5.9				6.8
Th		3.43	3.42				6.71
U		1.11	0.83				1.04
Sc		22.4	31.7				21.1
V		170	206				162
Cr		29.6	234				91.4
Co		20.4	32.5				21.9
Ni		12.6	47.9				31.2
Cu		26.7	55.4				39.4
Zn		67.1	84.4				64.8
Ga		17.2	18.5				16.4
Eu/Eu*		0.86	0.84				0.83
$^{87}Sr/^{86}Sr$		0.704946±4	0.704825±11				0.705170±12
$^{143}Nd/^{144}Nd$		0.512847±45	0.512737±17				0.512693±71
$^{206}Pb/^{204}Pb$		18.8300±30	18.8418±43				
$^{207}Pb/^{204}Pb$		15.6248±43	15.6275±57				
$^{208}Pb/^{204}Pb$		38.7238±92	38.7464±154				
$^{207}Pb/^{206}Pb$		0.82979±12	0.82941±14				
$^{208}Pb/^{206}Pb$		2.05650±21	2.05640±39				

Major oxides in wt%, trace elements in ppm.

Table A5. Continued.

Sample	MSR15024	MSR15025	MSR15026	MSR15027	MSR15028	MSR15029	MSR15030
SiO_2	56.72	65.87	60.45	59.72	57.61	57.48	57.14
TiO_2	0.70	0.48	0.81	0.81	0.68	0.67	0.67
Al_2O_3	16.58	16.15	17.08	17.07	15.21	16.18	16.12
Fe_2O_3 total	7.89	4.60	7.23	7.33	7.79	7.65	7.64
MnO	0.13	0.08	0.12	0.12	0.13	0.13	0.13
MgO	5.48	1.94	2.89	2.98	6.43	5.53	5.49
CaO	8.08	4.64	6.18	6.06	8.38	7.25	6.96
Na_2O	3.03	3.54	3.53	3.45	2.90	2.99	2.93
K_2O	1.00	1.95	1.56	1.61	1.15	1.32	1.27
P_2O_5	0.14	0.13	0.15	0.16	0.14	0.14	0.12
LOI	0.39	0.37	0.11	0.09	0.00	0.37	1.74
Total	100.26	99.85	100.16	99.53	100.54	99.84	100.28
Ba (XRF)	284	384		332	252	273	
Sr (XRF)	456	177		229	317	304	
Rb		67.7					
Sr (ICP-MS)		199					
Y		21.6					
Zr		136.1					
Nb		4.93					
Mo		1.26					
Cd		0.05					
In		0.02					
Sn		1.0					
Cs		1.93					
Ba (ICP-MS)		412					
La		12.1					
Ce		26.8					
Pr		3.25					
Nd		13.1					
Sm		3.06					
Eu		0.81					
Gd		3.13					
Tb		0.52					
Dy		3.30					
Ho		0.73					
Er		2.09					
Tm		0.34					
Yb		2.20					
Lu		0.35					
Hf		3.75					
Ta		0.4					
Tl		0.3					
Pb		8.0					
Th		6.28					
U		1.83					
Sc		11.5					
V		100					
Cr		19.6					
Co		11.4					
Ni		10.4					
Cu		25.7					
Zn		49.8					
Ga		14.4					
Eu/Eu*		0.80					
$^{87}Sr/^{86}Sr$							
$^{143}Nd/^{144}Nd$							
$^{206}Pb/^{204}Pb$							
$^{207}Pb/^{204}Pb$							
$^{208}Pb/^{204}Pb$							
$^{207}Pb/^{206}Pb$							
$^{208}Pb/^{206}Pb$							

Major oxides in wt%, trace elements in ppm.

Table A5. Continued.

Sample	MSR15031	MSR15032	MSR15033	MSR15034	MSR15035	MSR15037	MSR15038
SiO_2	57.32	57.18	55.94	56.93	57.60	56.19	60.12
TiO_2	0.68	0.68	0.70	0.68	0.68	0.69	0.80
Al_2O_3	15.14	15.17	15.64	15.20	15.32	15.70	17.06
Fe_2O_3 total	7.82	7.88	8.01	7.90	7.85	7.89	7.31
MnO	0.13	0.13	0.14	0.14	0.14	0.14	0.11
MgO	6.48	6.51	6.55	6.70	6.61	6.35	2.85
CaO	8.61	8.50	8.47	8.35	7.98	8.17	6.06
Na_2O	2.79	2.76	2.76	2.82	2.74	2.65	3.57
K_2O	1.08	1.08	0.99	1.11	1.10	0.95	1.66
P_2O_5	0.14	0.14	0.14	0.14	0.13	0.13	0.17
LOI	-0.21	-0.11	0.43	-0.18	0.46	1.38	0.04
Total	100.29	100.15	99.89	100.07	100.66	100.31	99.84
Ba (XRF)	240	225	199	223			267
Sr (XRF)	339	353	327	305			228
Rb							
Sr (ICP-MS)							
Y							
Zr							
Nb							
Mo							
Cd							
In							
Sn							
Cs							
Ba (ICP-MS)							
La							
Ce							
Pr							
Nd							
Sm							
Eu							
Gd							
Tb							
Dy							
Ho							
Er							
Tm							
Yb							
Lu							
Hf							
Ta							
Tl							
Pb							
Th							
U							
Sc							
V							
Cr							
Co							
Ni							
Cu							
Zn							
Ga							
Eu/Eu*							
$^{87}Sr/^{86}Sr$							
$^{143}Nd/^{144}Nd$							
$^{206}Pb/^{204}Pb$							
$^{207}Pb/^{204}Pb$							
$^{208}Pb/^{204}Pb$							
$^{207}Pb/^{206}Pb$							
$^{208}Pb/^{206}Pb$							

Major oxides in wt%, trace elements in ppm.

Table A5. Continued.

Sample	RPC110 (RPC090)	TG084	TG088
SiO_2	58.14	58.69	59.39
TiO_2	0.68	0.73	0.73
Al_2O_3	17.00	16.96	16.54
Fe_2O_3 total	6.82	7.51	7.31
MnO	0.13	0.12	0.12
MgO	4.62	3.86	4.37
CaO	7.19	7.21	7.29
Na_2O	3.03	3.23	3.16
K_2O	1.19	1.30	1.48
P_2O_5	0.13	0.14	0.14
LOI	1.45	-0.18	-0.54
Total	101.37	99.57	99.99
Ba (XRF)	245	304	317
Sr (XRF)	225	267	295
Rb	39.8	44.1	46.6
Sr (ICP-MS)	240	270	288
Y	13.5	23.1	20.4
Zr	67.1	121.1	127.7
Nb	3.75	4.72	5.07
Mo	0.34	0.42	0.87
Cd	0.06	0.07	0.07
In	0.03	0.01	0.01
Sn	0.4	1.5	1.6
Cs	1.46	1.32	2.23
Ba (ICP-MS)	266	312	307
La	7.5	13.8	12.9
Ce	15.8	28.6	28.5
Pr	1.99	3.64	3.44
Nd	8.3	15.3	14.3
Sm	2.14	3.63	3.37
Eu	0.86	0.97	0.93
Gd	2.05	3.69	3.34
Tb	0.37	0.59	0.55
Dy	2.49	3.78	3.52
Ho	0.53	0.81	0.73
Er	1.53	2.32	2.18
Tm	0.25	0.35	0.32
Yb	1.61	2.25	2.05
Lu	0.24	0.33	0.30
Hf	1.74	3.27	3.98
Ta	0.3	0.5	0.6
Tl	0.1	0.1	0.1
Pb	5.0	7.7	9.5
Th	2.73	4.56	5.21
U	0.56	1.08	1.29
Sc	25.6	23.7	25.0
V	204	195	193
Cr	62.5	11.1	104
Co	26.3	23.7	23.7
Ni	32.0	9.0	26.5
Cu	19.4	23.6	19.6
Zn	63.8	73.0	70.0
Ga	17.3	17.4	16.5
Eu/Eu*	1.26	0.81	0.85
$^{87}Sr/^{86}Sr$	0.705253±11	0.705268±11	0.705059±11
$^{143}Nd/^{144}Nd$	0.512672±31	0.512743±18	0.512713±18
$^{206}Pb/^{204}Pb$	18.8344±30	18.8413±30	18.8447±30
$^{207}Pb/^{204}Pb$	15.6290±43	15.6278±43	15.6336±43
$^{208}Pb/^{204}Pb$	38.7385±92	38.7447±93	38.7541±92
$^{207}Pb/^{206}Pb$	0.82982±12	0.82945±12	0.82960±12
$^{208}Pb/^{206}Pb$	2.05679±21	2.05637±21	2.05649±21

Major oxides in wt%, trace elements in ppm.

Appendix 6

Groundmass separates major element, trace element and Sr-Nd-Pb isotopic composition

A6.1. INTRODUCTION

This chapter reports ICP-MS and TIMS analyses for groundmass separates which have paired whole-rock samples (see Appendix 5). Groundmass samples are denoted with a 'GM' suffix, relative to whole-rock samples which share the same sample code. Trace elements, Ti, Fe, Mn, Na and P concentrations were determined via solution ICP-MS. Sr, Ba and Zr were analysed on both low and medium resolution (MR), as indicated in Table A6.1, below. Sr-Nd-Pb isotopic compositions were determined via TIMS and are reported with quadratically combined 2 s.e. internal errors and 2 s.d. external reproducibility errors. Major oxide data is reported in wt% and trace element data is reported in ppm. Eu/Eu* values are calculated as $Eu_N/sqrt(Sm_N*Gd_N)$ after normalisation with the values of McDonough and Sun (1995). $^{87}Sr/^{86}Sr$ data are reported relative to NBS987 = 0.710248 (Thirlwall, 1991). $^{143}Nd/^{144}Nd$ data are reported relative to JNdi-1 = 0.512515 which is equivalent to La Jolla = 0.511858 (Lugmair and Carlson, 1978; Tanaka et al., 2000). Pb isotope data are reported relative to NBS981 values recommended by Thirlwall (2000) of $^{206}Pb/^{204}Pb$ = 16.9409, $^{207}Pb/^{204}Pb$ = 15.4956, $^{208}Pb/^{204}Pb$ = 38.7228, $^{207}Pb/^{206}Pb$ = 0.91469, $^{208}Pb/^{206}Pb$ = 2.16770.

Table A6. Groundmass major element, trace element and Sr-Nd-Pb isotopic compositions.

Sample	CC351GM	GL2223GM	LP001GM	LP010GM	LP023GM	LP033GM	LP036GM
Digestion batch	5	5	5	8	5	5	8
ICP-MS batch	T5	T5	T5	T8	T5	T5	T8
TiO_2 (wt%)	0.74	0.87	0.88		0.82	0.55	
Fe_2O_3	5.48	4.86	4.30		5.24	3.89	
MnO	0.12	0.11	0.09		0.12	0.10	
Na_2O	2.59	2.83	2.82		2.64	3.04	
P_2O_5	0.13	0.19	0.20		0.16	0.13	
Rb (ppm)	35.9	52.7	67.9	64.5	49.8	47.7	52.8
Sr	401	303	314	202	228	201	242
Y	16.4	19.2	17.9	26.0	21.0	19.4	19.6
Zr	111	143	160	149	135	126	122
Nb	4.83	6.55	5.95	6.31	5.72	4.66	4.60
Mo	0.43	0.78	1.11	0.41	0.54	0.59	0.56
Cd	0.14	0.16	0.56	0.12	0.18	0.18	0.09
In	0.04	0.04	0.04	0.04	0.05	0.03	0.02
Sn	1.3	1.4	2.8	1.4	1.5	0.9	0.1
Cs	2.2	1.7	4.5	1.7	1.2	1.5	1.3
Ba	258	331	423	355	336	386	382
La	13.0	15.1	15.4	16.6	15.5	12.8	12.7
Ce	27.7	33.2	33.6	35.5	33.9	25.3	26.1
Pr	3.43	4.06	4.08	4.48	4.24	3.33	3.37
Nd	14.1	16.8	16.9	18.4	17.7	13.9	14.0
Sm	3.15	3.78	3.75	4.28	4.04	3.14	3.26
Eu	0.92	1.01	1.02	0.86	0.96	0.88	0.86
Gd	3.29	3.97	3.84	4.18	4.25	3.44	3.18
Tb	0.57	0.66	0.64	0.67	0.71	0.59	0.51
Dy	3.35	3.85	3.65	4.25	4.21	3.59	3.20
Ho	0.71	0.80	0.74	0.92	0.87	0.77	0.71
Er	2.11	2.37	2.18	2.53	2.58	2.33	1.99
Tm	0.31	0.35	0.31	0.39	0.38	0.35	0.31
Yb	2.04	2.27	2.07	2.50	2.52	2.33	2.06
Lu	0.32	0.35	0.31	0.37	0.39	0.37	0.32
Hf	3.25	3.79	4.34	4.26	3.72	3.49	3.16
Ta	0.6	0.5	0.5	0.7	0.5	0.5	0.4
Tl	0.2	0.2	0.4	0.3	0.3	0.3	0.2
Pb	8.0	9.7	12.6	7.6	7.0	8.9	5.5
Th	4.98	6.06	7.17	6.33	5.87	5.23	4.97
U	1.12	1.48	1.99	1.53	1.41	1.50	1.52
Na	4809	5245	5238		4900	5632	
P	553	825	879		703	588	
Sc	24.2	20.5	17.7	20.5	22.7	17.6	17.8
Ti	4409	5225	5300		4924	3288	
V	213	213	178	170	212	125	161
Cr	34.1	43.3	130	90.6	78.4	42.8	52.6
Mn	948	882	702		958	800	
Fe	37650	33397	29550		36000	26693	
Co	23.9	18.8	21.9	17.3	22.1	16.6	17.9
Ni	22.9	16.0	77.9	17.8	26.2	18.0	14.0
Cu	61.6	51.6	169	42.9	80.9	71.9	45.9
Zn	94.5	105.4	85.3	65.8	116	100.5	67.9
Ga	18.9	17.6	18.1	15.8	16.6	15.0	14.9
Sr (MR)	432	320	330	191	236	205	223
Zr (MR)	114	143	158	153	136	126	118
Ba (MR)	259	324	408	354	317	367	365
Eu/Eu*		0.79	0.82	0.62	0.71	0.82	0.81
$^{87}Sr/^{86}Sr$		0.704589±11					
$^{143}Nd/^{144}Nd$		0.512758±17					
$^{206}Pb/^{204}Pb$		18.8247±16					
$^{207}Pb/^{204}Pb$		15.6288±23					
$^{208}Pb/^{204}Pb$		38.7331±68					
$^{207}Pb/^{206}Pb$		0.83023±6					
$^{208}Pb/^{206}Pb$		2.05757±24					

Major oxides in wt%, trace elements in ppm.

Table A6. Continued.

Sample	LP039GM	LP051GM	LP062GM	LP072GM	LP074GM	LP080GM	LP097GM
Digestion batch	5	5	5	5	5	8	8
ICP-MS batch	T5	T5	T5	T5	T5	T8	T8
TiO_2 (wt%)	0.65	0.76	0.66	0.62	0.73		
Fe_2O_3	4.04	3.66	4.53	3.72	4.82		
MnO	0.10	0.06	0.11	0.09	0.11		
Na_2O	3.23	3.06	2.80	3.27	3.44		
P_2O_5	0.14	0.16	0.13	0.15	0.18		
Rb (ppm)	47.2	104	37.1	47.6	31.3	70.1	23.0
Sr	240	152	357	245	238	277	326
Y	17.5	30.3	14.7	20.0	20.5	25.2	19.7
Zr	117	225	108	135	108	177	121
Nb	4.90	8.39	4.41	4.72	4.16	6.83	3.43
Mo	0.57	1.17	0.51	0.62	0.53	0.64	0.37
Cd	0.13	0.18	0.14	0.14	0.14	0.12	0.11
In	0.04	0.04	0.04	0.03	0.05	0.04	0.03
Sn	1.0	1.3	1.3	1.0	0.9	1.3	0.5
Cs	1.5	3.2	0.9	1.2	0.7	4.1	1.3
Ba	362	530	255	388	324	398	231
La	12.0	33.1	12.1	12.1	11.0	17.8	11.1
Ce	24.0	50.5	26.4	25.7	23.6	39.6	23.9
Pr	3.12	7.68	3.21	3.38	3.23	4.74	3.07
Nd	13.1	30.6	13.2	14.2	14.2	19.2	12.7
Sm	3.02	6.29	2.92	3.35	3.41	4.35	3.02
Eu	0.87	1.17	0.84	0.92	1.00	0.99	0.88
Gd	3.26	6.66	3.13	3.68	3.72	4.16	3.07
Tb	0.56	1.04	0.51	0.63	0.65	0.66	0.50
Dy	3.34	6.00	3.00	3.83	3.97	4.22	3.34
Ho	0.71	1.22	0.62	0.82	0.84	0.89	0.73
Er	2.12	3.59	1.85	2.44	2.52	2.47	2.05
Tm	0.31	0.51	0.27	0.37	0.37	0.38	0.33
Yb	2.13	3.31	1.78	2.51	2.49	2.48	2.13
Lu	0.34	0.51	0.27	0.40	0.40	0.37	0.32
Hf	3.20	5.82	3.02	3.69	3.06	4.42	2.98
Ta	0.4	0.7	0.5	0.4	0.4	0.6	0.3
Tl	0.3	0.5	0.2	0.3	0.2	0.3	0.2
Pb	6.7	10.1	4.9	6.4	6.2	10.4	4.8
Th	4.78	10.0	4.36	5.01	3.19	7.40	4.19
U	1.40	2.84	1.07	1.48	0.92	1.64	0.93
Na	5991	5671	5196	6070	6383		
P	607	709	575	640	807		
Sc	15.6	12.6	24.0	14.8	16.5	20.1	26.6
Ti	3869	4554	3932	3703	4387		
V	151	129	187	146	189	198	219
Cr	15.6	7.8	161	48.2	17.5	64.4	35.0
Mn	771	497	855	669	861		
Fe	27775	25135	31124	25563	33089		
Co	15.1	12.1	24.5	13.9	17.0	18.4	23.8
Ni	8.6	10.7	66.0	13.6	10.0	16.4	9.0
Cu	29.4	48.5	151	49.4	36.2	33.1	20.6
Zn	76.4	71.8	66.7	67.1	85.9	72.4	83.1
Ga	16.2	15.6	16.7	16.2	18.2	17.5	18.2
Sr (MR)	246	151	365	253	245	264	312
Zr (MR)	116	218	106	129	107	162	108
Ba (MR)	344	505	240	376	311	376	223
Eu/Eu*	0.84	0.55	0.85	0.80	0.86	0.71	0.88
$^{87}Sr/^{86}Sr$					0.704905±11		0.704748±9
$^{143}Nd/^{144}Nd$					0.512852±19		0.512795±5
$^{206}Pb/^{204}Pb$					18.8307±15		
$^{207}Pb/^{204}Pb$					15.6278±22		
$^{208}Pb/^{204}Pb$					38.7228±66		
$^{207}Pb/^{206}Pb$					0.82991±6		
$^{208}Pb/^{206}Pb$					2.05637±24		

Major oxides in wt%, trace elements in ppm.

Table A6. Continued.

Sample	LP103GM	LP109GM	LP113GM	LP118GM	LP126GM	LP129GM	LP147GM
Digestion batch	5	8	8	5	5	5	5
ICP-MS batch	T5	T8	T8	T5	T5	T5	T5
TiO_2 (wt%)	0.98			0.91	0.72	0.90	0.86
Fe_2O_3	4.86			5.22	4.89	5.30	5.10
MnO	0.11			0.12	0.12	0.12	0.13
Na_2O	3.05			2.71	2.52	2.57	2.60
P_2O_5	0.17			0.18	0.15	0.19	0.15
Rb	90.7	49.1	42.7	58.9	44.3	69.3	57.0
Sr	169	235	258	234	375	194	226
Y	28.1	12.7	10.3	21.9	16.1	23.9	21.7
Zr	216	54.0	102	146	108	157	144
Nb	8.74	3.70	3.08	6.23	4.62	6.07	6.16
Mo	0.66	0.48	0.16	0.77	0.51	0.91	0.48
Cd	0.17	0.05	0.06	0.15	0.15	0.19	0.17
In	0.07	0.02	0.02	0.04	0.04	0.05	0.06
Sn	2.3	0.5	0.3	1.5	1.3	1.5	1.4
Cs	2.6	1.7	1.1	2.0	0.9	2.6	1.8
Ba	524	433	368	345	260	371	350
La	26.4	10.5	9.0	15.9	13.5	15.6	16.0
Ce	38.2	19.3	17.6	34.3	27.9	33.8	35.9
Pr	6.92	2.48	2.10	4.37	3.64	4.34	4.36
Nd	27.9	9.6	8.0	18.7	15.0	18.4	18.2
Sm	5.88	2.05	1.67	4.19	3.23	4.23	4.09
Eu	1.17	0.67	0.59	1.11	0.93	1.04	1.03
Gd	6.14	2.05	1.67	4.47	3.47	4.65	4.39
Tb	0.99	0.32	0.26	0.74	0.56	0.78	0.73
Dy	5.78	2.03	1.68	4.36	3.29	4.72	4.36
Ho	1.17	0.43	0.37	0.90	0.67	0.99	0.91
Er	3.46	1.21	1.05	2.65	1.97	2.93	2.66
Tm	0.51	0.19	0.17	0.39	0.28	0.43	0.39
Yb	3.28	1.27	1.19	2.54	1.88	2.80	2.54
Lu	0.52	0.20	0.19	0.40	0.29	0.44	0.39
Hf	5.60	1.70	2.55	3.96	2.96	4.17	3.84
Ta	0.7	0.3	0.3	0.6	0.4	0.5	0.5
Tl	0.5	0.1	0.2	0.3	0.2	0.4	0.4
Pb	10.8	9.1	6.4	9.0	6.7	9.1	8.4
Th	9.30	3.65	3.98	6.07	4.31	6.29	6.09
U	2.29	0.94	1.07	1.51	1.08	1.71	1.40
Na	5658			5024	4672	4765	4819
P	752			767	667	825	669
Sc	18.8	10.0	9.5	22.5	24.0	22.0	25.3
Ti	5890			5428	4334	5414	5167
V	164	136	72	211	188	223	217
Cr	0.9	27.0	14.0	9.6	111	15.4	14.7
Mn	849			917	925	919	990
Fe	33407			35845	33577	36398	35012
Co	11.6	10.1	10.8	19.5	23.6	20.9	19.5
Ni	1.7	17.0	11.9	5.5	22.7	15.0	4.5
Cu	10.5	16.4	23.9	13.7	55.3	29.6	15.6
Zn	98.5	56.1	49.9	83.9	73.8	89.5	87.9
Ga	17.9	16.4	15.9	17.1	16.5	16.0	17.6
Sr (MR)	171	218	252	240	386	194	230
Zr (MR)	208	48	96	143	106	152	141
Ba (MR)	500	418	366	331	251	355	338
Eu/Eu*	0.60	0.99	1.08	0.78	0.84	0.71	0.74
$^{87}Sr/^{86}Sr$	0.706137±11		0.705357±11				0.705718±11
$^{143}Nd/^{144}Nd$	0.512631±18		0.512791±22				0.512671±18
$^{206}Pb/^{204}Pb$	18.8623±15		18.8285±20				18.8403±17
$^{207}Pb/^{204}Pb$	15.6391±22		15.6223±28				15.6339±24
$^{208}Pb/^{204}Pb$	38.7851±67		38.7122±87				38.7617±71
$^{207}Pb/^{206}Pb$	0.82912±6		0.82972±7				0.82981±7
$^{208}Pb/^{206}Pb$	2.05622±24		2.05604±28				2.05738±25

Major oxides in wt%, trace elements in ppm.

Table A6. Continued.

Sample	LP149GM	LP151GM	LP187GM	LP198GM	LP211GM	LP214GM	LP234GM
Digestion batch	5	8	8	9	8	8	8
ICP-MS batch	T5	T8	T8	T8	T8	T8	T8
TiO_2 (wt%)	0.62						
Fe_2O_3	3.79						
MnO	0.09						
Na_2O	3.13						
P_2O_5	0.14						
Rb (ppm)	47.4	84.4	93.9	59.4	86.2	79.9	109
Sr	230	240	216	312	219	174	156
Y	16.5	28.4	29.3	22.4	28.6	24.9	21.9
Zr	119	206	193	139	183	165	205
Nb	4.98	7.89	7.19	5.39	7.20	6.58	7.66
Mo	0.48	0.54	0.65	2.83	0.79	0.72	0.74
Cd	0.13	0.11	0.14	0.07	0.11	0.10	0.11
In	0.04	0.03	0.04	0.01	0.04	0.03	0.03
Sn	0.9	1.5	1.4	1.4	1.4	1.2	1.9
Cs	1.2	2.0	3.4	1.9	3.4	2.5	3.1
Ba	370	458	425	360	433	399	513
La	11.4	20.7	20.0	14.7	18.5	18.5	12.9
Ce	24.3	45.5	44.8	30.6	40.2	32.9	28.9
Pr	3.01	5.53	5.46	4.10	4.99	4.64	3.60
Nd	12.5	22.1	22.1	16.8	20.3	18.6	14.8
Sm	2.84	5.01	5.12	3.92	4.69	4.14	3.61
Eu	0.87	1.11	1.04	1.01	1.07	0.84	0.92
Gd	3.08	4.81	4.96	3.92	4.57	4.03	3.42
Tb	0.53	0.76	0.78	0.63	0.74	0.64	0.58
Dy	3.26	4.84	5.00	3.83	4.76	4.13	3.74
Ho	0.69	1.02	1.05	0.79	1.01	0.88	0.80
Er	2.05	2.79	2.92	2.31	2.84	2.44	2.28
Tm	0.31	0.43	0.45	0.34	0.44	0.38	0.36
Yb	2.06	2.77	2.92	2.16	2.88	2.46	2.41
Lu	0.33	0.42	0.44	0.31	0.44	0.37	0.37
Hf	3.30	5.26	4.89	3.98	4.87	4.39	5.26
Ta	0.5	0.7	0.6	0.6	0.7	0.6	0.6
Tl	0.3	0.3	0.5	0.1	0.3	0.3	0.6
Pb	6.4	9.5	14.6	11.0	9.9	11.8	12.9
Th	4.88	8.88	8.62	6.14	8.09	8.07	9.77
U	1.42	2.09	2.18	1.50	2.01	2.14	2.80
Na	5806						
P	627						
Sc	14.6	15.8	18.9	18.8	19.2	18.6	10.5
Ti	3735						
V	136	121	200	186	182	182	107
Cr	12.7	18.4	12.9	92.6	12.1	14.8	14.2
Mn	733						
Fe	26027						
Co	13.4	12.4	16.6	19.1	15.2	16.2	6.8
Ni	7.2	8.0	6.8	24.8	8.4	6.7	6.5
Cu	27.3	25.3	16.5	35.2	20.4	21.2	25.7
Zn	69.3	63.4	73.8	79.4	73.8	65.3	51.7
Ga	15.9	17.6	17.0	17.1	17.7	15.5	15.3
Sr (MR)	234	230	202	320	208	166	147
Zr (MR)	117	191	184	134	181	164	202
Ba (MR)	361	454	417	381	429	396	507
Eu/Eu*	0.90	0.69	0.63	0.79	0.70	0.62	0.79
$^{87}Sr/^{86}Sr$	0.704870±15		0.705243±11		0.705559±11		0.705381±11
$^{143}Nd/^{144}Nd$	0.512818±17		0.512725±17		0.512696±17		0.512744±17
$^{206}Pb/^{204}Pb$	18.8284±15		18.8448±15		18.8496±15		18.8394±15
$^{207}Pb/^{204}Pb$	15.6267±22		15.6290±22		15.6308±22		15.6300±22
$^{208}Pb/^{204}Pb$	38.7226±67		38.7481±67		38.7513±67		38.7432±66
$^{207}Pb/^{206}Pb$	0.82996±6		0.82936±6		0.82924±6		0.82965±6
$^{208}Pb/^{206}Pb$	2.05660±24		2.05616±24		2.05581±24		2.05649±24

Major oxides in wt%, trace elements in ppm.

Table A6. Continued.

Sample	LP239GM	LP245GM	LP250GM	MSR15018GM	MSR15019GM	MSR15020AGM
Digestion batch	10	8	10	8	5	10
ICP-MS batch	T10	T8	T10	T8	T5	T10
TiO_2 (wt%)					0.73	
Fe_2O_3					5.00	
MnO					0.13	
Na_2O					2.40	
P_2O_5					0.15	
Rb (ppm)	83.8	80.2	77.3	51.2	29.8	42.9
Sr	171	243	224	228	335	227
Y	37.6	22.6	25.1	22.4	15.9	21.1
Zr	167	171	157	128	106	121
Nb	6.83	6.89	6.71	4.91	4.43	4.79
Mo	1.67	0.78	0.60	0.27	0.53	0.67
Cd	0.23	0.11	0.16	0.09	0.16	0.14
In	0.05	0.03	0.07	0.03	0.04	0.03
Sn	1.2	1.2	1.7	0.8	1.0	0.9
Cs	2.4	3.8	2.1	1.1	1.6	1.5
Ba	434	442	384	373	268	371
La	19.3	16.5	15.7	13.7	12.4	12.2
Ce	45.8	35.9	34.5	28.2	26.6	25.3
Pr	5.94	4.34	4.32	3.63	3.37	3.34
Nd	24.7	17.3	17.1	15.0	14.1	13.4
Sm	6.04	4.00	4.02	3.49	3.18	3.08
Eu	1.34	1.02	1.02	0.91	0.93	0.94
Gd	6.67	3.85	4.31	3.52	3.34	3.43
Tb	1.05	0.62	0.69	0.58	0.55	0.56
Dy	6.40	3.95	4.17	3.73	3.25	3.38
Ho	1.35	0.84	0.92	0.81	0.68	0.76
Er	3.88	2.36	2.58	2.27	2.00	2.16
Tm	0.58	0.37	0.39	0.35	0.29	0.33
Yb	3.79	2.45	2.59	2.32	1.92	2.20
Lu	0.55	0.37	0.37	0.36	0.30	0.36
Hf	4.68	4.35	4.47	3.25	2.91	3.16
Ta	0.5	0.5	0.5	0.4	0.4	0.4
Tl	0.1	0.4	0.1	0.2	0.2	0.1
Pb	12.3	9.5	15.7	5.4	6.7	9.2
Th	7.43	7.58	7.05	4.89	4.25	4.84
U	1.97	2.01	1.69	1.43	1.03	1.29
Na					4444	
P					658	
Sc	17.1	16.2	21.1	15.8	24.7	16.7
Ti					4352	
V	190	149	183	137	196	143
Cr	10.9	4.2	85.9	6.1	157	6.1
Mn					989	
Fe					34357	
Co	26.9	13.2	20.3	14.3	25.2	15.6
Ni	11.0	46.4	26.1	6.5	34.1	6.9
Cu	42.2	8.0	44.8	65.4	50.3	57.4
Zn	134	65.2	78.4	67.8	80.1	92.6
Ga	17.0	17.5	17.5	16.7	16.6	16.7
Sr (MR)		228		207	337	
Zr (MR)	166	170	161	126	106	121
Ba (MR)		433		368	257	
Eu/Eu*	0.64	0.79	0.74	0.79	0.87	0.88
$^{87}Sr/^{86}Sr$						
$^{143}Nd/^{144}Nd$						
$^{206}Pb/^{204}Pb$						
$^{207}Pb/^{204}Pb$						
$^{208}Pb/^{204}Pb$						
$^{207}Pb/^{206}Pb$						
$^{208}Pb/^{206}Pb$						

Major oxides in wt%, trace elements in ppm.

Table A6. Continued.

Sample	MSR15023GM	RPC110GM	TG084GM	TG088GM
Digestion batch	8	8	10	8
ICP-MS batch	T8	T8	T10	T8
TiO_2 (wt%)				
Fe_2O_3				
MnO				
Na_2O				
P_2O_5				
Rb (ppm)	26.3	62.6	60.7	74.4
Sr	195	210	224	267
Y	19.2	14.8	27.1	24.2
Zr	111	98.8	145	159
Nb	3.91	4.56	6.16	6.57
Mo	0.39	0.34	0.49	0.83
Cd	0.08	0.07	0.18	0.15
In	0.03	0.03	0.07	0.05
Sn	0.7	0.6	0.8	4.0
Cs	1.4	2.5	1.5	3.0
Ba	358	284	390	432
La	11.1	8.6	16.8	16.8
Ce	22.0	18.2	35.0	36.5
Pr	2.88	2.25	4.60	4.19
Nd	11.6	9.1	18.5	18.3
Sm	2.75	2.32	4.21	4.23
Eu	0.74	0.86	1.07	1.00
Gd	2.81	2.26	4.68	4.05
Tb	0.48	0.40	0.73	0.69
Dy	3.15	2.68	4.45	4.15
Ho	0.69	0.58	0.95	0.85
Er	1.95	1.68	2.77	2.65
Tm	0.31	0.27	0.40	0.39
Yb	2.06	1.85	2.67	2.49
Lu	0.32	0.28	0.40	0.42
Hf	2.88	2.74	4.05	4.35
Ta	0.4	0.4	0.4	0.6
Tl	0.2	0.2	0.0	0.3
Pb	7.4	5.8	9.1	9.8
Th	4.86	4.00	6.07	7.49
U	1.29	0.88	1.39	1.84
Na				
P				
Sc	19.9	27.0	21.3	18.2
Ti				
V	150	217	208	176
Cr	60.6	66.8	6.8	32.7
Mn				
Fe				
Co	18.1	26.1	20.8	16.0
Ni	22.1	31.9	6.7	11.8
Cu	67.6	20.8	25.9	18.1
Zn	71.9	69.3	78.8	59.6
Ga	15.9	16.2	17.2	17.9
Sr (MR)	180	196		
Zr (MR)	107	94	148	
Ba (MR)	343	275		
Eu/Eu*	0.81	1.15	0.73	0.74
$^{87}Sr/^{86}Sr$				0.704924±11
$^{143}Nd/^{144}Nd$				
$^{206}Pb/^{204}Pb$				18.8336±19
$^{207}Pb/^{204}Pb$				15.6218±24
$^{208}Pb/^{204}Pb$				38.7274±72
$^{207}Pb/^{206}Pb$				0.82947±7
$^{208}Pb/^{206}Pb$				2.05629±24

Major oxides in wt%, trace elements in ppm.

Appendix 7

Xenolith major oxide, trace element and Sr-Nd-Pb isotopic compositions

A7.1. INTRODUCTION

This appendix reports all major oxide (in wt%), trace element (in ppm) and Sr-Nd-Pb isotope compositions measured in metasedimentary xenoliths and one non-arc type basement xenolith (LP168X). The data were previously reported in section 4.3.2. Sr-Nd-Pb isotope ratios are reported with quadratically combined 2 s.e. internal analytical uncertainties and 2 s.d. external reproducibilities. Eu/Eu* values are calculated as $Eu_N/sqrt(Sm_N*Gd_N)$ after normalisation with the values of McDonough and Sun (1995). $^{87}Sr/^{86}Sr$ data are reported relative to NBS987 = 0.710248 (Thirlwall, 1991). $^{143}Nd/^{144}Nd$ data are reported relative to JNdi-1 = 0.512515 which is equivalent to La Jolla = 0.511858 (Lugmair and Carlson, 1978; Tanaka et al., 2000). Pb isotope data are reported relative to NBS981 values recommended by Thirlwall (2000) of $^{206}Pb/^{204}Pb$ = 16.9409, $^{207}Pb/^{204}Pb$ = 15.4956, $^{208}Pb/^{204}Pb$ = 38.7228, $^{207}Pb/^{206}Pb$ = 0.91469, $^{208}Pb/^{206}Pb$ = 2.16770.

Table A7. Major oxide, trace element and Sr-Nd-Pb isotopic compositions of metasedimentary xenoliths and LP168X (non-arc type basement xenolith).

Sample	LP134X	LP147X	LP168X	LP181X	LP182X	LP186X
SiO_2 (wt%)	63.24	48.17	49.33	49.89	49.40	50.73
Al_2O_3	19.61	25.07	19.97	20.15	25.46	15.10
TiO_2	0.36	1.53	1.29	1.57	0.91	0.75
MnO	0.07	0.11	0.19	0.15	0.09	0.22
Fe_2O_3 total	3.19	8.92	10.59	10.96	7.80	10.65
MgO	1.04	3.15	2.59	3.74	2.84	5.28
CaO	6.53	8.86	10.50	7.47	8.39	11.12
Na_2O	3.90	3.69	2.53	3.78	3.95	2.33
K_2O	1.18	0.34	0.30	0.79	0.47	1.06
P_2O_5	0.19	0.23	0.28	0.55	0.24	0.11
LOI	0.20	-0.34	1.64	-0.35	0.11	2.97
Total	99.68	100.16	99.32	99.17	99.75	100.39
Rb (ppm)	23.71	6.49	20.84	19.86	10.78	38.43
Sr	879.3	487.5	694	540.2	495.9	235.9
Y	27.00	20.91	51.21	46.37	22.36	25.79
Zr	39	46.4	64.1	71.7	28.3	62.1
Nb	5.12	19.27	2.37	20.25	10.86	2.59
Mo	0.20	0.48	1.5	0.59	0.41	0.74
Cd	0.03	0.06	0.11	0.06	0.03	0.14
In	0.01	0.03	0.05	0.04	0.02	0.05
Sn	0.23	0.36	1.27	1.11	0.75	1.37
Cs	0.37	0.96	4.63	1.17	1.72	1.4
Ba	513	320	116	614	371	184
La	24.21	40.03	12.01	53.21	37.63	10.98
Ce	49.87	80.52	18.1	115.01	77.53	21.97
Pr	5.96	8.81	4.58	13.53	8.83	2.84
Nd	24.55	34.14	22.43	52.86	32.57	12.01
Sm	4.74	6.27	6.32	10.85	6.14	3.03
Eu	1.15	1.71	1.76	2.3	1.82	0.84
Gd	4.53	5.75	7.45	10.43	5.82	3.43
Tb	0.68	0.78	1.28	1.54	0.77	0.58
Dy	4.03	4.21	8.27	8.62	4.12	3.81
Ho	0.85	0.80	1.74	1.67	0.78	0.82
Er	2.32	2.18	4.82	4.51	2.11	2.37
Tm	0.34	0.30	0.72	0.65	0.29	0.38
Yb	2.14	1.84	4.41	4.12	1.68	2.44
Lu	0.31	0.27	0.67	0.55	0.24	0.39
Hf	1.10	1.62	1.94	2.46	0.93	2.08
Ta	0.42	1.64	0.21	1.72	0.99	0.27
Tl	0.09	0.08	0.08	0.09	0.08	0.19
Pb	7.02	5.16	13.84	10.73	7.33	6.03
Th	3.01	11.52	0.19	19.5	10.67	2.9
U	0.55	0.92	0.34	3	1.25	0.71
Sc	6.9	22.1	41.8	31.8	13.3	36.9
V	53.1	218	312	248	149	322
Cr	3.2	103	695	102	57.6	154
Co	5.5	22.7	46.5	23.1	15.6	31.2
Ni	1.9	22.5	99.6	26.2	12.9	20.8
Cu	0.70	4.9	133	6.6	6.4	37.9
Zn	31.1	160	211	153	135	101
Ga	21.9	39.3	19.0	26.4	33.1	15.5
Eu/Eu*	0.72	0.82	0.78	0.66	0.93	0.79
$^{87}Sr/^{86}Sr$	0.707199±23	0.706825±23	0.707761±23	0.708062±23	0.707823±23	0.705449±23
$^{143}Nd/^{144}Nd$	0.512748±9	0.512488±9	0.512835±8	0.512470±9	0.512427±10	0.512722±9
$^{206}Pb/^{204}Pb$	18.8303±17	18.8702±33	18.8085±15	18.8855±16	18.8760±30	18.8460±30
$^{207}Pb/^{204}Pb$	15.6285±23	15.6428±45	15.6544±22	15.6531±23	15.6473±44	15.6309±43
$^{208}Pb/^{204}Pb$	38.7396±68	38.7865±97	38.7965±66	38.8305±69	38.8017±94	38.7539±92
$^{207}Pb/^{206}Pb$	0.82997±6	0.82897±12	0.83231±6	0.82885±7	0.82895±12	0.82940±12
$^{208}Pb/^{206}Pb$	2.05730±24	2.05543±21	2.06271±24	2.05610±24	2.05561±22	2.05634±21

Note: major oxides in wt% and trace elements in ppm.

Table A7. Continued.

Sample	LP187X	LP202X	LP204X	LP205X	LP214X
SiO_2 (wt%)	49.32		52.06		50.23
Al_2O_3	25.35		22.31		26.56
TiO_2	1.33		1.23		1.17
MnO	0.09		0.07		0.12
Fe_2O_3 total	7.83		9.23		8.83
MgO	2.17		3.18		2.48
CaO	9.65		6.48		4.77
Na_2O	3.43		4.69		3.63
K_2O	0.37		0.68		1.15
P_2O_5	0.14		0.25		0.29
LOI	0.71		0.27		1.29
Total	100.48		100.69		100.64
Rb (ppm)	7.94	11.39	19.2	17.79	31.38
Sr	415.6	412.2	619.7	481.9	504.5
Y	6.46	10.29	27.23	9.96	38.19
Zr	27.5	34.6	87.6	46.8	40.1
Nb	5.33	5.7	15.52	1.97	16.99
Mo	0.3	0.29	1.52	0.28	0.77
Cd	0.04	0.03	0.05	0.04	0.07
In	0.02	0.02	0.03	0.02	0.01
Sn	0.73	0.56	0.84	0.89	0.89
Cs	0.59	0.99	1.3	1.09	2.99
Ba	147	181	782	155	503
La	7.31	13.9	42.35	11.31	47.42
Ce	13.67	27.56	87.79	21.37	98.03
Pr	1.62	3.25	10.06	2.52	11.5
Nd	6.39	12.81	38.08	9.76	43.65
Sm	1.27	2.51	7.21	1.88	8.53
Eu	0.99	1.22	2.11	0.9	2.02
Gd	1.32	2.52	6.88	1.96	8.21
Tb	0.19	0.34	0.93	0.28	1.15
Dy	1.08	1.88	5.02	1.68	6.4
Ho	0.23	0.37	0.96	0.35	1.27
Er	0.64	0.99	2.61	0.98	3.43
Tm	0.1	0.14	0.37	0.15	0.48
Yb	0.66	0.92	2.24	0.97	2.78
Lu	0.1	0.14	0.32	0.15	0.4
Hf	0.93	1.07	2.67	1.47	1.59
Ta	0.5	0.41	0.87	0.16	1.09
Tl	0.32	0.1	0.14	0.12	0.31
Pb	5.34	4.57	10.36	4.15	19.17
Th	0.91	2.29	16.76	2.13	17.05
U	0.22	0.35	2.62	0.52	2.8
Sc	11.0	12.6	22.5	12.0	20.4
V	289	202	195	231	211
Cr	91.7	55.1	61.6	61.1	81.7
Co	21.3	21.6	17.5	23.2	26.3
Ni	13.7	13.0	21.2	31.3	32.8
Cu	15.5	6.4	25.1	29.7	30.7
Zn	113	179	168	99.4	183
Ga	31.8	31.7	32.6	31.3	37.8
Eu/Eu*	2.33	1.48	0.91	1.43	0.74
$^{87}Sr/^{86}Sr$	0.705549±4	0.706155±23	0.706367±23	0.705379±23	0.708505±37
$^{143}Nd/^{144}Nd$	0.512702±9	0.512559±9	0.512558±9	0.512678±9	0.512431±10
$^{206}Pb/^{204}Pb$	18.8466±31	18.8522±16	18.8632±15	18.8318±155	18.8615±15
$^{207}Pb/^{204}Pb$	15.6322±44	15.6325±22	15.6447±22	15.6332±139	15.6468±22
$^{208}Pb/^{204}Pb$	38.7536±94	38.7546±68	38.8053±67	38.7429±363	38.8067±67
$^{207}Pb/^{206}Pb$	0.82945±12	0.82921±6	0.82938±6	0.83015±17	0.82956±6
$^{208}Pb/^{206}Pb$	2.05627±21	2.05571±24	2.05720±24	2.05732±54	2.05745±24

Major oxides in wt%, trace elements in ppm.

Table A7. Continued.

Sample	LP215X	LP233X	LP242X	LP245X	TG088X
SiO_2 (wt%)	49.82				
Al_2O_3	23.94				
TiO_2	1.06				
MnO	0.10				
Fe_2O_3 total	8.61				
MgO	2.77				
CaO	8.02				
Na_2O	3.81				
K_2O	0.73				
P_2O_5	0.23				
LOI	0.23				
Total	99.42				
Rb (ppm)	22.42	10.29	25.36	14.85	4.71
Sr	456	510.2	385.5	433.6	399.8
Y	20.9	12.32	16.15	16.57	47.67
Zr	41.2	26	92	63.6	29
Nb	13.41	12.84	6.29	9.2	4.64
Mo	0.76	0.33	2.88	0.43	0.27
Cd	0.04	0.03	0.1	0.04	0.04
In	0.02	0.02	0.04	0.02	0.03
Sn	0.81	0.51	1.63	0.99	0.71
Cs	1.01	0.59	1.28	0.79	0.54
Ba	477	812	279	286	128
La	31.83	24.16	14.38	27.49	36.97
Ce	62.35	50.87	28.24	55.34	85.69
Pr	7.38	6.03	3.49	6.45	11.57
Nd	27.97	22.8	13.94	24.64	52.1
Sm	5.4	4.2	2.89	4.57	11.45
Eu	1.5	1.73	1.22	1.28	1.92
Gd	5.22	3.77	2.99	4.35	11.87
Tb	0.71	0.46	0.45	0.57	1.63
Dy	3.84	2.31	2.8	3.09	8.95
Ho	0.74	0.44	0.59	0.6	1.72
Er	1.99	1.21	1.68	1.63	4.31
Tm	0.27	0.17	0.27	0.23	0.55
Yb	1.65	1.08	1.77	1.44	3.14
Lu	0.24	0.16	0.29	0.22	0.44
Hf	1.34	1.19	2.69	1.77	0.93
Ta	0.91	1	0.41	0.66	0.43
Tl	0.14	0.09	0.13	0.09	0.06
Pb	6.23	6.13	67.24	6.47	4.61
Th	10.77	10.81	3.01	8.45	1.22
U	1.28	0.64	0.91	0.98	0.35
Sc	17.5	13.2	22.9	12.1	23.6
V	191	165	180	174	302
Cr	68.8	52.6	45.3	65.9	115
Co	22.8	16.0	19.1	18.4	27.2
Ni	26.4	13.4	20.4	10.7	17.1
Cu	24.1	7.2	1095	11.3	7.6
Zn	164	86.6	134	144	100
Ga	36.9	34.5	19.9	29.4	26.0
Eu/Eu*	0.86	1.33	1.27	0.88	0.50
$^{87}Sr/^{86}Sr$	0.705893±23	0.706794±23	0.706845±23	0.706475±23	0.705629±23
$^{143}Nd/^{144}Nd$	0.512515±8	0.512496±9	0.512611±12	0.512528±10	0.512564±9
$^{206}Pb/^{204}Pb$	18.8513±30	18.8653±30	18.8448±16	18.8548±30	18.8339±21
$^{207}Pb/^{204}Pb$	15.6361±43	15.6405±43	15.6297±22	15.6339±43	15.6180±27
$^{208}Pb/^{204}Pb$	38.7660±92	38.7867±92	38.7537±67	38.7668±92	38.7177±80
$^{207}Pb/^{206}Pb$	0.82945±12	0.82906±12	0.82939±6	0.82918±12	0.82925±7
$^{208}Pb/^{206}Pb$	2.05641±21	2.05598±21	2.05647±24	2.05607±21	2.05575±26

Major oxides in wt%, trace elements in ppm.

Appendix 8

Electron probe microanalysis (EPMA) data

A8.1. INTRODUCTION AND DATA QUALITY

This appendix presents electron probe microanalysis (EPMA) data for melt inclusions in orthopyroxene crystals, interstitial glasses in metasedimentary xenoliths and interstitial glasses in crystal clots. Analytical accuracy and precision were monitored with glass standards VG-A99 (Table A8.1) and VG-568 (Table A8.2). External reproducibilities for these standards is generally poor, being <5 % (2 s.d.) only for SiO_2, TiO_2, MgO and CaO. Full methods for EPMA analyses are described in Chapter 2.

Table A8.1. EPMA standard data and external reproducibility of VG-A99 (Makaopuhi Lava Lake, Hawai'i, USA: USNM 113498/1).

		Major oxide (wt%)										
B	**no.**	**SiO_2**	**TiO_2**	**Al_2O_3**	**FeO***	**MnO**	**MgO**	**CaO**	**Na_2O**	**K_2O**	**P_2O_5**	**Total**
1	1	49.62	3.91	11.93	13.40	0.26	4.70	9.16	3.52	0.79	0.38	97.66
1	2	49.70	3.92	12.04	14.30	0.22	4.63	9.15	3.44	0.91	0.54	98.83
2	1	50.04	3.96	12.03	13.59	0.30	4.79	9.17	2.59	0.75	0.26	97.48
2	2	50.00	4.04	11.72	13.23	0.26	4.88	9.46	2.46	0.75	0.28	97.08
2	3	50.25	4.00	11.95	13.49	0.25	4.74	8.87	2.66	0.76	0.24	97.21
2	4	50.03	4.02	11.53	13.71	0.24	4.72	9.01	2.61	0.84	0.29	97.00
2	5	49.91	3.98	11.59	12.92	0.30	4.77	9.44	2.31	0.84	0.30	96.34
2	6	49.92	4.03	11.64	13.02	0.27	4.68	9.18	2.69	0.75	0.24	96.41
2	7	50.12	3.98	11.86	13.45	0.29	4.77	9.06	2.78	0.82	0.26	97.40
2	8	49.55	3.99	11.95	13.48	0.30	4.77	9.32	2.87	0.83	0.23	97.29
3	1	49.81	4.00	12.23	13.21	0.18	4.84	8.85	2.58	0.84	0.61	97.14
3	2	49.68	4.05	12.25	13.05	0.16	4.92	9.35	2.75	0.87	0.34	97.43
3	3	50.21	4.05	12.17	13.60	0.17	4.74	9.28	2.34	0.84	0.53	97.94
3	4	49.08	3.94	12.04	12.76	0.18	4.86	9.21	2.82	0.96	0.35	96.20
3	5	48.63	4.39	9.82	14.86	0.15	5.01	9.54	2.24	0.82	0.46	95.91
3	6	49.58	4.05	11.70	12.91	0.18	4.81	9.37	3.01	0.80	0.40	96.81
3	7	49.11	4.04	11.98	12.88	0.16	4.80	9.34	2.75	0.86	0.33	96.26
3	8	49.01	4.03	12.11	12.56	0.20	4.88	8.85	2.79	0.96	0.40	95.79
Average		49.68	4.02	11.81	13.36	0.23	4.80	9.20	2.73	0.83	0.36	97.01
2 s.d.		0.89	0.20	1.05	1.08	0.10	0.18	0.41	0.66	0.12	0.22	1.50
2 s.d. (%)		1.79	4.90	8.91	8.11	46.34	3.75	4.43	24.02	14.78	61.55	1.54
Instr. cal.		51.01	4.12	12.47	13.35	0.20	5.05	9.23	2.68	0.84	0.44	99.39
Rec. values		50.94	4.06	12.49	13.49	0.15	5.08	9.30	2.66	0.82	0.38	99.39

B = batch, no. = replicate number.
Analyses were performed on 4 Oct 2019 (Batch 1), 4 Dec 2019 (Batch 2) and 5 Dec 2019 (Batch 3).
2 s.d. indicates external reproducibility.
Instr. cal. = values used for instrument calibration, which are similar to recommended values (Rec. values) of Jarosewich et al. (1980).

Table A8.2. EPMA standard data and external reproducibility of VG-568 (Yellowstone National Park, USA: USNM 72854).

		Major oxide (wt%)										
B	**no.**	**SiO_2**	**TiO_2**	**Al_2O_3**	**FeO***	**MnO**	**MgO**	**CaO**	**Na_2O**	**K_2O**	**P_2O_5**	**Total**
1	1	76.80	0.09	12.13	0.98	0.05	0.03	0.42	3.91	5.21		99.62
1	2	76.61	0.06	12.33	1.39	0.01	0.04	0.43	3.87	5.16		99.91
1	3	76.02	0.09	11.84	1.28	0.05	0.05	0.46	4.33	5.14		99.27
1	4	76.73	0.08	11.98	1.34	0.06	0.02	0.41	4.83	5.21		100.66
1	5	76.60	0.07	12.47	1.00	0.04	0.02	0.39	4.44	5.22		100.25
1	6	76.59	0.06	12.35	1.19	0.03	0.03	0.38	4.26	5.34		100.22
1	7	75.87	0.06	12.28	1.21	0.02	0.03	0.46	4.80	5.04		99.78
2	1	76.76	0.07	12.12	0.92	0.01	0.03	0.42	3.38	4.65		98.36
2	2	76.97	0.09	12.21	0.88	0.02	0.02	0.43	3.26	4.62		98.50
2	3	76.90	0.08	11.72	1.20	0.06	0.05	0.42	3.49	5.12		99.04
2	4	77.33	0.06	11.45	1.19	0.04	0.02	0.49	3.92	4.72		99.21
2	5	77.24	0.05	11.71	1.00	0.05	0.04	0.45	3.79	4.89		99.23
2	6	77.03	0.09	11.68	1.15	0.07	0.04	0.45	3.43	4.71		98.64
2	7	77.49	0.06	11.68	1.12	0.00	0.02	0.43	3.52	5.02		99.34
2	8	75.59	0.06	11.97	1.05	0.04	0.04	0.45	3.64	4.95		97.77
3	1	76.53	0.06	12.27	0.87	0.02	0.04	0.49	3.98	4.99		99.24
3	2	76.40	0.07	12.19	1.11	0.03	0.03	0.46	3.72	5.02		99.03
3	3	77.22	0.06	12.26	0.91	0.03	0.02	0.42	3.76	5.16		99.83
3	4	76.68	0.08	12.03	1.29	0.00	0.03	0.44	3.69	5.56		99.80
3	5	75.83	0.05	12.19	0.99	0.03	0.02	0.45	4.17	4.92		98.65
3	6	76.06	0.05	11.92	1.04	0.01	0.04	0.42	3.81	5.03		98.40
3	7	76.03	0.06	12.12	0.89	0.01	0.03	0.42	3.87	5.19		98.63
Average		76.60	0.07	12.04	1.09	0.03	0.03	0.44	3.90	5.04		99.24
2 s.d.		1.02	0.02	0.52	0.31	0.04	0.02	0.05	0.83	0.45		1.41
2 s.d. (%)		1.34	36.36	4.35	28.10	127.53	61.71	12.53	21.18	8.94		1.42
Instr. cal.		76.96	0.08	12.17	1.08	0.02	0.03	0.45	3.52	4.93		99.24
Rec. values		76.71	0.12	12.06	1.28	0.03	<0.1	0.50	3.75	4.89	<0.01	99.56

B = batch, no. = replicate number.

Analyses were performed on 4 Oct 2019 (Batch 1), 4 Dec 2019 (Batch 2) and 5 Dec 2019 (Batch 3).

2 s.d. indicates external reproducibility.

Instr. cal. = values used for instrument calibration, which are similar to recommended values (Rec. values) of Jarosewich et al. (1980).

P_2O_5 was not analysed.

Table A8.3. EPMA analyses of non-homogenised silicate melt inclusions in Tongariro (and Ruapehu: LP007) eruptives.

				Major oxide (wt%)										
S	**H**	**B**	**MI**	**SiO_2**	**TiO_2**	**Al_2O_3**	**FeO***	**MnO**	**MgO**	**CaO**	**Na_2O**	**K_2O**	**P_2O_5**	**Total**
LP007		1	1	69.88	0.79	15.10	2.06	0.05	0.14	1.99	4.14	4.55	0.22	98.92
		1	2	70.63	0.59	15.09	1.51	0.05	0.13	1.88	4.71	4.29	0.20	99.08
		1	3	70.27	0.68	14.83	2.00	0.03	0.14	1.78	3.97	4.54	0.21	98.46
		1	4	70.19	0.53	14.95	1.90	0.06	0.13	1.89	4.02	4.43	0.18	98.28
		1	5	69.88	0.75	15.04	1.53		0.15	2.01	4.95	4.48	0.28	99.06
		1	6	70.14	0.72	14.70	2.10	0.04	0.14	1.87	4.49	4.53	0.19	98.92
		1	7	70.61	0.62	14.71	1.71	0.03	0.15	1.91	5.09	4.49	0.19	99.51
		1	8	70.03	0.57	15.07	1.89	0.07	0.41	1.64	5.18	4.89	0.31	100.05
	opx3	1	9	70.17	0.52	13.79	1.82		0.13	1.43	4.63	5.11	0.03	97.62
LP011		1	1	69.13	0.45	16.20	1.50	0.04	0.10	3.03	5.49	2.41	0.03	98.37
	opx1	1	3	67.73	0.36	16.55	1.65	0.06	0.12	3.23	5.25	2.68	0.18	97.81
		1	2	71.52	0.31	14.50	1.27	0.08	0.11	2.13	3.83	4.81	0.27	98.82
		1	3	65.97	0.56	13.57	5.89	0.06	1.05	2.12	4.79	2.67	0.13	96.80
		1	4	68.03	0.33	16.68	1.16	0.03	0.12	1.67	5.38	5.54	0.20	99.12
		1	5	69.97	0.32	14.30	1.87	0.08	0.34	2.71	3.89	4.53	0.07	98.06
		1	7	72.74	0.28	14.15	1.64	0.04	0.12	2.27	5.24	2.75	0.09	99.31
	opx2	1	9	71.97	0.26	14.49	1.25	0.02	0.15	2.62	5.97	2.56	0.07	99.36
LP140		1	8	70.51	0.25	13.35	1.02		0.02	1.05	2.87	5.38		94.44
	opx1	1	9	74.23	0.18	12.86	0.66	0.06	0.17	2.51	4.77	2.60		98.05
		1	1	66.90	0.06	17.75	0.78	0.03		4.77	4.26	3.80		98.34
		1	4	62.67	0.73	13.89	5.94	0.07	1.27	2.20	4.80	2.55	0.17	94.28
	opx2	1	5	67.10	0.02	17.16	0.95		0.01	0.21	4.46	10.49		100.41
LP058		2	1	71.49	0.93	12.05	1.88	0.01	0.17	0.62	3.11	6.19	0.08	96.54
		2	3	71.35	0.81	11.65	2.43	0.06	0.17	0.71	2.85	5.38	0.22	95.63
		2	4	71.52	0.73	12.01	2.61		0.19	0.98	3.39	4.73	0.02	96.16
		2	5	70.53	0.80	11.87	2.38		0.35	0.68	2.61	5.58	0.15	94.94
	CC1	2	6	69.55	0.86	12.31	3.09	0.06	0.32	1.13	3.41	4.76	0.07	95.55
LP064		2	1	61.26	0.40	17.55	5.92	0.22	0.50	3.06	5.85	1.99	1.66	98.40
		2	2	60.76	0.38	17.60	4.88	0.13	0.40	3.44	5.51	2.01	1.63	96.74
		2	3	61.07	0.40	17.70	3.51	0.12	0.58	3.24	5.80	2.03	1.72	96.16
		2	4	60.17	0.37	17.45	5.79	0.25	0.97	3.17	5.95	1.91	1.66	97.67
		2	5	62.36	0.43	16.65	3.92	0.21	0.84	2.94	4.83	2.61	1.15	95.94
		2	6	66.90	0.68	14.66	5.03	0.15	0.43	4.25	3.84	0.97	0.19	97.08
		2	7	68.24	0.60	14.87	4.08	0.15	0.36	4.52	4.00	0.84	0.09	97.75
		2	8	67.11	0.73	15.39	4.28	0.10	0.44	4.23	4.21	1.64	0.11	98.24
		2	11	67.28	0.65	14.30	4.40	0.13	0.38	3.61	3.95	2.21		96.91
		2	14	69.01	0.59	15.43	3.33	0.10	0.24	3.84	4.04	1.96	0.07	98.60
		2	15	70.83	0.64	15.34	3.74	0.08	0.23	3.54	4.08	1.18	0.06	99.71
		2	16	66.33	0.61	15.03	5.04	0.12	0.37	3.48	4.52	1.33	0.01	96.84
	MS1	2	17	68.51	0.58	15.60	2.15	0.08	0.05	2.42	4.49	4.07	0.13	98.08

S = sample, H = host material (opx = orthopyroxene phenocryst, CC = crystal clot [interstitial melt between crystals], MS = metasedimentary xenolith, ol = olivine) MI = melt inclusion, B = batch.
Tongariro samples: LP011 (Te Rurunga Member [**atr**]), LP140 (Waitakatorua Member [**awu**]), LP058 (Te Porere Member [**dtp**]), LP064 (Rangitaupahi Member [**ari**]), LP032 (Otamangakau Member [**aok**]), LP096 (Pukeonake Formation [**PN**]).
Ruapehu sample: LP007 (this is the voluminous lava—probably from Ruapehu's Mangawhero Formation—in the Tongariro River, discussed in section 3.5.7).

Table A8.3. Continued.

S	H	B	MI	Major oxide (wt%)										
				SiO_2	TiO_2	Al_2O_3	FeO*	MnO	MgO	CaO	Na_2O	K_2O	P_2O_5	Total
LP064			18	66.31	0.60	14.83	4.92	0.09	0.33	3.59	4.14	2.04	0.05	96.90
		2	19	69.13	0.59	14.86	2.66	0.09	0.12	3.15	4.00	2.78	0.03	97.42
		2	20	66.86	0.58	14.59	4.58	0.12	0.30	3.65	3.82	2.25		96.75
		2	21	66.41	0.61	14.86	5.43	0.12	0.44	3.58	3.91	2.06	0.06	97.47
	MS1	2	22	66.60	0.59	15.16	4.47	0.06	0.57	4.03	4.70	1.10	0.05	97.33
LP032		2	1	67.46	0.99	10.99	6.04	0.06	1.09	1.70	2.74	4.68	0.17	95.91
		3	2	66.33	0.93	11.36	7.00	0.07	1.06	2.27	3.00	3.81	0.37	96.19
		3	3	66.51	1.16	10.15	6.89	0.15	1.51	1.68	2.45	4.84	0.28	95.61
		3	4	66.56	1.23	10.09	6.45	0.09	1.44	1.56	2.52	4.84	0.30	95.07
		3	5	65.58	1.17	10.07	8.16	0.15	1.51	1.88	2.12	4.50	0.41	95.54
		3	6	64.99	1.12	13.05	6.46	0.14	1.26	4.11	3.70	2.49	0.02	97.34
		3	7	67.04	0.80	13.69	5.04	0.03	0.82	3.78	3.77	2.73	0.07	97.77
		3	8	65.97	1.37	9.65	8.24	0.12	1.63	2.02	2.36	4.42	0.38	96.18
		3	9	65.31	0.79	15.76	3.63	0.07	0.54	4.32	3.98	2.49	0.14	97.02
		3	10	67.62	1.14	11.05	5.88	0.09	1.07	1.89	3.14	4.28	0.31	96.45
		3	11	66.45	1.22	11.39	6.53	0.11	1.07	2.04	3.24	3.61	0.08	95.75
		3	12	67.41	1.01	13.63	5.20	0.07	0.94	3.45	3.64	3.08	0.03	98.44
		3	13	67.06	1.12	10.23	6.26	0.10	1.45	1.64	2.58	5.16	0.10	95.67
		3	14	65.10	0.89	13.07	6.48	0.10	1.21	3.54	3.89	3.19	0.03	97.49
		3	15	66.02	0.64	16.39	2.16	0.04	0.26	4.00	4.13	2.94	0.10	96.68
		3	16	66.48	1.11	11.73	7.08	0.10	1.39	2.73	3.05	3.48	0.08	97.23
		3	17	64.66	0.85	13.62	5.70	0.10	1.08	3.64	3.60	2.85	0.04	96.14
		3	18	64.07	1.14	10.08	8.21	0.14	1.68	2.41	2.35	4.30	0.22	94.59
		3	19	64.88	1.10	10.18	8.22	0.14	1.61	2.41	2.55	4.66	0.27	96.02
	MS1	3	20	65.05	1.14	10.12	7.78	0.16	1.65	1.95	2.37	4.47	0.20	94.89
LP096		3	1	62.36	2.44	15.97	1.31	0.04	1.37	5.43	5.13	2.59	0.66	97.30
		3	2	62.66	2.67	15.66	1.45	0.00	1.49	5.54	4.55	2.68	0.88	97.58
		3	3	64.91	1.99	16.74	0.80		0.60	4.95	5.44	1.82	0.50	97.75
		3	7	63.87	2.47	13.17	0.89	0.02	0.96	3.81	2.88	6.20	0.63	94.89
		3	9	62.02	2.20	17.46	0.78		0.82	5.58	3.92	5.25	0.37	98.40
		3	10	65.25	2.15	16.35	0.74	0.00	0.46	3.69	3.85	6.13	0.46	99.08
		3	11	64.85	3.36	13.80	1.23	0.04	0.98	4.55	3.99	2.90	0.70	96.41
		3	12	65.55	1.88	14.37	0.94		0.76	4.98	3.57	4.01	0.36	96.41
		3	13	60.16	2.04	15.83	0.87	0.01	0.33	1.03	3.68	6.67	0.46	91.09
		3	15	62.89	1.21	17.55	0.64		0.46	5.54	4.12	3.63	0.48	96.52
		3	16	63.25	0.59	16.72	0.79	0.01	0.33	4.87	4.43	3.51	0.29	94.78
		3	18	64.01	2.22	13.29	1.03	0.03	0.96	2.97	3.42	6.09	0.42	94.42
		3	19	64.34	2.36	14.05	0.76	0.05	1.22	0.94	3.95	6.91	0.31	94.88
		3	20	65.06	2.22	14.03	1.02		0.91	0.90	4.27	6.82	0.54	95.77
	ol1	3	21	62.21	2.40	18.12	0.64	0.02	0.95	5.83	4.54	2.99	0.20	97.89

A8.2. EPMA ANALYSIS LOCATIONS

This subsection is a compilation of EPMA analysis locations for glassy melt inclusion in crystals, interstitial melts in crystal clots and patches of glass in partially-fused metasedimentary xenoliths.

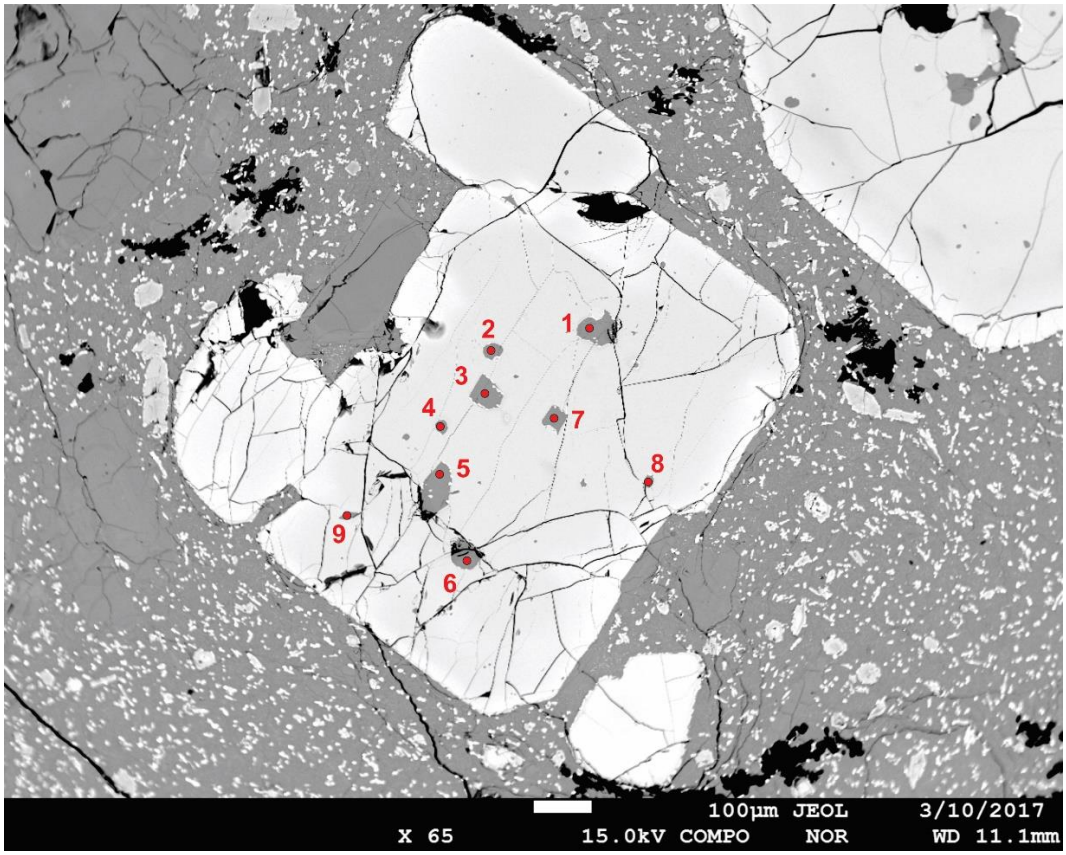

Figure A8.1. LP007 opx3 analysis locations corresponding to Table A8.3.

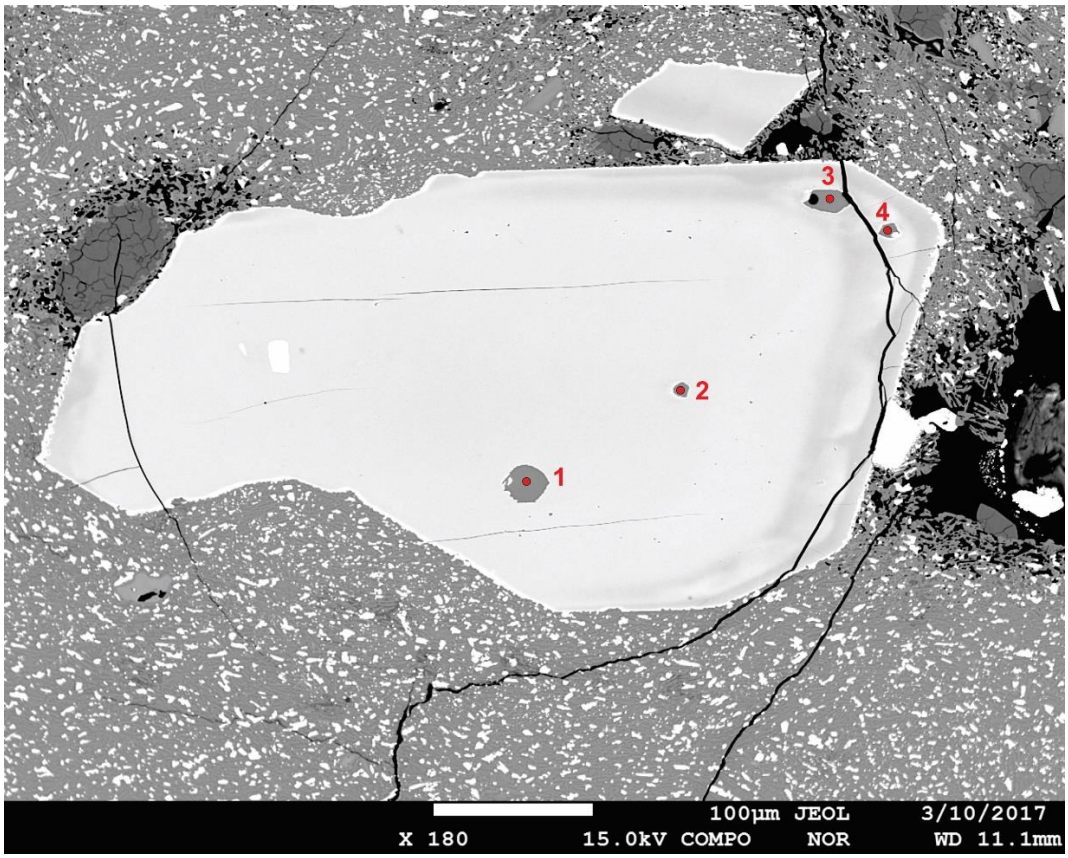

Figure A8.2. LP011 opx1 analysis locations corresponding to Table A8.3.

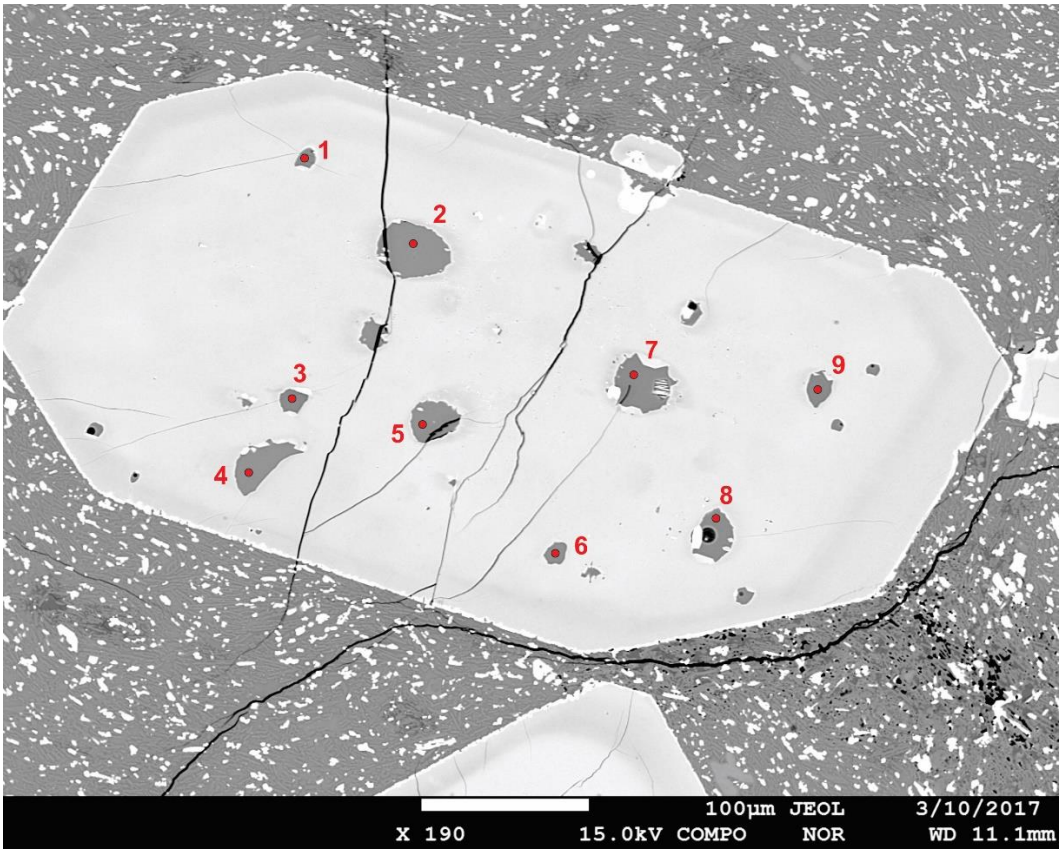

Figure A8.3. LP011 opx2 analysis locations corresponding to Table A8.3.

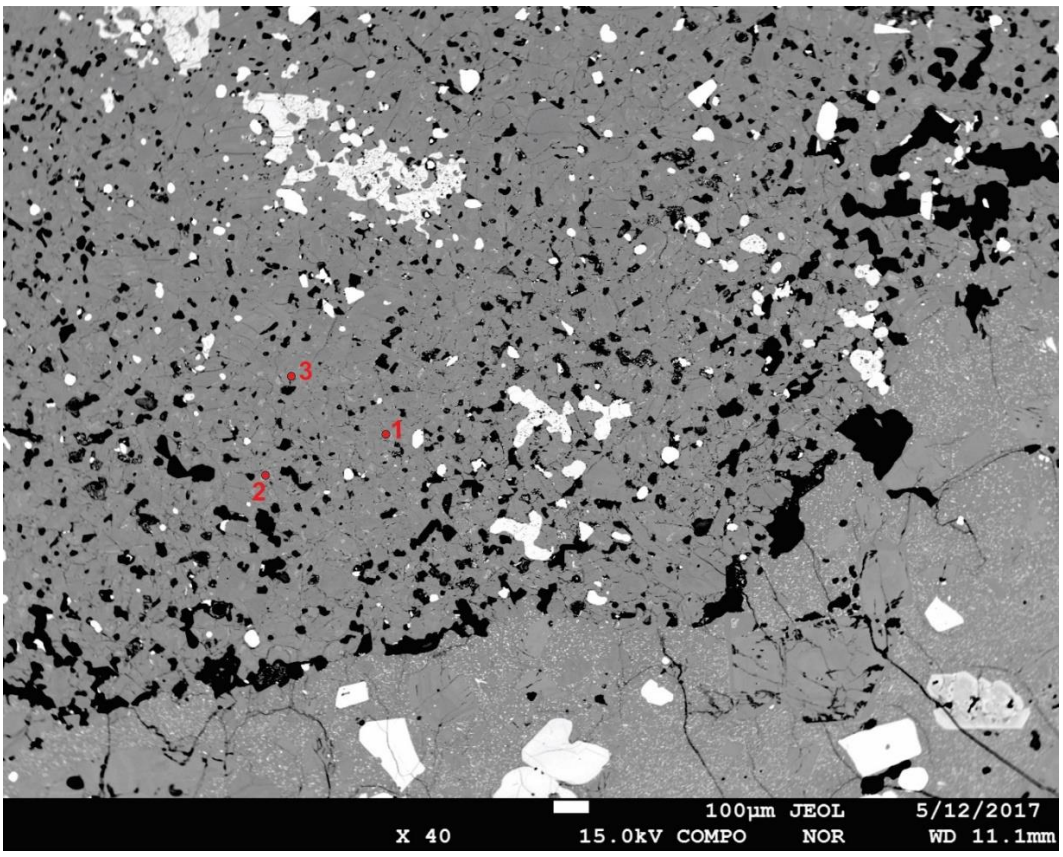

Figure A8.4. LP032 glass analyses within MS1 for locations 1-3, corresponding to Table A8.3.

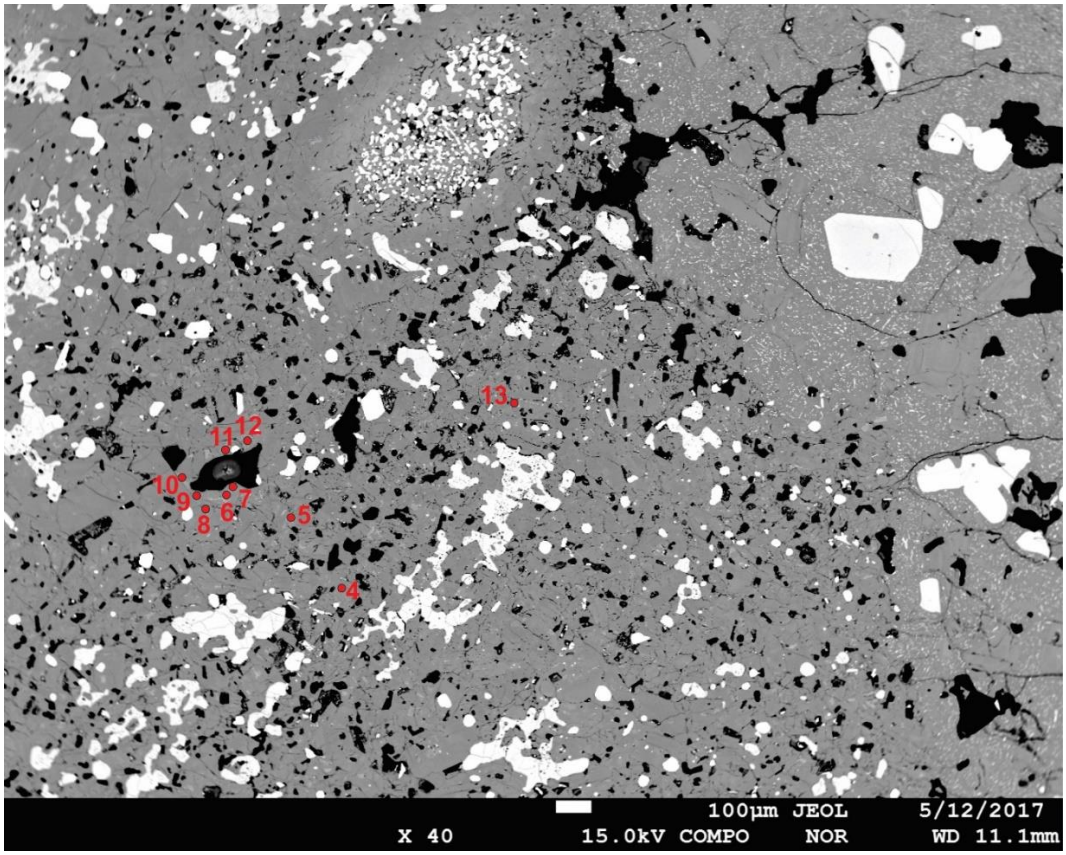

Figure A8.5. LP032 glass analyses within MS1 for locations 4-13, corresponding to Table A8.3.

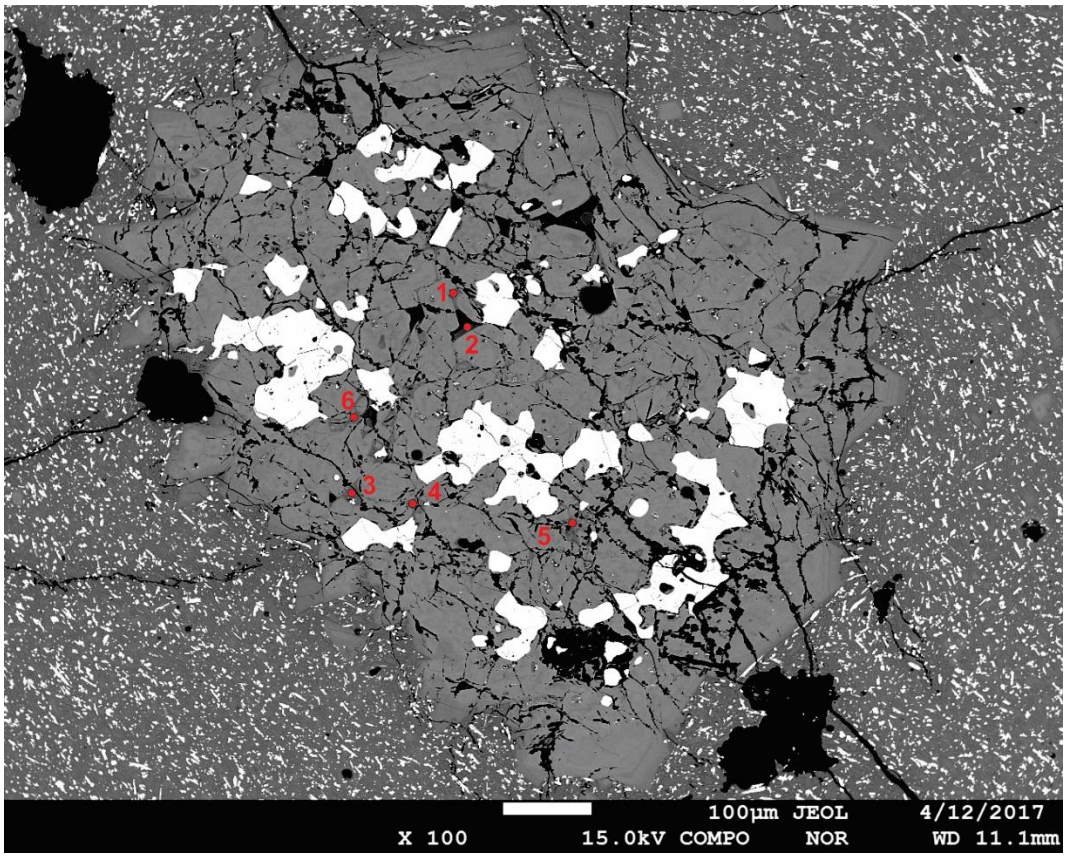

Figure A8.6. LP058 CC1 analysis locations corresponding to Table A8.3.

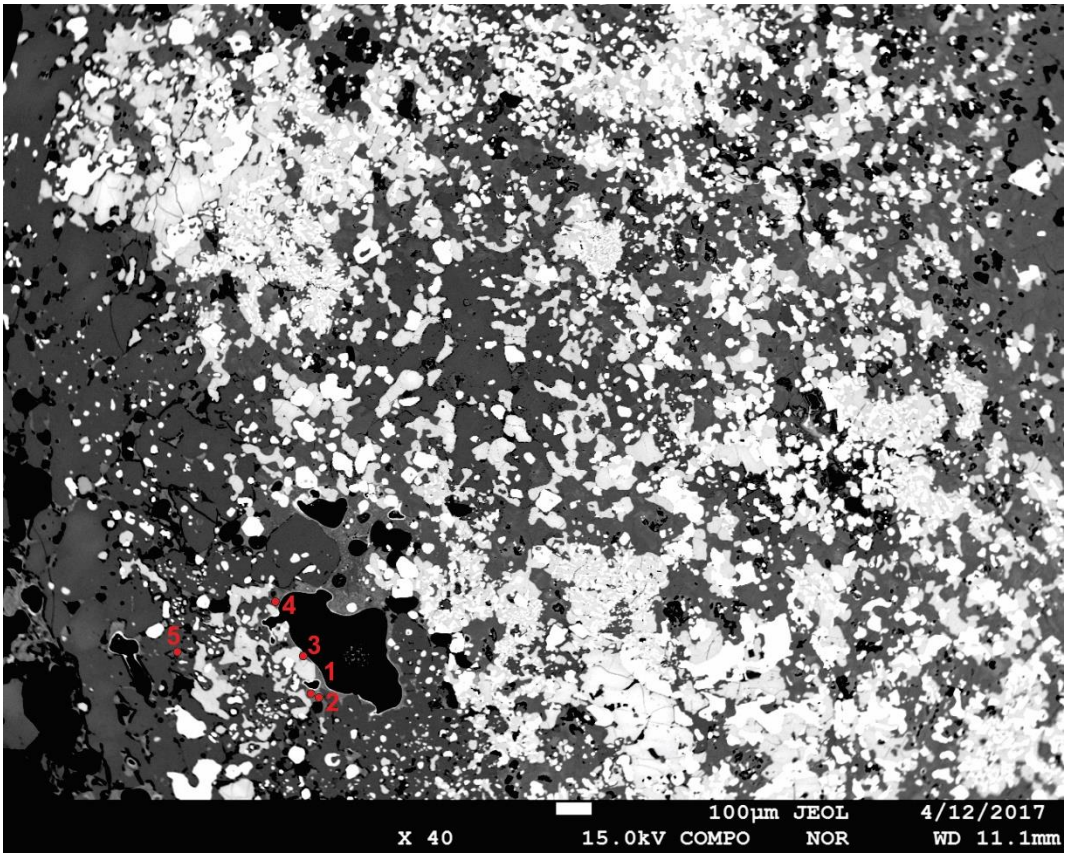

Figure A8.7. LP064 MS1 analysis locations corresponding to Table A8.3.

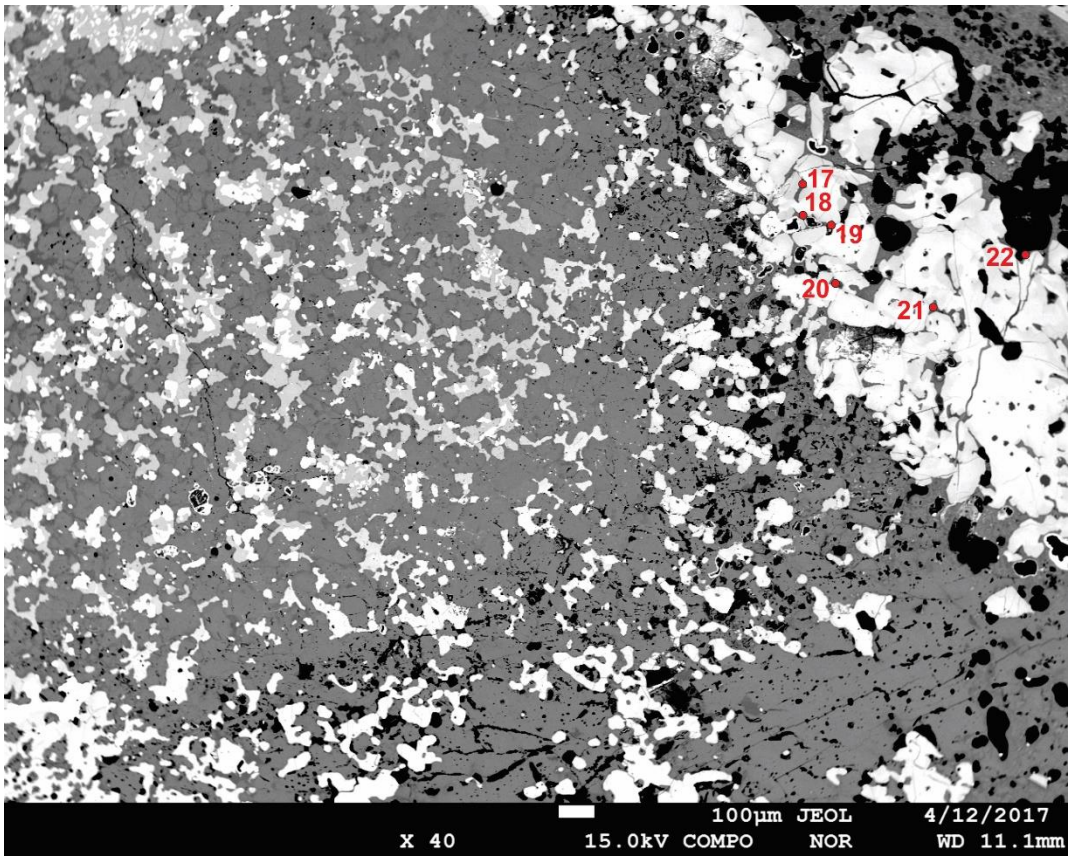

Figure A8.8. LP064 MS1 analysis locations corresponding to Table A8.3.

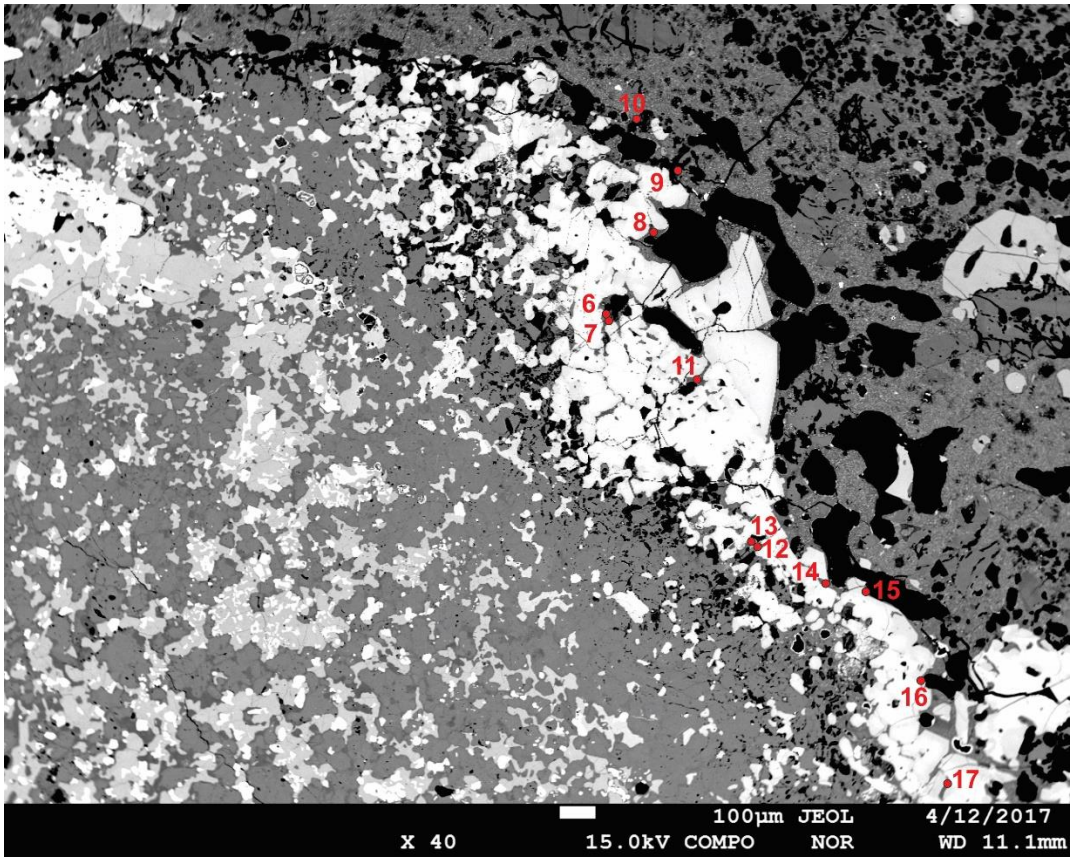

Figure A8.9. LP064 MS1 analysis locations corresponding to Table A8.3.

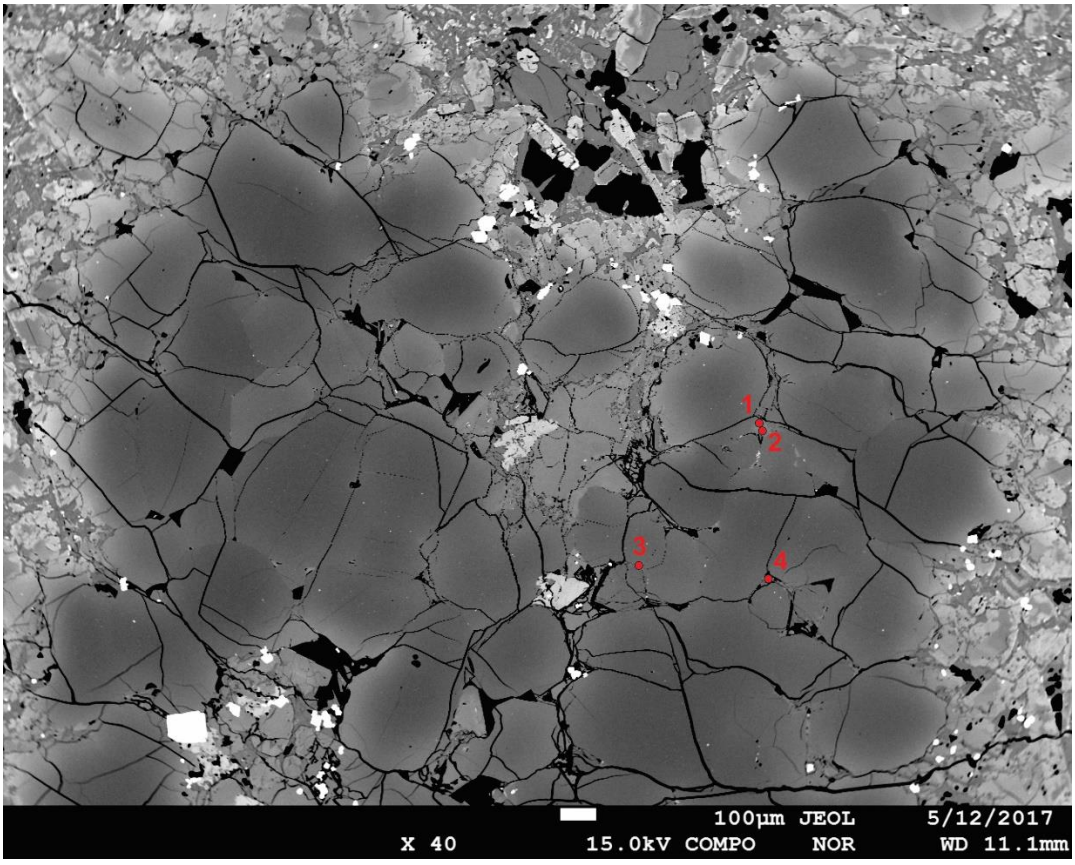

Figure A8.10. LP096 ol1 analysis locations corresponding to Table A8.3.

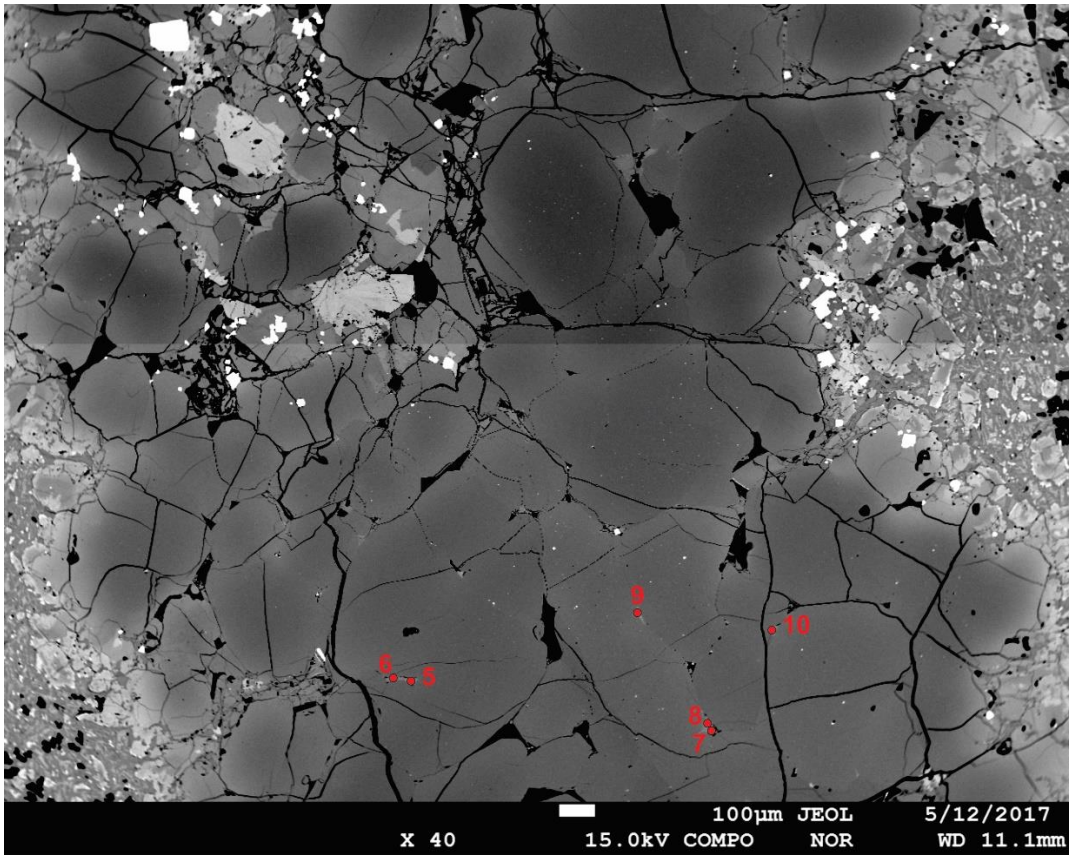

Figure A8.11. LP096 ol1 analysis locations corresponding to Table A8.3.

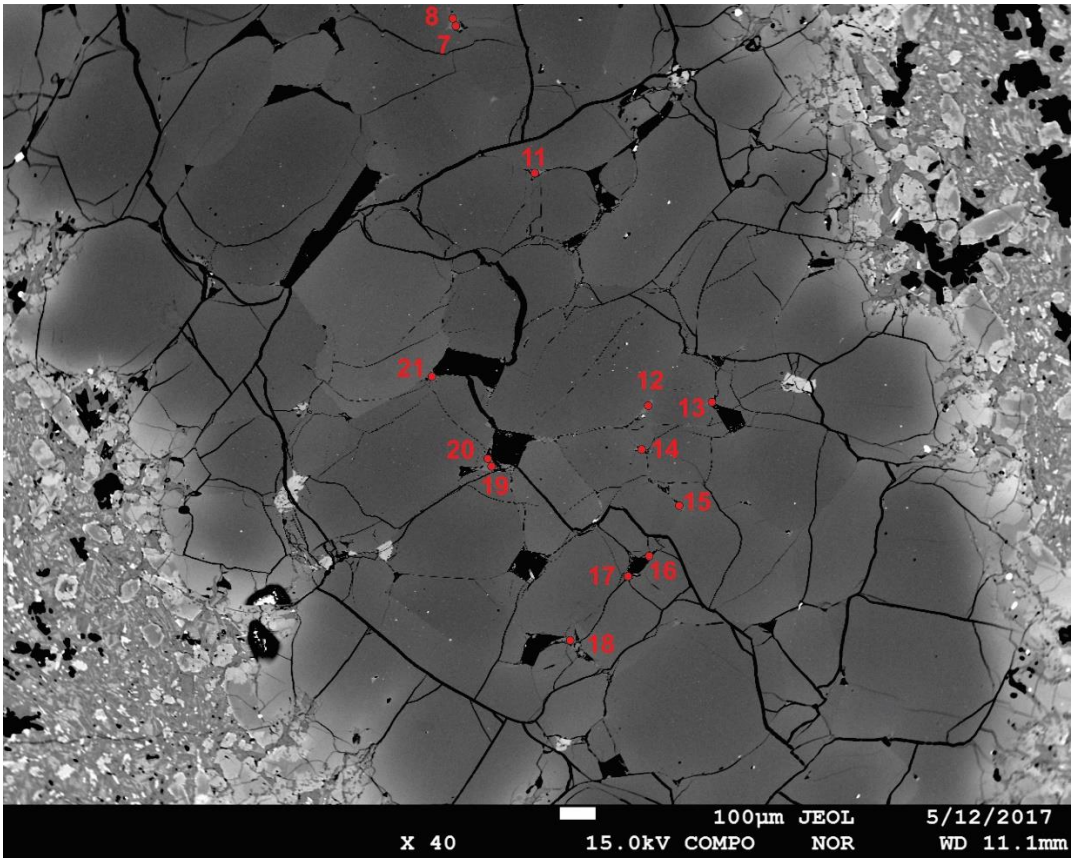

Figure A8.12. LP096 ol1 analysis locations corresponding to Table A8.3.

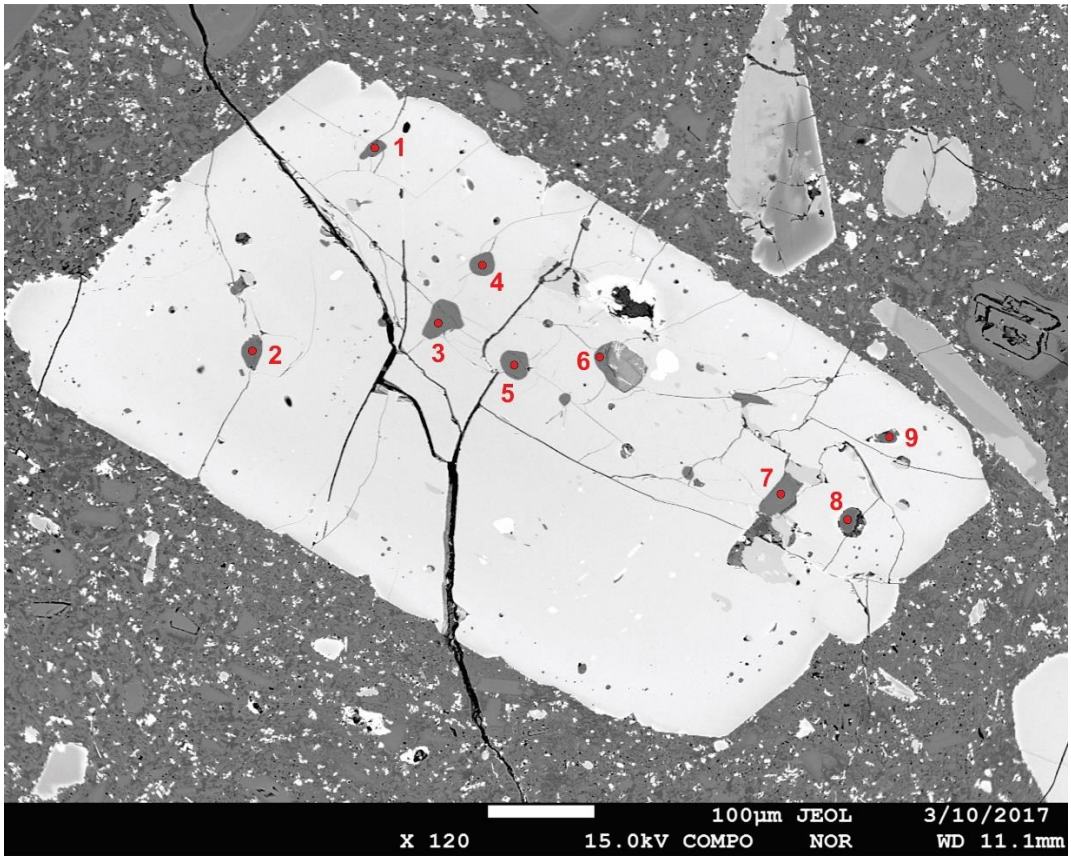

Figure A8.13. LP140 opx1 analysis locations corresponding to Table A8.3.

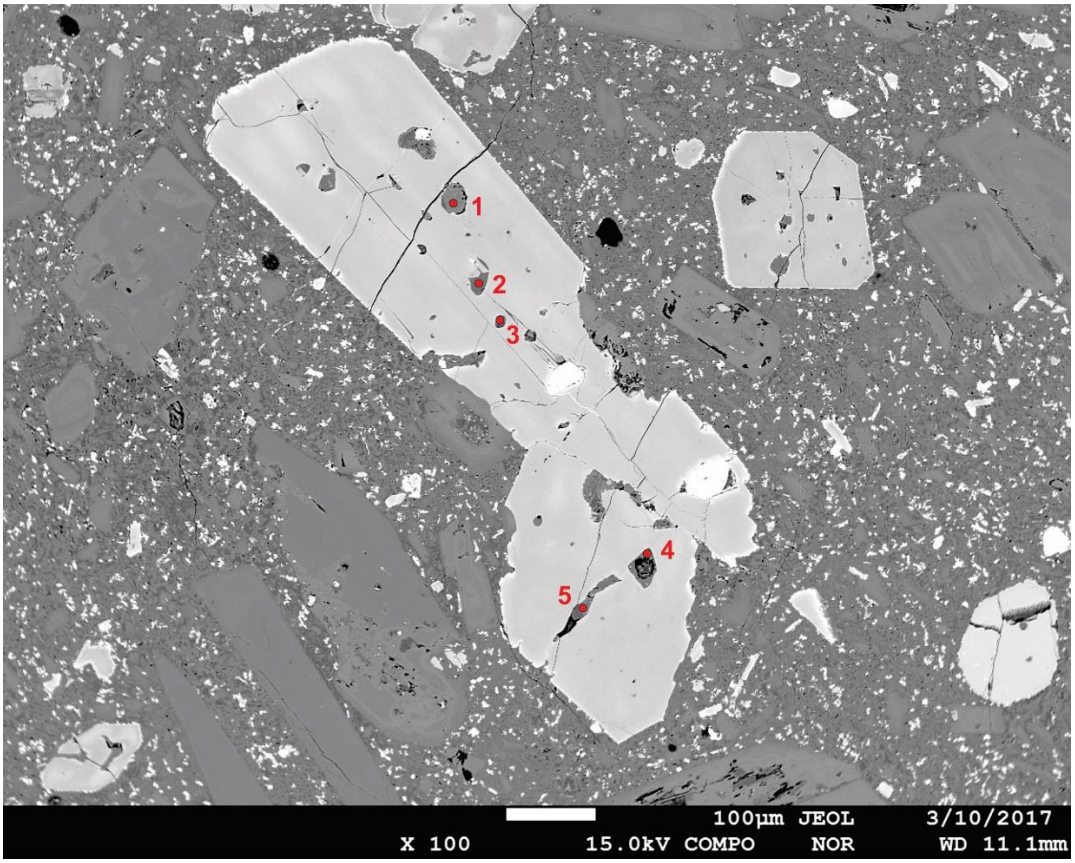

Figure A8.14. LP140 opx2 analysis locations corresponding to Table A8.3